PLASMA INTERACTIONS IN TITAN'S IONOSPHERE

by

Matthew Scott Richard

Submitted to the graduate degree program in Physics and Astronomy
and the Graduate Faculty of the University of Kansas in partial fulfillment of
the requirements for the degree of Doctor of Philosophy.

_____

Chairperson Professor Thomas Cravens

_____

Professor Philip Baringer

_____

Professor Barbara Anthony-Twarog

_____

Professor Gregory Rudnick

_____

Professor Peter Hierl

Date Defended: January 24, 2013

The Dissertation Committee for Matthew Scott Richard

certifies that this is the approved version of the following dissertation:

PLASMA INTERACTIONS IN TITAN'S IONOSPHERE

_____

Chairperson Professor Thomas Cravens

Date approved: January 31, 2013

Abstract

The Cassini mission has collected vast amounts of *in situ* data within the ionosphere of Saturn's moon Titan and has shown the complexity of the interaction of Saturn's magnetospheric plasma with Titan. Models of the interactions have been created; however, none have been able to completely describe the observed phenomena. Most notably, modeled electron densities are much larger than the electron densities observed by instruments aboard the Cassini spacecraft. This thesis will explore the possible causes of this discrepancy between measured and modeled electron densities using models calculating the production of ions due to solar photons and magnetospheric electrons precipitating down magnetic field lines and into the ionosphere, temperature calculations of the thermal electron population (electrons with energies less than 2 eV), and chemical reactions in the ionosphere. The results of these models will be compared to data collected by instruments aboard Cassini.

Modeled ion production rates and thermal electron temperature profiles will be shown to be in good agreement with ion production rates derived from data collected by the Ion-Neutral Mass Spectrometer (INMS) and electron temperatures measured by the Radio and Plasma Wave Science – Langmuir Probe above 1000 km. Modeled ion mass spectra will be generated near the ionospheric peak and will be compared with the INMS measured mass spectra to examine the effects of chemical loss processes on the ion densities. From this analysis it will be shown that the overabundance of modeled electrons is not caused by over production of ions and that chemical loss processes, predominantly the electron dissociative recombination coefficient of $HCNH^+$, need to be reexamined.

After the model has been proven to reproduce accurate profiles of ion production and temperature, ion production profiles will be generated using solar photons and magnetospheric electron fluxes for four canonical cases detailed in the work of *Rymer et al.* [2009] and a globally averaged model of the neutral densities based on INMS neutral measurements from more than 30 flybys of Titan. These generic profiles can be combined to predict ionospheric observations made by the Cassini spacecraft for a variety of solar zenith angles and magnetospheric conditions.

Acknowledgements

I would like to thank Dr. Tom Cravens for helping me get started in this research field and providing constant guidance and support throughout my course of study. Your help and advice was always invaluable and helped me become the physicist that I am today. Thank you to Dr. Greg Rudnick, Dr. Phil Baringer, Dr. Barbara Anthony-Twarog, and Dr. Peter Hierl for serving on my defense committee.

I would like to thank my wife Meg for all of her love, support and encouragement throughout this process. There isn't enough space here to thank you for all you have done and tell you how much I appreciate you. All.

Thank you to my parents, Bob and Judy Richard, for all of your support over the years.

I would like to say thank you to Ina Robertson, whose expertise with previous versions of the model allowed me to build upon a firm foundation of research. Thank you to Tizby Hunt-Ward for reading and editing the journal submissions and poster projects that would eventually become this dissertation. I would like to acknowledge the help of Calvin Wylie and Daniel Webb who helped with the running of the model and formatting data. Their efforts helped this work immensely.

Support from the NASA Cassini Project (Grant 699081KC via subcontract from Southwest Research Institute) is acknowledged. Model development at the University of Kansas was also supported by the NASA Planetary Atmospheres Grant NNX10AB86G.

Solar Irradiance Platform historical irradiances are provided courtesy of W. Kent Tobiska and Space Environment Technologies. These historical irradiances have been developed with partial funding from the NASA UARS, TIMED, and SOHO missions.

Table of Contents

Chapter 1 Introduction and Background Information

Saturn's largest moon Titan has been an object of interest since its discovery in 1665 by Christiaan Huygens. In 1997, NASA launched the Cassini Spacecraft with the European Space Agency's Huygens probe to study Saturn and its moons, particularly Titan and Enceledus. With the arrival of Cassini into the Saturn system in late 2004, a wealth of in situ data is now available to analyze and has greatly improved our understanding of Titan's ionosphere's complex interactions within the Saturnian system. The goal of this dissertation is to present the insights that have been gained into Titan's ionospheric processes and models of the particles therein as a result of these new measurements.

In Chapter 1, background information will be presented to provide a context for this study. In order to understand the interactions within the magnetosphere of Saturn it is important to first examine the role of plasma physics; as the particles of interest in this study exist as plasma and exhibit collective behaviors. Next, an overview of magnetospheres is given to aid in explanation of the external conditions Titan will experience as it orbits in the magnetosphere of Saturn. A review of ionospheres follows, as it is important to recognize that Titan's dense ionosphere is the reason that it interacts with the Saturnian magnetospheric plasma. Next, examples are given for potential plasma interactions with objects in the solar system. Finally an overview of the literature about Titan with a description of previous works is given that will serve as the starting point for this research.

Chapters 2 and 3 set up the procedures used in constructing the models in this work. A brief overview of the instruments aboard the Cassini spacecraft is given in Chapter 2. This

includes a discussion of what the instruments are capable of measuring and how those measurements are used to parameterize and constrain model values. Experimental methodologies used in this study are described in Chapter 3. The theoretical model is composed of several codes (i.e. photoionization, two-stream electron transport, photochemical model, etc.) that are implemented in conjunction with one another to describe the processes taking place in Titan's ionosphere. Each program is elaborated upon in a separate subsection detailing the ideas governing the program's operation and the results that the program will produce.

Next, the key results of the photoionization, two-stream electron transport, energetics and photochemical modeling programs will be analyzed. Chapter 4 details how primary (ions produced through photoionization) and secondary (ions produced via electron-impact ionization) ion production rates are calculated in the programs. These modeled production rates are then compared to empirical production rates derived from in situ measurements of ion densities collected by the Cassini Ion and Neutral Mass Spectrometer (INMS). The two-stream electron transport code also generates heating rates for the thermal electron population, electrons with energies less than 2 eV. Electron and ion temperatures will be calculated for a dayside flyby of Titan (Chapter 5). After the initial production of ions through photoionization and electron-impact ionization various chemical reactions will occur between ions and neutral species that will create heavier ions. These processes and chemical modeling efforts as well as comparisons to data are described in Chapter 6. Ion production and electron temperature profiles for nightside flybys of Titan will be compared to data and then generated for generic nightside cases in Chapter 7.

Finally, in Chapter 8 the major conclusions of this work are discussed. This chapter will not only state the important finding of this research endeavor; it will also outline areas of possible interest for the future.

1.1 General Background of Plasma Physics

Plasmas are abundant in the solar system and are created when the sun ejects energetic particles (the solar wind) as well as when atmospheres, comets, and planetary neutrals become ionized (thus becoming plasma). In the treatment of Saturn's moon Titan which interacts with Saturnian magnetospheric plasma via a dense ionosphere, it is beneficial to know what will be defined as plasma in this study.

Chen [2006] defines plasma as a "quasineutral gas of charged and neutral particles which exhibits a collective behavior". Unlike a neutral gas, the "collective behavior" of a plasma is dominated by electromagnetic fields and the Lorentz force [*Chen,* 2006*; Cravens,* 1997]. There are three main conditions necessary for a charged gas to be considered plasma [*Chen,* 2006*; Cravens,* 1997]. The first condition states that the length scale of the system must be much larger than the Debye length (λ_D) given by equation (1.1) where n_e and T_e represent the electron density and electron temperature respectively, k_b stands for Boltzmann's constant, q_e represents the charge of an electron and the permittivity of free space is given by ε_0.

$$\lambda_D = \sqrt{\frac{\varepsilon_0 k_B T_e}{n_e q_e^2}} \qquad \textbf{(1.1)}$$

At the Debye length a charge is shielded so that the observed charge decreases by an e-folding, and the first condition will ensure the quasi-neutrality of the system. The second relates to the number of particles in a Debye sphere (a sphere with the radius of a Debye length) which must be much larger than one so that the charges can be shielded, again enforcing quasi-neutrality. The third condition requires the plasma oscillation frequency to be greater than the collision frequency such that the system does not behave like a neutral gas.

Cravens [1997] classified plasma interactions with different solar system objects based on the nature of the interaction. The classifications discussed are the direct result of the solar wind pressure, magnetic dipole moment of the object and the interaction of the flowing plasma with an atmosphere or ionosphere.

For an object lacking a large magnetic dipole or atmosphere, the interaction is classified as "Lunar". The magnetic field of the solar wind will pass through the object but the particles will impact the surface creating a wake behind the object. If the object has a strong magnetic dipole the magnetosphere will create an obstacle to the flow, resulting in a bow shock [Cravens, 1997; *Schrijver and Siscoe,* 2009] in what is called an "Earth-like" interaction. A "comet-like" interaction occurs when the solar wind impacts an active (one in which cometary neutrals are flowing away from the comet creating a coma) cometary nucleus. As the coma is ionized, the gravity of the comet will not hold the particles and they will be carried downstream with the solar wind, mass-loading the solar wind plasma [*Cravens et al*., 1997]. The "Venus-like" interaction is the most applicable to the environment of Titan as it has a strong source of ions. In this interaction the ionosphere serves as a good conductor and acts as an obstacle to the solar wind flow

1.2 Magnetospheres

Any object in the solar system with a strong magnetic field will impede the flow of the supermagnetosonic solar wind, as the wind must slow down in order to divert its flow around the object. The term "magnetosphere" originated in 1959 from the work of Gold [*Gold*, 1959] following the discovery of the Van Allen Belts. The term "magnetosphere" is defined as the region of space around a central object within which the object's magnetic field has a dominant influence on the dynamics of the local medium [*Cravens et al.,* 1997; *Schrijver and Siscoe,* 2009]. Mercury, Earth, Jupiter, Saturn and Uranus all have an intrinsic dipole that creates a magnetosphere that interacts with the solar wind in a non-negligible manner.

The structure of the magnetosphere is relevant to this study so that the environment of Titan can be understood as it encounters various plasma environments based on its location in the magnetosphere of Saturn. Note how the plasma sheet encircles the whole of Saturn which is in contrast to how the plasma sheet of the Earth is confined to the region downstream of the solar wind due to the strength of Saturn's magnetic field relative to the solar wind velocity near 9.5 AU. As the solar wind flows out past a few solar radii it has a velocity above the magnetosonic velocity [*Cravens,* 1997; *Schrijver and Siscoe,* 2009]. Due to this occurrence, the plasma is dominated by convection instead of magnetic diffusion and the magnetic flux becomes "frozen" into the plasma. When supermagnetosonic solar wind encounters a magnetic object, the flow of the wind must slow down and a shock develops. The magnetosheath resides between the bow shock and the magnetopause. Here the shocked solar wind plasma will slowly cool and speed up. The magnetopause is the location where the solar wind pressure is balanced by the total plasma. Plasma lobes are formed from the draping of the solar magnetic field lines which result in regions of high magnetic fields, but lower density, which balances the pressures in the plasma

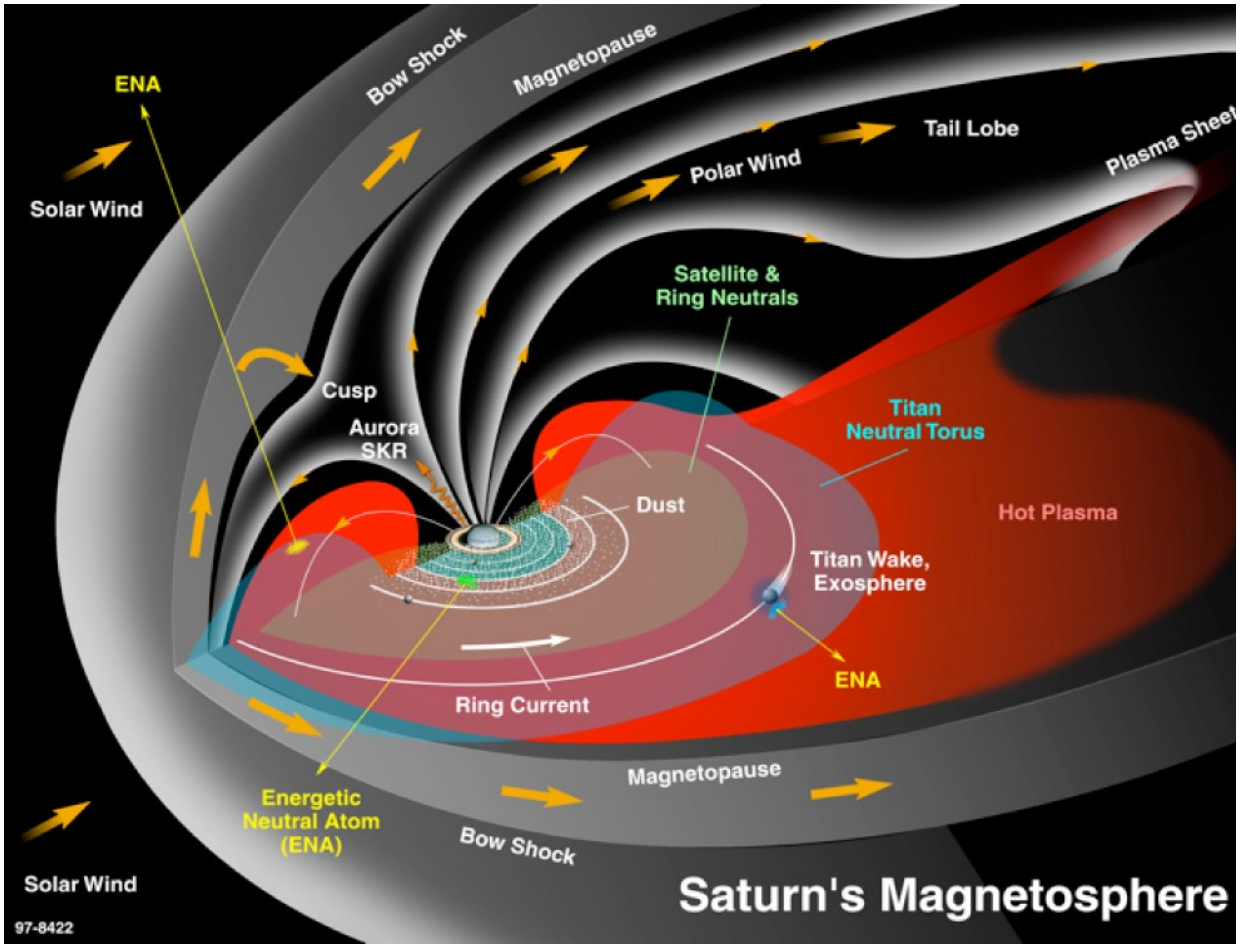

Figure 1.1: Schematic of the Magnetosphere of Saturn presented by *Krimigis et al.* [2004]

sheet (a high temperature, high density environment found in the equatorial plane of the object) [*Cravens*, 1997].

Titan orbits Saturn at 20 Saturn radii (R_s) and as a result can exist in a variety of plasma environments as a result of three main processes [*Rymer et al*., 2009 and references therein]. In the first process, the magnetosphere of Saturn (Figure 1.1) responds to the variability of the solar wind pressure by moving closer and farther away from Saturn which in turn can leave Titan outside of the magnetopause [*Arridge et al.,* 2006; *Bertucci et al.,*2008]. Another source of variability is the asymmetry of the environments on the day and night sides of Saturn [*Sergis et*

al., 2009] resulting in a thicker and more dense plasma sheet developing on the dayside of Saturn. The other main phenomenon that influences the plasma environment, though still not fully explained, is the observed periodic "flapping" in the equatorial plane of the plasma sheet of Saturn [*Carbary and Krimingis*, 1982; *Carbary et al*., 2007, *Coates et al*., 2007; *Arridge et al*., 2009]. It is possible that this flapping may be an effect of the corotation of Saturn on the organization of magnetospheric phenomena [cf. *Rymer et al.,* 2009].

Rymer et al., [2009] compared energetic electron spectra from the Cassini Plasma Science Electron Spectrograph (CAPS-EL, discussed in Section 2.1) and Magnetospheric Imaging Instrument (MIMI, see Section 2.4) to create a classification system based on the magnetospheric environment of Titan consisting of four cases (Figure 1.2). The first case ("plasma sheet") shows a relatively high peak energy (120 – 600 eV) and density ($3.5x10^5$ – $1.2x10^6$ $cm^{-2}s^{-1}sr^{-1}$) that are typical characteristics of the plasma sheet environment. The second case (lobe) is for the lobe-like environment characterized by high peak energy (150 – 820 eV), but a lower density ($5.3x10^4$ – $2.4x10^5$ $cm^{-2}s^{-1}sr^{-1}$) than the plasma sheet. The magnetosheath environment is the third classification and here Cassini observes lower energy electrons (few hundred eV) with a higher flux (~ 10^6 $cm^{-2}s^{-1}sr^{-1}$). The final case established was the bi-modal case that appeared to show two superimposed electron populations. The higher energy population peaked between 200 eV and 3.4 keV similar to the plasma sheet and lobe with fluxes between $9.0x10^4$ – $2.4x10^5$ $cm^{-2}s^{-1}sr^{-1}$ and the lower energy population (5.3 – 16.3 eV) had a peak flux of $5.7x10^5$ – $1.6x10^6$ $cm^{-2}s^{-1}sr^{-1}$. This bi-modality is thought to be caused by a lobe-like or plasma sheet environment with a local pick-up population from the neutrals [*Rymer et al.,* 2007, 2009; *Sittler et al.,* 2008; *Wilson et al.,* 2008]. Using these classifications, in conjunction with the global average model of the neutral atmosphere described in Section 3.4.2.2, it is

possible to create ion production and heating rate profiles for Titan, and its plasma environment, that more accurately reflect the varied ionospheric environment. The impacts of these cases on ion production and electron temperature are discussed in Chapter 7.

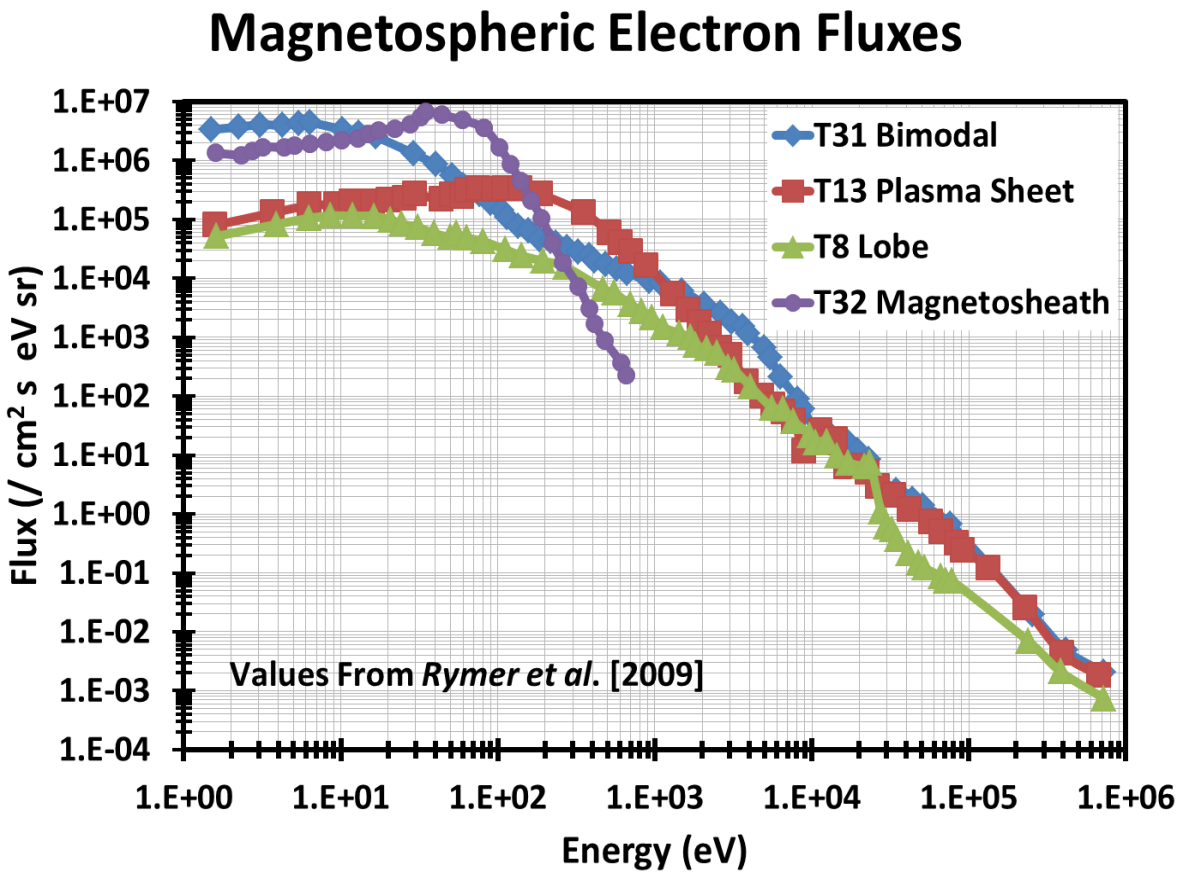

Figure 1.2 Superthermal electron fluxes plotted against energy for the four magnetospheric plasma environments presented by *Rymer et al.*, [2009]. Flybys are labeled in chronological order are Ta, Tb, Tc and then T followed by a sequential number

1.3 Neutral Atmosphere of Titan

Titan's dense neutral atmosphere is primarily composed of nitrogen (92-94%), methane (~4%), and molecular hydrogen (~1-2%), along with minor hydrocarbon and nitrile species [*Waite et al.,* 2005b, 2007; *Vuitton et al*., 2006, 2007; *Magee et al.,* 2009] (see Figure 1.3). *In situ* measurements of the ion composition were first conducted by the Ion and Neutral Mass Spectrometer (INMS) on the Cassini spacecraft on the outbound leg of the T5 flyby of Titan [*Cravens et al.,* 2006]. Flybys labeled in chronological order are Ta, Tb, Tc and then T followed by a sequential number. The temperature of the neutral atmosphere is estimated to be between 145 and 160 K (See Figure 1.4)[*Waite et al*., 2005b; *Vervack et al*., 2004; *Shemansky et al*., 2005; *De La Haye et al*., 2007].

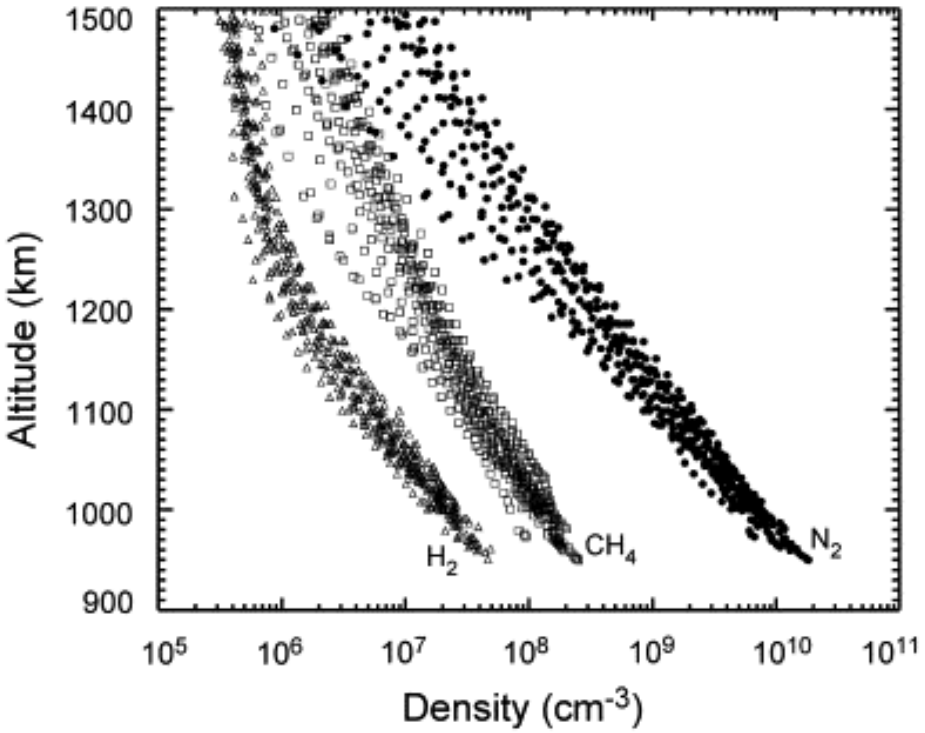

Figure 1.3 Measurements of densities in the neutral atmosphere of Titan collected by the Cassini INMS instrument from the 20 Titan encounters between TA through T40 flybys [*Magee et al*., 2009]

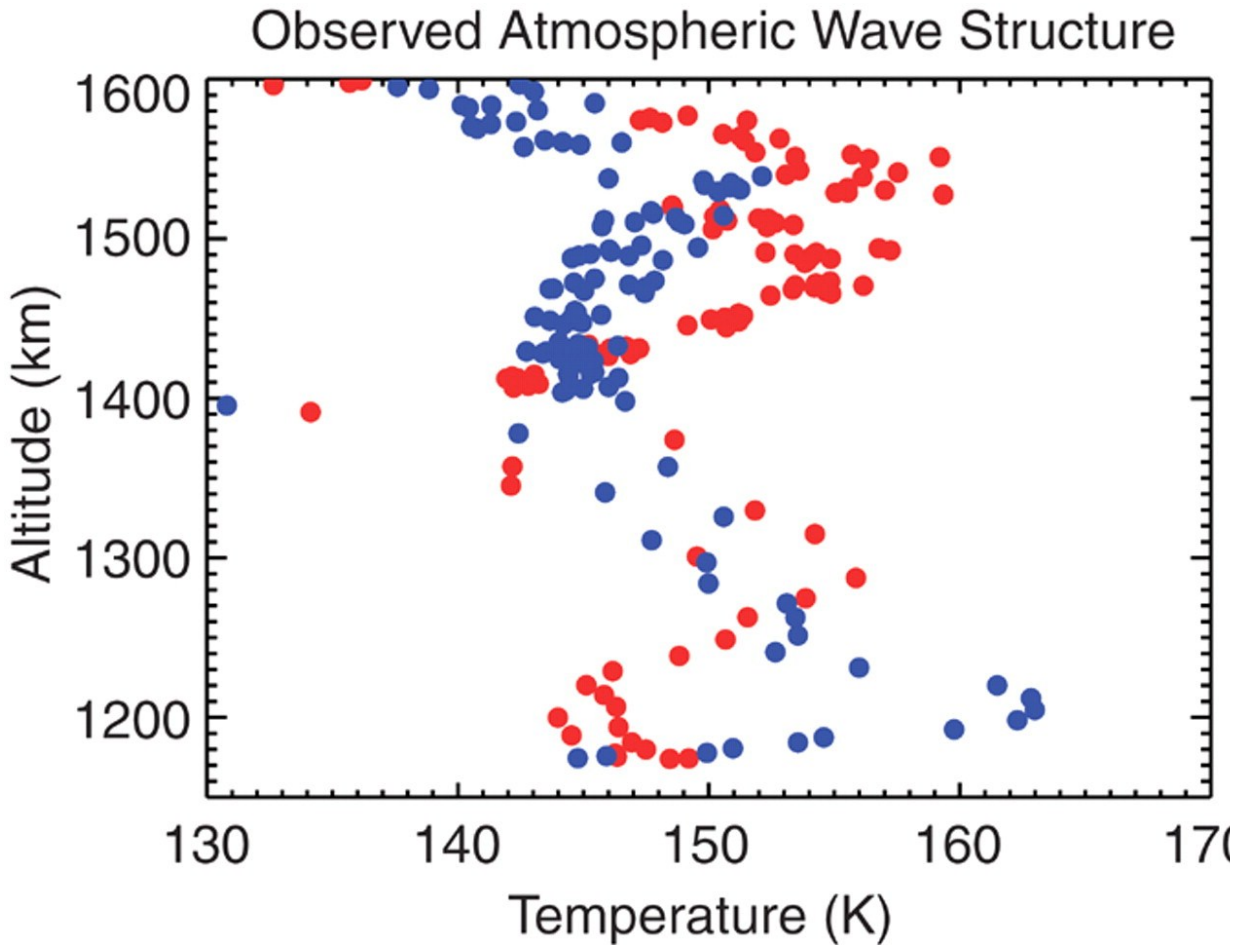

Figure 1.4 Temperature of Titan's neutral atmosphere derived from N_2 and CH_4 measurements made by INMS during TA presented by *Waite et al.,* [2005b]. Red data points were obtained during ingress while blue were obtained during egress.

The upper atmosphere of Titan, like most upper atmospheres, assumes a structure formed by hydrostatic equilibrium (see Equation (1.2)) in which the derivative of the pressure p_s of a species s with respect to the altitude z is balanced by the gravitational force represented by the number density of the species n_s multiplied by the mass of the species m_s and the acceleration due to gravity of the body g [*Schunk and Nagy,* 2009].

$$\frac{dp_s}{dz} + n_s m_s g = 0 \qquad \textbf{(1.2)}$$

Integration of the above equation for an isothermal atmosphere gives the solution

$$p_s = p_{s0} e^{-\frac{z}{H}} \qquad \textbf{(1.3)}$$

where p_{s0} represents the pressure at a reference altitude and H is the atmospheric scale height. This scale height of a neutral species s can be calculated as a function of the temperature T_s and

$$H = \frac{k_B T_s}{m_s g} \qquad \textbf{(1.4)}$$

mass m_s, as shown in Equation (1.4) which yields information about the vertical scale as a function of hydrostatic balance [*Cravens,* 1997; *Schunk and Nagy,* 2000]. In this equation H is the scale height, k is Boltzmann's constant, T and m are the temperature and mass of a member of the species respectively and g is the acceleration due to gravity that a particle will experience. Equation (1.4) is only valid for altitudes above the homopause where individual atoms are separated by their mass due to diffusive equilibrium. Below the homopause, turbulence will mix the various species within the atmosphere into a homogeneous mixture [*Schunk and Nagy,* 2009]. This scale height represents the altitude range at which the density of a species decreases by a factor of e, which affects the distance that solar photons can penetrate (the optical depth) and thus influence ion production.

1.4 Ionosphere of Titan

Ionospheres are regions of plasma formed by the photoionization and the electron impact ionization of an object's neutral atmosphere [*Cravens,* 1997; *Schunk and Nagy,* 2009]. Ionospheres have been detected on every planet in the solar system. Here the focus will be placed on the ionosphere of Titan as it orbits Saturn $20R_S$ from the planet and approximately 9.5 AU from the sun.

Radio occultation data generated from Voyager 1 [*Bird et al.,* 1997] gave the first glimpse of Titan's ionosphere. This observation has been corroborated by the Cassini Radio Science Subsystem [*Kliore et al*., 2008], as well as *in situ* measurements made by the Cassini spacecraft (see review by *Cravens et al.* [2009b]), which have shown that an ionosphere exists on Titan above 400 km with peak ionospheric electron densities between 900 and 1200 km depending on the conditions of Titan [*Wahlund et al.,* 2005; *Young et al.,* 2005; *Keller et al.,* 1992; *Gan et al.,* 1992; *Cravens et al.,* 2004, 2005, 2008; *Galand et al*., 1999; *Banaskiewicz et al*., 2000; *Molina-Cuberos et al*., 2001; *Lilensten et al.,* 2005a, 2005b; *Agren et al.,* 2007*; Kliore et al*., 2008]. On the dayside of Titan, photoionization of the neutral atmosphere from solar irradiance is usually the dominant source of the ionosphere above 800 km [*Robertson et al.,* 2009; *Cravens et al.,* 2004, 2005]. Electron impact ionization of the neutral atmosphere by energetic electrons from Saturn's outer magnetosphere (Figure 1.5) has been shown in models to adequately reproduce the nightside ionosphere in some cases (e.g., T5) [*Cravens et al.,* 2006, 2009a; *Agren et al.,* 2007].

Titan has no intrinsic magnetic field and data from the Voyager 1 encounter with Titan [*Hartle et al.,* 1992; *Neubauer et al.,* 1984] showed that Saturnian magnetic field lines drape

around Titan (Figure 1.5) and this has been confirmed by Cassini observations of the magnetic interaction with Titan [cf. review by *Sittler et al.*, 2009]. It has been shown that the magnetic field line topology is important for models of Titan's ionosphere and its energetics as heat will transfer between altitudes due to conduction along field lines [*Roboz and Nagy,* 1994; *Gan et al*., 1992; *Cravens et al*., 2005, 2009a; *Robertson et al*., 2009; *Galand et al*., 2006]. The specific three-dimensional details of the field topology are less important for the energetics than the degree to which the field lines connect different altitudes.

Titan features complex neutral and ion chemistry and various pre- and post-Cassini chemical models of Titan's atmosphere and ionosphere have been created to explain observed densities [Krasnopolsky, 2009; Lavvas et al., 2008a; 2008b; Robertson et al., 2009; Wilson and Atreya, 2004]. Pre-Cassini models included complex hydrocarbon chemistry [Keller et al., 1992] and with the work of Vuitton et al. [2007, 2008], various nitrile species have been added to the ion-neutral chemistry.

1.5 Previous and Current Research

The two-stream electron transport method was originally used to calculate suprathermal electron fluxes in the terrestrial ionosphere [*Nagy and Banks,* 1970] and has previously been used in models of both the energetics and composition of Titan's ionosphere [*Gan et al.,* 1992; *Cravens et al.,* 2009a; *Robertson et al.,* 2009]. This method derives from a gyrotropic distribution function averaged over a gyroperiod [cf. *Schunk and Nagy,* 2009]. As photoelectrons and magnetospheric electrons move along field lines they may scatter in a new direction or ionize a neutral thus creating another electron. This secondary electron must then also be tracked along the field line. Monte Carlo simulations have shown that considering only

two streams, one up and one down [cf. *Schunk and Nagy,* 2009 and references therein] is usually sufficient in the ionosphere.

Robertson et al. [2009] used a steady-state photochemical model of the ion-neutral chemistry that, coupled with a photoionization and two-stream code (see Sections 3.2 and 3.3), generated the primary (those caused by photoionization) and secondary (those caused by electron impact ionization) ion production rates and calculated ion densities as a function of altitude as was done in the model of *Keller et al*. [1992]. *Robertson et al.* found that their model's predictions of dayside ion densities below 1400 km agreed well with the *in situ* measurements made by the IMNS for the T18 flyby; however, low modeled electron densities and disagreement between modeled and measured ion densities below 1100 km indicated the need for improved high mass (m > 100 amu) chemistry for ions outside of the detection range of INMS. The model of *Robertson et al.* also did not contain information about negative ion chemistry which could be important in the lower ionosphere [*Vuitton et al.,*2009] or ion transport effects which limit the applicability of this model above 1400 km where ion transport becomes non-negligible [*Ma et al*., 2006].

Crary et al. [2009] published densities for possible high mass species (Figure 1.7) that were detected by a combination of CAPS and INMS measurements. They determined the species based on the recurring peak structure that appears in mass spectra about every 12 amu. This is attributed to higher mass carbon families of ions. Chemical pathways to species such as $C_7H_5N^+$, $C_{10}H_2^+$, $C_9H_7N^+$ and $C_{11}H_9N^+$ have been implemented in this model.

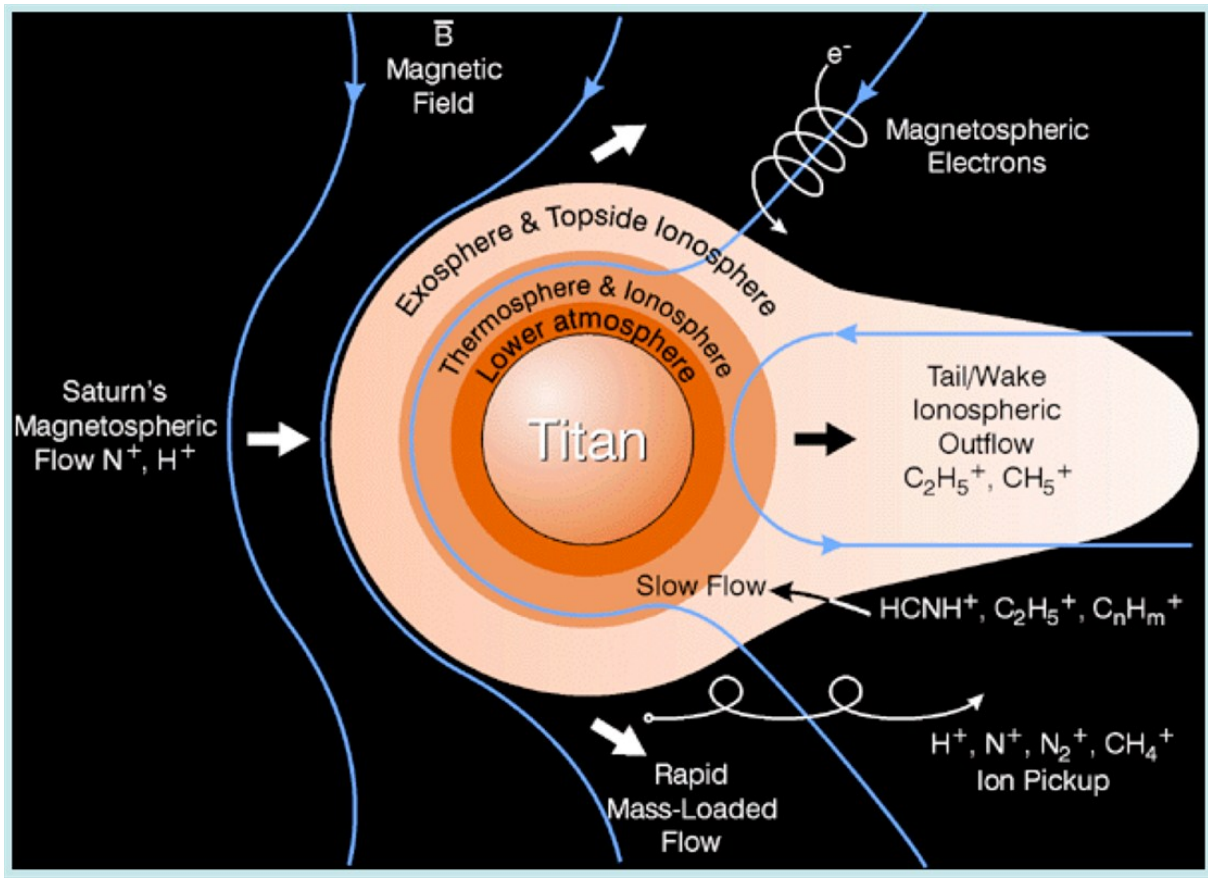

Figure 1.5 Schematic of the ionosphere of Titan with the magnetosphere of Saturn originally presented by *Waite et al*. [2004]. The diagram shows how the Saturnian magnetic field lines are bent around Titan due to the interaction with the ionosphere of Titan. The figure also illustrates how magnetospheric electrons travel along a magnetic field line and reach the ionosphere where the electron can ionize the upper atmosphere.

To improve upon the model of *Robertson et al.* [2009] updates of the ion chemistry are needed. *Anicich* [2003], *Woodall et al.* [2007] and *McEwan and Anicich,* [2007] have compiled detailed listings of ion-neutral reaction coefficients from various sources. The reaction list in this study's model will be updated to reflect the most accurate values. Further updates to the chemical models have been done in accordance with the model of Westlake et al. [2012].

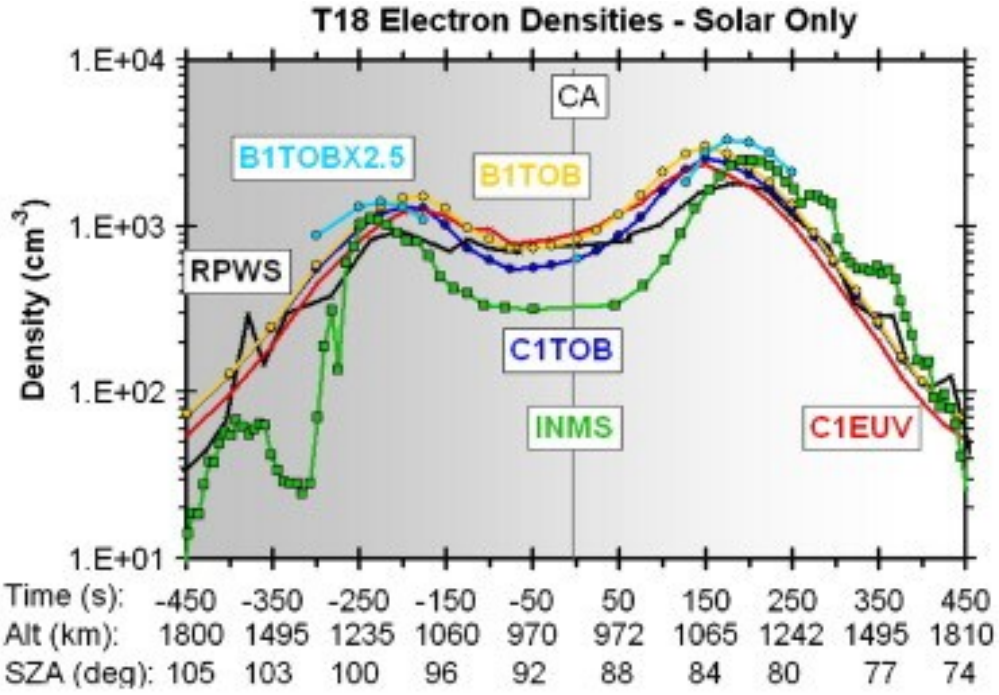

Figure 1.6 Electron density comparisons between the models of *Robertson et al.* [2009], and originally presented in their work, using only solar photons as the initial ionization source of the ionosphere and in situ measurements. The black and green lines represent measurements made by the Cassini Radio and Plasma Wave Science – Langmuir Probe (RPWS/LP) and the Cassini Ion and Neutral Mass Spectrometer (INMS) respectively. CA denotes the point of closest approach between the Cassini orbiter and Titan. The light blue, yellow and dark blue lines are marked with TOB indicating that the Tobiska SOLAR 2000 model of the solar flux was used while the EUVAC model was used for the red line. In the case represented by the light blue line, the neutral densities used in the model have been increases by a factor of 2.5. Cases starting with B use mixing ratios for minor neutral species that show preference to the ratios presented by *Magee et al.* [2009] while the C denotes preference to the mixing ratios given by *Vuitton et al.* [2006].

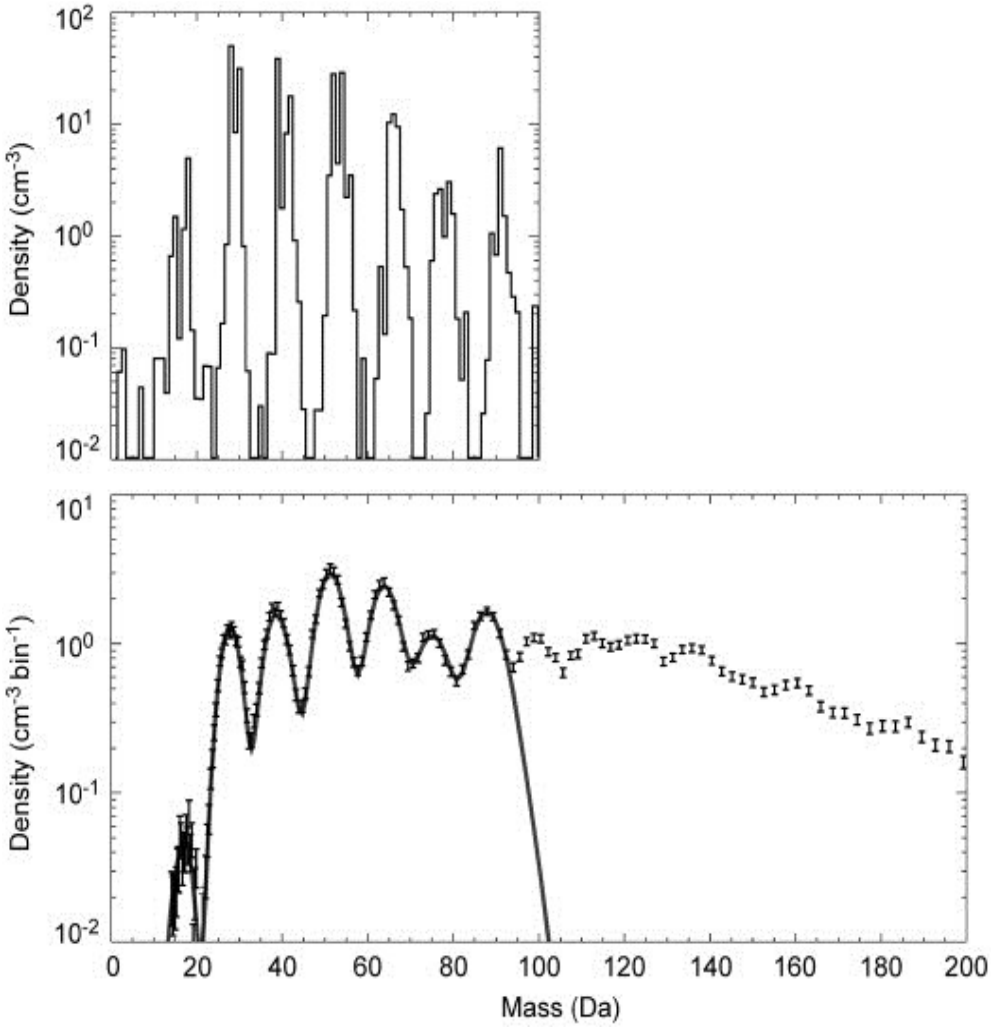

Figure 1.7 Ion spectra for the T26 flyby of Titan at 1025 km during ingress from the INMS (above) and the Cassini Plasma Spectrometer's Ion Beam Sensor (CAPS-IBS) (below) presented by *Crary et al.* [2009]. The line on the lower part of the figure is a fit to the CAPS-IBS data using the INMS spectra as input.

Thermal electron temperatures were first measured in the ionosphere during the Cassini Ta flyby of Titan by the Langmuir Probe (LP), part of the Radio and Plasma Wave Science (RPWS) experiment [*Wahlund et al*., 2005] (Figure 1.8). Temperatures and densities of ionospheric thermal electrons (that is, electrons with energies less than about 1 eV) were measured by RPWS/LP with temperature values measured to be between 400 and 1200 K [*Agren et al*., 2009]. Energetic suprathermal electrons with energies ranging from 10's of eV for photoelectrons to MeV for electrons in Saturn's magnetosphere were also measured by the Cassini Plasma Spectrometer (CAPS) [*Coates et al*., 2007] and the MIMI instrument [*Krimigis et al*., 2005] both in Titan's ionosphere and in the near-by Saturnian magnetosphere (Figure 1.9). Prior to the Cassini mission *Gan et al.* [1992, 1993] modeled ionospheric suprathermal fluxes using a two-stream method originally constructed by *Nagy and Banks* [1970] for the terrestrial ionosphere. Post-Cassini models of suprathermal electron fluxes using this general approach have been discussed for the nightside [*Cravens et al*., 2009a] and the dayside [*Galand et al.,* 2006; *Robertson et al*., 2009].

Prior to the Cassini mission a one-dimensional heat transport (along the magnetic field lines) model of electron temperatures was developed by *Gan et al*. [1992], and a one-dimensional electron and ion temperature model was created by *Roboz and Nagy* [1994]. In both of these models the energy equation for thermal electrons was solved. *Roboz and Nagy* [1994] indicated that the electron temperatures (T_e) above 1000 km had reached a steady state.

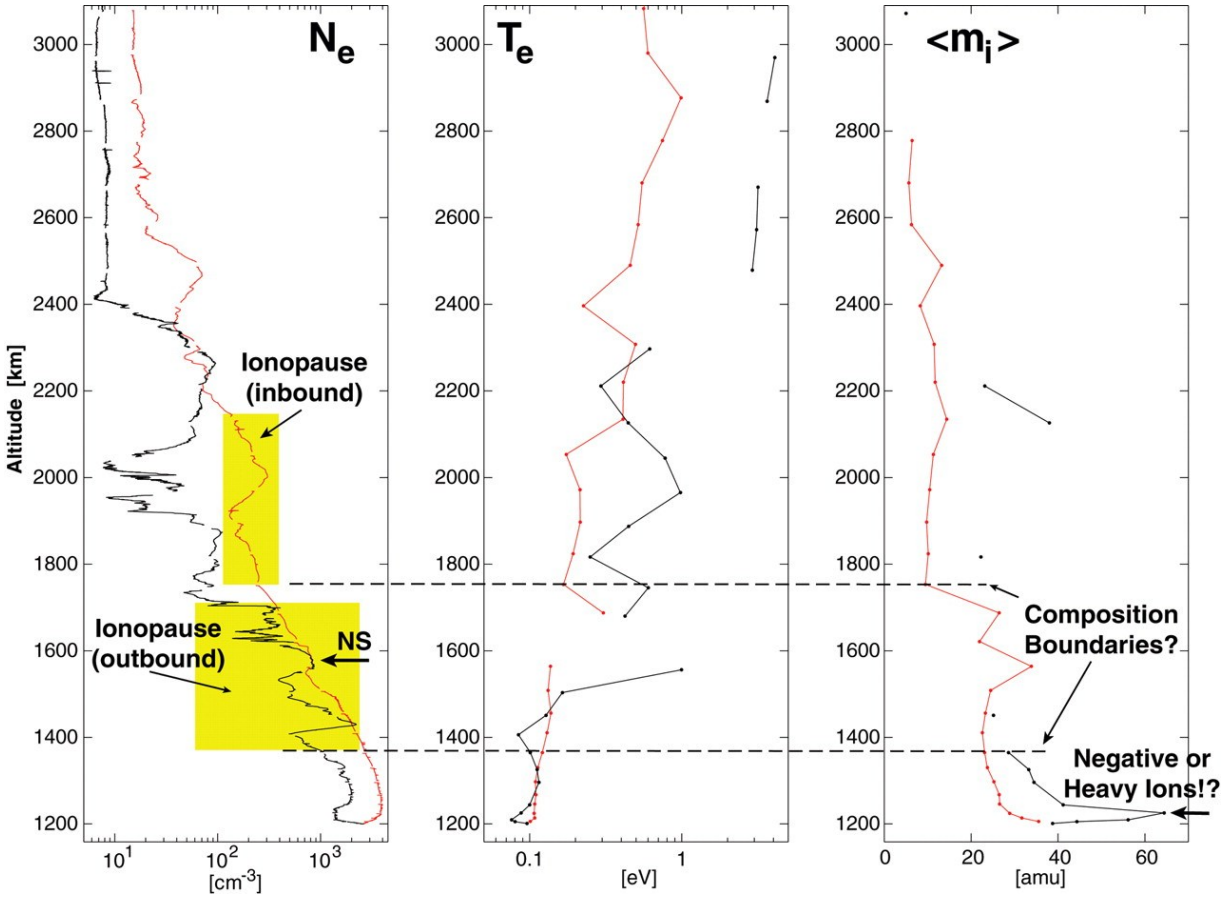

Figure 1.8 Altitude profiles for electron density (N_e), temperature (T_e) and average ion mass as measured by the RPWS/LP during the T_A flyby. The yellow blocks indicate the ionospheric boundaries as proposed by *Wahlund et al.* [2005]. Figure from *Wahlund et al.* [2005].

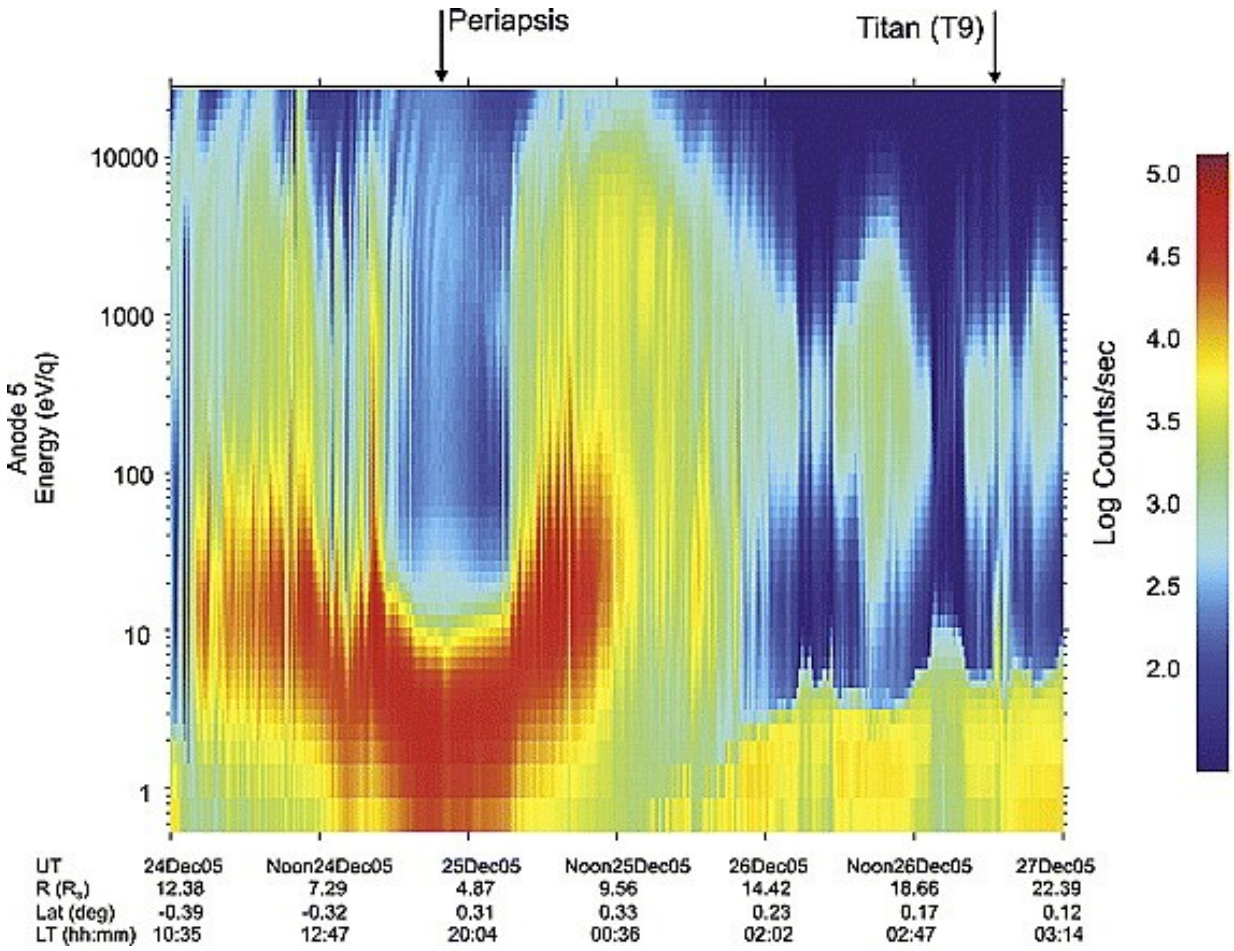

Figure 1.9 Electron energy spectra obtained by the CAPS/ELS instrument from the magnetosphere of Saturn near the T9 encounter with Titan [*Coates et al.,* 2009]. As expected, there are larger amounts of electrons with lower energies than higher energies. As the spacecraft approaches periapsis the higher energy electrons are thought to disappear as a result of interaction with atmospheric neutrals [*Young et al.,* 2005] forming a "V" shape. The higher energy observations near T9 are thought to be plasma injections. (from *Coates et al,* [2009])

Post-Cassini, *Galand et al*. [2006] presented an electron energetics model (thermal energy equation and suprathermal electron transport equation) for Titan and compared modeled electron temperatures with data for the first pass of the Cassini spacecraft through Titan's upper atmosphere (i.e., the Ta encounter). Note that subsequent Cassini passes, or encounters with Titan, are labeled Tb, Tc, T1, T2…., although the current paper focuses on just two passes (T5

and T18) as described later. The energetics model of *Galand et al.* [2006] (Figure 1.10) generated temperatures at two locations (near 1200 and 1350 km) on two separate magnetic field lines using independent solutions of the energy equation. *Galand et al.* [2006] also noted that the electron temperature along a radial field line was too low by several hundred K because heat from the upper atmosphere is readily conducted to lower altitudes where the cooling rate is large. No comparisons or temperatures were provided below 1200 km. The post-Cassini global MHD model of *Ma et al.* [2009] demonstrated that structure of the magnetic field lines at Titan is very complex and that the magnetic field produced by MHD models does not generally agree with magnetometer data at lower altitudes below 1300 k or so [*Ulusen et al.,* 2010]. This suggests that usefulness of using detailed field line topology from MHD models in ionospheric energetics models is limited. In this paper we adopt rather simple field-line topologies in order to explore how basically radial versus horizontal field configurations affect the electron energetics.

Crary et al. [2009] recently showed a measured global average ion temperature altitude profile (Figure 1.11). The profile has a temperature minimum of about 110 K around 1250 km and an approximate temperature of 260 K is reached at an altitude of 1600 km. *Crary et al*. [2009] compared data from the CAPS Ion Beam Sensor (CAPS-IBS) and INMS to generate ion fluxes as a function of energy that were fit to a Maxwellian distribution. The width of the peak ion flux is related to the thermal velocity of the ion species and hence the temperature of the ions. In order to obtain their global average results, data was collected from 14 flybys of Titan with varying solar zenith angle and at varying Saturn local times.

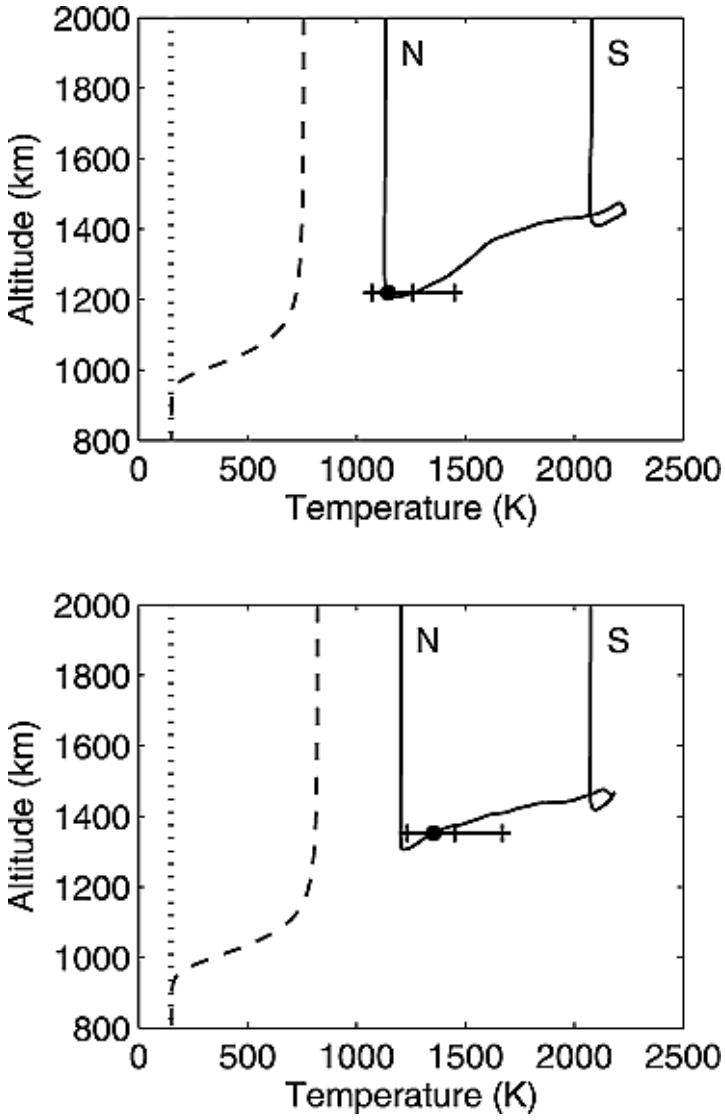

Figure 1.10 Electron temperatures from the model of *Galand et al.* [2006] for the Ta flyby of Titan at 100 s and 200 s before closest approach for the top and bottom figure respectively. The dot and bar represents the RPWS/LP derived electron temperature with error estimates of ±15%. The solid line represents *Galand et al.*'s model temperatures along a field line with the N and S representing the northern and southern hemisphere. The dotted line shows the INMS inferred neutral temperatures and the dashed line shows the results for a purely radial field line. Figure originally appeared in the work of *Galand et al.* [2006]

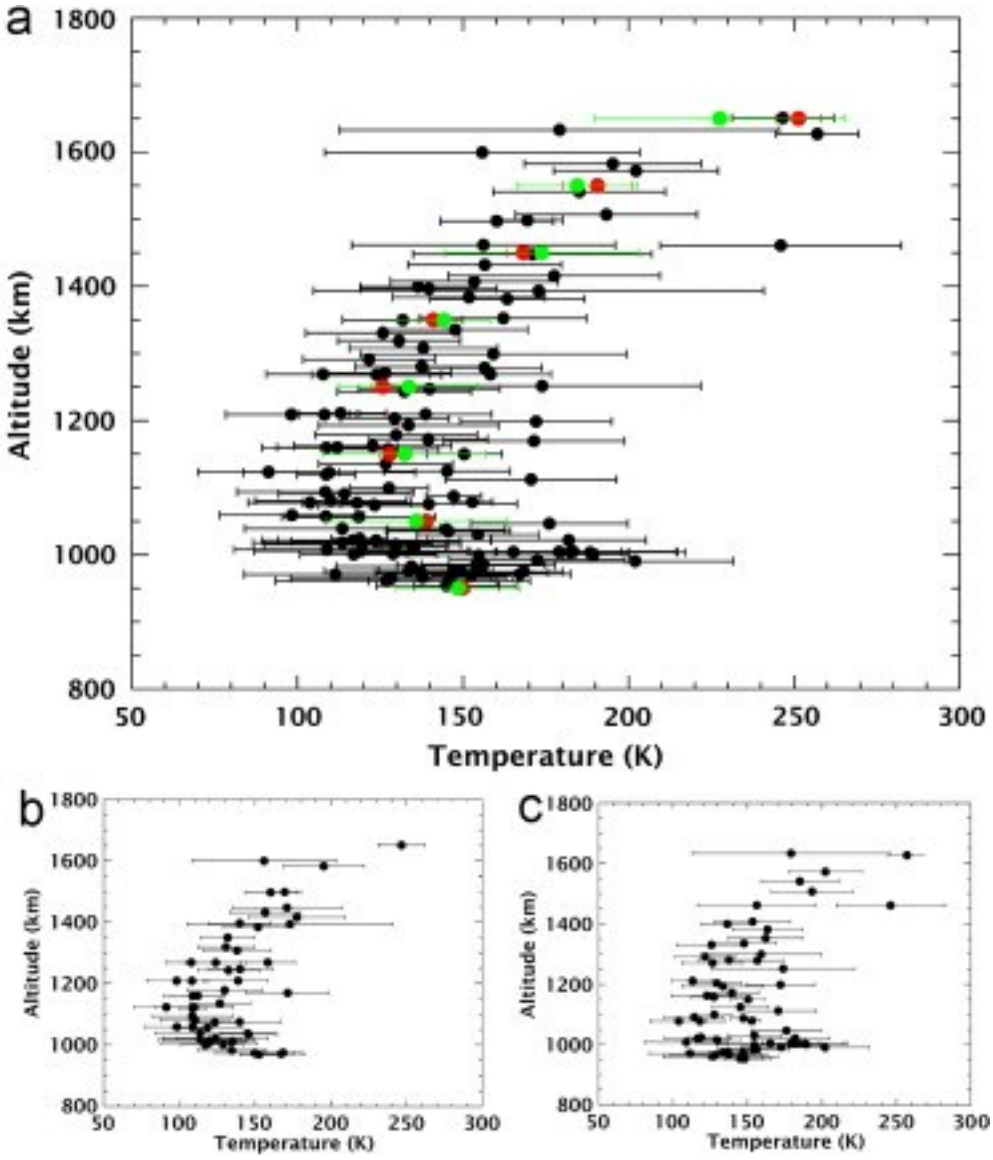

Figure 1.11 Ion temperature profile presented by *Crary et al.* [2009] calculated from the analysis of INMS and the Cassini Plasma Spectrometer Ion Beam Sensor (CAPS-IBS) acquired during 14 Titan encounters. The red and green data sets correspond to the mean and weighted-mean values. Parts b and c display the data for the dayside and nightside respectively. Figure originally appeared in the work of *Crary et al.* [2009].

The works of *Gan et al.* [1992], *Roboz and Nagy* [1994] and *Galand et al.* [2006] are the only works to date that present detailed calculations of the electron temperature at Titan. *Gan et al.* [1992] showed with their pre-Cassini model that that solar ionizing radiation is the dominant source of electron heating on the dayside. *Galand et al.* [2006] used horizontal magnetic field lines (that is, field lines with a strong component parallel to Titan's surface) in their model and also found that solar radiation was sufficient to explain the measured temperatures near the terminator. The subject of nightside and non-Ta dayside electron temperatures has yet to be explored in the literature.

The goal is to use in situ data collected by the Cassini spacecraft and Huygens probe to further the understanding of mechanisms involved in the creation and sustainment of Titan's ionosphere. Models of the electron and ion production, energetics of electrons and ions and photochemical models of chemistry have been constructed and are able to examine various components of the formation of the ionosphere.

Current models for the ion and electron densities are all found to produce electron and ion (most notably $HCNH^+$) densities that are higher than the measurements recorded by the INMS aboard Cassini [e.g. *Robertson et al.*, 2009; *Westlake et al*., 2012]. To understand the source of this problem the production of ions and electrons is evaluated in light of new photoabsorption cross sections mentioned in *Lavvas et al.* [2011]. The results from the production model are compared to empirical values derived from data and will be shown to be adequate and not the source of the model discrepancies. After the initial production is verified, the chemical processes (electron-ion dissociative recombination, ion-neutral reactions) will be evaluated and various chemical pathways will be explored for the transition of one ion species to another in the hopes

of reconciling the differences between the models and observations. Possible cases will be outlined that bring the model and data into better agreement.

There are many open-ended questions regarding the ionosphere and plasma interactions of Titan that guide this study. Below is a list of the questions that form by the path this study will follow in order to illuminate possible solutions to each question.

1. Is the current model (to be defined in later chapters) employed by this study valid near the ionospheric peak?
    - Comparisons will be drawn between modeled electron temperature profiles and compared to measurements made by the Radio Plasma Wave Science – Langmuir Probe.
    - Modeled ion production rates and the resulting modeled ion density spectrum for the ionospheric peak will be compared to empirical ion production rates and ion densities measured by the Ion Neutral Mass Spectrometer aboard Cassini for several flybys of Titan which include measurements of the dayside and nightside ionosphere.
2. How can the observed electron and ion temperatures, which are much higher than the neutral temperatures, be explained?
    - Temperature profiles versus altitude between 800 and 1800 km are calculated for electrons and ions and for the dayside (T18) and the nightside (T5).
    - Different configurations of the modeled magnetic field line geometry, verified from data from the Cassini Magnetometer, are implemented and the impacts on the electron and ion temperatures are examined.

- Various heating sources such as magnetospheric electrons, photoelectrons produced by solar photons, and terms depending on the flow speed of the plasma are considered and the results are given.

3. What is the cause of the discrepancy between the measured and modeled electron densities [i.e. *Robertson et al.*, 2009; *Westlake et al*., 2012]?

- Ion production rate profiles from the current model are examined in light of updated photo-absorption and photoionization cross sections at a variety of solar zenith angles to determine if the discrepancy is due to an overproduction of primary ions.
- Ion production rates for primary species, ions created from the photoionization or electron-impact ionization of N_2 and CH_4 (i.e. N_2^+,CH_4^+, CH_3^+ etc.), have been derived empirically from data from Cassini spacecraft instruments for flybys encompassing solar zenith angles between 15˚ and 90˚ on the dayside and for various nightside conditions are compared with model runs of Titan flybys.
- The two major chemical processes (ion-neutral reactions and electron dissociative recombination) are reconsidered for the ion species to ensure up-to-date values are implemented in the model to examine if the excess electrons are the result of missing or insufficient loss processes. Chemical reactions transition lower mass ions to higher mass ions that recombine more readily with electrons .
- Modeled temperature profiles are implemented that are closer to the neutral temperatures at altitudes near and below 1000 km than the values obtained from the Cassini Radio and Plasma Wave Science – Langmuir Probe which raises

electron recombination rates of ions at lower altitudes in order to examine the reliability of the measurements and if the modeled profile is preferable.

4. How can this information be applied to the global picture of Titan's ionosphere and its interaction with the Saturnian magnetospheric plasma?

- Model runs yielding ion production rates and densities for various solar zenith angles on the dayside and for the cases presented by *Rymer et al.* [2009] on the nightside are constructed using a globally averaged neutral atmosphere.

Chapter 2 **Instrument Overview**

The Cassini spacecraft (Figure 2.1) launched on October 15, 1997 and entered its orbit around Saturn on July 1, 2004. Cassini has been sending information about the environment of Saturn and its moons, with flybys of Titan occurring almost monthly, since its arrival and will continue to do so for the remainder of the current mission (Cassini Solstice) which ends in 2017. In this chapter an overview is given of the instruments aboard the Cassini spacecraft whose measurements compose the dominant share of the data used in this study (Table 2.1). A brief outline of the instrument operations, the type of data each instrument collects and a reference to papers with in-depth descriptions of the instruments is presented in each subsection. More space is devoted to the Cassini Ion and Neutral Mass Spectrometer as it is the main source of data used in this research.

2.1 Cassini Plasma Spectrometer (CAPS)

The CAPS instrument [*Young et al*., 2005] includes an electron spectrograph (ELS), ion beam Sensor (IBS) and ion mass spectrometer (IMS) for measuring energetic electrons and ions in the magnetosphere of Saturn and in the ionosphere of Titan. The CAPS-ELS measures suprathermal electron fluxes with energies between 0.6 and 28,250 eV and will be used for model comparison. The CAPS-IMS measures ions with energies between 1 and 50,280 eV. The resolution of the IMS and ELS is 0.17 $(E/\Delta E)_{FWHM}$ which means that although the energy range of measured electrons and ions is high, the spectral resolution of the instrument is lower than the Cassini Ion and Neutral Mass Spectrometer described in Section 2.3. The IBS measures the flux of ions as a function of their kinetic energy and direction and can be used to gather information

about the ion flow velocity and temperature. *Crary et al*. [2009] used this sensor for their comparisons with INMS mass spectra in the ionosphere and for their determination of the ion temperature. For additional information see *Young et al.* [2005] and *Coates et al.* [2007].

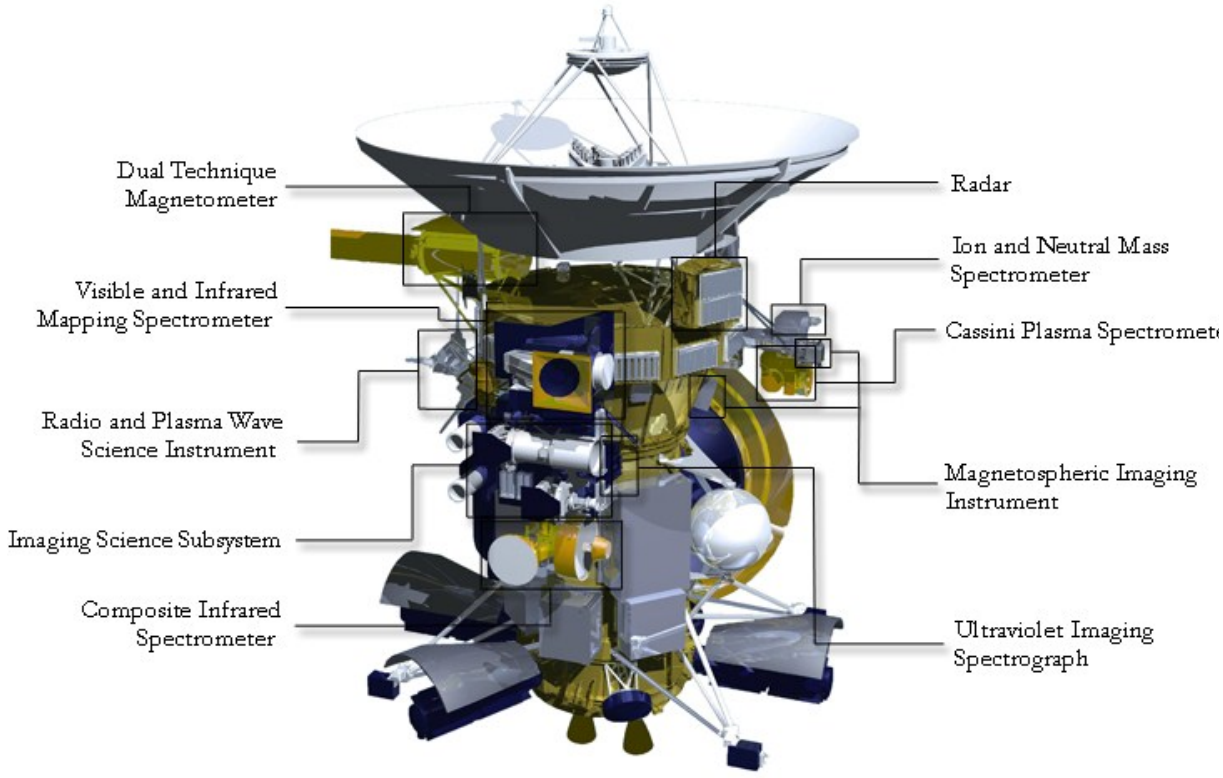

Figure 2.1 Rendered image of the Cassini spacecraft with instrument subsystems labeled. Note the magnetometer boom in the image is not fully extended. [Image courtesy of NASA JPL]

Table 2.1 Overview of relevant Cassini instrumentation

Instrument Name	Acronym	Types of Measurement
Cassini Plasma Spectrometer Ion Beam Sensor	CAPS - IBS	Ion flow velocity and temperature
Cassini Plasma Spectrometer - Ion Mass Spectrometer	CAPS - IMS	Flux of ions with energies between 1 and 50,280 eV
Cassini Plasma Spectrometer Electron Spectrograph	CAPS - ELS	Superthermal electron fluxes with energies between 0.6 and 28,250 eV
Cassini Radio and Plasma Wave Science – Langmuir Probe	RPWS - LP	Electron density and temperature
Ion and Neutral Mass Spectrometer	INMS	Ion and neutral densities from 0.5 to 8.5 and 11.5-99.5 Daltons
Magnetospheric Imaging Instrument – Lower Energy Magnetospheric Measurement System	MIMI - LEMMS	Flux of electrons with 0.015 MeV< E < 0.884 MeV and 0.1 < E <5 MeV and ions with 0.03 < E < 18 MeV and 1.6 < E < 160 MeV
Magnetospheric Imaging Instrument – Ion and Neutral Camera	MIMI - INCA	Flux of ions and energetic neutrals with energies per nucleon between 7keV and 3MeV
Magnetospheric Imaging Instrument – Charge-Energy-Mass Spectrometer	MIMI - CHEMS	Flux of ions with energies between 3 and 220 keV/e
Cassini Magnetometer	MAG	Direction and strength of magnetic field to within one nT

2.2 Cassini Radio and Plasma Wave Spectrometer (RPWS)

The Cassini RPWS/LP instrument is a Langmuir Probe (LP), which measures electron densities (n_e) and temperature (T_e). A brief overview of the instrument is provided below and further details on this instrument can be found in *Wahlund et al*. [2005], *Ågren et al.* [2009], and *Gurnett et al.* [2004]. The Langmuir probe is composed of a sphere with a diameter of 5 cm at the end of a 1 m boom. The current flowing from the spacecraft to the probe is measured as the

potential on the probe is changed. As the probe's positive potential increases the current will also increase to the electrons that are being picked up from Titan's ionosphere or Saturn's magnetosphere and measurements of the electron density and temperature can be obtained.

2.3 Ion and Neutral Mass Spectrometer (INMS)

The INMS instrument is a radio-frequency quadrupole mass spectrometer. It is capable of operating in multiple modes in order to measure the ion and neutral composition of the ionosphere with a mass to charge ratio of 0.5 to 8.5 Daltons and from 11.5 to 99.5 Daltons [*Waite et al*., 2004]. The gap in these measurements is caused by the choice of radio frequencies used in the quadrupole mass analyzer to cover the low and high mass measurement regime. For more in-depth information see *Kasprzak et al.* [1996] and *Waite et al.* [2004] in addition to the overview below. The neutral density profiles needed as inputs by this model are based on INMS data (also see *Cravens et al*. [2009a], *Robertson et al*. [2009], *Cui et al*. [2009a, 2009b], and *Magee et al*. [2009]) and the ion density profiles produced in this study are compared to measurements made by the INMS.

The INMS will operate in a closed source neutral mode in order to measure the non-reactive neutral species such as N_2 and CH_4. In this mode neutrals enter the instrument through the spherical antechamber shown in Figure 2.2 taken from [*Waite et al*., 2004]. In the antechamber the ions will collide with the walls of the chamber and thermalize to the surface temperature while the ram pressure builds up as more neutrals are pushed into the chamber than are allowed to escape. After the neutrals have thermalized they will travel down the transfer tube into a chamber where a collimated beam of electrons produced by the electron gun will ionize the neutral atoms. These newly formed ions are then deflected into the quadrupole switching

lenses where the ions will be directed into the quadrupole mass analyzer and counted. The mass analyzer will vary the voltage of the quadrupole at a rate of 3.57 MHz for M=1-8 Daltons and 1.64 MHz for M=12-99 Daltons in accordance with Equation (2.1) in order to select different masses to count. In Equation (2.1) M represents the mass of the species, f is the frequency of the voltage modulation and V_{ac} is the radiofrequency potential amplitude. Each mass scan is taken over an integration period of 34 ms which corresponds to approximately 200 m along the spacecraft trajectory assuming a velocity of 6 km/s which is a good estimate of the spacecraft velocity on a Titan flyby.

$$M = \frac{0.55V_{ac}}{f^2} \qquad \textbf{(2.1)}$$

When measuring ions or more reactive neutrals (i.e. N) the open source mode is used. In this mode the ion or neutral species enters through the lower opening on the left of Figure 2.2. Ions are guided to into the focusing lenses in the open ion source by four ion deflectors. Neutrals that have arrived in the open ion source are ionized by a pair of electron guns at this stage and then the ion and ionized neutral beams will be directed by focusing lenses (OL 1-4) into the quadrupole switching lens which will subsequently guide the ions into the mass analyzer. In the mass analyzer a dc voltage is applied to the RF mass analyzer rods in order to slow the ions and enable better mass resolution.

The INMS has a mass resolution M/ΔM of 100 at 10% of the mass peak height enabling the instrument to differentiate between ions species with mass to charge ratios only one Dalton apart from one another. The threshold density for detection of ions in the closed source ion mode is 5 x 10^4 cm^{-3}. For the open source neutral mode the limits of detection for neutrals and

ion species are 2 x 10^5 and on the order of 10^{-2} cm^{-3} respectively. These values represent the detection thresholds for conditions when the spacecraft is travelling near 6 km/s and will be adjusted for varying spacecraft velocity and when the spacecraft becomes charged due to the ambient plasma.

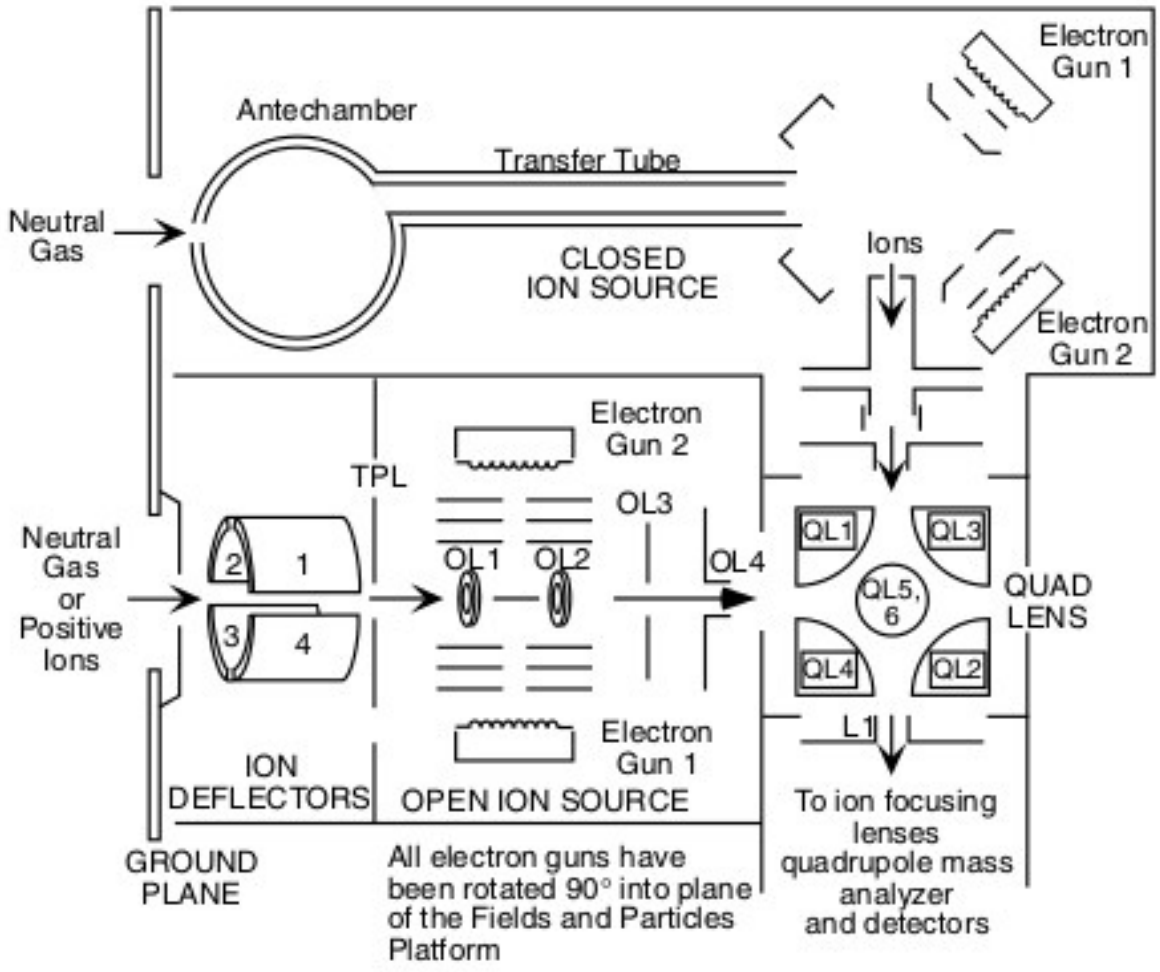

Figure 2.2 Schematic of the Cassini Ion and Neutral Mass Spectrometer originally appearing in *Waite et al*. [2009].

2.4 Magnetospheric Imaging Instrument (MIMI)

The Magnetospheric Imaging Instrument (MIMI) [discussed in detail by *Krimigis et al.*, 2004] consists of three sensors that will provide information about the energetic neutral, ion and electrons that reside within the magnetosphere of Saturn and the ionosphere of Titan. Ions and energetic neutrals with energies per nucleon between 7keV and 3MeV will be detected with the Ion and Neutral (INCA) which utilizes a foil time-of flight-camera to collect information. The Low Energy Magnetosphere Measurements System (LEMMS) is a spinning two-ended telescope that will collect information from both sides in a 360˚ arc with 15 and 30˚ full angle conical fields of view for the lower and higher energy ranges respectively. LEMMS is capable of detecting electrons with energies between 0.015 and 0.884 MeV and 0.1-5 MeV and ions with energies between 0.03 and 18 MeV and 1.6-160 MeV. The third instrument composing MIMI is the Charge-Energy-Mass-Spectrometer (CHEMS) which gathers data about ions with energies between 3 and 220 keV/e using time-of-flight and energy measurements in conjunction with electrostatic deflection. MIMI is capable of collecting measurements over a large energy range which provides this study with information regarding the superthermal electrons in the magnetosphere of Saturn that can travel along magnetic field lines and deposit their energy into the ionosphere of Titan. These energetic electrons can become the primary source of the ionosphere on Titan [*cf. Cravens et al.*, 2009a]

2.5 Cassini Magnetometer (MAG)

Information regarding the ambient magnetic field is obtained through in situ measurements of the Cassini Magnetometer (MAG) [*Dougherty et al.*, 2009]. MAG is classified

as a dual-technique magnetometer as consists of a flux gate magnetometer (FGM) mounted in the middle of an 11 m boom extending from the Cassini spacecraft and a helium magnetometer (S/VSM) that can operated in vector and scalar modes. Measurements can be obtained to within a nT using cross calibration between the FGM and the S/VHM operated in its scalar mode over a frequency range of 0-20 Hz with the S/VHM favoring frequencies below 1 Hz.

A brief overview of both magnetometers is given below. The FGM consists of three single axis core rings mounted orthogonally to one another. Each ring contains a core and is driven by a 15.625 kHz square wave that will drive the core into saturation twice per cycle. When the instrument encounters an external magnetic field the core will saturate asymmetrically and this signal can be used to determine the ambient magnetic field.

The helium magnetometer excites helium gas using a radiofrequency signal so that the gas will emit infrared photons with a wavelength of 1083 nm. These photons are passed through a circular polarizer and the signal is collected by a detector. In the presence of a magnetic field there is a decrease in optical pumping efficiency due to the Zeeman effect which results in less photons being collected by the detector. By using sweeping magnetic fields it is possible to ascertain the direction of the field from these measurements. When the S/VHM is operating in its scalar mode a weak AC is applied to the cell at the Larmor frequency, (the frequency that a charged object completes a rotation in a magnetic field) which opposes the optical pumping. This method makes use of the fact that the Larmor frequency is proportional to the ambient magnetic field by the gyromagnetic ratio of helium in this device. The frequency of the signal is then modulated in order to track changes in the magnetic field.

Chapter 3 **Methodology**

This chapter describes the methodology employed in the current study which is similar to the methods of *Gan et al.* [1992], *Keller et al.* [1992], and *Robertson et al.*, [2009]. Constructing a model of a flyby of Titan entails running a sequence of programs (Figure 3.1) to determine the primary population of ions from photoionization, ionization from electron-impact ionization, electron and ion temperatures, and the ion densities. Inputs into this sequence include a profile of the neutral densities, flux of solar photons, and the flux of electrons from the magnetosphere of Saturn. Each section of this chapter explains a section of the diagram below and a short description can be found in Table 3.1.

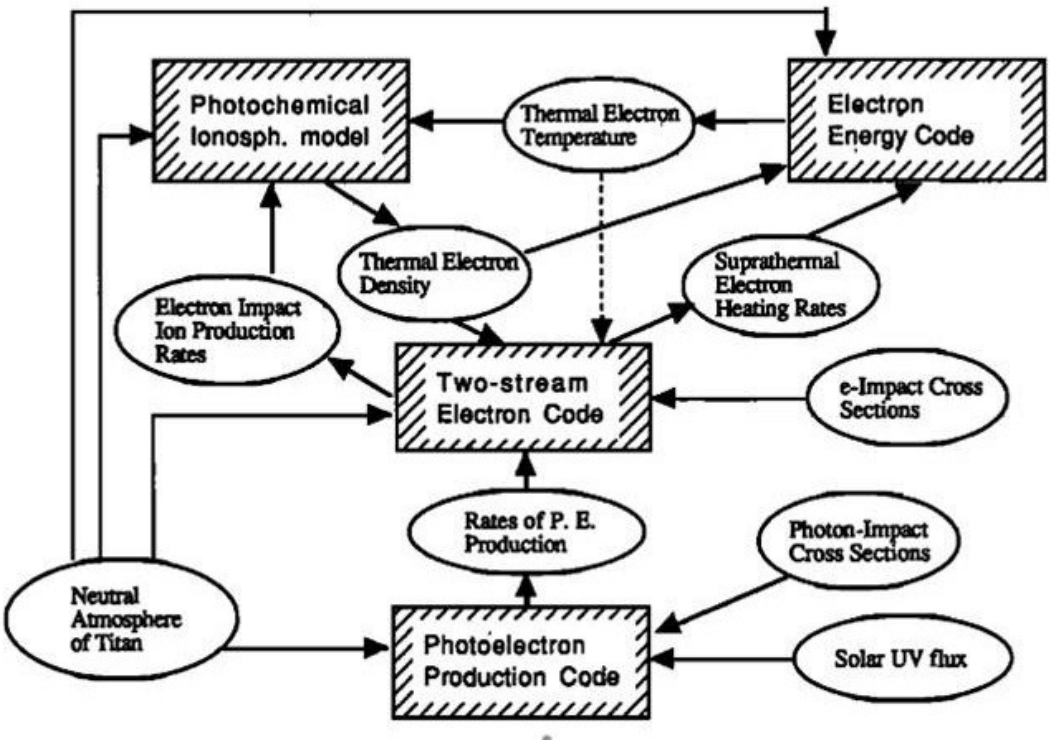

Figure 3.1 Schematic of the current model. Programs are indicated with the rectangular boxes while input and products are denoted by ovals. Arrows pointing toward a box are inputs for that program while arrows pointing away are output by the program. (From *Keller et al.* [1992])

Table 3.1 Description of Model Programs

Program	Description
Photoionization, Ion and Photoelectron Production Code	Given a neutral atmosphere, solar UV flux, solar zenith angle and photoabsorption and photoionization cross sections this program will determine the rates of photoelectron production and photoionization as a function of altitude.
Two-Stream Electron Code	Using the two-stream methodology of *Nagy and Banks* [1970] this program produces the rate of electron impact ionization of a given neutral atmosphere using electron-impact ionization cross sections, magnetospheric electron fluxes and photoelectron production rates from the Photoelectron Production Code.
Electron and Ion Energy Code	Produces profiles of electron and ion temperatures using electron heating rates from the Two-Stream Code and a neutral atmosphere to determine electron cooling from collisions with neutral molecules. Ions are heated via collisions with electrons and cooled by collisions with the neutral species.
Photochemical Ionospheric Model	Uses a photochemical approximation (ion production equals ion loss) to determine the density of an ion species. The code currently has 38 and 136 neutral and ion species respectively with production rates determined by a chemical reaction list (see Appendix C) and production rates determined by the Photoionization, Ion and Photoelectron Production Code and the Two-Stream Electron Code.

3.1 Magnetic Field Line Geometry

The magnetic field line topology needed for the magnetospheric and photoelectron transport in this model of Titan's ionosphere is essentially derived from the models of *Gan et al*. [1992, 1993] and *Cravens et al*. [2008]. Magnetic field line topologies are taken to be radial or parabolic in accordance with the magnetometer data from Cassini (see Figure 3.2 for an example of magnetometer data consistent with a parabolic field line configuration for the T18 and T5

flyby of Titan). Parabolic field lines are used to simulate the draping of Saturn's magnetic field around Titan. The radius of curvature at the subsolar point, or anchor point, (where the parabola intersects the x-axis in Figure 3.3) is the distance from the subsolar point to the center of Titan. This configuration gives the tightest possible parabola with monotonically increasing radial distances (see Figure 3.4 for a sample of the correlation between the distance along the field line and altitude). The model uses grid spacing of 35 km along magnetic field lines [*Gan et al*., 1992, 1993; *Cravens et al*., 2004] for the superthermal electron flux calculations, and also for the calculation of thermal electron and ion temperatures from the coupled electron and ion energy equations.

Even though the current model is one-dimensional along magnetic field lines, it is not strictly one-dimensional in space as the magnetic field can curve due to the field line topology. For this model the field line configuration serves as a path for superthermal electrons and photoelectrons that influence how much of the atmosphere a particle potentially interacts with; hence, the heating rates and ion production rates. The overall field configuration in this study is not as important as the local configuration, as conductivity along the field lines will transport heat in the ionosphere between altitudes. For example, if the local fields are horizontal, little heat will be transported between altitudes. MHD models are capable of providing more accurate field line topologies and velocity flow fields to provide insight into terms in the energy equation (Section 3.5) that depend on the bulk plasma velocity [*Cravens et al*., 2009a; *Ma et al*., 2007, 2009].

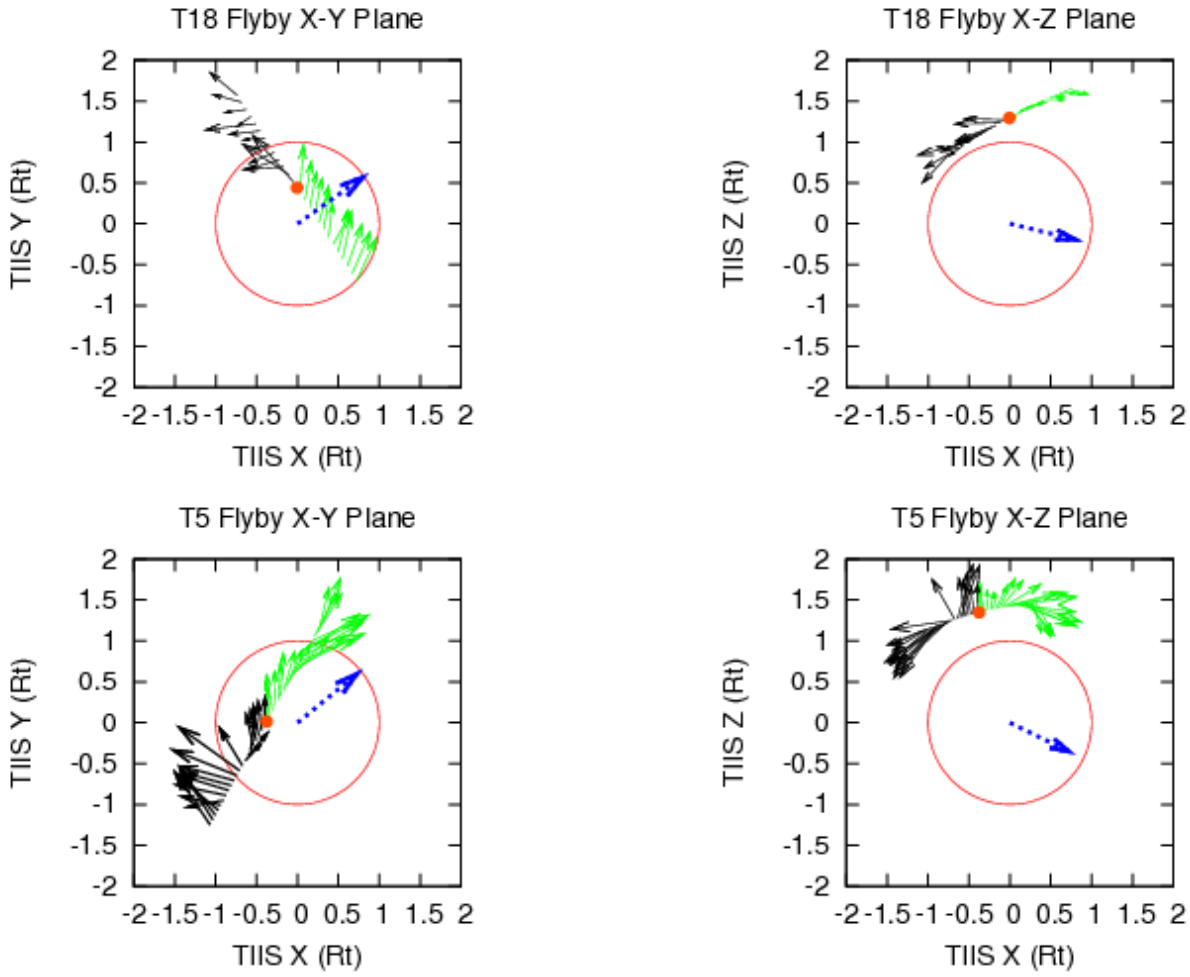

Figure 3.2 Magnetometer data along Cassini's trajectory for the T18 (above) and T5 (below) flyby of Titan [cf. *Bertucci* 2009; *Cravens et al.*, 2010, and references therein] in TIIS coordinates. The x-axis points in the corotational flow direction, y is directed to Saturn and z completes the right-handed coordinate system. The solid arrows indicate the magnetic field vector at one-tenth scale in nT (i.e. one unit on the graph is equal to 10 nT) with the green and black arrows indicating the inbound and outbound portion of the flyby, respectively. The dashed blue arrow points to the sun and the filled circle indicates the location of the spacecraft's closest approach.

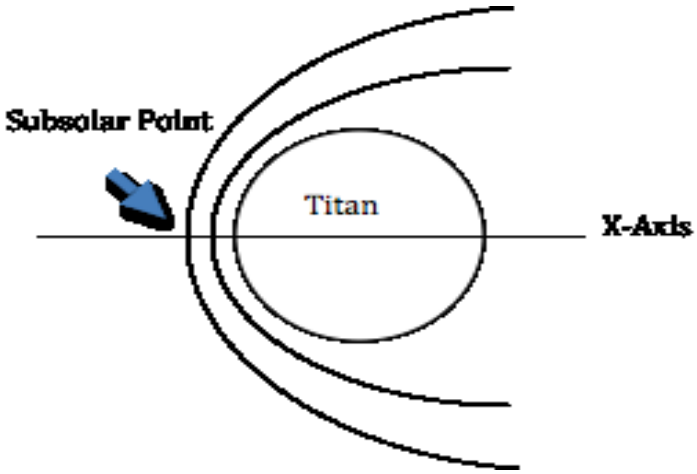

Figure 3.3 Sketch of the magnetic field line configuration for the parabolic (one line) and nested cases (combination of lines). Distance along the field line s is measured from the apex point. The parabolas may be implemented with different solar zenith angles and different locations with respect to the external flow direction.

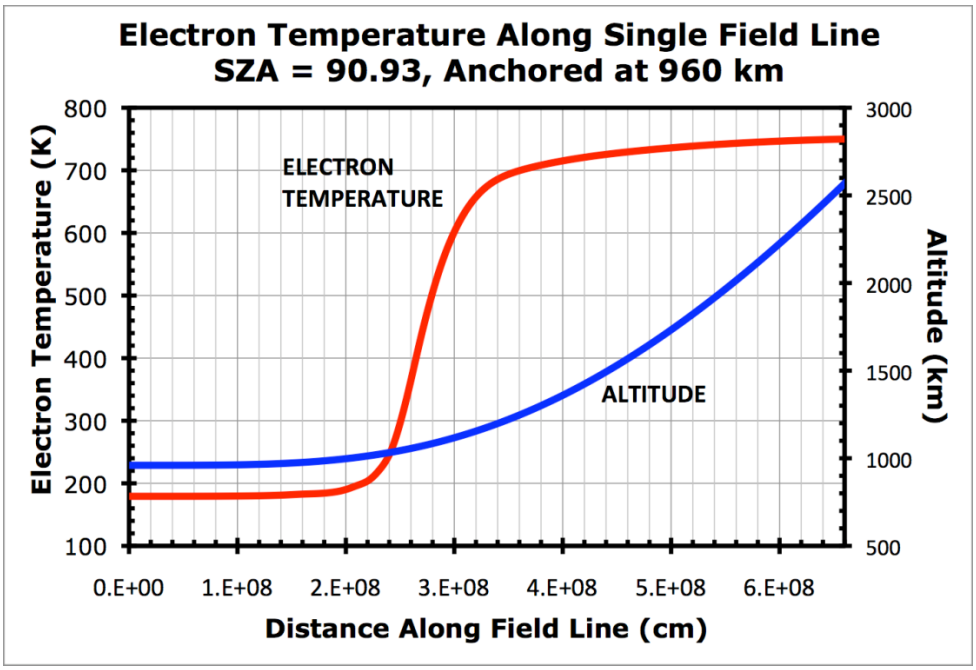

Figure 3.4 Thermal electron temperature and altitude plotted against the distance along the magnetic field line from the anchor point. (From *Richard et al.*[2011])

3.2 Photoionization Code

Photoionization is the main source of Titan's ionosphere between 900 and 1400 km on the dayside of Titan [c.f. *Cravens et al.,* 2005; *Robertson et al.*, 2009]. As shown in Figure 3.5, solar photons of energy hν travel into the upper atmosphere at a solar zenith angle of χ and deposit their energy at altitude z which can result in the photoionization or excitation of atmospheric neutrals. In this model photoionization rates are calculated as a function of altitude and solar zenith angle for photons at various energies.

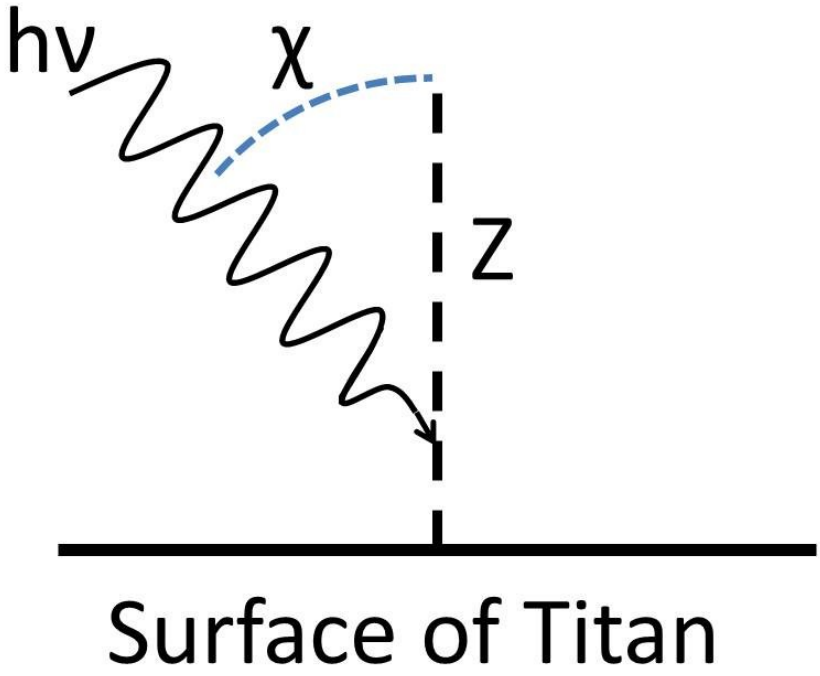

Figure 3.5 Schematic of photoionization of Titan's upper atmosphere.

The optical depth, the depth that a photon will penetrate into the atmosphere, can be approximated by Equation (3.1):

$$\tau_\lambda \approx \frac{1}{\cos\chi} n_s(z) H_s(z) \sigma_\lambda \qquad \textbf{(3.1)}$$

where χ is the solar zenith angle, σ_λ is the photoabsorption cross-section at wavelength λ, and n is the density of a species. H_s is the scale height of the atmosphere for species s given by Equation (1.4). In order to account for ion production with the solar zenith above 90˚, Chapman functions along with spherical geometry have been utilized [*Cravens et al.*, 2009] which have been calculated by *Smith and Smith* [1972] [cf. *Schunk and Nagy,* 2009]. The production P of a species m in the ionosphere is given by Equation (3.2):

$$P_m = \int F_\lambda(z) n_n(z) \sigma_{\lambda,i} d\lambda \qquad \textbf{(3.2)}$$

with $n_n(z)$ representing the number density of a neutral species in the atmosphere as a function of altitude z, $\sigma_{\lambda,i}$ representing the photoionization cross section at a wavelength λ and the incident photon flux as a function of altitude $F_\lambda(z)$ given by Equation (3.3).

$$F_\lambda(z) = F_{\lambda_0} e^{-\tau_\lambda} \qquad \textbf{(3.3)}$$

The incident flux of photons at a given wavelength λ at an altitude depends on the initial flux of photons at the top of the atmosphere which decreases by an e-folding with the optical depth.

3.2.1 Solar Flux Modeling

The principles discussed above are used in the photoelectron production code shown in Figure 3.1 in order to produce a primary population of electrons from the photoionization of the

neutral atmosphere of Titan by solar photons. The initial flux of solar photons is derived using the EUVAC [*Richards et al*., 1994] or the Solar Irradiance Platform or SIP (formerly SOLAR2000) [*Tobiska et al.*, 2000; *Tobiska*, 2007] models of solar flux based on measurements. Both of these models are designed to give the flux of solar photons at Earth; however, a scaling factor of $1/9.5^2$ is introduced in order to create an appropriate incident flux for Titan's environment 9.5 AU from the sun. The EUVAC model provides data at a lower wavelength resolution than the SIP and, for these cases, photon fluxes from the larger EUVAC wavelength bins are divided, proportional to the relative size of each bin to one another, into wavelength bins matching the structure of the SIP model. For the solar flux between 0 and 30 Angstroms, wavelength resolution of one Angstrom was implemented by scaling YOHKOH observations (Figure 3.6) [*Acton et al*, 1999; *Cravens et al*., 2006] so that the total flux obtained matched the total flux in the wavelength range of the EUVAC and SIP models. Figure 3.7, Figure 3.8, and Figure 3.9 show the modeled solar photon fluxes at Earth generated by both solar flux models and the F10.7 index, the 10.7 cm radio wave flux in $WHz\text{-}^1m^{-2}$ multiplied by 10^{22} serving as an indicator of solar activity and a proxy for the solar extreme ultraviolet (EUV) flux, for the T17, T18 and T40 flybys respectively. These fluxes are distributed amongst 320 wavelength bins, whose structure appears as a table in Appendix A-1, and are used as inputs in the photoionization routine. The resulting ion production rates will be discussed in Chapter 4.

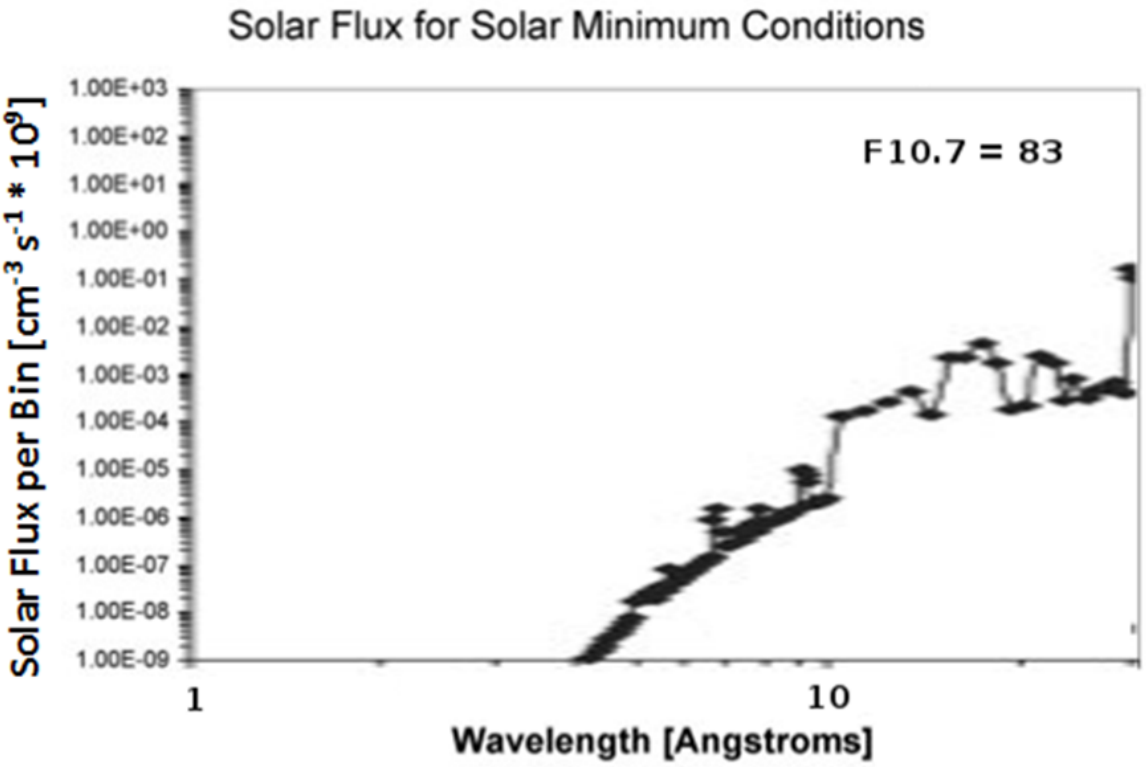

Figure 3.6 Yohkoh observations of the solar flux below 30 Åwhen the F10.7 index was 83. The portion of this graph between zero and thirty angstroms is scaled so that the total photon flux matches the flux generated by the EUVAC or SIP model. (Figure from *Cravens et al.* [2006])

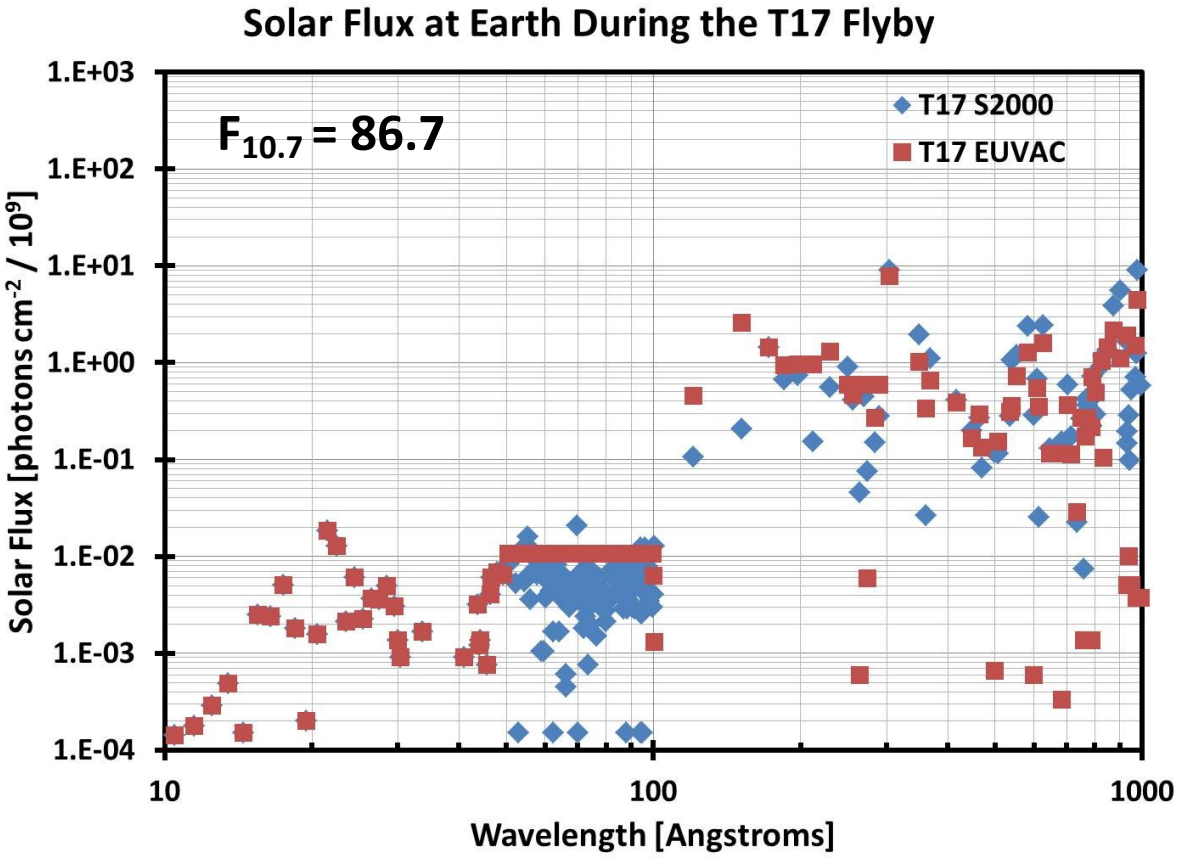

Figure 3.7 Flux of solar photons per bin at Earth in solar flux units (flux cm^{-2} / 10^9) during the T17 Flyby of Titan. The binning structure appears in Appendix A. Red squares denote the values produced by the SIP model [Tobiska et *al.*, 2000; *Tobiska*, 2007] while the blue diamonds represent the flux generated by the EUVAC model [*Richards et al.*, 1994].

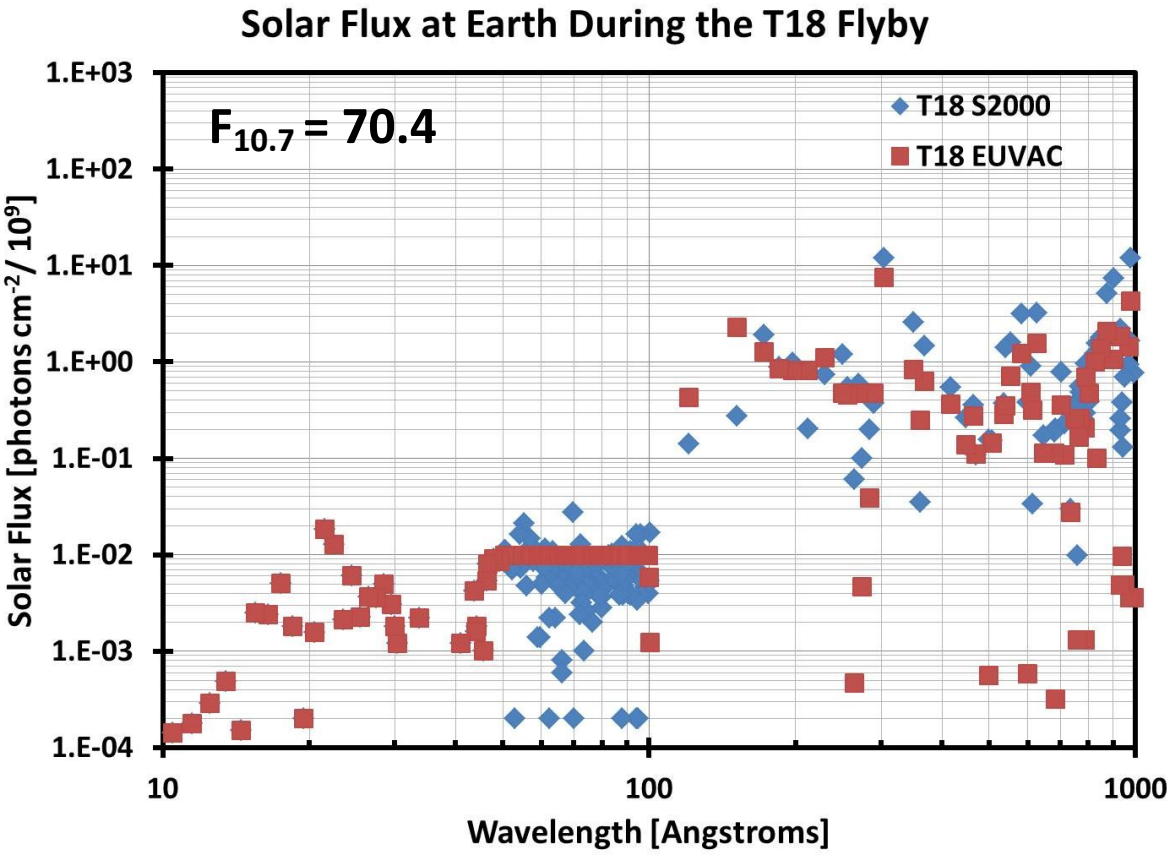

Figure 3.8 Flux of solar photons per bin at Earth in solar flux units (flux cm^{-2}/ 10^9) during the T18 Flyby of Titan. The binning structure appears in Appendix A. Red squares denote the values produced by the SIP model [Tobiska et *al.*, 2000; *Tobiska*, 2007] while the blue diamonds represent the flux generated by the EUVAC model [*Richards et al.*, 1994].

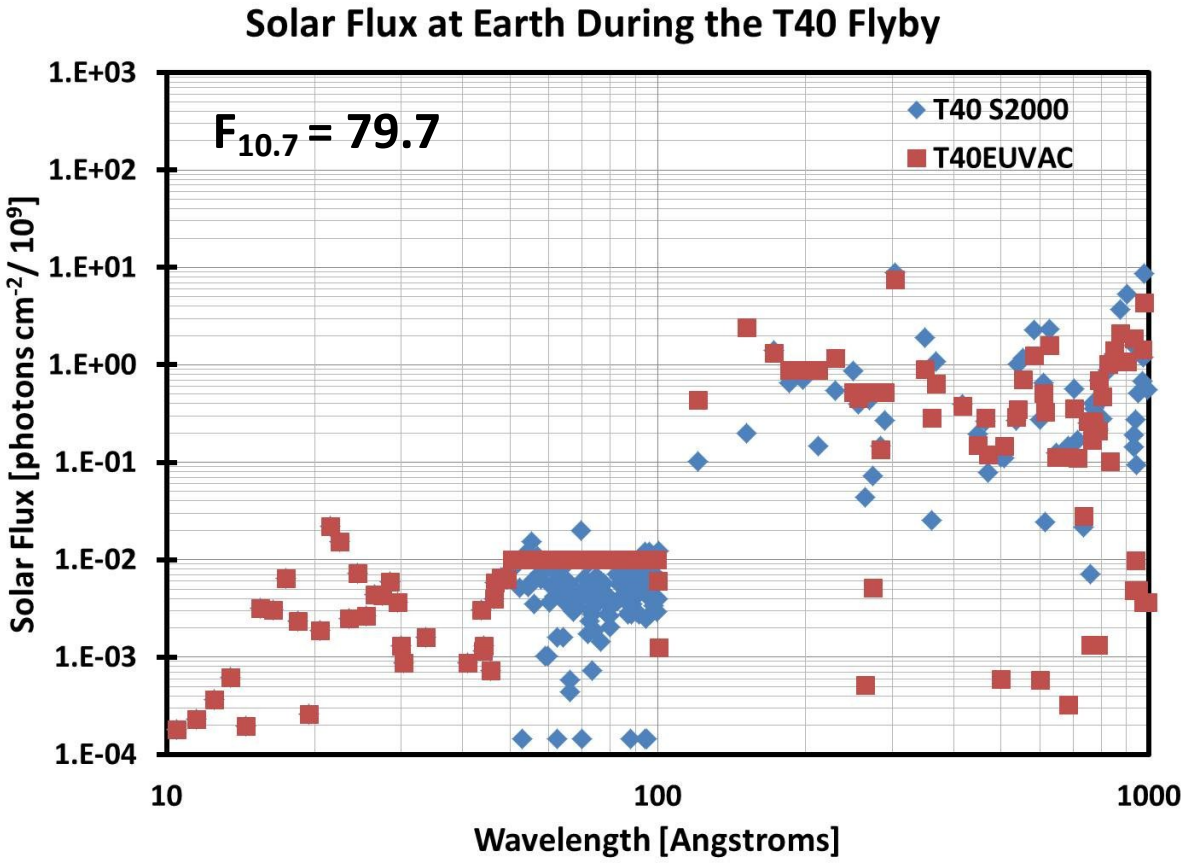

Figure 3.9 Flux of solar photons per bin at Earth in solar flux units (flux cm^{-2}/ 10^9) during the T40 Flyby of Titan. The binning structure appears in Appendix A. Red squares denote the values produced by the SIP model [Tobiska et *al.*, 2000; *Tobiska*, 2007] while the blue diamonds represent the flux generated by the EUVAC model [*Richards et al.*, 1994].

3.2.2 Photoabsorption and Photoionization Cross Sections

Like the incident solar flux of photons, photoabsorption and photoionization cross sections for the two major neural species (N_2 and CH_4) are also given as input to the photoelectron code. The values are compiled from multiple sources and tables of the values used will appear in Appendix B-1 in addition to the discussion given below.

3.2.2.1 Photoabsorption and Photoionization Cross Sections of N_2

The N_2 cross sections for photoabsorption and photoionization used in this work follow the work done by *Gan* [1991] and are used to compute the production of photoelectrons, N_2^+ and N^+ from the photoionization of N_2. *Gallagher et al.* [1988] compiled data between 50 and 770 Å from several sources and their results are shown in Figure 3.10. Using the cross sections presented in Figure 3.10 branching ratios are determined for each ionization state of nitrogen. For the cross sections between 100 and 1000 Å the values from *Solomon et al.* [1988] are used which are in good agreement with those of *Gallagher et al*. Ionization cross sections for the $2\sigma^{-1}$ state are taken from the theoretical works of *Langhoff et al.* [1981]. Below 100 Å the data from *Banks and Kockarts* [1973] and *Denne* [1970] are implemented which clearly show a peak due to K-shell ionization (Figure 3.11). The N^+/N_2 photofragmentation cross section (Figure 3.12) is derived from data from *Wight et al.* [1976] and presented by *Gallagher et al.* [1988].

Liang et al. [2007] have derived higher resolution (0.04 Å) cross sections for the photoabsorption of molecular nitrogen for wavelengths between 800 and 1000 Å (Figure 3.13) using a coupled-Schrodinger equation (CSE) model to obtain information regarding transitions of electrons between higher Rydberg states and starting energy levels. Photons in this wavelength range have energies below the ionization threshold of N_2 (800 Å or 15.53 eV), but are capable of ionizing CH_4 if they are allowed to penetrate into the atmosphere. *Lavvas et al.*

[2011] have shown that the use of the N_2 photoabsorption cross sections of *Liang et al.* (shown in Chapter 4) is able to help explain the production of CH_4^+ in the ionosphere. This topic is addressed in Chapter 4 and an in-depth discussion appears there.

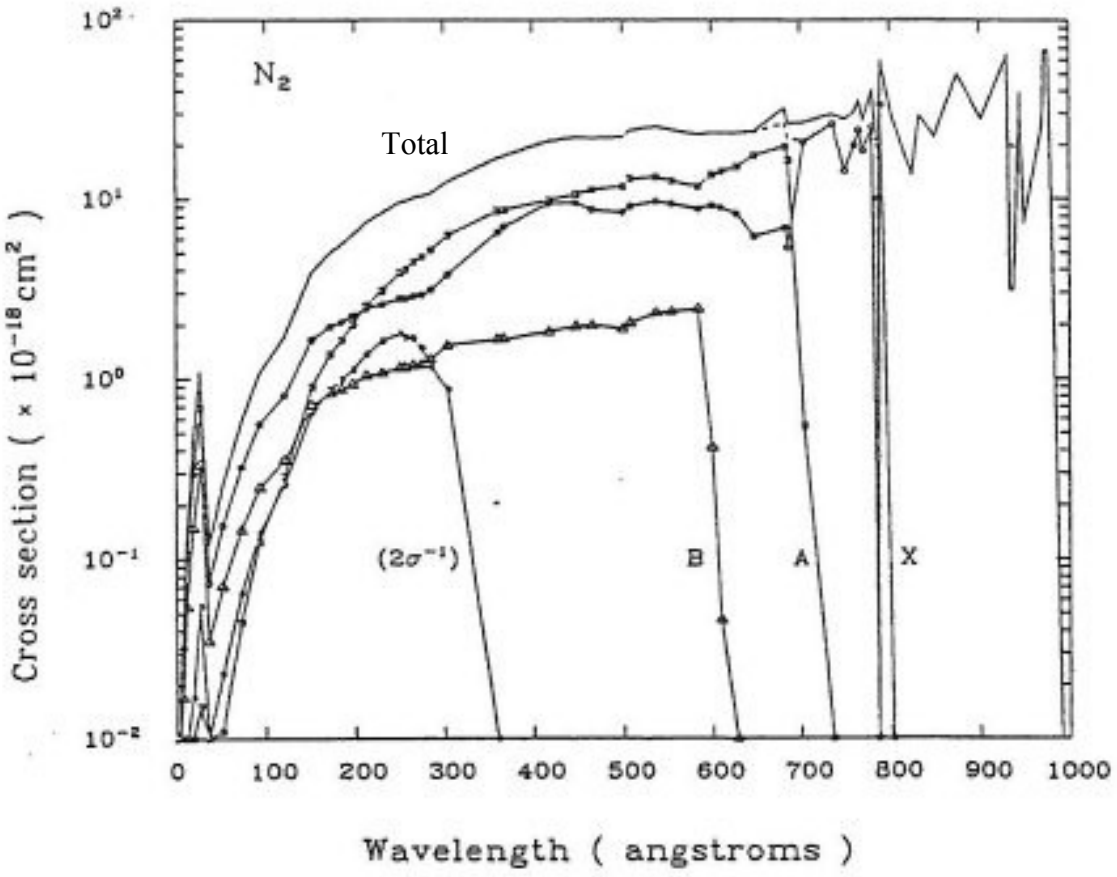

Figure 3.10 Photoabsorption (topmost line) and photoionization cross sections (lines are labeled according to the final ionization state, X, A, B, and $2\sigma^{-1}$) for N_2. The dashed line indicates the total ionization cross section. (From [*Gan*, 1991])

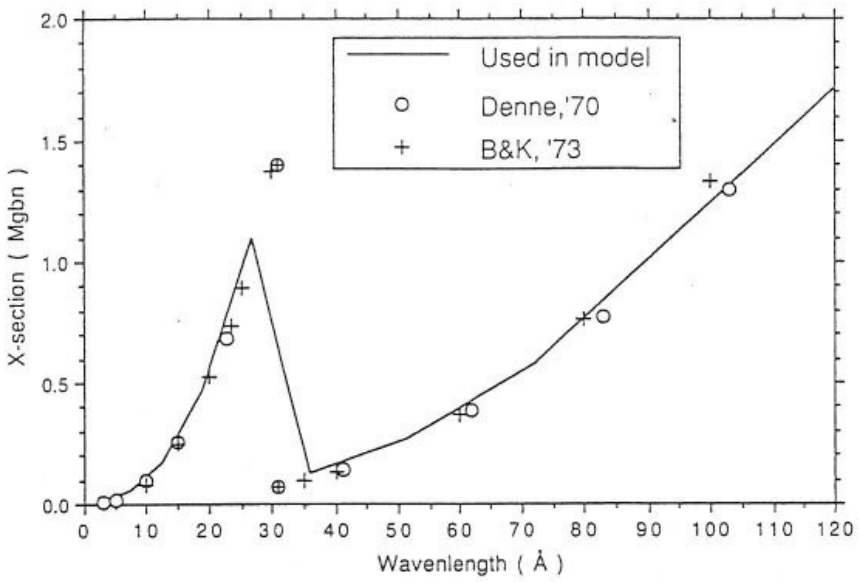

Figure 3.11 Photoabsorption cross sections of N_2 in the X-ray range from *Gan* [1991]. The peak in the data represents the K-shell edge for ionization. The cross sections of Denne [1970] and Banks and Kockarts [1973] are represented by circles and crosses respectively.

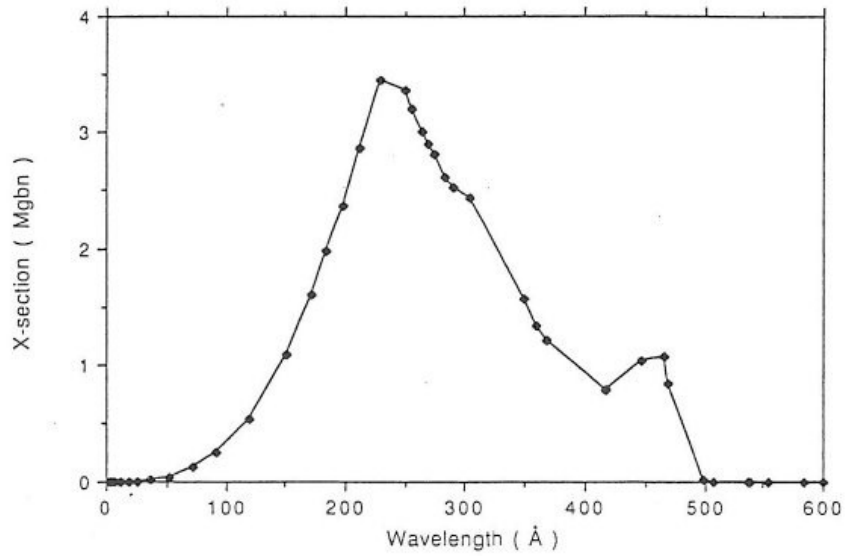

Figure 3.12 Dissociative ionization cross section of N_2 going to N^+. (From *Gan* [1991])

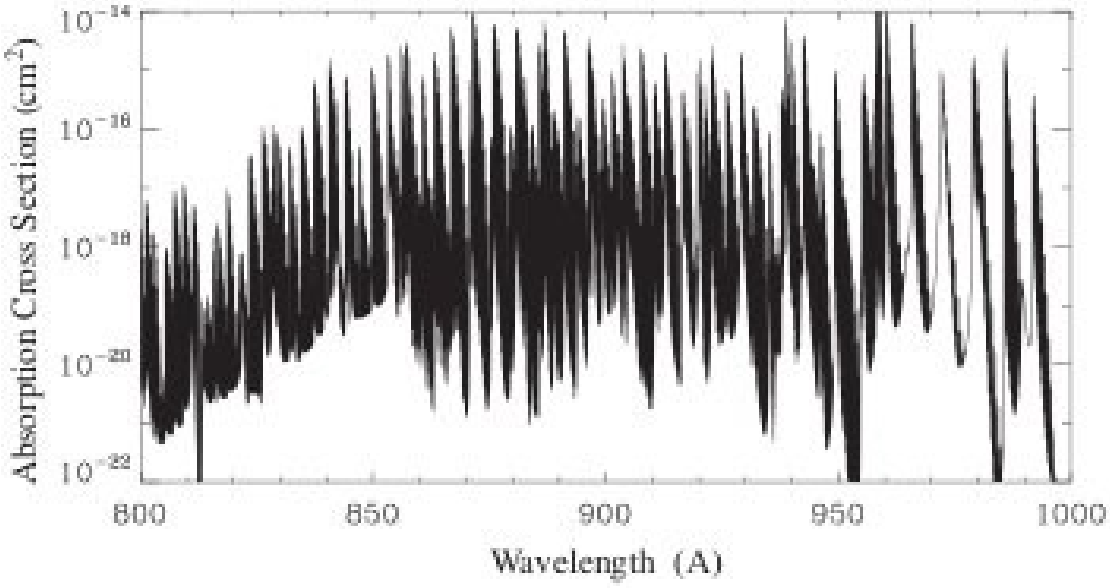

Figure 3.13 N_2 Photoabsorption cross sections for photons with wavelengths between 800 and 1000 Å calculated by *Liang et al.* [2007] using a coupled Schrodinger Equation and 0.04 Å resolution. Figure originally appearing in *Lavvas et al.* [2011].

3.2.2.2 Photoabsorption and Photoionization Cross Sections of CH_4

For the photoabsorption of CH_4, cross sections compiled by *Gan* [1991] and *Gan et al.* [1992] for photons with wavelengths between 4 and 1305.45 Å are used. The cross sections of *Watanabe et al.* [1953], *Ditchburn* [1955], and *Rustgi* [1964] are used between 950 and 1305.45 Å. For photons in the wavelength range 300 – 950 Å values obtained by *Samson et al.* [1989] are implemented. Below 300 Å cross sections from *Lukirskii et al.* [1964] are employed with values for photons with $\lambda < 25$ Å obtained from a power law extrapolation (Equation (3.4)) of their data [*Gan,* 1992] where σ is in units of 10^{-18} cm^2 and λ is in Å .

$$\sigma_{abs}(\lambda) = 1{,}368 \times 10^{-4}\lambda^{2.4} \qquad \textbf{(3.4)}$$

Photoionization cross sections are obtained by *Gan et al.* [1992] from the data of *Samson et al.* [1989] and *Backx and Van der Wiel* [1975] for seven ion species. These cross sections are shown in Figure 3.14 and appear again in Appendix B-2 in tabular form.

The end result of the photoelectron code is a primary production rate profile of ions and an initial population of electrons caused by the photoionization of N_2 and CH_4 in Titan's atmosphere. The photoelectron population is then used as input into the two-stream electron code (Figure 3.1) and discussed in Section 3.3 where they may interact with the neutral population via electron-impact ionization.

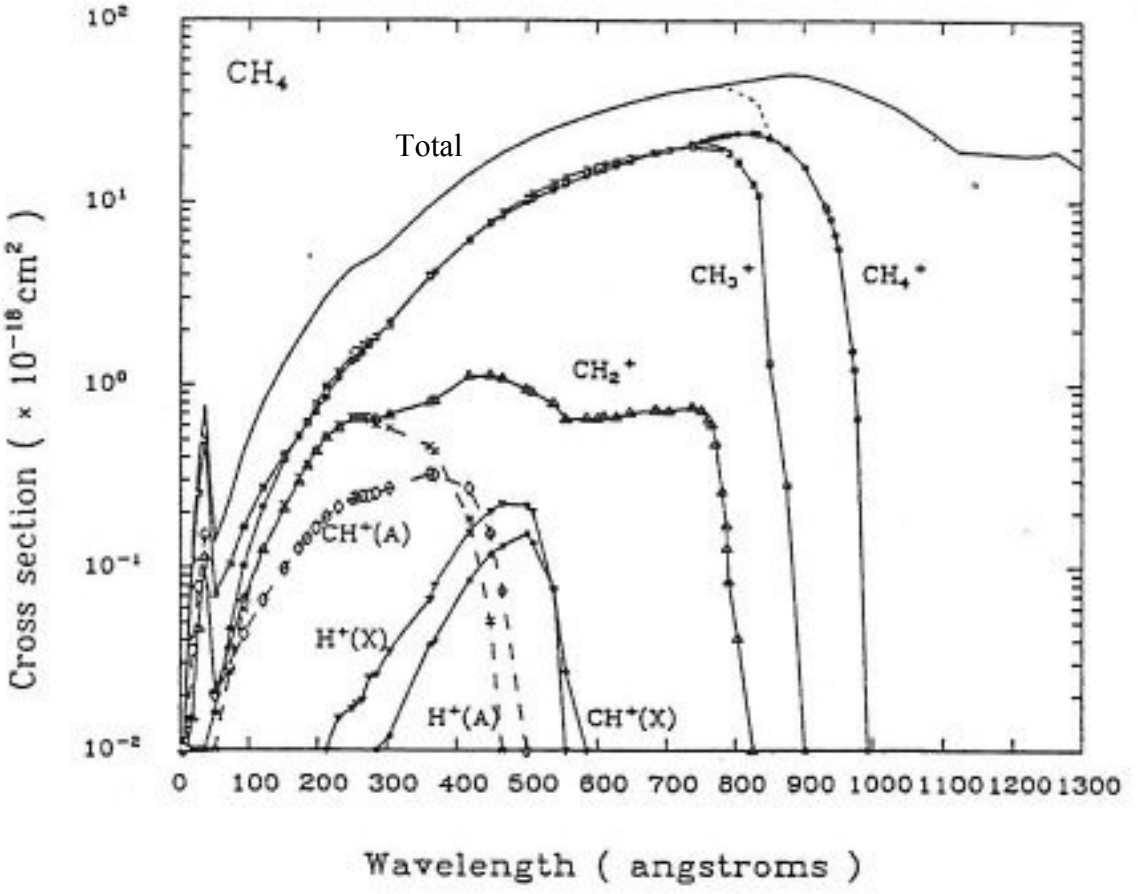

Figure 3.14 Total photoabsorption (solid black line), total photoionization (dashed line) and photoionization cross sections (labeled by final state) for CH_4. (From *Gan* et al. [1992])

3.3 Two-Stream Equations for Suprathermal Electron Flux and Electron Heating Rates

Electron impact ionization of the neutral atmosphere is responsible for the bulk of ion production on the nightside of Titan above 1000 km and for a substantial portion of the energy deposition of the region below 1000 km on the day and nightside [cf. *Cravens et al*.; 2009a; *Cravens et al,*. 2009b; *Robertson et al*., 2009]. These electrons, originating from photoionization of the neutral atmosphere (Section 3.2) or from Saturn's magnetosphere, travel down Saturn's magnetic field lines that drape around Titan (see Section 3.1) and through the ionosphere to lower altitudes. The heating rate of the thermal electron population of Titan's ionosphere (electrons with energy less than 2 eV) as well as the ion production rate from electron impact ionization are calculated using the two-stream model [*Nagy and Banks*, 1972; cf. *Schunk and Nagy,* 2009] and the results are then used in conjunction with the photochemical model to determine ion densities (Section 3.4) and the energetics code to determine the temperature of the thermal electron and ion temperature (Section 3.7).

3.3.1 General Overview

This two-stream electron flux model was adopted to calculate heating rates and ion production rates at various points along a magnetic field line. The two-stream equation for electron fluxes up and down a magnetic field line is as follows (see *Nagy and Banks*, [1972]):

$$\frac{d\Phi^{\pm}}{ds} = \frac{\mp 1}{\langle cos\Theta \rangle}\sum_k n_k[\sigma_e^k + p_e^k\sigma_e^k]\Phi^{\pm} + \frac{\pm 1}{\langle cos\Theta \rangle}\sum_k n_k p_e^k \sigma_e^k \Phi^{\mp} \pm \frac{q}{2\langle cos\Theta \rangle} \pm \frac{q^{\pm}}{\langle cos\Theta \rangle} \quad \textbf{(3.5)}$$

where Φ^+ and Φ^- are the electron fluxes away and toward the apex point as a function of the energy of the electron, E, and the distance along the field line, s. The number density of the k^{th} neutral species (i.e., N_2 or CH_4) is represented by n_k. The total electron scattering cross-section for elastic collisions with the k^{th} species is represented by σ_e^k. The electron backscatter probability for elastic collisions with the k^{th} species is given by p_e^k. The electron production rate in the range E to E + dE and at a given location, due to photoionization by solar radiation, is denoted by q. That is, q is the primary photoelectron production rate as a function of energy and location. The suprathermal electron production rate in the energy range E to E + dE due to electrons at higher energies that undergo inelastic collisions is the cascading production rate, denoted $q^{\pm}$. This production rate also included the secondary electrons produced by primary electron impact ionization of neutrals. The average cosine of the pitch angle is assumed to be ½ (i.e., isotropic upward and downward distributions).

Electron fluxes as a function of energy were calculated by solving Equation (3.5) as described by *Gan et al*. [1992, 1993] using the primary population created as the result of photoionization of the neutral atmosphere by solar extreme ultraviolet (EUV) and solar X-ray radiation (Section 3.2) along with the electron flux from Saturn's magnetosphere (i.e. Figure 1.2), if desired. The fluxes were assumed to be symmetric about the x-axis shown in Figure 3.3. The energy grid consisted of discrete energy bins starting with a bin size of 0.5 eV and increasing to 10 keV at the maximum energy in the code of 194 keV (see for Table 3.2 details). A sample flux of electrons for the dayside case is given in Figure 3.15. Note the photoelectron peak at an energy of 25 eV is due to photoionization caused by the strong solar HeII resonance line at 30.4 nm [*Nagy and Banks,* 1970; *Gan et al.*, 1992; Robertson et al., 2009].

Table 3.2 Binning Structure of electron energy in two-stream code

Energy Range Covered	Number of Bins	Size Of Bin (eV)
0 - 10 eV	20	0.5
10 - 80 eV	70	1.0
80 - 100 eV	10	2.0
100 - 200 eV	20	5.0
200 – 500 eV	30	10.0
500 – 1000 eV	10	50.0
1 – 2 keV	10	100.0
2 – 10 keV	40	200.0
10 – 14 keV	10	400.0
14 – 24 keV	10	1,000.0
24 – 44 keV	10	2,000.0
44 – 94 keV	10	5,000.0
94 – 194 keV	10	10,000.0

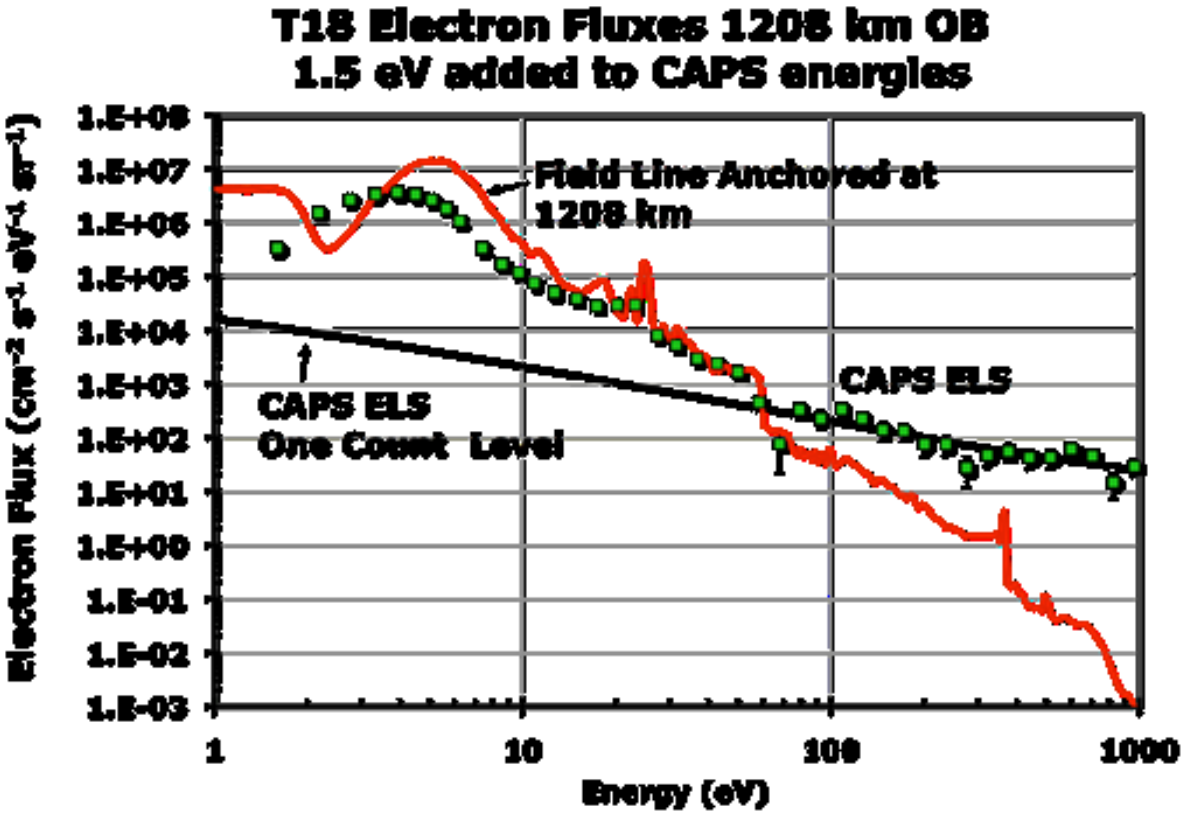

Figure 3.15 Dayside electron fluxes measured by CAPS-ELS and reported by *Robertson et al.* [2009]. The one count level shows the sensitivity limits of the spectrometer. The measured values from CAPS have been shifted by 1.5 eV to account for the spacecraft potential at this time. The solid line shows the electron flux that was generated in the model using the two-stream approach and shows reasonable agreement with the CAPS spectra below 100 eV until the instrument readings approach the one count level.

Suprathermal and secondary electrons are transported up and down magnetic field lines in this model and, through Coulomb collisions, provide heating to the thermal electron population and generate ion production rates from electron impact ionization of the neutral atmosphere. Equation (3.6) shows how the electron heating rate Q_e as a function of altitude was calculated with Φ_e representing the flux of electrons and E_T representing the transition energy that separates thermal and superthermal electrons [*Schunk and Nagy*, 2009]. This transition energy is defined as the point where the electron distribution deviates noticeably from a Maxwellian distribution in velocity space, about 2 eV at Titan. The rate at which an superthermal electron loses energy to the ambient thermal electrons, $\left(\frac{dE}{dz}\right)_e$, is defined in Equation (3.7) where E_e is given by 8.618×10^5 eV/K multiplied by the thermal electron temperature. The heating rate is computed along the field line as a function of distance from the apex point and used as an input in the energetics code shown in Figure 3.16 for a dayside (T18) case for an altitude of 1007 km and a solar zenith angle of 90.93º where magnetometer data has shown the field to be mainly horizontal, parallel to the surface of Titan (a case discussed in Chapter 5). The ion production rates are used in the chemical models presented in Chapter 5.

$$Q_e(z) = \int_{E_T}^{\infty} \Phi_e(z, E) \left(\frac{dE}{dz}\right)_e dE \qquad \textbf{(3.6)}$$

$$\left(\frac{dE}{dz}\right)_e = \frac{3.37\ x\ 10^{-12}}{E^{0.94} n_e^{0.03}} \left(\frac{E - E_e}{E - 0.53E_e}\right)^{2.36} \qquad \textbf{(3.7)}$$

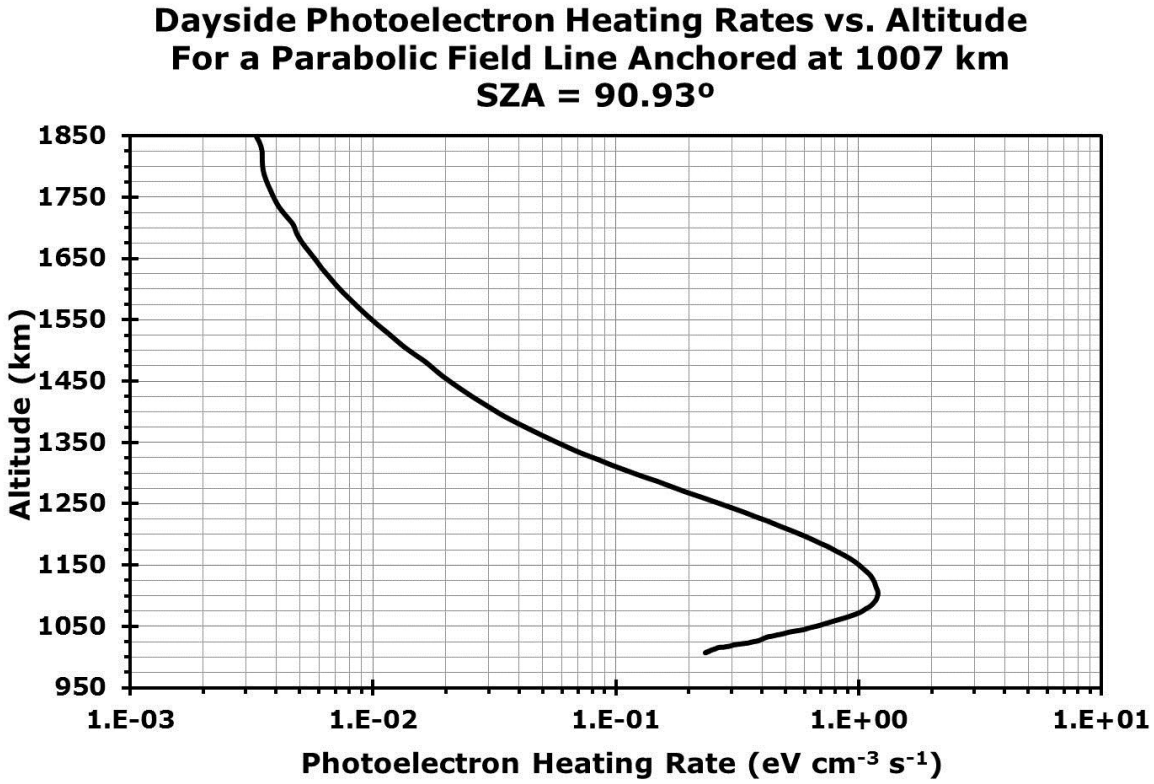

Figure 3.16 Heating rate of thermal electrons by photoelectrons for the dayside/terminator case (T18). The majority of energy is deposited between altitudes of 950 and 1250km, generally consistent with the location of the ionospheric density peak [cf. *Robertson et al*., 2009].

3.3.2 Electron Impact Cross Sections

This subsection details the electron-impact ionization cross sections used in this study for molecular nitrogen and methane. An analytical approach to finding these cross sections and graphs appear below.

3.3.2.1 General Analytical Approach

Following the methodology of *Gan et al.* [1992], the inelastic electron impact cross sections σ for a species j with an electron of energy E are calculated using the parametric formula of *Green and Dutta* [1967]

$$\sigma_j(E) = \frac{q_0 f_0 C_0}{W^2}\left(\frac{W}{E}\right)^{\Omega}\left[1 - \left(\frac{W}{E}\right)^{\beta}\right]^{\nu} \qquad \textbf{(3.8)}$$

which can accurately represent experimental data. In Equation (3.8), $q_0 = 4\pi a_0 R^2 = 6.514 \times 10^{-14}$ eV^2cm^2 with a_0 and R representing the Bohr radius and Rydberg energy respectively. The remaining parameters (f_0C_0, W, Ω, β, and ν) are known as the Generalized Optical Strength (GOS) parameters.

For the differential ionization cross section S of a species j as a function of the energy E of the electron j collides with and the energy T of the released secondary electron the expression developed by *Green and Sawada* [1972] is implemented.

$$S_j(E,T) = \frac{A(E)\Gamma^2(E)}{[T - T_0(E)]^2 + \Gamma^2(E)} \qquad \textbf{(3.9)}$$

$$A(E) = \left(\frac{K}{E + K_B}\right)\ln\left(\frac{E}{J} + J_B + \frac{J_C}{E}\right) \qquad \textbf{(3.10)}$$

$$\Gamma(E) = \Gamma_s\frac{E}{E + \Gamma_B} \qquad \textbf{(3.11)}$$

$$T_0(E) = T_s - \frac{T_A}{E + T_B} \qquad \textbf{(3.12)}$$

In the above equations K, K_B, J, J_B, J_C, Γ_S, Γ_B, T_S, and T_B are adjustable parameters. To obtain the total ionization cross section $\sigma_j(E)$ of species j as a function of the initial electron energy E, Equation (3.9) is integrated over T from 0 to $T_M = (E-I)/2$ where I is the ionization threshold energy yielding:

$$\sigma_j(E) = A(E)\Gamma(E)\left[\tan^{-1}\frac{T_M - T_0}{\Gamma} + \tan^{-1}\frac{T_0}{\Gamma}\right] \qquad \textbf{(3.13)}$$

Although graphs of the cross sections are presented below, tables of the parameters used in this study appear in Appendix B-2.

3.3.2.2 Electron Impact Cross Sections for N_2

Elastic electron differential cross sections are calculated from the values of *Trajemar et al*. [1983] and *Solomon et al.* [1988] and have been integrated by *Gan et al.* [1992] in order to obtain the backscatter probabilities and the elastic cross section as a function of energy for electron-N_2 collisions shown in Figure 3.17.

The sum of vibrational excitations of molecular nitrogen through inelastic collisions was taken from *Porter et al.* [1976]. For the cross section of the A, B, B', W, C, a, a' and W states the revised cross sections of *Cartwright et al.* [1977] by *Trajmar et al.* [1983] were used. The cross sections of the b' and $^1\Pi_u$ were obtained from *Zipf and McLaughlin* [1978]. The sum of the Rydberg states was derived by normalizing the values from *Green and Stolarski* [1972] to the total dissociation cross sections of *Zipf and McLaughlin* when they are added to the cross sections of the b' and $^1\Pi_u$ states. A representation of the excitation cross sections appears in Figure 3.18 and the GOS parameters for these cross sections appear in Appendix B-2.

The ionization cross sections of *Tabata et al.* [2006] and *Itikawa* [2006] are found to be in good agreement with one another and so their results were used in the current work. The cross sections for total ionization, ionization of N_2 forming N_2^+ and ionization of N_2 forming N^+ are shown below in Figure 3.19, Figure 3.20 and Figure 3.21.

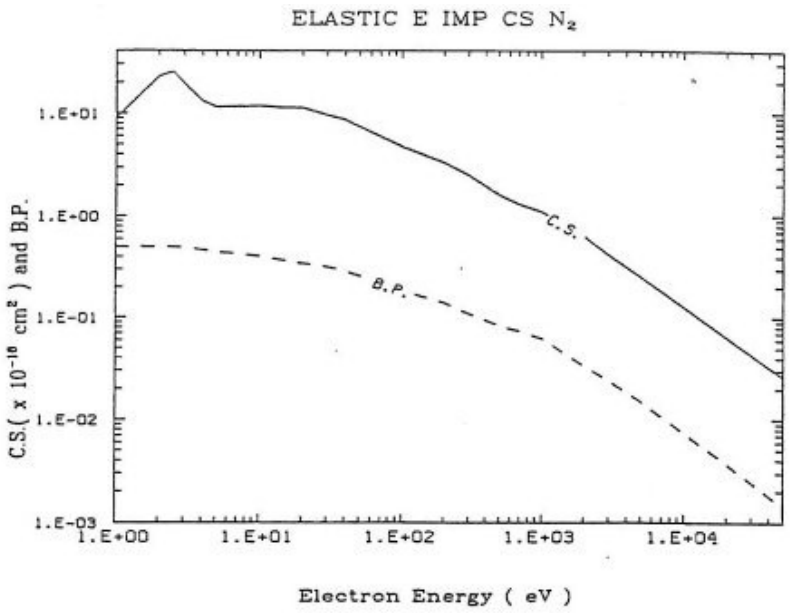

Figure 3.17 Total elastic cross section (C.S.) and backscatter probability (B.P.) for electron collisions with N_2. (From *Gan* [1991])

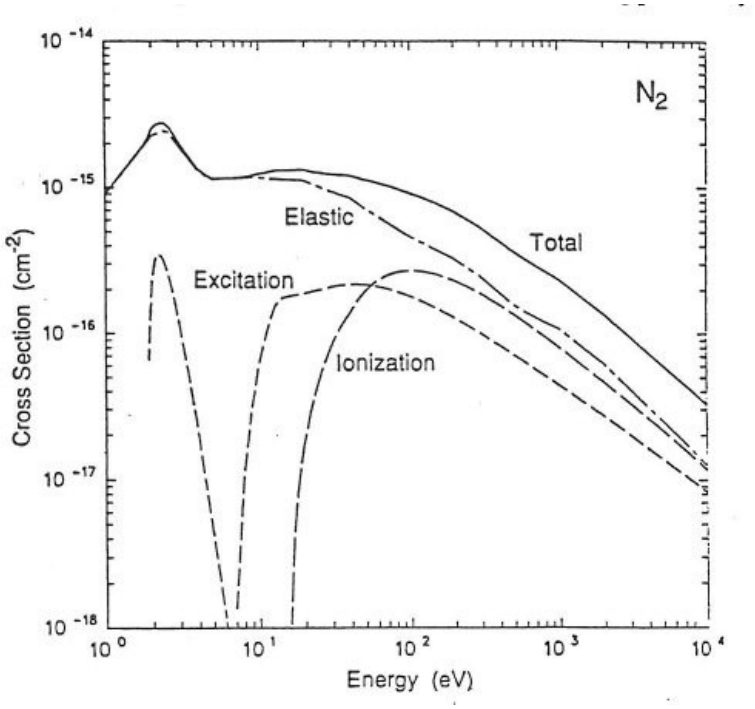

Figure 3.18 Electron impact cross sections of N_2. Note that even though this figure displays the ionization cross section, this study uses the electron impact ionization cross sections from *Itikawa* [2006]. (From *Solomon et al.* [1988])

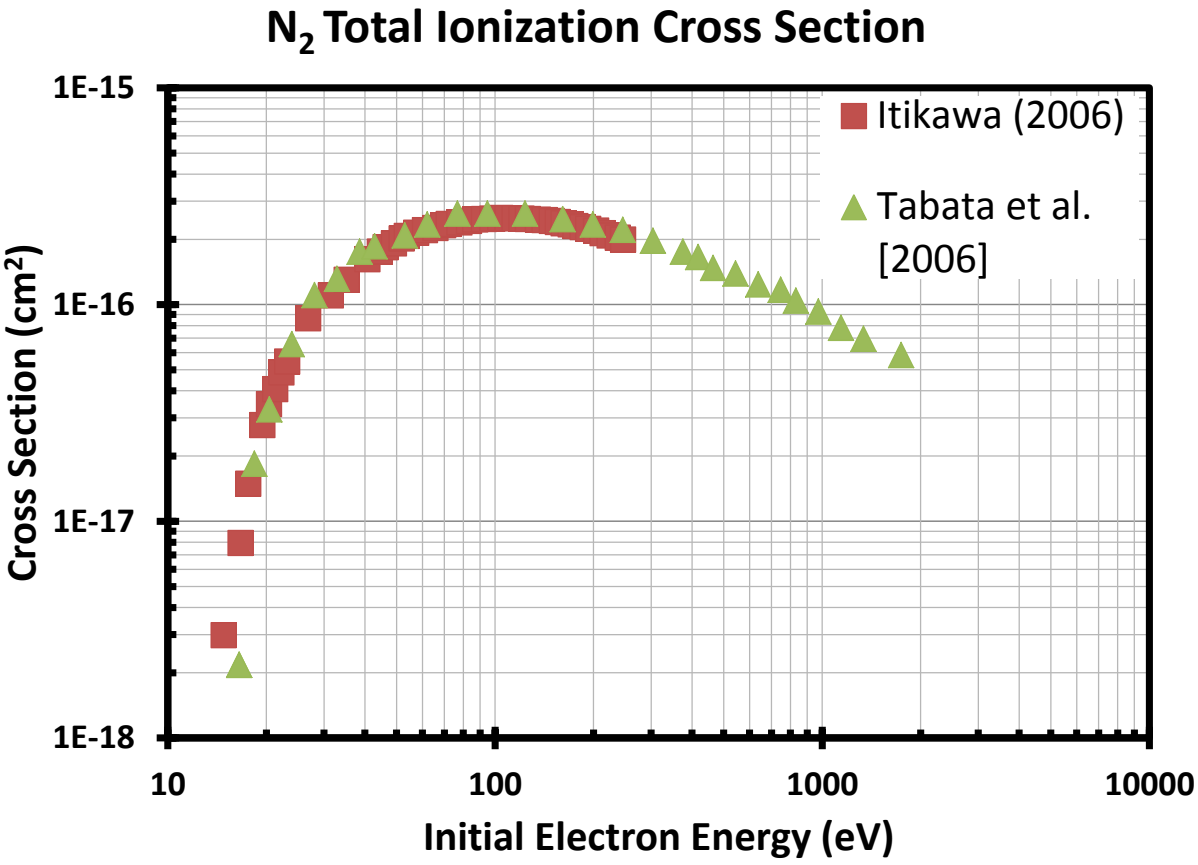

Figure 3.19 Total Electron impact ionization cross sections of N_2. Data is shown from *Tabata et al.* [2006] (green triangles) and *Itikawa* [2006]. (red squares).

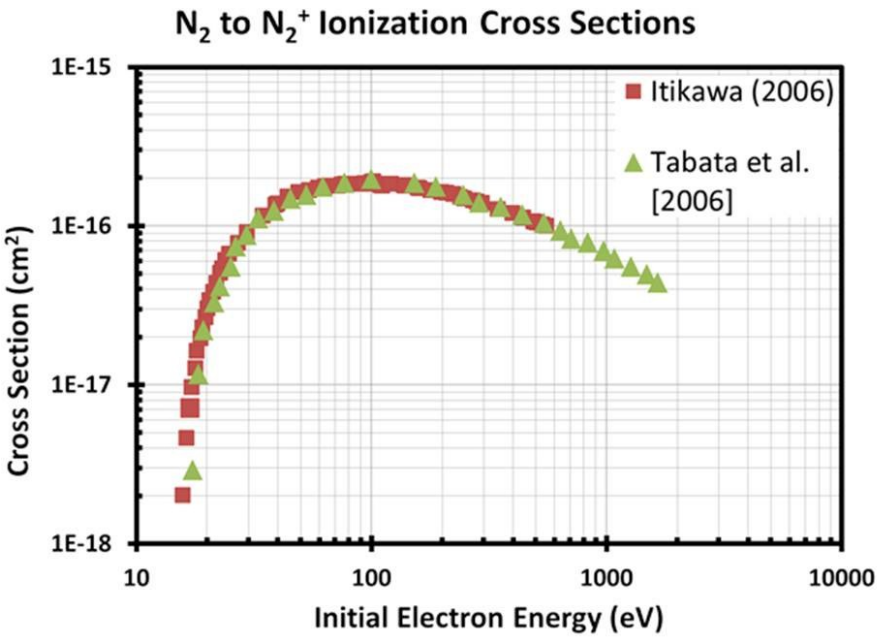

Figure 3.20 Electron impact ionization cross sections of N_2 to N_2^+. Data is shown from *Tabata et al.* [2006] (green triangles) and *Itikawa* [2006]. (red squares).

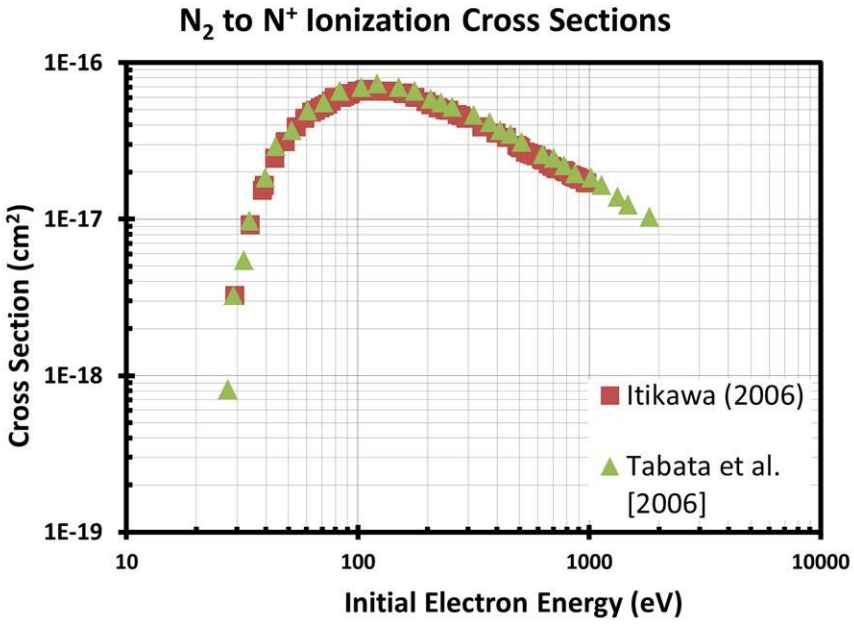

Figure 3.21 Electron impact ionization cross sections of N_2 to N^+. Data is shown from *Tabata et al.* [2006] (green triangles) and *Itikawa* [2006]. (red squares).

3.3.2.3 Electron Impact Cross Sections for CH_4

Differential elastic electron-impact cross sections of methane have been taken from the theoretical work of *Jain* [1986] over energy ranges from 0.1–1 eV, 2.5-20 eV, and 30–400 eV. Backscattering probabilities, integrated cross sections and momentum transfer cross sections have been calculated from these results and are shown in Figure 3.22.

The dominant vibrational modes for CH_4 are denoted as v_1, v_2, v_3, and v_4; however the difference in energy thresholds of v_1 and v_3 and that of v_2 and v_4 are unresolved. Due to this, a combination of vibrational states $v_{1,3}$ and $v_{2,4}$ are used with threshold energies of 0.367 eV and 0.175 eV. The results of *Tanaka et al.* [1983] are used for the differential cross sections above 2 eV. Measurements are provided between 3 and 20 eV while the following extrapolations are used for energies above 20 eV:

$$\sigma_T^{v1,3}(E) = 265.4E^{-0.871} \quad \textbf{(3.14)}$$

$$\sigma_M^{v1,3}(E) = 91.16E^{-0.491} \quad \textbf{(3.15)}$$

$$\sigma_T^{v2,4}(E) = 157.57E^{-0.868} \quad \textbf{(3.16)}$$

$$\sigma_M^{v2,4}(E) = 56.44E^{-0.477} \quad \textbf{(3.17)}$$

where σ is in units of 10^{-18} and E is in eV. Their vibrational excitation cross section at 2 eV is taken from those of *Rohr* [1980] and for energies below 2 eV cross sections are used from the measurements of *Sohn et al.* [1983]. The compilation of the vibrational excitation cross sections appears in Figure 3.23.

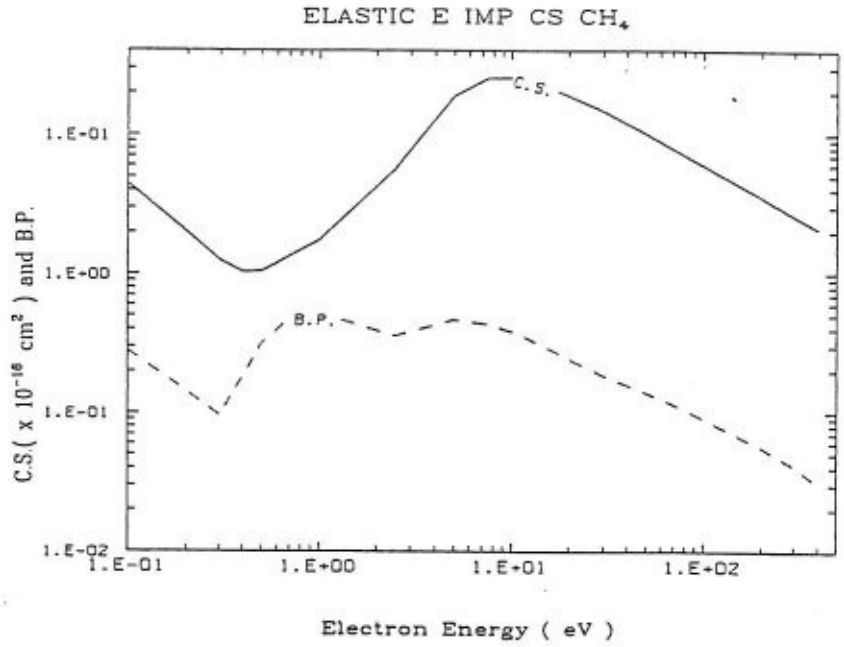

Figure 3.22 Total elastic cross section (C.S.) and backscatter probability (B.P.) for electron collisions with CH_4. (From *Gan* [1992])

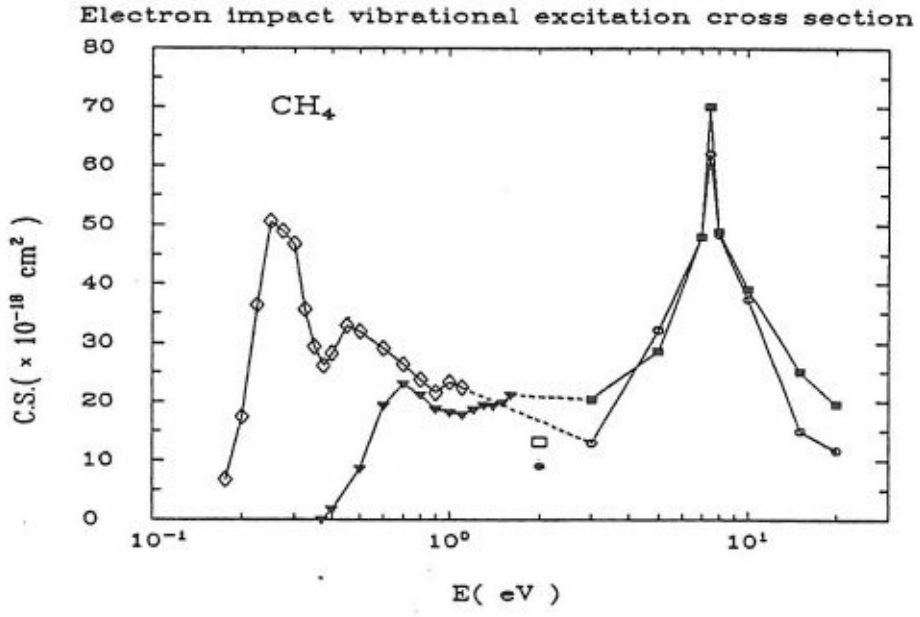

Figure 3.23 Compilation of vibrational excitation for CH_4. Solid symbols represent cross sections for the $v_{1,3}$ state while open symbols are for $v_{2,4}$. Below 2 eV the values from *Sohn et al.* [1983] are used. At 2 eV the cross section of *Rohr* [1980] is implemented. Cross sections from or derived from *Tanaka et al.* [1983] are used above 2 eV. (From [*Gan et al.*, 1992])

The electronic excitation cross sections of methane are fit to Equation (3.8) using GOS parameters derived from the measurements of *Vuskovic and Trajmar* [1983] (Figure 3.24). *Vuskovic and Trajmar* presented cross sections measured at 20, 30, and 200 eV. The GOS parameters for electronic excitation via electron impact appear in Appendix B-2.

Rotational excitation cross sections for methane are taken from the theoretical work of *Jain and Thompson* [1983] and multiplied by a factor of 2 in order to bring their work into better agreement with measurements of *Muller et al.* [1985], *Brescansin et al.* [1989], and *Shimamura* [1983] (Figure 3.25). Only the results for transitions from the J=0 to the J=3 and 4 rotational states are shown. Nuclear spin statistics dictate that the change in angular momentum J_t cannot be 1, 2, or 5 [*Herzberg*, 1945].

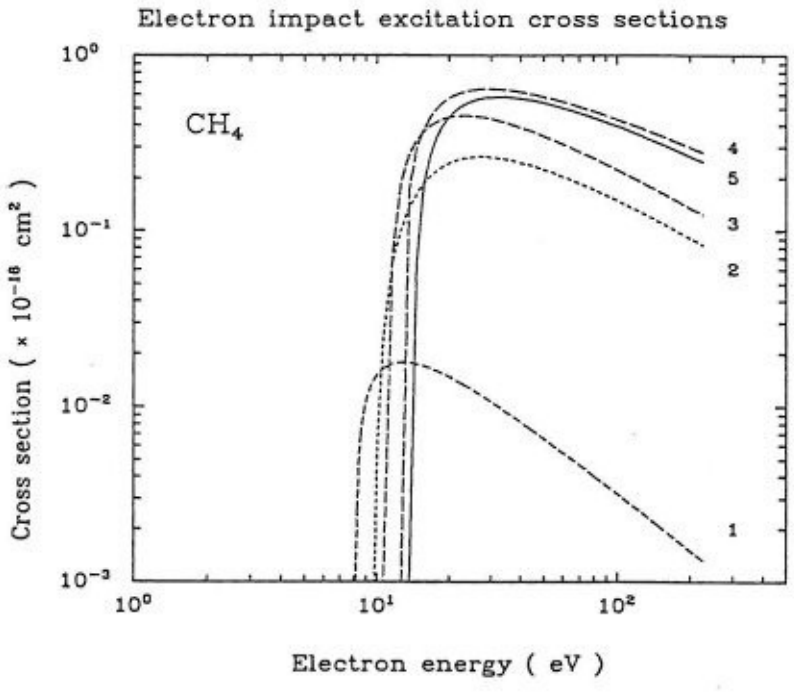

Figure 3.24 Electron impact cross sections for electronic excitation of CH_4 based on measurements of *Vuskovic and trajmar* [1983]. From *Gan et al.* [1992]. The numbers next to the curve indicate the excited state.

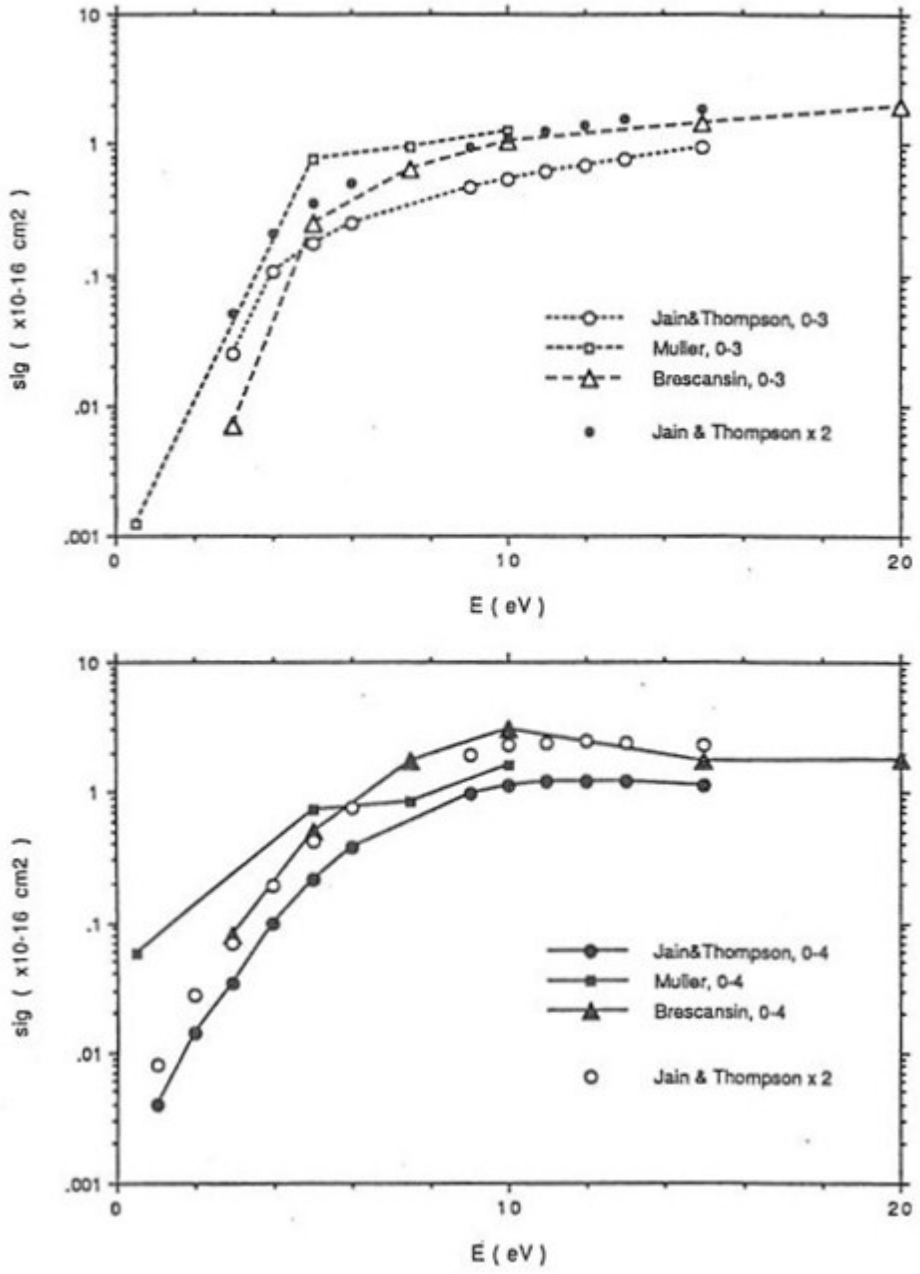

Figure 3.25 Electron impact cross sections for the rotational excitation of methane for the 0→ 3 (upper panel) and the 0→4 (lower panel) transitions. The values of *Jain and Thompson* [1983] multiplied by 2 (open circles) are the adopted values. (From [*Gan*, 1991])

Seven products resulting from the ionization of methane are considered in this study CH_4^+, CH_3^+, CH_2^+, CH^+, C^+, H_2^+ and H^+). Cross sections for these processes resulting from collisions with electrons have been reviewed by *Liu and Shemansky* [2006], whose results have indicated a preference for the cross sections of *Straub et al.* [1997] as revised by *Lindsay and Mangan* [2003]. The current code uses the two different implementations of the cross sections as a result of past coding decisions *Gan et al.* [1992]. First, curves fit to the data using the GOS parameters in Equation (3.13) are used to calculate energy absorption and electron heating and cooling rates. For calculating the ion production rates, direct extrapolations of the data of *Lindsay and Mangan* were used. Beginning with Figure 3.26 and ending with Figure 3.32 the cross sections for methane ionization via electron impact are presented. Parameters for the fitting equations and a table of the cross sections appear in Appendix B-2.

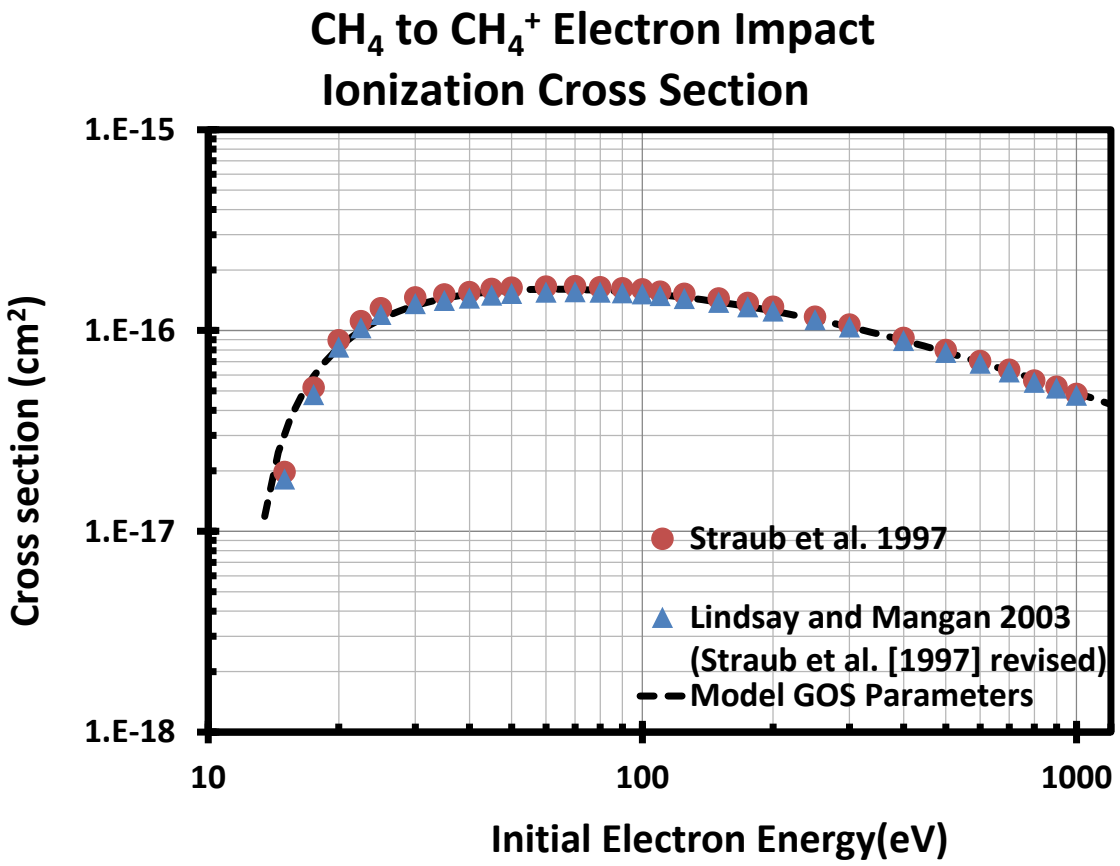

Figure 3.26 Cross sections for the electron impact ionization of methane producing CH_4^+. Red circles indicate the values of *Straub et al.* [1997], blue triangles represent the revised cross sections of *Straub et al.* [*Lindsay and Mangan*, 2003] that are used in this work and the dashed line shows the fit to the revised values using the GOS parameters.

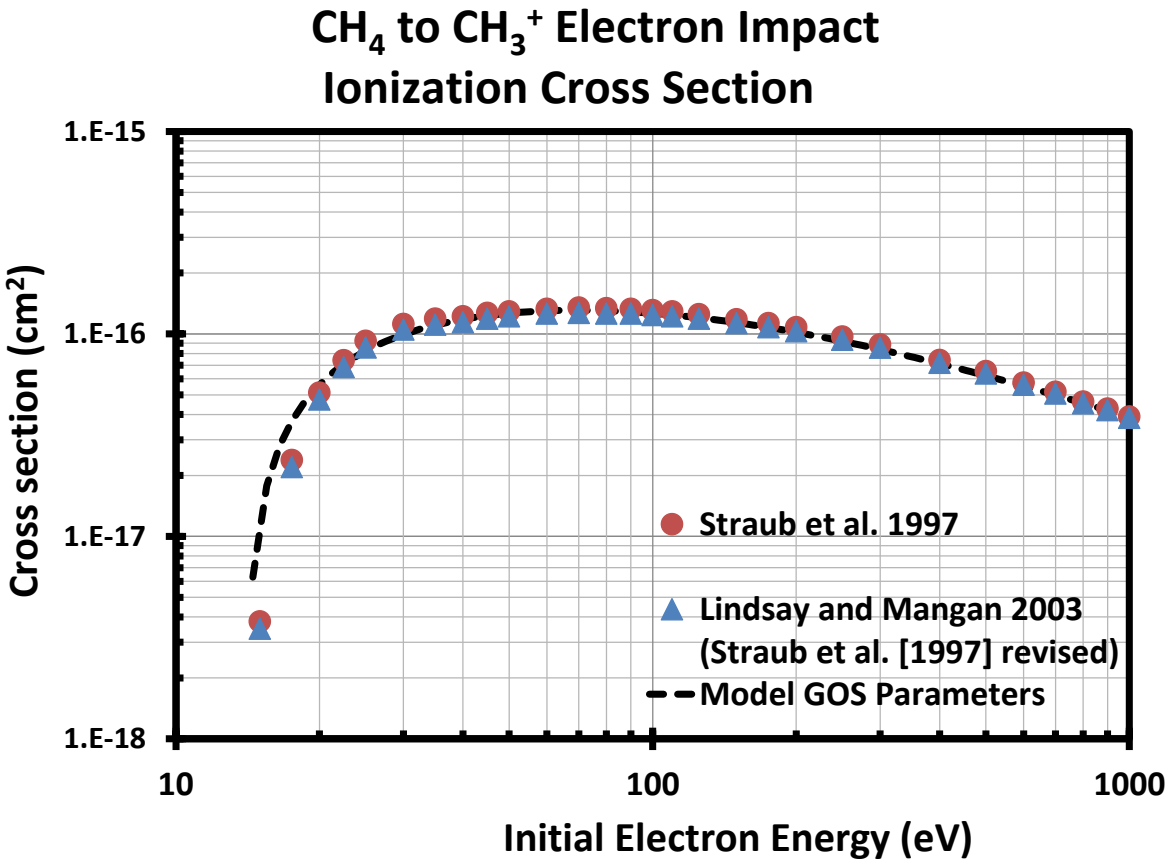

Figure 3.27 Cross sections for the electron impact ionization of methane producing CH_3^+. Red circles indicate the values of *Straub et al.* [1997], blue triangles represent the revised cross sections of *Straub et al.* [*Lindsay and Mangan*, 2003] that are used in this work and the dashed line shows the fit to the revised values using the GOS parameters.

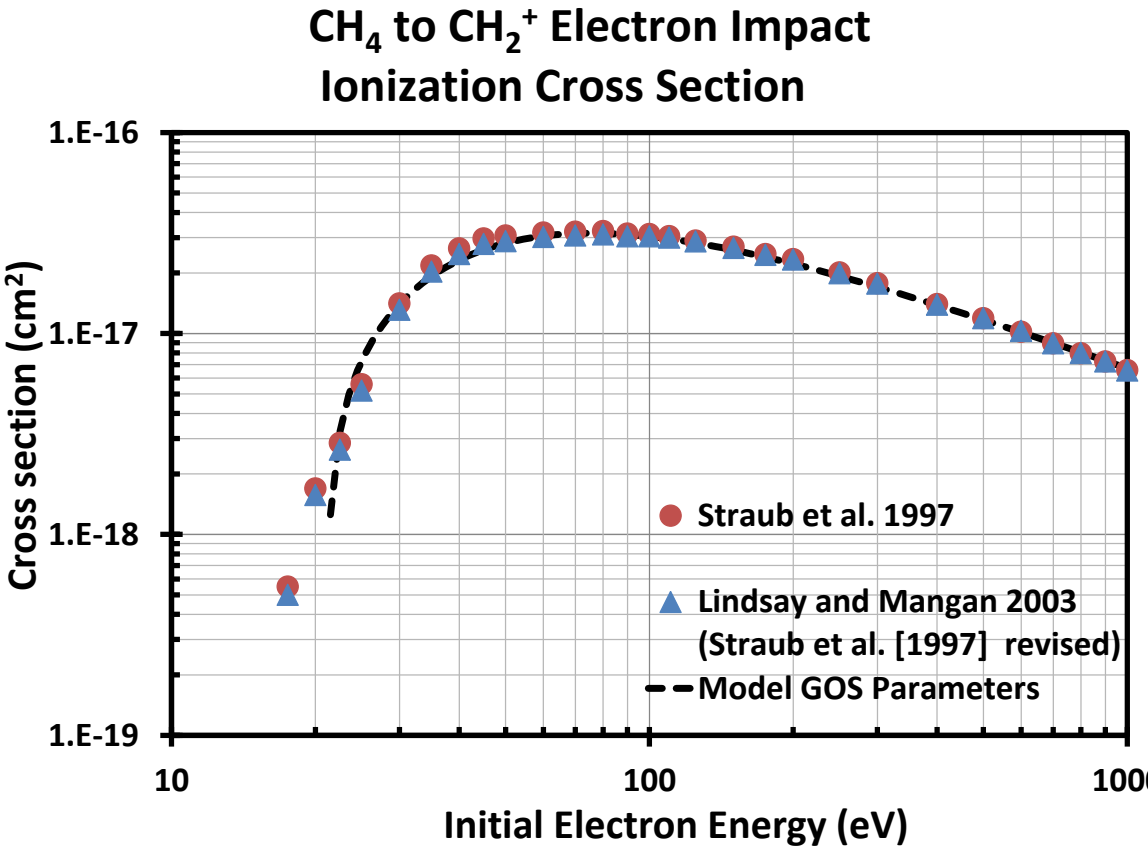

Figure 3.28 Cross sections for the electron impact ionization of methane producing CH_2^+. Red circles indicate the values of *Straub et al.* [1997], blue triangles represent the revised cross sections of *Straub et al.* [*Lindsay and Mangan,* 2003] that are used in this work and the dashed line shows the fit to the revised values using the GOS parameters.

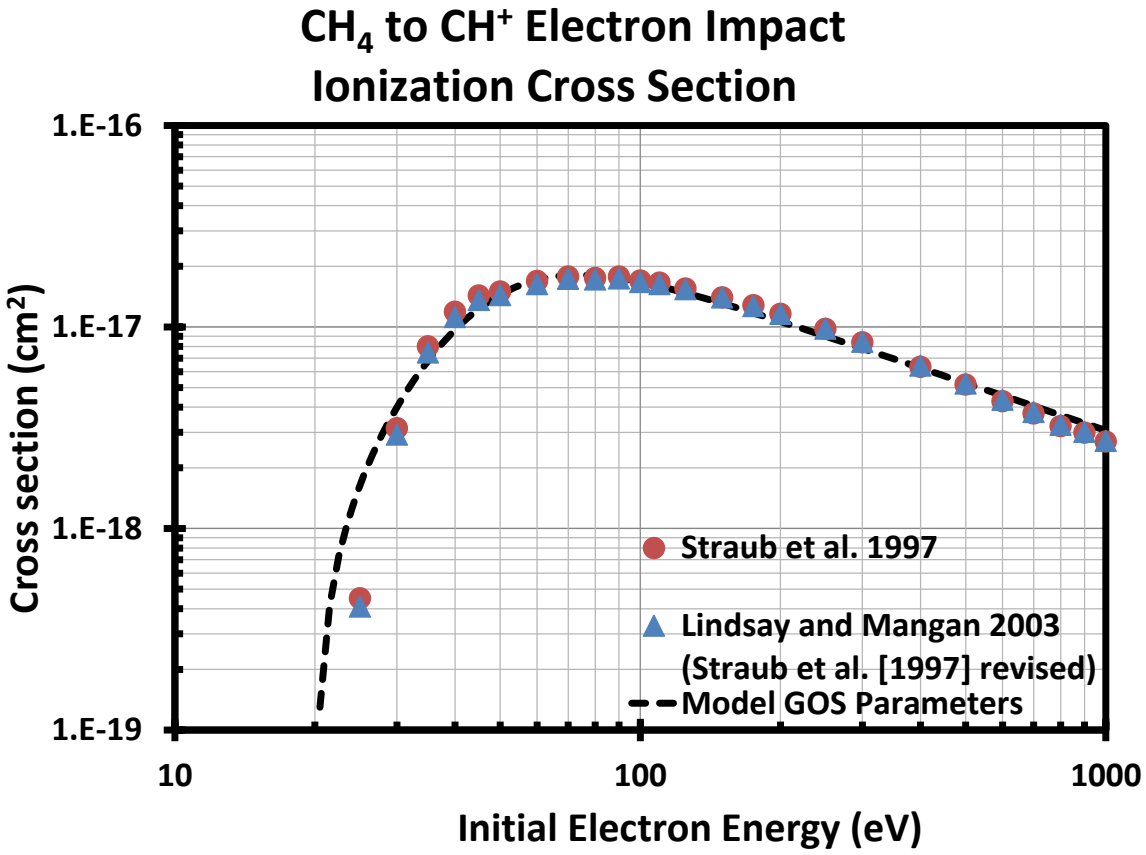

Figure 3.29 Cross sections for the electron impact ionization of methane producing CH^+. Red circles indicate the values of *Straub et al.* [1997], blue triangles represent the revised cross sections of *Straub et al.* [*Lindsay and Mangan,* 2003] that are used in this work and the dashed line shows the fit to the revised values using the GOS parameters.

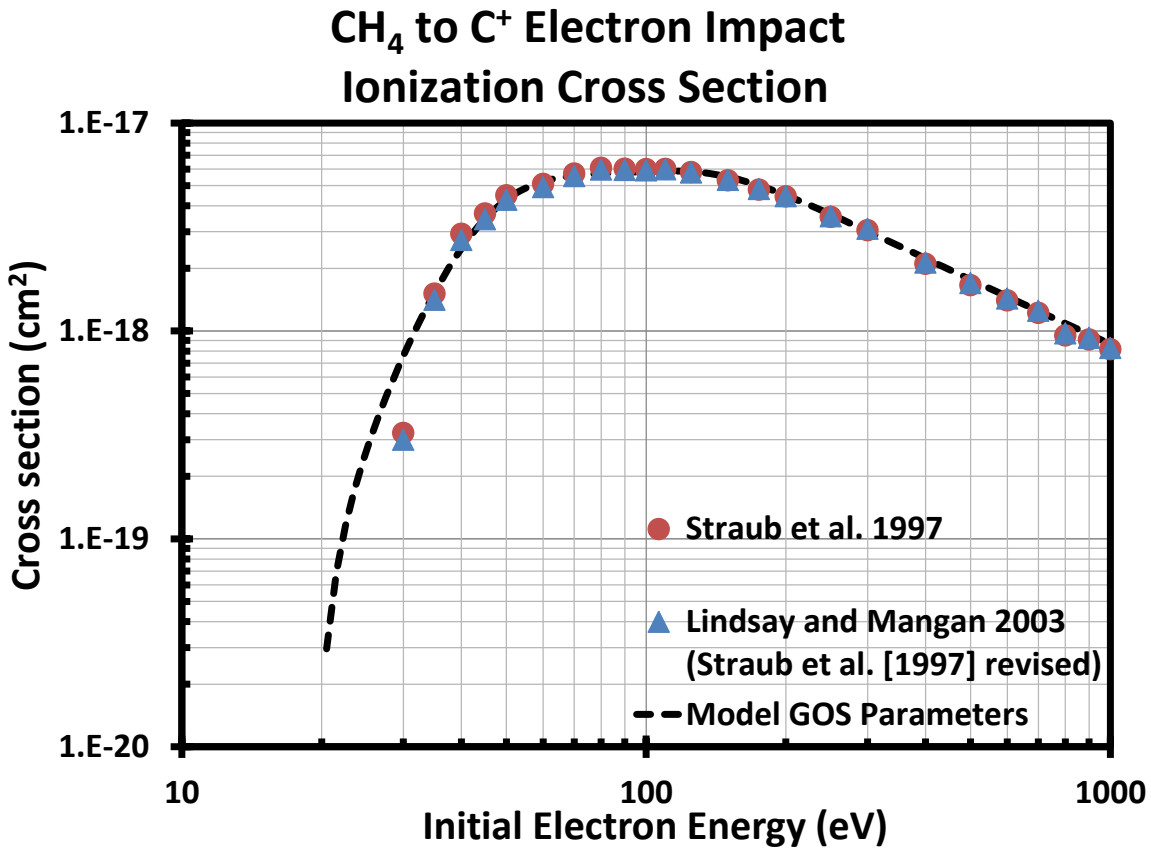

Figure 3.30 Cross sections for the electron impact ionization of methane producing C^+. Red circles indicate the values of *Straub et al.* [1997], blue triangles represent the revised cross sections of *Straub et al.* [*Lindsay and Mangan*, 2003] that are used in this work and the dashed line shows the fit to the revised values using the GOS parameters.

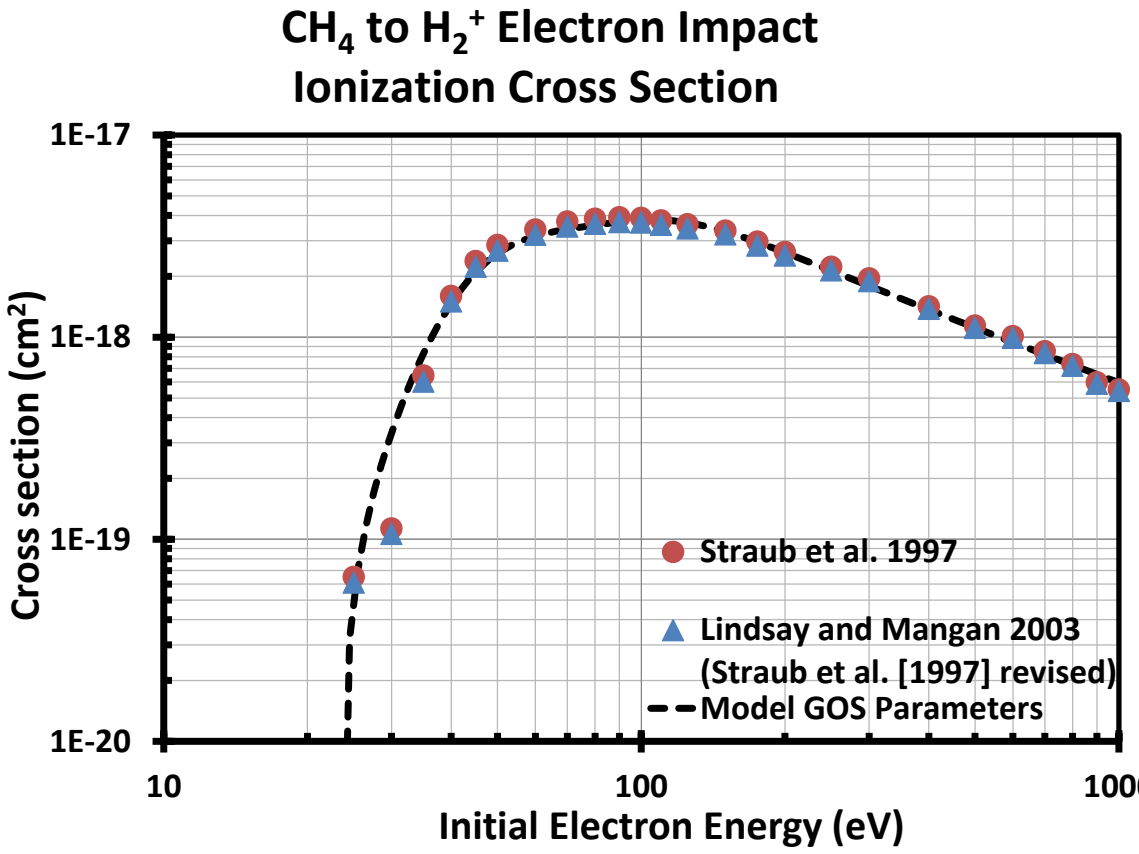

Figure 3.31 Cross sections for the electron impact ionization of methane producing H_2^+. Red circles indicate the values of *Straub et al.* [1997], blue triangles represent the revised cross sections of *Straub et al.* [*Lindsay and Mangan*, 2003] that are used in this work and the dashed line shows the fit to the revised values using the GOS parameters.

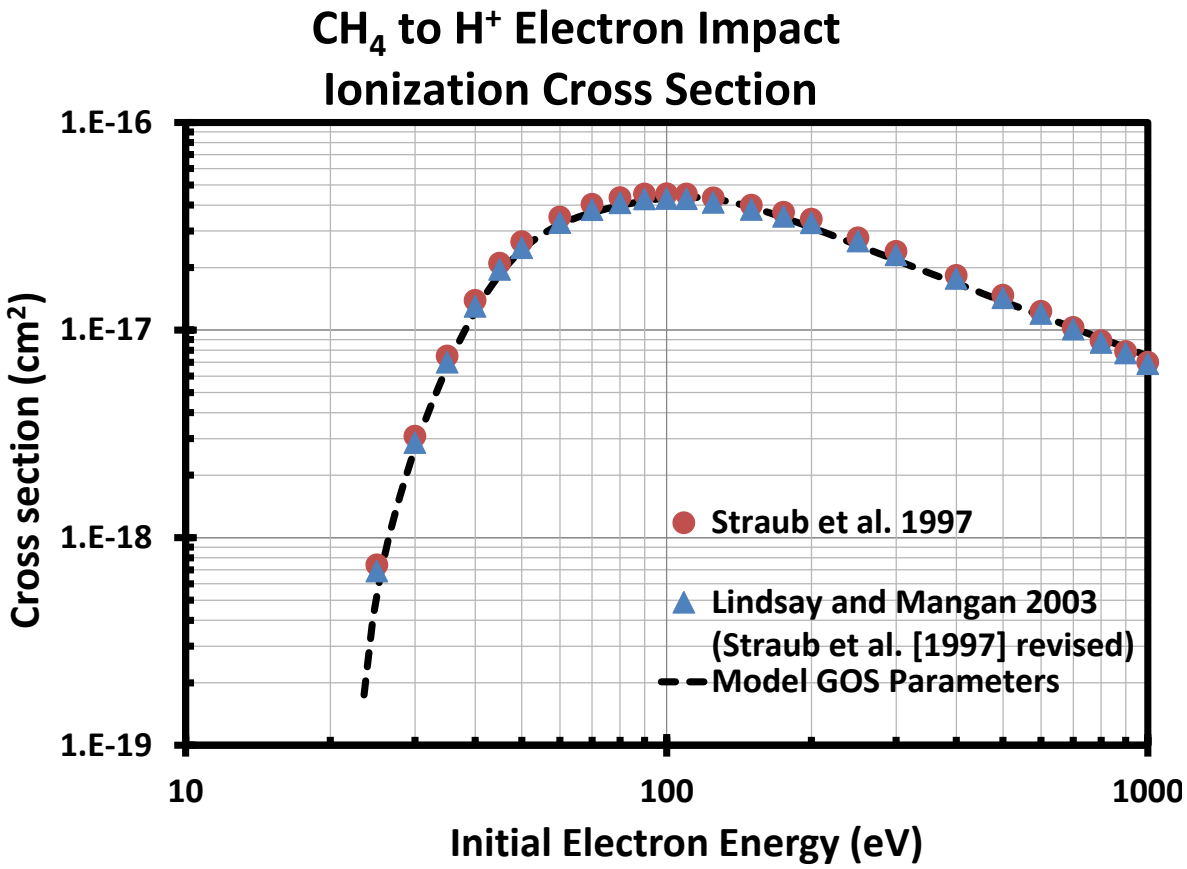

Figure 3.32 Cross sections for the electron impact ionization of methane producing H^+. Red circles indicate the values of *Straub et al.* [1997], blue triangles represent the revised cross sections of *Straub et al.* [*Lindsay and Mangan*, 2003] that are used in this work and the dashed line shows the fit to the revised values using the GOS parameters.

3.4 Photochemical Modeling

The Cassini spacecraft is equipped with mass spectrometers to measure the ion density (see Chapter 2). Thus, a chemical model of the ionosphere that combines ion-neutral chemistry with the ion production rates generated in the photoionization and two-stream codes is necessary to create an ion density profile that can be compared directly to INMS and CAPS measurements. For this a photochemical model is needed which balances the ion production rate from chemical pathways, photoionization and electron-impact ionization with ion loss rates from dissociative electron recombination and reactions with neutral ions at each altitude for 136 ion species and 38 neutral species. In a purely photochemical model transport of ions between altitudes as a result of the bulk motion of plasma is not included. In this section the workings of the photochemical model will be examined. Specific ion chemistry will be discussed in Section 3.5 and a complete list of reactions in tabular form can be found in Appendix C.

3.4.1 Description of Model

The photochemical ionospheric model (Figure 3.1) is derived from the earlier photochemical models of *Keller et al.* [1992, 1998], *Cravens et al.* [2004], and *Robertson et al.* [2009]. This model is time-independent and does not include ion transport between altitudes as a result of bulk plasma flow. The production of ions is governed by photoionization, electron-impact ionization, and chemical reactions while the loss processes are dictated by chemical loss processes and electron dissociative recombination. Production and loss processes are assumed to be in equilibrium, an assumption that is valid below 1350 km [*Ma et al*. 2006,2009; *Cravens et al,* 2010], and solutions for the neutral densities are obtained using Newton-Raphson iterative techniques [*Press et al*., 1986] for altitudes between 725 and 2715 km in 10 km intervals. Primary (caused by photoionization) and secondary (caused by electron impact ionization)

production rates of ions have been calculated as a function of altitude (Sections 3.2 and 3.3) and used as inputs in the photochemical model along with a neutral atmosphere (see Section 3.4.2), an ion neutral reaction scheme (shown in Appendix C-1) and dissociative electron recombination rates (see Appendix C-2).

3.4.2 Neutral Densities

This subsection details how the neutral densities used in the model were obtained.

3.4.2.1 Flyby Specific Densities

For the major neutral ion species (N_2, CH_4 and H_2) density measurements made by the INMS instrument during ingress of each flyby were used in this model (See Figure 3.33 through Figure 3.38 for neutral density measurements for flybys considered in this study). INMS measurements taken during egress have been shown to be less accurate due to potential sticking effects of ions as they make their way through the antechamber in the instrument [*Magee et al.,* 2009; *Westlake et al.,* 2011, 2012]. Profiles of the major neutral species for the Titan flybys studied appear below. Major neutral densities in the figures above have been multiplied by a factor of 3.15 in order to account for a possible recalibration of the INMS instrument [c.f. *Robertson et al.* 2009; *Westlake et al,.*2011, 2012; *Waite et al.*, 2013, in preparation].

To determine the neutral density of the remaining 35 species the mixing ratio profiles of *Krasnopolsky* [2009], or *Lavvas et al.* [2011] for the case of CH_2NH, were anchored to mixing ratios reported by *Magee et al.*[2009], *Cui et al.* [2009b], *Robertson et al.* [2009] or fit as a model parameter (see Table 3.3). If the neutral density was treated a model parameter the mixing ratio was set such that the ion spectrum created with the neutral density profile would be in relatively good agreement with INMS measurements at the ionospheric peak.

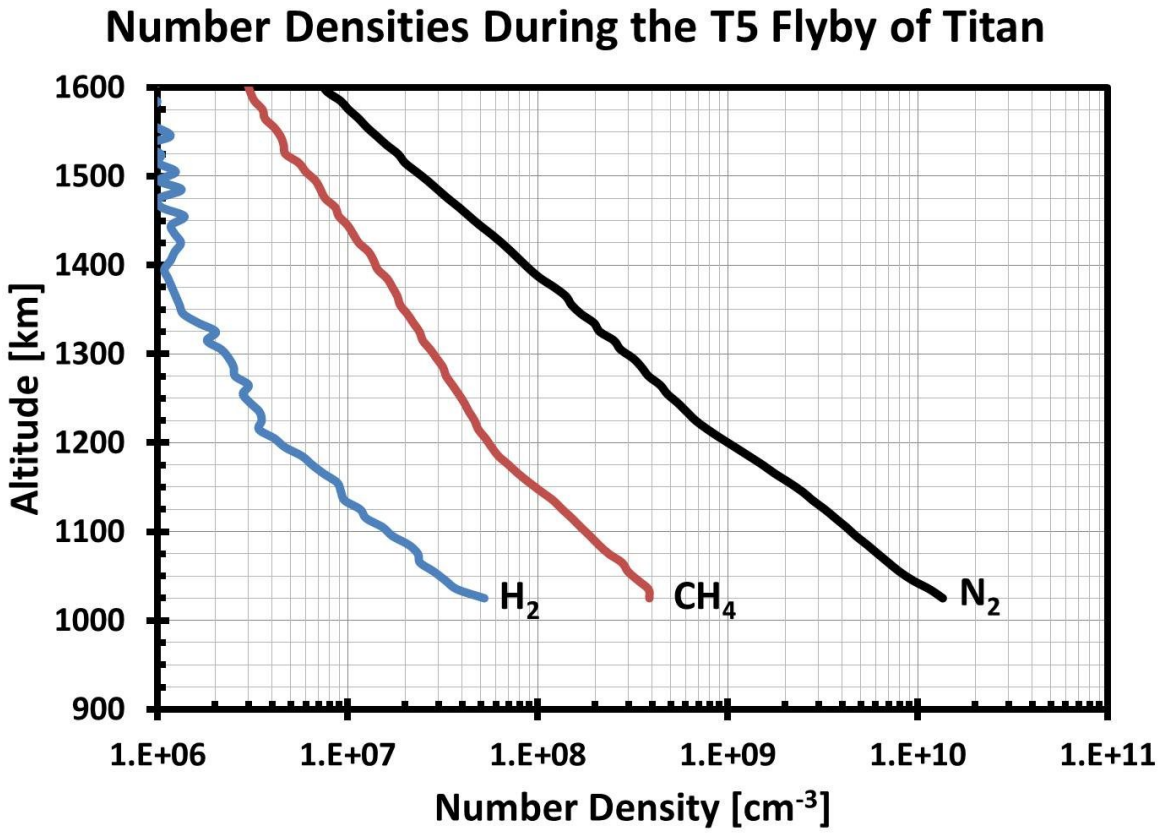

Figure 3.33 Number Density of major neutral species derived from INMS measurements for the T5 flyby of Titan. N_2, CH_4 and H_2 are indicated by the black, red and blue line respectively. The number densities have been multiplied by a factor of 3.15 in this figure in order to account for a potential recalibration of the INMS instrument.

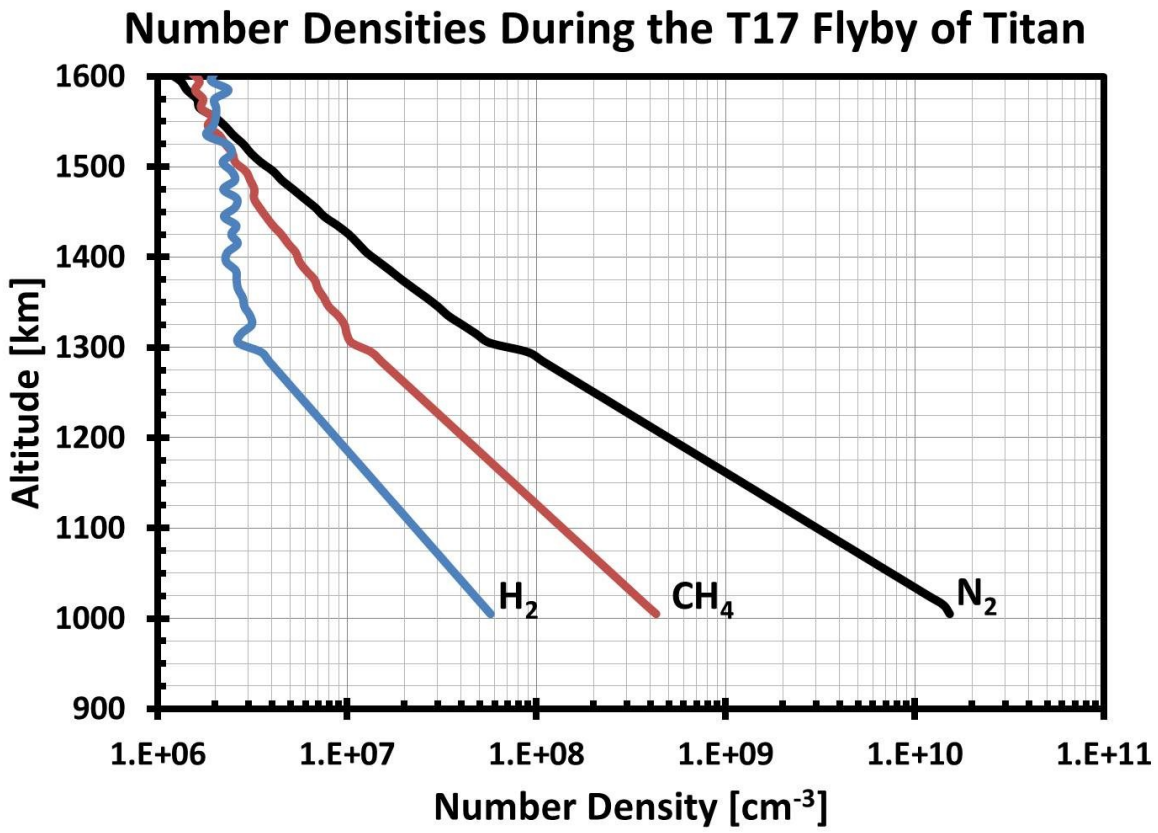

Figure 3.34 Number Density of major neutral species derived from INMS measurements for the T17 flyby of Titan. N_2, CH_4 and H_2 are indicated by the black, red and blue line respectively. The number densities have been multiplied by a factor of 3.15 in this figure in order to account for a potential recalibration of the INMS instrument.

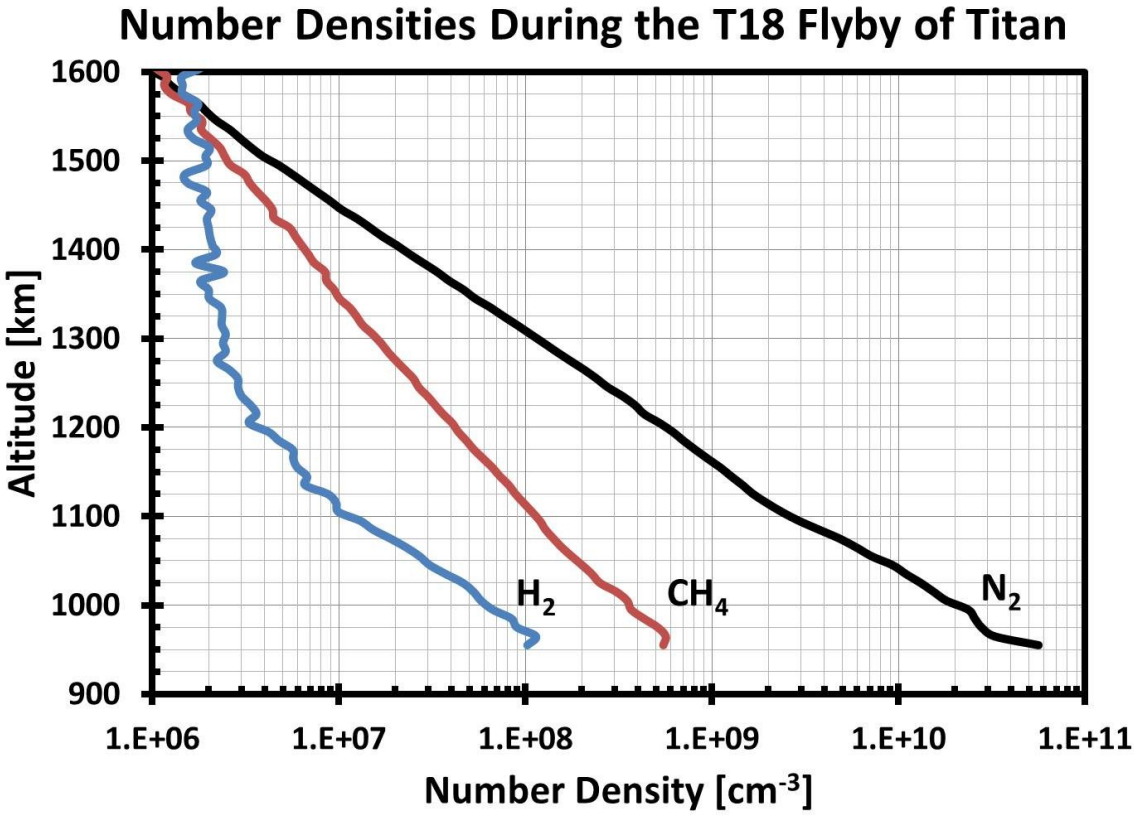

Figure 3.35 Number Density of major neutral species derived from INMS measurements for the T18 flyby of Titan. N_2, CH_4 and H_2 are indicated by the black, red and blue line respectively. The number densities have been multiplied by a factor of 3.15 in this figure in order to account for a potential recalibration of the INMS instrument.

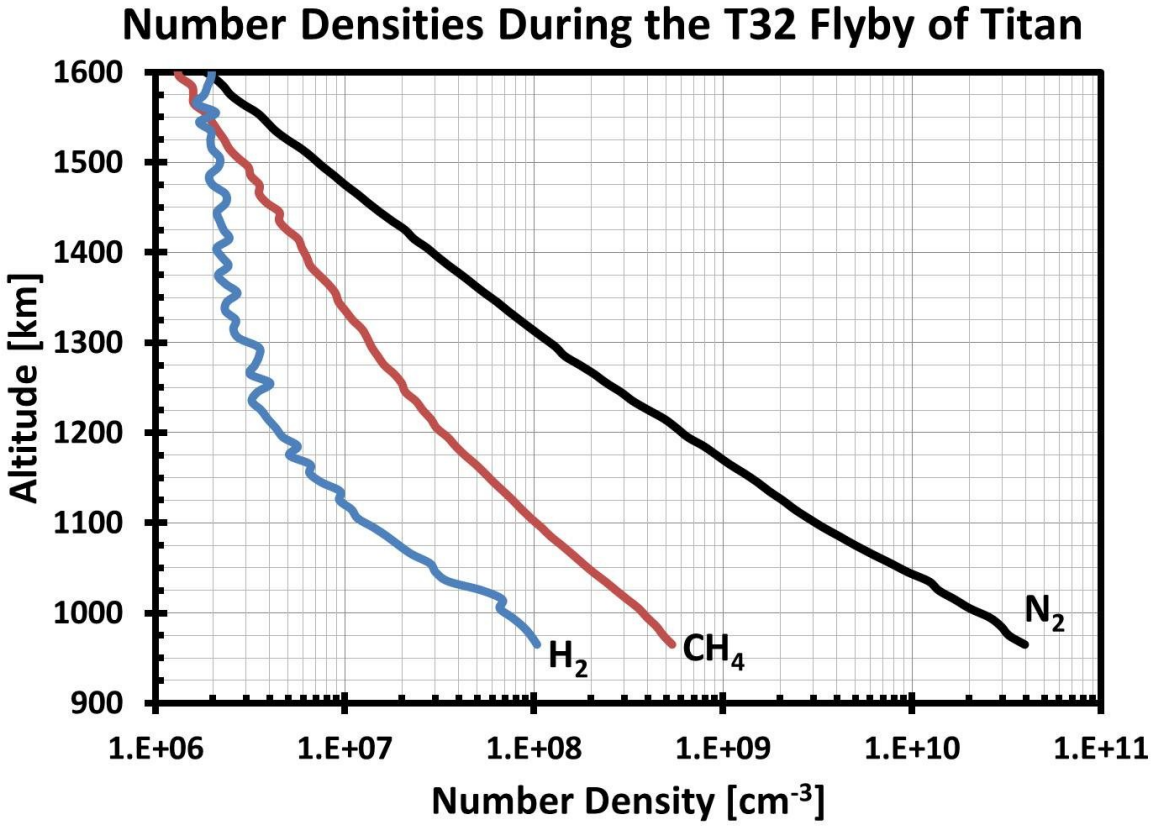

Figure 3.36 Number Density of major neutral species derived from INMS measurements for the T32 flyby of Titan. N_2, CH_4 and H_2 are indicated by the black, red and blue line respectively. The number densities have been multiplied by a factor of 3.15 in this figure in order to account for a potential recalibration of the INMS instrument.

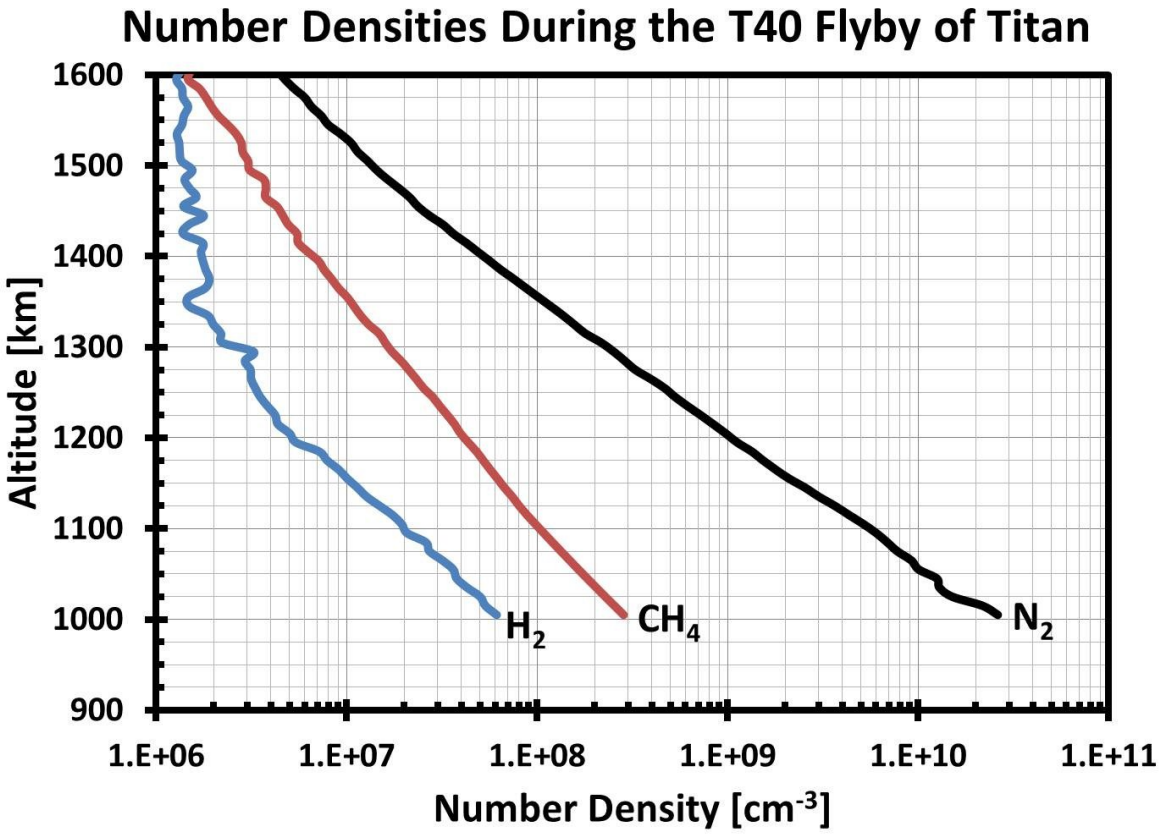

Figure 3.37 Number Density of major neutral species derived from INMS measurements for the T40 flyby of Titan. N_2, CH_4 and H_2 are indicated by the black, red and blue line respectively. The number densities have been multiplied by a factor of 3.15 in this figure in order to account for a potential recalibration of the INMS instrument.

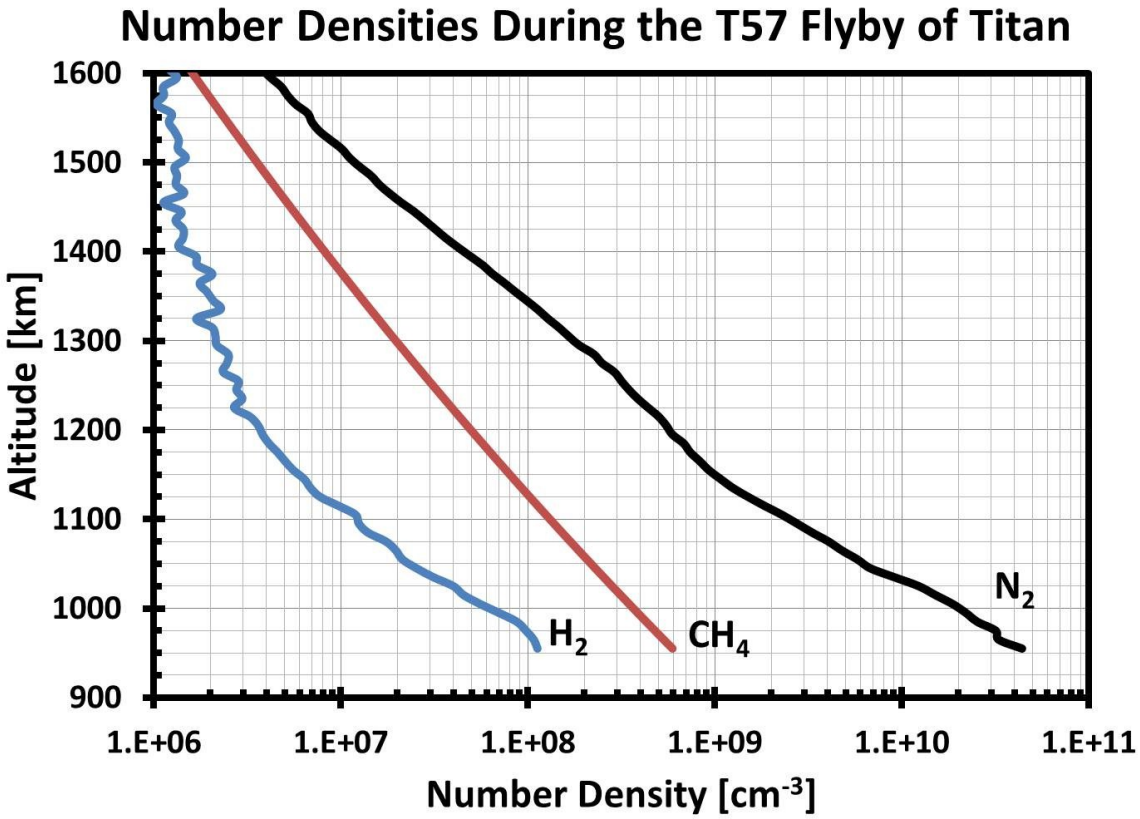

Figure 3.38 Number Density of major neutral species derived from INMS measurements for the T57 flyby of Titan. N_2, CH_4 and H_2 are indicated by the black, red and blue line respectively. The number densities have been multiplied by a factor of 3.15 in this figure in order to account for a potential recalibration of the INMS instrument.

Table 3.3 Mixing ratios for the minor neutral species

Neutral	Mixing Ratio	Anchor Point [km]	Source	Notes
N	6.560E-05	1100	*Robertson et al.* [2009]	
NH	5.920E-04	1100	*Robertson et al.* [2009]	
C_2H_2	3.420E-04	1050	*Magee et al.* [2009]	
C_2H_4	3.910E-04	1050	*Magee et al.* [2009]	
HCN	2.440E-04	1050	*Magee et al.* [2009]	
C_2H_6	4.570E-05	1050	*Magee et al.* [2009]	
H	9.790E-04	1100	*Robertson et al.* [2009]	
C_3HN	1.480E-06	1050	*Magee et al.* [2009]	
C_3H_4	9.200E-06	1050	*Magee et al.* [2009]	
H_2O	2.79E-06	1025	*Cui et al.* [2009b]	
C_3H_8	2.870E-06	1050	*Magee et al.* [2009]	
C_4H_2	5.550E-06	1050	*Magee et al.* [2009]	
CO	7.680E-06	1100	*Robertson et al.* [2009]	
C_3H_6	2.330E-06	1050	*Magee et al.* [2009]	
C_2N_2	2.140E-06	1050	*Magee et al.* [2009]	
C_3H_2	4.320E-05	1100	*Robertson et al.* [2009]	
C_4N_2	2.250E-05	1100	*Robertson et al.* [2009]	
CH_3	2.609E-03	1100	*Robertson et al.* [2009]	
NH_3	4.220E-05	1025	*Cui et al.* [2009b]	
O	0.0E+00	1100	*Robertson et al.* [2009]	
CH_2NH	1.020E-04	1100	*Robertson et al.* [2009]	Profile from *Lavvas et al.* [2011]
CH_3CN	1.510E-06	1025	*Cui et al.* [2009b]	
C_2H_3CN	3.460E-07	1050	*Magee et al.* [2009]	
C_2H_5CN	1.540E-07	1050	*Magee et al.* [2009]	
CH_3NH_2	1.0E-08	1100	*Robertson et al.* [2009]	
C_6H_6	2.480E-06	1050	*Magee et al.* [2009]	

Neutral	Mixing Ratio	Anchor Point [km]	Source	Notes
C_6H_2	8.0E-07	1100	*Robertson et al.* [2009]	
C_7H_4	3.0E-07	1100	*Robertson et al.* [2009]	
C_7H_8	2.510E-08	1050	*Magee et al.* [2009]	
C_8H_2	2.0E-07	1100	*Robertson et al.* [2009]	
C_4H_3N	4.0E-06	1100	*Robertson et al.* [2009]	
HC_5N	1.0E-06	1100	*Robertson et al.* [2009]	
C_5H_5N	4.0E-07	1100	*Robertson et al.* [2009]	
C_6H_3N	3.0E-07	1100	*Robertson et al.* [2009]	profile of C_5H_5N
C_6H_7N	1.0E-07	1100	*Robertson et al.* [2009]	profile of C_5H_5N

3.4.2.2 Global Average Densities

In order to complete generic model runs to obtain ion production rates, profiles of the electron and ion temperature and density for arbitrary solar zenith angles and fluxes of precipitating magnetospheric electrons, a global average model of the neutral atmosphere was developed. As above in Section 3.4.2.1, the densities of N_2, CH_4 and H_2 are derived from in situ measurements made by INMS presented in *Magee et al*. [2009] by applying the basic fitting equation (3.18) used by *Keller et al*. [1992] with the parameters found in Table 3.4 and multiplying the results by a factor of 3.15. Figure 3.39 shows the neutral densities resulting from this parameterization of Equation (3.18) as well as the data of *Magee et al.* [2009]. In Equation (3.18) n is the number density corresponding to altitude r, r_1 is a reference altitude and C is an adjustable fitting parameter.

$$n(r) = n(r_1)\exp\left(-C\left[\frac{1}{r_1} - \frac{1}{r}\right]\right) \qquad \textbf{(3.18)}$$

Table 3.4 Fitting parameters of Equation (3.18) for the major neutral densities

Neutral Species	Reference Altitude [km]	Value of C
N_2	1050	2.2E5
CH_4	1050	1.35E5
H_2	1050	1.7E5
	1245	5.4E4

Spacecraft trajectories set the lower altitude limit of the INMS measurements between 960-1020 km, depending on the flyby, thus a transition region between 785 and 1065 km was used to evenly shift the total neutral number density profile from the flyby specific INMS values extrapolated to lower altitudes to the total atmospheric density profile obtained by the Huygens Atmospheric Structure Instrument (HASI) during its landing on Titan [*Fulchignoni et al*., 2005] (see Figure 3.40). The mixing ratio from the three major neutrals shown in Figure 3.39 and Table 3.3 were used to convert the HASI measured mass densities into number densities for the 38 neutral species considered.

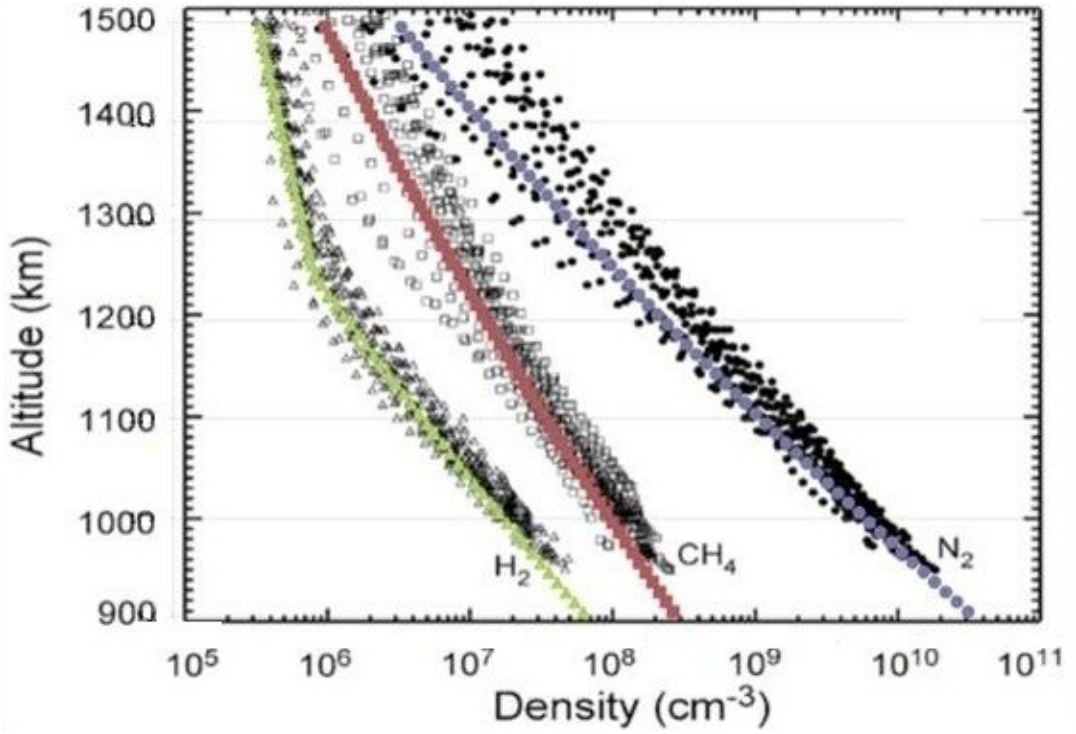

Figure 3.39 Global average neutral densities obtained by parameterizing the fitting equation of *Keller et al.* [1992] to agree with INMS measurements from many Cassini flybys of N_2 (blue circles), CH_4 (red squares) and H_2 (green triangles). The underlying black circles, squares and triangles are the data presented by *Magee et al*/ [2009] for N_2, CH_4, and H_2 respectively. Figure modified from *Magee et al.* [2009].

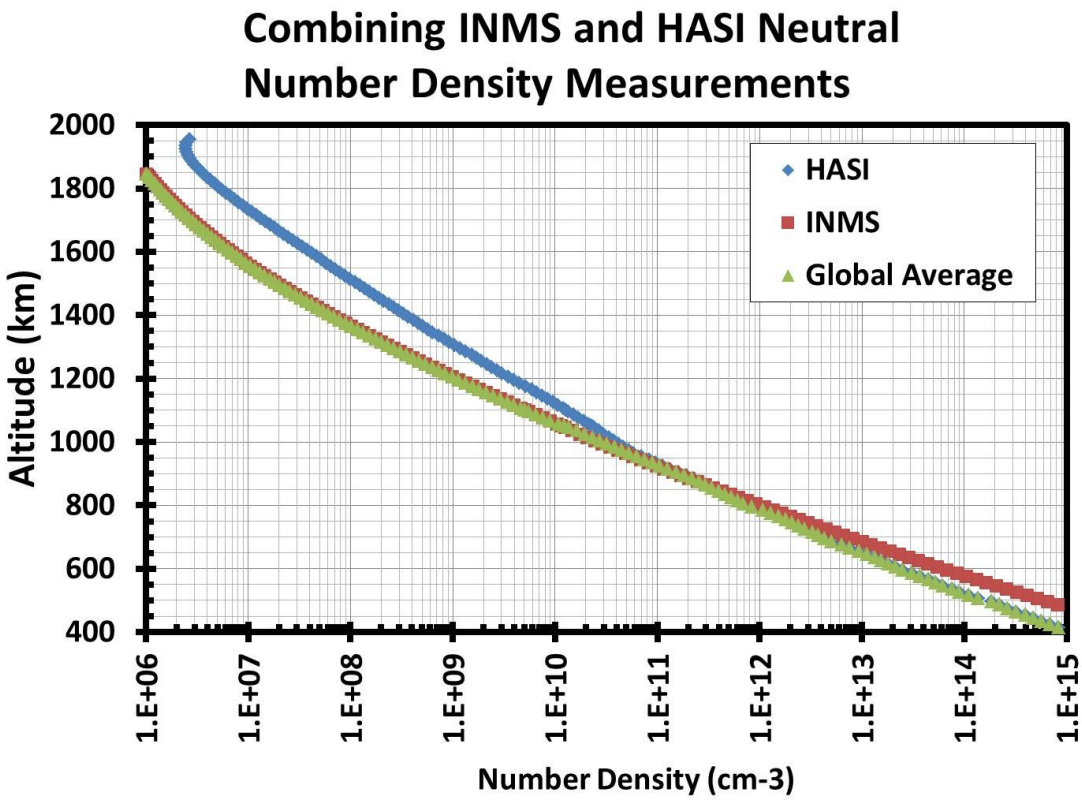

Figure 3.40 Total number density of neutral atoms in the global average model (green triangles) compared with the global average total neutral density values derived from INMS (red squares) multiplied by a factor of 3.15 [*Magee et al.*, 2009] (Figure 3.39) and total density measurements of HASI (blue diamonds) [*Fulchignoni et al.*, 2005]. The altitude region between 785 and 1065 km is used to gradually shift the Global Average Model's total number density from the upper altitude region using INMS data to a lower altitude region using the Huygens Atmospheric Structure Instrument (HASI) data.

3.5 Ion Chemistry

Titan boasts a complex nitrile and hydrocarbon chemistry starting with the ionization products of the major neutral constituents of the atmosphere (N_2, CH_4 and H_2) and a host of minor neutrals which then react with neutrals to produce hydrocarbons and nitriles with masses well above 100 amu [*Crary et al*. 2009; *Cravens et al*., 2009b; *Vuitton et al*, 2007; 2007; *Westlake et al.*, 2012]. Figure 3.41 shows a schematic of the ion chemistry that is by no means complete, but shows the general progression of molecular growth along various chemical production pathways from initial ionization caused by solar photons, photoelectrons and magnetospheric electrons to high mass terminal ions that are removed primarily through electron dissociative recombination. For the lower mass ion species, chemical reactions comprise the bulk of the production and loss processes for an ion in contrast to the high mass, or so called terminal ion species, where dissociative electron recombination is the sole loss process. In this subsection, details of the ion chemistry will be discussed such as reaction and dissociative recombination rates in order to more accurately model the ion densities observed by the INMS and CAPS instrument aboard the Cassini spacecraft during flybys of Titan.

3.5.1 Electron Dissociative Recombination Rates

Electron dissociative recombination occurs when an ion and an electron collide resulting in two or more neutral fragments (Equation (3.19)). Although chemical reactions will remove one ion, they will produce another ion and will not deplete the thermal electron density, thus,

$$Ion + e^- \rightarrow Neutral_1 + Neutral_2 \qquad \textbf{(3.19)}$$

dissociative electron recombination is responsible for the removal of excess thermal electrons and ions from the ionosphere of Titan.

The dissociative electron recombination loss rate expressed in Equation (3.20) is a function of the electron and ion density, n_e and n_i, a dissociative recombination coefficient $\alpha_{e,i}$ derived at 300 K in units of cm^3s^{-1} and a factor β showing the dependence on the electron temperature T_e. Note that as the temperature of the thermal ions and electrons diminishes, the loss rate from dissociative electron recombination will increase. This is important in the ionosphere of Titan where electron temperatures will decrease as you move closer to the surface where neutral densities are larger and thermal coupling between the ions and neutrals becomes more prevalent.

$$Loss_{ER} = \alpha_{e,i} n_e n_i \left(\frac{300\ K}{T_e}\right)^{\beta} \qquad \textbf{(3.20)}$$

The values of the electron dissociative recombination coefficients and temperature dependence factors are predominantly taken from the work of *Anicich and McEwan* [1997], *McEwan and Anicich* [2007], and *Vuitton et al.* [2007]. *McLain et al*. [2004; 2006] and *McLain and Adams* [2007] measured the recombination rates of several ions found in the ionosphere of Titan and obtained measurements that were best fit using a larger value of β when T_e is larger than 300 K. By using two different values of β above and below 300 K, they were able to produce a power law fit to their observations that indicated a larger electron recombination rate below 300 K and a lower rate above 300 K. Updated measurements for dissociative electron coefficients at room temperature have been obtained by *Osborne et al*. [2011a, 2011b] for several larger ions species and for nitrile species by *Vigren et al*. [2009]. *Westlake et al*. [2012]

have also suggested several modifications to the dissociative electron recombination coefficients as a result of their empirical chemical modeling work. These modifications have been implemented in the current model. For high mass molecules containing more than six carbon atoms, a reaction rate coefficient α of 1.00x10^{-6} and a temperature dependence factor, β, of 0.3 is assumed when there are no relevant measurements. Below, in Table 3.5, the dissociative electron recombination coefficients and temperature dependence factors for some important and updated ion species can be found. A complete list appears in Appendix C-1.

Table 3.5 Dissociative electron recombination coefficients. A * in the reference column means the result is attributed to the works of *Anicich and McEwan* [1997], *McEwan and Anicich* [2007], and *Vuitton et al.* [2007].

Ion	$\alpha_{e,i}$ $[cm^3 s^{-1}]$	β	Reference
N_2^+	$1.70\ x\ 10^{-7}$	0.3	*
N^+	$4.00\ x\ 10^{-12}$	0.58	*, Radiative Recombination
CH_5^+	$1.10\ x\ 10^{-6}$	1.5, $T_e > 300\ K$ 0.7, $T_e < 300\ K$	*McLain et al.* [2004]
CH_4^+	$3.5\ x\ 10^{-7}$	0.5	*
CH_3^+	$2.97\ x\ 10^{-7}$	0.5	*
HN_2^+	$1.70\ x\ 10^{-7}$	0.92	*Vigren et al.* [2009]
$HCNH^+$	$3.50\ x\ 10^{-7}$	1.38	*McLain and Adams* [2007]
$C_2H_5^+$	$1.20\ x\ 10^{-6}$	1.2, $T_e > 300\ K$ 0.8, $T_e < 300K$	*McLain et al.* [2004]
$C_3H_5^+$	$1.50\ x\ 10^{-6}$	1.4, $T_e > 300\ K$ 0.7, $T_e < 300\ K$	*Westlake et al.*[2012]
$C_5H_5^+$	$1.50\ x\ 10^{-6}$	1.4, $T_e > 300\ K$ 0.7, $T_e < 300\ K$	*Westlake et al.*[2012]
$C_6H_7^+$	$2.80\ x\ 10^{-6}$	1.3	*McLain and Adams* [2007]
$C_7H_7^+$	$2.80\ x\ 10^{-6}$	1.3	*McLain and Adams* [2007]

Ion	$\alpha_{e,i}$ $[cm^3 s^{-1}]$	β	Reference
$C_4H_3^+$	$1.50\ x\ 10^{-6}$	0.7	*Westlake et al.* [2012]
$C_5H_7^+$	$1.10\ x\ 10^{-6}$	1.4, $T_e > 300\ K$ 0.7, $T_e < 300\ K$	*Westlake et al.* [2012]
CH_3CNH^+	$3.40\ x\ 10^{-7}$	1.03	*McLain and Adams* [2007]
$C_2H_3CNH^+$	$1.78\ x\ 10^{-6}$	0.8	*Vigren et al.* [2009]
$C_7H_9^+$	$3.80\ x\ 10^{-7}$	0.7	*Osborne et al.* [2011a, 2011b]
$C_4H_5NH^+$	$4.00\ x\ 10^{-7}$	0.7	*Osborne et al.* [2011a, 2011b]
$C_5H_6N^+$	$8.50\ x\ 10^{-7}$	0.7	*Osborne et al.* [2011a, 2011b]
$CH_3C_5H_5N^+$	$2.83\ x\ 10^{-7}$	0.7	*Osborne et al.* [2011a, 2011b]

3.5.2 Chemical Reaction Scheme

The reaction list used in this model is based upon several previous efforts to model the ionosphere of Titan. [*Keller et al.,* 1992, 1998; *Vuitton et al.*, 2007; *Cravens et al*., 2005, *Robertson et al*., 2009; *Westlake et al*., 2012]. For lower mass hydrocarbons the model used the reaction rate coefficients compiled by *Anicich and McEwan* [1997] with the addition of heavier hydrocarbon reactions shown by *McEwan and Anicich* [2007]. Additional chemical reaction pathways for heavier hydrocarbons from reactions with benzene and nitrile species were added by *Vuitton et al.* [2006, 2007]. Recently, *Westlake et al.* [2012] highlighted the reaction rates of *Edwards et al.* [2008] for CH_2NH, C_2H_5CN and C_2H_6 and the rates of *Zabka et al*. [2009] for reactions between $C_2H_5^+$ and benzene which have been implemented in this model. *Westlake et al.* also postulated several reaction pathways in which ions react with C_2 hydrocarbons (i.e. C_2H_2,

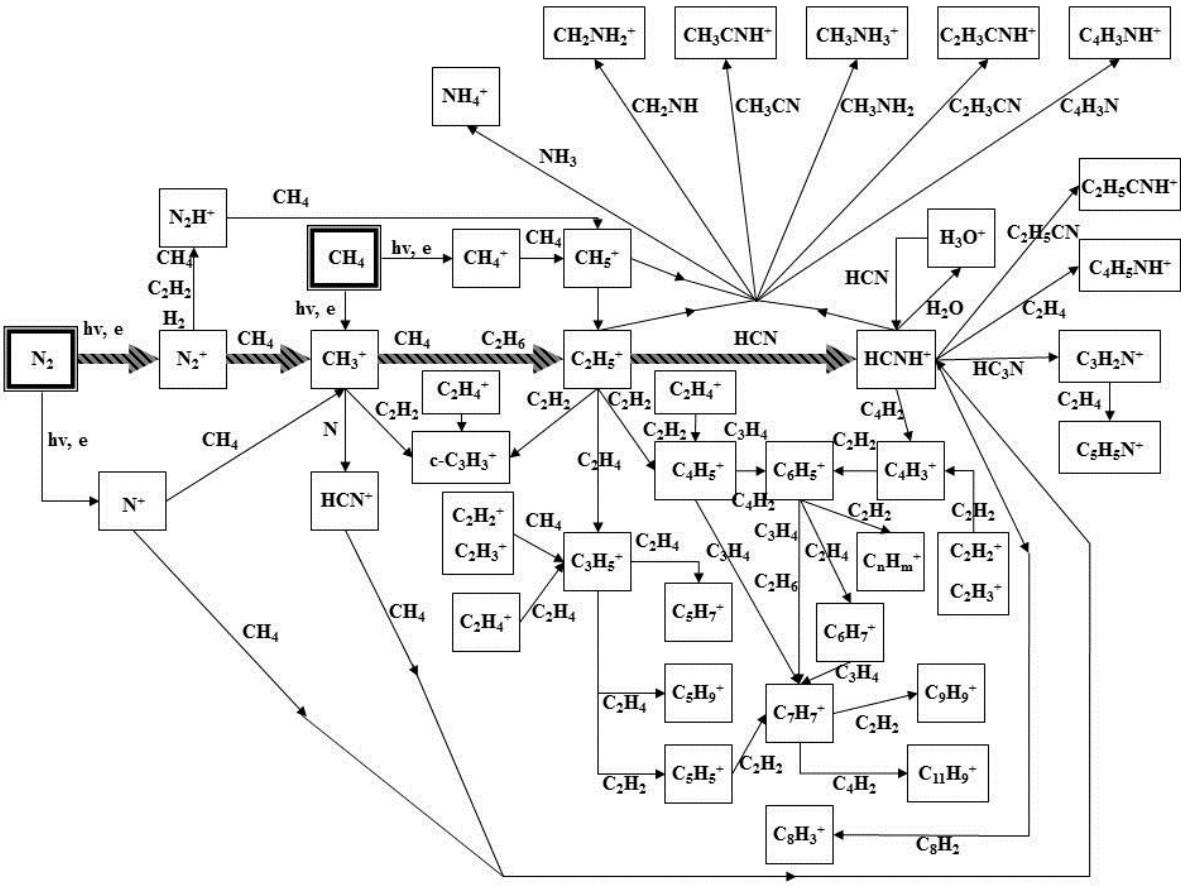

Figure 3.41 Schematic of the ion chemistry at Titan. Dark boxes indicate the major neutral species N_2 and CH_4 which are ionized. Boxes bordered by a thin line are ion species that react with neutrals shown in bold along the reaction pathway indicated by an arrow. Reactions proceed in the direction of the arrows. Large arrows indicate major ion production pathways for key ion species.

C_2H_4, C_2H_6) resulting in higher mass ions from their observations of correlations between ion groups approximately 24 amu apart in data from CAPS-IBS and INMS.

The chemical reaction rate $k_{i,n}$ between an ion species i and a neutral species n directly impacts the production rate, in $cm^{-3}s^{-1}$, of an ion species as indicated in Equation (3.21). Here the production rate of an ion s is determined by multiplying $k_{i,n}$ in cm^3s^{-1} by the density of the neutral species and the density of the ion species in units of cm^{-3}, represented in Equation (3.21) by n_n and n_i respectively. Reaction rates for some important chemical pathways will be discussed in the following sub-section. The complete reaction list appears in tabular form in Appendix C.

$$Prod_s = k_{i,n} n_n n_i \qquad \textbf{(3.21)}$$

3.5.2.1 Reaction Pathways for the Ionization Products of N_2

The ionization products of N_2 and CH_4 are the primary building blocks of the ionosphere. Although there are other ions that are produced through ionization of the neutral atmosphere, the abundance of N_2 and CH_4 ensures that their reaction products are the most prevalent.

The ionization products of molecular nitrogen are N_2^+ and N^+. As Figure 3.41 shows, these two products are major building blocks in the ionosphere of Titan due to their role in the reaction chain producing $HCNH^+$, the most abundant ion in the ionosphere of Titan.

The overwhelming majority (<99%) of N_2^+ is produced directly from the photoionization and electron impact ionization of N_2 so the other production pathways will not be mentioned here. The loss processes of N_2^+ are far more interesting though (Table 3.6), particularly the reaction in which N_2^+ reacts with CH_4 to produce CH_3^+ which accounts for upwards of 65% of the loss of N_2^+ due to the relatively large reaction rate coefficient (1.04×10^{-9} cm^3s^{-1}) and the

large abundance of methane. N_2^+ can also react with C_2H_4 and C_2H_6 to produce $C_2H_5^+$ and $HCNH^+$ respectively which are major contributors to the total ion density in Titan's ionosphere. In Table 3.6 mention is also made of the reactions between methane or molecular hydrogen and N_2^+ resulting in HN_2^+, which will produce $HCNH^+$, and the reaction with methane that will produce CH_2^+, which will react to produce heavier hydrocarbons and nitriles (see Section 3.5.2.2).

Table 3.6 Chemical loss processes of N_2^+

Chemical Reaction	Reaction Rate Coefficient [cm^3s^{-1}]
$N_2^+ + CH_4 \rightarrow CH_3^+$	$1.04\ x\ 10^{-9}$
$N_2^+ + H_2 \rightarrow HN_2^+$	$2.00\ x\ 10^{-9}$
$N_2^+ + CH_4 \rightarrow HN_2^+$	$1.71\ x\ 10^{-10}$
$N_2^+ + CH_4 \rightarrow CH_2^+$	$1.03\ x\ 10^{-10}$
$N_2^+ + C_2H_4 \rightarrow HCNH^+$	$1.30\ x\ 10^{-10}$
$N_2^+ + C_2H_6 \rightarrow C_2H_5^+$	$2.16\ x\ 10^{-10}$

Unlike N_2^+, photoionization and electron impact ionization only account for around 50-60% of the N^+ production at the peak. The remaining N^+ occurs as the result of a reaction between N_2^+ and N (Table 3.7) noted by *Anicich* [2003]. The main contributions of N^+ in the chemical reaction chain are the products of its reactions with methane to produce CH_3^+, $HCNH^+$ and HCN^+ (Table 3.8).

Table 3.7 Chemical production processes of N^+

Chemical Reaction	Reaction Rate Coefficient [cm^3s^{-1}]
$N_2^+ + N \rightarrow N^+$	$1.00\ x\ 10^{-11}$

Table 3.8 Chemical loss processes of N^+

Chemical Reaction	Reaction Rate Coefficient [cm^3s^{-1}]
$N^+ + CH_4 \rightarrow CH_3^+$	$5.75\ x\ 10^{-10}$
$N^+ + CH_4 \rightarrow HCNH^+$	$4.14\ x\ 10^{-10}$
$N^+ + CH_4 \rightarrow\ HCN^+$	$4.14\ x\ 10^{-10}$
$N^+ + H_2^+ \rightarrow HN^+$	$1.00\ x\ 10^{-9}$
$N^+ + CH_4 \rightarrow CH_4^+$	$5.75\ x\ 10^{-11}$
$N^+ + HCN \rightarrow HCN^+$	$2.41\ x\ 10^{-9}$

3.5.2.2 Reaction Pathways for Major Ionization Products of CH_4

Methane is the second most abundant neutral in the upper atmosphere of Titan and its primary ionization products that have the greatest impact on the ion-neutral chemistry at Titan are CH_4^+ and CH_3^+.

CH_4^+ is primarily produced via photoionization and electron impact ionization, but reactions with CH_5^+ contribute a non-negligible amount (upwards of 33%) to this ion's population due to the large abundance of CH_5^+ in the ionosphere (Table 3.9). The major chemical loss pathway for CH_4+ (Table 3.10), accounting for more than 80% of the loss at altitudes near the ionospheric peak, is through reactions with neutral methane that produce CH_5^+. The second largest sink, roughly 10-15% of the total loss rate near the peak, of CH_4^+ is through reactions with HCN to produce $HCNH^+$. Both of these ions are in high abundance in the ionosphere of Titan and serve as building blocks to produce higher mass ions and will be discussed in Section 3.5.2.3.

Table 3.9 Chemical production processes for CH_4^+

Chemical Reaction	Reaction Rate Coefficient [cm^3s^{-1}]
$CH_5^+ + H \rightarrow CH_4^+$	$1.50\ x\ 10^{-10}$

Table 3.10 Chemical loss processes of CH_4^+

Chemical Reaction	Reaction Rate Coefficient [cm^3s^{-1}]
$CH_4^+ + CH_4 \rightarrow CH_5^+$	$1.14\ x\ 10^{-9}$
$CH_4^+ + HCN \rightarrow HCNH^+$	$3.23\ x\ 10^{-9}$
$CH_4^+ + C_2H_4 \rightarrow C_2H_4^+$	$1.38\ x\ 10^{-9}$
$CH_4^+ + C_2H_2 \rightarrow C_2H_2^+$	$1.44\ x\ 10^{-9}$
$CH_4^+ + C_2H_2 \rightarrow C_2H_3^+$	$1.12\ x\ 10^{-9}$

The other main ionization product of methane that impacts the ion chemistry substantially is CH_3^+. This ion is produced through a combination of photoionization and electron impact ionization of methane (~60%) and through chemical reactions between methane and N_2^+ (Table 3.11). Two chemical loss processes of CH_3^+ are of great importance to the ion composition of Titan: reactions with methane to produce CH_5^+ and reactions with NH to produce $HCNH^+$ (Table 3.12). As mentioned above, these two reaction products are among the most abundant ion species in the ionosphere of Titan and are discussed in Section 3.5.2.3.

Table 3.11 Chemical production processes of CH_3^+

Chemical Reaction	Reaction Rate Coefficient [cm^3s^{-1}]
$N_2^+ + CH_4 \rightarrow CH_3^+$	$1.04\ x\ 10^{-9}$

Table 3.12 Chemical loss processes of CH_3^+

Chemical Reaction	Reaction Rate Coefficient [cm^3s^{-1}]
$CH_3^+ + CH_4 \rightarrow C_2H_5^+$	$1.10\ x\ 10^{-9}$
$CH_3^+ + C_2H_4^+ \rightarrow C_2H_2^+$	$1.70\ x\ 10^{-9}$
$CH_3^+ + NH \rightarrow HCNH^+$	$7.4\ x\ 10^{-10}$

3.5.2.3 Reaction Pathways for CH_5^+, $C_2H_5^+$ and $HCNH^+$

After the initial ionization of methane and molecular nitrogen in Titan's ionosphere the next major ions in the reaction chain are CH_5^+, $C_2H_5^+$ and $HCNH^+$ (see Figure 3.41). These ions represent the most abundant ions in the ionosphere of Titan and the correct modeling of these ion species has been a difficulty in previous modeling attempts [i.e. *Robertson et al.,* 2009; *Westlake et al.,* 2012]. These difficulties arise from the fact that all of these ions are chemically linked to one another such that adjusting the reaction pathways of one ion directly impacts both of the other ion species.

The main production of CH_5^+ comes from reactions between HN_2^+ and CH_4^+ and methane (Table 3.13) with the former reaction providing the bulk of the ion production rate. The main loss processes of CH_5^+ are reactions with HCN to produce $HCNH^+$, C_2H_2 to produce $C_2H_3^+$ and C_2H_4 to produce $C_2H_5^+$ (Table 3.14). This means that an overabundance of CH_5^+ will increase the production rate of $HCNH^+$ and $C_2H_5^+$.

The overwhelming majority of $C_2H_5^+$ is produced as a result of the reaction of CH_3^+ and methane (Table 3.15) which emphasizes the role that a correct production rate of N_2^+, which reacts to produce CH_3^+, has on the $C_2H_5^+$ density. The main loss process for $C_2H_5^+$ is via reactions with HCN to produce $HCNH^+$ (Table 3.16).

Table 3.13 Chemical production processes of CH_5^+

Chemical Reaction	Reaction Rate Coefficient [cm^3s^{-1}]
$HN_2^+ + CH_4 \rightarrow CH_5^+$	$8.90\ x\ 10^{-10}$
$CH_4^+ + CH_4 \rightarrow\ CH_5^+$	$1.14\ x\ 10^{-9}$
$HN_2^+ + C_2H_6 \rightarrow\ CH_5^+$	$1.13\ x\ 10^{-9}$

Table 3.14 Chemical loss processes of CH_5^+

Chemical Reaction	Reaction Rate Coefficient [cm^3s^{-1}]
$CH_5^+ +\ HCN \rightarrow HCNH^+$	$2.70\ x\ 10^{-9}$
$CH_5^+ +\ C_2H_2 \rightarrow C_2H_3^+$	$1.48\ x\ 10^{-9}$
$CH_5^+ +\ C_2H_4 \rightarrow C_2H_5^+$	$1.00\ x\ 10^{-9}$
$CH_5^+ +\ NH \rightarrow NH_2^+$	$7.10\ x\ 10^{-9}$
$CH_5^+ +\ H \rightarrow CH_4^+$	$1.50\ x\ 10^{-9}$

Table 3.15 Chemical production processes of $C_2H_5^+$

Chemical Reaction	Reaction Rate Coefficient [cm^3s^{-1}]
$CH_3^+ + CH_4 \rightarrow C_2H_5^+$	$1.10\ x\ 10^{-9}$

Table 3.16 Chemical loss processes of $C_2H_5^+$

Chemical Reaction	Reaction Rate Coefficient [cm^3s^{-1}]
$C_2H_5^+ + HCN \rightarrow HCNH^+$	$5.00\ x\ 10^{-9}$
$C_2H_5^+ +\ C_2H_4 \rightarrow C_3H_5^+$	$3.35\ x\ 10^{-10}$
$C_2H_5^+ +\ C_2H_2 \rightarrow C_4H_5^+$	$1.22\ x\ 10^{-10}$

Chemical production pathways for the most abundant ion in Titan's ionosphere are shown in Table 3.17. Approximately 80% of the production of $HCNH^+$ comes from the reaction of HCN and $C_2H_5^+$ while almost 10% comes from reactions between CH_5^+ and HCN. Not only does this illustrate the interconnectivity of CH_5^+, $C_2H_5^+$, and $HCNH^+$, but also the importance of correctly determining the amount of HCN in the neutral atmosphere as small changes in the mixing ratio can have profound impacts on the ion densities of these three species as will be discussed in Chapter 6.

Table 3.17 Chemical production processes of $HCNH^+$

Chemical Reaction	Reaction Rate Coefficient [cm^3s^{-1}]
$C_2H_5^+ + HCN \rightarrow HCNH^+$	$5.00\ x\ 10^{-9}$
$CH_5^+ + HCN \rightarrow HCNH^+$	$2.70\ x\ 10^{-9}$
$HN_2^+ + HCN \rightarrow HCNH^+$	$3.20\ x\ 10^{-9}$

3.5.2.4 High Mass Chemistry

Ions with masses greater than 29 amu are the result of chemical reactions with lighter ions (N_2^+, CH_3^+, CH_4^+, CH_5^+, $C_2H_5^+$, $HCNH^+$, etc.) with atmospheric neutrals such as C_2H_2, C_2H_4, C_2H_6, and heavier neutrals (see Table 3.3 for a complete list of minor neutral species) as shown in Figure 3.41. Reaction rate coefficients have been used from *Anicich and McEwan* [1997], *McEwan and Anicich* [2007], and *Vuitton et al.* [2007]. Recently, *Westlake et al.* [2012] proposed using reactions with C_2H_2 and C_2H_4 to construct higher mass ions from their observations of correlations between ions whose masses differed on the order of 24 amu, the size of two carbon atoms. As these reactions will be too numerous to list, the reader is directed to the complete list of chemical reactions found in Appendix C-2.

3.6 Fluid Equations

It becomes advantageous, when working with plasma, to use a statistical approach, assuming a distribution function of the plasma as a function of position, velocity, and time [*Chen,* 2006*; Cravens,* 1997]. This distribution function $f(\vec{x},\vec{v},t)$ with units of number of particles $cm^{-6}s^3$ represents a distribution of identical particles per unit volume in phase space. If this function is integrated over all velocities, one will arrive at an expression for the number density of the particles, $n(\vec{x},t)$ as a function of position and time. An example of a distribution function for a Maxwellian centered on the origin of velocity space is shown below in Equation (3.23).

$$f(x,v,t) = n\left(\frac{m}{2\pi k_B T}\right)^{\frac{3}{2}} \exp\left(-\frac{m\left(v_x^2+v_y^2+v_z^2\right)}{2k_b T}\right) \qquad \textbf{(3.22)}$$

3.6.1 Derivation of the Fluid Equation

If one looks at the rate of change of the distribution function one will arrive at

$$\frac{df(\vec{x},\vec{v},t)}{dt} = \frac{\partial f}{\partial \vec{x}}\frac{d\vec{x}}{dt} + \frac{\partial f}{\partial \vec{v}}\frac{d\vec{v}}{dt} + \frac{\partial f}{\partial t} \qquad \textbf{(3.23)}$$

which can be rewritten as the Boltzmann Equation (3.24) when the rate of change of the distribution function is assumed to be caused by collisional processes.

$$\frac{\partial f}{\partial t} + \nabla\cdot(f\vec{v}) + \nabla_{\vec{v}}(f\vec{a}) = \left.\frac{\delta f}{\delta t}\right|_{coll.} \qquad \textbf{(3.24)}$$

The term on the right of Equation (3.24) represents the change in the distribution function due to collisions and the term on the left is the time derivative of the distribution function. Moments of

the distribution function are calculated by integrating the product of $v^{(moment)}$ and the distribution function over all velocities. By taking the 0^{th} moment of this function it is possible to derive the continuity equation (3.25) [*Schunk and Nagy*, 2009]:

$$\frac{\partial n_s}{\partial t} + \nabla \cdot (n_s \vec{v}) = S_s \qquad \textbf{(3.25)}$$

where n represents the density, $\vec{v}$ is the velocity and S_s represents the source term of the species. Taking successive moments of the Boltzmann equation one can arrive at the momentum equation and energy equation. If the source term S_s Equation (3.26)and the bulk velocity of the plasma $\vec{v}$ are zero then in the production rate of each ion is balanced by the loss rate of the ion at each altitude, which are the conditions used in the photochemical model in Section 3.4.

$$S_s = 0 \qquad \textbf{(3.26)}$$

The second moment of the Boltzmann Equation (3.24), found by integrating the product of the distribution function and $m_s v$, where m_s is the mass of the species s and v is its velocity, over all velocities will provide information about the transfer of momentum $\vec{M}$, in the plasma. *Schunk and Nagy* [1980] derived the form of this equation presented as Equation (3.27) [cf. *Schunk and Nagy,* 2009].

$$n_s m_s \frac{D_s \vec{u}_s}{Dt} + \nabla p_s + \nabla \cdot \tau_s - n_s m_s \vec{G} - n_s e_s \{\vec{E} + u_s \times \vec{B}\} = \frac{\delta \vec{M}}{\delta t} \qquad \textbf{(3.27)}$$

In the momentum equation $p_s = n_s k_B T_s$, the scalar partial pressure of species s, T_s is the temperature, k_B is Boltzmann's constant and τ is the stress tensor. The expression for the change

in momentum (Equation (3.28)), neglecting mass loading, is taken from the work *Schunk and Nagy* [2009]. $\frac{D_s}{Dt}$ is the convective derivative and is defined by Equation (3.29) and ν_{st} is the momentum transfer collision frequency.

$$\frac{\delta \vec{M}}{\delta t} = \sum_t n_s m_s \nu_{st} \{\vec{u}_t - \vec{u}_s\} \qquad \textbf{(3.28)}$$

$$\frac{D_s}{Dt} = \frac{\partial}{\partial t} + \vec{u}_s \cdot \nabla \qquad \textbf{(3.29)}$$

3.7 Energy Equation and Temperature Modeling

Electron and ion temperatures for the relatively cold thermal electron and ion species were calculated by solving the coupled electron and ion energy equation (defined below) that includes heat transport via thermal conduction, heating rates, cooling rates, and dynamical terms. Solutions of the energy equation are calculated in 10 km intervals along magnetic field lines. The thermal populations of electrons (electrons with energies less than about 2 eV), heated by Coulomb collisions with the superthermal electron population of magnetospheric or atmospheric origin, were considered. Ions are heated by collisions with the thermal electrons. For electrons, the cooling rate includes contributions from vibrational, rotational, and electronic excitational cooling from electron-neutral collisions as well as heat lost by the thermal electrons to the thermal ion species [*Gan et al.,* 1992, 1993]. Methane provides a large contribution to the cooling rate of the thermal electrons despite its relatively low abundance compared to molecular nitrogen [*Gan et al*., 1992, 1993]. Ions are cooled (or heated if there is drift motion) through elastic collisions with the neutral species.

This section will discuss the electron energy code shown in Figure 3.1. This code has been modified to include a general ion species of mass 29 amu ($C_2H_5^+$) which will be heated by collisions with the thermal electrons and thus will provide a temperature profile along a magnetic field line for electrons and the ion species. A general overview of the theory behind the energy balance of ions and electrons is presented along with the necessary parameters used in this model.

Multiplying the distribution function by $\frac{1}{2}m_s v^2$ and integrating over all velocities will yield the energy equation for a species s of electrons or ions (s = e or i) [cf. *Schunk and Nagy,* 2009] as follows:

$$\frac{D_s}{Dt}\left(\frac{3}{2}p_s\right) + \frac{5}{2}p_s(\nabla \cdot \vec{u}_s) + \nabla \cdot \vec{q}_s + \tau_s : \nabla\vec{u}_s = \frac{\delta E}{\delta t} + Q_s - L_s \quad \textbf{(3.30)}$$

The heating rate of species s is Q_s. Electrons are heated by Coulomb collisions with suprathermal electrons and ions are heated through Coulomb collisions with the thermal electron population. The cooling rate of a species is denoted by L_s. For electrons the cooling rate includes contributions from vibrational, rotational, and electronic excitational cooling from electron-neutral collisions as well as heat lost by the thermal electrons to the thermal ion species [*Gan et al.,* 1992, 1993]. The heat flow vector $\overrightarrow{q_s}$ is defined as:

$$\overrightarrow{q_s} = -\kappa_s \nabla T \quad \textbf{(3.31)}$$

where κ_s is the modified Spitzer thermal conductivity equation which takes into account Coulomb collisions [*Gan et al*., 1992, 1993] of species s and will be explained for electrons and

ions in Sections 3.7.1 and 3.7.3 respectively. The expression derived by *Schunk* [1977] is used for the change in energy, $\frac{\delta E}{\delta t}$ defined in (3.32).

$$\frac{\delta E}{\delta t} = \sum_t \frac{n_s m_s \nu_{st}}{m_s + m_t} (3k_B[T_t - T_s] + m_t(\vec{u}_s - \vec{u}_t)^2) \qquad \textbf{(3.32)}$$

In this formulation of the change in energy between species s and t, ν_{st} is the momentum transfer collision frequency (described in Section 3.7.1) between the two species presented by *Schunk and Nagy* [2009]. Changing the indices of the ν_{st} will not give identical results as the momentum transfer cross section is not symmetrical but follows the relation:

$$n_s m_s \nu_{st} = n_t m_t \nu_{ts} \qquad \textbf{(3.33)}$$

By combining the energy equation (3.30) with the continuity equation (3.25) the form of the energy equation used in the electron and ion energy code was obtained (Equation (3.34)).

$$\begin{aligned} &\frac{3}{2}k_B n_s \frac{\partial T_s}{\partial t} + \frac{3}{2}k_b n_s \overrightarrow{u_s} \cdot \nabla T_s + \frac{3}{2}k_B T_s n_s \nabla \cdot \overrightarrow{u_s} \\ &\quad + \frac{3}{2}k_B(T_s - T_n)S_s + \nabla \cdot (-K_s \nabla T_S) \\ &\quad = \sum_m \frac{n_s m_s \nu_{sm}}{m_s + m_m}[3k_B(T_m - T_s) \\ &\quad + m_m(\overrightarrow{u_s} - \overrightarrow{u_m})^2] + Q_s - L_s \end{aligned} \qquad \textbf{(3.34)}$$

In Equation (3.34) k_B is Boltzmann's constant, n_s represents the number density, T denotes the temperature, $\mathbf{u}_s$ represents the bulk velocity of species s, m_s is the mass, and t represents time. Mass-loading (the addition of newly formed ions to the plasma flow) is implemented with the

term S_s which represents a source of species s. T_n is the temperature of the ionized neutral species.

Steady-state solutions to the time-dependent energy equation (3.34) were obtained after running the model for 10^6 seconds during which time the solutions for the electron and ion temperature converged (Figure 3.42). The equations were calculated along a single magnetic field line and a constant solar zenith angle with parameters (solar zenith angle, shape, altitude of the apex point etc.) determined by a combined analysis of magnetometer data and the spacecraft trajectory (see Figure 3.2). The results of these calculations are displayed versus altitude above the surface of Titan. The temperature model provided its results in terms relative to the neutral temperature (T_i-T_n); however, for comparison purposes with *Crary et al*. [2009], the temperatures have been readjusted so that the neutral temperature is 150 K.

3.7.1 Electron Energetics

The heating of the thermal electron population by Coulomb collisions with the superthermal electron heating appears in the Q_s term in Equation (3.34). In order to calculate the deposition of energy along the magnetic field line due to these collisions the effective Coulomb cross section for each energy bin in units of cm^2 derived by *Swartz et al*. [1971] was used (shown below) where $\Delta\varepsilon$ represents the size of the energy bin.

$$\sigma_{eff} = \frac{1}{\Delta\varepsilon}\frac{1}{n_e}\frac{d\varepsilon}{dx} \qquad \textbf{(3.35)}$$

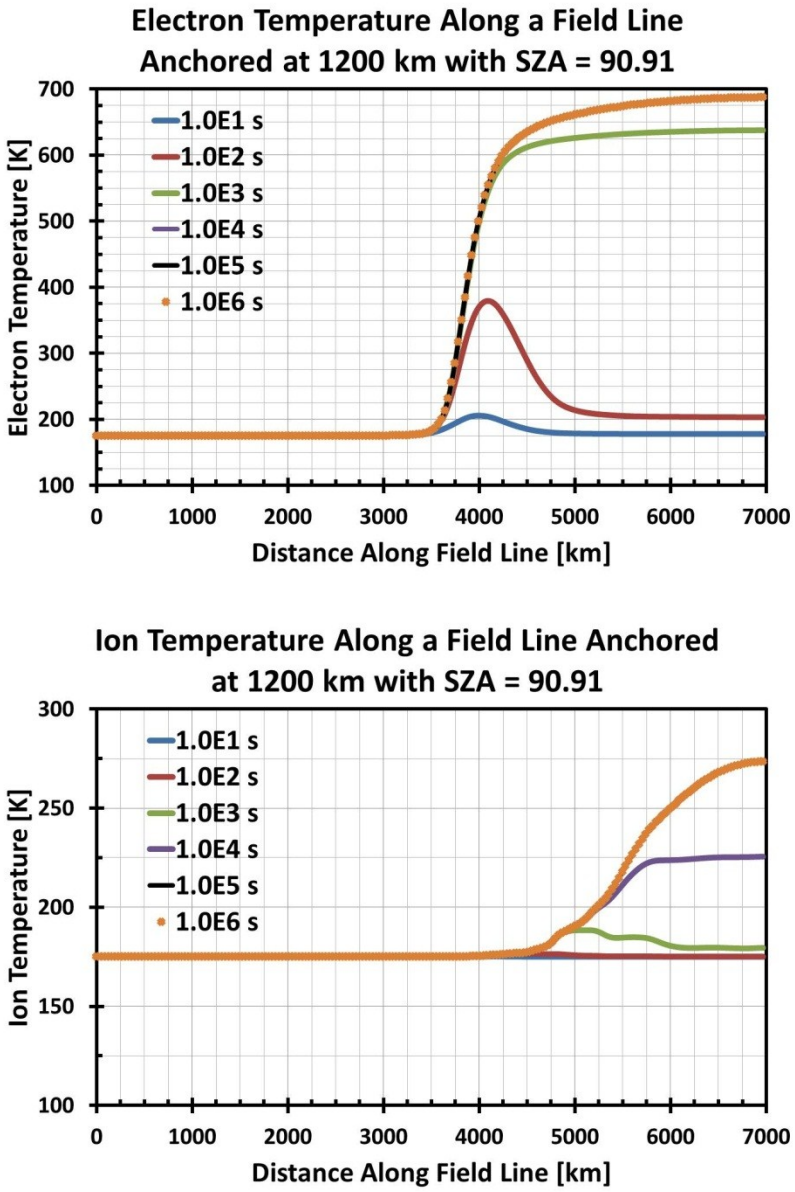

Figure 3.42 Electron (top) and Ion (bottom) temperature computed along a magnetic field line anchored at 1200 km for a solar zenith angle of 90.91˚. Solutions obtained after 10 (blue line), 10^2 (red line), 10^3 (green line), 10^4 (purple line), 10^5 (black line) and 10^6 (orange dot) seconds are indicated. After 10^6 seconds both the ion and electron temperature had reached a steady state.

In the above cross section the electron energy loss per unit length is defined by the following equations:

$$\frac{1}{n_e}\frac{d\varepsilon}{dx} = \frac{3.37 \times 10^{-12}}{E^{0.94} n_e^{0.03}} \left(\frac{E - E_e}{E - 0.53E_e} \right)^{2.36} \quad \textbf{(3.36)}$$

$$E_e = 8.618 \times 10^{-5} T_e \quad \textbf{(3.37)}$$

where E is the incident photoelectron energy in eV, n_e is the thermal electron density and $\Delta\varepsilon$ is the width of the energy bin (Table 3.2).

The thermal electron population is cooled through collisions with the neutral atmosphere and ions. When an electron collides with a neutral species it is possible that the collision will be elastic, in which case very little energy is transferred between the species, or inelastic which can induce rotational and vibrational excitation of the neutral molecule. Observations indicate that these inelastic collisions are capable of transferring large amounts of energy from the electrons to atmospheric neutrals [cf. *Banks and Kockarts,* 1973]. Expressions for the cooling rates mentioned above will be discussed in the following paragraphs.

The exact form of the equation for the cooling of a species 1 from elastic collisions with species 2 in a stationary gas has been derived from Equation (3.30) by *Banks and Kockarts* [1973] and is shown in Equations (3.38) -(3.43).

$$\frac{dU_1}{dt} = -\left[\frac{2m_1 m_2}{(m_1 + m_2)^2} \right] n_1 \bar{\nu}_{12} \frac{3}{2} k_B (T_1 - T_2) \quad \textbf{(3.38)}$$

$$\bar{\nu}_{12} = \frac{4}{3} \left(\frac{8k_B}{\pi} \right)^{\frac{1}{2}} \left[\frac{T_1}{m_1} + \frac{T_2}{m_2} \right]^{\frac{1}{2}} \bar{Q}_D \quad \textbf{(3.39)}$$

$$\bar{Q}_D = K^3 \int_0^\infty g^5 q_D(g) \exp(-Kg^2) dg \qquad \textbf{(3.40)}$$

$$U_1 = \frac{1}{2} \int m_1 v_1^2 f_1 d^3 v \triangleq \frac{3}{2} n_1 k_B T_1 \qquad \textbf{(3.41)}$$

$$K = \left[\frac{2k_B T_1}{m_1} + \frac{2k_B T_2}{m_2} \right]^{-1} \qquad \textbf{(3.42)}$$

$$q_D(g) = 2\pi \int \sigma(g, \theta)[1 - \cos\theta] \sin\theta d\theta \qquad \textbf{(3.43)}$$

In the above set of equations dU_1/dt is the rate of energy transfer of species 1 in eV cm^{-3} sec^{-1}, $\bar{\nu}_{12}$ is the average momentum transfer collision frequency, $\bar{Q}_D$ is the average momentum transfer cross section, g is the relative velocity, q_D is the velocity dependent momentum transfer cross section and σ is the differential scattering cross section for electron impact described in Sections 3.3.2.2 and 3.3.2.3.

Using the general set of equations above *Banks* [1966] derived the following representation for the cooling of thermal electrons in a neutral gas.

$$\frac{dU_{en}}{dt} = \frac{3m_e}{m_n} n_e k_B \bar{\nu}_{en} [T_e - T_n] \qquad \textbf{(3.44)}$$

$$\bar{\nu}_{en} = \frac{4}{3} n_n \left(\frac{8k_B T_e}{\pi m_e} \right)^{\frac{1}{2}} \bar{Q}_D \qquad \textbf{(3.45)}$$

$$\bar{Q}_D = \left(\frac{m_e}{2k_B T_e} \right)^3 \int_0^\infty v q_D \exp\left(-\frac{m_e v^2}{2k_B T_e} \right) dv \qquad \textbf{(3.46)}$$

For elastic electron-neutral collisions with N_2, *Banks and Kockarts* [1973] obtained the expression for the cooling of electrons given in Equation (3.47) and this is used in the current model.

$$\frac{dU_{eN_{2,elastic}}}{dt} = -1.2 \times 10^{-19} n_e n_{N_2} \times [1 - 1.2 \times 10^{-4} T_e] T_e \left(T_e - T_{N_2}\right) \quad \textbf{(3.47)}$$

The rate of energy transfer from the electrons to methane via elastic electron-neutral collisions was computed using Equations (3.44) - (3.46) by *Gan* [1991] and *Gan et al.* [1992] (Figure 3.43).

Expressions for the inelastic cooling rate due to energy transfer rate between the electron and target neutral gas are given by the set of equations below [*Banks and Kockarts,* 1973].

$$\frac{dU}{dt} = \int_0^\infty L(\varepsilon) v F(\varepsilon) d\varepsilon \quad \textbf{(3.48)}$$

$$\frac{dU}{dt} = 2n_e \sqrt{\frac{2}{m_e \pi (k_B T_e)^3}} \int_0^\infty L(\varepsilon) \varepsilon \exp\left(-\frac{\varepsilon}{k_B T_e}\right) d\varepsilon \quad \textbf{(3.49)}$$

$$F(\varepsilon) = 2n_e \sqrt{\frac{\varepsilon}{\pi (k_B T_e)^3}} \exp\left(-\frac{\varepsilon}{k_B T_e}\right) \quad \textbf{(3.50)}$$

$$L(\varepsilon) = \sum_{j, \varepsilon > w_j} W_j \sigma_j(\varepsilon) \quad \textbf{(3.51)}$$

In this set of equations $F(\varepsilon)$ is the Maxwellian energy distribution function in cm^{-3} eV^{-1}, $L(\varepsilon)$is the electron impact loss function in eV cm^2, j denotes different inelastic collisional

processes, and W_j is the energy loss in eV for each electron which equals the threshold of the excitation process. The rate of the transfer of energy dU/dt has units of eV sec^{-1}.

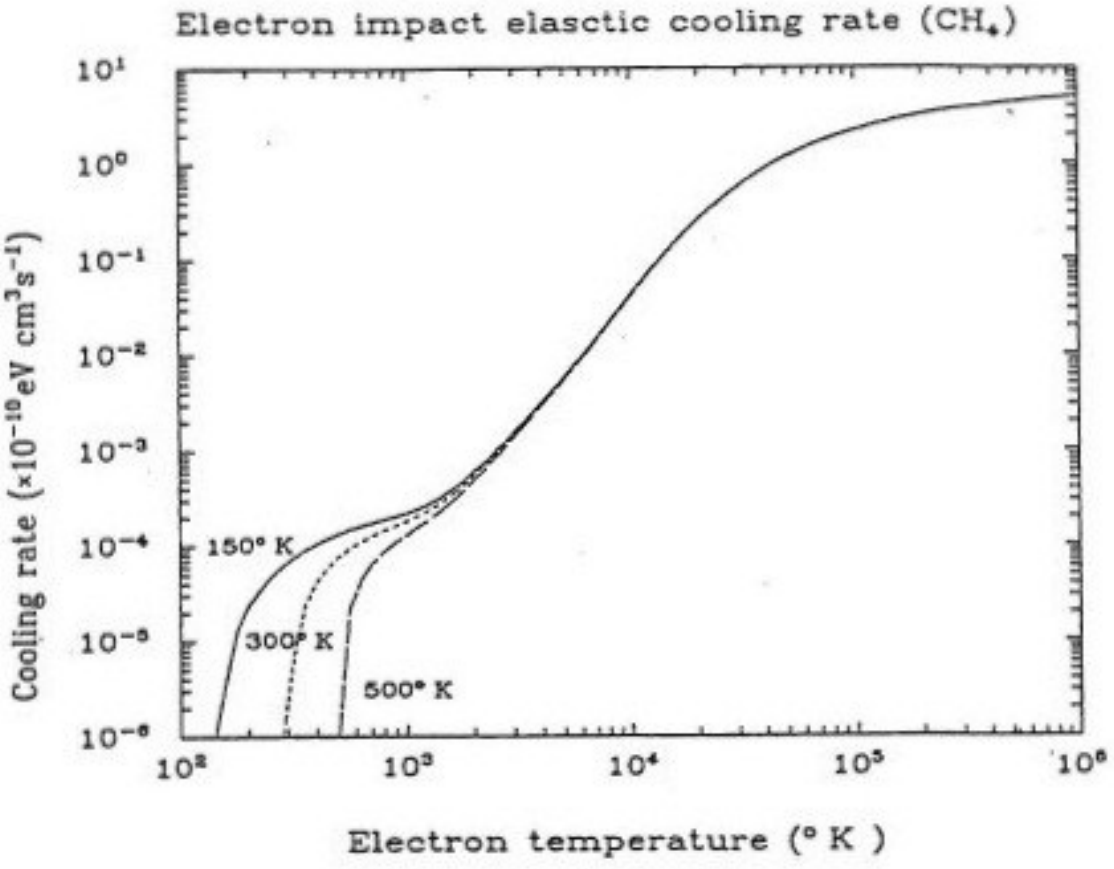

Figure 3.43 Electon impact cooling rates for elastic collisions with CH_4. The temperature of methane is labeled on the each curve. (From *Gan* [1991])

As was the case for the elastic collisions with N_2, inelastic collisions resulting in the rotational excitation of N_2 have been calculated and the simpler expression shown in Equation (3.52) is used [*Dalgarno*, 1968; *Mentzoni and Row*, 1963]. The exact expression has not been calculated and it is possible that this equation could produce an uncertainty of as much as a factor of 2.

$$\frac{dU_{eN_2,rotational}}{dt} = -2 \times 10^{-14} n_e n_{N_2} \frac{\left(T_e - T_{N_2}\right)}{T_e^{\frac{1}{2}}} \qquad \textbf{(3.52)}$$

Inelastic collisions producing excited vibrational states of N_2 have been shown to cool electrons with temperatures above 1500 K more effectively than collisions that produce a rotationally excited state [*Dalgarno*, 1968; *Dalgarno and Henry*, 1965]. *Roble* [1969] fit the following expression to the data of *Dalgarno* [1968] and *Dalgarno and Henry* [1965] which is used in the current model.

$$\frac{dU_{eN_2,vibrational}}{dt} =$$

$$-1.3 \times 10^{-4} n_e n_{N_2} \left\{1 - \exp\left[3200\left(\left[\frac{1}{T_e} - \frac{1}{T_{N_2}}\right]\right)\right]\right\} C \qquad \textbf{(3.53)}$$

In Equation (3.53), C has the values assigned in Equation (3.54).

$$C = \begin{cases} 5.715 \times 10^{-8} \exp(-3352.6/T_e), & T_e < 1000\ K \\ 2.0 \times 10^{-7} \exp(-4605.2/T_e), & 1000 < T_e < 2000\ K \\ 2.53 \times 10^{-8}\, T_e^{\frac{1}{2}} \exp(-17620/T_e), & T_e > 2000\ K \end{cases} \qquad \textbf{(3.54)}$$

For methane, de-excitation processes complicate the inelastic electron collision cross sections that produce rotationally and vibrationally excited final states. *Mott and Massey* [1965]

have shown that these de-excitation cross sections can be related to the excitation cross sections by balancing the collision strengths [*Gan,* 1991]. *Waite and Cravens* [1981] calculated the rotational de-excitation cross sections used in this model and presented in Equation (3.55) where $R_{J'\leftarrow J''}$=(2J'+1)^2 is the degeneracy factor.

$$\sigma_{J'\leftarrow J''}(E) = \frac{R_{J'\leftarrow J''}}{R_{J''\leftarrow J'}} \frac{E + W_{J',J''}}{E} \sigma_{J''\leftarrow J'}\left(E + W_{J',J''}\right) \qquad \textbf{(3.55)}$$

Using the above function for the de-excitation cross section the loss function becomes

$$L(E,T) = \sum_{J',J} \left[E_{J'} - E_J\right] \times \left\{f(J,T)\sigma_{J'\leftarrow J}(E) - f(J',T)\sigma_{J\leftarrow J'}(E)\right\} \qquad \textbf{(3.56)}$$

$$f(J,T) = \frac{1}{Q(T)} g_r(J) \exp\left(\frac{-BJ(J+1)}{k_B T}\right) \qquad \textbf{(3.57)}$$

where B = 5.25 cm^{-1} for methane, f(J,T) is the distribution function as a function of the rotational state J and temperature T and Q(T) is the partition function which is equal to 608.9 at a temperature of 300 K. *Herzberg* [1945] provides values of the weighting function $g_r(J)$. *Gan* [1991] and *Gan and Cravens* [1992] calculated the loss of energy due to the rotational processes and the results are shown in Figure 3.44.

The loss function for the vibrational states is given below [*Gan,* 1991] and when used with Equation (3.48) vibrational cooling rates for methane are obtained (Figure 3.45).

$$L_{vJ}(E, T_n) =$$

$$W_J \left\{ \sigma_{vJ}(E) - \exp\left[- W_J / k_B T_n \right] \frac{E + W_J}{k_B T_n} \, \sigma_J\left(E + W_J\right) \right\} \tag{3.58}$$

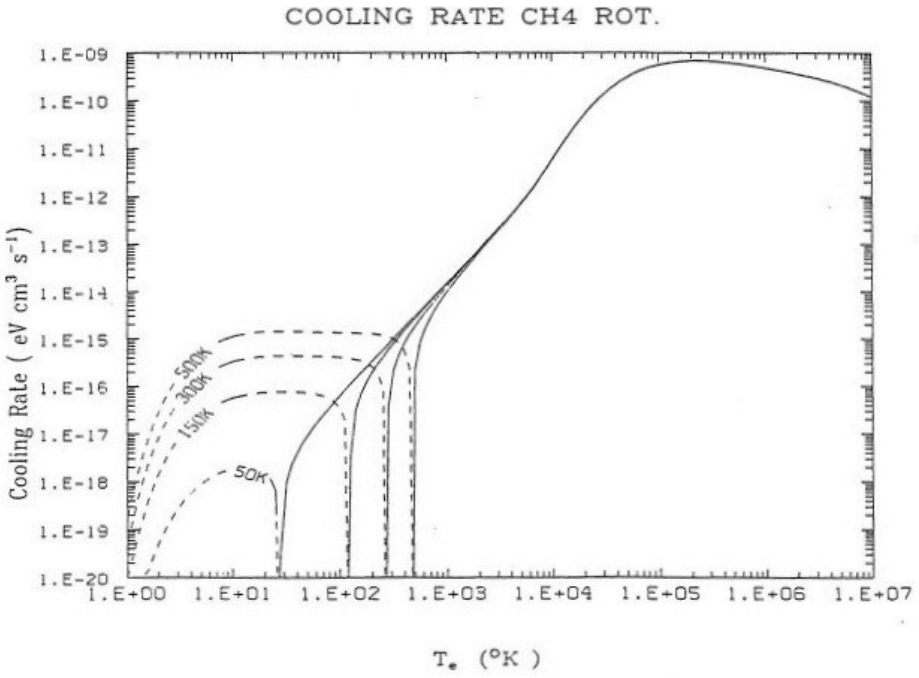

Figure 3.44 Cooling rates of electrons for rotational excitation of CH_4 with a neutral temperature of 50, 150, 300, or 500 K. (From *Gan* [1991])

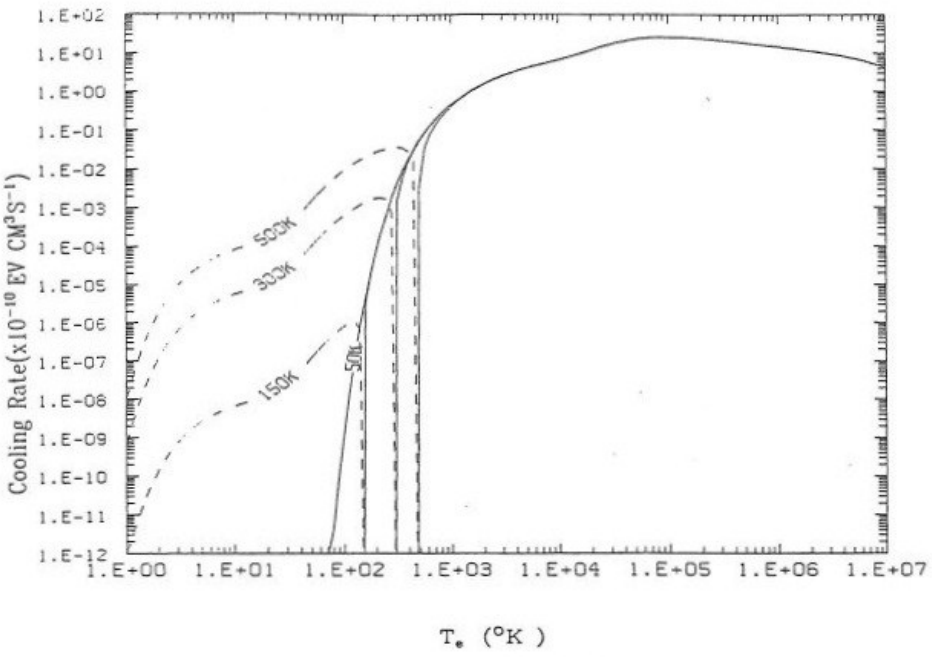

Figure 3.45 Cooling rates of electrons for vibrational excitation of CH_4 with a neutral temperature of 50, 150, 300, or 500 K as indicated on each line. (From *Gan* [1991])

Another representation of the cooling rates of thermal electrons as a result of electron-impact excitation and ionization of N_2 and CH_4 is shown in Figure 3.46 and Figure 3.47 respectively.

Collisions with the ion species also provides cooling to the thermal electron population. *Banks and Kockarts* [1973] have derived Equation (3.59) for use in determining the energy loss rate $\frac{dU_{ei}}{\delta t}$ for electrons in electron-ion Coulomb collisions. It should be noted that while the electrons are losing energy, the ion population is gaining energy indicated by the difference of signs of $\frac{dU_{ei}}{\delta t}$ and $\frac{dU_{ie}}{dt}$.

$$-\frac{dU_{ei}}{\delta t} = \frac{dU_{ie}}{dt} = 7.7 \times 10^{-6} n_e n_i \left[\frac{(T_e - T_i)}{A_i T_e^{\frac{3}{2}}} \right] \qquad \textbf{(3.59)}$$

In Equation (3.59), n denotes the number density (subscript e for electrons and i for ions), T is the temperature and A_i is the mass of the ion in atomic mass units.

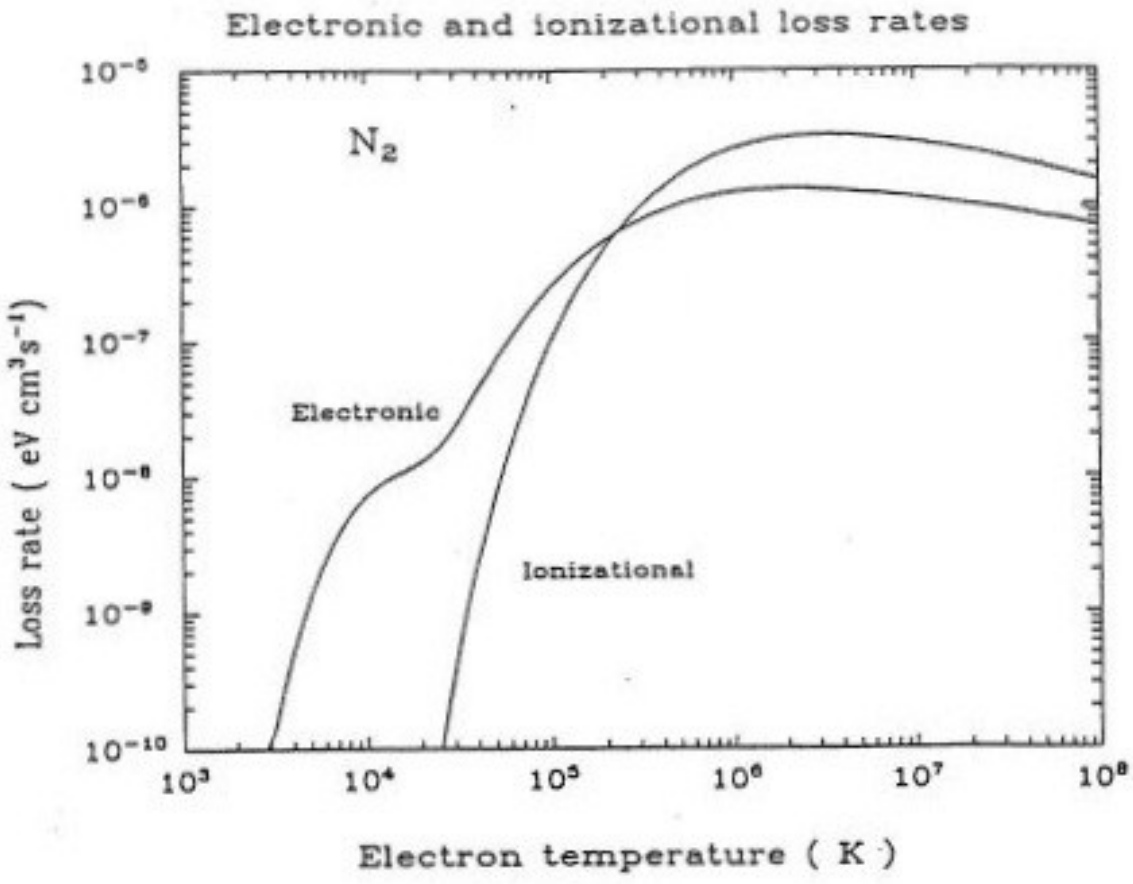

Figure 3.46 Electronic and ionizational loss rates for electron impact collisions with N_2. (From *Gan* [1991])

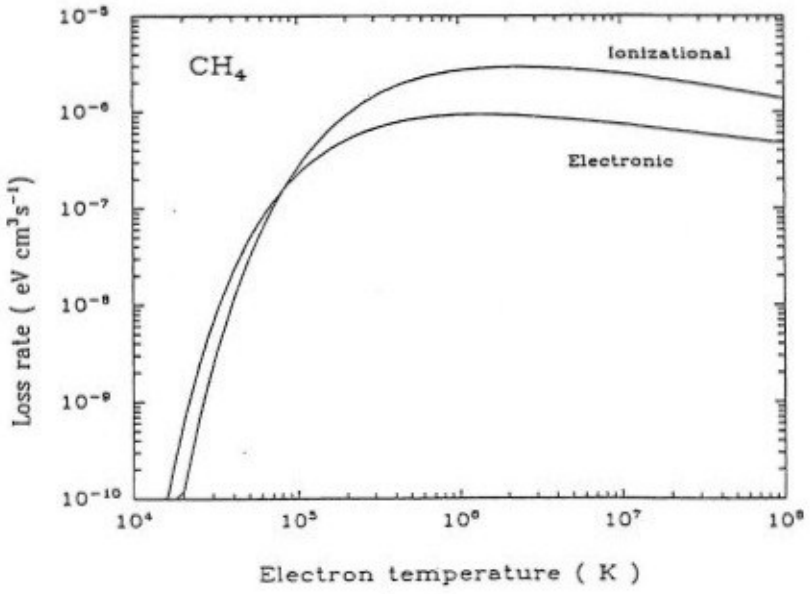

Figure 3.47 Electronic and ionizational loss rates for electron impact collisions with CH_4. (From *Gan* [1991])

3.7.2 Electron Conductivity

In addition to the transfer of energy between different species, energy may be conducted along the magnetic field line. The expression for the thermal electron conductivity κ_e in units of $eV\ cm^{-1}s^{-1}K^{-1}$ is obtained from *Banks and Kockarts* [1973] and *Korosmezey* et al. [1987].

$$\kappa_e = \frac{\kappa_{ei}}{1 + \kappa_{ei}[\sum_k 1/\kappa_{en}]} = \frac{7.7 \times 10^5 T_e^{\frac{5}{2}}}{1 + 3.22 \times 10^4 (T_e^2/n_e) \sum_k n_n \bar{Q}_D} \quad \textbf{(3.60)}$$

where κ_{ei} is the thermal electron conductivity resulting from electron-ion collisions for a fully ionized plasma, κ_{en} is the thermal conductivity from electron-neutral collisions, n is the number density, T is the temperature and $\bar{Q}_D$ is the average momentum transfer cross section defined by Equation (3.46). The numerator of Equation (3.60) corresponds to the Spitzer-Harm conductivity

[*Spitzer*, 1962] which over-estimates the heat flux when the electron density is low [*Merrit and Thompson*, 1980] and so a correction to the flux is implemented (Equation (3.61)). *Rosner et al*. [1986] used the data of *Matte and Virmont* [1982] to limit the heat flux to a value known as the saturation flux defined as the flux of energy of all thermal electrons moving at the thermal speed.

$$F_c = \frac{F_{classical}}{1 + \left[9.1\left(\frac{\lambda_e}{L_T}\right)^{0.36}\right]} \qquad \textbf{(3.61)}$$

In the above equation F_c represents the corrected heat flux, $F_{classical}$ is the heat flux calculated by Equation (3.31), λ_e is the mean free path of the electrons and L_T is the scale length of the electron temperature's spatial variations. The 1 that appears in the denominator is a construct that was added by *Gan et al.* [1992] in order to limit the corrected heat flux to a maximum value of the classical heat flux.

3.7.3 Ion Energetics

Until very recently no published ion temperatures for Titan were presented. *Crary et al*. [2009] presented a global average ion temperature altitude profile with a temperature minimum of about 110 K around 1250 km, reaching an approximate temperature of 260 K at an altitude of 1600 km. The temperatures reported were obtained by comparing data from the INMS and the CAPS Ion Beam Sensor (CAPS-IBS*). Crary et al*. [2009] used the CAP-IBS and INMS data to generate ion fluxes as a function of energy that were then fit to a Maxwellian distribution, where the width of the peak indicated the temperature of the ions.

One "average" ion species is considered in this model with an average mass of 29 amu (i.e., $C_2H_5^+$ [*Robertson et al*., 2009]), which is found to be a major species in the ion chemistry [*Cravens et al.,* 2008]. This mass value also serves as a pseudo-average between the average

mass in the lower ionosphere (which contains more massive species) and the upper ionosphere (which contains less massive ion species from data reviewed by *Cravens et al*. [2009a]). The ion densities were taken to be equal to the electron density as the plasma was assumed to be quasi-neutral.

Dynamical terms in the energy equation (Equation (3.34)) depending on individual species flow velocities, $\mathbf{u}_{s,}$ could play an important role in establishing the ion temperature. The effect that such terms have on the electron temperature is negligible essentially due to the low mass of electrons compared to ions. The impact dynamical terms such as Joule heating, which is shown to be able to provide a non-negligible heat source to the thermal ion population with relative ion-neutral velocities on the order of the estimates made by *Cravens et al.* [2010], are examined further in Section 5.3.1. Three-dimensional MHD models are needed to provide accurate information regarding flow velocities above 1100 km [*Backes,* 2004; *Ma et al*., 2009].

Collisions with the thermal electrons represent the main source of heating for the ions even though they are a relatively small loss process for the electron species. The amount of energy transferred to an ion from the electrons is equal to the amount of energy lost by the electrons and is calculated using Equation (3.59).

The ion species will lose energy through collisions with the neutral atmosphere. Here the Maxwell molecule collision formulae are used instead of a hard sphere interaction which is reasonable for elastic collisions [*Schunk,* 1977]. This approach is taken due to the fact that the ion will induce a charge in the polarizable neutral atom and the ion will experience and interaction potential of the form:

$$V = -\frac{1}{4\pi\varepsilon_0}\frac{\gamma_n e^2}{2r^4} \qquad \textbf{(3.62)}$$

which *Schunk* and *Schunk and Nagy* [2009] manipulate to arrive at the ion-neutral momentum transfer frequency in Equation (3.63).

$$\nu_{in} = 2.21\pi\frac{n_n m_n}{m_i + m_n}\left(\frac{\gamma_n e^2}{\mu_{in}}\right)^{\frac{1}{2}} \qquad \textbf{(3.63)}$$

In this equation ions and neutrals are indicated with the subscript i and n, n is the number density, m is the mass, μ_{in} is the reduced mass of the ions and neutrals, e denotes the charge of an electron and γ_n is the neutral molecular polarizability. Table 3.18 provides the values of γ_n used in this model from *Lide* [2008].

Table 3.18 Neutral molecular polarizability

Species	γ_n [10^{-24}cm^3]
CH_4	2.593
N_2	1.7403

As was the case with electrons (see Equation (3.60)), ions are also capable of moving energy along the magnetic field through thermal conduction. *Burgers* [1969] derived a general expression for the ion conductivity κ_i as follows:

$$\kappa_i = \frac{5k_B p_s}{2m_s}\left\{\frac{4}{5}\nu_{ss} + \sum_{t\neq s}\nu_{st}\left[D_{st}^{(1)} + \frac{5z_{st}\mu_{st}}{2m_s}\frac{T_s}{T_{st}}\right]\right\}^{-1} \qquad \textbf{(3.64)}$$

where p_s = $n_s k_B T_s$, m is the ion mass k_B represents Boltzmann's constant and T stands for the temperature. This is a more generic case of Equation (3.60). Momentum transfer frequencies for

Coulomb collisions between species s and t, ν_{st}, are defined in Equation (3.65) [*Schunk and Nagy*, 2009]

$$\nu_{st} = \frac{16\sqrt{\pi}}{3} \frac{n_t m_t}{m_s + m_t} \left(\frac{2k_B T_{st}}{\mu_{st}}\right)^{-\frac{3}{2}} \frac{e_s e_t}{\mu_{st}^2} \ln \Lambda \qquad \textbf{(3.65)}$$

where T_{st} is the reduced temperature given by

$$T_{st} = \frac{m_s T_t + m_t T_s}{m_s + m_t} \qquad \textbf{(3.66)}$$

and Λ is the Coulomb logarithm [*Chen,* 2006] where λ_D is the Debye length given in Equation (1.1).

$$\Lambda = 12\pi n_i \lambda_D^3 \qquad \textbf{(3.67)}$$

The correction factor z_{st} for Coulomb collisions, depending on the reduced interaction potential, and the term $D_{st}^{(1)}$ have been determined by *Schunk* [1977] to be in the form of Equations (3.68) and (3.69).

$$z_{st} = \frac{3}{5} \qquad \textbf{(3.68)}$$

$$D_{st}^{(1)} = \frac{3m_s^2 + \frac{1}{10} m_s m_t - \frac{1}{5} m_t^2}{(m_s - m_t)^2} \qquad \textbf{(3.69)}$$

Using the above equations and the methodology described in this section, temperature profiles are derived for the ions and thermal electrons for a number of Titan flybys. The results of these temperature modeling efforts are presented in Chapter 5.

This section has described the model that will be used in this study. In the following chapters, results calculated using this model will be compared to measurements of ion density collected by INMS (Chapter 6 for the dayside and Chapter 7 for the nightside) and electron temperatures observed by RPWS-LP on the dayside (Chapter 5) and nightside (Chapter 7).

Chapter 4 **Dayside Primary Ion Production Rates**

Previous efforts into modeling electron and ion densities observed in Titan's ionosphere have found that the models produce an excess of ionospheric electrons [*Robertson et al*., 2009, *Westlake et al*., 2012] (see Section 1.5). The model used in this study had similar problems to the previous modeling efforts as shown in (Figure 4.1) where it is evident that the modeled electron densities at the peak are higher than the densities observed by the RPWS-Langmuir Probe as reported by *Agren et al.* [2009].

This discrepancy in the peak electron densities prompted an investigation into the possible causes of this increased density. The first step in modeling the ion densities of Titan's dayside ionosphere is to produce a primary population of ions via photoionization of the neutral upper atmosphere. As such, a method of evaluation of the primary ion production rates of the model using comparisons to empirical production rates derived from in situ measurements was used. The process used for these comparisons as well as the results from the T17, T40 and outbound leg of T18 appear in this chapter, which cover a wide range of solar zenith angles (See Table 4.1). For comparisons with the dayside measurements, the nested magnetic field line topology has been adopted (see Section 3.1) and the electron precipitation of magnetospheric electrons has not been considered. In addition to comparisons with the data, production rate profiles for various solar zenith angles have been generated for more generic modeling purposes.

Table 4.1 Solar zenith angles for the Titan passes examined in this section

Flyby	F10.7 Index	Solar Zenith Angle at Closest Approach	Solar Zenith Angle at an Altitude of 1400 km
T40 - Outbound	79.7	37˚	15˚
T40 - Inbound	79.7	65˚	37˚
T17 - Outbound	86.7	44˚	31˚
T17 - Inbound	86.7	45˚	65˚
T18 - Outbound	70.4	90˚	78˚

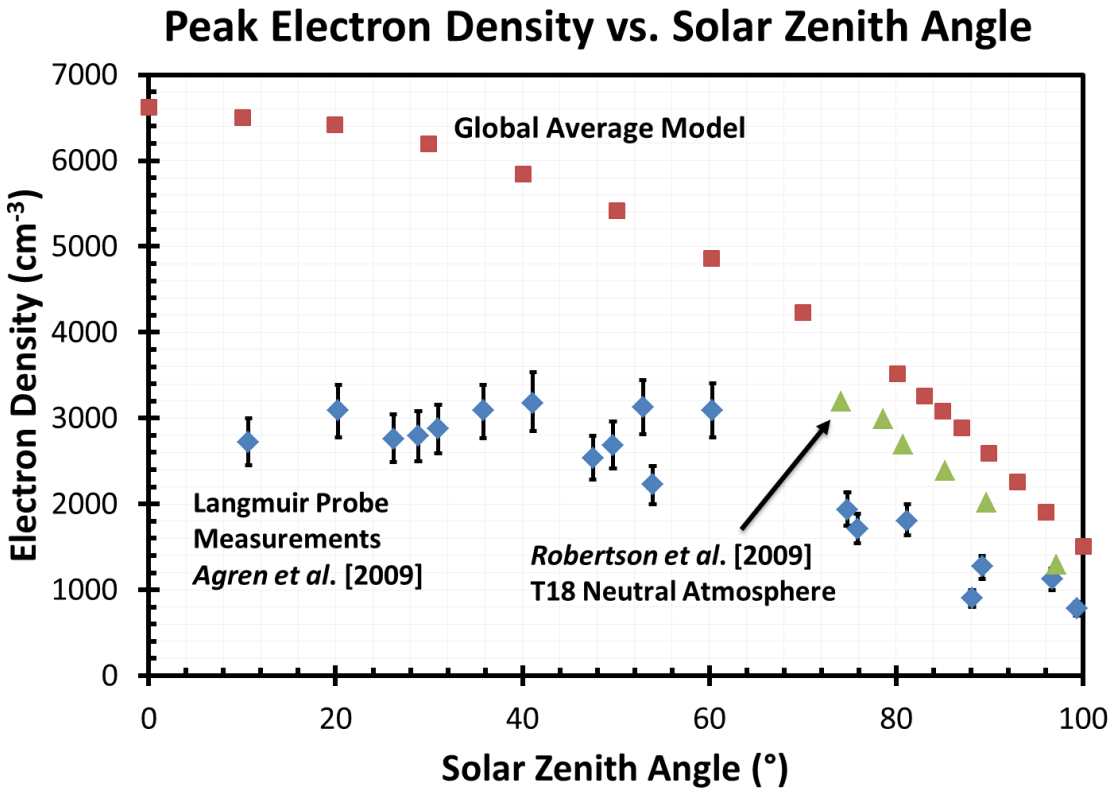

Figure 4.1 Peak electron density vs. solar zenith angle. Measurements taken by the Langmuir probe and presented by *Agren et al.* [2009] are shown with blue circles while the ionospheric modeling efforts of *Robertson et al.* [2009] are indicated with green triangles. The red squares show the peak electron densities generated using the first iteration of the global average model of Titan's ionosphere. The discrepancy between the modeling efforts and the measured electron densities will serve as the impetus for the current section.

4.1 Method for Verifying the Primary Ion Production

In order to investigate the cause of the abnormally large electron densities produced by the photochemical model, the primary population of ions produced in the photoionization code as well as ions produced by collisions with photoelectrons was examined. Give that the primary ion densities are used as inputs in the photochemical model, it follows that overproduction of the primary ions, the building blocks of the atmosphere, would cause an increase in the electron and ion densities further down in the modeling chain. In order to ensure that reasonable primary densities are produced, data collected by the Cassini Spacecraft was compared to densities obtained by the model. Production rates of ions in the model are also compared to production rates derived empirically from INMS. When discussing the methods used in verifying the model, the analysis of the outbound leg of T40 will be to illustrate the process. Incident photoelectron fluxes for T40 can be found in Figure 3.9.

4.1.1 Verification of N_2^+ Production Rate

As N_2 is the major constituent of the atmosphere of Titan, the production rate of N_2 must be examined carefully. This comparison is complicated by the fact that INMS is a mass spectrometer and with its mass of 28 amu, N_2 shares the same collection bin as the most abundant ion ($HCNH^+$) which outnumbers N_2 by two or three orders of magnitude.

As a solution to this observational difficulty the chemical reaction rates of *Anicich* [2003] were used in conjunction with the photochemical model (see Section 3.4). The photochemical model has shown that 90-99% of the CH_3^+ produced in Titan's ionosphere is a product of the reaction of N_2^+ and CH_4. Using this fact it is possible to use density comparisons between the CH_3^+ density and the density measured by INMS (shown in Figure 4.2) to evaluate the efficacy

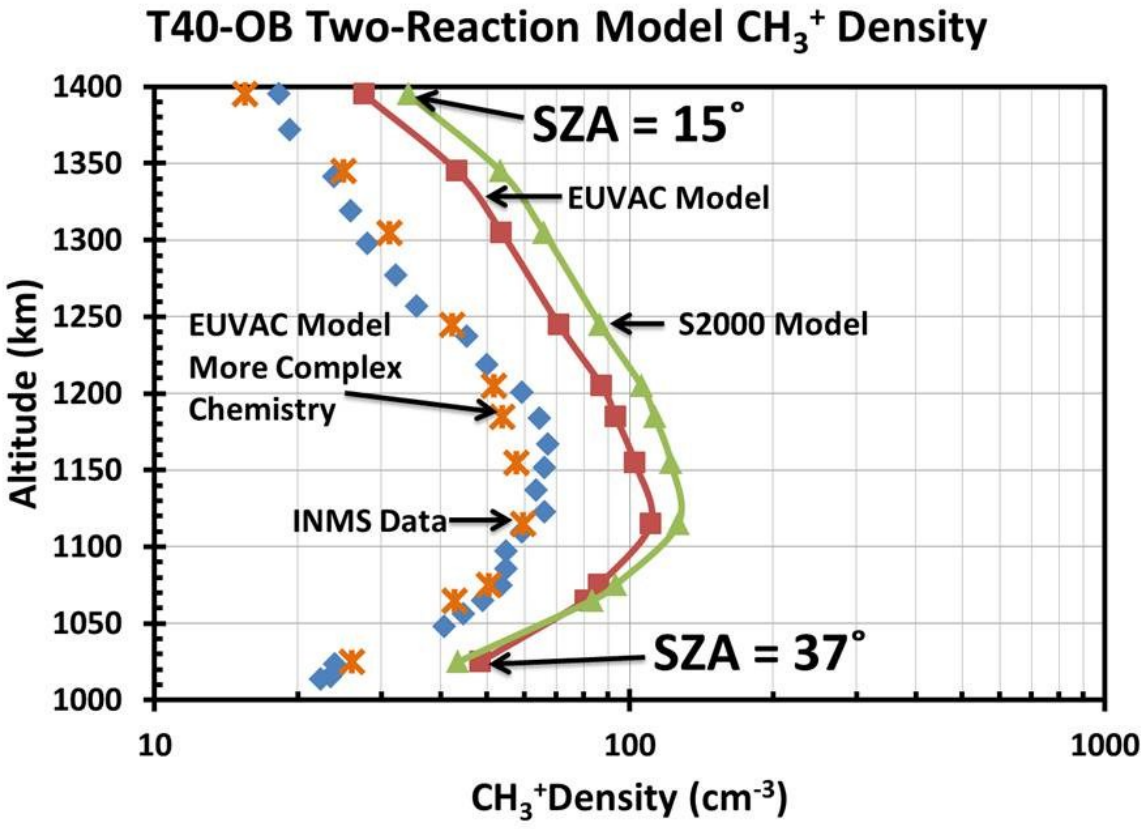

Figure 4.2 Density of CH_3^+ derived from model production rates using a simple two reaction chemical model compared to INMS data from the T40-Outbound flyby of Titan. INMS data is indicated with the blue diamonds, results for the Solar 2000 and EUVAC models of the solar flux are shown with green triangles and red squares respectively. The orange crosses indicate the CH_3^+ density derived from model production rates and the more complex ion chemistry given in Equation (4.5). The solar zenith angle at closest approach and at the uppermost altitude are indicated at the bottom and top of the figure. The solar zenith angle is adjusted to reflect the conditions observed by the Cassini spacecraft.

of the photoproduction model. At this point the opportunity was taken to evaluate the impact of the choice of solar flux model (EUVAC or SOLAR2000) on the model as well.

The CH_3^+ density presented in Figure 4.2 was obtained using a simple two-reaction model. In order to calculate the density with this simple two-reaction model, 0 the ion density was assumed to be purely photochemical, meaning that the production rate of an ion at a given altitude is equal to its loss rate (Equation (4.1)) at that altitude where production and loss of the ion occur locally (i.e. no neutral winds). Equation (4.2) shows that in our approximation the production of CH_3^+ from reactions with N_2^+ and CH_4 is balanced by the loss of CH_3^+ from reactions with CH_4 (the main loss process of CH_3^+) with a reaction rate coefficient of 1.10×10^{-9} $cm^3 s^{-1}$ [*Anicich,* 2003]. From these equations an expression for the density of CH_3^+ was obtained using a simple two-reaction model (Equation (4.3)) where the production of CH_3^+ is assumed to be the production of N_2^+ (Equation (4.4)) which is graphed in Figure 4.2.

$$Production_{CH_3^+} = Loss_{CH_3^+} \tag{4.1}$$

$$k_{N_2^+,CH_4^+}[N_2^+][CH_4] = k_{CH_3^+,CH_4}[CH_3^+][CH_4] \tag{4.2}$$

$$[CH_3^+] = \frac{k_{N_2^+,CH_4}[N_2^+]}{k_{CH_3^+,CH_4}} \tag{4.3}$$

$$[CH_3^+] \approx \frac{Prod_{N_2^+}}{k_{CH_3^+,CH_4}} \tag{4.4}$$

$$[CH_3^+] \approx \frac{k_{N_2^+,CH_4}[N_2^+]_{model}[CH_4]}{k_{CH_3^+,CH_4}[CH_4] + k_{CH_3^+,C_2H_4^+}[C_2H_4] + k_{CH_3^+,NH}[NH]} \tag{4.5}$$

Figure 4.2 shows that at the ionospheric peak the density of CH_3^+ is near 60 ions/cc while the SOLAR 2000 model produces almost twice as much and the EUVAC model overprices the

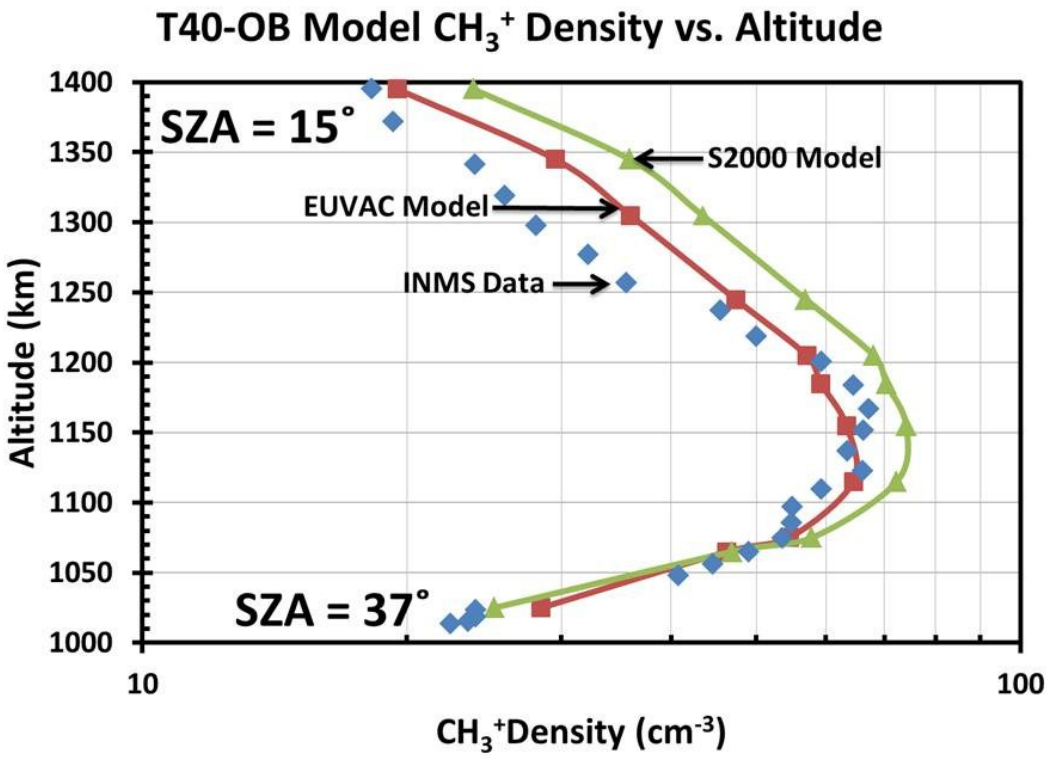

Figure 4.3 CH_3^+ density produced by the full photochemical model compared to INMS data from the T40-Outbound flyby of Titan. INMS data is indicated with the blue diamonds, results for the Solar 2000 and EUVAC models of the solar flux are shown with green triangles and red squares respectively. The solar zenith angle at closest approach and at the uppermost altitude are indicated at the bottom and top of the figure. The solar zenith angle is adjusted to reflect the conditions observed by the Cassini spacecraft.

INMS measured density by 80%. This abundance of CH_3^+ is a product of the assumption that methane is the only loss pathway for CH_3^+. For a more accurate calculation for the density of CH_3^+, the other major loss processes of CH_3^+ (reactions with C_2H_4 and NH as noted in Table 3.11) would need to be considered (Equation (4.5)), which, as the orange crosses in Figure 4.2 show, greatly increases the agreement between the model and INMS measured densities using the EUVAC solar flux model. At this point, it becomes advantageous to use the full photochemical model (Appendix C) to account for additional minor loss pathways of CH_3^+. Density profile comparisons between the measured and modeled CH_3^+ density profiles are shown in Figure 4.3 and are in much better agreement when the EUVAC solar flux model is used.

After verifying that the CH_3^+ densities produced in the model are in reasonable agreement with the INMS measured densities, the production rate profile of N_2^+ from photoionization of N_2 and electron impact ionization due to photoelectrons was compared to a production rate derived from INMS measurements using the simple two-reaction chemical model. This production rate was found using the same approximations used in Equation (4.2) and (4.4) but now the densities of CH_3^+ and CH_4 are taken directly from INMS measurements (see Equation (4.6)).

$$Prod_{N_2^+} \approx k_{CH_3^+,CH_4}[CH_3^+]_{INMS}[CH_4]_{INMS} \qquad \textbf{(4.6)}$$

Figure 4.4 shows a comparison of the production rate profile of N_2^+ derived from INMS measurements using the simple two-reaction model compared to that which is produced in the model using the SOLAR2000 and EUVAC modeled solar photon fluxes. Note how both models of the solar flux have production rates that are larger than those derived from the INMS measurements. This difference is caused by the fact that even though the overwhelming majority

of CH_3^+ is produced directly from N_2^+, not all N_2^+ reacts with methane to form CH_3^+ (see Table 3.6). Thus, the production rate of N_2^+ can more accurately be expressed by Equation (4.7).

$$\begin{aligned} & Prod_{N_2^+} \\ & \approx k_{N_2^+,CH_4}[N_2^+][CH_4] \\ & + k_{N_2^+,H_2}[N_2^+][H_2] \\ & + k_{N_2^+,C_2H_4}[N_2^+][C_2H_4] \\ & + k_{N_2^+,C_2H_6}[N_2^+][C_2H_6] \end{aligned} \qquad \textbf{(4.7)}$$

Instead of using Equation (4.7) to determine the fraction of N_2^+ that will form CH_3^+, the photochemical model is used once again. A correction factor was obtained by taking the ratio of the production rate of CH_3^+ to the production rate of N_2^+ (shown in Figure 4.5). In most cases only 60-85% of the N_2^+ produced will interact with methane to form CH_3^+ and dividing the N_2^+ production rate by this factor will account for the remaining N_2^+ production.

This adjustment to the empirical INMS N_2^+ production rate, shown in Figure 4.6, brings the modeled production rates within 10% of the empirical values using both the EUVAC and SOLAR2000 models of the solar flux at the peak and within 20% at higher altitudes using the EUVAC solar flux. This trend is also seen in the CH_3^+ production rates (Figure 4.7) which provides evidence that the CH_3^+ production rate is also reasonable.

These results produce confidence that the model is reliably accounting for the photoionization and electron impact ionization of molecular nitrogen in the upper atmosphere of Titan. This in turn indicates that the major source of ion production on the dayside has been implemented in a reliable and accurate manner.

4.1.2 Verification of CH_4^+ Production Rates

After the verification of the photoionization and electron impact ionization of the most abundant molecule in Titan's upper atmosphere, it becomes important to verify that the model produces the ionization products of methane sufficiently. The study will use the ion CH_4^+ as an indicator of the abundance of the products formed from the ionization of methane.

In light of the higher resolution N_2 photoabsorption cross sections for photons between 800 and 1000 Angstroms published by *Liang et al.* [2007] and utilized by *Lavvas et al.* [2011], multiple instances of this model have been run. The higher resolution cross sections have sharply defined peaks that will allow more photons to pass through more of the upper atmosphere without interacting with nitrogen than the cross sections of *Gallagher et al.* [1988]. In order to simulate this lack of interaction shown by *Liang et al.*, the percentage of photons that interact with the *Gallagher et al.* cross sections was adjusted for a case where all photons interact with the *Gallagher et al.* cross sections, a case where half of the photons interact with the *Gallagher et al.* cross sections and a case where photons in this regime do not interact with N_2. These additional model runs were not necessary for the discussion of the N_2^+ production rates as the energies of these photons are below the photoionization threshold for N_2; however, as photons in this energy range can ionize methane.

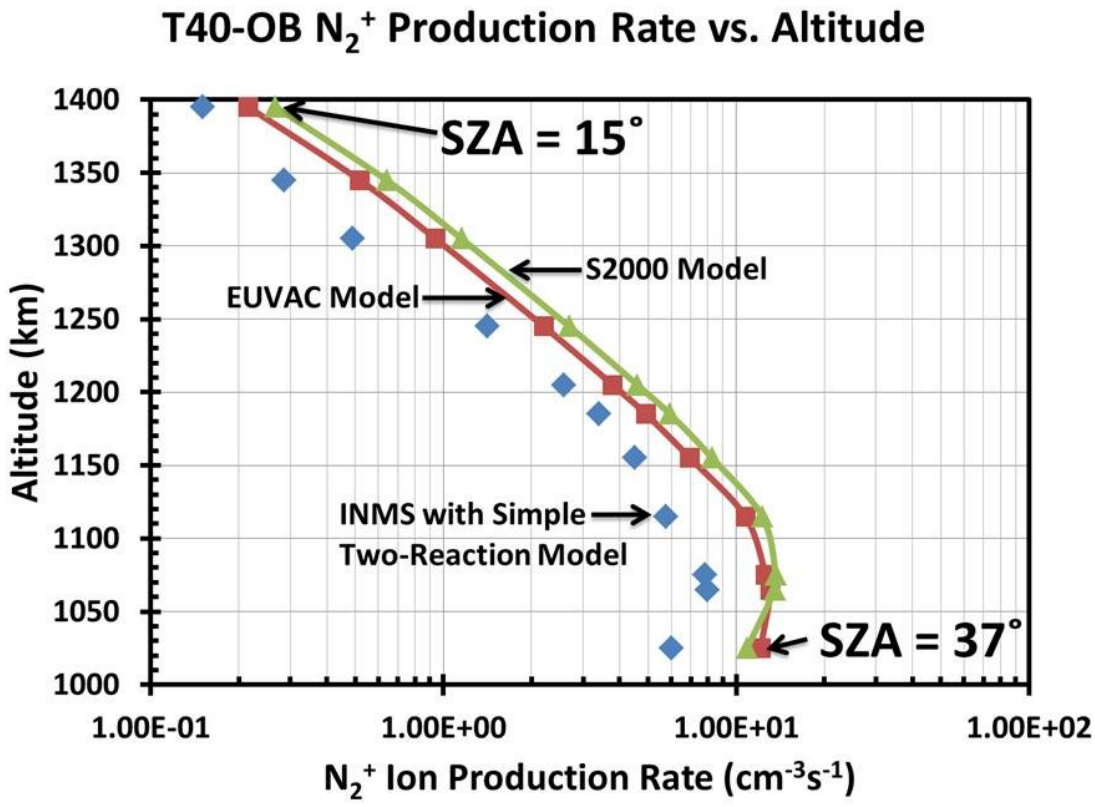

Figure 4.4 Modeled photoionization production rates of N_2^+ compared to the empirical production rate of N_2^+ derived from INMS data from the T40-Outbound flyby of Titan using the simple two reaction chemical model. INMS data is indicated with the blue diamonds, results for the Solar 2000 and EUVAC models of the solar flux are shown with green triangles and red squares respectively. All N_2^+ production is assumed to produce CH_3^+. The solar zenith angle at closest approach and at the uppermost altitude are indicated at the bottom and top of the figure. The solar zenith angle is adjusted to reflect the conditions observed by the Cassini spacecraft.

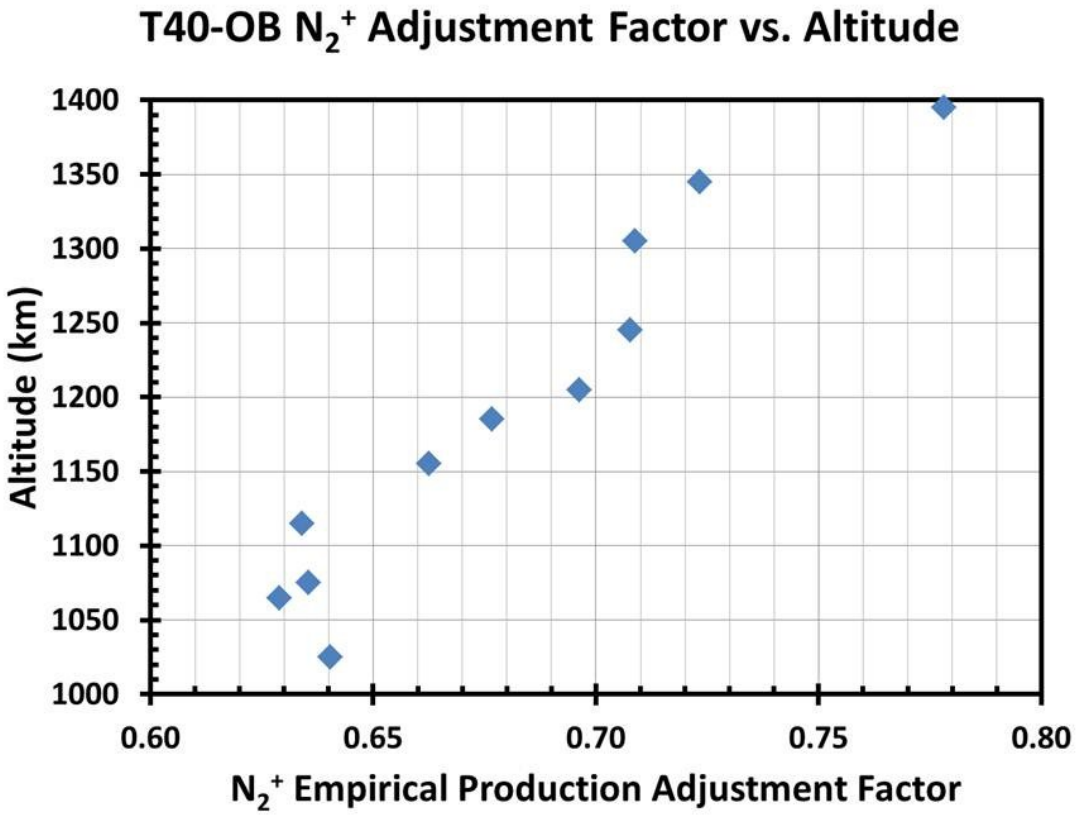

Figure 4.5 Factor used to adjust the empirical INMS N_2^+ production rate for the T40-Outbound flyby of Titan. This correction factor is the ratio of N_2^+ production rate from photoionization to the N_2^+ production rate from the full photochemical model (production from photoionization and chemical pathways).

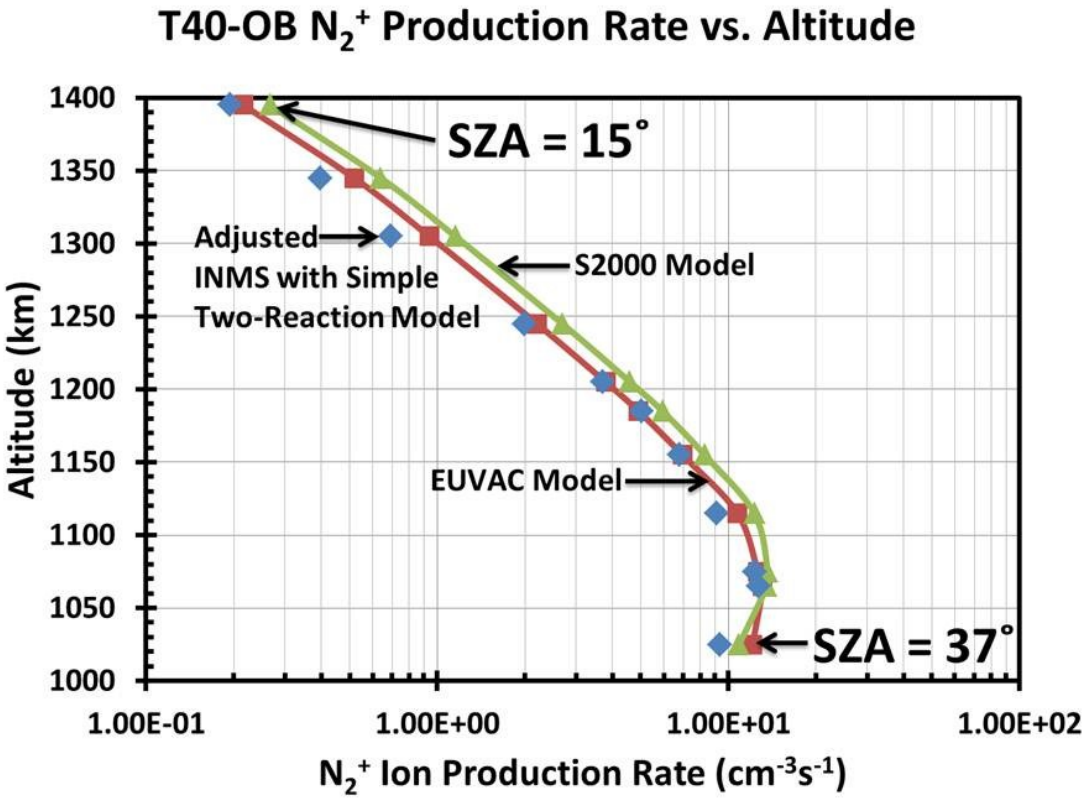

Figure 4.6 Modeled photoionization production rates of N_2^+ compared to the empirical production rate of N_2^+ derived from INMS data using the simple two reaction chemical model adjusted by the factor shown in Figure 4.5 from the T40-Outbound flyby of Titan. INMS data is indicated with the blue diamonds, results for the Solar 2000 and EUVAC models of the solar flux are shown with green triangles and red squares respectively. Not all N_2^+ production is assumed to produce CH_3^+. The solar zenith angle at closest approach and at the uppermost altitude are indicated at the bottom and top of the figure. The solar zenith angle is adjusted to reflect the conditions observed by the Cassini spacecraft.

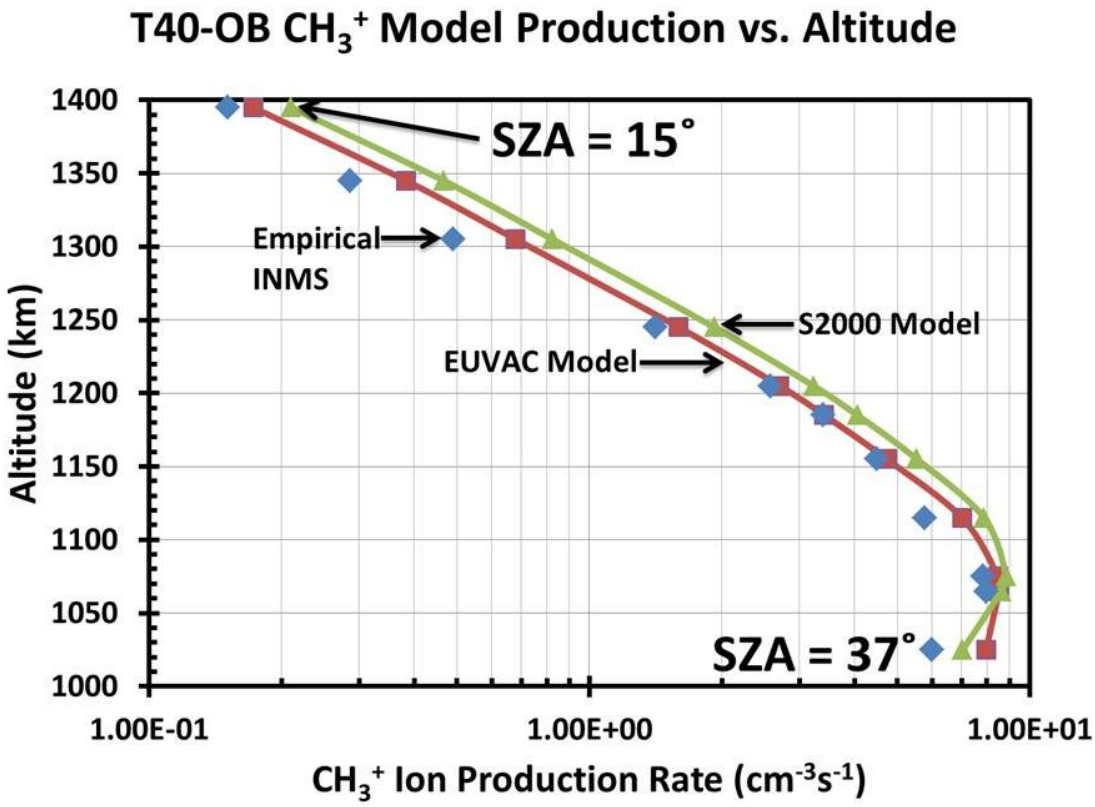

Figure 4.7 A comparison of the modeled production rates of CH_3^+ to the empirical production rate of CH_3^+ derived from INMS data from the T40-Outbound flyby of Titan. INMS data is indicated with the blue diamonds, results for the Solar 2000 and EUVAC models of the solar flux are shown with green triangles and red squares respectively. The solar zenith angle at closest approach and at the uppermost altitude are indicated at the bottom and top of the figure. The solar zenith angle is adjusted to reflect the conditions observed by the Cassini spacecraft.

As was done for the verification of the N_2^+ production rates, an empirical density of CH_4^+ was derived by assuming photochemical equilibrium for the ion (Equation (4.8)). Figure 4.8, Figure 4.9, and Figure 4.10 show the CH_4^+ density derived from assuming that all of the CH_4^+ is produced via the photoionization and electron impact ionization from photoelectrons and that the major loss process of CH_4^+ is through interactions with CH_4 with all, half and none of the photons interacting with N_2 using the photoabsorption cross section of *Gallagher et al.* [1988] respectively. The reaction coefficient used for CH_4^+ reacting with CH_4 is 1.14×10^{-9} $cm^3 s^{-1}$ [*Anicich*, 2003] as shown in Equation (4.9). Rearranging the variables will yield an expression for the density of CH_4^+ shown in Equation (4.10).

$$Production_{CH_4^+} = Loss_{CH_4^+} \quad \textbf{(4.8)}$$

$$Prod_{CH_4^+} = k_{CH_4^+,CH_4}[CH_4]_{INMS}[CH_4^+] \quad \textbf{(4.9)}$$

$$[CH_4] = \frac{Prod_{CH_4^+}}{k_{CH_4^+,CH_4}[CH_4]_{INMS}} \quad \textbf{(4.10)}$$

In looking at Figure 4.8 it appears that using the SOLAR2000 model of the solar flux produces the best agreement between the empirical densities and the measured INMS values; however, the empirical densities are too low below 1200 km and too large above 1200 km. Decreasing the percentage of photons that interact with molecular nitrogen will improve the agreement at altitudes below 1200 km (Figure 4.9 and Figure 4.10), but there is still a substantial disagreement in the upper altitude range. This overall discrepancy is due to the fact that not all of the CH_4^+ is produced from the photoionization and photoelectron impact ionization of methane (see Table 3.9). In some cases, this primary and secondary production only accounts for 65% of the total production of CH_4^+ while other sources, primarily chemical reactions between CH_5^+ and H, provide the bulk of the remaining production.

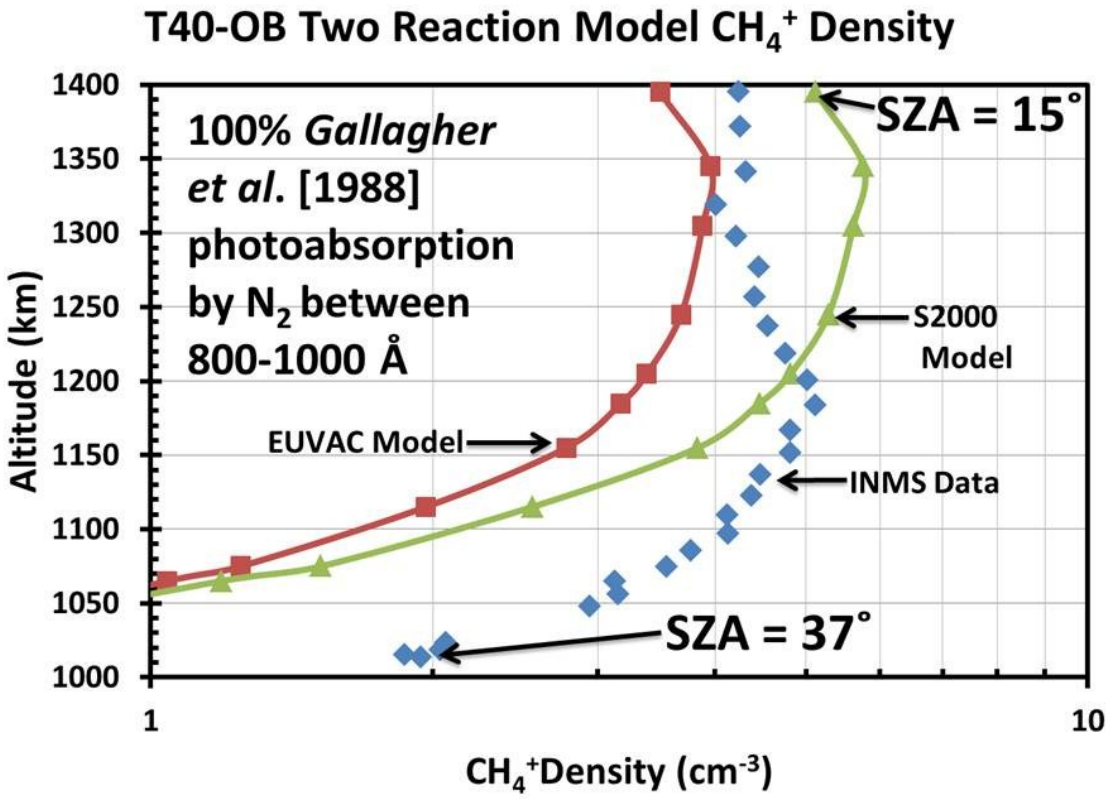

Figure 4.8 Density of CH_4^+ calculated using the simple two reaction chemical model (Equation (4.10)) and the photoionization model compared to INMS data from the T40-Outbound flyby of Titan. N_2 photoabsorption cross sections for photons with wavelengths between 800 and 1000 Å of *Gallagher et al.* [1988] were used. INMS data is indicated with the blue diamonds, results for the Solar 2000 and EUVAC models of the solar flux are shown with green triangles and red squares respectively. The solar zenith angle at closest approach and at the uppermost altitude are indicated at the bottom and top of the figure. The solar zenith angle is adjusted to reflect the conditions observed by the Cassini spacecraft.

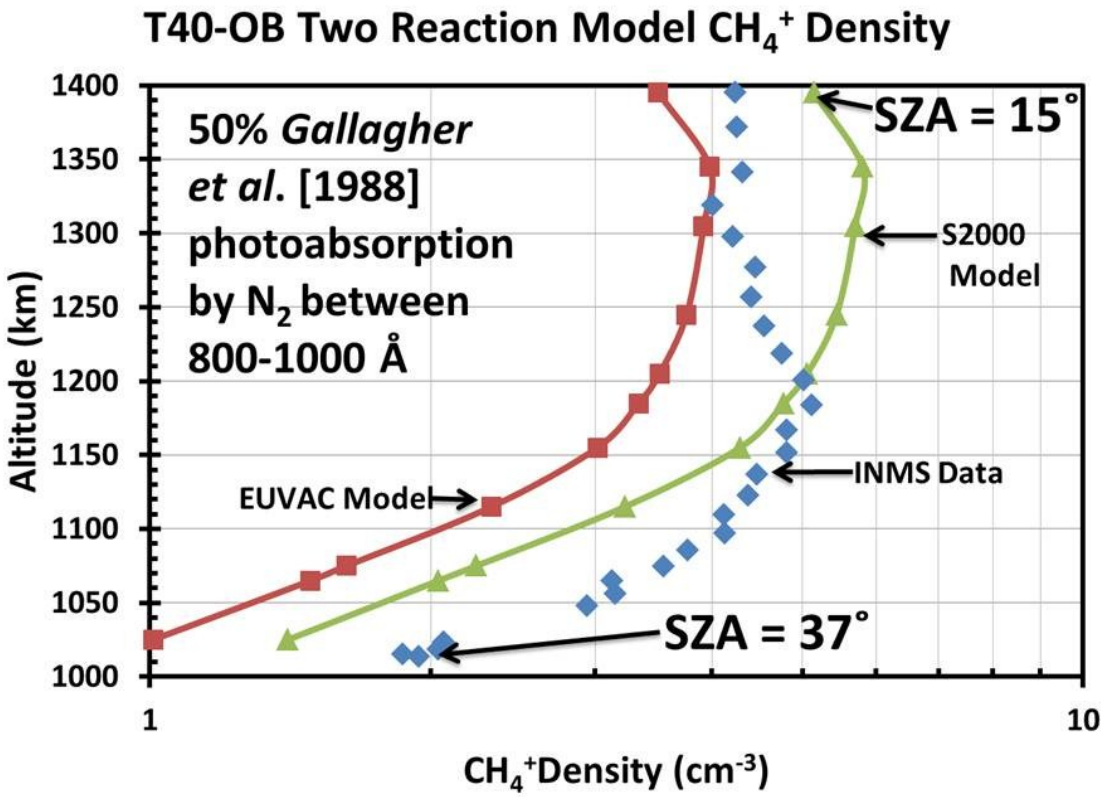

Figure 4.9 Density of CH_4^+ calculated using the simple two reaction chemical model (Equation (4.10)) and the photoionization model compared to INMS data from the T40-Outbound flyby of Titan. 50% of solar photons with wavelengths between 800 and 1000 Å interact with N_2 using photoabsorption cross sections of *Gallagher et al.* [1988]. INMS data is indicated with the blue diamonds, results for the Solar 2000 and EUVAC models of the solar flux are shown with green triangles and red squares respectively. The solar zenith angle at closest approach and at the uppermost altitude are indicated at the bottom and top of the figure. The solar zenith angle is adjusted to reflect the conditions observed by the Cassini spacecraft.

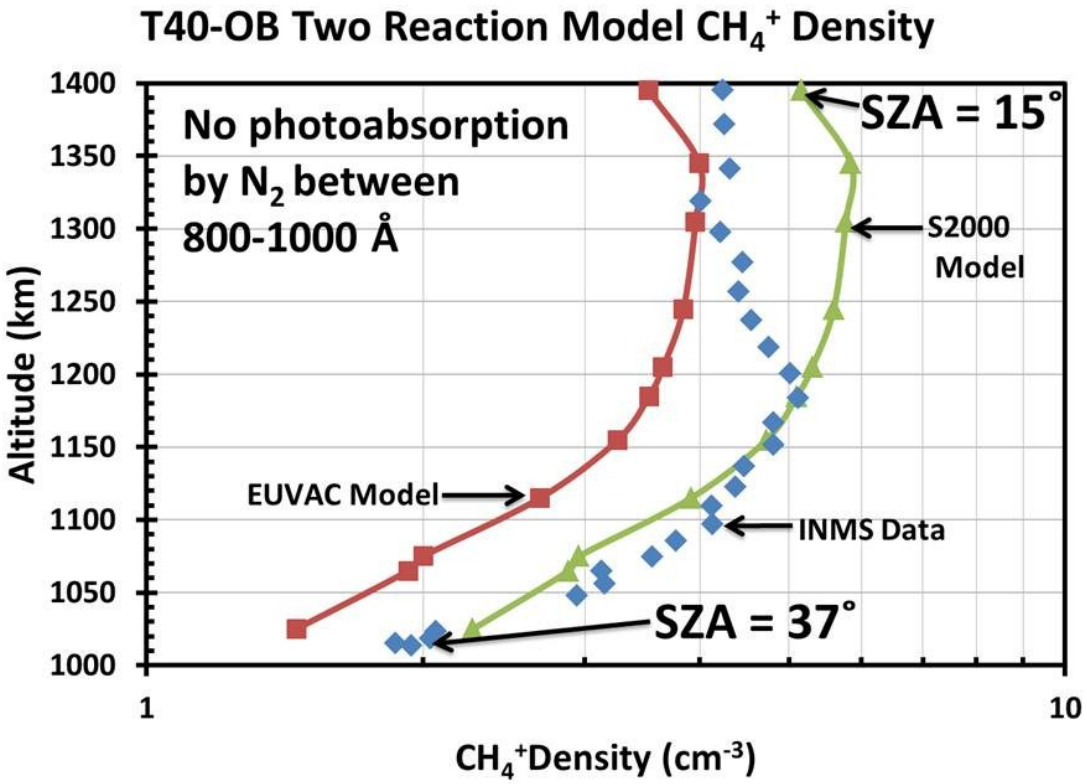

Figure 4.10 Density of CH_4^+ calculated using the simple two reaction chemical model (Equation (4.10)) and the photoionization model compared to INMS data from the T40-Outbound flyby of Titan. solar photons with wavelengths between 800 and 1000 Å did not interact with N_2. INMS data is indicated with the blue diamonds, results for the Solar 2000 and EUVAC models of the solar flux are shown with green triangles and red squares respectively. The solar zenith angle at closest approach and at the uppermost altitude are indicated at the bottom and top of the figure. The solar zenith angle is adjusted to reflect the conditions observed by the Cassini spacecraft.

To account for these other production pathways of CH_4^+ (CH_5^+ reacting with H, methane reacting with H_2^+, H^+, and N^+, see Appendix C for the full list) the photochemical model is implemented and the results are displayed in Figure 4.11, using the full *Gallagher et al.* [1988] N_2 cross sections, Figure 4.12 for the case where 50% of the photons interact with N_2 and Figure 4.13 for the instance where there is no interaction with nitrogen for photons with wavelengths between 800 and 1000 Angstroms. Viewing the results of the model indicates that the EUVAC model produces an initial population of solar photons that brings the model into better agreement with the INMS observed densities than the SOLAR2000 model. This is consistent with the results from the production verification of N_2^+. It should be noted that all of the model runs give densities that are too small above 1200 km but this is on the order of 10%. For altitudes less than 1200 km the best agreement is found in the case where 50% of the photons interact with the cross sections of *Gallagher et al.* [1988].

After demonstrating that the model can produce a CH_4^+ density profile that is near the measured density profile, the production rate of CH_4^+ was examined. As before, the results where the only source of CH_4^+ is the photoionization and photoelectron impact ionization of methane were examined first. Beginning with Figure 4.14 and ending with Figure 4.16 the production rate profiles of CH_4^+ are shown and compared to an empirical production rate determined by Equation (4.9) where the density of methane was measured by INMS. Unlike N_2^+, the major loss process of CH_4^+ (reactions with neutral methane) accounts for more than 90% of the loss of the ion; thus using the local approximation, the adjustment factor for the empirical production rate is not considered.

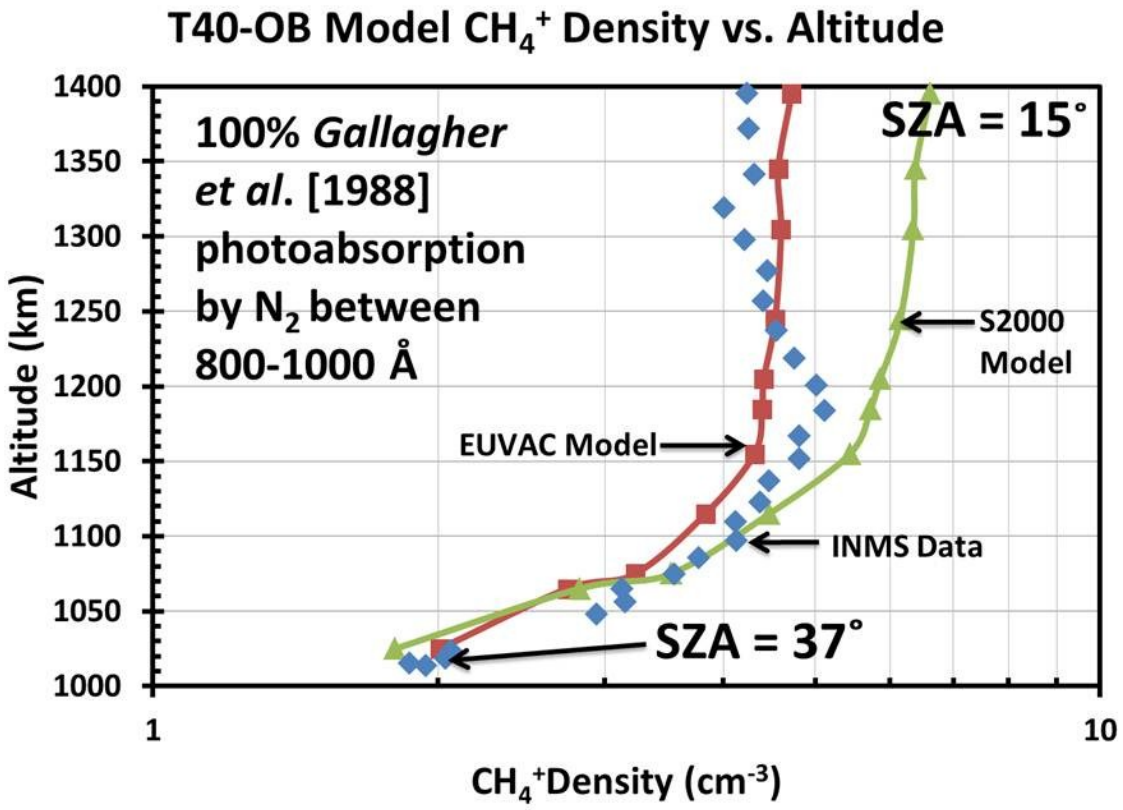

Figure 4.11 CH_4^+ density produced with the full photochemical model compared to INMS data from the T40-Outbound flyby of Titan. N_2 photoabsorption cross sections for photons with wavelengths between 800 and 1000 Å of *Gallagher et al.* [1988] were used. INMS data is indicated with the blue diamonds, results for the Solar 2000 and EUVAC models of the solar flux are shown with green triangles and red squares respectively. The solar zenith angle at closest approach and at the uppermost altitude are indicated at the bottom and top of the figure. The solar zenith angle is adjusted to reflect the conditions observed by the Cassini spacecraft.

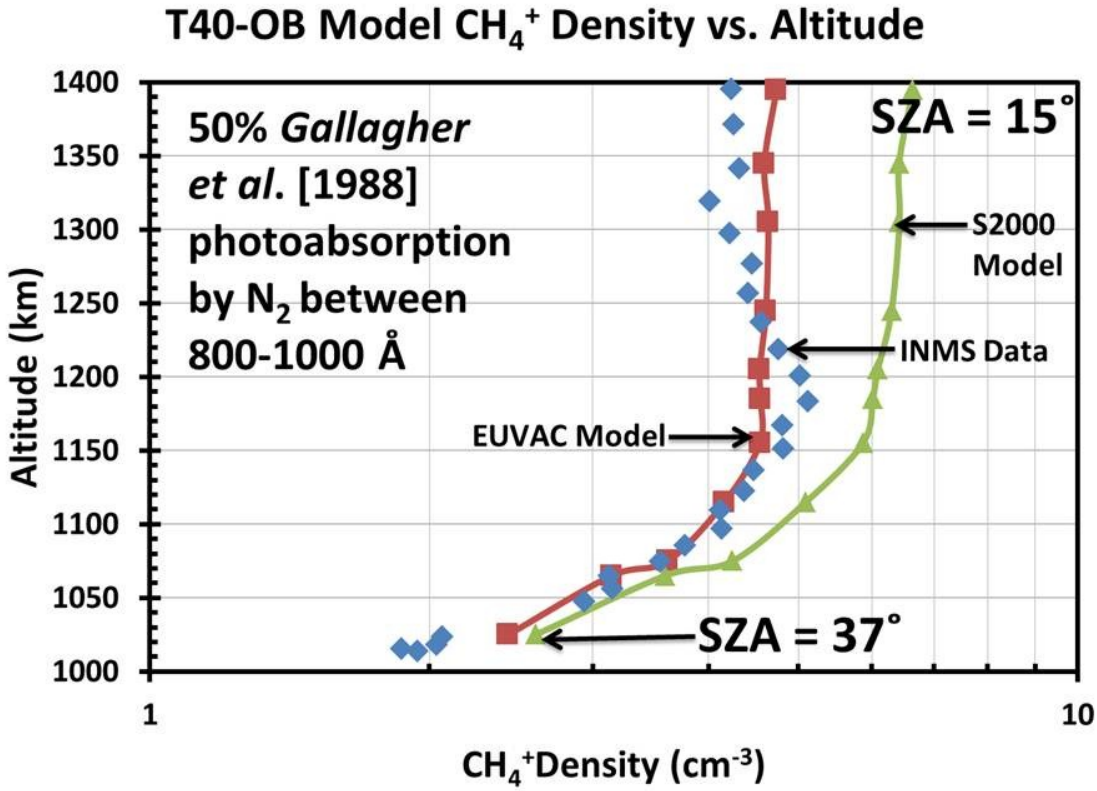

Figure 4.12 CH_4^+ density produced by the full photochemical model compared to INMS data from the T40-Outbound flyby of Titan. 50% of solar photons with wavelengths between 800 and 1000 Å interact with N_2 photoabsorption using cross sections of *Gallagher et al.* [1988]. INMS data is indicated with the blue diamonds, results for the Solar 2000 and EUVAC models of the solar flux are shown with green triangles and red squares respectively. The solar zenith angle at closest approach and at the uppermost altitude are indicated at the bottom and top of the figure. The solar zenith angle is adjusted to reflect the conditions observed by the Cassini spacecraft.

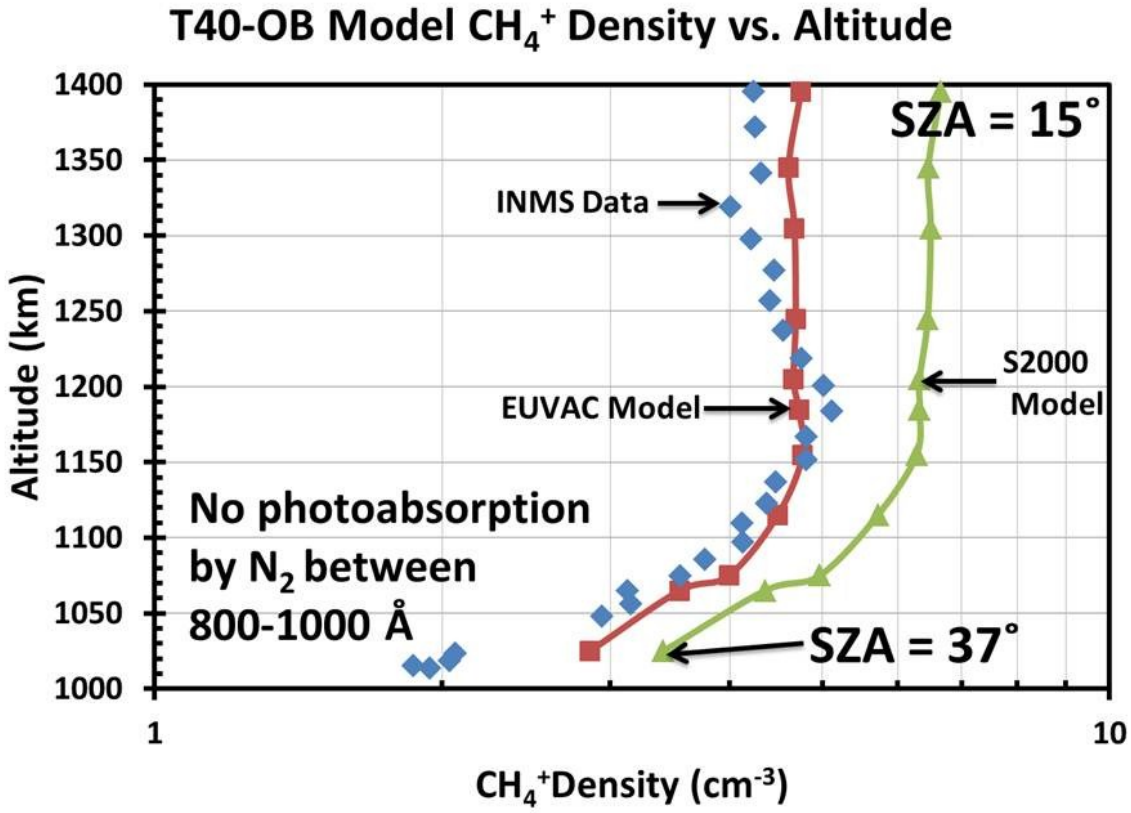

Figure 4.13 CH_4^+ density produced by the full photochemical model compared to INMS data from the T40-Outbound flyby of Titan. solar photons with wavelengths between 800 and 1000 Å did not interact with N_2. INMS data is indicated with the blue diamonds, results for the Solar 2000 and EUVAC models of the solar flux are shown with green triangles and red squares respectively. The solar zenith angle at closest approach and at the uppermost altitude are indicated at the bottom and top of the figure. The solar zenith angle is adjusted to reflect the conditions observed by the Cassini spacecraft.

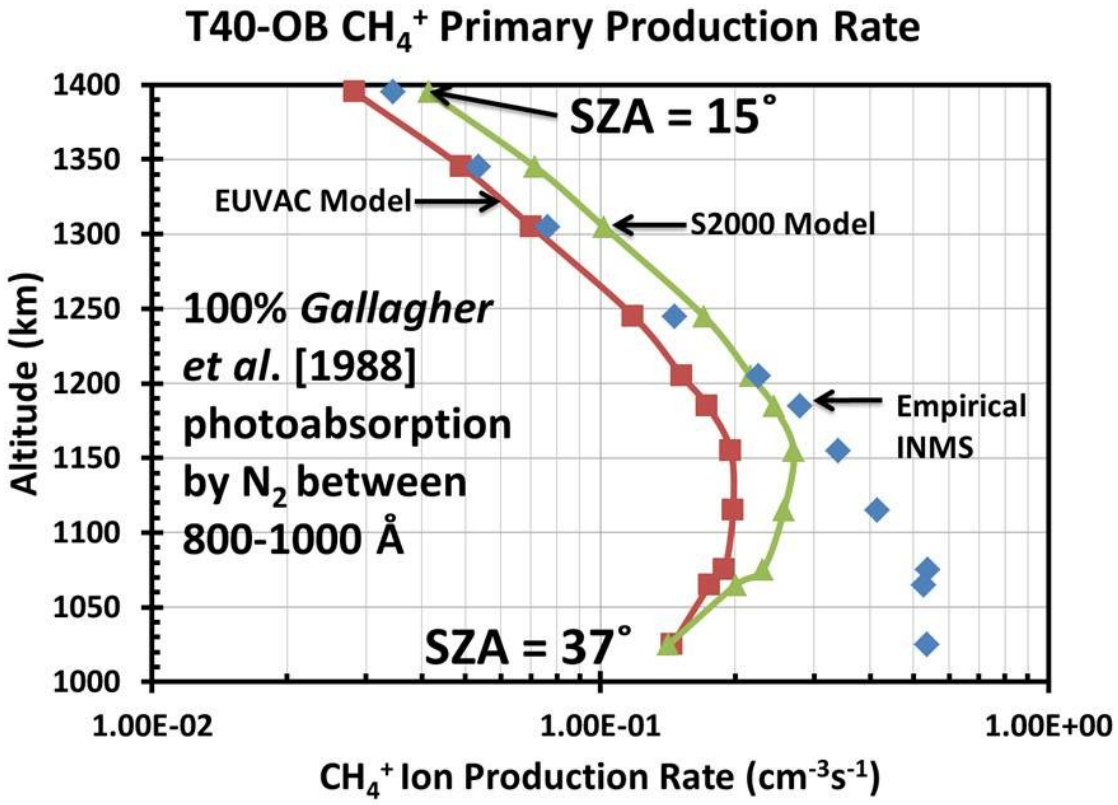

Figure 4.14 Modeled photoionization production rates of CH_4^+ from photoionization and electron impact ionization by photoelectrons compared to the empirical production rate of CH_4^+ derived from INMS data from the T40-Outbound flyby of Titan. N_2 photoabsorption cross sections for photons with wavelengths between 800 and 1000 Å of *Gallagher et al.* [1988] were used. INMS data is indicated with the blue diamonds, results for the Solar 2000 and EUVAC models of the solar flux are shown with green triangles and red squares respectively. The solar zenith angle at closest approach and at the uppermost altitude are indicated at the bottom and top of the figure. The solar zenith angle is adjusted to reflect the conditions observed by the Cassini spacecraft.

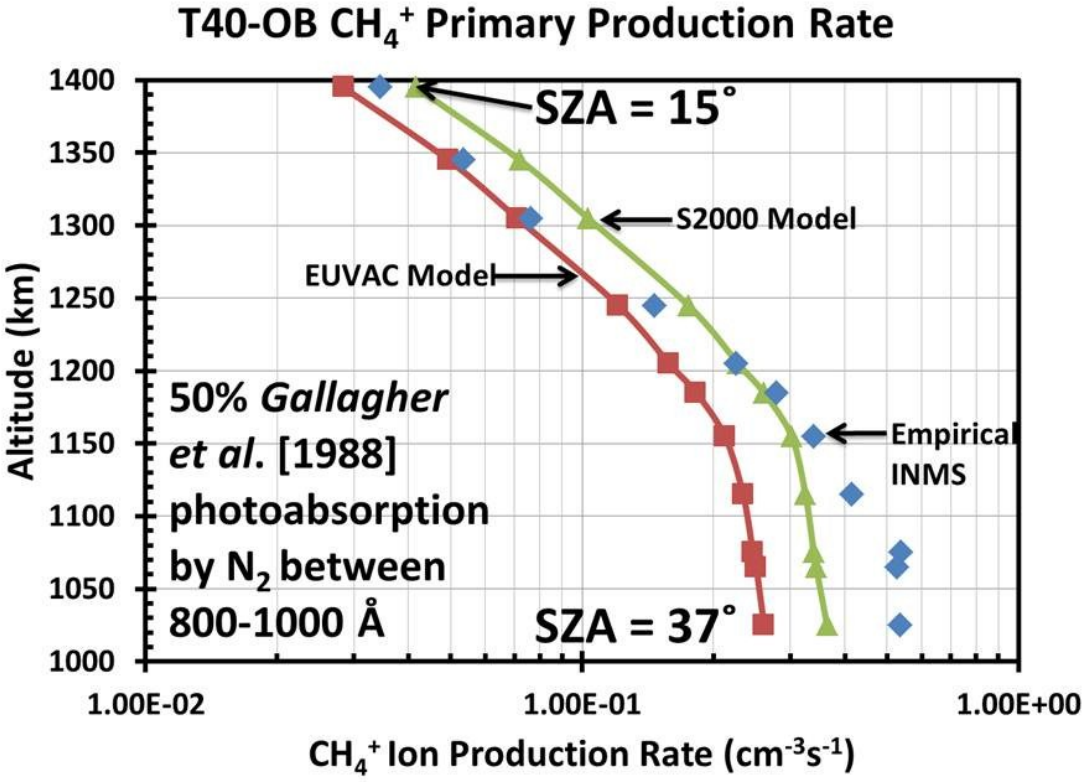

Figure 4.15 Modeled photoionization production rates of CH_4^+ from photoionization and electron impact ionization by photoelectrons compared to the empirical production rate of CH_4^+ derived from INMS data from the T40-Outbound flyby of Titan. 50% of solar photons with wavelengths between 800 and 1000 Å interact with N_2 using photoabsorption cross sections of *Gallagher et al.* [1988]. INMS data is indicated with the blue diamonds, results for the Solar 2000 and EUVAC models of the solar flux are shown with green triangles and red squares respectively. The solar zenith angle at closest approach and at the uppermost altitude are indicated at the bottom and top of the figure. The solar zenith angle is adjusted to reflect the conditions observed by the Cassini spacecraft.

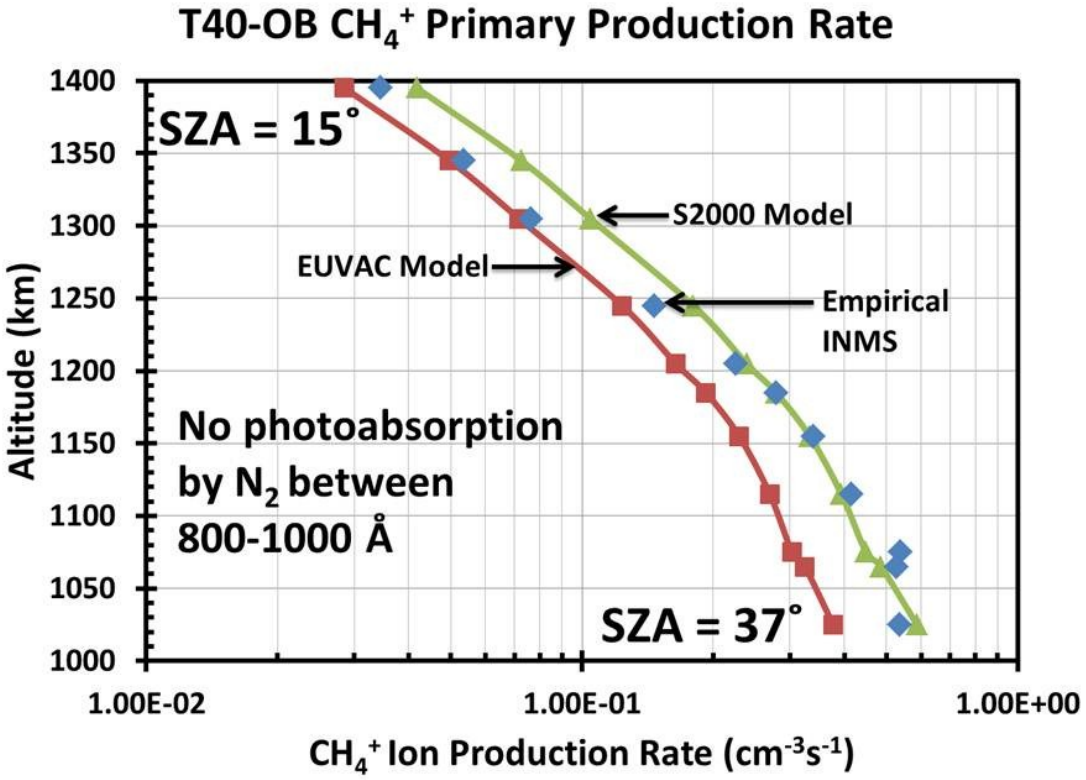

Figure 4.16 Modeled photoionization production rates of CH_4^+ from photoionization and electron impact ionization by photoelectrons compared to the empirical production rate of CH_4^+ derived from INMS data from the T40-Outbound flyby of Titan. solar photons with wavelengths between 800 and 1000 Å did not interact with N_2. INMS data is indicated with the blue diamonds, results for the Solar 2000 and EUVAC models of the solar flux are shown with green triangles and red squares respectively. The solar zenith angle at closest approach and at the uppermost altitude are indicated at the bottom and top of the figure. The solar zenith angle is adjusted to reflect the conditions observed by the Cassini spacecraft.

As expected, patterns similar to those observed in the density profiles emerge when examining the primary and secondary production rate profiles. All of the production rate profiles were below the empirical production rate profile derived from INMS values. The production rate profile deviates from the empirical production rate by as much as a factor of two at altitudes below 1200 km when the full photoabsorption by molecular nitrogen is considered with the cross sections of Gallagher *et al.* [1988]. When the photoabsorption of nitrogen is neglected for photons with wavelengths between 800 and 1000 Angstroms, the production rate at the upper altitudes (above 1200km) agrees with the empirical production rate for the EUVAC model while the lower altitude production rates show better agreement with the SOLAR2000 model. None of the models in this case have shown sufficient agreement between the photoproduction and secondary ion production of CH_4^+.

Once again the focus turns to the results of the production rate profiles made by the full photochemical model (Figure 4.17, Figure 4.18, and Figure 4.19). Using the full photochemical model to account for the additional production processes of CH_4^+ shows a much better agreement with the empirical production rates. In all cases, using the EUVAC model of the solar flux has yielded production rate profiles where that are in the best agreement with the empirical production rate profiles. Again, this is consistent with the results above. When all of the photons interact with nitrogen, (Figure 4.17) the closest agreement between the model production rates and the empirical production rates was obtained. There is less than a 10% discrepancy between the modeled and empirical production rates except at the lowest altitudes where there is a 15% discrepancy. When half and none of the photons with wavelengths between 800 and 1000 Angstroms interact with nitrogen (Figure 4.18 and Figure 4.19 respectively) the upper altitude modeled production rates are still within 10% of the empirical

values. At the lower altitudes the empirical production rates differ from the modeled production rates by almost 80% and a factor of 2 for the case where half and none of the photons with wavelengths between 800 and 1000 Angstroms interact with nitrogen respectively.

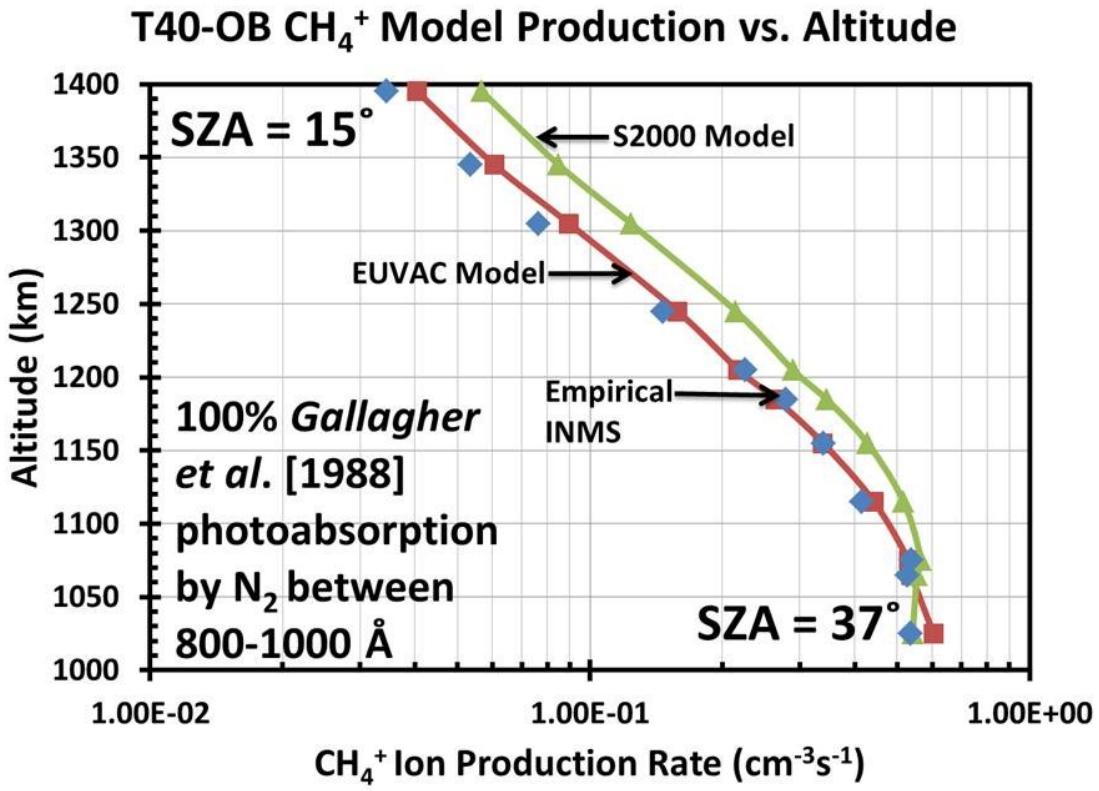

Figure 4.17 Modeled production rates of CH_4^+ using the full photochemical model compared to the empirical production rate of CH_4^+ derived from INMS data from the T40-Outbound flyby of Titan. N_2 photoabsorption cross sections for photons with wavelengths between 800 and 1000 Å of *Gallagher et al.* [1988] were used. INMS data is indicated with the blue diamonds, results for the Solar 2000 and EUVAC models of the solar flux are shown with green triangles and red squares respectively. The solar zenith angle at closest approach and at the uppermost altitude are indicated at the bottom and top of the figure. The solar zenith angle is adjusted to reflect the conditions observed by the Cassini spacecraft.

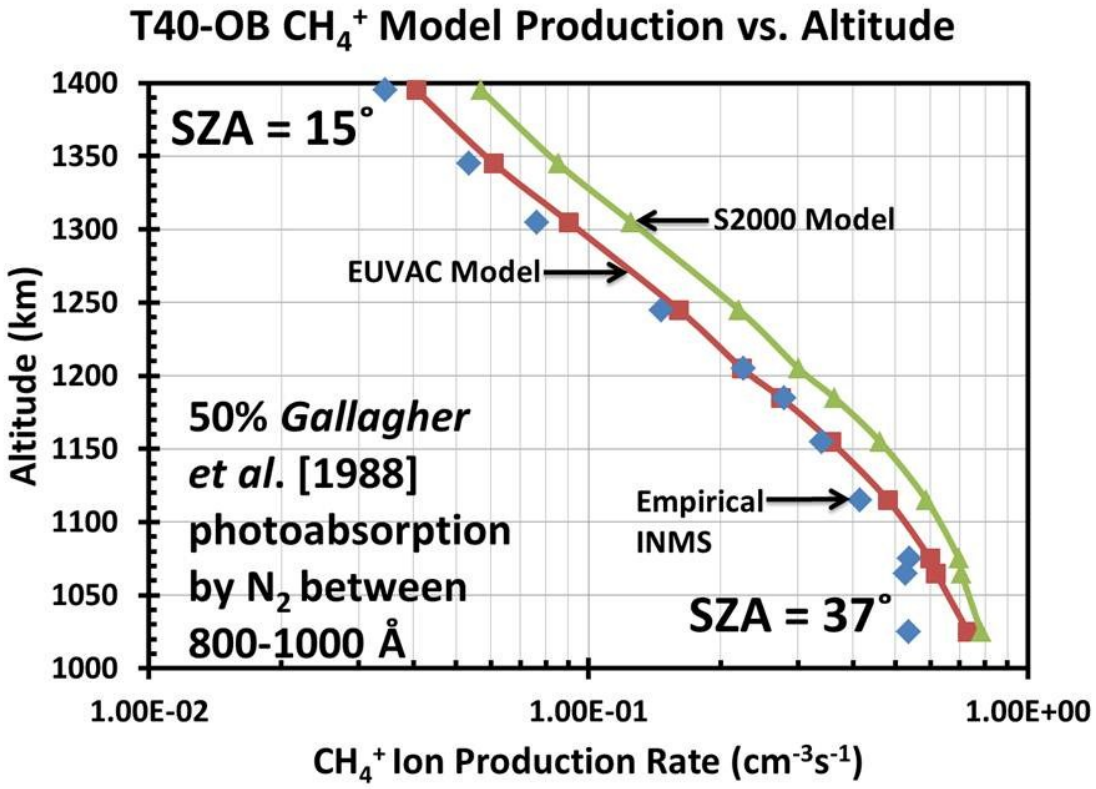

Figure 4.18 Modeled production rates of CH_4^+ using the full photochemical model compared to the empirical production rate of CH_4^+ derived from INMS data from the T40-Oubound flyby of Titan. 50% of solar photons with wavelengths between 800 and 1000 Å interact with N_2 using the photoabsorption cross sections of *Gallagher et al.* [1988]. INMS data is indicated with the blue diamonds, results for the Solar 2000 and EUVAC models of the solar flux are shown with green triangles and red squares respectively. The solar zenith angle at closest approach and at the uppermost altitude are indicated at the bottom and top of the figure. The solar zenith angle is adjusted to reflect the conditions observed by the Cassini spacecraft.

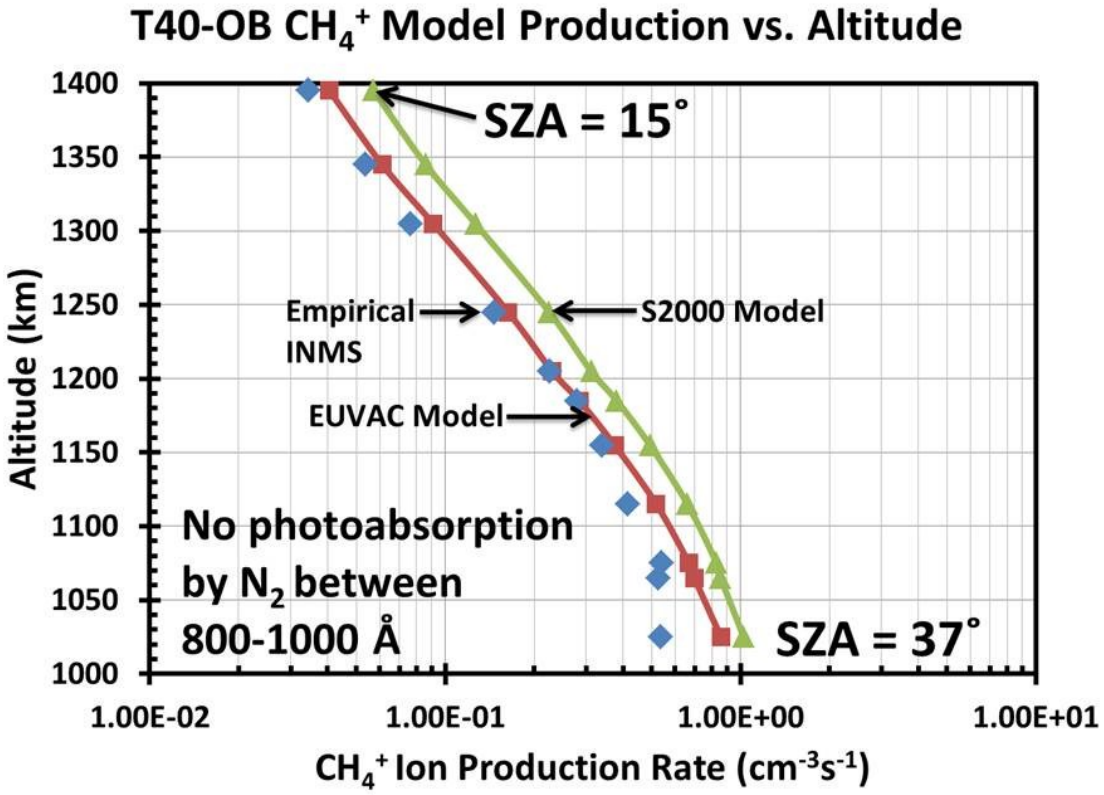

Figure 4.19 Modeled production rates of CH_4^+ using the full photochemical model compared to the empirical production rate of CH_4^+ derived from INMS data from the T40-Outbound flyby of Titan. solar photons with wavelengths between 800 and 1000 Å did not interact with N_2. INMS data is indicated with the blue diamonds, results for the Solar 2000 and EUVAC models of the solar flux are shown with green triangles and red squares respectively. The solar zenith angle at closest approach and at the uppermost altitude are indicated at the bottom and top of the figure. The solar zenith angle is adjusted to reflect the conditions observed by the Cassini spacecraft.

The results from this comparison between the modeled and empirical production rate profiles of CH_4^+ are found to be in reasonable agreement. This agreement builds confidence in the model and demonstrates that the increased electron densities are not an artifact from the overproduction of ion species for the outbound leg of T40 and demonstrates that the model is capable of producing realistic production rates of CH_4^+ at lower solar zenith angles. This particular case shows that the EUVAC model for the incident flux of solar photons produces better agreement between ion densities and production rates between modeled values and observed densities and empirically derived production rates for the primary ions N_2^+ and CH_4^+.

These results are by no means conclusive and the results of further modeling efforts are discussed in the next section for flybys of Titan at higher dayside solar zenith angles.

4.2 Flyby Specific Results

Now that the methodology for verifying the primary ion production rates of N_2^+ and CH_4^+ has been demonstrated for the outbound leg of T40 (and therefore solar zenith angles between 15˚ and 37˚) this method will be applied to the inbound leg of T40, covering solar zenith angles between 37˚ and 45˚), both legs of the T17 encounter (spanning solar zenith angles between 31˚ and 65˚), and the outbound leg of T18 which includes solar zenith angles between 78˚ and 90˚ (see Table 4.1). This will justify the use of the model for solar zenith angles up to 90˚ as well as examine the impact that the choice of solar flux model has on the results.

In Section 4.1 the verification process was discussed in depth. In this section, similar methods are used and so only the pertinent results are shown (N_2^+ and CH_4^+ production rate profiles). All of the figures that have been left out of this section, but are necessary for completeness, are shown in 0.

For each flyby of Titan, the photoionization (see Section 3.2) and two-stream (see Section 3.3) codes were run using the neutral atmosphere and the solar photon flux appropriate to each flyby producing production rate profiles of N_2^+ and CH_4^+ from photoionization and electron impact ionization due to photoelectrons of the neutral atmosphere. Using the fact that the vast majority of CH_3^+ is produced from reactions between methane and N_2^+ (see Table 3.11), the production rate of CH_3^+ was assumed to be the production rate of N_2^+, which in the photochemical model is equal to the loss rate of CH_3^+ from reactions with methane. This is represented by the simple two reaction model shown in Equation (4.6), which has been used to calculate the production rate of N_2^+ using the ion densities measured by the INMS instrument. In reality, not all N_2^+ reacts with methane to form CH_3^+, so the ratio of CH_3^+ production to N_2^+ production computed in the photochemical model was used as a correction factor. Dividing the loss rate of CH_3^+ by this correction factor accounts for the additional chemical sinks of N_2^+ and gives a more accurate representation of the N_2^+ production rate based on INMS density measurements of methane and CH_3^+.

An empirical production rate for CH_4^+ was calculated using the assumption of photochemical equilibrium to set the production rate of the ion equal to its loss rate by reactions between CH_4^+ and methane (see Table 3.10), both of whose densities have been measured by INMS, as shown in Equation (4.9). Unlike N_2^+, which is overwhelmingly produced by photoionization and electron impact ionization, a substantial portion of the CH_4^+ production comes from chemical reactions between CH_5^+ and H (see Table 3.9). To account for both of these production processes, the production rate of CH_4^+ from the full chemical model is compared to the production rate of the ion derived empirically from INMS measurements.

In light of the photoabsorption cross sections presented by *Liang et al.* [2007], the percentage of photons between 800 and 1000 Å that interact with N_2 using the photoabsorption cross sections of *Gallagher et al.* [1988] has been varied. The fine structure of the cross sections of *Liang et al.* allows a larger amount of photons to pass through the atmosphere without interacting with molecular nitrogen. These photons, that do not have a high enough energy to ionize molecular nitrogen, will then interact with methane lower in the ionosphere and increase the production rate at lower altitudes.

4.2.1 T40-Inbound

The outbound leg of the T40 pass covers the range of solar zenith angles from 37° at closest approach up to 65° at an altitude of 1400 km. The comparison of the N_2^+ production rates from photoionization and electron impact ionization from photoelectrons and the empirical production rate derived from INMS measurements adjusted by the correction factor obtained from the photochemical model is shown in Figure 4.20. This figure shows a good agreement, less than 10% difference, between the model and data when using both models of the solar flux; however, the best agreement was obtained when the EUVAC model of the solar flux was used. The peak production rate N_2^+ production rate approached 10 ions per second near 1050 km.

Once again, three cases varying the percentage of photons that interact with nitrogen via the photoabsorption cross sections of *Gallagher et al.* [1988] with wavelengths between 800 and 1000 Angstroms were implemented to account for the higher resolution cross sections of *Liang et al.* [2007]. When all of the photons interact with the *Gallagher et al.* cross sections the complete photochemical production rate produced by the EUVAC model corresponds with the empirically derived production rates from INMS (see Figure 4.21). Below 1050 km the modeled production rates are 20% lower than the empirically derived densities indicating that a greater

percentage of photons must be passing through the upper ionosphere and are not being absorbed by nitrogen. When half of the photons between 800 and 1000 Å interact with nitrogen (Figure 4.22) the best agreement between the modeled and the empirically derived production rate profile is obtained. The only modeled point that is not within 15% of the empirical rate is at 1015 km. For the case where the photons of wavelength 800-1000 Å did not interact with nitrogen (Figure 4.23) the model production was too high in all but the highest altitudes. The discrepancy is exceptionally noticeable at the lowest altitudes.

The results for the outbound leg of T40 further verify that the production rates of N_2^+ and CH_4^+ are within acceptable error bounds (15-20%) of the empirically modeled production rates. Furthermore, the EUVAC model with 50% of the photons interacting with nitrogen had been shown to give the best agreement for the T40 inbound and outbound legs. This instills confidence in the model for solar zenith angles between 15 and 65˚. More cases are still to be considered to provide a more in depth look at the dependence of the model on solar zenith angles and solar flux model.

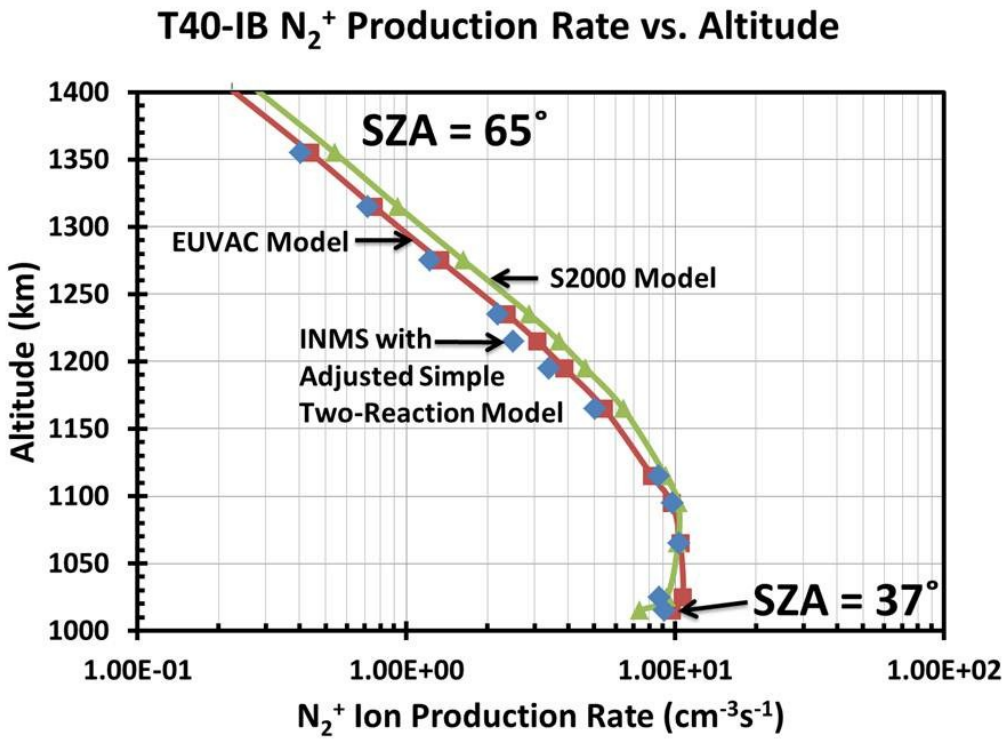

Figure 4.20 Modeled photoionization production rates of N_2^+ compared to the empirical production rate of N_2^+ derived from INMS data adjusted by the factor shown in Appendix Figure C.4 from the T17-Inbound flyby of Titan. INMS data is indicated with the blue diamonds, results for the Solar 2000 and EUVAC models of the solar flux are shown with green triangles and red squares respectively. The solar zenith angle at closest approach and at the uppermost altitude are indicated at the bottom and top of the figure. The solar zenith angle is adjusted to reflect the conditions observed by the Cassini spacecraft.

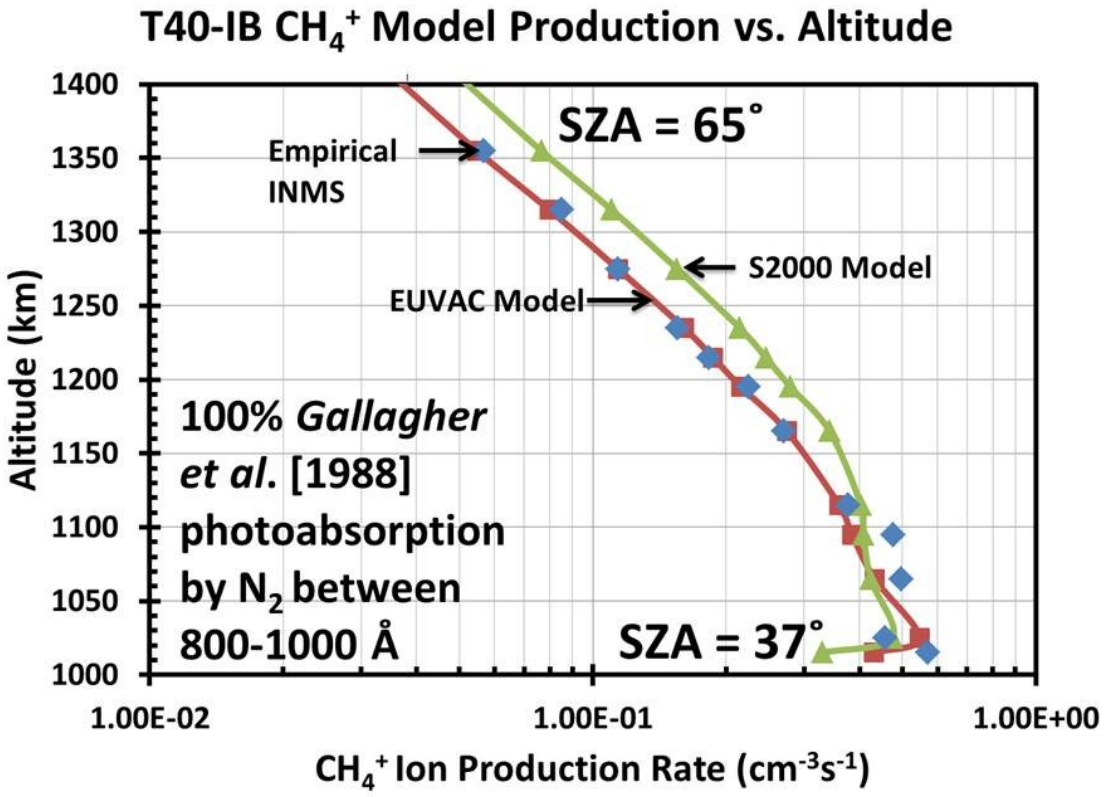

Figure 4.21 Modeled production rates of CH_4^+ compared to the empirical production rate of CH_4^+ derived from INMS data from the T40-Inbound flyby of Titan. N_2 photoabsorption cross sections for photons with wavelengths between 800 and 1000 Å of *Gallagher et al.* [1988] were used. INMS data is indicated with the blue diamonds, results for the Solar 2000 and EUVAC models of the solar flux are shown with green triangles and red squares respectively. The solar zenith angle at closest approach and at the uppermost altitude are indicated at the bottom and top of the figure. The solar zenith angle is adjusted to reflect the conditions observed by the Cassini spacecraft.

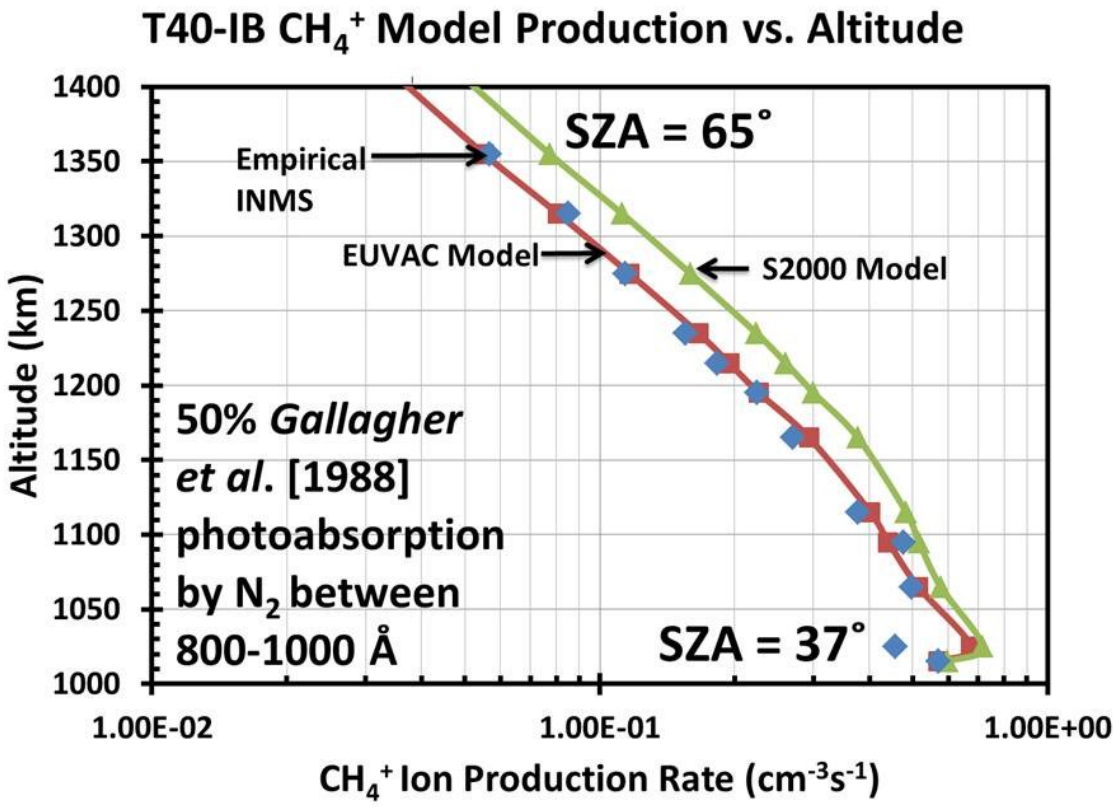

Figure 4.22 Modeled production rates of CH_4^+ to the empirical production rate of CH_4^+ derived from INMS data from the T40-Inbound flyby of Titan. 50% of solar photons with wavelengths between 800 and 1000 Å interact with N_2 using photoabsorption cross sections of *Gallagher et al.* [1988]. INMS data is indicated with the blue diamonds, results for the Solar 2000 and EUVAC models of the solar flux are shown with green triangles and red squares respectively. The solar zenith angle at closest approach and at the uppermost altitude are indicated at the bottom and top of the figure. The solar zenith angle is adjusted to reflect the conditions observed by the Cassini spacecraft.

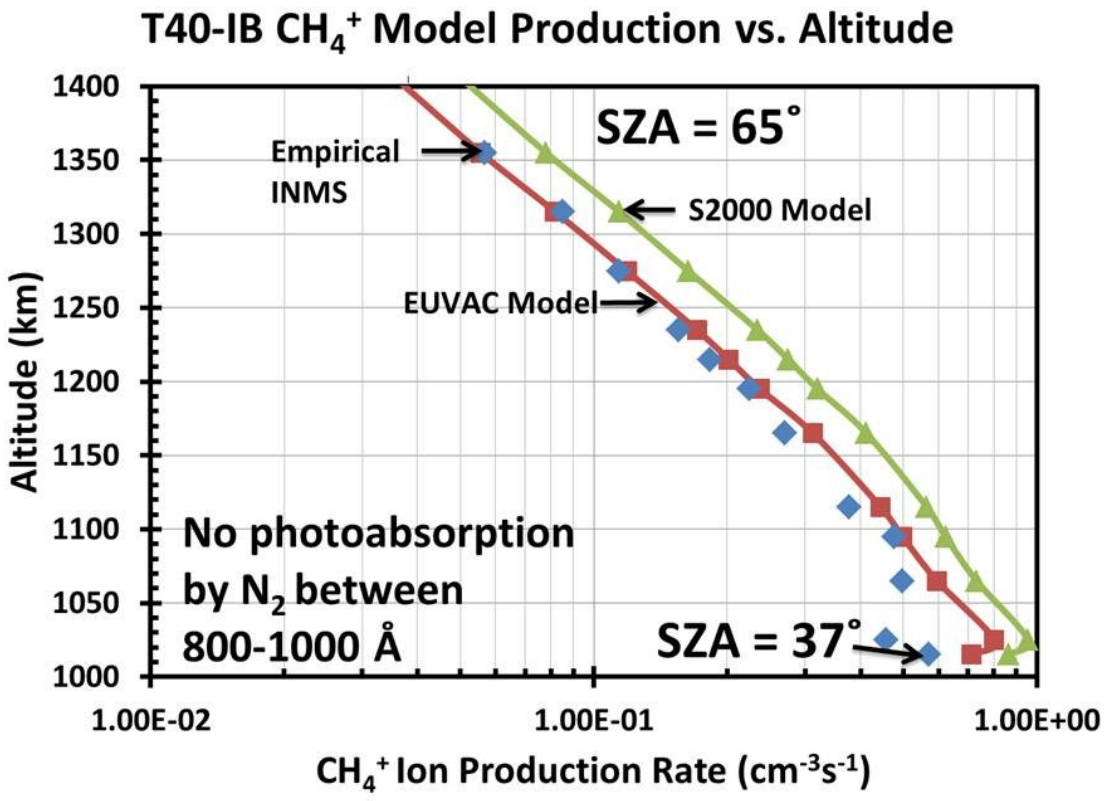

Figure 4.23 Modeled production rates of CH_4^+ compared to the empirical production rate of CH_4^+ derived from INMS data from the T40-Inbound flyby of Titan. solar photons with wavelengths between 800 and 1000 Å did not interact with N_2. INMS data is indicated with the blue diamonds, results for the Solar 2000 and EUVAC models of the solar flux are shown with green triangles and red squares respectively. The solar zenith angle at closest approach and at the uppermost altitude are indicated at the bottom and top of the figure. The solar zenith angle is adjusted to reflect the conditions observed by the Cassini spacecraft.

4.2.2 T17-Outbound

The T17 flyby of Titan will be used to examine the middle range of solar zenith angles. The outbound leg started at a solar zenith angle of 31° and proceeded to a solar zenith angle of 44° at closest approach. The adjusted empirical N_2^+ production rates appear to match the modeled production rate when the SOLAR2000 model was used above 1145 km while below 1145 km the empirical production rates are closer to the EUVAC model (Figure 4.24). At altitudes above 1250 km the modeled production rates are a factor of two lower than the empirical production rates. At the production rate peak near 1045 km the model is within 5% of the empirical production rates indicating that the model is providing a sufficiently reliable rate of N_2^+ production.

For the production rate profiles of CH_4^+ a transition region where the favored solar flux model switches from the EUVAC to SOLAR2000 model is also observed but the transition occurs at 1200 km as opposed to 1145 km as was the case for the N_2^+ production rate. For the case where the all of the photons with wavelengths 800-1000 Å interact with nitrogen (Figure 4.25) the modeled production rate of CH4+ is within 20% of the empirically derived production rate for the SOLAR2000 model above 1200 km and the EUVAC model below 1200 km until 1050 km where both models underestimate the empirical production by at least 150%. When half of the photons of wavelength 800-1000 Å pass through the ionosphere without interacting with nitrogen (Figure 4.26) the discrepancy below 1050 km drops to 25%. Figure 4.27 shows the case when none of the photons with wavelengths between 800 and 1000 Å interact with nitrogen. This case yields the best agreement between the modeled and empirically derived production rates of CH_4^+. At the closest approach the empirical production rate is closer to the modeled production rate using the SOLAR2000 model which is a deviation from the pattern

where the production rate profile at lower altitudes aligns more readily with the EUVAC model; however, at closest approach the discrepancy between the EUVAC model and the empirical production rate is only 20%.

The outbound leg of T17 has shown that the modeled production rates are in reasonable agreement with the empirically derived production rates for N_2^+ and CH_4^+. In contrast to the T40 flyby where using the solar flux generated with the EUVAC model of the solar flux produced better agreement between the model and the empirical production rates, the T17-Outbound leg showed better agreement when the SOLAR2000 model was used above 1200 km and for the EUVAC model below 1200 km. The CH_4^+ production rate profiles were also in better agreement when photons with wavelengths in the range of 800-1000 Å did not interact with nitrogen.

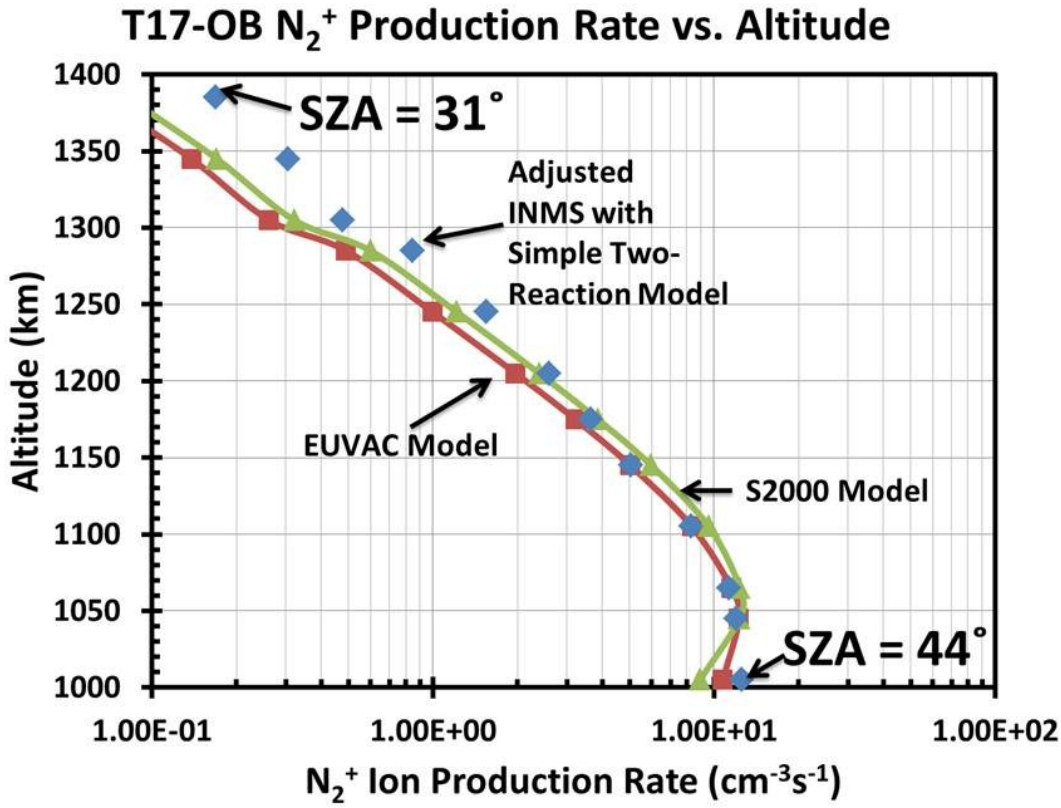

Figure 4.24 Modeled photoionization production rates of N_2^+ compared to the empirical production rate of N_2^+ derived from INMS data adjusted by the factor shown in Appendix Figure C.18from the T17-Outbound flyby of Titan. INMS data is indicated with the blue diamonds, results for the Solar 2000 and EUVAC models of the solar flux are shown with green triangles and red squares respectively. The solar zenith angle at closest approach and at the uppermost altitude are indicated at the bottom and top of the figure. The solar zenith angle is adjusted to reflect the conditions observed by the Cassini spacecraft.

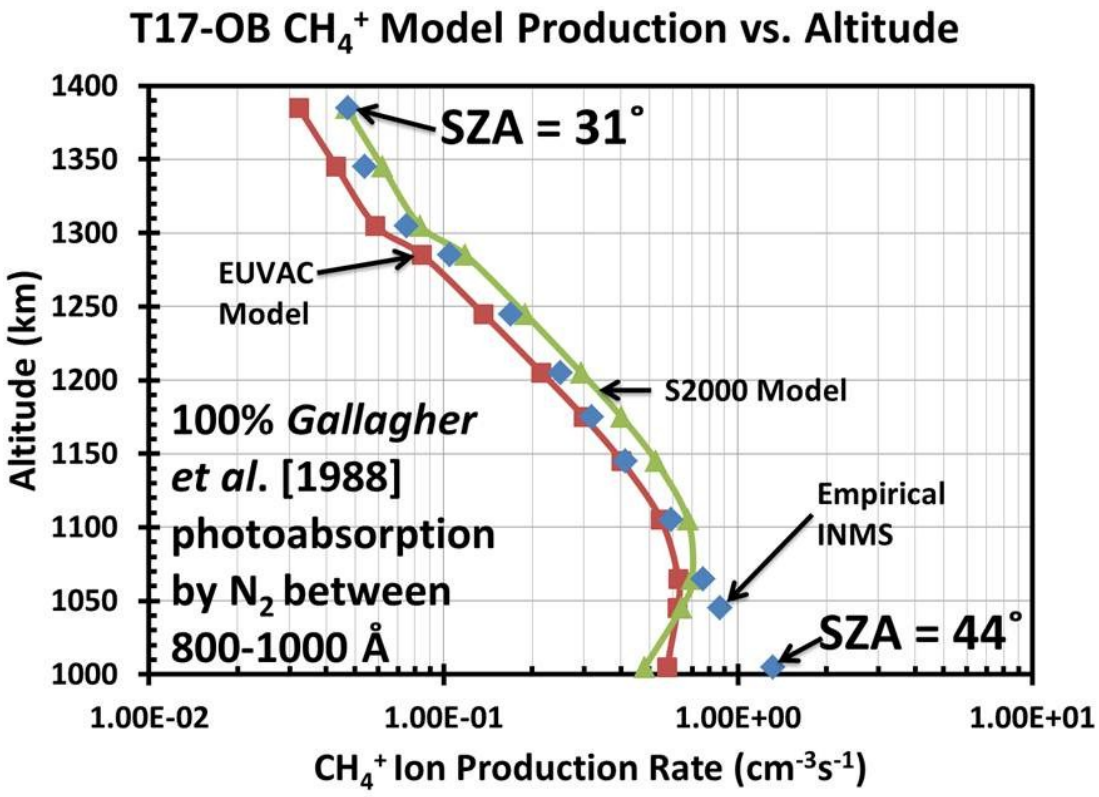

Figure 4.25 Modeled production rates of CH_4^+ compared to the empirical production rate of CH_4^+ derived from INMS data from the T17-Outbound flyby of Titan. N_2 photoabsorption cross sections for photons with wavelengths between 800 and 1000 Å of *Gallagher et al.* [1988] were used. INMS data is indicated with the blue diamonds, results for the Solar 2000 and EUVAC models of the solar flux are shown with green triangles and red squares respectively. The solar zenith angle at closest approach and at the uppermost altitude are indicated at the bottom and top of the figure. The solar zenith angle is adjusted to reflect the conditions observed by the Cassini spacecraft.

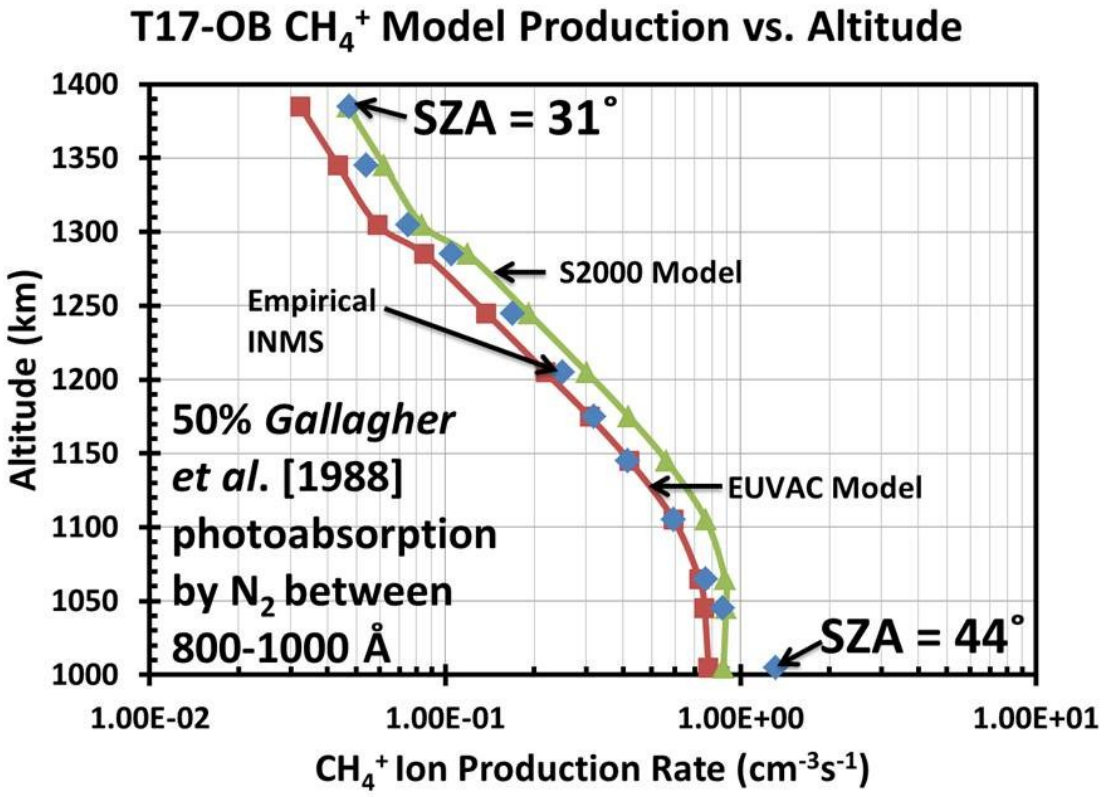

Figure 4.26 Modeled production rates of CH_4^+ to the empirical production rate of CH_4^+ derived from INMS data from the T17-Outbound flyby of Titan. 50% of solar photons with wavelengths between 800 and 1000 Å interact with N_2 using photoabsorption cross sections of *Gallagher et al.* [1988]. INMS data is indicated with the blue diamonds, results for the Solar 2000 and EUVAC models of the solar flux are shown with green triangles and red squares respectively. The solar zenith angle at closest approach and at the uppermost altitude are indicated at the bottom and top of the figure. The solar zenith angle is adjusted to reflect the conditions observed by the Cassini spacecraft.

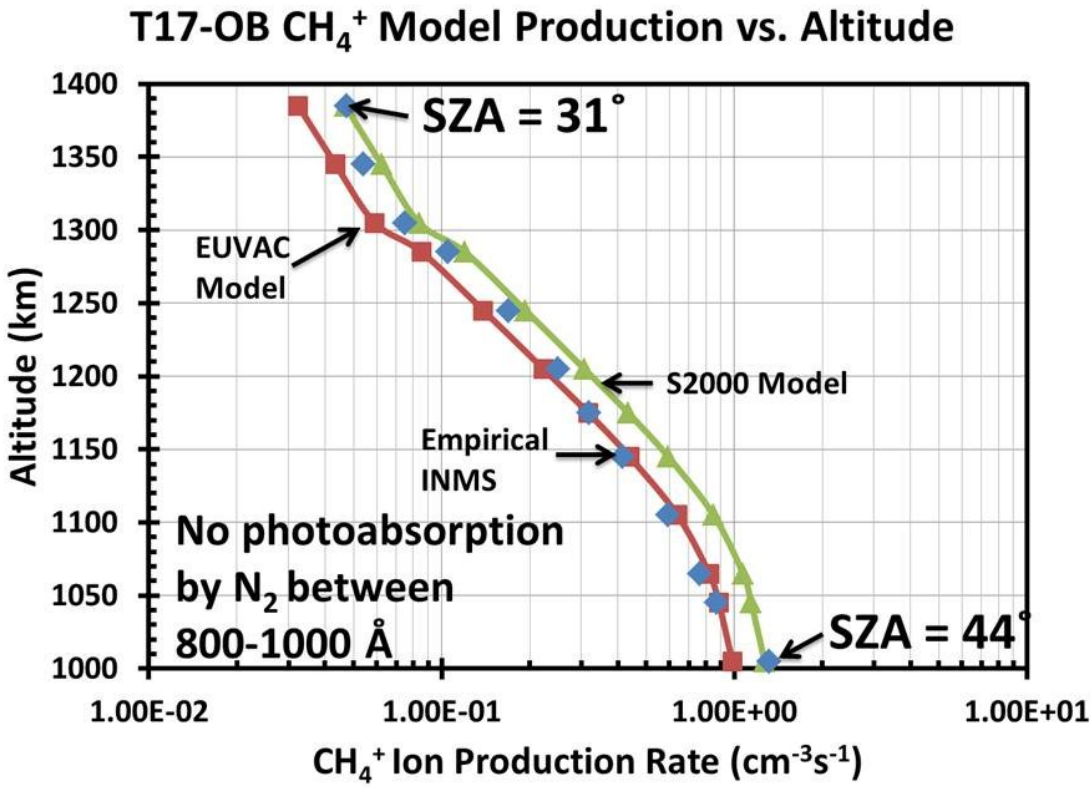

Figure 4.27 Modeled production rates of CH_4^+ compared to the empirical production rate of CH_4^+ derived from INMS data from the T17-Outbound flyby of Titan. solar photons with wavelengths between 800 and 1000 Å did not interact with N_2. INMS data is indicated with the blue diamonds, results for the Solar 2000 and EUVAC models of the solar flux are shown with green triangles and red squares respectively. The solar zenith angle at closest approach and at the uppermost altitude are indicated at the bottom and top of the figure. The solar zenith angle is adjusted to reflect the conditions observed by the Cassini spacecraft.

4.2.3 T17-Inbound

After examining the outbound leg of T17, production rates of N_2^+ and CH_4^+ for the inbound leg of the flyby will be analyzed. Figure 4.28 shows the model and adjusted empirical production rates of N_2^+. For this case using the flux of photons from the SOLAR2000 model produced a higher production rate than the EUVAC model, but the two models differed consistently by about 10%. Above 1175 km the model production using both solar flux models falls within 10% of the empirically derived production rates. Below 1175 km the empirical production rates become 15% larger than the modeled rate using the SOLAR2000 flux and 25% larger below 1100 km. Even when considering this, the model agrees reasonable well with data.

A similar result pattern is observed when comparing the CH_4^+ production rates to the empirical production rates. Above 1200 km the model production rate using both solar flux models agreed to within 10% of the empirically derived production rates in all cases. For the case where all of the photons interact with nitrogen via the *Gallagher et al.* [1988] (Figure 4.29) the modeled production rates using the SOLAR2000 incident photon flux agree with the empirical production rate to within 10%. Below 1200 km, the disagreement between the modeled and empirical production rate of N_2^+ increases to a factor of two at closest approach. This trend is similar to that seen in the N_2^+ production rate profile. Decreasing the amount of photons with wavelengths between 800 and 1000 Å that interact with nitrogen to 50% (see Figure 4.30) will not greatly impact the upper altitude production rates but it will move the discrepancy below 1200 km to approximately 20%. This lower altitude discrepancy between the empirical and modeled production rates is further reduced to between 5 and 10% if photons of wavelength 800-1000 Å do not interact at all with atmospheric nitrogen (Figure 4.31).

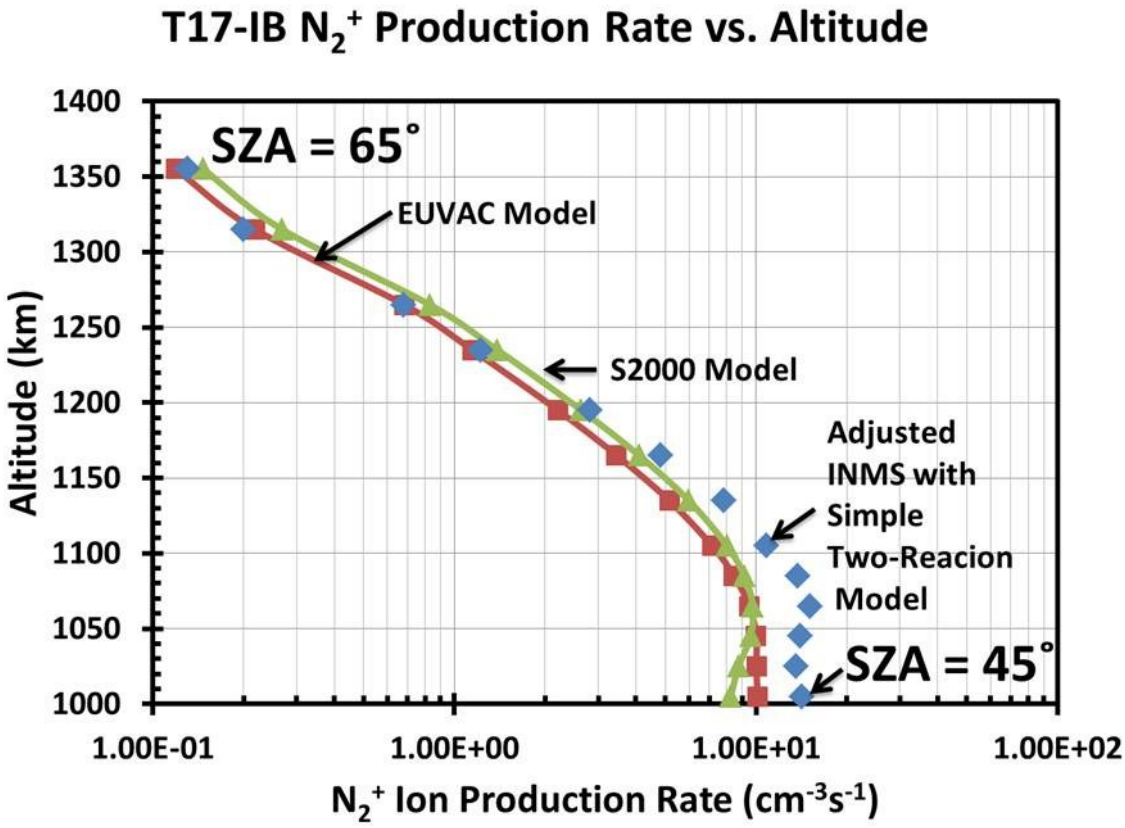

Figure 4.28 Modeled photoionization production rates of N_2^+ compared to the empirical production rate of N_2^+ derived from INMS data adjusted by the factor shown in Appendix Figure C.32from the T17-Inbound flyby of Titan. INMS data is indicated with the blue diamonds, results for the Solar 2000 and EUVAC models of the solar flux are shown with green triangles and red squares respectively. The solar zenith angle at closest approach and at the uppermost altitude are indicated at the bottom and top of the figure. The solar zenith angle is adjusted to reflect the conditions observed by the Cassini spacecraft.

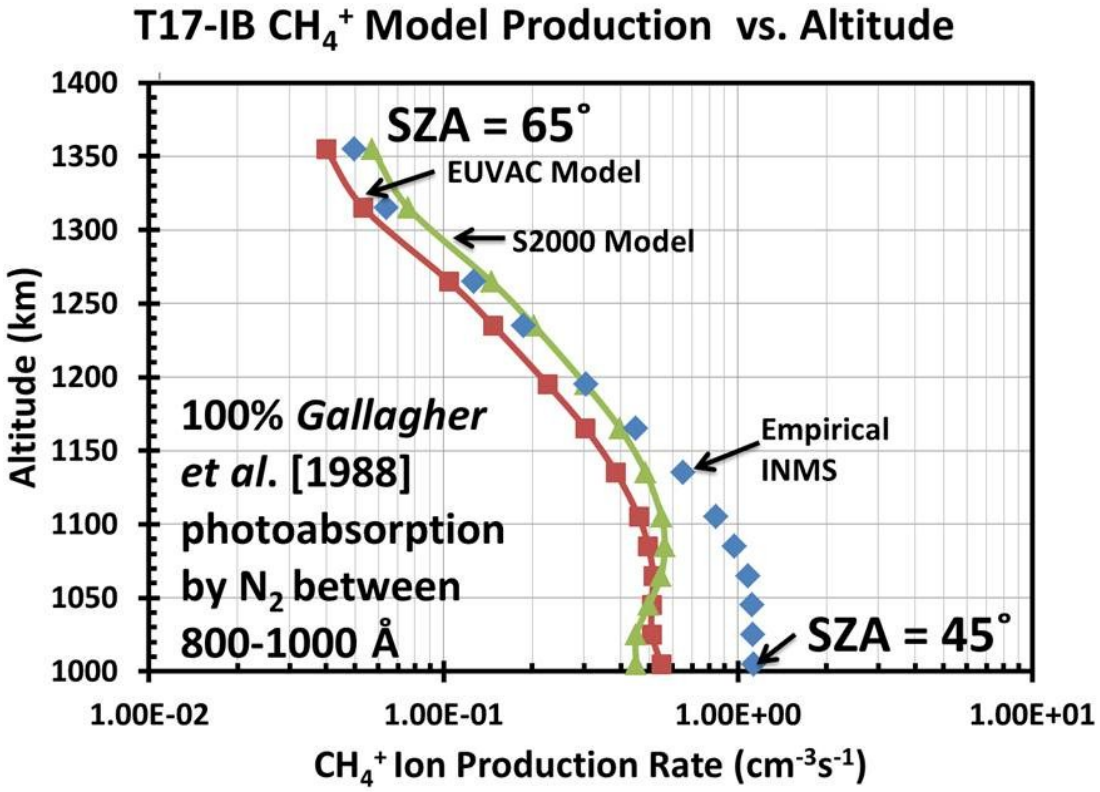

Figure 4.29 Modeled production rates of CH_4^+ compared to the empirical production rate of CH_4^+ derived from INMS data from the T17-Inbound flyby of Titan. N_2 photoabsorption cross sections for photons with wavelengths between 800 and 1000 Å of *Gallagher et al.* [1988] were used. INMS data is indicated with the blue diamonds, results for the Solar 2000 and EUVAC models of the solar flux are shown with green triangles and red squares respectively. The solar zenith angle at closest approach and at the uppermost altitude are indicated at the bottom and top of the figure. The solar zenith angle is adjusted to reflect the conditions observed by the Cassini spacecraft.

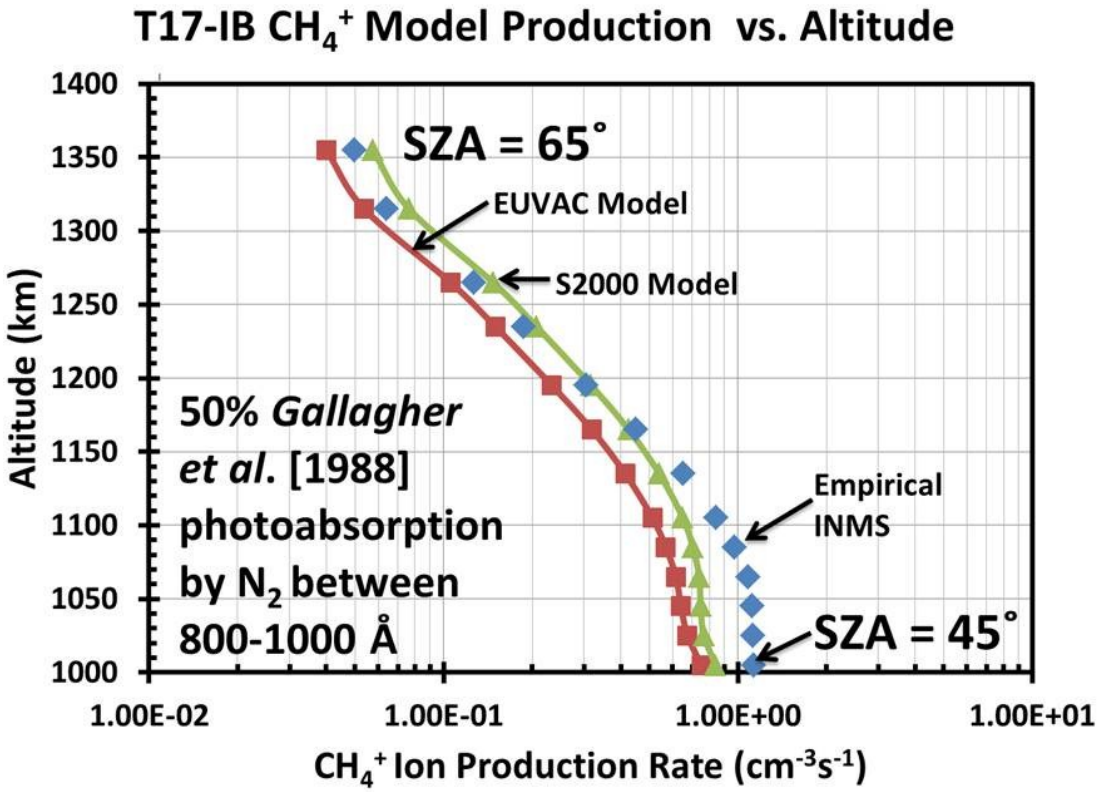

Figure 4.30 Modeled production rates of CH_4^+ to the empirical production rate of CH_4^+ derived from INMS data from the T17-Inbound flyby of Titan. 50% of solar photons with wavelengths between 800 and 1000 Å interact with N_2 photoabsorption cross sections of *Gallagher et al.* [1988]. INMS data is indicated with the blue diamonds, results for the Solar 2000 and EUVAC models of the solar flux are shown with green triangles and red squares respectively. The solar zenith angle at closest approach and at the uppermost altitude are indicated at the bottom and top of the figure. The solar zenith angle is adjusted to reflect the conditions observed by the Cassini spacecraft.

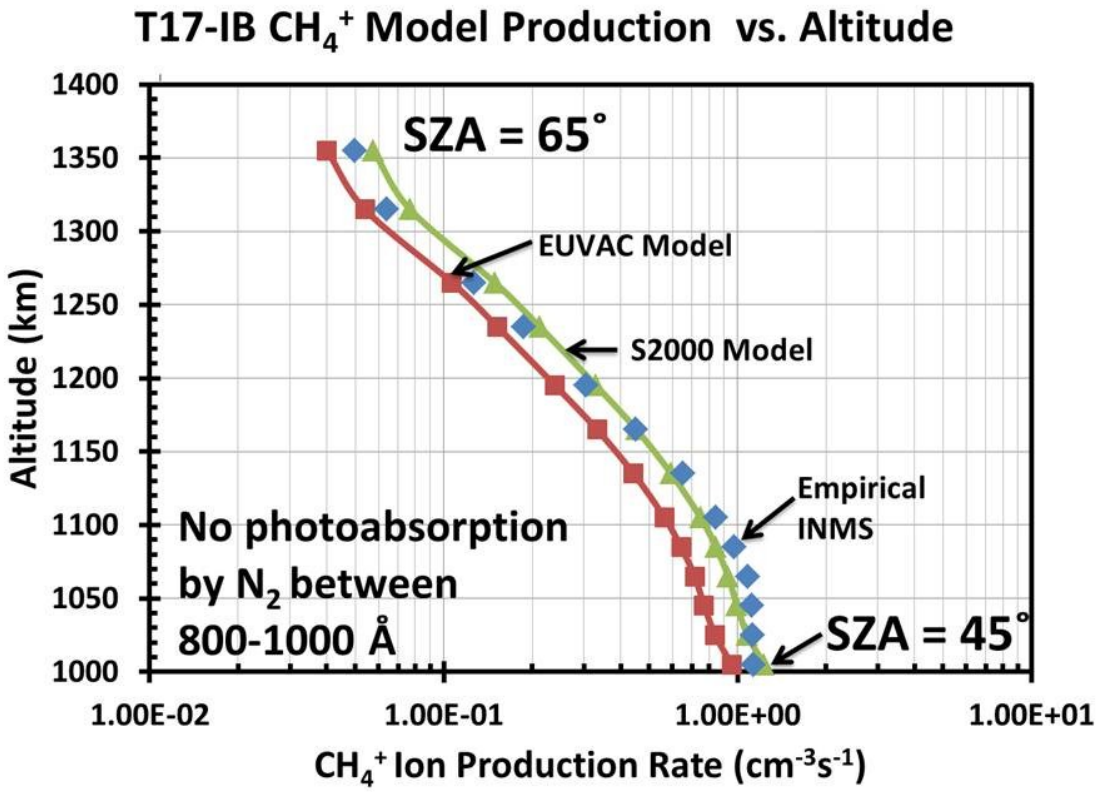

Figure 4.31 Modeled production rates of CH_4^+ compared to the empirical production rate of CH_4^+ derived from INMS data from the T17-Inbound flyby of Titan. solar photons with wavelengths between 800 and 1000 Å did not interact with N_2. INMS data is indicated with the blue diamonds, results for the Solar 2000 and EUVAC models of the solar flux are shown with green triangles and red squares respectively. The solar zenith angle at closest approach and at the uppermost altitude are indicated at the bottom and top of the figure. The solar zenith angle is adjusted to reflect the conditions observed by the Cassini spacecraft.

The favored case for the outbound leg of the T17 flyby of Titan uses the SOLAR2000 model of the solar flux and neglects the photoabsorption of molecular nitrogen for wavelengths between 800 and 1000 Å. It should be noted that even though the SOLAR2000 model of the solar flux has been indicated as the favored case, the modeled production rate profiles for N_2^+ and CH_4^+ showed only minor differences. This was in contrast to the T40 case where the EUVAC model of the solar flux produced a substantially more reasonable production rate profile when compared with the empirically derived production rate profile of the SOLAR2000 model. Overall the modeled production rates were found to be in reasonable agreement with the empirical production rates, although for altitude below 1100 km the modeled production rates were generally low.

4.2.4 T18-Outbound

The outbound leg of the T18 flyby of Titan was used to verify the production rates for solar zenith angles between 78 and 90˚ for altitudes near 1400 km and closest approach (near 950 km) respectively. Comparisons between the adjusted empirical and modeled production rates of N_2^+ are shown in Figure 4.32. At altitudes above 1100 km the empirical production rates appear to agree with the model using the EUVAC model solar flux inputs. At 1100 km the EUVAC model falls below the empirical model by a factor of two which increases to a discrepancy of a factor of three at closest approach. Upon further inspection it appears that the empirically derived production rate profile of N_2^+ actually follows the model profile of using the SOLAR2000 incident photon flux but has been shifted down by 50 km. The difference in altitudes at which the N_2^+ production rate peaks for the INMS derived and modeled production rate profile could be caused by; (1) a missing source of N_2^+ production in the model such as magnetospheric electron fluxes, (2) using neutral densities that are too high which cause energy

to be deposited higher in the ionosphere, or (3) a missing component in the X-ray solar flux that was used in the model. This is most evident when looking at the peak production rates where the empirically determined peak production rate is a factor of two larger that the model using the EUVAC photon flux but only 20% larger than the peak production rate when the SOLAR2000 photon flux was used.

The preferred choice for the model of the incident solar flux becomes apparent when examining the CH_4^+ production rate profiles. When all of the photons interact with nitrogen (Figure 4.33), the production empirical production rate profile above 1150 km agrees with the modeled production rate profile of using the SOLAR2000 model of the photon flux. This is in contrast to production rates modeled with the EUVAC solar flux which is lower than the empirical production rates by factors of two and three. Below 1150 km, there is a large discrepancy between the modeled and empirical production rates and they cannot be said to agree. Increasing the number of photons with wavelengths between 800 and 1000 Å that do not interact with nitrogen to 50% (Figure 4.34) will improve the agreement between the empirical and modeled production rates using the SOLAR2000 photon flux to within 10% down to 1100 km but below this the discrepancy increases from a factor of 2 at 1050 km to a factor of 5 at closest approach. It can be shown that the best agreement between the modeled and empirical production rates is obtained when photons with wavelengths between 800 and 1000 Å do not interact with the molecular nitrogen (Figure 4.35). Allowing these photons to pass though the atmosphere and ionize methane will bring the modeled production rates using with the SOLAR2000 incident photon flux to within 15% of the empirical production rate down to an altitude near 1000 km. Below 1000 km both of the modeled production rates drop off rapidly indicating that there is a need for an addition production pathway for CH_4^+. Using the EUVAC

model of the solar flux produces a production rate profile that is a factor of two lower than the SOLAR2000 model thus ruling the EUVAC model of the solar flux out as the preferred choice for the model.

Using an analysis of the outbound leg of the T18 flyby of Titan it has been shown once again that the photoionization model used in this study is capable of producing production rate profiles of CH_4^+ and N_2^+. Although the N_2^+ production rate profile did not perfectly match up to the modeled production rate profile using the SOLAR2000 flux of photons, confidence in the model was gained due to the fact that the shape of the production rate profile follows the shape of the modeled production rate very closely and that the modeled and empirical peak production rates are close to one another. The modeled CH_4^+ production rate profile when all photons with wavelengths in the range of 800-1000 Å do not interact with nitrogen and using the SOLAR2000 model photon flux agreed very well (within 15%) with the empirically derived production rates making this the favored case for this flyby. After making these observations it can be said that the modeled production rates are in reasonable agreement with empirically derived production rates for solar zenith angles between 78 and 90˚.

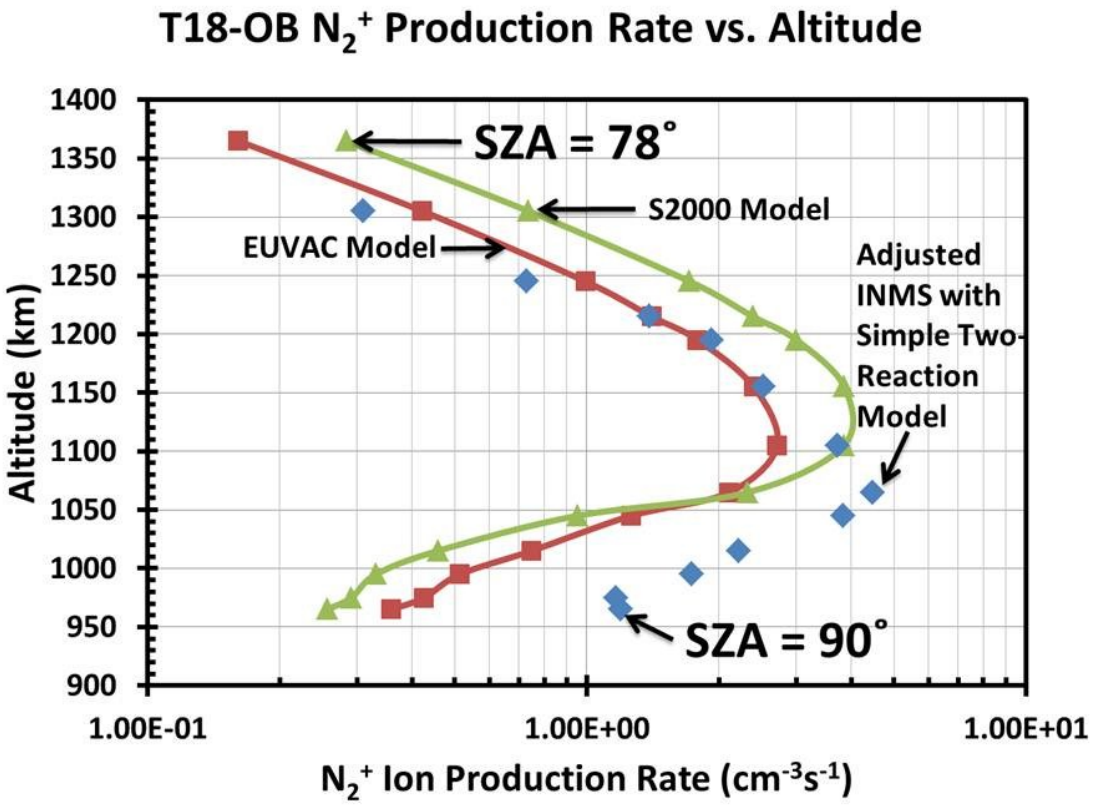

Figure 4.32 Modeled photoionization production rates of N_2^+ compared to the empirical production rate of N_2^+ derived from INMS data adjusted by the factor shown in Appendix Figure C.46 from the T18-Outbound of Titan. INMS data is indicated with the blue diamonds, results for the Solar 2000 and EUVAC models of the solar flux are shown with green triangles and red squares respectively. The solar zenith angle at closest approach and at the uppermost altitude are indicated at the bottom and top of the figure. The solar zenith angle is adjusted to reflect the conditions observed by the Cassini spacecraft.

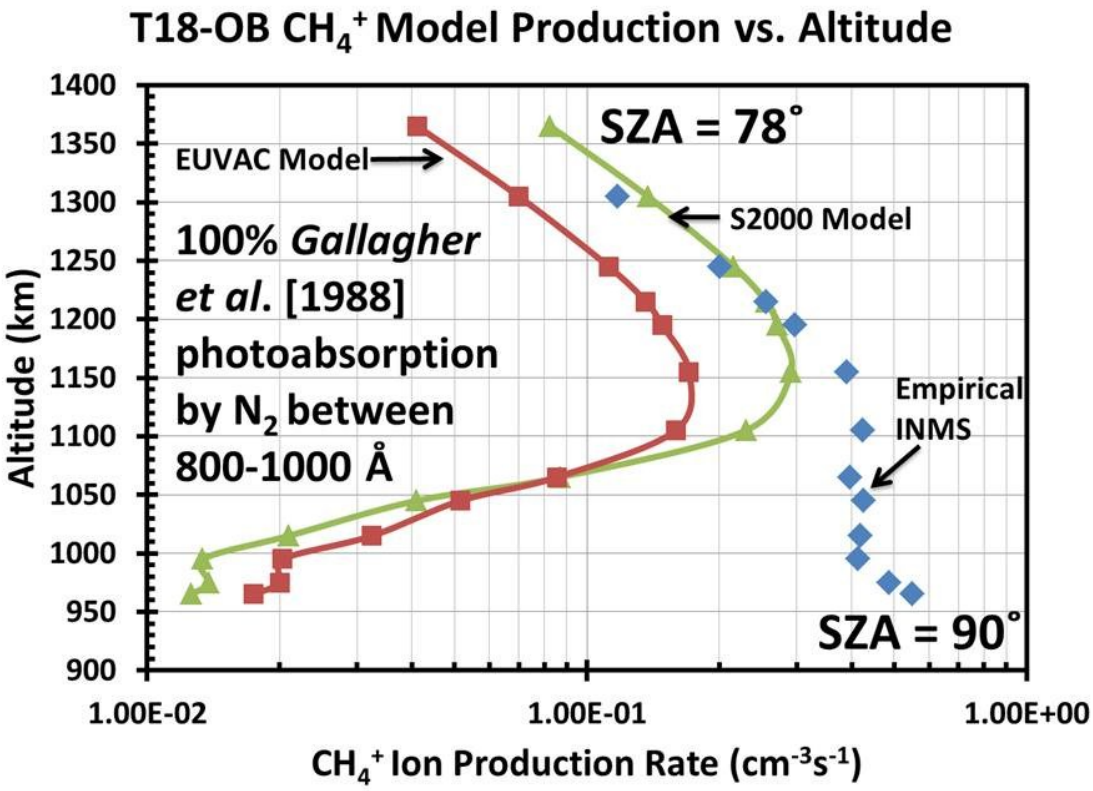

Figure 4.33 Modeled production rates of CH_4^+ compared to the empirical production rate of CH_4^+ derived from INMS data from the T18-Outbound flyby of Titan. N_2 photoabsorption cross sections for photons with wavelengths between 800 and 1000 Å of *Gallagher et al.* [1988] were used. INMS data is indicated with the blue diamonds, results for the Solar 2000 and EUVAC models of the solar flux are shown with green triangles and red squares respectively. The solar zenith angle at closest approach and at the uppermost altitude are indicated at the bottom and top of the figure. The solar zenith angle is adjusted to reflect the conditions observed by the Cassini spacecraft.

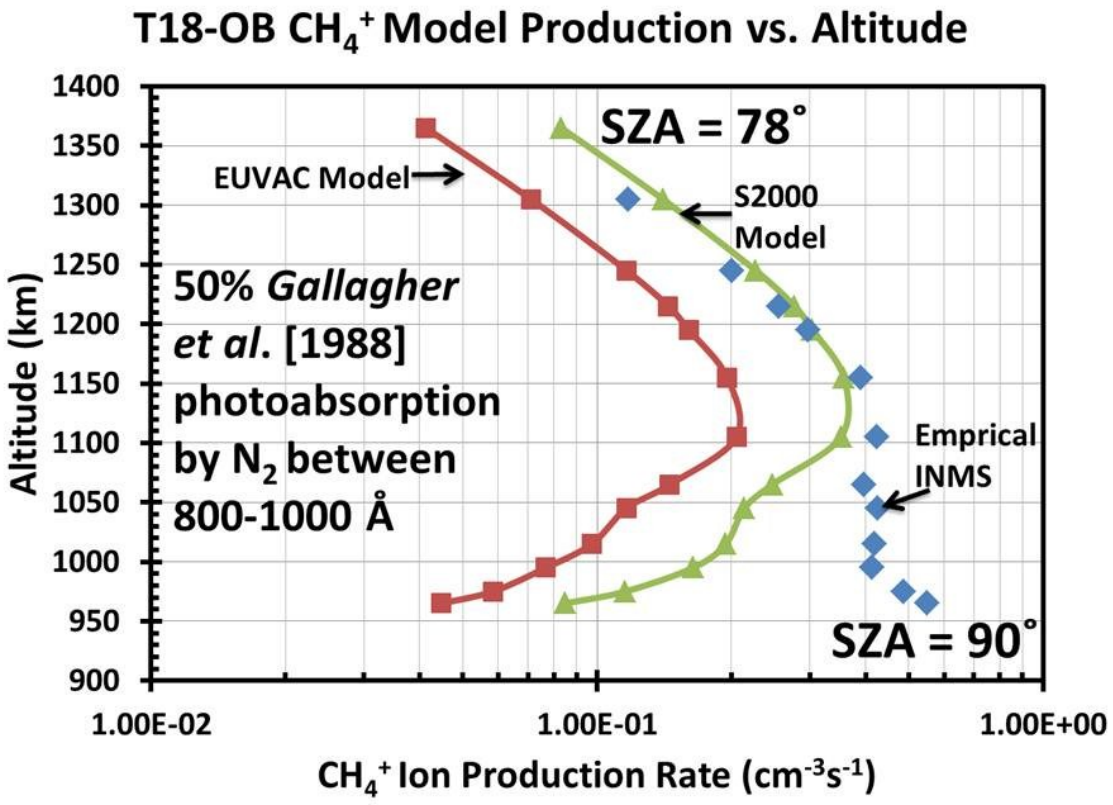

Figure 4.34 Modeled production rates of CH_4^+ to the empirical production rate of CH_4^+ derived from INMS data from the T18-Outbound of Titan. 50% of solar photons with wavelengths between 800 and 1000 Å interact with N_2 using photoabsorption cross sections of *Gallagher et al.* [1988]. INMS data is indicated with the blue diamonds, results for the Solar 2000 and EUVAC models of the solar flux are shown with green triangles and red squares respectively. The solar zenith angle at closest approach and at the uppermost altitude are indicated at the bottom and top of the figure. The solar zenith angle is adjusted to reflect the conditions observed by the Cassini spacecraft.

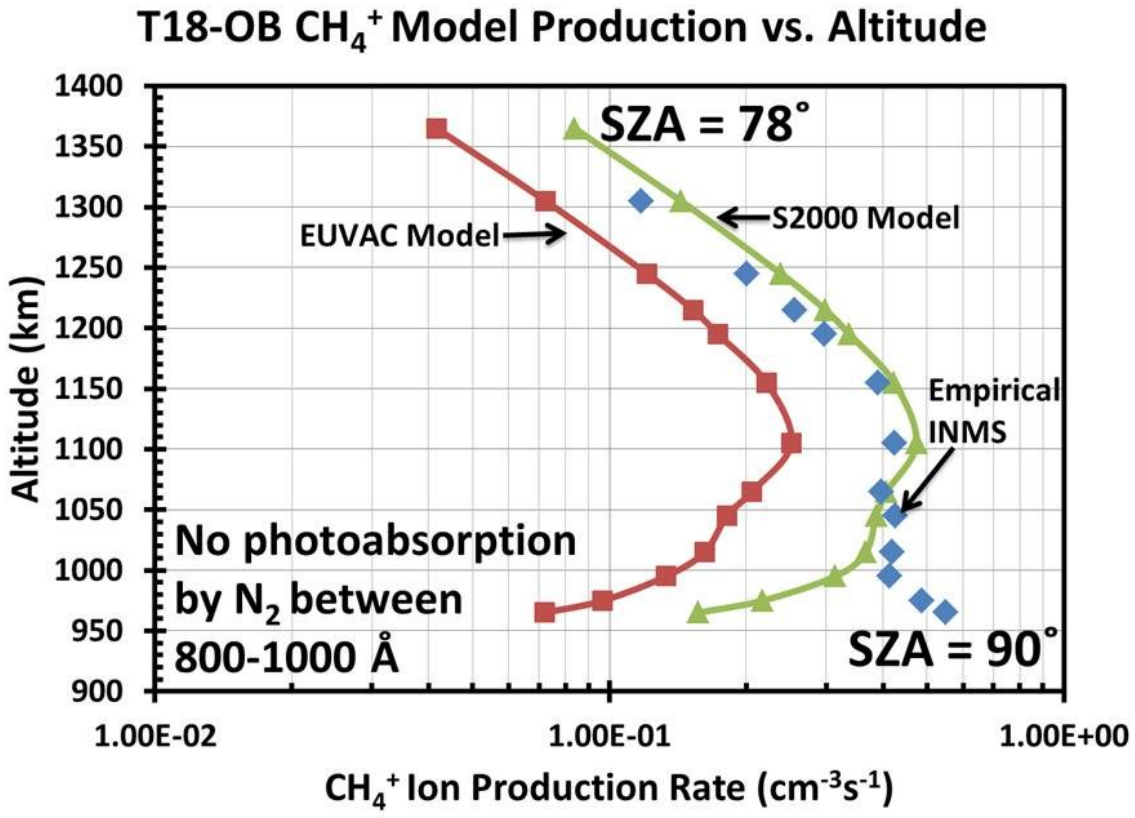

Figure 4.35 Modeled production rates of CH_4^+ compared to the empirical production rate of CH_4^+ derived from INMS data from the T18-Outbound flyby of Titan. solar photons with wavelengths between 800 and 1000 Å did not interact with N_2. INMS data is indicated with the blue diamonds, results for the Solar 2000 and EUVAC models of the solar flux are shown with green triangles and red squares respectively. The solar zenith angle at closest approach and at the uppermost altitude are indicated at the bottom and top of the figure. The solar zenith angle is adjusted to reflect the conditions observed by the Cassini spacecraft.

4.3 Globally Averaged Production Rate Profiles for Primary Ionization Products of N_2 and CH_4

After verifying that the model is capable of producing reasonable production rates the stage was set to complete one of the major goals of this study: creating production rate profiles for a variety of solar zenith angles. Production rate profiles have previous been examined for the nightside of Titan by *Gronoff et al.* [2009b] who calculated an ion production rate using magnetospheric electron impact ionization, energetic ions and cosmic rays, and for the dayside for a radial case by *Lavvas et al*. [2011] with a focus on the effects of the revised N_2 photoabsorption cross sections of *Liang et al.* [2007] (Figure 3.13).

The model of *Lavvas et al.* computed ion production rates using the magnetospheric superthermal electron flux and solar photon flux for the T40 flyby of Titan for a radial magnetic field line and a solar zenith angle of 60˚. Both superthermal electron and solar sources are included in their model as the ionization from solar sources dominates near 1000 km while the contribution from electron impact ionization caused by superthermal electrons dominates between 700 and 900 km. From these production rates, a diurnal average was presented by multiplying the results by one-half. For comparison purposes the results from the model of *Lavvas et al.* will be compared to the results of this model using the T40 solar photon flux and a radial magnetic field line.

4.3.1 Production Rate Profiles Using Nested Magnetic Field Lines and the T40 Solar Flux

In order to produce a generalized production rate, the global average model of the neutral atmosphere described in Section 3.4.2.2 with major neutral densities shown in Figure 3.39 utilizing the minor neutral mixing ratios given in Table 3.3 was used. This neutral atmosphere was compiled by fitting INMS measurements of the major atmospheric neutrals (N_2, CH_4, and

H_2) [*Magee et al.,* 2009] and then multiplying the densities by a factor of 3.15 to reflect a recalibration of the INMS instrument [*Mandt et al.,* 2012]. In the following discussion the results are presented of the photoionization and electron impact ionization using the EUVAC solar photon flux for the T40 case (Figure 3.9), where only half of the solar photons are subject to photoabsorption by N_2, in conjunction with nested magnetic field lines effectively limiting the vertical transport of electrons. These parameters were chosen because of the agreement between the modeled and empirical production rates and modeled and measured ion densities presented in Section 4.1.

Figure 4.36 and Figure 4.37 show the ionization products of molecular nitrogen for solar zenith angles ranging from 0˚ to 90˚ between 725 and 1400 km. Figure 4.38 through Figure 4.44 show the ionization products of methane (CH_4^+, CH_3^+, CH_2^+, CH^+, C^+, H_2^+, and H^+) for the same conditions over the same range of altitudes. In all cases a strong atmospheric peak is observed with a secondary shelf caused by soft x-rays. The only cases where this was not apparent were CH_4^+, H_2^+, and H^+ where the ionization thresholds tend to exhibit a single elongated peak.

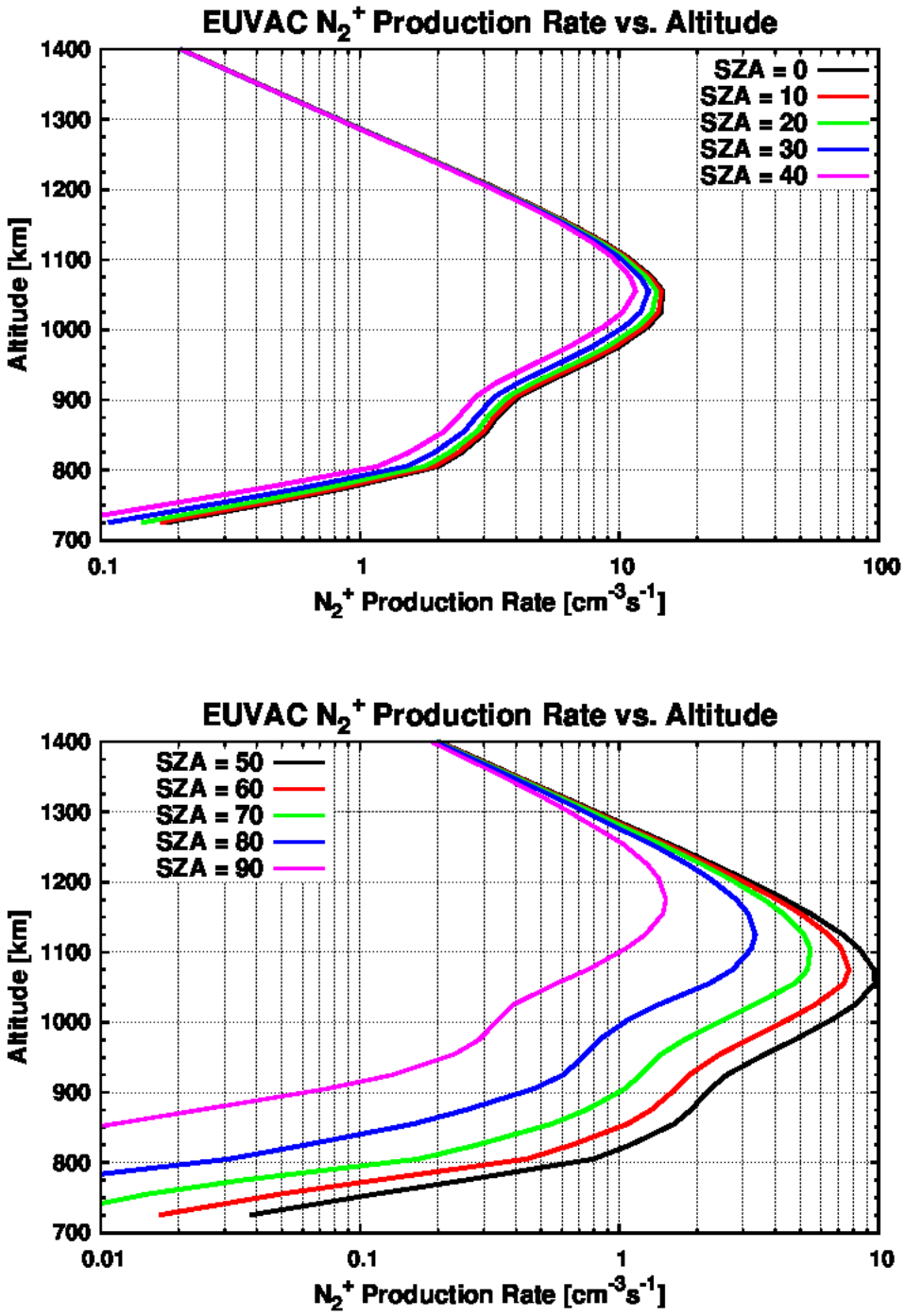

Figure 4.36 Production rate of N_2^+ resulting from the photoionization and photoelectron impact ionization of the global average model of the ionosphere of Titan using the EUVAC model of the solar photon flux for T40 conditions and nested magnetic field lines for solar zenith angles between 0° and 40° (above) and between 50° and 90° (below).

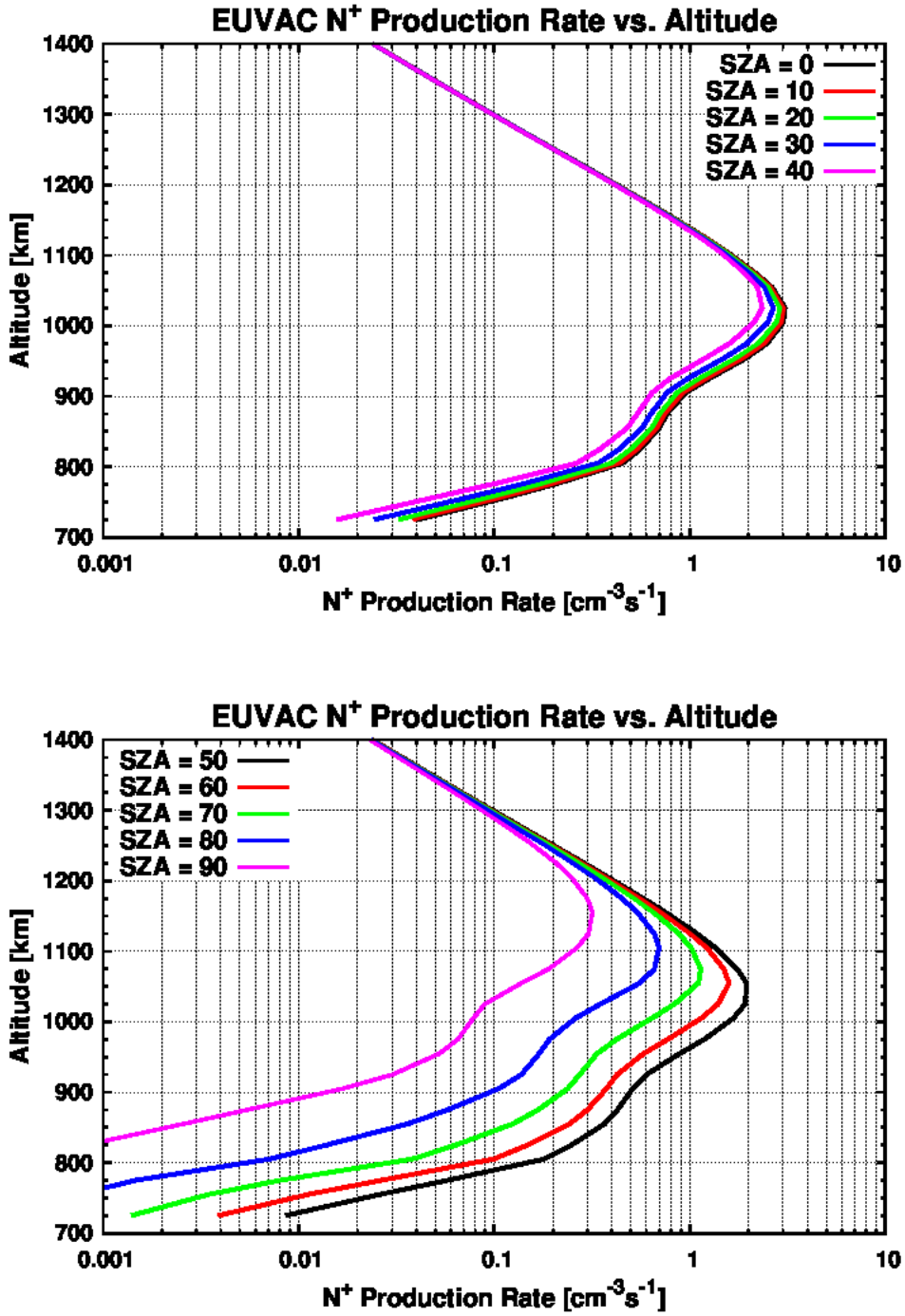

Figure 4.37 Production rate of N^+ resulting from the photoionization and photoelectron impact ionization of the global average model of the ionosphere of Titan using the EUVAC model of the solar photon flux for T40 conditions and nested magnetic field lines for solar zenith angles between 0° and 40° (above) and between 50° and 90° (below).

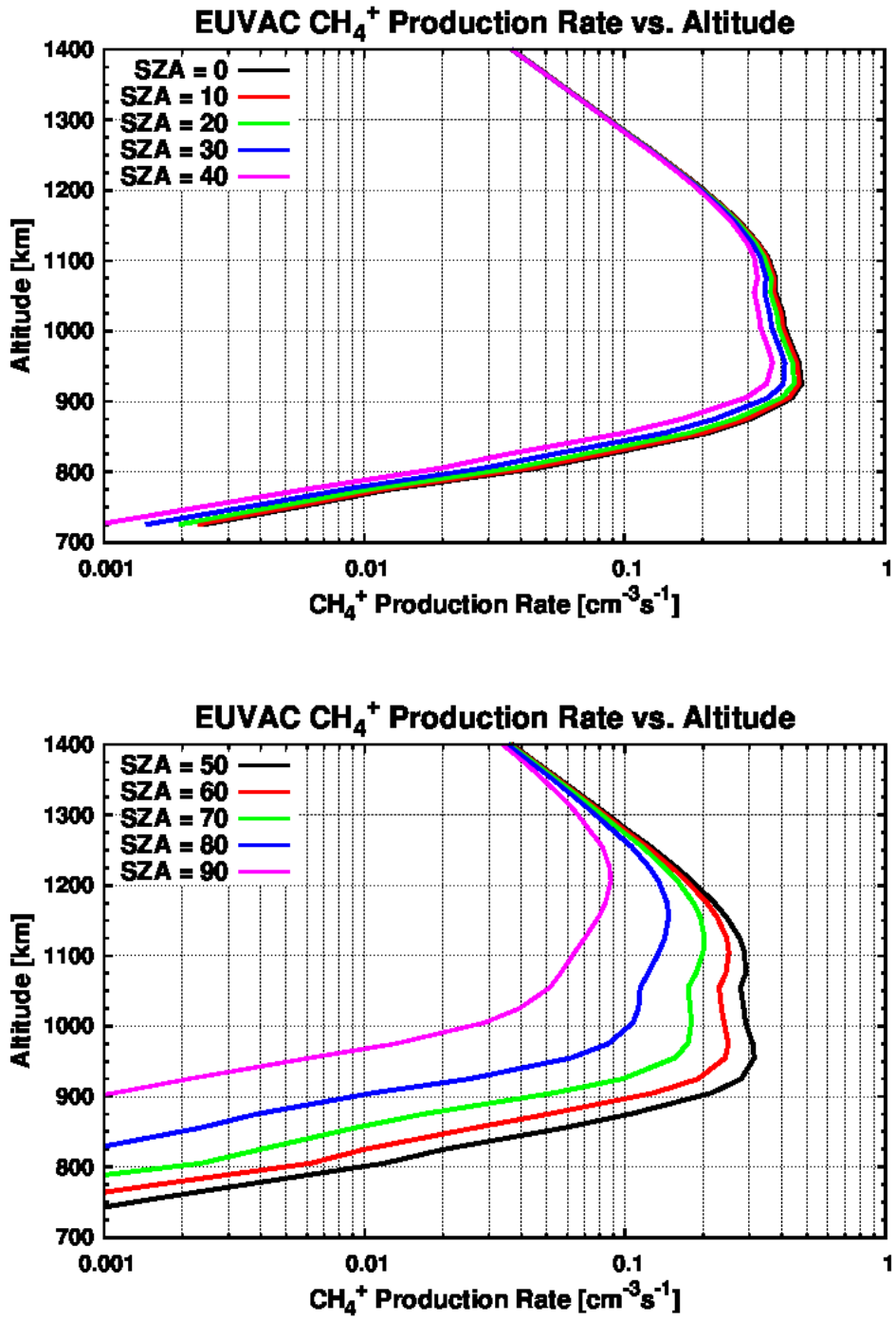

Figure 4.38 Production rate of CH_4^+ resulting from the photoionization and photoelectron impact ionization of the global average model of the ionosphere of Titan using the EUVAC model of the solar photon flux for T40 conditions and nested magnetic field lines for solar zenith angles between 0° and 40° (above) and between 50° and 90° (below). In this model half of the solar photons with wavelengths between 800 and 1000 Å interact with molecular nitrogen.

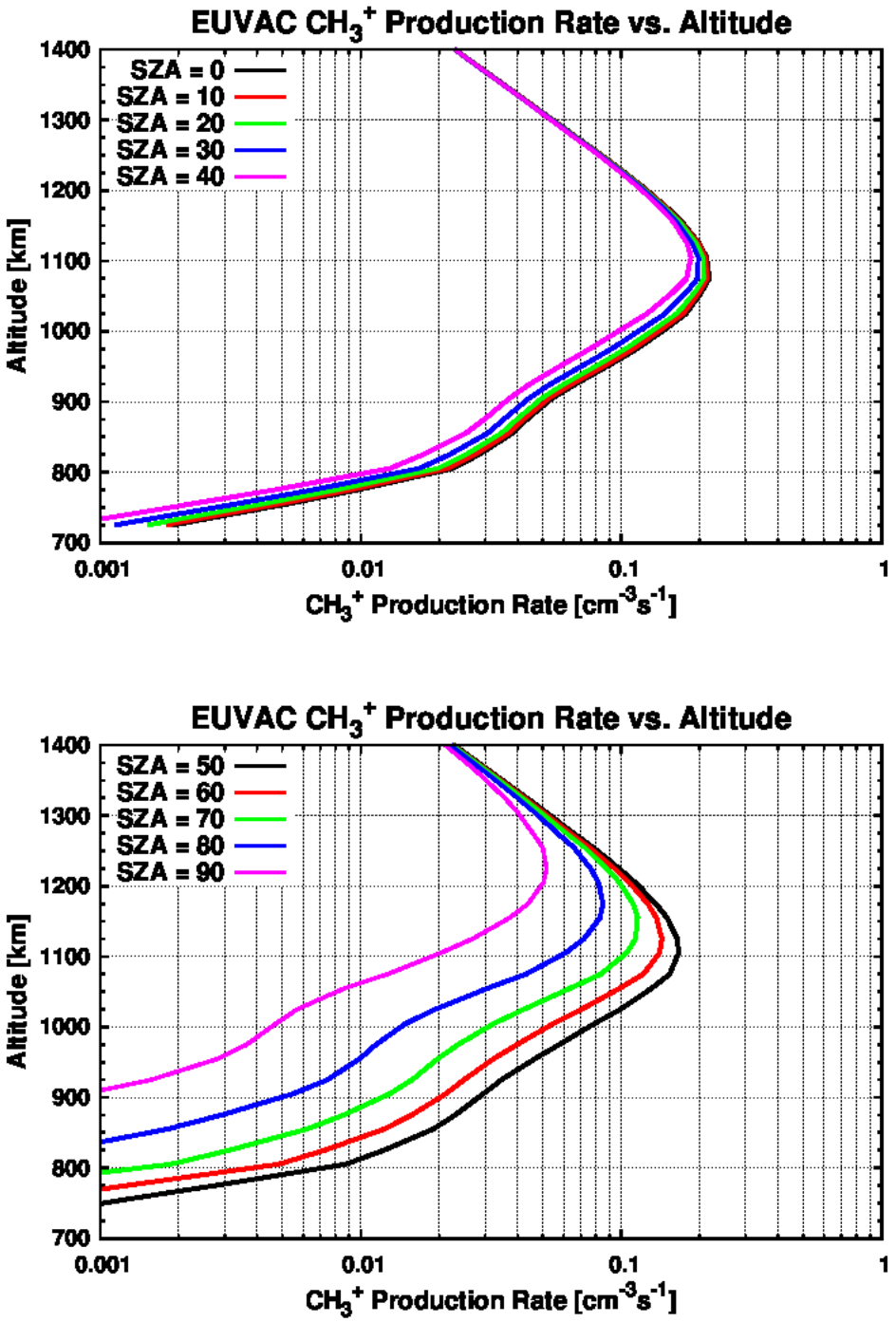

Figure 4.39 Production rate of CH_3^+ resulting from the photoionization and photoelectron impact ionization of the global average model of the ionosphere of Titan using the EUVAC model of the solar photon flux for T40 conditions and nested magnetic field lines for solar zenith angles between 0° and 40° (above) and between 50° and 90° (below). In this model half of the solar photons with wavelengths between 800 and 1000 Å interact with molecular nitrogen.

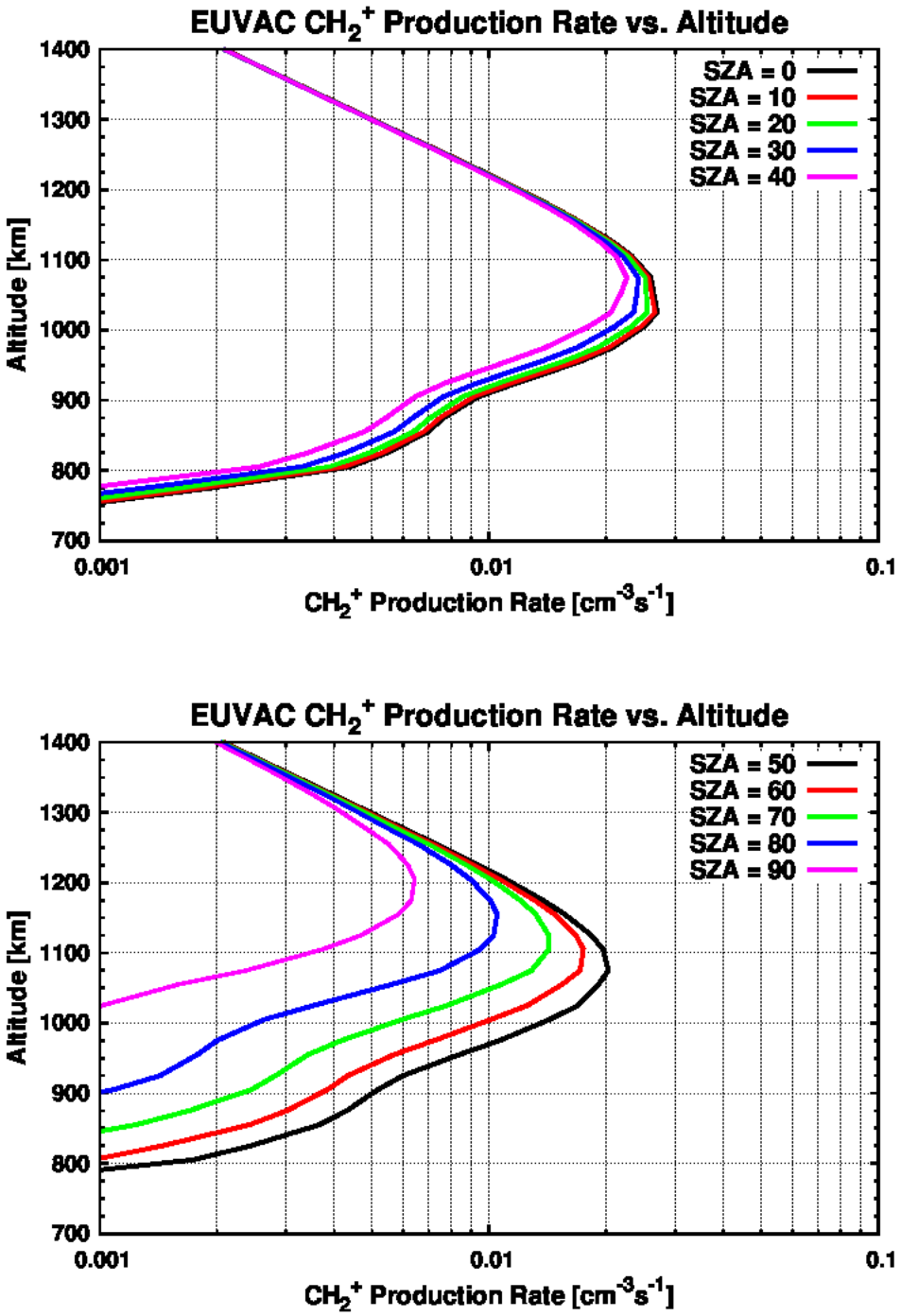

Figure 4.40 Production rate of CH_2^+ resulting from the photoionization and photoelectron impact ionization of the global average model of the ionosphere of Titan using the EUVAC model of the solar photon flux for T40 conditions and nested magnetic field lines for solar zenith angles between 0° and 40° (above) and between 50° and 90° (below). In this model half of the solar photons with wavelengths between 800 and 1000 Å interact with molecular nitrogen.

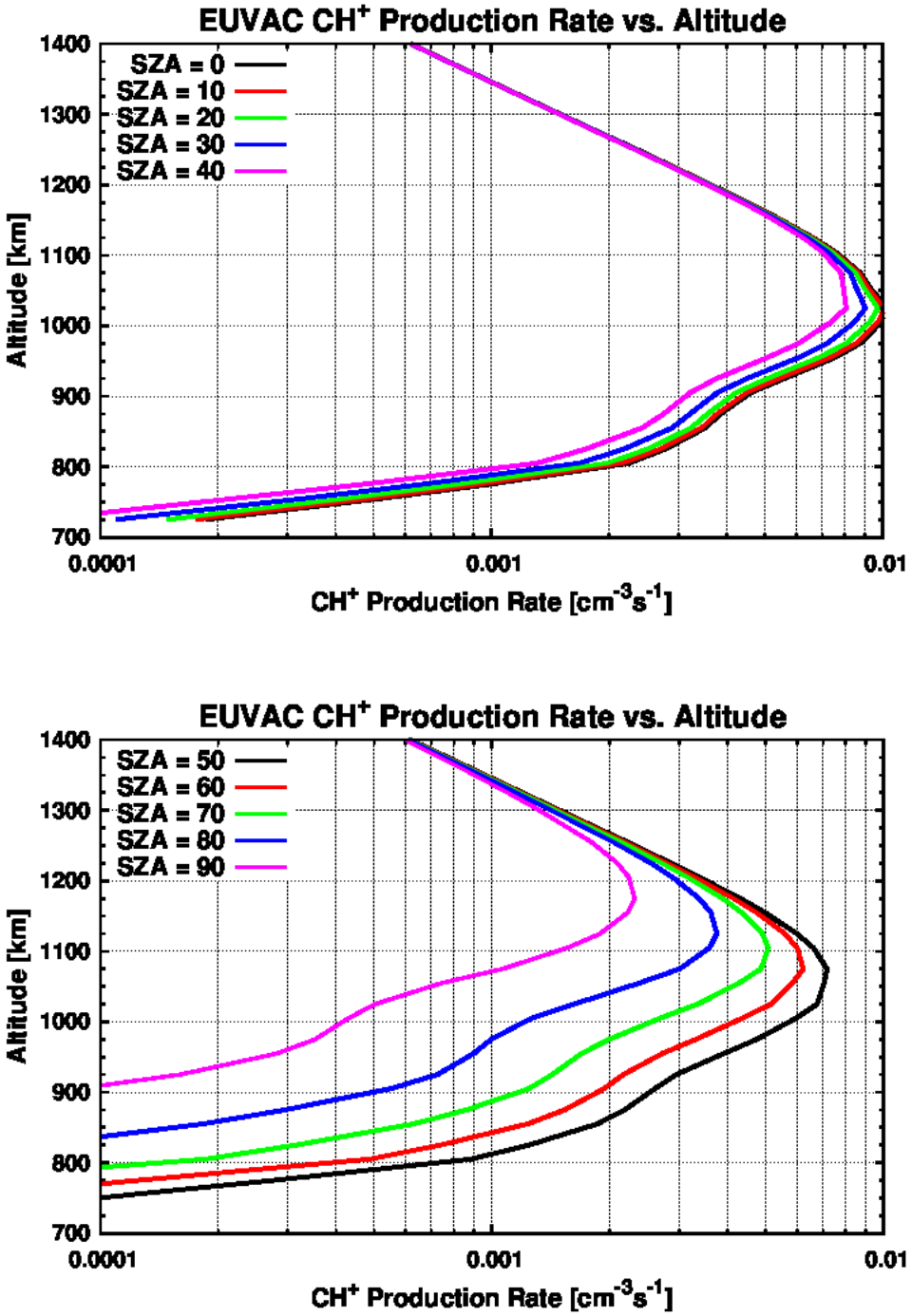

Figure 4.41 Production rate of CH^+ resulting from the photoionization and photoelectron impact ionization of the global average model of the ionosphere of Titan using the EUVAC model of the solar photon flux for T40 conditions and nested magnetic field lines for solar zenith angles between 0° and 40° (above) and between 50° and 90° (below). In this model half of the solar photons with wavelengths between 800 and 1000 Å interact with molecular nitrogen.

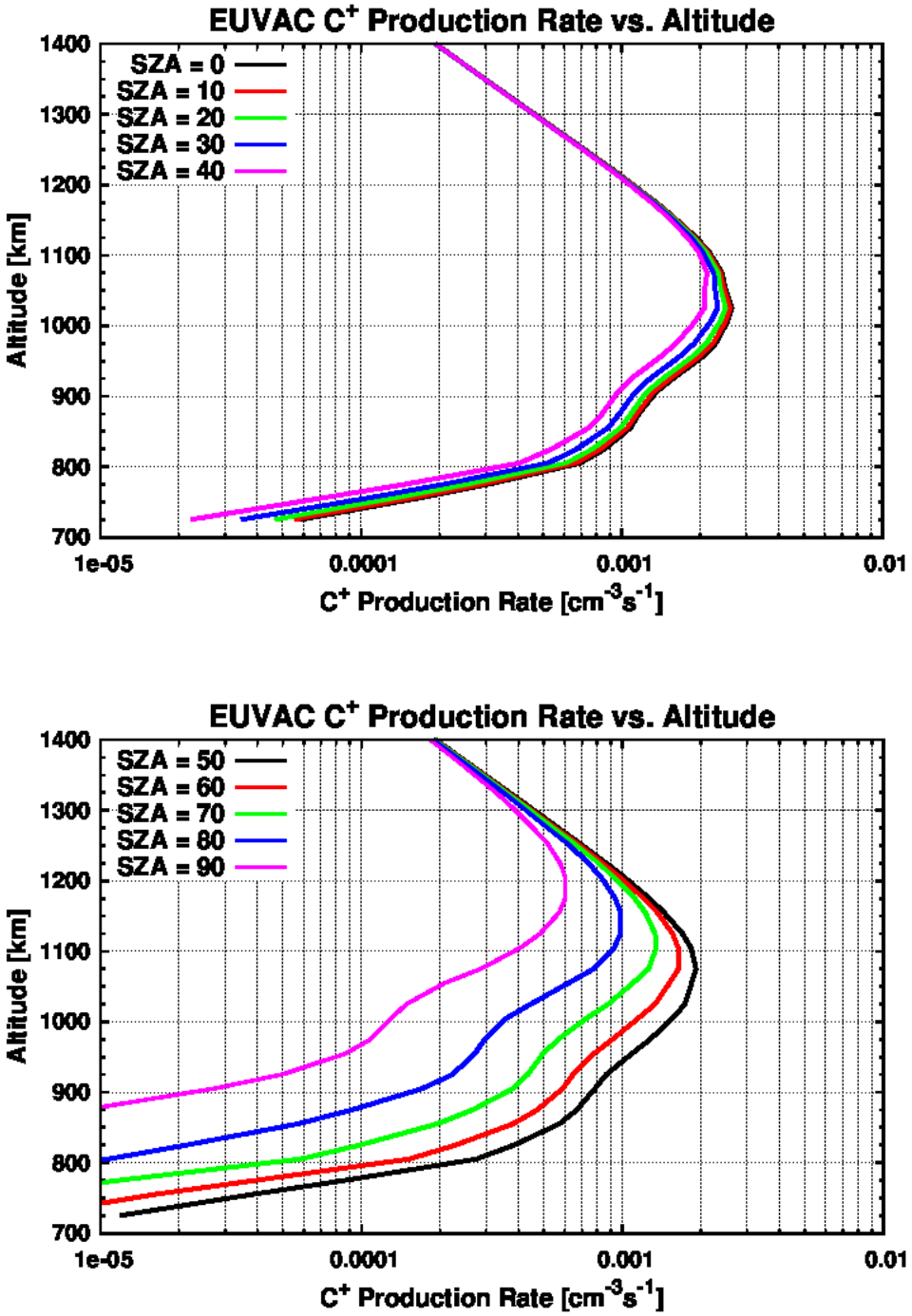

Figure 4.42 Production rate of C^+ resulting from the photoionization and photoelectron impact ionization of the global average model of the ionosphere of Titan using the EUVAC model of the solar photon flux for T40 conditions and nested magnetic field lines for solar zenith angles between 0° and 40° (above) and between 50° and 90° (below). In this model half of the solar photons with wavelengths between 800 and 1000 Å interact with molecular nitrogen.

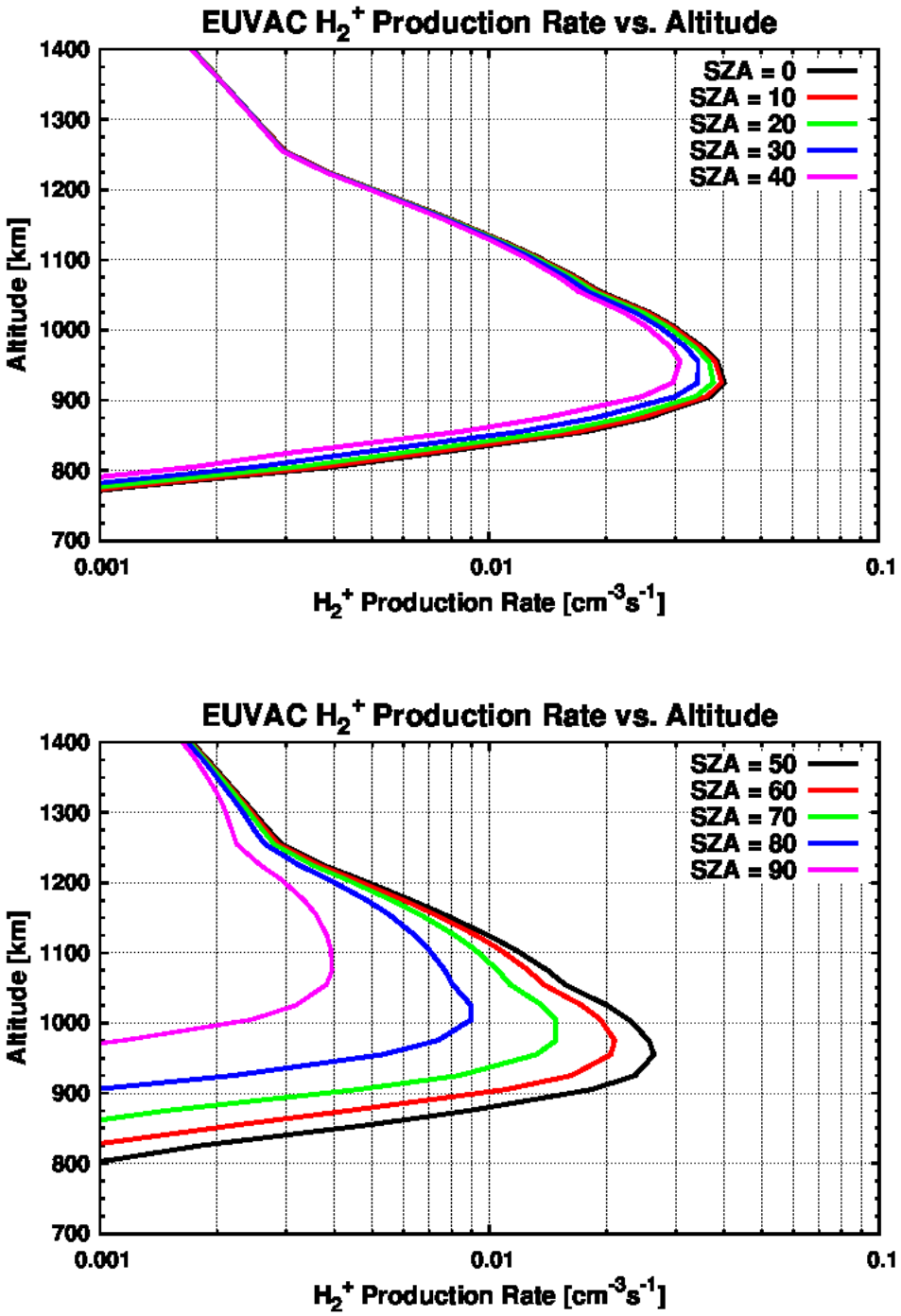

Figure 4.43 Production rate of H_2^+ resulting from the photoionization and photoelectron impact ionization of the global average model of the ionosphere of Titan using the EUVAC model of the solar photon flux for T40 conditions and nested magnetic field lines for solar zenith angles between 0° and 40° (above) and between 50° and 90° (below). In this model half of the solar photons with wavelengths between 800 and 1000 Å interact with molecular nitrogen.

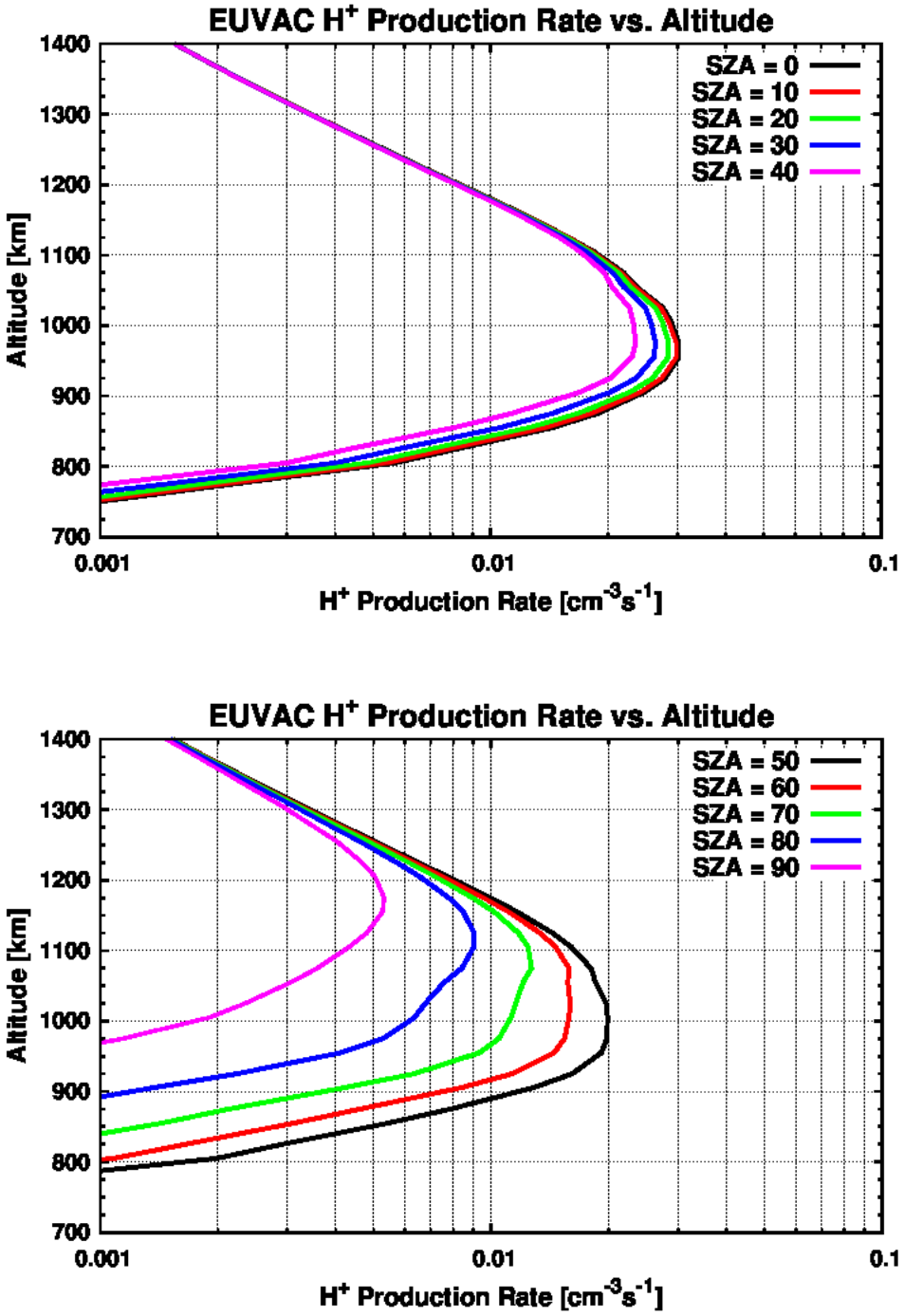

Figure 4.44 Production rate of H^+ resulting from the photoionization and photoelectron impact ionization of the global average model of the ionosphere of Titan using the EUVAC model of the solar photon flux for T40 conditions and nested magnetic field lines for solar zenith angles between 0° and 40° (above) and between 50° and 90° (below). In this model half of the solar photons with wavelengths between 800 and 1000 Å interact with molecular nitrogen.

4.3.2 Production Rate Profiles Using Radial Magnetic Field Lines and the T40 Solar Flux

The previous models of *Lavvas et al.* [2011] and *Mandt et al.* [2012] have used radial magnetic field lines in their efforts and, so that direct comparisons can be drawn between the models, the analysis done in the previous section will be repeated using radial magnetic field line geometry. This case will also demonstrate the effects that field line geometry has on the current model using the global average model of the neutral atmosphere. Comparisons will be drawn between the modeled production rates of *Lavvas et al.* and the current study for solar zenith angles of 0˚ and 60˚. In this case, as above, half of the photons, determined from the photon flux of the EUVAC model, with wavelengths between 800 and 1000 Å are not subject to photoabsorption by molecular nitrogen as was determined to be the favored case for the T40 flyby in Section 4.1. For the production rate profiles displaying results obtained using the EUVAC model of the solar flux where none and all photons with wavelengths between 800 and 1000 Å and all cases utilizing the SOLAR2000 solar flux model, please see 0.

The ionization products of N_2 are shown in Figure 4.45 (N_2^+) and in Figure 4.46 (N^+). For a solar zenith angle of 0˚(60˚) N_2^+ the production rate peaked at 14 (8) $cm^{-3}s^{-1}$ at an altitude of 1050 km (1075 km) compared to the values of 9 (5) $cm^{-3}s^{-1}$ obtained for altitudes near 1030 km (1065 km) for the model of *Lavvas et al.* [2011]. In both models a secondary shelf is observed about 150 km below the peak with a production rate of approximately 10% of the peak value. For the production of N^+, this model predicts rates slightly above 3 cm^3s^{-1} (1.4 $cm^{-3}s^{-1}$) for solar zenith angles of 0˚ (60˚) which is in agreement with the models of *Lavvas et al.* albeit at an altitude roughly 20 km higher.

The analysis of the production rates of the ionization products of methane begin with Figure 4.47 for CH_4^+. Unlike the products of nitrogen and the other ionization products of

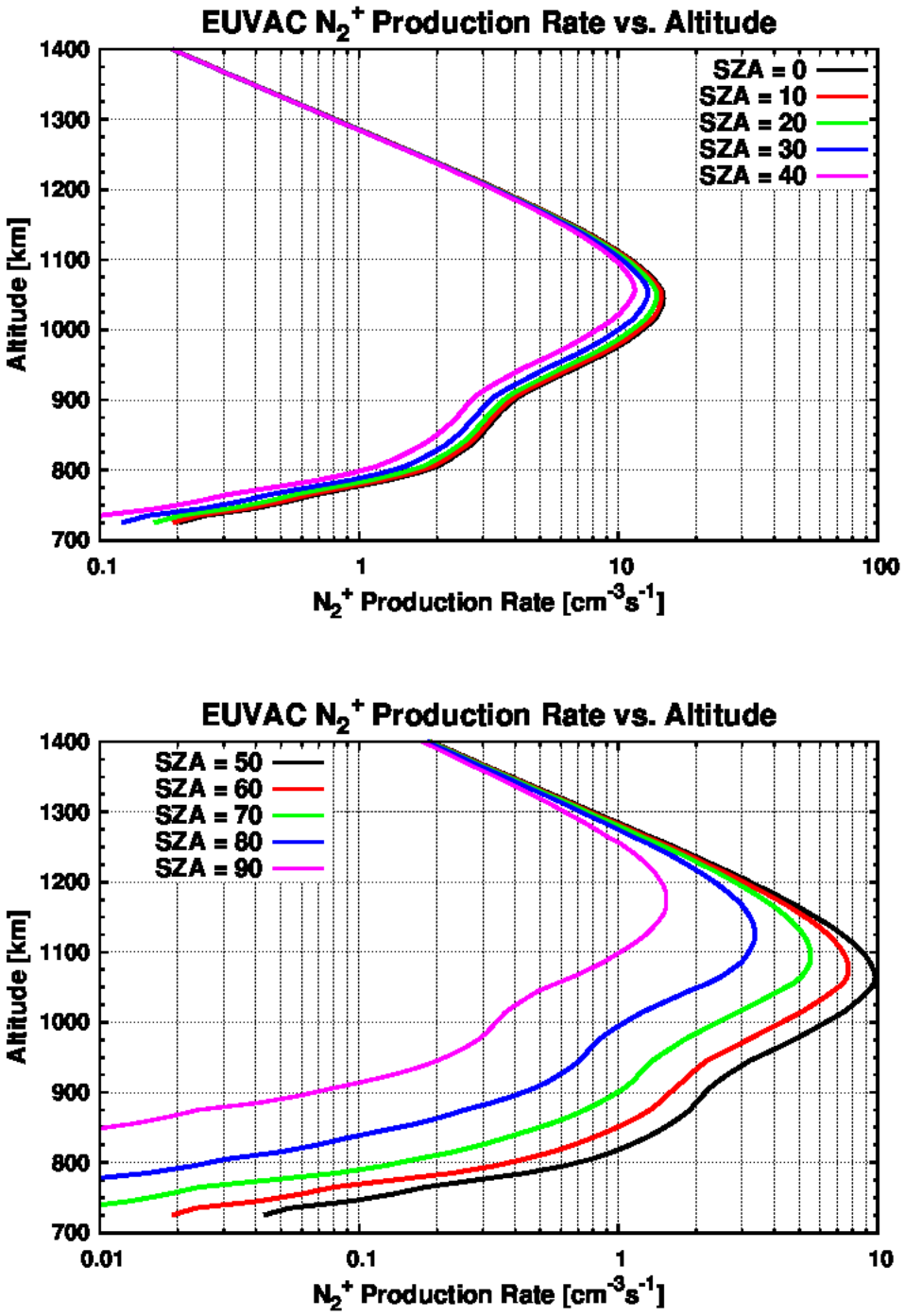

Figure 4.45 Production rate of N_2^+ resulting from the photoionization and photoelectron impact ionization of the global average model of the ionosphere of Titan using the EUVAC model of the solar photon flux for T40 conditions and a radial magnetic field line for solar zenith angles between 0° and 40° (above) and between 50° and 90° (below).

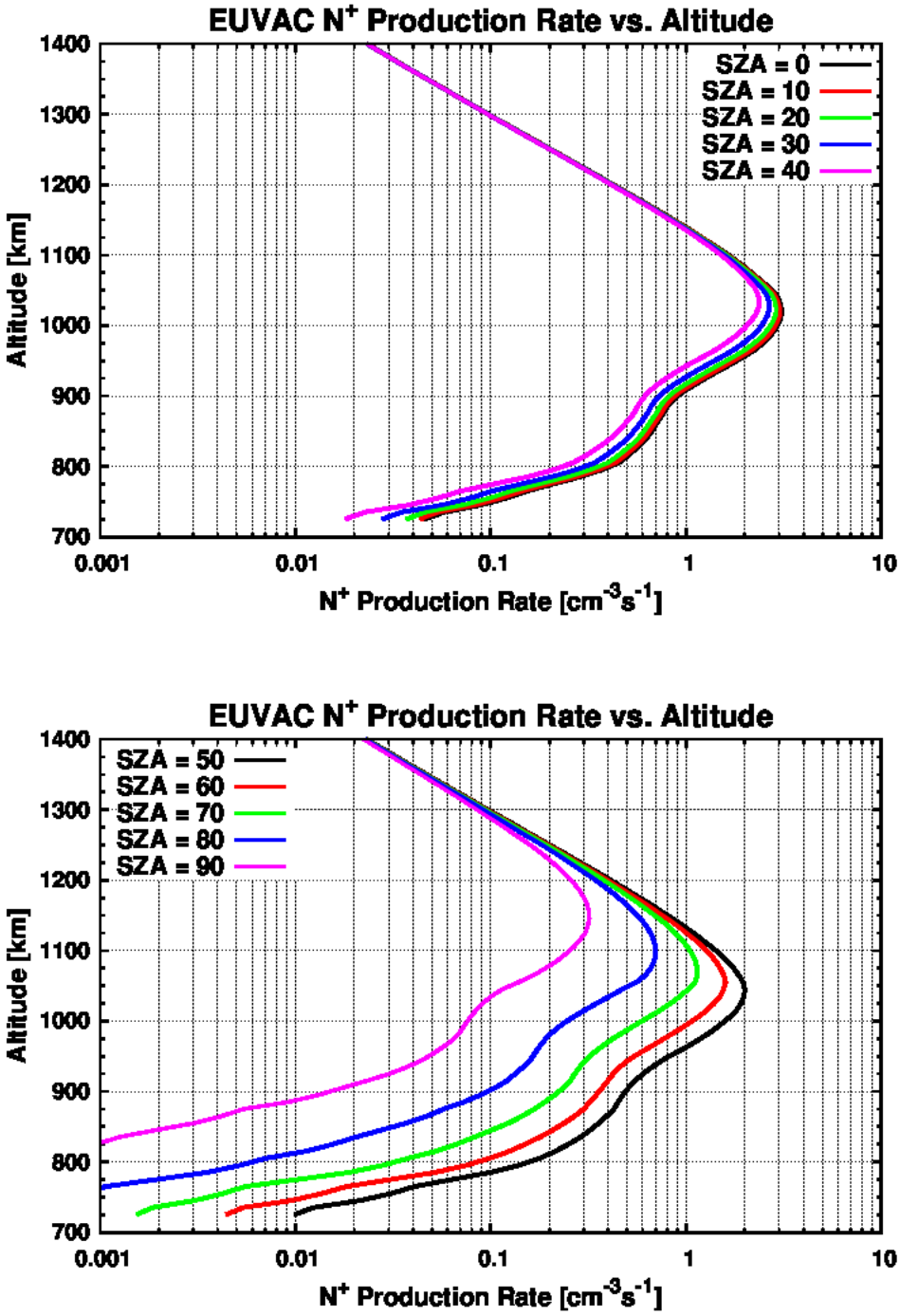

Figure 4.46 Production rate of N^+ resulting from the photoionization and photoelectron impact ionization of the global average model of the ionosphere of Titan using the EUVAC model of the solar photon flux for T40 conditions and a radial magnetic field line for solar zenith angles between 0° and 40° (above) and between 50° and 90° (below).

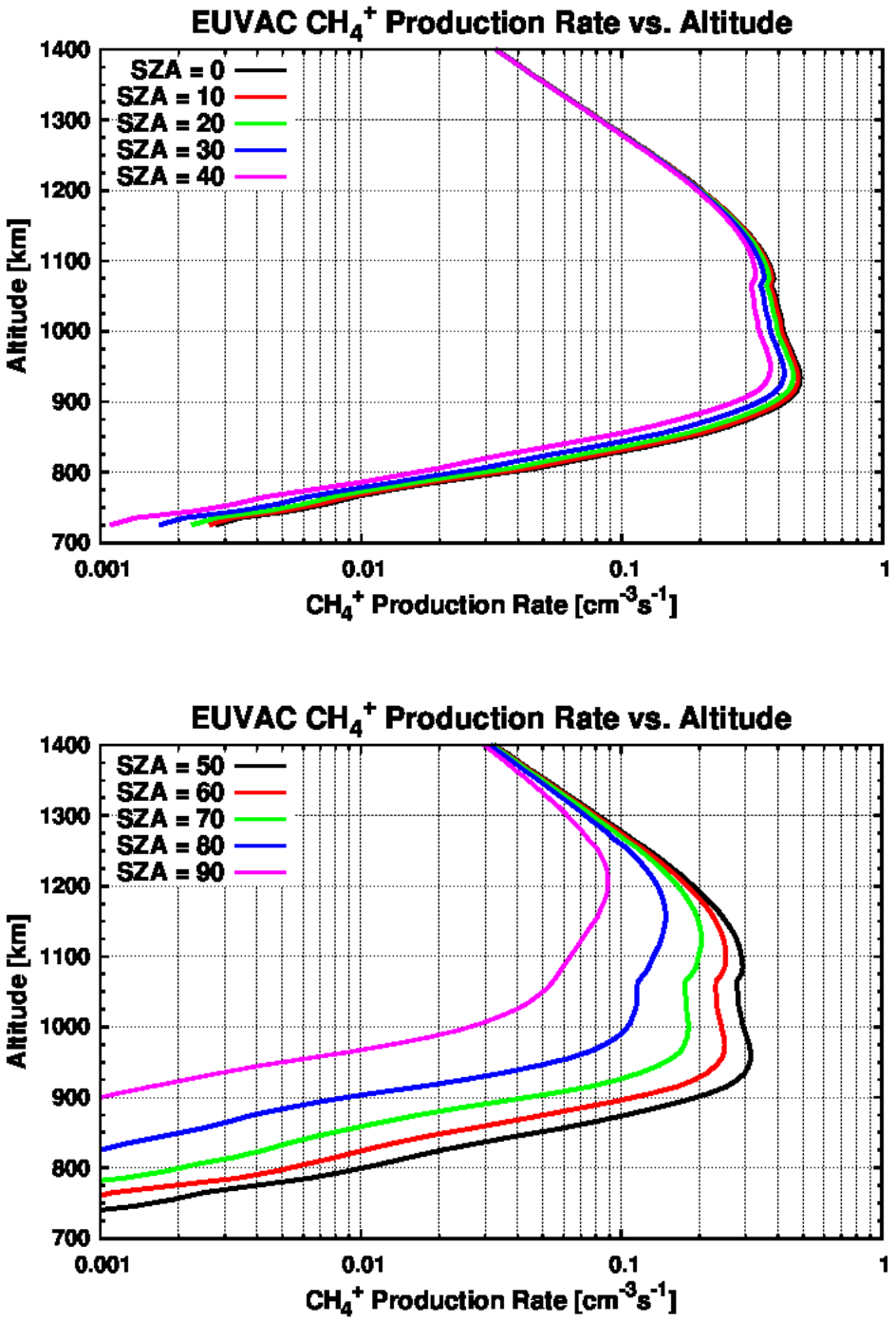

Figure 4.47 Production rate of CH_4^+ resulting from the photoionization and photoelectron impact ionization of the global average model of the ionosphere of Titan using the EUVAC model of the solar photon flux for T40 conditions and a radial magnetic field line for solar zenith angles between 0° and 40° (above) and between 50° and 90° (below). In this model half of the solar photons with wavelengths between 800 and 1000 Å interact with molecular nitrogen.

methane, the production rate profile of CH_4^+ exhibits an elongated peak with a slight increase that eventually peaks at 925 km at a value of 0.5 $cm^{-3}s^{-1}$ in this model and at 875 km with a rate of 0.6 $cm^{-3}s^{-1}$ in the model of *Lavvas et al.* [2011]. This flatter distribution is caused from the lack of photoabsorption of molecular nitrogen in the upper atmosphere [*Liang et al.*, 2007], which allows more photons with energies near the threshold energy of ionization for methane to penetrate deeper into the atmosphere. This flat feature is not observed in other cases due to the fact that the updated cross sections of *Liang et al.* only affect the absorption of photons near the threshold energy and so the contribution to other ionization products is negligible.

For CH_3^+ (Figure 4.48), the shape of the production rate profile consists of a peak with a less well defined shelf compared to the N_2^+ production rate profiles. The current model produced a peak CH_3^+ production rate of 0.21 $cm^{-3}s^{-1}$ (0.14 $cm^{-3}s^{-1}$) at an altitude of 1075 km (1125 km) and a production rate of 0.054 $cm^{-3}s^{-1}$ (0.03 $cm^{-3}s^{-1}$) at the point of inflection near 900 km (950 km) for a solar zenith angle of 0˚ (60˚). *Lavvas et al.* [2011] have shown peak production rates of 0.2 $cm^{-3}s^{-1}$ (0.12 $cm^{-3}s^{-1}$) at 1070 km (1150 km) with a production rate at the point of inflection near 900 km (1000 km) of 0.09 $cm^{-3}s^{-1}$ (0.06 $cm^{-3}s^{-1}$) for a solar zenith angle of 0˚ (60˚). Again, it is noted that the peak production values are in reasonable agreement between the two models; however, there is a minor altitude discrepancy that shows our model peaks slightly higher than that of *Lavvas et al.*

The current model produces peak ion densities of CH_2^+ (Figure 4.49) of 0.026 $cm^{-3}s^{-1}$ (0.018 $cm^{-3}s^{-1}$) at 1030 km (1100 km) for a solar zenith angle of 0˚ (60˚). As before, the same trend is evident that the production rate profiles yield similar values to the model of *Lavvas et al*. [2011], but at an altitude 20 km above the values of *Lavvas et al*. [2011].

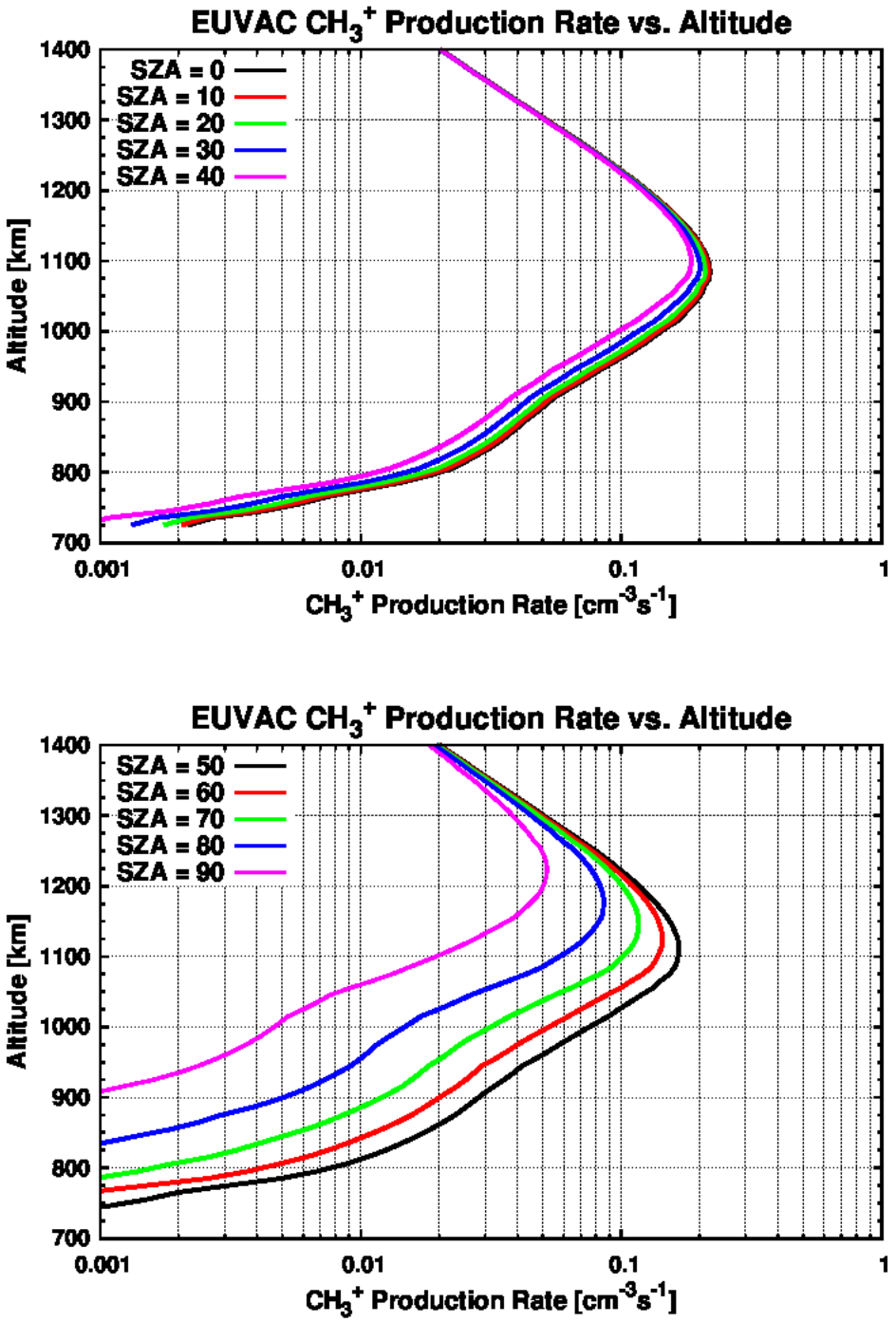

Figure 4.48 Production rate of CH_3^+ resulting from the photoionization and photoelectron impact ionization of the global average model of the ionosphere of Titan using the EUVAC model of the solar photon flux for T40 conditions and a radial magnetic field line for solar zenith angles between 0° and 40° (above) and between 50° and 90° (below). In this model half of the solar photons with wavelengths between 800 and 1000 Å interact with molecular nitrogen.

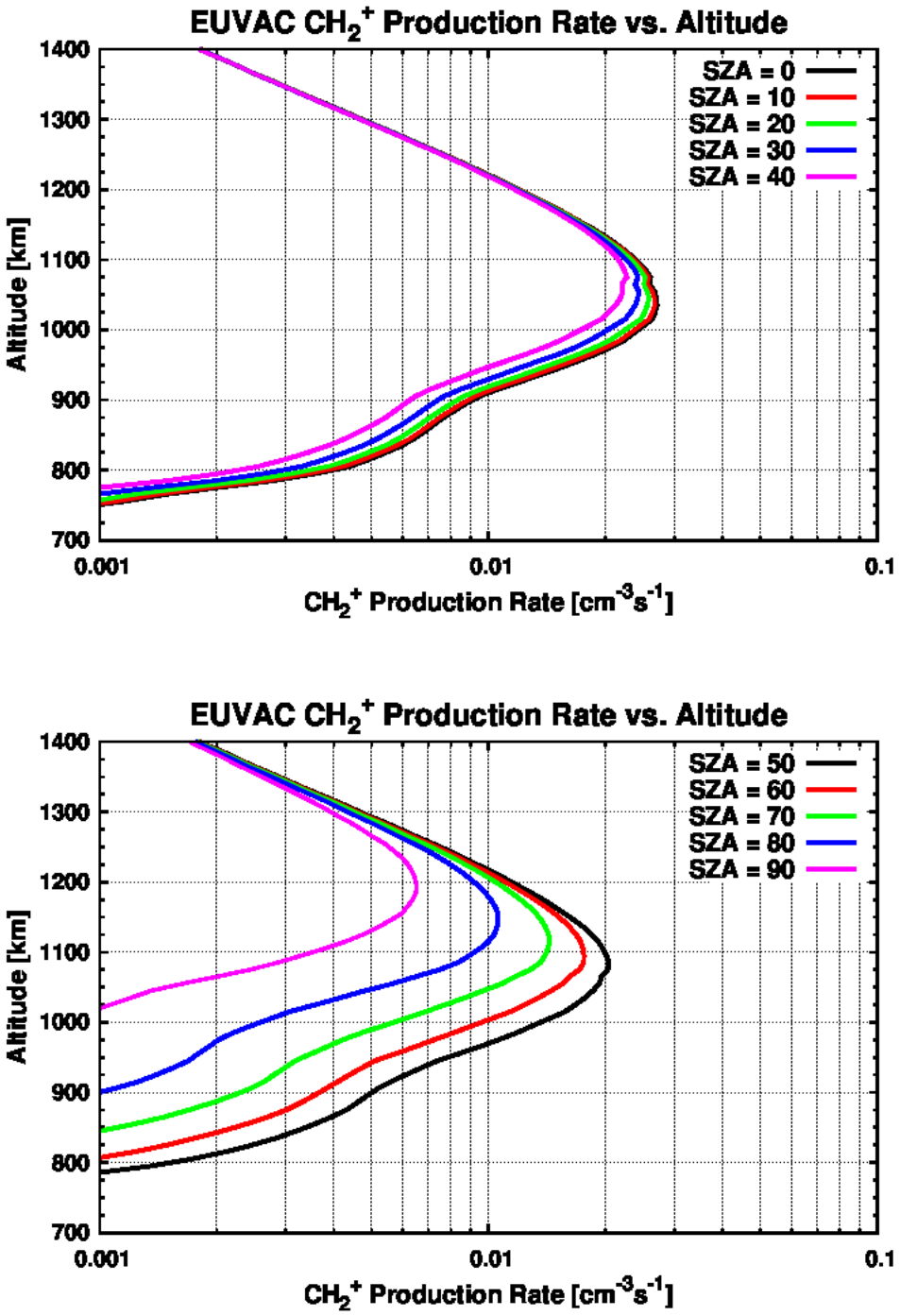

Figure 4.49 Production rate of CH_2^+ resulting from the photoionization and photoelectron impact ionization of the global average model of the ionosphere of Titan using the EUVAC model of the solar photon flux for T40 conditions and a radial magnetic field line for solar zenith angles between 0° and 40° (above) and between 50° and 90° (below). In this model half of the solar photons with wavelengths between 800 and 1000 Å interact with molecular nitrogen.

This agreement between the current model and the model of *Lavvas et al.* [2011] continues in the production rate profiles of CH^+ (Figure 4.50) and C^+ (Figure 4.51). The production rate of CH^+ peaks at 0.01 $cm^{-3}s^{-1}$ (0.006 $cm^{-3}s^{-1}$) near 1025 km (1175 km) for a solar zenith angle of 0˚ (60˚) with a shelf beginning at 900 km (950 km) with a production rate of 0.0046 $cm^{-3}s^{-1}$ (0.0023 $cm^{-3}s^{-1}$). For the same solar zenith angle of 0˚ (60˚) the C^+ production rate profile peaked at 0.0025 $cm^{-3}s^{-1}$ (0.0017 $cm^{-3}s^{-1}$) at 1030 km (1175 km) with the shelf beginning at 900 km (960 km) with a production rate of 0.0013 $cm^{-3}s^{-1}$ (0.0007 $cm^{-3}s^{-1}$).

Lavvas et al. [2011] did not show production rate profiles for H_2^+ and H^+ so comparisons between the two models cannot be drawn. It is shown that the production rate profiles of H_2^+ (Figure 4.52) and H^+ (Figure 4.53) follow the same shape as the profile of CH_4^+. It should also be noted that the effect of lowering the amount of photons with wavelengths between 800 and 1000 Å that interact with molecular nitrogen, allowing more electrons to penetrate the ionosphere without being absorbed, increases the peak production rate near 900 km. In this instance the profile of the production rate of H_2^+ has a singular peak at a value of 0.04 $cm^{-3}s^{-1}$ (0.02 $cm^{-3}s^{-1}$) at an altitude of 930 km (960 km) for a solar zenith angle of 0˚ (60˚). The production rate profile of H+ shows a singular broad peak between the altitudes of 950 km (950 km) and 1025 km (1060 km) with a production rate of approximately 0.03 $cm^{-3}s^{-1}$ (0.016 $cm^{-3}s^{-1}$) for a solar zenith angle of 0˚ (60˚).

A comparison between the production rates of N_2^+ and CH_4^+ computed by this model for a solar zenith angle of 60˚ using radial and nested magnetic field line topologies appears in Figure 4.54. As this figure shows, the choice of magnetic field line topology makes very little difference in the production rate. This is due to the fact that this model considers only ionization from solar sources (photoionization and electron impact ionization caused by photoelectrons).

The altitude at which photoionization occurs does not depend on the magnetic field line topology and this accounts for upwards of 90% of the ion production. Another reason for this similarity is that as the parabolas used to build the nested case are anchored closer and closer to the surface of Titan, the radial component of the field line increases and so the difference between the angle of the radial and parabolic field line decreases.

4.4 Conclusions of Production Rate Modeling

As a response to the results of modeled electron densities that were found to be a factor of two larger than the observed electron densities at low solar zenith angles measured by RPSW-LP [*Agren et al.*,2007] (Figure 4.1), an investigation into the model's production rate of the primary ion species resulting from the photoionization and electron impact ionization by subsequent photoelectrons was launched. This was to ensure that the cause of the discrepancy between the model and observations was not due to the fact that there was simply an overabundance of primary ions that were used as a starting point in the photochemical model. Evaluating the primary production rates of the model would also allow the construction of a global average model of the ionosphere of Titan that could be used in future modeling efforts and in order to make predictions about future flybys in a variety of conditions at Titan.

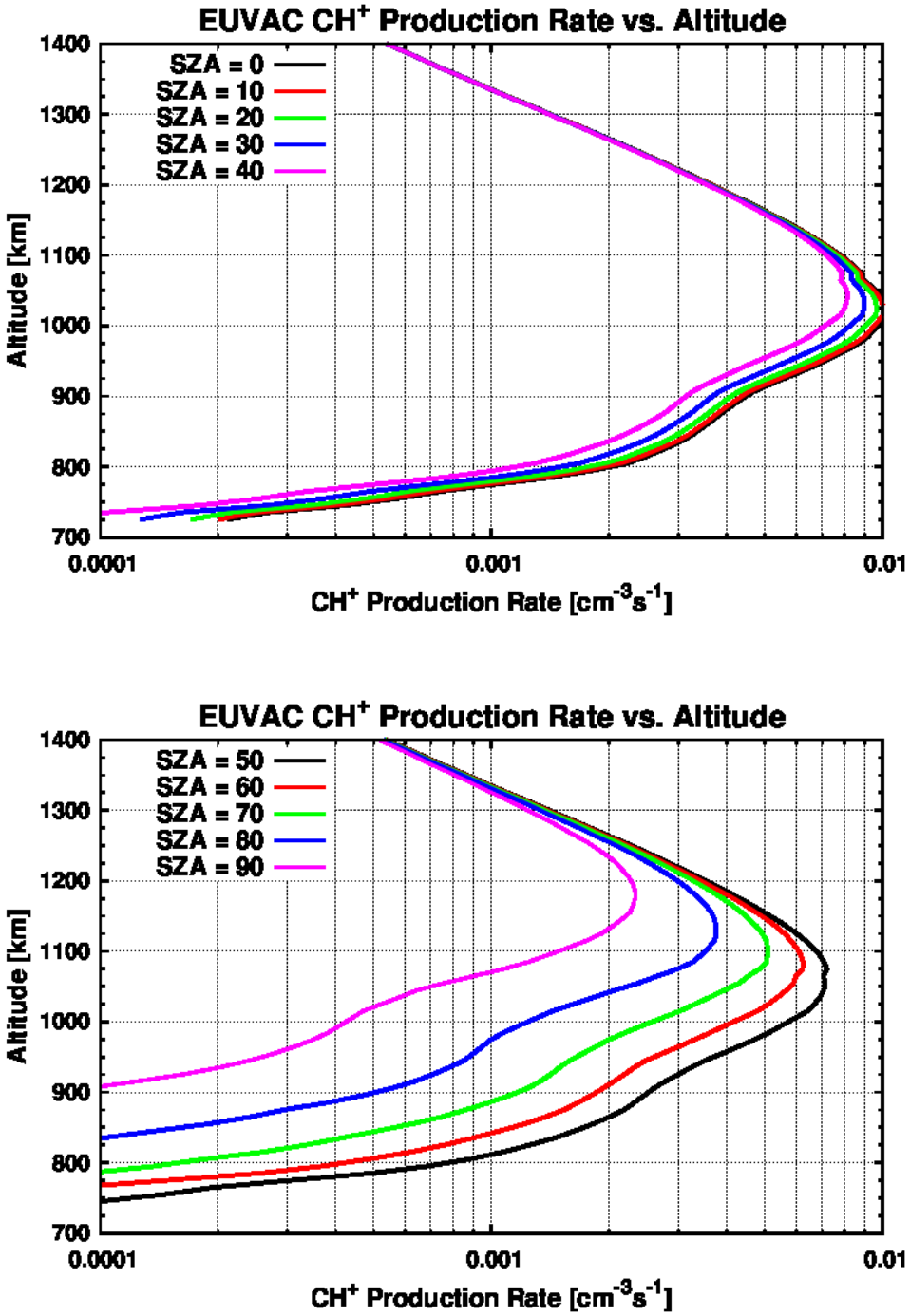

Figure 4.50 Production rate of CH^+ resulting from the photoionization and photoelectron impact ionization of the global average model of the ionosphere of Titan using the EUVAC model of the solar photon flux for T40 conditions and a radial magnetic field line for solar zenith angles between 0° and 40° (above) and between 50° and 90° (below). In this model half of the solar photons with wavelengths between 800 and 1000 Å interact with molecular nitrogen.

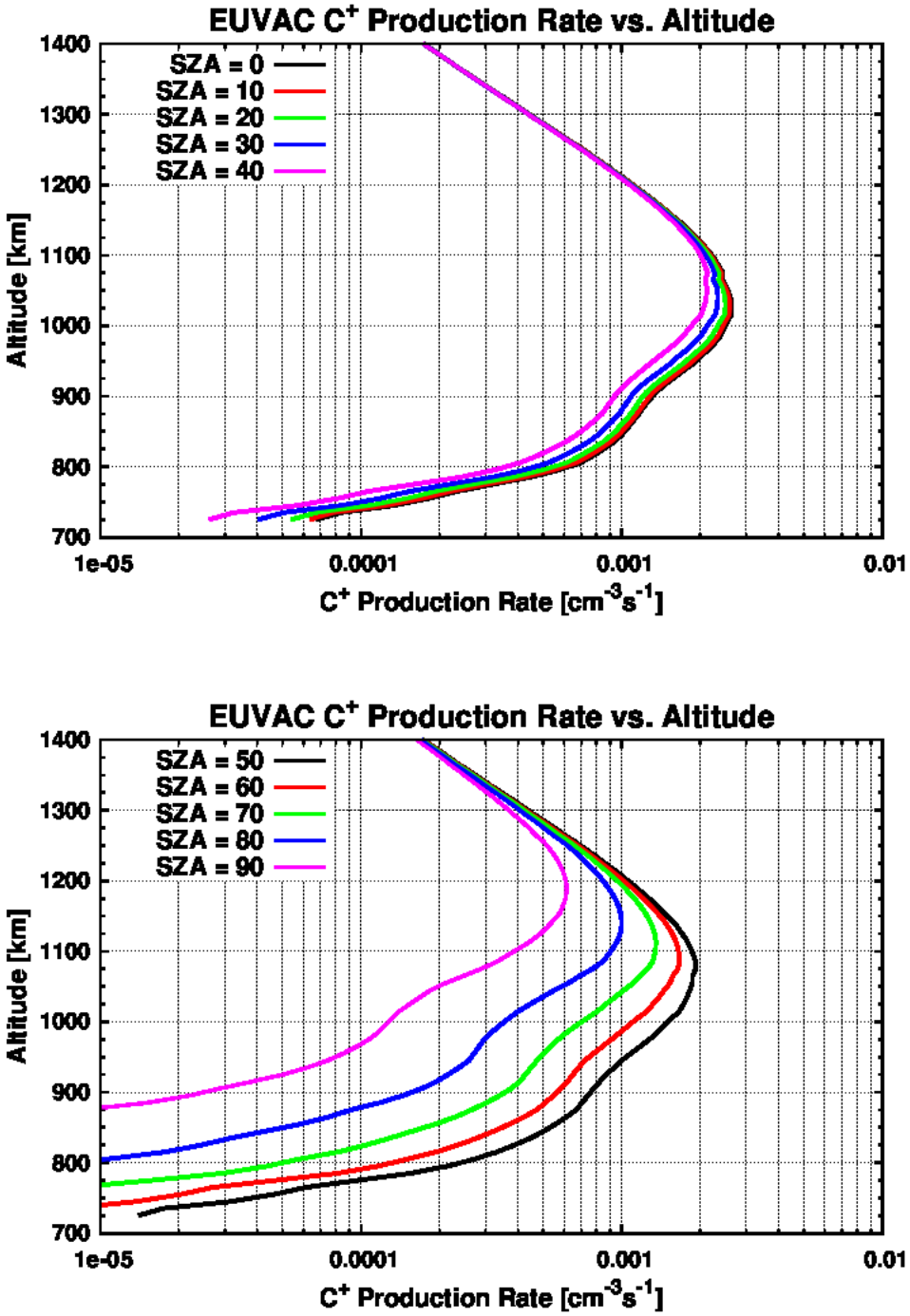

Figure 4.51 Production rate of C^+ resulting from the photoionization and photoelectron impact ionization of the global average model of the ionosphere of Titan using the EUVAC model of the solar photon flux for T40 conditions and a radial magnetic field line for solar zenith angles between 0° and 40° (above) and between 50° and 90° (below). In this model half of the solar photons with wavelengths between 800 and 1000 Å interact with molecular nitrogen.

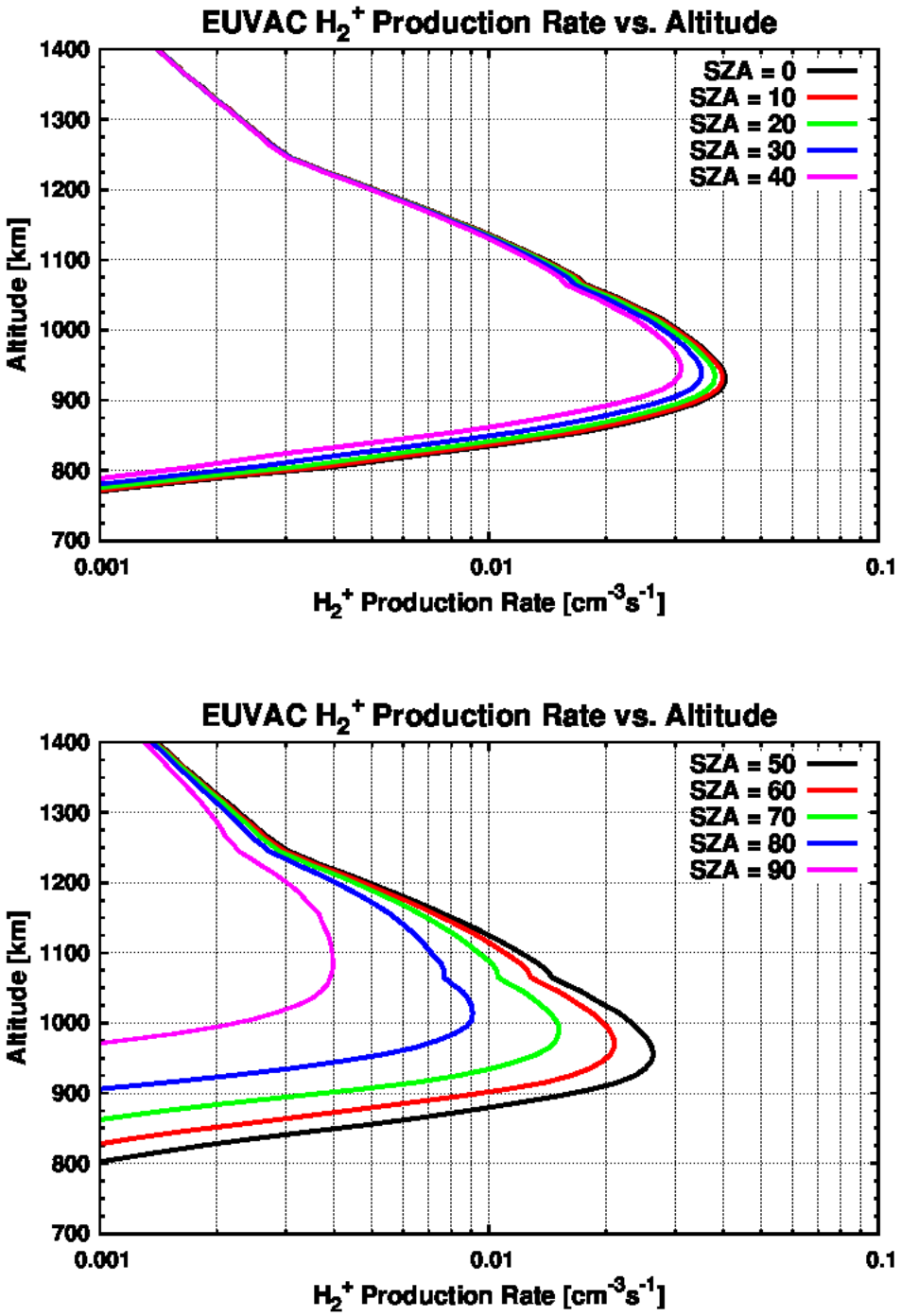

Figure 4.52 Production rate of H_2^+ resulting from the photoionization and photoelectron impact ionization of the global average model of the ionosphere of Titan using the EUVAC model of the solar photon flux for T40 conditions and a radial magnetic field line for solar zenith angles between 0° and 40° (above) and between 50° and 90° (below). In this model half of the solar photons with wavelengths between 800 and 1000 Å interact with molecular nitrogen.

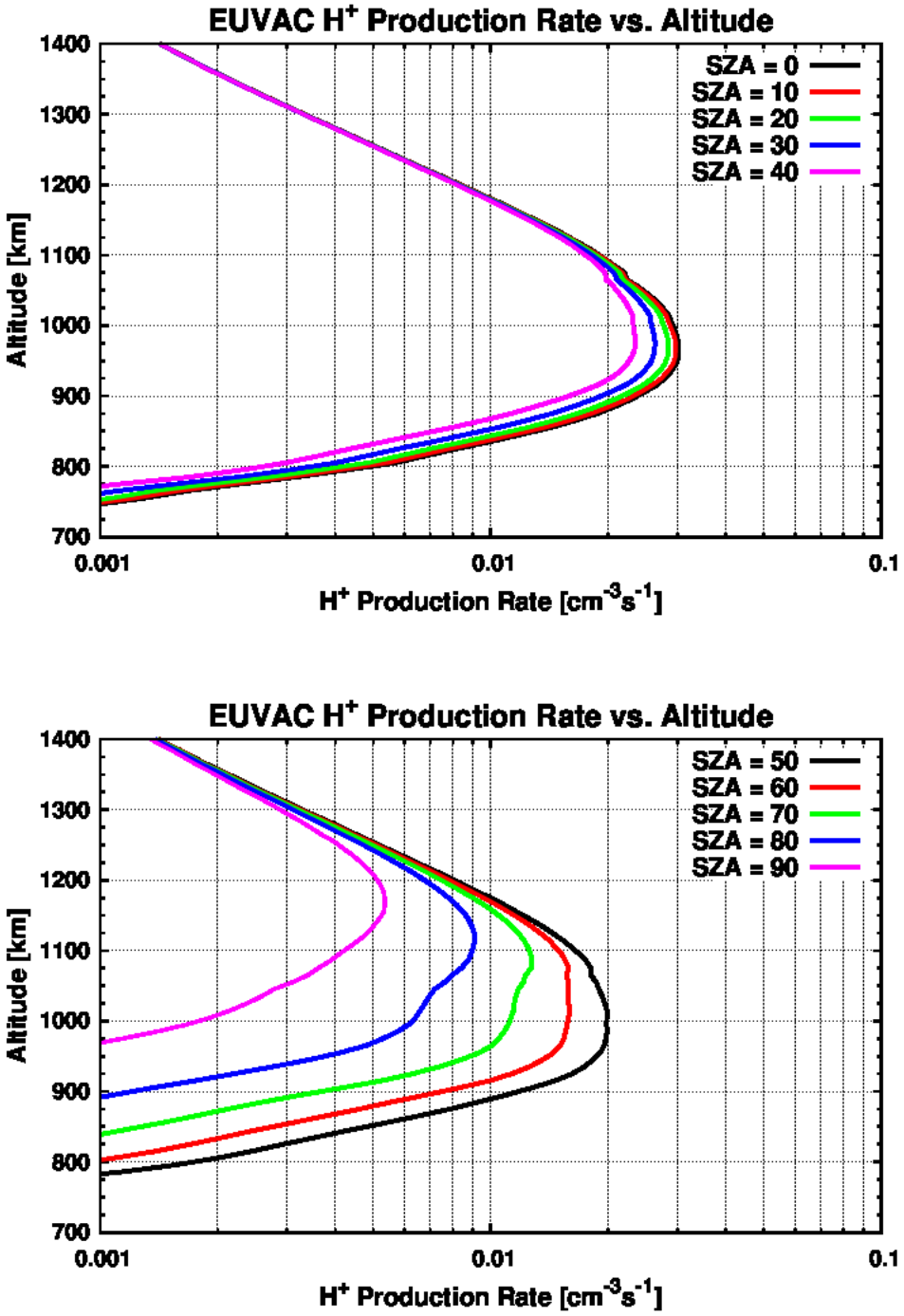

Figure 4.53 Production rate of H^+ resulting from the photoionization and photoelectron impact ionization of the global average model of the ionosphere of Titan using the EUVAC model of the solar photon flux for T40 conditions and a radial magnetic field line for solar zenith angles between 0° and 40° (above) and between 50° and 90° (below). In this model half of the solar photons with wavelengths between 800 and 1000 Å interact with molecular nitrogen.

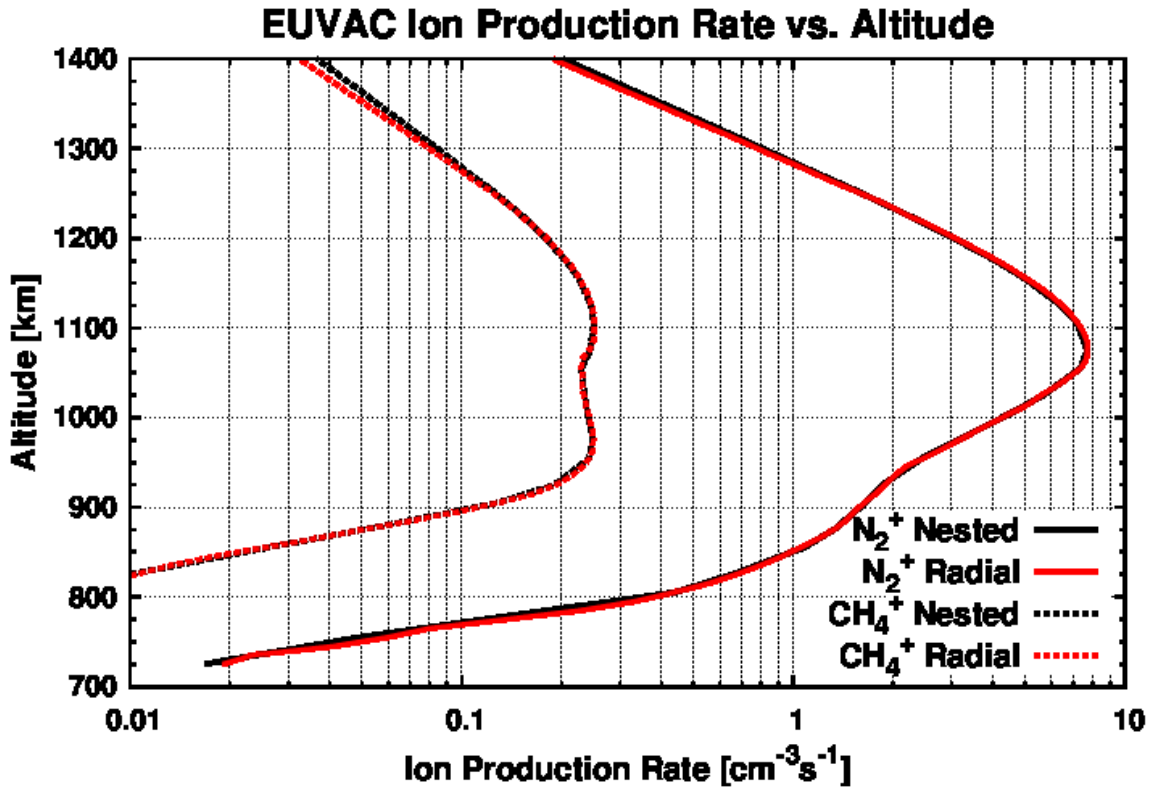

Figure 4.54 Production rate profiles for N2 (solid lines) and CH4 (dashed lines) for nested (black lines) and radial (red lines) magnetic field line topologies using the global average model of the neutral atmosphere, the incident solar flux from the T40 flyby of Titan and a solar zenith angle of 60˚. No magnetospheric inputs are considered.

In order to validate the model (Section 4.1) comparisons between the modeled results and observations for the T17, T18, and T40 flyby of Titan were used covering a range of solar zenith angles from 15˚ – 90˚. In order to verify the N_2^+ production, empirical production rates were derived from the CH_3^+ density based on the fact that reactions between N_2^+ and methane are the main producer of CH_3^+ in the ionosphere of Titan and that the main loss process of CH_3^+ is from reactions with methane. By balancing the production and loss terms and using the model to correct for the fact that not all N_2^+ reacts with methane to become CH_3^+, an empirical production

rate was derived and compared to the modeled production rate of N_2^+. Using neutral atmospheres tuned to each specific flyby and the EUVAC and SOLAR2000 models of the solar flux it was possible to model the empirical production rates and densities of CH_3^+ for all of the passes to within 20% for all cases using nested magnetic field lines which reflect magnetometer observations. It should be noted that the model appears to show flyby specific preferences to the model of the solar photon flux with the EUVAC model being the preferred case for the T40 flyby, the SOLAR2000 model being preferred by the T18 flyby, and the T17 flyby being modeled at high altitudes by the EUVAC solar flux model and at low altitudes by the SOLAR2000 model.

Next the CH_4^+ production rate from the photoionization and electron impact ionization from photoelectrons was examined. In light of the revised photoabsorption cross sections presented by *Liang et al.* [2007] for photons with wavelengths between 800 and 1000 Å, the percentage of solar photons in this wavelength range that interact with molecular nitrogen in the aforementioned wavelength regime was adjusted to 100, 50 and 0% for three model runs. This had the effect of allowing more photons to penetrate deeper into the atmosphere which increases the amount of ionization of methane. For CH_4^+ it is shown that the best agreement between the measured and modeled densities was for the case where 50% of the photons interact with N_2 using the photoabsorption cross sections of *Gallagher et al.* [1988]. Using these conditions, the modeled and observed densities were within 15% of one another.

An empirical production rate of CH_4^+ was derived by assuming photoequilibrium of the ion species and using the fact that the main loss process of the ion is through reactions with neutral methane. The modeled production rate obtained using photoionization and electron impact ionization by photoelectrons was found to be as much as a factor of 2 lower than the

empirical production rate for altitudes below 1100 km. This discrepancy arose from the fact that production of CH_4^+ from chemical reactions at lower altitudes becomes non-negligible. This production from various chemical pathways has been accounted for by implementing the full reaction chemistry of the photochemical model which brings the production rate of CH_4^+ within 10% of the empirical value derived from Cassini INMS observations.

After verifying the production rates of the major ionization products of molecular nitrogen and methane for solar zenith angles between 15 and 90˚ using comparisons between the models and the T40, T17 and T18 flybys, generic production rate profiles were made of all of the primary ionization products of methane and nitrogen for nested and radial magnetic field line configurations. The results from the radial magnetic field line case have been compared to the ion production models of *Lavvas et al.* [2011] and have been found to be in reasonable agreement, which instills confidence in the methodologies that have been used throughout this section even through the higher resolution photoabsorption cross sections of *Liang et al.* [2007] have not been explicitly implemented. There is little difference between the dayside production rate profiles for the radial and nested magnetic field line cases. This is to be expected as the majority of ionization on the dayside is caused by photoionization [cf. *Robertson et al.*, 2009].

In this chapter the production rate profiles of the primary ion species have been examined and found to agree with empirical production rate profiles derived from Cassini INMS observations. Several flybys were chosen so that the results of the model could be evaluated at a variety of solar zenith angles. After comparing with empirical results, comparisons were then drawn between this ion production model and the model of *Lavvas et al*. [2011] and the results were found to be in reasonable agreement. From this, it is concluded that the primary production of ions on the dayside of Titan resulting from photoionization and the electron impact ionization

of molecular nitrogen and methane has been reasonably modeled. Production rate profiles have also been presented for all of the major primary ionization products of N_2 and CH_4 with a resolution of 25 km for a case using nested magnetic field lines and 10 km for radial magnetic field lines utilizing a global averaged model of the atmosphere for solar zenith angles between 0˚ and 90˚. The global average production rate profiles are shown using the photon spectrum generated by the EUVAC model of the solar flux where 50% of the photons with wavelengths between 800 and 1000 Å interact with molecular nitrogen. By only allowing 50% of photons within this wavelength range to interact with N_2, the high-resolution photoabsorption cross sections of *Liang et al.* [2007] were simulated using the photoabsorption cross sections of *Gallagher et al.* [1988]. Profiles using the SOLAR2000 model flux of solar photons and various interaction percentages are shown in 0. This will enable future modelers of the ionosphere of Titan to choose between generic primary ion production rate profiles in order to represent the conditions at Titan using the solar flux model and solar zenith angle(s) of interest to them.

In summary the key findings of this chapter are:

1. Solar flux empirical models (i.e. EUVAC and SOLAR2000) only make a 25% difference in the modeled ion production rates.
2. Allowing 50% of solar photons with wavelengths between 800 and 1000 Å to interact with molecular nitrogen using the photoabsorption cross sections of *Gallagher et al.* [1988] is a good approximation to the high resolution photoabsorption cross sections of *Liang et al.* [2007] and will aid the model in reproducing the lower altitude shelf in the CH_4^+ production.
3. Model ion production rates agree with empirical ion production rates determined using INMS ion neutral density profiles to within 20%.

4. On the dayside of Titan, the choice of magnetic field line topology (radial or nested) makes very little difference in the production rates of N_2^+ and CH_4^+ at the ionospheric peak as the production rate is dominated by solar sources.
5. The discrepancy between modeled and measured (data taken by INMS, RSS, and RPWS-LP) electron and ion density is not due to overproduction of the primary ion species and therefore must be caused by insufficient electron recombination rates.

Chapter 5 **Dayside Electron and Ion Temperature**

In Figure 4.1, it was shown that a discrepancy exists between the measured ion densities and those produced by the model used in this study. In the ionosphere of Titan electron dissociative recombination is the primary cause of ion loss. This loss process of an ion species i is expressed as a dissociative recombination coefficient α multiplied by the product of the electron density n_e and ion density n_i and a factor of 300 K divided by the electron temperature T_e to the power β as shown in Equation (5.1). These coefficients are taken from *Anicich* [2003] and following the

$$Loss_i = \alpha n_e n_i \left(\frac{300K}{T_e}\right)^{\beta} \qquad \textbf{(5.1)}$$

modeling efforts of *Robertson et al.* [2009] and *Westlake et al.* [2012] and are shown in Appendix C-1. Equation (5.1) shows that lower electron temperatures will result in larger electron dissociative recombination rates. The goal of this section is to accurately model the electron and ion temperatures in order to verify that the electron dissociative loss rates used in this model are representative of those occurring in the ionosphere of Titan.

The current model is essentially taken from the models of *Gan et al*. [1992, 1993] and *Cravens et al*. [2008] but has been updated to reflect new observations made by in situ by the Cassini spacecraft and Huygens probe. Magnetic field line topologies were chosen such that the field orientation at the spacecraft location is in general agreement with magnetometer observations for each flyby considered (see Figure 3.2) [*Dougherty et al.,* 2004; *Backes et al.,* 2005; *Bertucci et al.,* 2009; *Cravens et al.*, 2010]. Parabolic field lines were used to approximately simulate the draping of Saturn's magnetic field around Titan. This has been discussed in Section3.1. See Figure 3.4 for an example of altitude versus the distance along a

magnetic field line for a case with its apex point at an altitude of 960 km. The model uses a grid spacing of 35 km along magnetic field lines [*Gan et al*., 1992, 1993; *Cravens et al*., 2004] for the suprathermal electron flux calculations and also for the calculation of thermal electron and ion temperatures from the coupled electron and ion energy equations.

The main neutral species in the model are nitrogen and methane. A primary photoelectron population was created as the result of photoionization of these neutrals by solar extreme ultraviolet (EUV) and solar X-ray radiation (Section 3.2). The SOLAR2000 solar flux model (now the SIP) [*Tobiska et al*., 2000] was used to provide inputs from solar radiation for solar minimum conditions, as described by *Robertson et al*. [2009], and in Chapter 3 in Section 3.2.

The thermal population of electrons, heated by Coulomb collisions with the suprathermal electron population of magnetospheric or atmospheric origin, was considered. The two-stream electron transport code (Section 3.3) was used to calculate suprathermal electron fluxes along magnetic field lines and their code-generated thermal electron heating rate. Electron and ion temperatures for the thermal electron and ion species were calculated by solving the coupled electron and ion energy equation that includes heat transport via heat conduction, local heating sources/sinks, and dynamical terms that depend on the bulk flow of the plasma (Equation (3.34)) discussed in Section 3.3.

The temperature model gives its results in terms relative to the neutral temperature (T_i-T_n). For comparison purposes with the *Crary et al*. [2009] paper, the neutral temperature is set at 150 K.

5.1 Setup for Temperature Comparisons with Data

The T18 flyby of Titan took place on 23 September 2006 when Titan was located at 2.27 Saturn Local Time (SLT) and reached an altitude of 960 km at closest approach (CA) near the

dayside terminator as the Cassini spacecraft left the ionosphere on the dayside. Solar zenith angles (SZA) for the outbound, dayside part of this encounter ranged from 90.93º, just before CA, to 75º, later during egress. Magnetometer data along the spacecraft trajectory is presented in the upper portion of Figure 3.2. The neutral densities for molecular nitrogen and methane are taken from INMS measurements of the T18 neutral atmosphere reported in *Magee et al*. [2009] (Figure 3.35).

Photoionization from solar radiation alone was sufficient for a chemical model to produce the observed thermal electron and ion densities [*Cravens et al*., 2005; *Robertson et al*., 2009] and solar radiation is used as an "internal" source of the suprathermal electrons (that is, photoelectrons). For this T18 comparison the Tobiska SIP flux model with F10.7 = 70.4 [*Tobiska et al*., 2000] (Figure 3.8) was implemented as described by *Robertson et al*. [2009]. F10.7 is the solar radio intensity at 10.7 cm and is a common proxy for solar activity [c.f., *Schunk and Nagy*, 2009]. The conditions for this paper are solar minimum conditions. *Robertson et al.* [2009] and *Cravens et al.* [2009a] noted that the majority of photoelectrons are produced below 1400 km; however, above this altitude photoelectrons do not provide sufficient heating for thermal electrons and so other cases will be examined which include magnetospheric electron inputs as constrained by CAPS-ELS magnetospheric electron flux measurements. The comparison of the CAPS observed suprathermal fluxes and the suprathermal fluxes from the model near the ionospheric peak for dayside T18 conditions is shown in Figure 3.15. It should be noted that the CAPS fluxes presented in Figure 3.15 are shifted by 1.5 eV in order to account for the spacecraft potential; however, a further shift between 1-2 eV would have brought the model into better agreement with the data.

All the model temperatures for altitudes below 1000 km converge on the neutral temperature of about 150 K or so, but the measured electron temperatures remain higher at values of about 400 K (*Agren et al*., 2007). Electron-neutral thermal coupling is quite large at lower altitudes, so the 400 K temperatures will require a source of heat that is yet to be determined.

Analysis of the magnetic field data shown in Figure 3.2 [see discussion in *Cravens et al.,* 2010; *Robertson et al*., 2009] suggested that field lines were very close to being horizontal with respect to the radial direction for the outbound portion of the T18 flyby. This is especially evident when viewing the flyby in the X-Z plane in the Titan Interaction System (TIIS) coordinates. In Figure 3.2, you can see distinct magnetic field vectors almost parallel to the surface of Titan. In this coordinate system, x is the nominal corotational flow direction, y points toward Saturn and z completes the set of right-handed coordinates [*Backes et al.,* 2005].

MHD models of the Titan encounter [*Backes*, 2004; *Ma et al.,* 2009] also show the draping of magnetic field lines and hence that the field lines are horizontal at most altitudes. In order to simulate this configuration in the model and ensure that the local magnetic field lines are horizontal, a "nested" case was implemented using multiple parabolic field lines (described by *Gan et al*. [1992, 1993], *Cravens et al*. [2004], and *Robertson et al*. [2009] and in 3.1) as illustrated in Figure 3.3. An example of the thermal electron temperature obtained by solving Equation (3.34) along a single field line anchored at 960 km (closest approach for the T18 encounter) with a solar zenith angle of 90.93° is shown in Figure 3.4 along with the corresponding altitude. Figure 5.1 shows the heating and cooling rates of thermal electrons along this field line while the rate of cooling for the thermal electrons as a result of collisions with N2 and CH4 is displayed in Figure 5.2. The apex point of each parabola used to construct the nested

case was set to an altitude coinciding with an altitude where the Cassini spacecraft made measurements. The thermal electron and ion temperatures at each apex point, i.e. the s = 0 point in Figure 3.4, were taken and compiled from a large number of model runs and combined into a single case that will be referred to as the "nested case." For the dayside case, three field line configurations were tested and compared, including a radial field line, a single parabola anchored at the surface, and the nested case mentioned above.

The following dayside cases are considered in the model:

Case D1 – Radial: The adopted magnetic field line is anchored to the surface of Titan and extends outward in the radial direction. The solar zenith angle was set at a constant value of 90.93º to simulate T18 conditions near CA at the terminator.

Case D2 – Parabolic Surface Anchored Field Line: A single parabolic magnetic field line anchored at the surface of Titan was adopted and the solar zenith angle was set at 90.93º. This field line still has a significant radial component at ionospheric altitudes (about 45 degree angle with respect to radial).

Case D3 – Parabolic Field Line with Apex at Surface and with INMS Neutral Densities Increased by a Factor of 3: This case is identical to case D2 except that all of the neutral densities have been tripled to account for the INMS recalibration of neutral densities [*Mandt et al.*, 2012] that was not included in previous model runs. Increasing the neutral densities has the effect of shifting all curves upward by about one scale height such that the altitude at which the electrons and ions reach thermal equilibrium increases by approximately 70 km.

Case D4 – Nested Magnetic Field Lines: This case is composed of several model runs with the apex point of each parabolic field line serving as the location where the temperature

result is extracted from the model(s) (see Figure 3.3). For each run, the apex point of the parabola was set to an altitude where Cassini had recorded data for T18. The solar zenith angle was set to 90.93º for each parabola.

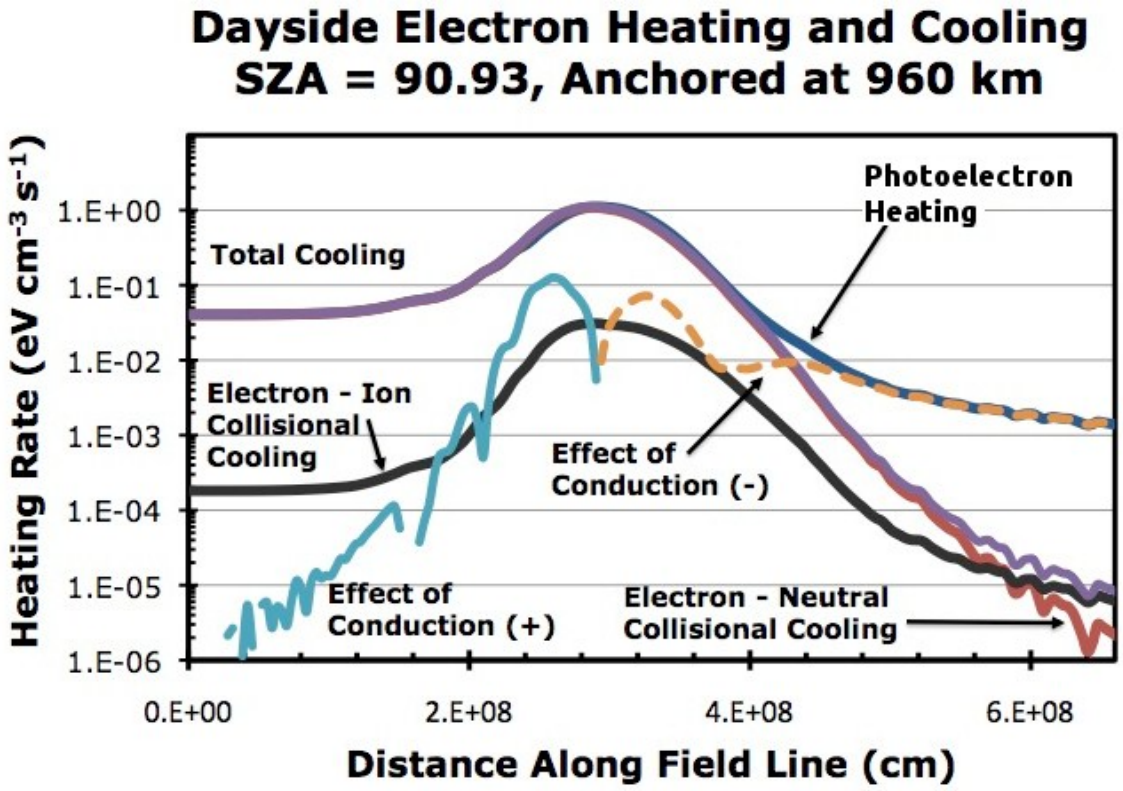

Figure 5.1 Heating and cooling rates for the thermal electron population along a single parabolic field line of the D4 case anchored at 960 km with SZA = 90.93˚. Magnetometer data [c.f. *Bertucci et al.*, 2009] shows that the magnetic field has a large horizontal component at this point on the Cassini trajectory. The purple line shows the total cooling rate with the effect of electron-ion collisional cooling and electron-neutral collisional cooling shown in black and red respectively. The dark blue indicates heating due to photoelectrons. The light blue and orange lines indicate the positive and negative effects of conduction respectively.

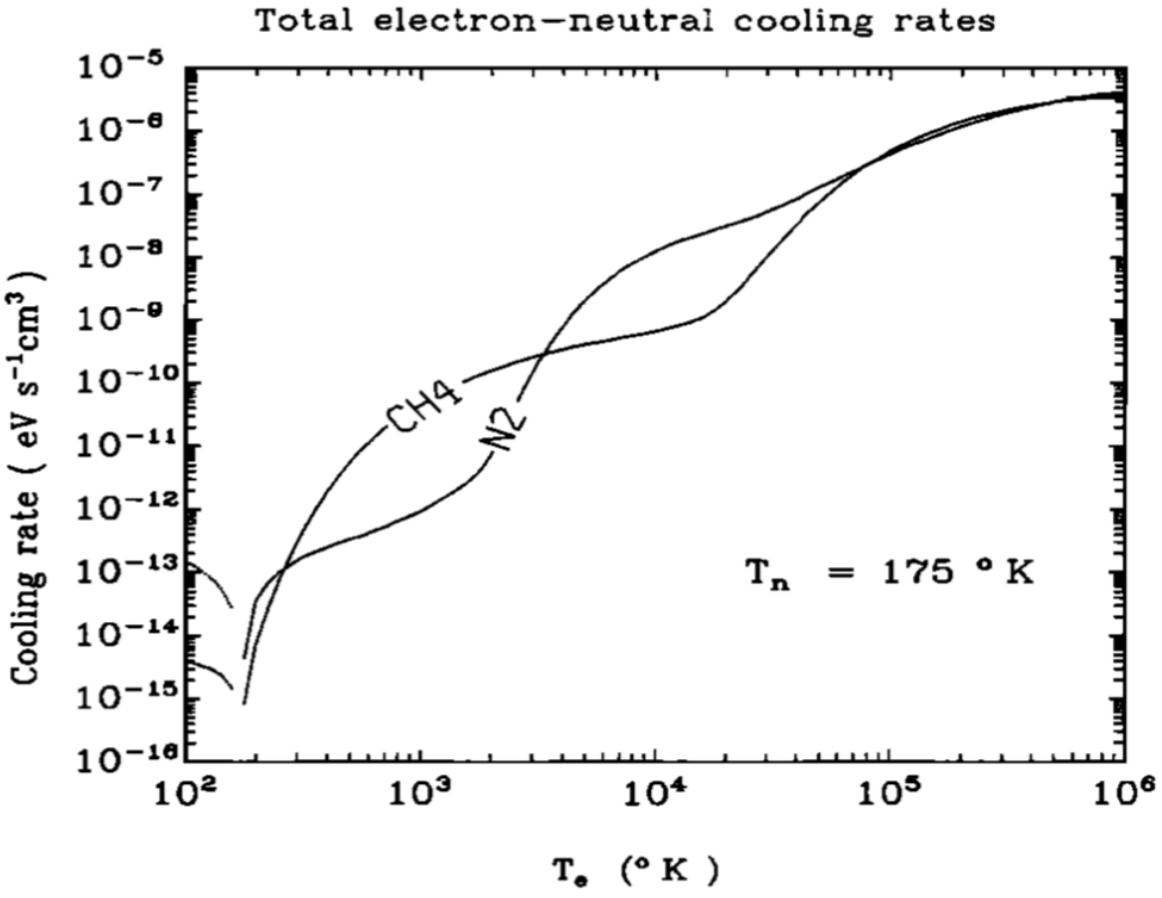

Figure 5.2 Cooling rates of thermal electrons as a result of inelastic collisions with methane and nitrogen taken from Gan et al. [1992]. Copyright 1992 American Geophysical Union; further reproduction or electronic distribution is not permitted.

Case D5 – Nested Field Line, SZA = Cassini: This case is identical to case D4 except that the solar zenith angle for each parabola was modified to reflect the solar zenith angle along the spacecraft track for T18 between 74.49° and 90.93°.

Case D6 – Nested Magnetic Field Lines with "Lobe-Like" Magnetospheric Electron Inputs: This case is identical to D5 except that it includes the T8 "lobe-like" magnetospheric electron flux (Figure 1.2) observed by the CAPS-ELS as an input at the upper boundary in an attempt to bring the modeled electron temperatures above 1400 km into agreement with RPWS measurements. The T8 electron flux data was adopted because of the lack of availability of a T18 suprathermal electron flux at very high altitudes for the boundary condition. *Rymer et al.* [2009] classified both the T8 and T18 flybys as "lobe like", meaning the upstream magnetospheric electron conditions for Titan were similar to the lobe regions of the Earth's ionosphere characterized by an electron density flux between $5.3 \times 10^4 - 2.4 \times 10^5$ $cm^{-2}s^{-1}sr^{-1}$ at the peak energy (150 - 820 eV). Thus, the T8 suprathermal electron flux is used as a representative suprathermal electron flux for the model's boundary conditions of the T18 encounter.

Case D7 - Nested Magnetic Field Lines with "Plasma Sheet-Like" Magnetospheric Electron Inputs: This case is identical to D5 except that it includes the T5 "plasma sheet-like" magnetospheric electron flux as an input at the upper boundary. It will be demonstrated in Section 5.2 that the T8 magnetospheric electron flux was not sufficient to bring the modeled electron temperatures into agreement with RPWS measurements and so the more robust T5 magnetospheric electron flux is used to examine its effect on the model.

5.2 Dayside Temperature Modeling Results

Results from the electron and ion energetics model for the dayside are described in this

section assuming that there is no bulk motion of the plasma. The different dayside cases considered in 5.1 are shown in Figure 5.3 and Figure 5.4. The resulting electron and ion temperatures determined for the various model cases show the importance of the local magnetic field line topology for the electron thermal balance. The calculated electron temperatures for the cases (D1and D2) in which the field has a significant radial component at ionospheric altitudes are much lower than the measured temperatures as shown in Figure 5.3. Both heat and suprathermal electrons can be transported downward to lower altitudes in this case, and higher neutral density allows collisional losses and cooling to operate more efficiently.

On the other hand, for the cases in which the field lines were horizontal at each altitude where Cassini measurements were made and model comparisons were carried out (D4 and D5), much higher calculated electron temperatures (see Figure 5.4) result and, at least below an altitude of about 1350 - 1400 km, better agreement is obtained with the measured temperatures. For these cases, the heat is bottled up at higher altitudes where cooling is less effective as the horizontal field lines limit the conduction between altitudes. This is consistent with the models of *Gan et al*. [1992, 1993], *Roboz and Nagy* [1994], and *Galand et al*. [2006]. The electron and ion temperatures obtained for case D5 were very similar to those obtained for case D4, indicating that the local magnetic field topology (and hence whether the field lines are locally horizontal or have strong radial components) has a greater effect on temperatures than the exact solar zenith angle does (as long as it is on the dayside at least).

The measured temperatures above 1350 km exceed the model temperatures for all cases except D7, suggesting that the model is missing some high altitude heat source. Recall that no magnetospheric inputs were included in model cases D1-D5 (Figure 5.3 and Figure 5.4), which might be unrealistic even on the dayside. In order to fix this problem and to increase the electron

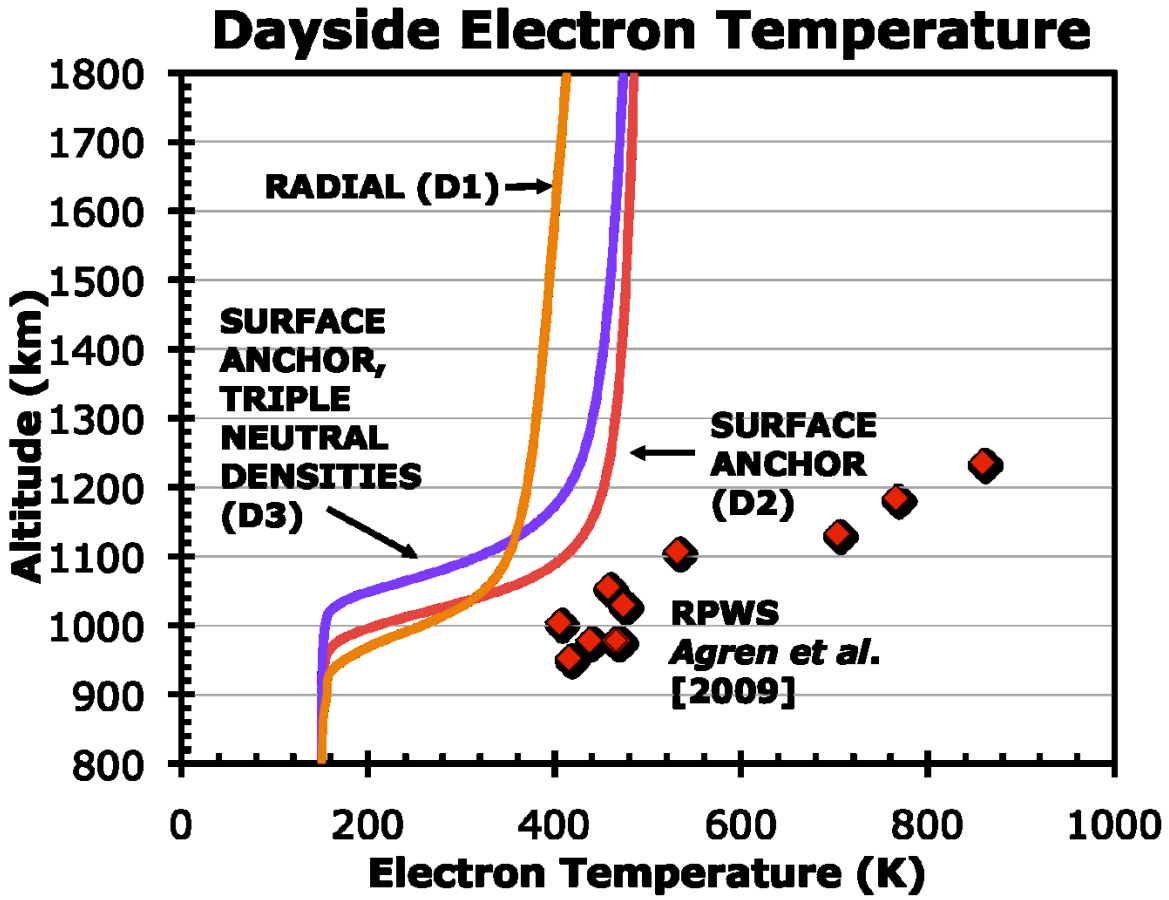

Figure 5.3 Electron temperatures vs. altitude for the dayside model case (T18 conditions) with both radial and single parabolic field line topologies (cases labeled D1, D2, and D3). For all these cases the magnetic field has a significant radial component, even though the magnetometer data indicates that the field is predominantly horizontal. These cases are shown to illustrate the importance of the field direction. For the case labeled "triple neutral densities" the INMS density measurements of N_2 and CH_4 have been tripled. For all of the field line cases shown here the model give temperatures are significantly greater than the neutral temperature of 150 – 170 K, but they are still much lower than the reported values. This is caused by efficient conduction of heat along the field line to lower altitudes where the electrons are cooled by collisions with the neutrals.

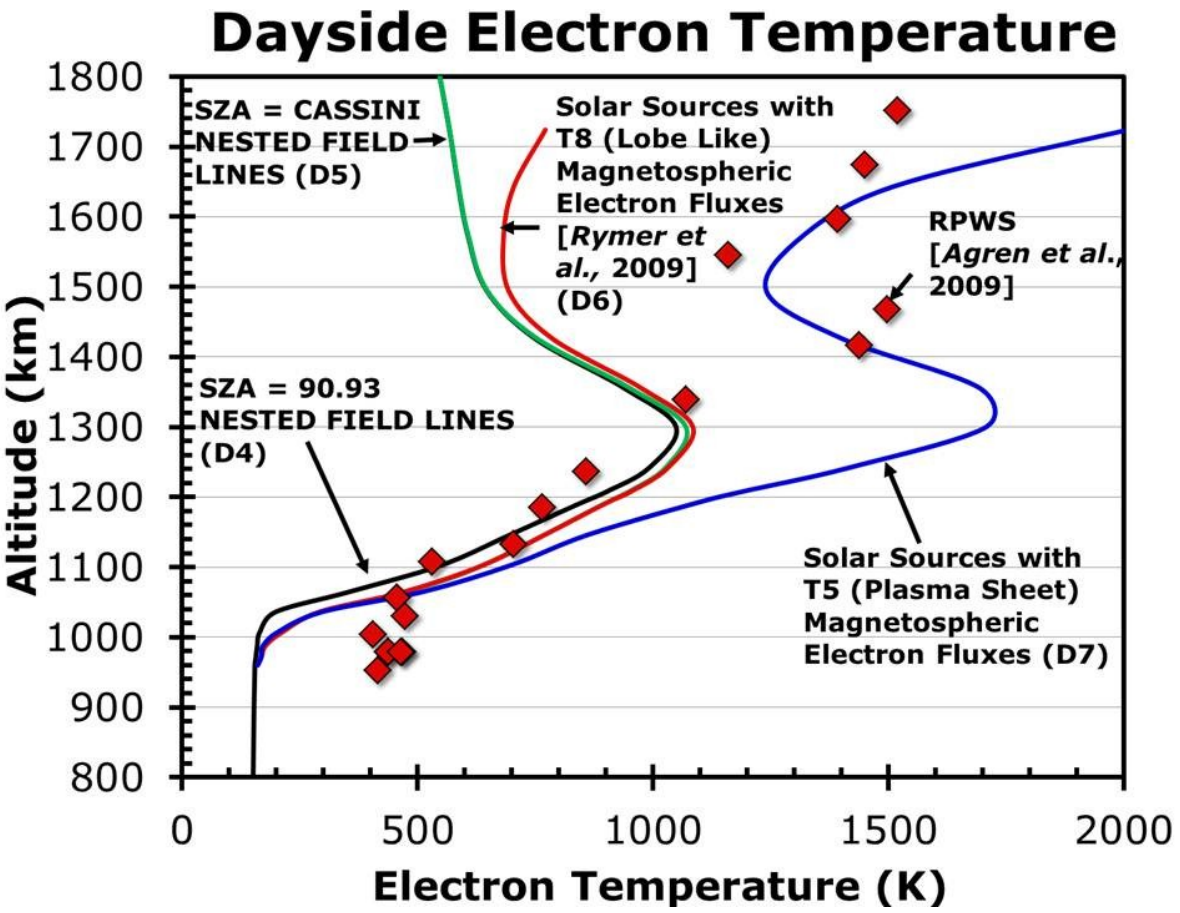

Figure 5.4 Cases D4, D5, D6, and D7 for the dayside/terminator ionosphere (as described in the test) are shown. All these cases have "nested" field lines, as described in the text, in which the field is horizontal at each location of the spacecraft during T18. The D4 and D5 cases did not include any external magnetospheric electron fluxes. Good agreement between modeled and measured temperatures exists up to about 1300 km. Above this altitude an additional source of energy is required to bring thermal electron temperatures into agreement with the RPWS/LP measured values so magnetospheric electron precipitation is considered. The D6 cases shows the impact of a typical "lobe-like" [*Rymer et al.*, 2009] magnetospheric electron flux, the same type of magnetospheric conditions observed during the T18 pass. A more energetic T5 magnetospheric electron flux is considered (D7) but overshoots the measured electron temperature.

temperature for the D4 case between 1500 and 1800 km, T8 suprathermal fluxes [*Rymer et al.*, 2009] were adopted as the upper boundary condition for the electron flux in the D6 case. The T8 flyby, like T18, was classified by *Rymer et al.* [2009] as a "lobe-like" plasma environment so the two flybys should have similar magnetospheric electron fluxes. The model electron temperatures with this addition (shown in Figure 5.4) increased the electron temperature by 200 K at 1700 km. RPWS thermal electron temperatures [*Agren et al*., 2009] still exceed the model temperature by 800 K at this altitude. Using the T5 magnetospheric flux brought the model electron temperatures into agreement with measured values from *Agren et al.* [2009] between 1500 and 1700 km; however, with this change the modeled temperatures exceed the measured temperatures at 1300 km by nearly 700 K. Unfortunately, T5 magnetospheric electrons are not appropriate for T18 conditions and were used in this study as an upper bound for the magnetospheric electron flux. The actual heat source for the T18 upper ionosphere is still under investigation.

Note that there is a dip in the modeled electron temperatures near 1500 km (Figure 5.4) due to an increase in the relative amount of methane to nitrogen this altitude. Electron collisions with methane are more effective at cooling the electrons due to methane's vibrational and rotational excitation modes. As altitude increases the neutral density decreases as does the electron density and the heating rate of the thermal electrons due to photo- and magnetospheric electron heating. The cooling rate of the thermal electrons due to collisions with neutral and ion species also decreases with altitude due to the decreased densities of the ions and neutral species. The balance of these terms, together with conduction, along the field line determines the thermal electron temperature, but for the nested field line case, heat conduction is less important. Photoelectron heating is mainly balanced by electron-neutral cooling but near 1500 km, electron-

ion cooling is relatively more important than at other altitudes.

Model cases (D6, D7) were run with external suprathermal electron fluxes, as described earlier. In particular we adopted, as inputs at the top of the atmosphere, magnetospheric electron fluxes as seen by Cassini outside Titan's ionosphere during the T8 and T5 encounters. Magnetospheric fluxes will increase the ion production rates at higher altitudes as magnetospheric electrons ionize the upper atmosphere while the rate of ion production near the peak (1.03×10^{-1} $cm^{-3}s^{-1}$ near 1208 km) is relatively unchanged. At an altitude of 1350 km the relative importance of magnetospheric electrons' contribution to the ion production rate becomes significant giving ion production rates at this altitude of 1.58×10^{-2} and 2.49×10^{-1} $cm^{-3}s^{-1}$ when the T8 "lobe-like" (D6) and T5 (D7) magnetospheric electron fluxes are used respectively. Neglecting the fluxes at 1350 km when the SZA is 78.38º (D5) as it was during the time when Cassini made measurements yielded an ion production rate of 7.64×10^{-3} $cm^{-3}s^{-1}$. Above 1350 km and SZA > 78º the impacts of magnetospheric electron precipitation on the ion production rates need to be considered.

Now consider the modeled electron temperature in the lower ionosphere. The calculated temperatures for all cases and for altitudes below 1000 km converge on the neutral temperature of about 150 K, but the measured electron temperatures remain at values of about 400 K (*Agren et al*., 2007). The electron-neutral thermal coupling is quite large at lower altitudes where the neutral density is high resulting in more electron-neutral collisions, so the 400 K measured temperatures are difficult to explain. A potential cause for these high measurements of electron temperature could be that the coating of the RPWS-LP restricts the accuracy of measurements near 0.015 eV [*Wahlund, J.-E., private communication*] (corresponding to temperatures of approximately 175 K) which are appropriate for the conditions in the ionospheric peak (cf.

Cravens et al. [2009b]).

5.3 Dayside Ion Temperature

Ions in the ionosphere of Titan are primarily heated by Coulomb collisions with the thermal electron population. In Section 3.5, the full energy balance equation for the ions was given as well as a description of the terms in the equation. In this section temperature profiles for an ion of mass 29 amu will be given. This mass was chosen as a pseudo-average of the masses of the heavy ions and lighter ions found in the lower and upper altitudes respectively. The results of the model will also be compared to ion temperatures that have been inferred by *Crary et al.* [2009].

Figure 5.5 shows the ion temperature altitude profiles for all of the cases mentioned in the previous section. The calculated temperatures for Cases D4, D5, D6, and D7 agree the best with the measured ion temperatures from *Crary et al*. [2009] below an altitude of 1600 km. The measured temperatures exceed the model temperatures for altitudes above 1600 km but no dynamical terms were included in the ion energy equation so this is perhaps not surprising given that dynamics should be important in the upper ionosphere [*Ma et al.,* 2006; 2009]. Including T8 magnetospheric suprathermal electron inputs in our model (case D6) had little impact on the modeled ion temperatures. Using the T5 magnetospheric electron flux (case D7) increased the modeled ion temperatures by almost 200 K at 1600 km and moved them into closer agreement with the measured values. However, the T5 electron flux introduces significantly more energy to the ionosphere than does the T8 flux and the temperature difference between the two cases is small compared to the error bars in the measured temperatures at higher altitudes.

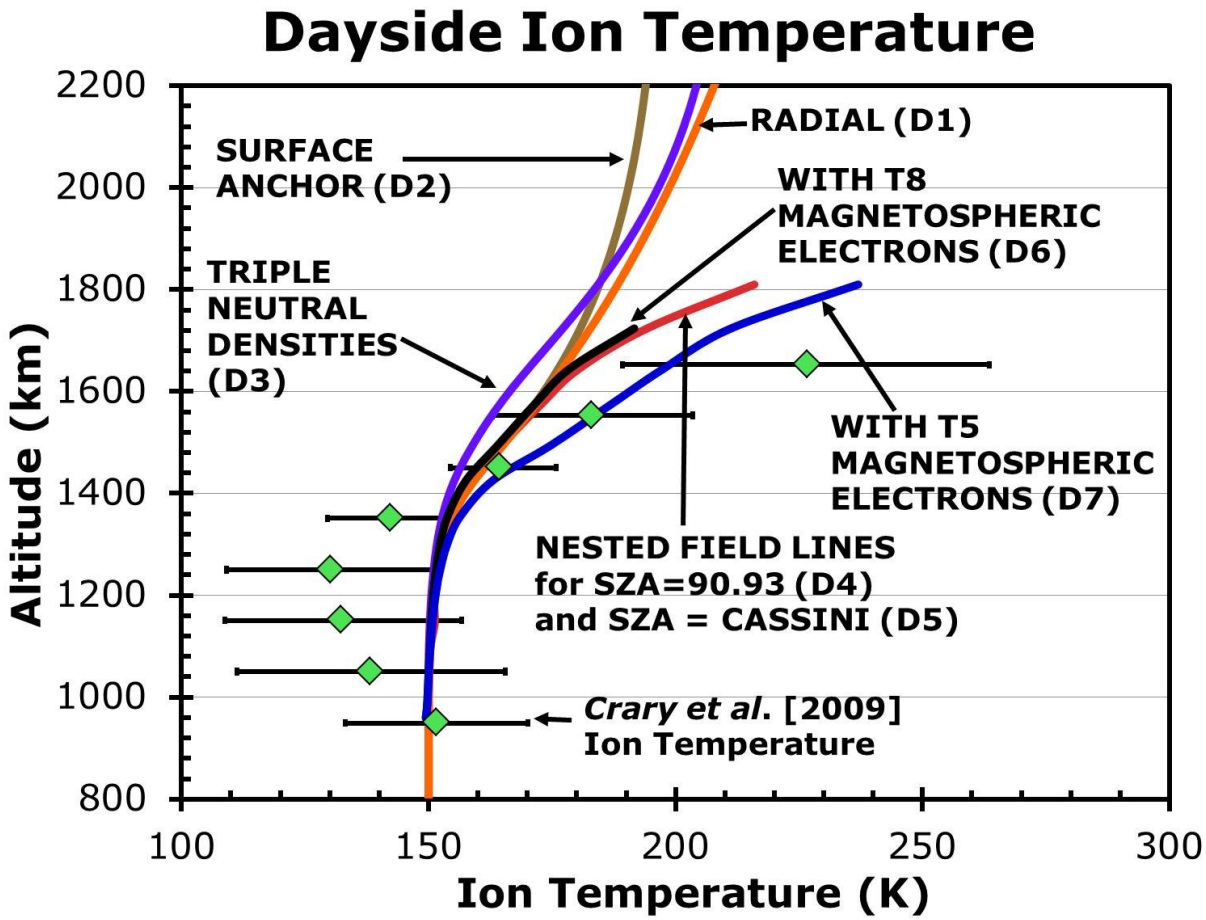

Figure 5.5 Ion temperatures vs. altitude for various field line cases. Again, the nested field line approach shows the best agreement with measured ion temperatures from Crary et al. [2009]. The triangles on the graph represent electron temperatures for the nested case (D4) with a magnetospheric suprathermal electron flux from the T5 flyby [Cravens et al., 2008].

5.3.1 Impacts of Dynamical Terms on Ion Temperature

Dynamical Terms, terms depending on the flow velocity of the plasma u in Equation (3.34), are capable of influencing the energy balance of the ions and therefore ion temperatures. In this subsection the impacts of mass loading, plasma flow speeds parallel to the direction of the field line, frictional heating between the ions and neutrals (Joule heating) and the divergence of plasma flow along a magnetic field line have been investigated for the conditions observed during the T18 flyby. Empirical estimates of possible velocities [*Cravens et al.,* 2010] and flow fields from MHD models will aid in the implementation of realistic values into the model [*Ma et al*., 2006; 2008; 2009].

First the impact of adding a source of ions (mass loading) to the plasma on the temperature of the ion species was examined. Figure 5.6 shows the effects of mass loading by multiplying the neutral density by an ion production factor indicated by the labels on the figure in order to derive the value of S_s in Equation (3.34). For nitrogen, the production factor at 1100 km would be roughly 10^{-9} according to ion production rates published by *Robertson et al*. [2009]. The mass loading term is capable of producing an effect on the ion temperature; however, this effect will be noticed at lower altitudes in Titan's ionosphere. Including the production rate factor is shown to bring the temperatures in the lower ionosphere, where neutral densities are greater, into better agreement with the data from *Crary et al.* [2009]; however, in the upper atmosphere, this lowered ion temperature increases the discrepancy between this model and the values shown by *Crary et al.* [2009]. In order to decrease the modeled ion temperature by the 20 K needed at 1100 km the ion production factor would need to be between 5×10^{-8} and 1×10^{-7}, 50-100 times larger than the production rates of *Robertson et al.* [2009] which is an indication that mass loading is not a dominant part of the ion energy balance.

Figure 5.7 shows the impact of the divergence of the plasma flow velocity (terms depending on $\nabla \cdot u_s$ in Equation (3.34)) along the field line. A positive value indicates that the divergence is up the field line away from the anchor point of the parabola and the surface of Titan. Estimated values of this parameter put its value close to 10^{-4} s^{-1} which does not produce a profound effect in the lower ionosphere and only a slight negative effect (~20 K) in the upper ionosphere at 1600 km. Near the ionospheric peak (1000-1200 km) even a divergence of the plasma flow 100 times larger than the estimated value is not enough to resolve the discrepancy between the ion temperatures reported by *Crary et al.* [2009] and therefore, like the mass loading term, the divergence of flow is not expected to play an important part in the ion energy balance.

Crary et al. [2009] calculated ion wind speeds on Titan between 100 and 260 m/s. Neutral wind speeds ranging from 245 ± 50 m/s were estimated by *Müller-Wodarg et al*. [2006], values up to 150 m/s by *Müller-Wodarg et al*. [2008] and up to 160 m/s in the lower atmosphere by *Flasar et al*. [2005]. Figure 5.8 shows the effect on the ion temperatures for the case where the bulk velocity of the ions and neutrals are directed parallel to the magnetic field line. The ion temperatures are strongly coupled below 1200 km. In the lower estimates for the wind speeds given above the neutral temperatures see a decrease of approximately 10K when the wind is parallel to the field line. When the wind is anti-parallel, the ion temperatures are increased by 15K for the lower estimate and almost 40 K for the higher estimates at altitudes above 1800 km. At altitudes below 1550 km estimates for the neutral and ion wind speeds used in the model will agree with the ion temperatures published by *Crary et al*. [2009]. Above this altitude, anti-parallel ion winds of 250 m/s bring the modeled ion temperature within the range reported by *Crary et al*. [2009].

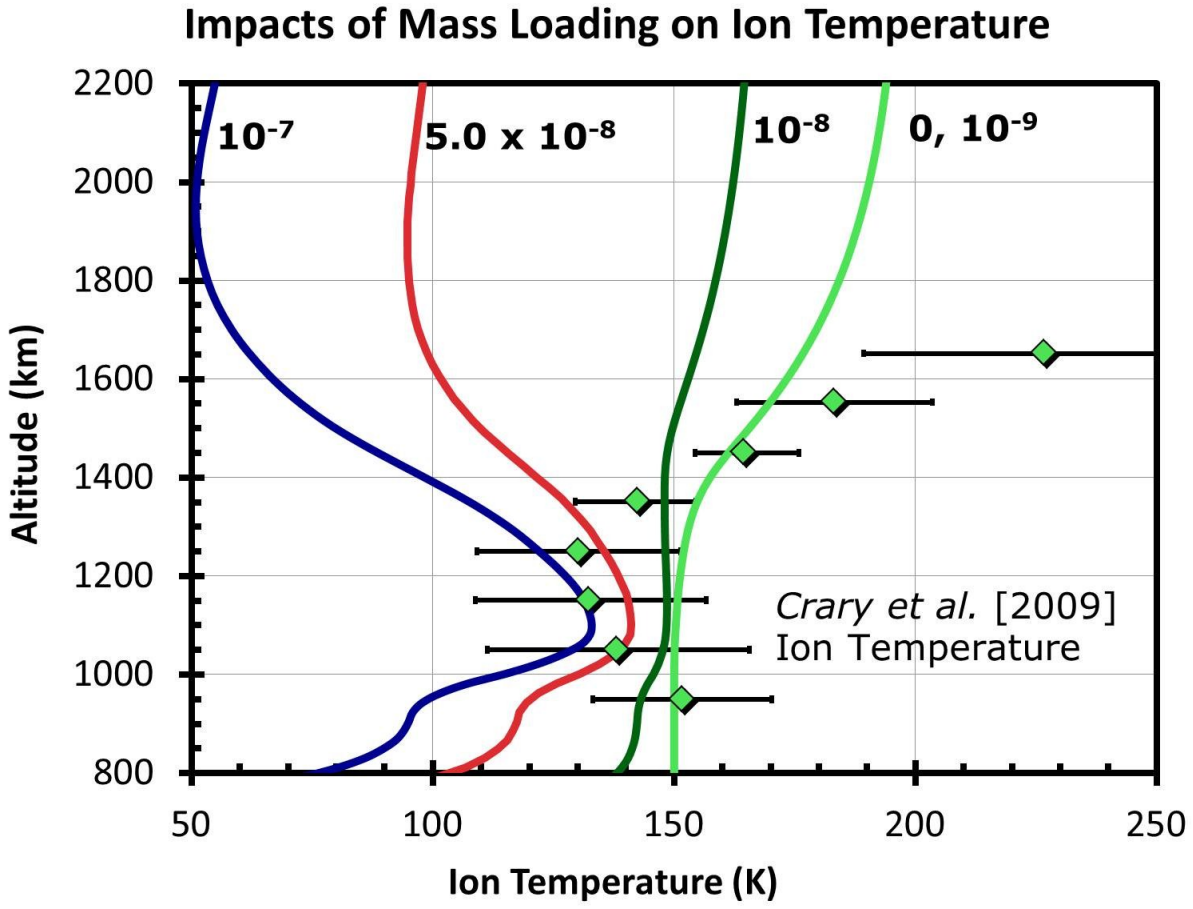

Figure 5.6 Impacts of mass loading on the ion temperature. The source term of the ion species S_s in Equation (3.34) is found by multiplying the production rate factor in s^{-1} by the sum of the molecular nitrogen and methane densities in cm^3. results for a production factor of 0 (light green), 10^{-9} (overlaps with light green) consistent with the production rate published by *Robertson et al.* [2009], 10^{-8} (dark green), $5x10^{-8}$ (red line), and 10^{-7} s^{-1} (blue line) were considered for T18 conditions.

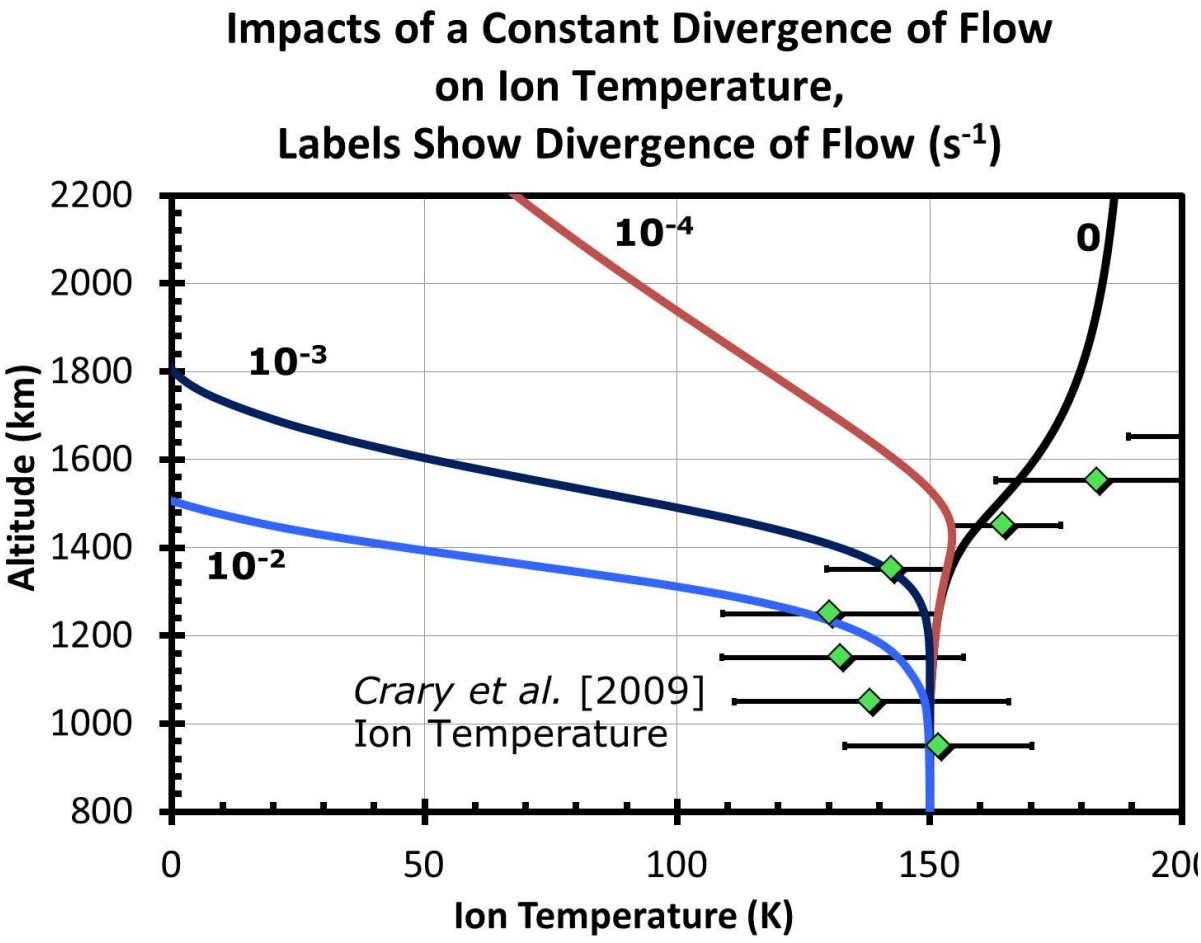

Figure 5.7 Effect of a divergence of the plasma flow velocity on the ion temperature for T18 conditions. Cases are shown for a divergence of plasma flow of 0 (black line), the estimated value of 10^{-4} (red line), 10^{-3} (dark blue) and 10^{-2} (light blue) as well as the ion temperature values of *Crary et al.* [2009] (green diamonds).

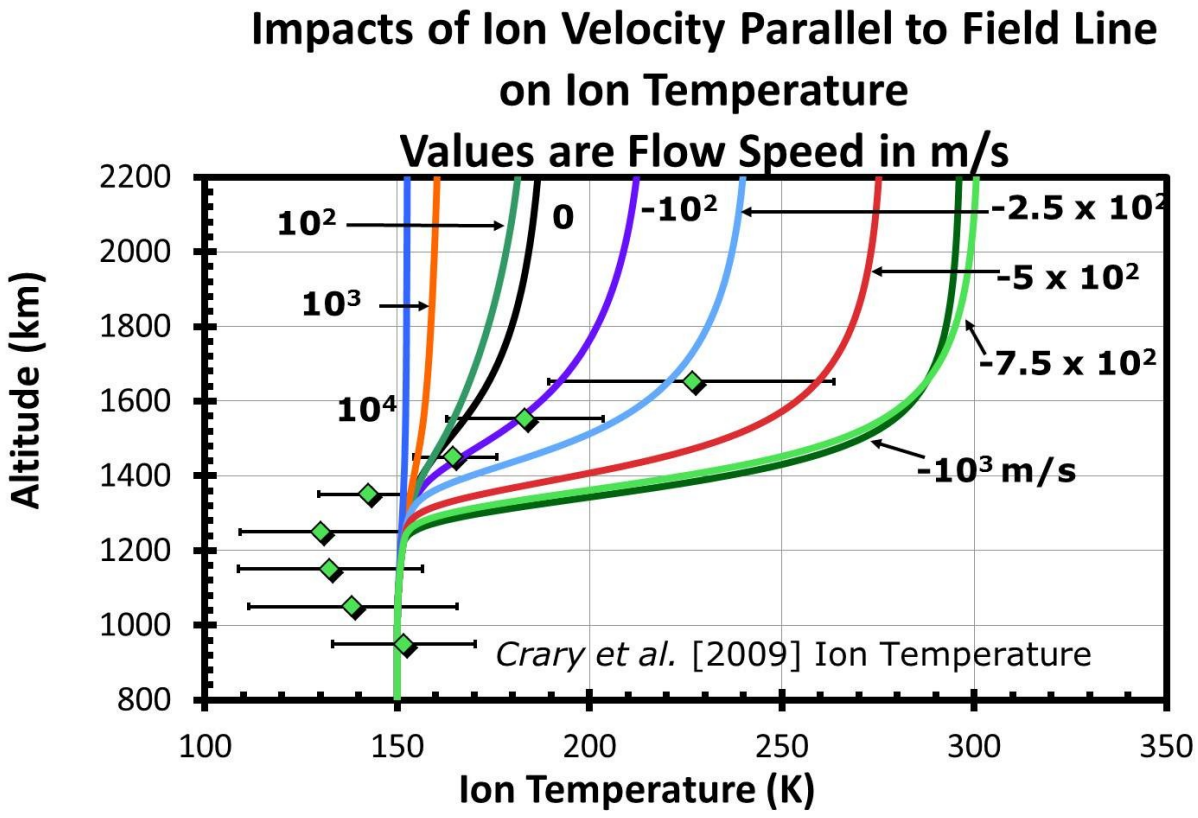

Figure 5.8 ion temperatures for T18 conditions with neutral flow speeds indicated by the number accompanying each curve (in m/s). Positive and negative numbers represent flow velocities parallel and anti-parallel to the magnetic field line (away and toward the apex point respectively). Flow velocities are kept constant along each curve.

The final dynamic term investigated, and the term that has been shown to be capable of producing profound effects on the ion temperature, is Joule heating shown in Figure 5.9. Joule heating occurs from the collisions between two species when ions and neutrals move at different velocities. This extra heating can significantly increase the ion temperature. In Equation (3.34), reprinted here as Equation (5.2),

$$\begin{aligned}&\frac{3}{2}k_B n_s \frac{\partial T_s}{\partial t} + \frac{3}{2}k_b n_s \overrightarrow{u_s} \cdot \nabla T_s + \frac{3}{2}k_B T_s n_s \nabla \cdot \overrightarrow{u_s} \\ &\quad + \frac{3}{2}k_B (T_s - T_n) S_s + \nabla \cdot (-K_s \nabla T_S) \\ &\quad = \sum_m \frac{n_s m_s \nu_{sm}}{m_s + m_m} [3k_B (T_m - T_s) \\ &\quad + m_m (\overrightarrow{u_s} - \overrightarrow{u_m})^2] + Q_s - L_s\end{aligned} \qquad \textbf{(5.2)}$$

Joule heating is represented by the term $\sum_t \frac{n_s m_s \nu_{st}}{m_s + m_t}\left[m_t(\vec{u}_s - \vec{u}_t)^2\right]$. To consider the effects of this term, we introduced into the model a range of ion-neutral relative velocities but kept the relative velocities constant with altitude (which will not be the case in reality). A more realistic variation of this relative velocity with altitude was presented in *Cravens et al.* [2010] who estimated velocities using pressure gradients and ion-neutral collision frequencies based on Cassini data. *Cravens et al.* [2010] adapted vertical and horizontal length scales (100 and 500 km respectively) when computing these estimates. The relative ion-neutral velocity near 1000 km was estimated to be only a few m/s or less, but increased up to a km/s or so by 1400-1500 km. Above 1500 km the estimated flow speeds approached or exceeded the magnetosonic speed and the assumptions used to estimate the velocities broke down. For the case of a relative ion-neutral velocity of 100 m/s the ion temperature increase is not significant ($\Delta T_i \approx 7$ K at an altitude of 2000 km);

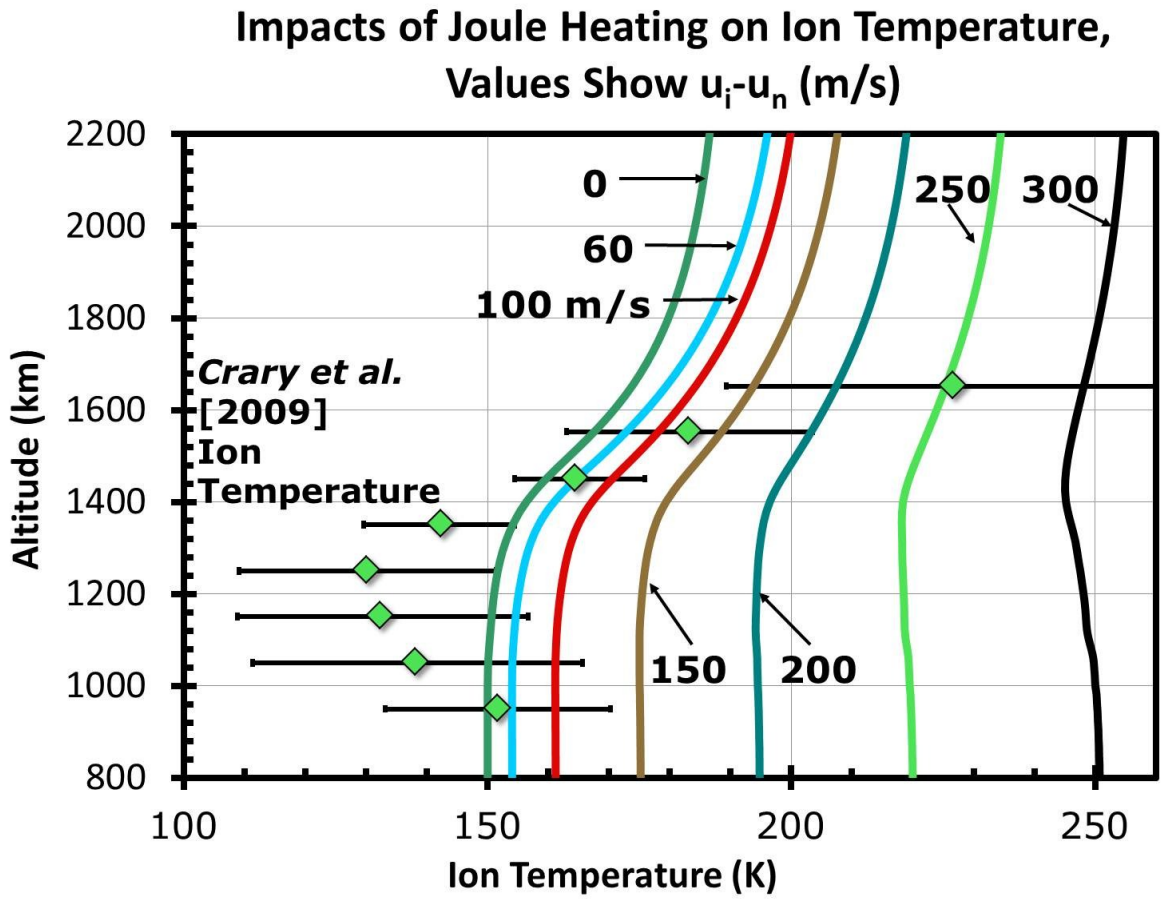

Figure 5.9 The effect of relative ion and neutral velocities (in m/s) on calculated ion temperatures is shown. That is, Joule heating is shown to be an effective heat source for ions for sufficiently high relative ion-neutral drift speeds. The value of u_i-u_n is kept constant for each line, but large values are expected only at higher altitudes.

however, for a relative velocity of 250 m/s, $\Delta T_i \approx 45$ K near 1500 km, which brings the model's ion temperature into reasonable agreement with the measured temperature at that altitude. Joule heating is an important source of ion heating in the upper ionosphere.

Cravens et al. [2010] pointed out that below an altitude of 1300 km the high ion-neutral collision frequency strongly couples the ion and neutral velocities such that the ion velocity tends to be brought near the neutral velocity which reduces Joule heating. In order to more accurately determine ionospheric flow velocities, and all of the dynamical terms in the ion energy equation (Equation (3.34)), global MHD or hybrid models are needed (see discussion in *Cravens et al*., 2009a; *Ma et al*., 2007, 2009].

5.4 Conclusions from Temperature Modeling

Thermal electron and ion temperature profiles from the ionospheric electron and ion temperature model were compared in this paper to ion and electron temperatures measured by Cassini instruments for a dayside (T18) and nightside (T5) case. Previously modeled temperatures were only available for electrons for the Ta encounter [*Galand et al.,* 2006]. The study by *Galand et al*. reported the electron temperature at two positions of the Cassini spacecraft (near 1200 and 1350 km) and did not include any information about the temperatures below 1200 km. The electron temperatures from our model were compared to RPWS-LP data [*Agren et al.,* 2007*,* 2009; *Cravens et al.,* 2009a; *Robertson et al.,* 2009] and ion temperatures were compared to the measured temperatures presented by *Crary et al.* [2009]. We show that the magnetic field line topology is important for the electron energetics due to its effect on heat conduction and transport of suprathermal electrons throughout the ionosphere. This conclusion appears in agreement with pre-Cassini models [*Gan et al.,* 1992, 1993; *Roboz and Nagy,* 1994]

and with Cassini Ta models of *Galand et al.* [2006]. It is also shown that one can create a reasonable model of the electron temperature below 1400 km with only "local" knowledge of the magnetic field line topology. For the day and nightside, our model also shows that the thermal electron temperature is strongly coupled to the neutral temperature below an altitude of 1000 km and that the ion temperature is strongly coupled to the neutral temperature below an altitude of 1400 km.

Analysis of the dayside (T18) case showed that suprathermal electrons (i.e., photoelectrons) produced by absorption of solar radiation are sufficient to heat the thermal electrons for altitudes below 1400 km if the field lines are kept largely horizontal. Our model did this using a "nested" field line approach to limit thermal conductivity between altitudes and simulate local magnetic topology. The nested approach is consistent with *Galand et al.*'s [2006] study of Titan's ionospheric electron temperature, which utilized various magnetic field lines. Above 1400 km magnetospheric electron inputs are needed to provide sufficient heat to the thermal electron population. The T8 magnetospheric suprathermal electron flux, while classified as "lobe-like" magnetospheric conditions similar to T18 [*Rymer et al,* 2009], did not provide sufficient heat for thermal electrons above 1400 km. Using the more robust T5 "plasma sheet" magnetospheric suprathermal electron flux brought the modeled electron temperatures between 1500 and 1600 km into agreement with measured temperatures but overshot measured temperatures between 1150 and 1350 km. However, it seems unlikely that the "lobe-like" magnetospheric suprathermal electron flux will provide sufficient heating to thermal electrons and that alternative heat sources need to be considered in the upper ionosphere.

For the ion temperature on the dayside, dynamical terms associated with the bulk ion plasma flow are potentially important in the upper ionosphere. In particular, Joule heating (i.e.

relative ion-neutral drift) was able to provide a sufficient temperature boost to the ions to bring the model temperature into agreement with measured values reported by *Crary et al.* [2010] for relative ion-neutral speed values in agreement with the empirical estimates made by *Cravens et al.* [2010]. A 3-D global MHD model similar to the type used by *Ma et al*. [2006, 2007, 2009] is able to constrain the values of the bulk flow velocity more accurately at the spacecraft position and in future studies this could improve the analysis of dynamical effects.

In conclusion, the key results of this chapter, as also shown by *Richard et al.* [2011], are:

1. Below approximately 1400 km on the dayside, solar inputs sufficiently explain ionospheric electron temperatures when appropriate magnetic field lines are adopted.
2. Dynamical terms, most notably Joule heating, play an important role at higher altitudes in the energy balance for the ions at Titan.

Chapter 6 **Dayside Chemical Modeling**

The discrepancy between the modeled electron densities and the peak electron densities measured by the RPWS-LP (Figure 4.1) has yet to be resolved. There are two possibilities for this increased density: (1) there is an overproduction of primary ions as was discussed in Chapter 4 or (2) the electron-ion dissociative recombination rate is not adequately removing ions from the ionosphere. The conclusions of Chapter 4 indicate that ion production rates in the model are reasonable and the model is not producing an overabundance of ions based on comparisons between modeled and measured ion densities of CH_3^+ and CH_4^+ and empirically derived production rates of N_2^+ and CH_4^+. This means that the electron dissociative recombination rates in the photochemical model (Section 3.4) must be examined.

The electron dissociative recombination rate can be increased by either lowering the thermal electron temperature using the modeled temperatures from Chapter 5 or by reacting lower mass ions with neutrals resulting in higher mass ions with higher dissociative recombination coefficients (see preliminary discussion on ion-neutral chemistry in Section 3.5). Effective recombination rate coefficients have been estimated by *Galand et al*. [2010], 5.9 x 10^{-6} cm^3s^{-1} at 970 km assuming an electron temperature of 500 K and a temperature dependence factor β of 0.7 (see Equation (3.20)), and *Kliore et al*. [2011], 1 x 10^{-6} cm^3s^{-1}, and have been found to be larger than those found by photochemical models, 2.5 x 10^{-7} cm^3s^{-1} when scaled to an electron temperature of 500 K at 1000 km [*Cravens et al.,* 2005; *Krasnopolsky,* 2009]. In this chapter the ion-neutral chemical pathways will be examined in order to create an updated model of the ion chemistry and the model will be used to evaluate new possible reaction mechanisms and chemical processes that are occurring in Titan's ionosphere.

6.1 Initial Modeling Efforts

To establish a baseline case for chemical modeling efforts a reaction chemistry similar to that of *Robertson et al.* [2009] and *Westlake et al.* [2012] was implemented (see Section 3.5). The density profiles of the major neutral species (N_2, CH_4 and H_2) have been taken directly from measurements made by the INMS instruments and the minor neutral densities are calculated using the mixing ratios calculated by *Magee et al.* [2009] (Section 3.4.2 and Table 3.3) . Chemical reaction rate coefficients of *Anicich and McEwan* [1997], *McEwan and Anicich* [2007], and *Vuitton et al.* [2006,2007] are used as a starting point with updated reaction rate coefficients measured by *Edwards et al.* [2008] and *Zabka et al.*[2009]. Electron dissociative recombination rates measured by *Anicich and McEwan* [1997], *McEwan and Anicich* [2007], and *Vuitton et al.* [2007] have been implemented. The model also includes updated electron dissociative reaction rates measured by McLain and Adams [2007], *McLain et al*. [2004], *Osborne et al.* [2011a, 2011b], and *Vigren et al*. [2009] (see Table 3.5). Full chemical reaction lists appear in tabular form in Appendix C.

For comparison purposes and to maintain consistency with the main case examined in Chapter 4, density profiles for the outbound leg of T40 will be examined at the ionospheric peak (1205 km). The solar zenith angle is set at 21.04˚ and a nested arrangement of magnetic field lines was used to implement an appropriate magnetic field line topology (see Section 3.1). Fifty percent of the solar photons with wavelengths between 800 and 1000 Å interact with molecular nitrogen using the photoabsorption cross sections of *Gallagher et al.* [1988] as was found to be the favored case for the outbound leg of T40 (Section 4.1).

Figure 6.1 shows the mass spectrum of ions with a mass to charge ratio between 1 and 100 Daltons for the outbound leg of the T40 flyby of Titan at the ionospheric peak at 1205 km. The red line indicates the measurements made by the INMS instrument at this altitude. Using the ion chemical model described above (shown by the black crosses in Figure 6.1), we can observe that the modeled production rates for the primary production of N_2^+ and CH_4^+ are being reproduced reasonably well given the agreement between the model and the measured ion density at m=14, 15, and 16 representing CH_2^+, CH_3^+, the main product of N_2^+ reactions with methane and CH_4^+ respectively (see discussion in Section 4.1). Although the CH_4^+ density is almost a factor of two too large, this is an artifact of the overabundance of CH_5^+ which reacts with methane to produce CH_4^+.

There are several ion species where the modeled densities are substantially larger than the measured densities, most notably at m=17 (CH_5^+), 18 (NH_4^+), 19 (H_3O^+), 28 ($HCNH^+$), and 29 ($C_2H_5^+$). The overabundance of CH_5^+, $HCNH^+$, and $C_2H_5^+$ represents a known problem in chemical modeling (c.f. *Robertson et al.* [2009] and *Westlake et al.* [2012]). This is due to the fact that these species are among the most abundant in the ionosphere of Titan and are chemically linked (see Section 3.5.2.3) by the reactions given in Table 6.1, meaning that an overproduction of one will cause discrepancies in the other two. This will be discussed in the following sections of this chapter.

Table 6.1 Chemical links between CH_5^+, $HCNH^+$, and $C_2H_5^+$

Chemical Reaction	Reaction Rate Coefficient [cm^3s^{-1}]
$CH_5^+ + HCN \rightarrow HCNH^+$	$2.70\ x\ 10^{-9}$
$CH_5^+ + C_2H_4 \rightarrow C_2H_5^+$	$1.00\ x\ 10^{-9}$
$C_2H_5^+ + HCN \rightarrow HCNH^+$	$5.00\ x\ 10^{-9}$

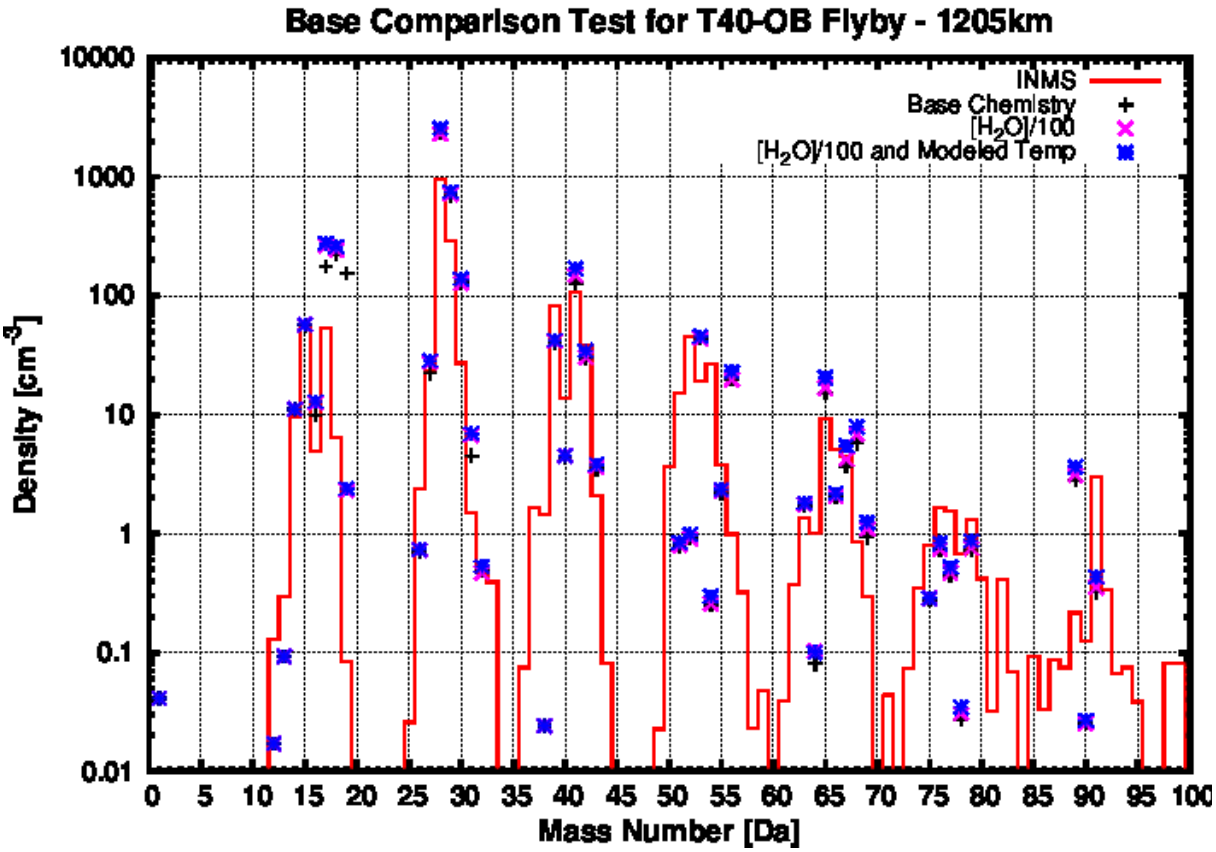

Figure 6.1 Ion density profile for the outbound leg of the T40 flyby of titan at 1205 km. Ion masses are given in Daltons. The red line indicates densities measured by the INMS instrument. Black crosses mark the densities obtained using the ion chemistry described in Section 3.5. The H_2O density has been decreased by a factor of 100 in order to bring the density of mass 19 down and the impacts of this change are shown when electron temperatures measured by RPWS/LP (pink 'X') and the modeled temperature (blue star) are used.

It should also be noted that there is an underproduction of ions between masses 48 and 60 Da. This fact is part of the reason *Westlake et al.* [2012] speculated on the existence of missing reactions between hydrocarbons containing two carbon atoms and $HCNH^+$ which would produce ions in this mass regime. This will be discussed in Section 6.3.

H_3O^+ is the product of chemical reactions involving ions and neutral H_2O in the upper atmosphere of Titan. The mixing ratio of H_2O in the ionosphere of Titan was inferred by *Cui et al.* [2009b] and found to be 2.79×10^{-6} and was not stated by *Magee et al.* [2009]. Since the only major impact that the H_2O density has on the ionospheric ion density profile is apparent in the H_3O^+ density, this mixing ratio was lowered by a factor of 100 bringing the H_3O^+ density within a factor of 10 of the measured value without significantly affecting the other ion species (see the pink X's in Figure 6.1). The remaining discrepancy will be resolved through chemical modeling.

It was also mentioned that modeled electron temperatures (see Chapter 5) are strongly coupled to the neutral temperature of 150 K below 1000 km due to the large amount of thermal coupling between neutrals and electrons at lower altitudes (Figure 6.2). In order to evaluate the impact that modeled temperatures have on the modeled ion densities the modeled electron temperature for the T40-Flyby of Titan was used in the photochemical model. As Figure 6.1 shows, using the modeled electron temperature profile (blue stars) did not significantly change the ion densities at the peak as the electron temperature measured by RPWS differs from the model by less than 10% at the ionospheric peak of outbound leg of the T40 flyby (Figure 6.2).

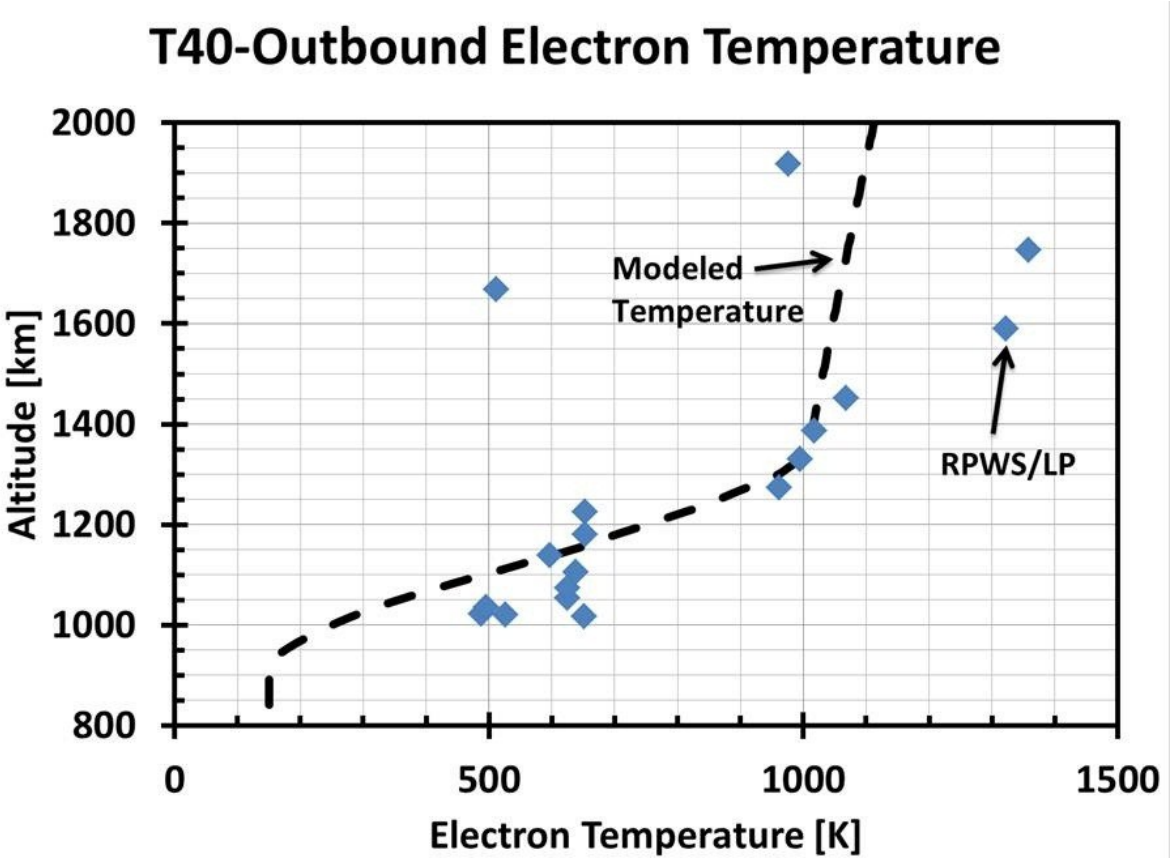

Figure 6.2 Electron temperature during the outbound leg of the T40 flyby of Titan measured by RPWS/LP (blue diamonds) and modeled using the energy equation (dashed line) and the neutral atmosphere shown in Figure 3.37.

6.2 HCN Density Modifications

The primary loss channel of both CH_5^+ and $C_2H_5^+$ is through chemical reactions with HCN to form $HCNH^+$ (Table 6.1). Thus the overabundance in the ion densities of mass 17 and 29 can be resolved by increasing the mixing ratio of HCN in the upper atmosphere which will increase the amount of CH_5^+ and $C_2H_5^+$ that are reacting to produce $HCNH^+$. This solution of increasing the HCN neutral density has been proposed by *Westlake et al.* [2009] in accordance with uncertainties in the HCN mixing ratio of *Magee et al.* [2009].

Figure 6.3 shows the effects of increasing the HCN density on the ion density spectrum at the ionospheric peak of the outbound leg of the T40 flyby. For comparison purposes the chemistry described in Section 6.1 with the H_2O densities reduced by a factor of 100 and using the modeled electron temperatures is used as a baseline (blue stars on Figure 6.3). Increasing the HCN density by a factor of 3 (green open boxes) as was done by *Westlake et al.* [2012] and a factor of 10 (filled grey boxes) both lowered the discrepancy in CH_5^+ and $C_2H_5^+$ at the cost of increasing the disparity in the $HCNH^+$ density. Using a factor of three increase to the HCN density brought the modeled density of CH_5^+ to within a factor of 4 or measured values and the modeled $C_2H_5^+$ density to within a factor of 1.5; however, the modeled $HCNH^+$ density increased by a factor of 1.5. Increasing the density of HCN by a factor of 10 brought the modeled CH_5^+ density to within a factor of 2 higher than measured values and the $C_2H_5^+$ was lower than the measured valued by a factor of 2 at the cost of increasing the modeled $HCNH^+$ density to 4 times the baseline value. As the density of $HCNH^+$ is two orders of magnitude larger than the CH_5^+ density and approximately twice the density of $C_2H_5^+$, the extra loss of CH_5^+ and $C_2H_5^+$ provided by using a factor of 10 instead of a factor of 3 increase to the HCN density actually increased the overall electron density and the discrepancy between measured and modeled electron densities

(Figure 4.1). Increasing the HCN density by a factor of three proved to provide the best balance between shifting CH_5^+ and $C_2H_5^+$ to $HCNH^+$ and keeping the electron density at a reasonable level. For these reasons, increasing the HCN density by a factor of 3, effectively increasing the mixing ratio from 2.44×10^{-4} [*Magee et al.*, 2009] to 7.320×10^{-4}, is the favored modification to the neutral density profile.

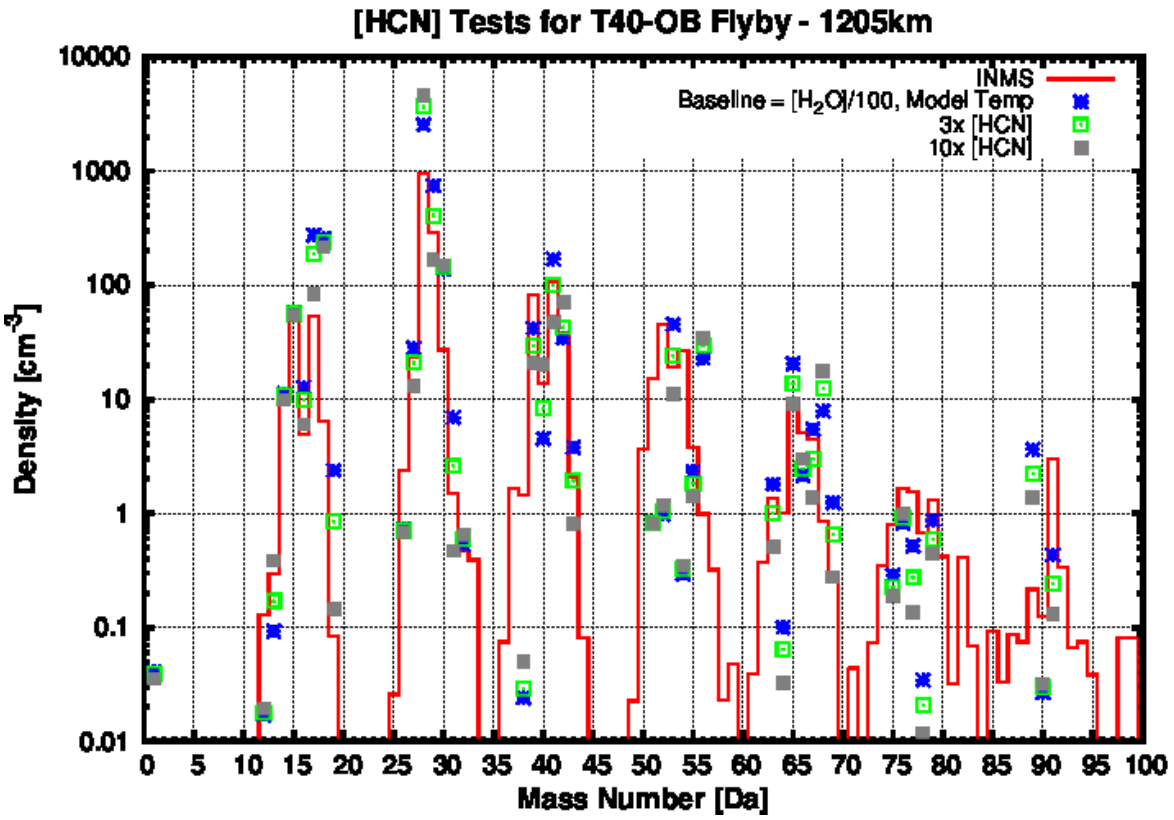

Figure 6.3 Ion density profile for the outbound leg of the T40 flyby of titan at 1205 km. Ion masses are given in Daltons. The red line indicates densities measured by the INMS instrument. A reference point is established using the baseline chemisty described in Section 6.1 using modeled electron temperatures and H_2O reduced by a factor of 100 (blue stars). Cases where the HCN density has been increased by a factor of 3 (green open boxes) and 10 (grey filled boxes) are also shown. Increasing the HCN density by a factor of 3 was found to be the favored case.

6.3 Additional Reactions with C2-Group Neutrals

Increasing the HCN density in the atmosphere had the impact of lowering the CH_5^+ and $C_2H_5^+$ densities and increasing the HCNH+ density. *Westlake et al.* [2012] attempted to remedy this by adding reactions between $HCNH^+$ and the neutrals C_2H_2 and C_2H_4 (Table 6.2). This was justified by their observation of correlations between ions with masses separated by 24 or 26 amu corresponding to chemical reactions resulting in the addition of two carbon atoms or two carbon atoms and two hydrogen atoms to an ion. *Westlake et al.* proposed a modest reaction rate coefficient of $5x10^{-11}$ as such a reaction rate coefficient was two orders of magnitude lower than typical reaction rate coefficients and there is no experimental evidence that such a process exists due to a lack of research on the reaction. These reactions would also help in the current model as the reactions would produce ions with masses 52 ($C_3H_2N^+$) and 54 ($C_2H_3CNH^+$) amu at which the previous model runs produced densities that were factors of 50 and 100 too low.

Table 6.2 Reactions proposed by *Westlake et al.* [2012]

Chemical Reaction	Reaction Rate Coefficient [cm^3s^{-1}]
$HCNH^+ + C_2H_2 \rightarrow C_3H_2N^+$	$5.00\ x\ 10^{-11}$
$HCNH^+ + C_2H_4 \rightarrow C_2H_3CNH^+$	$5.00\ x\ 10^{-11}$

Figure 6.4 shows the results of adding these reactions on the ion density profile for the ionospheric peak of the T40 outbound leg. The best case of the chemical model is shown as a reference point with green open boxes (chemistry from Section 6.1 using modeled temperatures, H_2O density reduced by a factor of 100, and HCN increased by a factor of 3). When the additional reactions from Table 6.2 are added the resulting ion spectrum (blue circles in Figure 6.4) shows a slightly decreased $HCNH^+$ density (m=28 Da) and the peaks at mass 52 and 54 Da

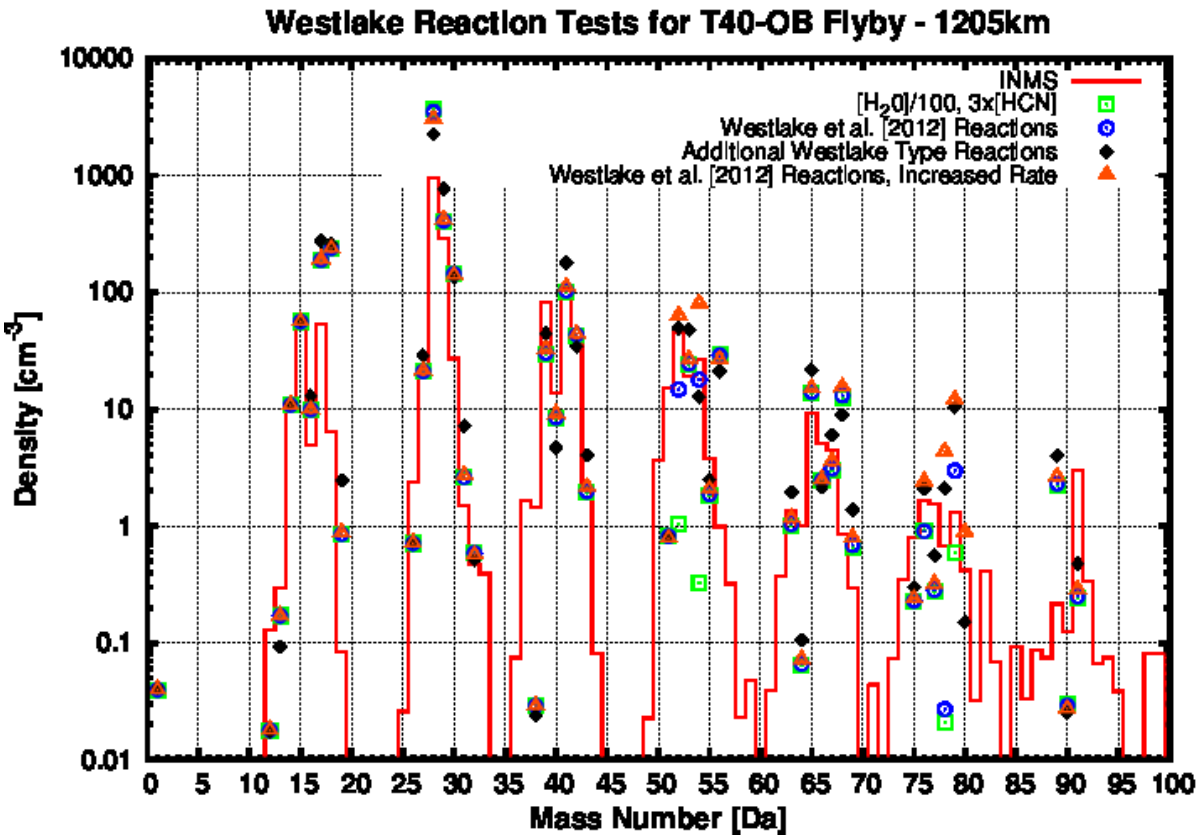

Figure 6.4 Ion density profile for the outbound leg of the T40 flyby of titan at 1205 km. Ion masses are given in Daltons. The red line indicates densities measured by the INMS instrument. A reference point is established using the baseline chemistry described in Section 6.1 using modeled electron temperatures and H_2O reduced by a factor of 100 and HCN increased by a factor of 3 (green open boxes). The reactions discussed by *Westlake et al.* [2012] (Table 6.2) have been implemented (blue circles) and compared with results when the reaction rate is multiplied by a factor of 5 (orange triangles). Black diamonds represent the case where the original *Westlake et al.* (Table 6.2) reaction rates are used along with additional reactions of the same type (Table 6.3).

are within a factor of 5 and 1.5 respectively, thus showing better agreement between modeled and measured ion densities in the middle mass regime. In an attempt to determine if the reaction rate coefficients proposed by *Westlake et al.* were sufficient, a case where the reaction rates were multiplied by 5, resulting in a reaction rate coefficient of 2.5×10^{-10} was implemented (orange triangles in Figure 6.3). This resulted in an overproduction of heavier ions with masses above 48 Da at several points in the spectrum showing a preference for the reaction rate coefficients of *Westlake et al.*

Westlake et al. [2012] mentioned the correlation of ion densities that were separated by what appeared to be reactions with C2-group hydrocarbons. The best case modeled ion density spectrum from Section 6.2 showed that the modeled densities for masses 76 (HC_5NH^+), 78 ($C_5H_4N^+$), and 80 ($C_5H_6N^+$) were lower than the INMS measurements by factors of 2, 10 and 50 respectively. In light of this under abundance, reactions following the scheme of *Westlake et al.* were added (Table 6.3) which react the products of *Westlake et al.*'s reactions with C_2H_2 and C_2H_4 with a reaction rate coefficient of 5.00×10^{-11} in order to form ions with masses where the ion density spectrum is deficient. Adding these reactions resulted in modeled ion densities at masses 76, 78 and 80 Da that were 1.25 times higher, 2 times higher and 3 times lower than INMS measured densities (black diamonds in Figure 6.4) while also lowering the $HCNH^+$ density by a factor of 2 with respect to the model run without these reactions bringing it to within a factor of 2 of the measured ion density at mass 28 Da. For this reason the case utilizing the *Westlake et al.* (Table 6.2) and similar reactions (Table 6.3) was found to be the favored case.

Table 6.3 Additional *Westlake et al.* type reactions

Chemical Reaction	Reaction Rate Coefficient [cm^3s^{-1}]
$C_3H_2N^+ + C_2H_2 \rightarrow HC_5NH^+$	$5.00\ x\ 10^{-11}$
$C_3H_2N^+ + C_2H_4 \rightarrow C_5H_4N^+$	$5.00\ x\ 10^{-11}$
$C_2H_3CNH^+ + C_2H_2 \rightarrow C_5H_4N^+$	$5.00\ x\ 10^{-11}$
$C_2H_3CNH^+ + C_2H_2 \rightarrow C_5H_6N^+$	$5.00\ x\ 10^{-11}$

6.4 C_2H_2 and C_2H_4 Density Modifications

In light of the reactions proposed by *Westlake et al.* [2012] where C_2H_2 and C_2H_4 react with $HCNH^+$, *Westlake et al.* also increased the density of C_2H_2 and C_2H_4 by a factor of 3 each (green triangles in Figure 6.5). This results in stronger loss processes of $HCNH^+$ which will pull ions out of the reaction triangle between $HCNH^+$, CH_5^+ and $C_2H_5^+$ (Table 6.1). When the densities of C_2H_2 and C_2H_4 were increased, the density of CH_5^+ goes from being a factor of 3 larger than the measured ion density from the best case in Section 6.3 (black diamonds in Figure 6.5) to within 15% of the measured value (Figure 6.5). The density of $C_2H_5^+$ decreases from being a factor of 3 too large to being a factor of 2 lower than the measured values. Increasing the density also increases the density of $HCNH^+$ by a factor of 2 making it 4 times larger than the measured value due to the reaction of C_2H_4 and N_2^+ which forms $HCNH^+$. An increase in the modeled densities of most ions with masses above 48 Da and a lowering of most ion densities with masses below 48 amu is also observed with the increase in C_2H_2 and C_2H_4.

In spite of these changes, the benefits of increasing the density of C_2H_2 and C_2H_4 by a factor of 3 on the resulting ion mass spectra outweigh the negative impacts on the $HCNH^+$ density. This addition lowers the ion densities of the lower mass ions, which have higher ion

densities than the heavier ion species, resulting in a general lowering of the electron densities. The increase in the modeled density of $HCNH^+$ can hopefully be resolved by additional studies of the loss processes of the ion. These processes have not been well studied in the lab so there may be additional loss processes that are missing in the current chemical reaction models as discussed in *Westlake et al.* [2012].

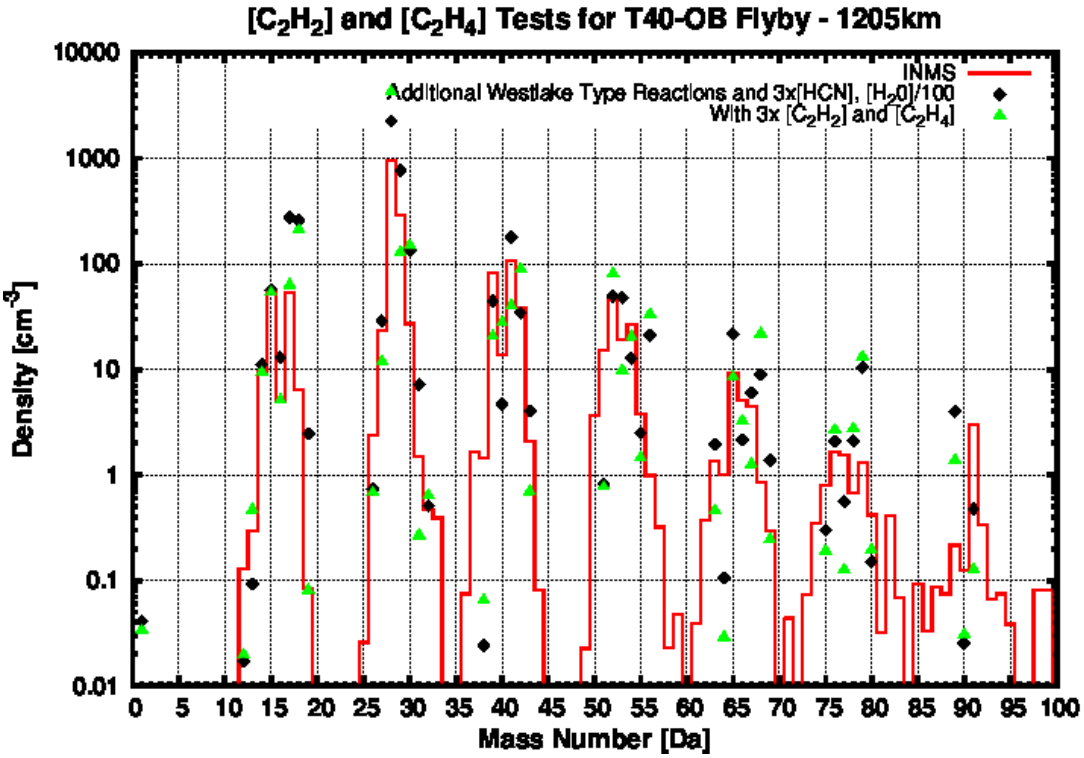

Figure 6.5 Ion density profile for the outbound leg of the T40 flyby of titan at 1205 km. Ion masses are given in Daltons. The red line indicates densities measured by the INMS instrument. Black diamonds represent the best case from Section 6.3 (base chemistry from Section 6.1, tripled HCN density, H_2O density divided by 100, and all *Westlake et al.* type reactions (Table 6.2 and Table 6.3)). The results obtained when the C_2H_2 and C_2H_4 densities are tripled are indicated with green diamonds.

6.5 NH_3 Density Tests

In Section 6.1 it was mentioned that the modeled ion density at a mass of 18 Da, representing NH_4^+, is a factor of 50 larger than the measured ion densities at the ionospheric peak of the outbound leg of the T40 flyby. The modifications to the neutral atmosphere and ionospheric chemistry discussed in the previous sections have not made an impact on the ion density of NH_4^+.

In order to decrease the ion density of NH_4^+ which is primarily (<50%) produced though reactions between NH_3 and $HCNH^+$ the density of NH_3, originally inferred by *Cui et al.* [2009b], has been reduced by a factor of 10 (black pentagons in Figure 6.6). When compared to the best case from Section 6.4 (green triangles in Figure 6.6), this resulted in lowering the modeled NH_4^+ density from 50 times larger than the measured values to within a factor of 10. Although this lowered the modeled NH_4^+ density, it raised the $HCNH^+$ density by 10%. This is because the reactions with NH_3 account for between 10 and 20% of the loss of $HCNH^+$. For this reason the reduction to the NH_3 density was set at a factor of 10 in order to balance the reduction of the NH_4^+ modeled density with the gain in the modeled density of $HCNH^+$, representing the new favored case.

6.6 $HCNH^+$ Dissociative Electron Recombination Rate

Ultimately, electrons are removed from the ionosphere through dissociative recombination reactions with ions. The dissociative recombination rates of heavier ions is typically larger than that of lower mass ions and thus lower mass ions are removed primarily though chemical loss process while heavier mass ions are removed via electron dissociative recombination (see discussion in Section 3.5.1).

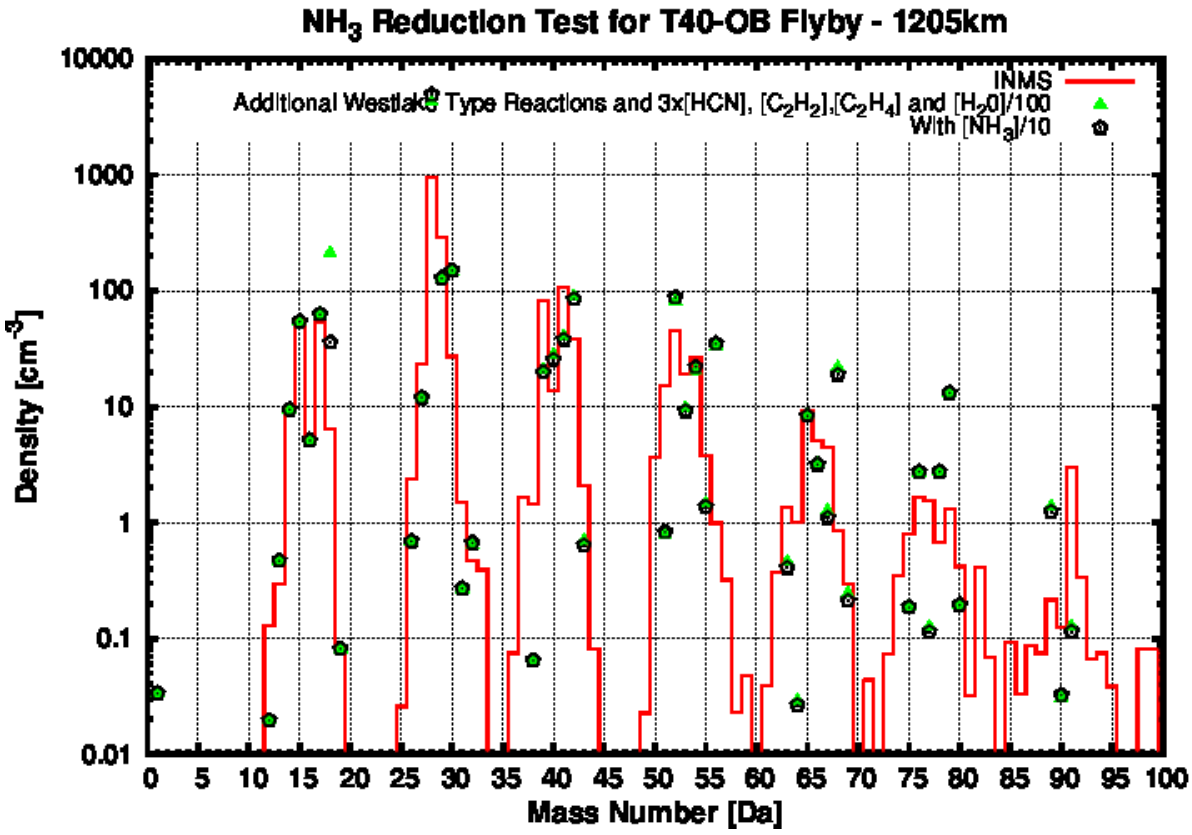

Figure 6.6 Ion density profile for the outbound leg of the T40 flyby of titan at 1205 km. Ion masses are given in Daltons. The red line indicates densities measured by the INMS instrument. Green triangles represent the best case from Section 6.4 (base chemistry from Section 6.1, tripled HCN, C_2H_2 and C_2H_4 density, H_2O density divided by 100, and all *Westlake et al.* type reactions (Table 6.2 and Table 6.3)). The black pentagons mark the modeled ion densities when the NH_3 density is lowered by a factor of 10.

Electron dissociative recombination accounts for between 60 and 90% of the loss of $HCNH^+$ which is the most abundant ion in the ionosphere of Titan. As was mentioned in Section 6.3, the chemical loss processes of $HCNH^+$ have not been well researched [c.f. *Westlake et al.*, 2012] and so in this section an approach to estimating the required electron recombination rate will be examined. This follows logically as the majority of the loss process for $HCNH^+$ is a product of this dissociative recombination reaction.

Figure 6.7 examines what dissociative recombination coefficient is needed to bring the $HCNH^+$ density produced in the original chemical model described in section 6.1 into agreement with the INMS measured density of the ion. The original chemical model is indicated with black crosses. Cases where the dissociative electron recombination rate of $HCNH^+$ of 3.5 x 10^{-7} cm^3s^{-1} [*McLain and Adams,* 2007] (Table 3.5) has been increased by a factor of 2 and 5 are marked with green diamonds and inverted blue triangles respectively. This brings the electron dissociative recombination coefficient at 300 K to 1.75 x 10^{-6}, a factor of 6.25 larger than the value of 2.8 x 10^{-7} [*Semaniak et al.,* 2001] used by *Galand et al.* Although increasing the electron dissociative recombination coefficient by a factor of 5 will bring the modeled $HCNH^+$ density within 10% of the measured value, there are no corrections to the modeled ion densities of CH_5^+, $C_2H_5^+$, NH_4^+, H_3O^+, and ions with masses between 48 and 60 Da. This indicates that chemical reactions involving $HCNH^+$, CH_5^+ and $C_2H_5^+$ cannot be neglected and reaction pathways need to be investigated to properly model the ion densities in Titan's ionosphere.

The electron dissociative recombination rate of $HCNH^+$ for the case involving the favored chemical model (base chemistry from Section 6.1, tripled HCN, C_2H_2 and C_2H_4 density, H_2O density divided by 100, NH_3 reduced by a factor of 10, and all *Westlake et al.* type reactions (Table 6.2 and Table 6.3)) is examined in Figure 6.8. This figure demonstrates that if all of the

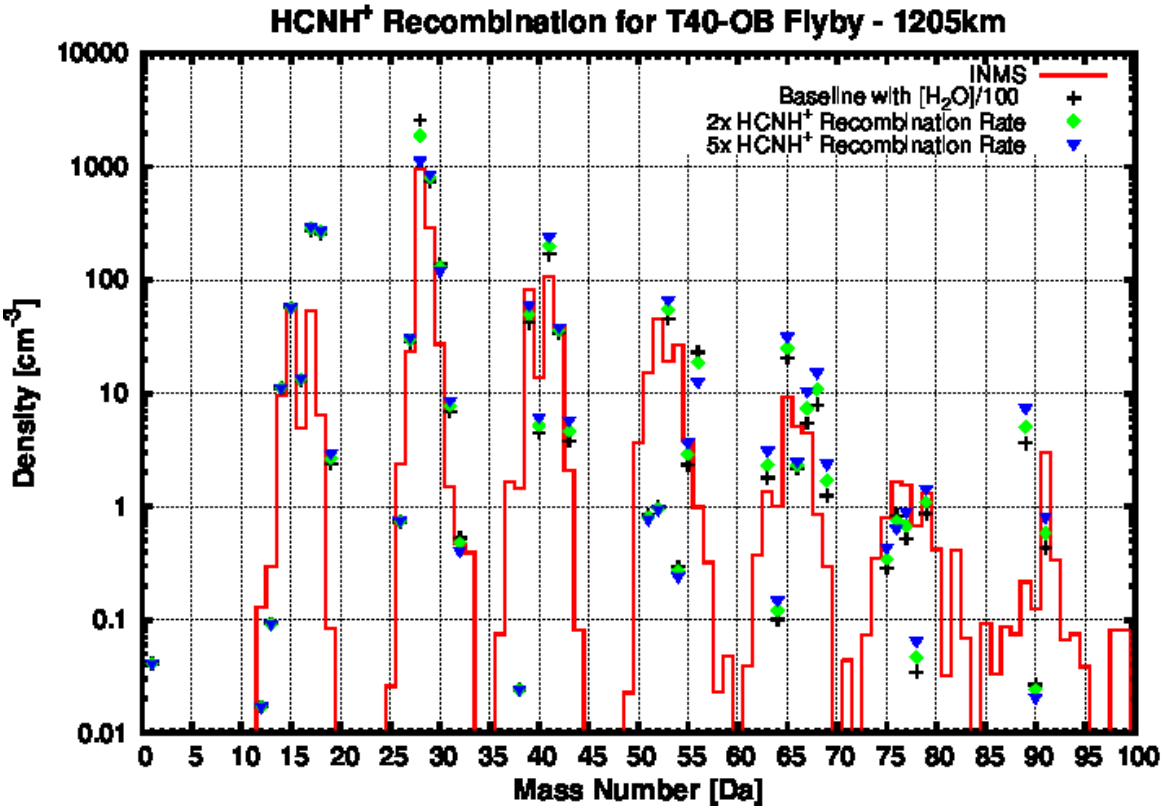

Figure 6.7 Ion density profile for the outbound leg of the T40 flyby of titan at 1205 km. Ion masses are given in Daltons. The red line indicates densities measured by the INMS instrument. The model implementing the basic ion chemistry discussed in section 6.1 is indicated with black crosses. Green diamonds and inverted blue triangles show the impacts of increasing the $HCNH^+$ electron dissociative recombination rate by a factor of 2 and 5 respectively.

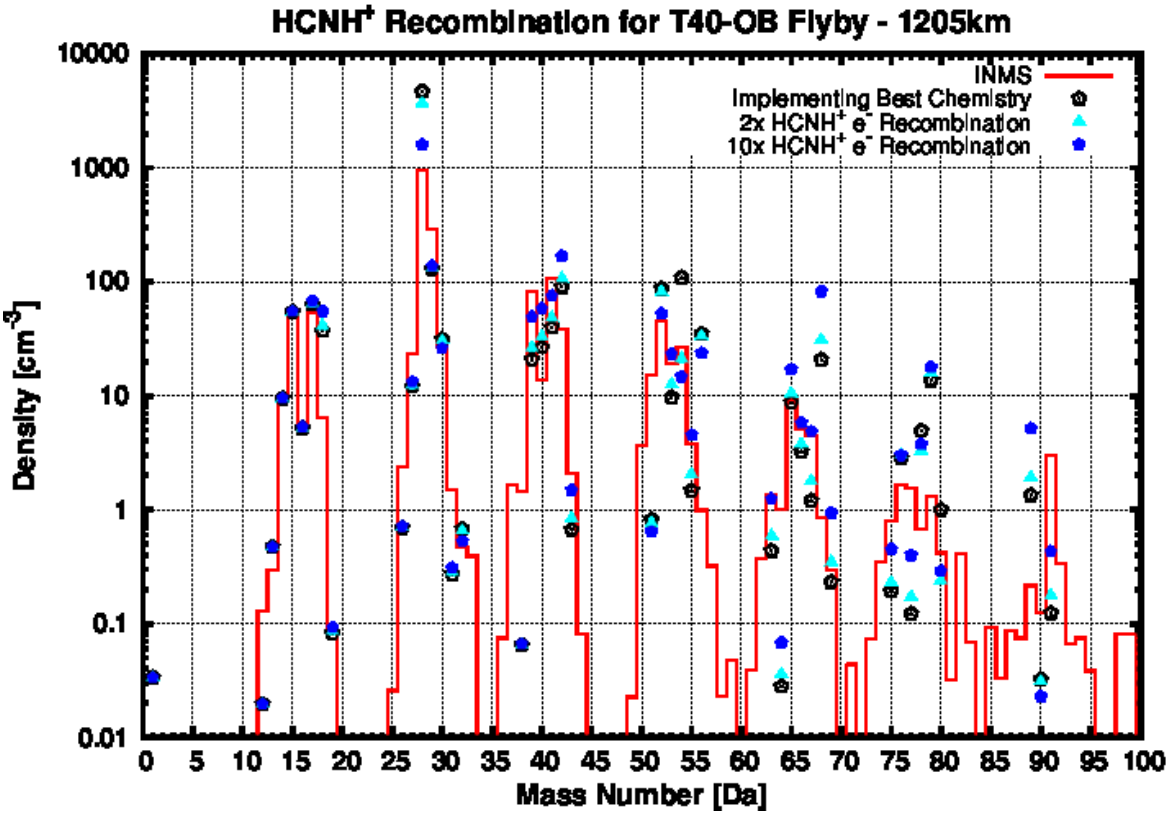

Figure 6.8 Ion density profile for the outbound leg of the T40 flyby of titan at 1205 km. Ion masses are given in Daltons. The red line indicates densities measured by the INMS instrument. The model run using the favored chemistry of the model (base chemistry from Section 6.1, tripled HCN, C_2H_2 and C_2H_4 density, H_2O density divided by 100, NH_3 reduced by a factor of 10, and all *Westlake et al.* type reactions discussed in Table 6.2 and Table 6.3) is shown with the black pentagon. Runs where the electron dissociative recombination rate of HCNH+ has been increased by a factor of 2 and a factor of 10 are indicated with the teal filled triangle and the filled blue pentagon respectively.

chemical reaction and neutral density modifications discussed in this section are enacted, then the electron dissociative recombination rate must be increased by at least a factor of 10 in order to bring the modeled $HCNH^+$ ion density to within 10% of the value measured by the INMS instrument. Although this model requires a larger electron dissociative recombination coefficient of $HCNH^+$, the resulting modeled ion density spectrum agrees with the data much more than the initial modeling effort. Modeled ion densities for several key ion species (CH_5^+, $C_2H_5^+$, heavier ions at mass 52, 54, 76, and 80 Da) are within a factor of 2 of the measured ion densities.

There are a couple noticeable exceptions to this improved agreement. The density of NH_4^+ is still a factor of 10 too large, but this can be resolved by further adjusting the mixing ratio of NH_3. The modeled densities of $C_7H_5^+$ (m=89 Da), the combination of $C_5H_5N^+$ and $C_6H_7^+$ (m=79 Da) and $C_4H_5NH^+$ (m=68 Da) are higher than the measured ion densities by factors of 50, 10, and 100 respectively while the modeled densities of the combination of C_3HN^+ and $C_4H_3^+$ (m=51 Da), the combination of $C_3H_2^+$ and CNC^+ (m=38 Da) and $C_5H_4^+$ (m=64 Da) are lower than the measured ion densities by a factor of 15. This demonstrates that more research into the chemical reaction pathways between lower and higher mass hydrocarbons and nitrile species needs to be done to accurately model the chemical composition of Titan's ionosphere.

6.7 Conclusions

Modeling the chemical processes in the ionosphere has proven to be a challenging endeavor [c.f. *Robertson et al*., 2009; *Cui et al*., 2009b; *Westlake et al*., 2012]. In an attempt to bring the modeled electron densities into agreement with the electron densities measured by RPWS/LP and recreate the ion density profile observed by the INMS instrument, several chemical models were implemented with the goal of accurately reproducing the observed ion

density spectrum. In this chapter the ionospheric peak (1205 km) of the outbound leg of the T40 flyby of Titan was studied as this was the primary case examined in Chapter 4 and in the work of *Westlake et al.* [2012]. For this modeling endeavor only half of the solar photons with wavelengths between 800 and 1000 Å interacted with molecular nitrogen via the photoabsorption cross sections of *Gallagher et al.* [1988]. The work described in Chapter 4 concluded that this was the favored case for the outbound leg of the T40 flyby and would accurately represent the high resolution photoabsorption cross sections of molecular nitrogen published by *Liang et al.* [2007].

The basic chemical reaction scheme came from the reaction lists compiled by *Anicich and McEwan* [1997], *McEwan and Anicich* [2007], and *Vuitton et al.* [2006,2007] with updated reaction rate coefficients observed by *Edwards et al.* [2008] and *Zabka et al.*[2009]. The density of H_2O was lowered by a factor of 100 from the value of *Cui et al.* [2009b] in order to bring the modeled ion density of mass 19 (H_3O^+) into agreement with the INMS observed values. Next the density of HCN was increased to allow the reaction pathways between CH_5^+, $C_2H_5^+$ and $HCNH^+$ (Table 6.1) to shift the excess ion density into the m=28 Da peak.

Westlake et al. [2012] proposed chemical pathways comprised of reactions between $HCNH^+$ and C_2H_2 and $HCNH^+$ and C_2H_4 with a reaction rate coefficient of 5.00×10^{-11} cm^3s^{-1} (Table 6.2). These were implemented based upon the correlation between the densities of ion species with mass differences of 24 and 26 Da [*Westlake et al.,* 2012]. These reactions proved helpful in moving the ions from $HCNH^+$, which had a previously modeled ion density a factor of 4 larger than the value measured by the INMS instrument, to within a factor of 2. In order to settle the discrepancy between the measured ion spectrum and the modeled ion densities at masses of 52 and 54 Da, additional *Westlake et al.* type reactions were hypothesized and

implemented into the model (Table 6.3). In light of the additional reactions, *Westlake et al.* proposed a three-fold increase in the neutral densities of C_2H_2 and C_2H_4 of *Magee et al.* [2009] in order to increase the rate of loss of $HCNH^+$. This change was then adopted in this model which brought the CH_5^+ model density into agreement with the measured values and brought the modeled $C_2H_5^+$ density to a value within a factor of 1.5 below the density observed by INMS. The final modification was a decrease in the ion density of *Cui et al*. [2009b] for NH_3 of 100. Although the modeled ion density of NH_4^+ is still a factor of 10 larger than the measured value, reactions with NH_3 account for 10-20% of the loss of $HCNH^+$ and thus reducing the NH_3 density further will result in a substantial increase in the $HCNH^+$ density that will need to be resolved in another manner. Combining these modifications represents the favored case of the ion chemistry as shown in Figure 6.6.

The only way to completely remove electrons from the ionosphere is through dissociative electron recombination (3.5.1). This is also the main loss process for $HCNH^+$ in the ionosphere of Titan, accounting for upwards of 65% of the $HCNH^+$ loss. It was found in Section 6.6, that if the basic chemical model discussed in Section 6.1 was used, then the dissociative electron recombination rate of $HCNH^+$ would have to be increased by a factor of 5 in order to bring the modeled $HCNH^+$ density into agreement with the ions densities measured by INMS (Figure 6.7). Although this is a modest correction, it did little for the modeled densities of the other ion species and there was still a large discrepancy in the densities of CH_5^+ and $C_2H_5^+$ as well as densities for ions with masses between 48 and 60 Da.

When the favored chemistry case was used (see Section 6.5) the $HCNH^+$ electron dissociative recombination rate needed to be increased by a factor of 10, bringing the electron dissociative recombination coefficient to 3.5×10^{-6} cm^3s^{-1}, for agreement between the measured

and modeled ion densities of $HCNH^+$ (Figure 6.8). This value for the electron dissociative recombination coefficient falls between the values of the total electron dissociative recombination coefficient estimated by *Galand et al*. [2010] for an electron temperature of 500 K at 970 and 1200 km in altitude, 5.9 x 10^{-6} and 6.9 x 10^{-7} cm^3s^{-1} respectively. These chemical changes bring the modeled ion densities for the majority of the ion species to within a factor of 2 of the INMS measured ion densities greatly improving the agreement between the model and the data.

Even though the chemical loss processes of the type proposed by *Westlake et al.* [2012] are shifting ion densities to higher masses where they can recombine with electrons more readily and help reproduce the mid- and upper-mass ion density spectra, they cannot solve the disagreement between the modeled and RPWS measured electron density or the modeled and INMS measured $HCNH^+$ density. As $HCNH^+$ is the most abundant ion in Titan's ionosphere the disparity in the electron density is symptomatic of the $HCNH^+$ density modeling problem. In order to effectively resolve both of these conflicts research must be conducted into reaction pathways for $HCNH^+$ and the dissociative electron recombination of this ion.

In summary, the following key conclusions can be made from this chapter:

1. Using the chemical reaction pathways of *Anicich and McEwan* [1997], *McEwan and Anicich* [2007], and *Vuitton et al.* [2006,2007] with updated reaction rate coefficients observed by *Edwards et al.* [2008] and *Zabka et al.*[2009] requires that the electron dissociative recombination of $HCNH^+$ be increased by a factor of 5 in order for modeled $HCNH^+$ densities to agree with INMS measured densities

but there were still large discrepancies between modeled and measured ion densities of many major ion species (i.e. CH_5^+ and $C_2H_5^+$).

2. Using the favored ion chemical scheme (reducing the H_2O and NH_3 densities by a factor of 100, tripling the HCN, C_2H_2, and C_2H_4 densities, using the modeled electron temperature, and including reactions between C_2H_2, C_2H_4 and $HCNH^+$) requires the electron dissociative recombination coefficient of $HCNH^+$ to be increased by a factor of 10 for the modeled ion density to agree with the measured ion density, but provides agreement between most modeled ion densities and the INMS measured values to within a factor of 2.

3. Reactions between C_2H_2 and C_2H_4 and ion species proposed by *Westlake et al.* [2012] are helpful in modeling the mid- and upper mass hydrocarbon and nitrile production in the ionosphere of Titan.

4. Electron dissociative recombination accounts for nearly 70% of the loss of $HCNH^+$ and therefore, updated recombination coefficients represent a more plausible sink for $HCNH^+$ loss.

Chapter 7 **Nightside Cases**

Photoionization or heating due to solar radiation does not occur on the nightside of Titan, but suprathermal electrons coming into the ionosphere from outside can provide energy to the ionospheric thermal electron population and ionize the neutral atmosphere. Ion precipitation can also take place and contribute to the ionization rate and heating of the thermal electrons [*Cravens et al.*, 2008; *Gronoff et al.*, 2009a]. Electrons that originate in the magnetosphere of Saturn gain access to the ionosphere along the induced magnetic field lines. The choice of field line topology determines how much of the atmosphere a suprathermal electron interacts with before reaching the altitude of interest and so an electron following a radial magnetic field line will take a more direct path through the atmosphere than an electron following a curved field line and will deposit their energy at a lower altitude. Thus, magnetic field line topology is especially important for the nightside (Section 3.1).

In addition to the magnetic field line topology, the location of Titan in Saturn's magnetosphere also plays an important role in determining the superthermal electron population that will precipitate into the ionosphere of Titan (see Section 1.4). *Kliore et al.* [2011] emphasized the large range of electron densities measured by the Cassini Radio Science Subsystem via radio occultation indicating wide variations in the superthermal electron population. *Rymer et al.* [2009] classified the superthermal electron population (electrons originating in the magnetosphere of Saturn with energies larger than 2 eV) of Titan based on its location in Saturn's magnetosphere (Figure 7.1 and Table 7.1).

Although this was discussed in Section 1.2, the magnetospheric electron flux classifications of *Rymer et al.* [2009] will be briefly discussed here (see Figure 7.2, repeated Figure 1.2, for the magnetospheric electron flux for each case). *Rymer et al* described a region in the plasma sheet with a high electron density and peak energy, a lobe-like region in the tail lobes of the ionosphere with high peak energy similar to the plasma sheet case; however, the densities are an order of magnitude lower than when Titan is located in the plasma sheet. The third case mentioned by *Rymer et al.* occurs when Titan is located between the bow shock and the magnetopause in a region known as the magnetosheath. The magnetosheath environment is characterized by low electron densities with lower peak energies. The final category is known as a bimodal distribution. As the name implies, the bimodal distribution's electron spectrum (see Figure 1.2) looks like the superposition of a lobe-like or plasma sheet electron flux with a lower energy electron population associated with pick-up ions.

Table 7.1 Peak electron fluxes and energies for categories of *Rymer et al.* [2009]

***Rymer et al.* [2009] Classification**	**Peak Electron Energy**	**Peak Electron Flux**
Lobe	120 – 600 eV	$5.3 \times 10^4 - 2.4 \times 10^5$ $cm^{-2}s^{-1}sr^{-1}$
Plasma sheet	150 – 820 eV	$3.5 \times 10^5 - 1.2 \times 10^6$ $cm^{-2}s^{-1}sr^{-1}$
Magnetosheath	few hundred eV	$\sim 10^6$ $cm^{-2}s^{-1}sr^{-1}$
Bimodal	200 eV and 3.4 keV 5.3 – 16.3 eV	$9.0 \times 10^4 - 2.4 \times 10^5$ $cm^{-2}s^{-1}sr^{-1}$ $5.7 \times 10^5 - 1.6 \times 10^6$ $cm^{-2}s^{-1}sr^{-1}$

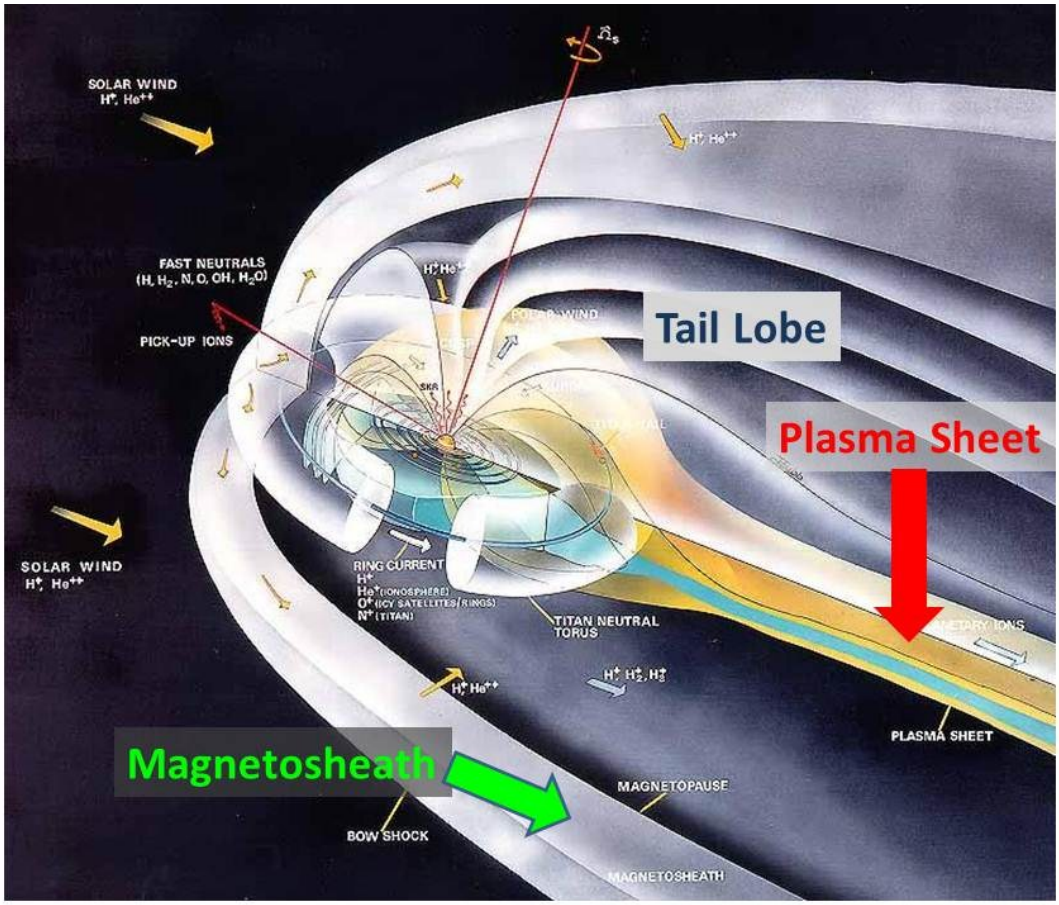

Figure 7.1 Rendition of the magnetosphere of Saturn. The areas marked with large text are the magnetospheric regions whose electron spectra have been categorized by *Rymer et al.* [2009] (tail lobe, plasma sheet, and magnetosheath). [Image courtesy of NASA]

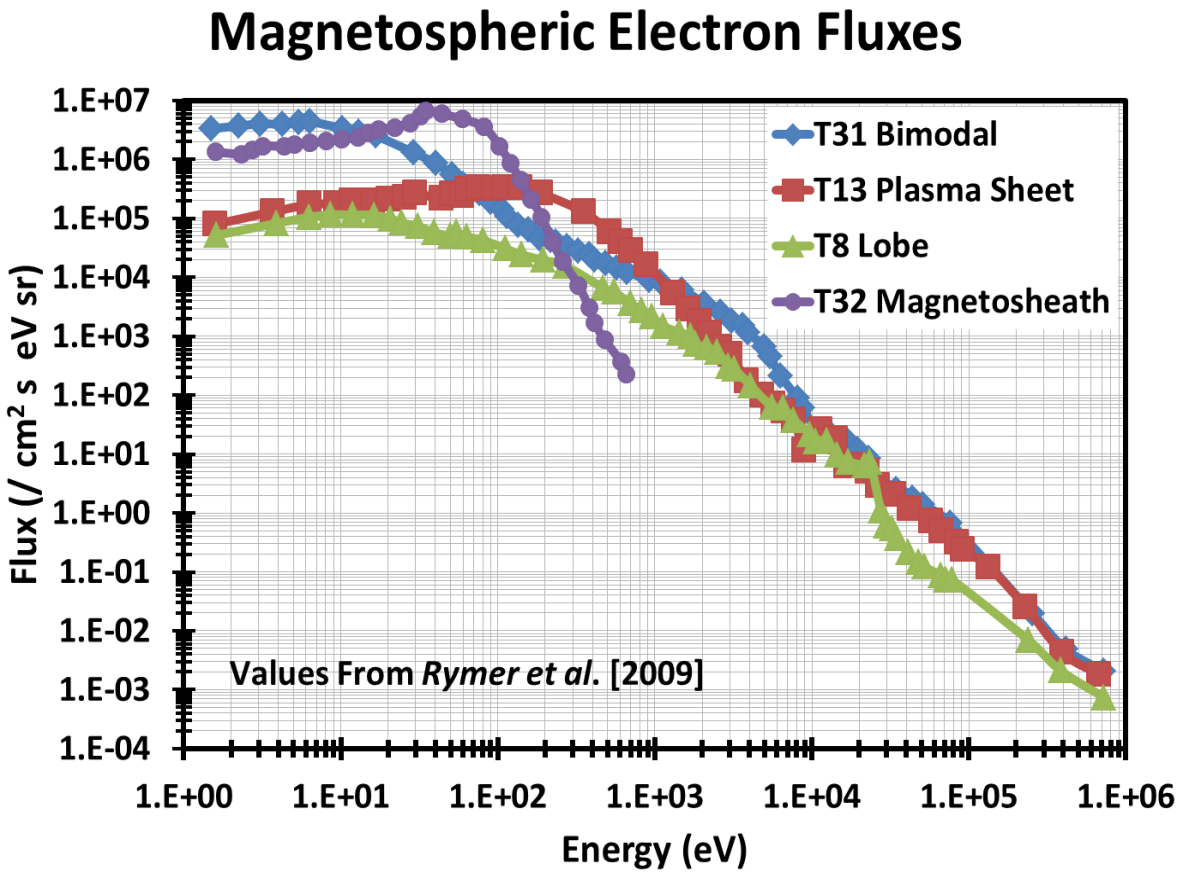

Figure 7.2 Superthermal electron fluxes plotted against energy for the four magnetospheric plasma environments presented by *Rymer et al.*, [2009]. Repeat of Figure 1.2

In this chapter the ion production rates in Titan's ionosphere due to magnetospheric electron precipitation will be examined. First comparisons will be drawn between INMS measurements taken on the nightside of Titan and modeled ion production rates similar to what was done for the dayside in Chapter 4. After verifying that the model ion production rate is comparable to production rates inferred from measurements, generic ion production profiles for the canonical cases discussed by *Rymer et al.* [2009] will be generated. The same process will be used to produce profiles for electron temperatures for magnetic field line topologies that are horizontal (nested), parabolic and radial (Section 3.1). The goal of this endeavor is to produce ion production and electron temperature profiles so that future modeling efforts can combine the solar ion production profiles (Chapter 4) with the ion production caused by magnetospheric electrons when Titan is located in an area of Saturn's magnetosphere characterized by *Rymer et al.* in order to accurately predict the ion production and density profiles for future flybys of Titan.

7.1 Ion Production Rates

As discussed in Chapter 4, the primary production rates of ion species are used in the photochemical model to accurately reproduce the ion densities that are measured in Titan's ionosphere. Ionization sources on the nightside of Titan have been discussed during the T5 encounter of Titan by *Agren et al.* [2007], *Cravens et al.* [2009a], *Robertson et al.* [2009], and *Gronoff et al.* [2009b] and all have concluded that the flux of magnetospheric electrons precipitating into Titan's ionosphere needs to be reduced by a factor of 10 in order to reproduce the electron flux observed by the CAPS/ELS instrument aboard the Cassini spacecraft.

Studies emphasizing the ion production at Titan have been carried out by *Galand et al.* [2010] in an attempt to determine an effective dissociative electron recombination rate in the ionosphere of Titan to examine the possibility of missing loss processes in the ionosphere of Titan. *Gronoff et al.* [2009b] have specifically examined the ion production of N_2^+, N^+ and CH_4^+ in the ionosphere of Titan using the TransTitan model [*Gronoff et al.,* 2009a] in order to consider effects of magnetic field line geometry on the ionization processes. This is similar to the work done by *Cravens et al.* [2009a].

In this section ion production rates resulting from magnetospheric electron precipitation down magnetic field lines will be presented for the ionization products of N_2 (N_2^+ and N^+) and CH_4 (CH_4^+, CH_3^+, CH_2^+, CH^+, C^+, H_2^+, and H^+) for the T5 and T57 flyby of Titan and the cases described by *Rymer et al.* [2009]. The two-stream methodology (see Section 3.3) will be implemented [*Schunk and Nagy*, 2009] along with the electron impact ionization cross sections for N_2 of *Itikawa et al.* [2006] and the revised electron impact ionization cross sections for methane from *Straub et al.* [1997] [*Lindsay and Mangan*, 2003], in order to produce these profiles (see Section 3.3.2). The modeled production rates of N_2^+, CH_3^+ and CH_4^+ will be compared to ion production rates derived empirically from ion density measurements collected by INMS for the T5 flyby, as this case has been previously discussed in the literature (i.e. *Cravens et al.,* [2009a], *Robertson et al.* [2009], and *Gronoff et al.* [2009b]), as well as the T57 flyby of Titan, as was done in Chapter 4. Examination of the model results of these two flybys will also allow the model to be evaluated for the plasma sheet (T5) and bimodal (T57) magnetospheric electron flux conditions of *Rymer et al*. After the model production rates of the primary ion species are shown to be in reasonable agreement with the production rates derived from INMS density measurements, production rate profiles using the magnetospheric electron

fluxes for the canonical cases of *Rymer et al.* [2009] (lobe-like, plasma sheet, bimodal, and magnetosheath) will be conducted using the magnetic field line topologies discussed in Section 3.1 (radial, single parabola, nested parabolas simulating horizontal field lines). Although the same methodology discussed in Chapter 4 will be used in this section, the discussion presented here will follow a more streamlined format. All of the ancillary figures appear in Appendix D-1 for the T5 flyby and in Appendix D-2 for the T57 flyby.

7.1.1 Verification of the Model Production Rates of N_2^+ and CH_4^+

7.1.1.1 T5 – Plasma Sheet

The deep nightside T5 flyby of Titan occurred on 16 April, 2005 when Titan was located near 5.27 SLT, and the spacecraft reached a closest approach altitude of 1027 km with a corresponding SZA of approximately 137º. Electron densities were adopted from RPWS-LP for this encounter [*Agren et al*., 2007]. The neutral density profile for the major ion species shown in Figure 3.33 (INMS measured densities multiplied by a factor of 3.15) was adopted along with the mixing ratios of *Magee et al.* [2009] (Table 3.3) in order to create a neutral density profile. The magnetometer data collected during the T5 outbound encounter with Titan showed that field lines were at an angle of approximately 45 degrees with respect to the surface and had a large radial component near closest approach (Figure 3.2) not predicted by MHD models [*Ulusen et al.,* 2010; *Backes et al*., 2005; *Cravens et al*., 2010; *Ma et al*., 2009]. To simulate the magnetic field lines our model uses a parabolic field line anchored at the surface of Titan, for which the field lines have approximately the correct orientation at ionospheric altitudes (see Figure 3.2).

Agren et al. [2007] and *Cravens et al*. [2008] have shown that the T5 electron density profile can be reproduced with this model using only production from precipitation of magnetospheric suprathermal electrons; however, both of their models compared the electron

density from the chemical model with the electron density measured by RPWS-LP. Using only comparisons of the modeled and measured electron density, *Cravens et al.* and *Agren et al.* concluded that the magnetospheric electron flux at the top of the magnetic field line would need to be reduced by a factor of 8-10 and 2.5 respectively and thus; there was attenuation of the incident magnetospheric electron flux. In this section, it will be shown that this attenuation of the magnetospheric electron flux is no longer needed to reproduce the primary ion densities.

A comparison of the observed CAPS ELS suprathermal electron flux, which has been divided by a factor of 4 to represent a recalibration of the instrument [*Cravens et al.,* 2008], and the electron spectrum from our two-stream model are shown in Figure 7.3. The fluxes measured by CAPS ELS well outside the ionosphere without attenuation were used for this model's "magnetospheric" input (i.e. boundary conditions for the two-stream code discussed in Section 3.3). Figure 7.3 also shows that the CAPS ELS superthermal electron flux measured at 1200 km, near the ionospheric peak, is within 5-10% of the downward superthermal electron flux and within 20% of the upward superthermal electron flux. This is in contrast to the modeled fluxes reported by *Cravens et al.* [2008] that were still a factor of 8 larger than the CAP ELS measurements. This is due to the recalibration of the INMS instrument as the neutral atmosphere of *Cravens et al.* did not include the factor of 3.15 increases to the neutral densities, as this model does, which results in the absorption of more superthermal electrons, thus lowering the flux at 1200 km.

As discussed in Section 3.5.2 and Chapter 4, the density of N_2^+ cannot be determined from in situ ion density measurements made by the INMS instrument as the mass 28 peak in the ion density spectrum is dominated by $HCNH^+$, the most abundant ion species in the ionosphere of Titan. As a consequence of this, the ion density measurements of CH_3^+ will be used as a

proxy for the N_2^+ production and density verifications. This approach is justified on the grounds that the overwhelming majority of N_2^+ is produced through electron impact ionization and lost primarily, between 60-85%, through chemical reactions with methane to produce CH_3^+ (Table 3.6), which coincidently is the major production source of CH_3^+ (Table 3.11). Roughly 99-90% of CH_3^+ is lost through reactions with methane to produce CH_4^+ (Table 3.12). This means that the production of CH_3^+ will serve as a good indicator of whether or not there is a sufficient production of N_2^+ in the ionosphere of Titan. This is the same methodology that has been detailed in Sections 3.5.2 and 4.1. As discussed in Section 4.1, this model is capable of producing reasonable ion production rates and densities for the dayside passes, so the same chemical modeling processes will be implemented here although magnetospheric electrons will provide the initial source of ionization and solar sources will not be considered.

Using the full photochemical model (see Section 3.4) and the CAPS ELS input superthermal electron fluxes, the density profile of CH_3+ as a function of altitude has been constructed using a single parabolic magnetic field line anchored at the surface of Titan. Using the full photochemical model accounts for the production of CH_3^+ from N_2^+ reactions with methane as well as the electron impact ionization of methane and all of the loss processes of CH_3^+ described in Table 3.12 (Figure 7.4). As Figure 7.4 shows, model CH_3^+ density is in agreement with the density measured by INMS to within 20% at altitudes below 1160 km and above 1280 km.

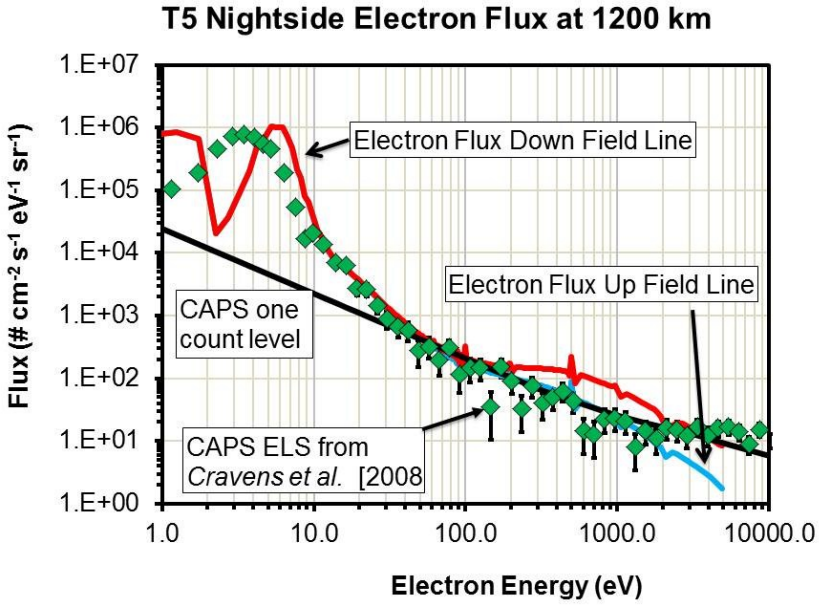

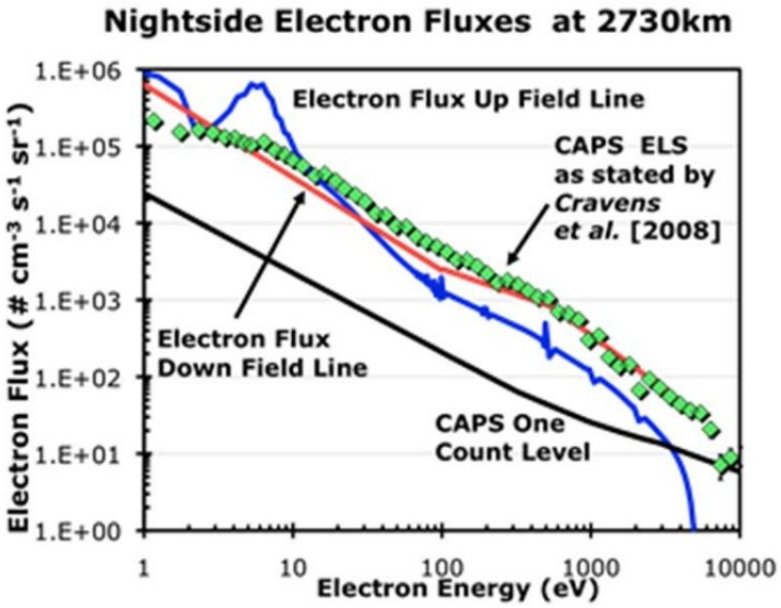

Figure 7.3 Suprathermal magnetospheric electron fluxes measured by CAPS during the T5 encounter as reported by *Cravens et al.* [2008] at 1200 km (above) and 2730 km (below). The downward flux comes from suprathermal electron transport along the field line from the magnetosphere to the ionosphere. These CAPS ELS fluxes for T5 were adopted as the boundary condition for the two-stream code. The upward electron fluxes appearing at higher energies are calculated from the model and are the result of backscattering and at lower energies are escaping secondary electrons produced by ionization deeper in the atmosphere.

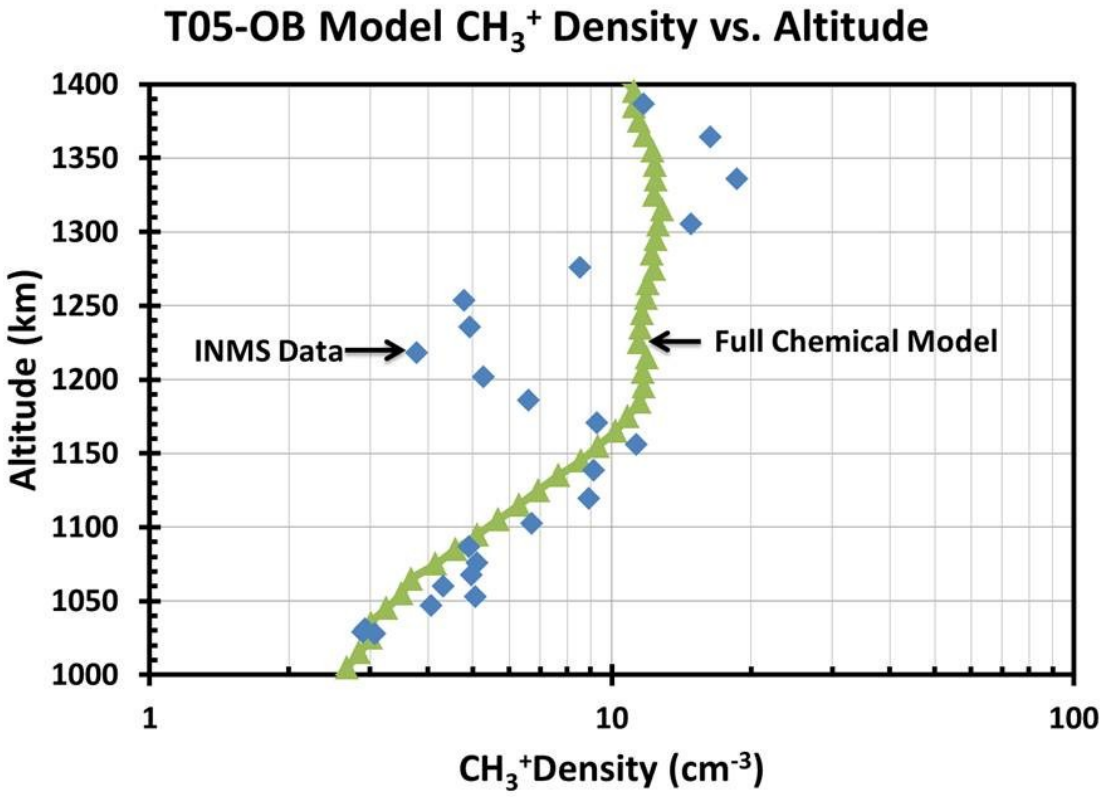

Figure 7.4 CH_3^+ density produced by the full photochemical model (green triangles) using the full T5 magnetospheric electron flux measured by CAPS/ELS [*Cravens et al.*, 2008] as an input (Figure 7.3) compared to INMS data from the T5-Outbound flyby of Titan. INMS data is indicated with the blue diamonds. This model uses the magnetic field topology of a single parabola anchored at the surface of Titan to simulate a curved field line with a large radial component.

Between 1160 and 1275 km (Figure 7.4), INMS and modeled CH_3^+ densities have a discrepancy as large as a factor of 2. This feature was noticed by both *Agren et al.* [2007] and *Cravens et al.* [2008]. As is shown in Figure 7.5, the CAPS ELS 4 eV electron flux, corresponding to secondary electrons, correlates well to the INMS measured ion density of CH_5^+, the product of the chemical reaction between CH_4^+ and methane (see Table 3.10), with a noticeable dip between 155 and 205 seconds after closest approach corresponding to altitudes of 1140 and 1220 km respectively. *Cravens et al.* also noted that the density profile of longer lived ions (such as $HCNH^+$) do not exhibit such a profound drop in density at these altitudes (Figure 7.6). As the drop in density was only prevalent in shorter lived ion species, *Cravens et al.* concluded that the production rate of ions, and hence the magnetospheric electron flux at the end

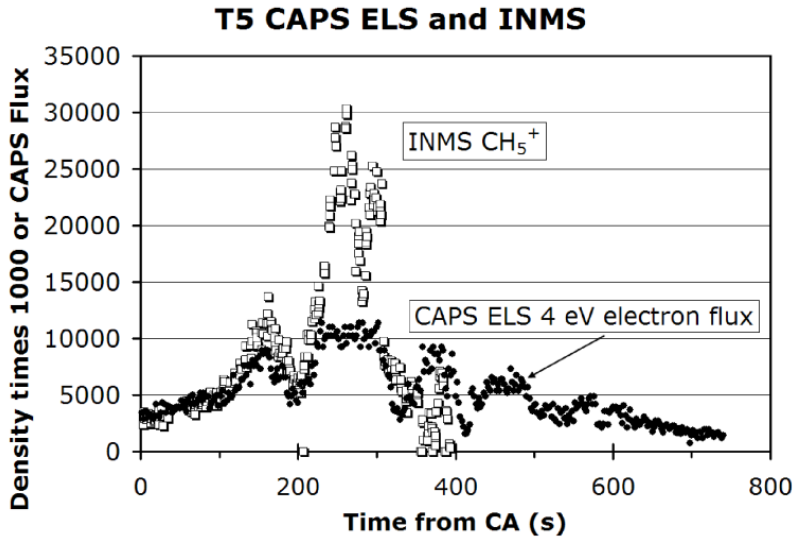

Figure 7.5 The CAPS ELS electron flux (actually count rate) for 4.06 eV and the m = 17, corresponding to CH_5^+, densities measured by INMS are plotted versus time for the outbound portion of the T5 Cassini encounter with Titan. Note that the times of 155 s and 205 s correspond to altitudes of 1140 and 1220 km respectively. Figure from *Cravens et al.* [2008]

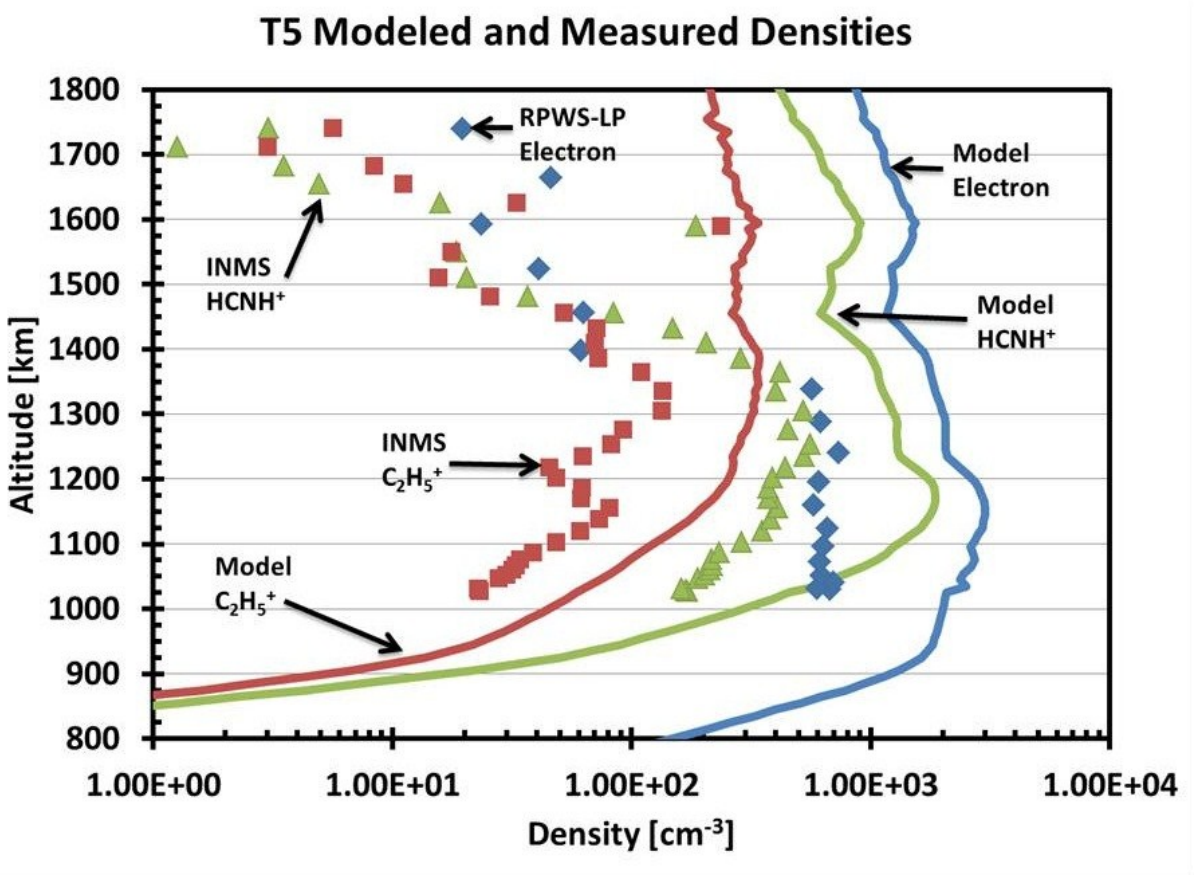

Figure 7.6 Modeled densities of electrons (blue line), $HCNH^+$ (green line) and $C_2H_5^+$ (red line) compared to their measured counterparts. Measurements of the densities of $C_2H_5^+$ (red squares) and $HCNH^+$ (green triangles) are made by the INMS instrument. Electron densities (blue diamonds) are measured by RPWS-LP.

of the flux tube connected to this region was passing through more of the neutral atmosphere and was being depleted of its electron content. This effect has been noted in several previous works [*Gan et al.,* 1992*; Agren et al.,* 2007; *Cravens et al.,* 2008; *Ma et al.,* 2006; 2009] and is the most plausible explanation for this feature.

Although the evidence for the case of depleted magnetic flux tubes leading to the spacecraft observations between 1140 and 1220 km is strong, the overall attenuation of the CAPS ELS measured magnetospheric electron flux is not needed to accurately reproduce the density profile of CH_3^+. Agreement between the measured and modeled densities (Figure 7.4) indicates that the full magnetospheric electron flux is needed, along with the factor of 3.15 increases in the neutral densities, to produce the amount of CH_3^+ observed. In the initial comparisons between modeled and measured electron densities of *Agren et al.* [2007] and *Cravens et al.* [2008] they concluded that in order to bring the modeled electron densities down, there would need to be attenuation of the incident magnetospheric flux. The results of this model shown in (Figure 7.6) show that the overabundance of electrons is the direct result of the overabundance of $HCNH^+$ which is not being sufficiently removed from the ionosphere (see Chapter 4).

It can be concluded from the agreement between the modeled and measured CH_3^+ densities that the model is producing a reasonable amount of N_2^+ (Figure 7.7). As was done in Section 4.1.1, an empirical production rate of N_2^+ has been derived using the simple two-reaction model assuming photoequilibrium (Equation (7.1)) and that the main loss process for CH_3^+ is through reactions with methane and that it is created by reactions between N_2^+ and methane (Equation (7.2)). As CH_3^+ is mainly produced via N_2^+ reactions with methane, but not all N_2^+ reacts with methane to form CH_3^+, the photochemical model was used to derive the percentage

ratio of CH_3^+ produced to the total amount of N_2^+ produced (mentioned in Equation (7.3) and shown in Figure 7.8). The CH_3^+ production factor divided by this correction factor will yield an empirical production rate of N_2^+ from the CH_3^+ density measurements taken by INMS (Equation (7.4)). The data shown in Figure 7.7 shows that the modeled production rate of N_2^+ using the full T5 CAPS ELS magnetospheric electron flux falls within 10 – 20% of the production rate that was empirically derived using the simple two reaction model (Equation (7.4)) with the implementation of the adjustment factor obtained using the photochemical model with the exception of the "bite-out" feature between 1140 and 1220 km. This in conjunction with the agreement between modeled and measured CH_3^+ densities suggests that the two-stream model is producing adequate amounts of N_2^+.

$$Production_{N_2^+} \sim Production_{CH_3^+} = Loss_{CH_3^+} \quad \textbf{(7.1)}$$

$$k_{N_2^+,CH_4^+}[N_2^+][CH_4] = k_{CH_3^+,CH_4}[CH_3^+][CH_4] \quad \textbf{(7.2)}$$

$$(Cor.Factor) * Production_{N_2^+} = k_{CH_3^+,CH_4}[CH_3^+]_{INMS}[CH_4]_{INMS} \quad \textbf{(7.3)}$$

$$Production_{N_2^+} = \frac{k_{CH_3^+,CH_4}[CH_3^+]_{INMS}[CH_4]_{INMS}}{Correction\ Factor} \quad \textbf{(7.4)}$$

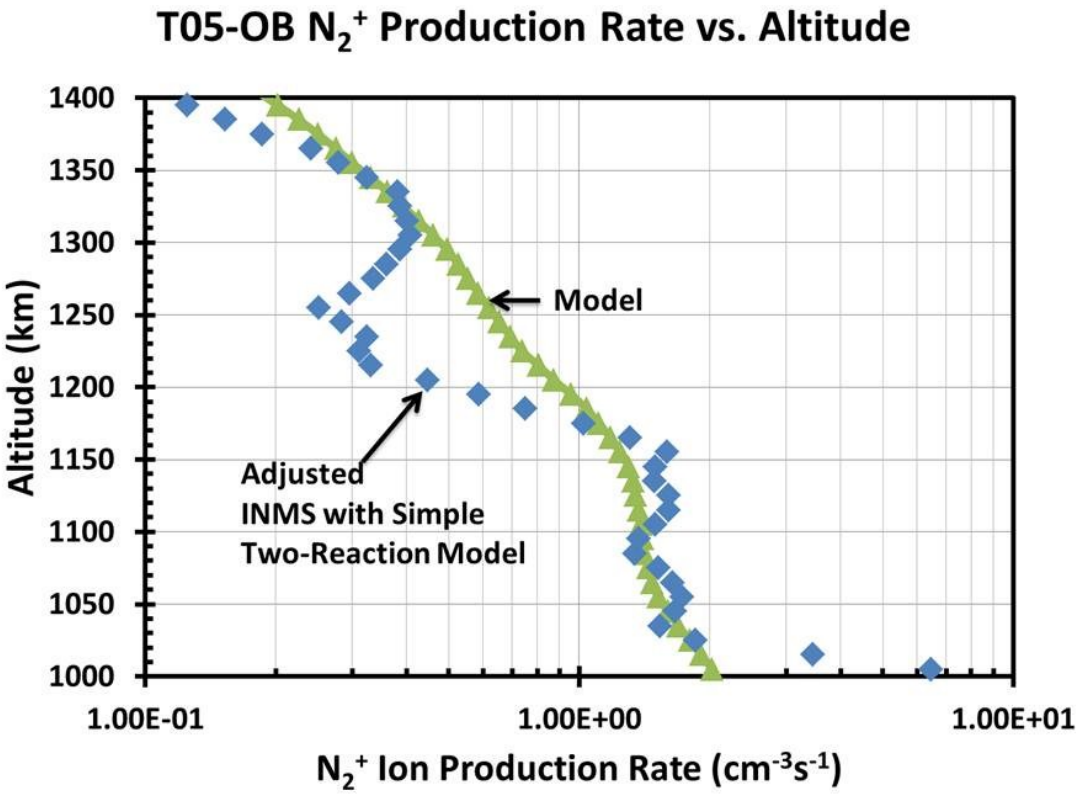

Figure 7.7 Modeled photoionization production rates of N_2^+ (green triangles) compared to the production rate of N_2^+ derived from INMS data using a simple two – reaction model adjusted by the factor shown in Figure 7.8 (blue diamonds) for the outbound leg of the T5 flyby of Titan. A single parabolic field line anchored at the surface of Titan for the magnetic field line topology.

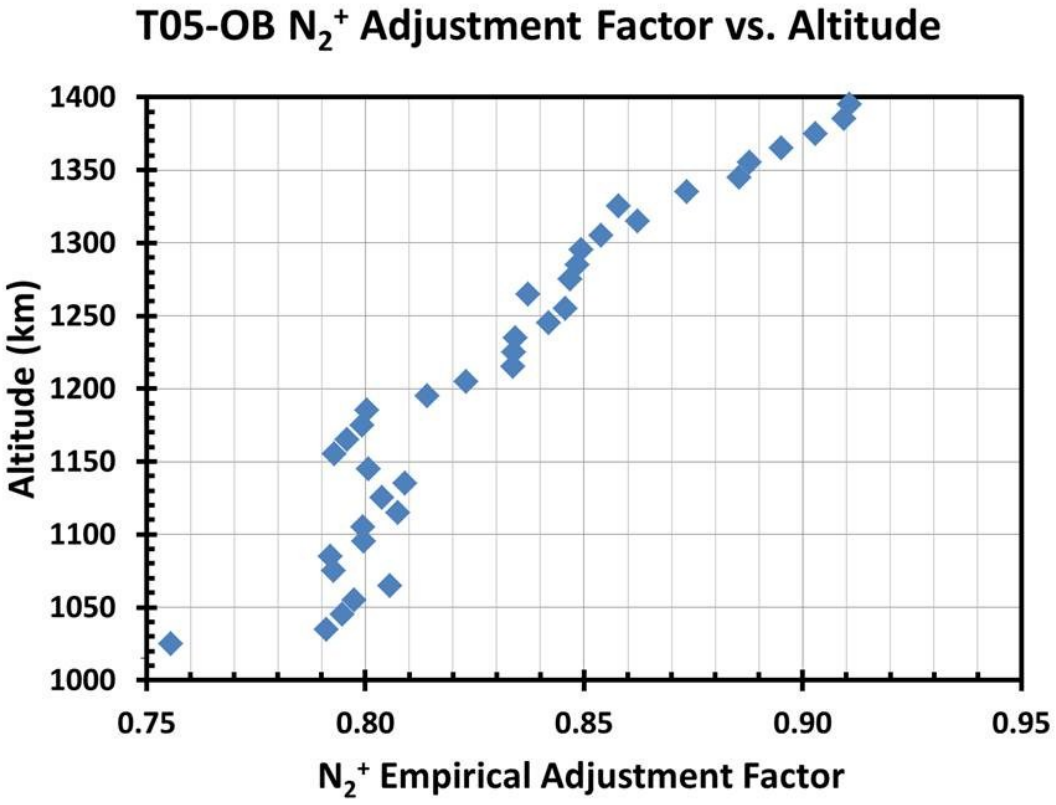

Figure 7.8 Factor used to adjust the production rate of N_2^+ derived from the simple two-reaction model using INMS data for the outbound leg of the T5 flyby of Titan. This correction factor is the ratio of the N_2^+ production rate from photoionization to the N_2^+ production rate from the full photochemical model (production from photoionization and chemical pathways).

Now the production rate of CH_4^+ must be examined in order to verify that the model is properly handling the electron impact ionization of methane. The first check on this is to examine how the modeled CH_4^+ density compares to the CH_4^+ densities measured by INMS (Figure 7.9). For this comparison the full photochemical model was used in order to account for the production of CH_4^+ from reactions between CH_5^+ and methane (see Section 3.5.2.3 and Table 3.14) which can contribute upwards of 35% of the production rate at lower altitudes. Even when using the full photochemical model, the CH_4^+ densities measured by INMS are 50% larger than the modeled CH_4^+ density below 1160 km and above 1300 km and are 50% higher than the "bite-out" feature between 1160 and 1275 km.

On the nightside of Titan, accurately modeling the magnetic field line topology becomes increasingly more important as the only source of energy deposition considered is from magnetospheric electrons that follow these magnetic field lines [c.f. *Cravens et al.,* 2009a; *Robertson et al.* 2009, *Galand et al,.*2006, 2010; *Gronoff et al,* 2009b; *Ulusen et al.*, 2010; *Richard et al.* 2011]. Thus, the field line determines how much of the neutral atmosphere an electron interacts with; the larger the radial component of the magnetic field line, the less of the atmosphere an electron will have to pass through in order to react at lower altitudes, as will be discussed in the next section.

After looking at the CH_4^+ density, the production rate of CH_4^+ from the two-stream code (Section 3.3) using only magnetospheric electrons as an input source and the production rate from the full photochemical model will be compared to empirical production rates derived from the INMS instrument using a simple two-reaction model with the assumption of photochemical equilibrium discussed in Section 4.1.2 (Figure 7.10). By setting the production

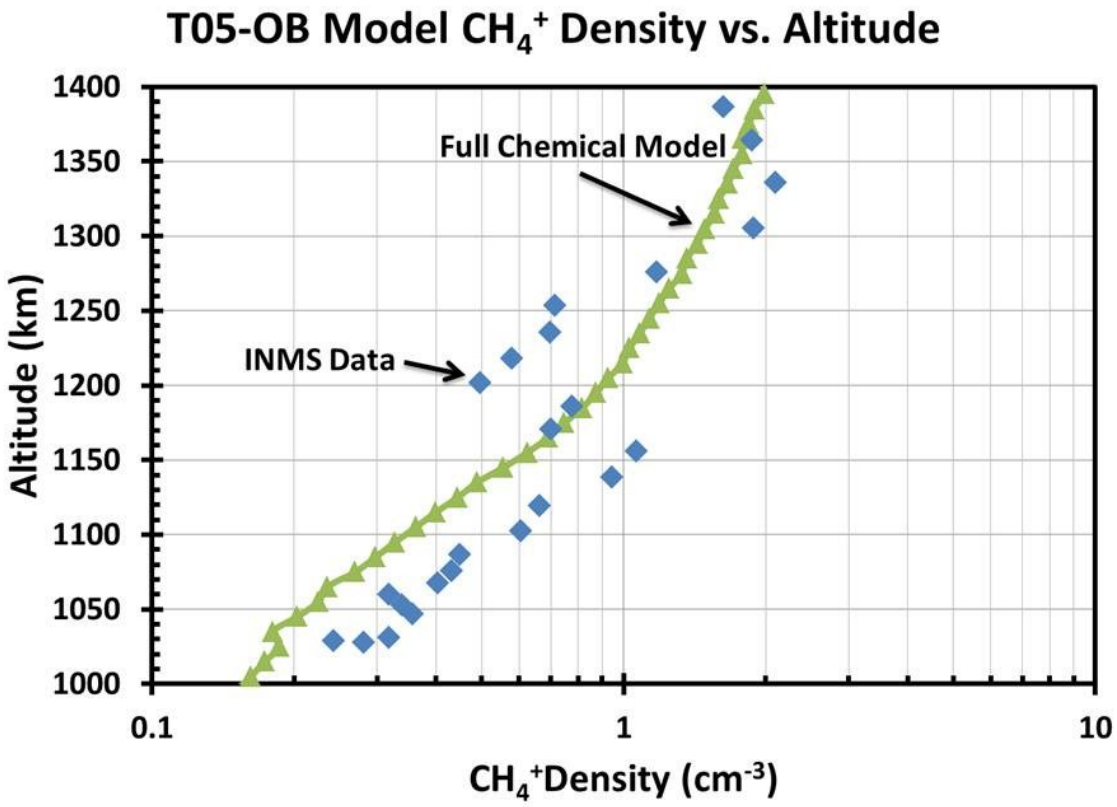

Figure 7.9 CH_4^+ density produced with the full photochemical model (green triangles) compared to INMS data (blue diamonds) from the T5-Outbound flyby of Titan. A single parabolic field line anchored at the surface of Titan for the magnetic field line topology.

rate of CH_4^+ equal to the loss rate (Equation (7.5)) of the ion and utilizing the fact that upwards of 90% of the CH_4^+ loss is due to reaction with methane to produce CH_5^+ (see Table 3.13), the empirical production rate can be expressed as the loss rate from this reaction where the densities of CH_4^+ and CH_4 are measured by INMS (Equation (7.6)).

$$Production_{CH_4^+} = Loss_{CH_4^+} \quad \textbf{(7.5)}$$

$$Prod_{CH_4^+} = k_{CH_4^+,CH_4}[CH_4]_{INMS}[CH_4^+]_{INMS} \quad \textbf{(7.6)}$$

When comparing the two-ion production rate of CH_4^+ from electron impact ionization of precipitating magnetospheric electrons to the production rate determined empirically from INMS data (upper portion of Figure 7.10), the production rates were found to be in agreement between 1350 and 1200 km. Between 1150 and 1000 km the modeled production of CH_4^+ from electron impact ionization is lower than the empirically derived production rate by a factor of 2; however, the production rate from electron impact ionization in this model is found to be in agreement with the radial case presented by *Gronoff et al.* [2009b] with a value of 0.04 $cm^{-3}s^{-1}$ between 1100 and 1000 km.

In order to account for the possible missing production pathways of CH_4^+, most notably the reactions between CH_5^+ and H (see Table 3.14), the full photochemical model (see Section 3.4 and Section 3.5) was used (lower panel of Figure 7.10). This brought the modeled production rate to within a factor of 1.5 at 1150 km and within 25% of the empirical production rates at all other altitudes. From this it can be concluded that the model production rate of CH_4^+ is reasonable (within 25% at most altitudes). Using more advanced magnetic field topologies from MHD models may help in bringing the modeled production rates into better agreement with the empirical production rates [c.f. *Ma et al.* 2006; 2007; 2009].

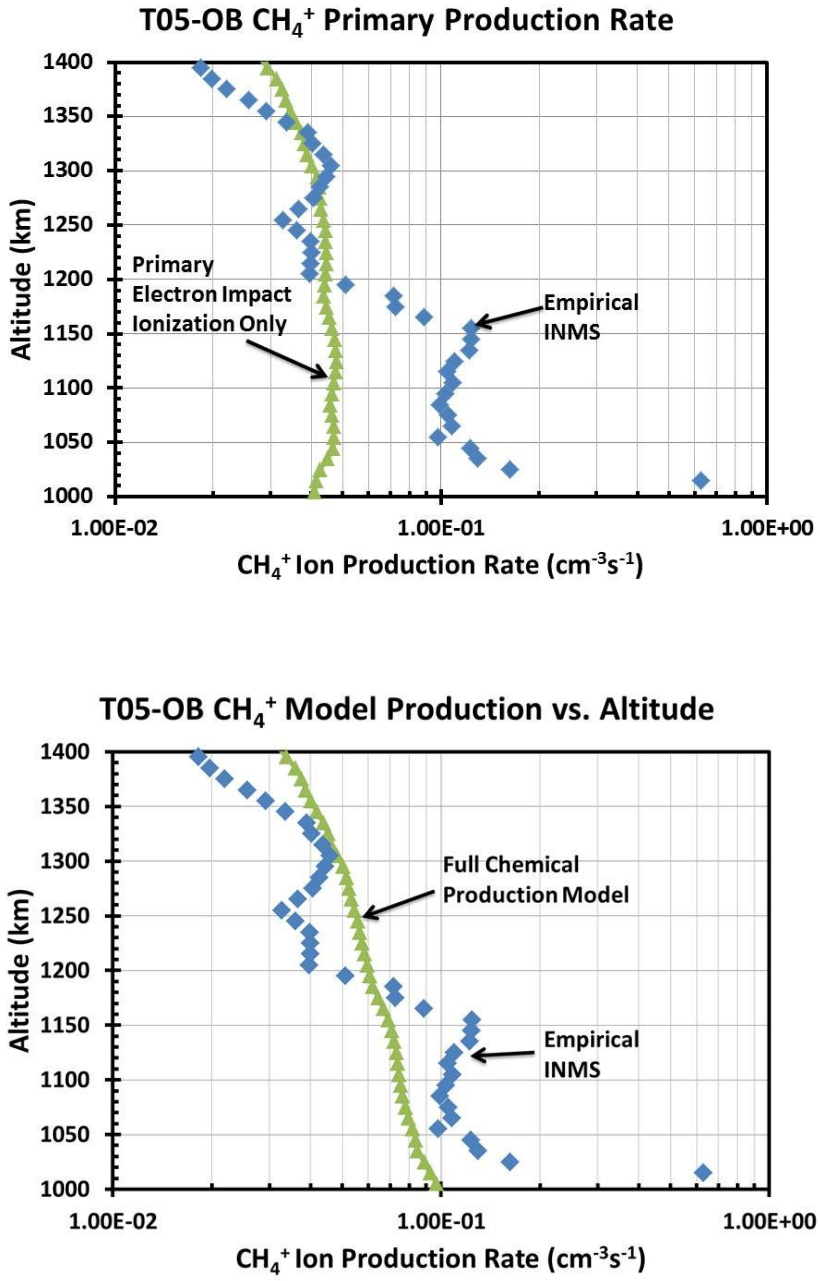

Figure 7.10 Modeled production rates (green triangles) of CH_4^+ compared to the empirical production rate of CH_4^+ derived from INMS data (blue diamonds) using the simple two-reaction chemical model for the T5-Outbound flyby of Titan. The primary production rate of CH_4^+ caused solely by electron impact ionization of methane by magnetospheric electron precipitation appears in the top panel while the bottom panel shows the modeled CH_4^+ production obtained using the full photochemical model to account for the production of CH_4^+ from reaction between CH_5^+ and H.

7.1.1.2 T57- Bimodal

The T57 flyby of Titan occurred on June 22, 2009 and reached an altitude of 955 km at the closest approach. During the inbound leg of T57 the solar zenith angle went from 165˚ at an altitude of nearly 2000 km to 128˚ at closest approach allowing the spacecraft to make observations of the nightside ionosphere. *Rymer et al.* [2009] classified this flyby as a bimodal case meaning that the electron flux (Figure 7.11) exhibited features of a high energy lobe or plasma sheet electron population as well as a lower energy electron peak believed to be caused by pick-up ions. This electron flux without attenuation will be used as an input into the two-stream code (Section 3.3) at the top of the magnetic field line where it will interact with the neutral atmosphere given in Figure 3.38 using the mixing ratios of *Magee et al*. [2009] (Table 3.3). This case has also been mentioned by *Kliore et al.* [2011] when discussing the variability of the magnetospheric electron fluxes precipitating into Titan's ionosphere. The same methodology used in Sections 4.1 and 7.1.1.1 will be used here to show that the model production rates of N_2^+ and CH_4^+ are reasonable thus increasing the confidence in the model and showing that the model is valid for use in a variety of magnetospheric electron flux environments.

Magnetometer data has shown that the magnetic field line topology for T57 has radial and horizontal (parallel to the surface of Titan) components and so model runs with three different magnetic field line topologies (nested, single parabola anchored at the surface, single parabola anchored at 725 km) will be shown (see Section 3.1). The nested case will represent completely horizontal field lines, the parabola anchored at the surface will represent a field line with a 45˚ angle with respect to Titan near 1200 km and the parabolic field line anchored at 725

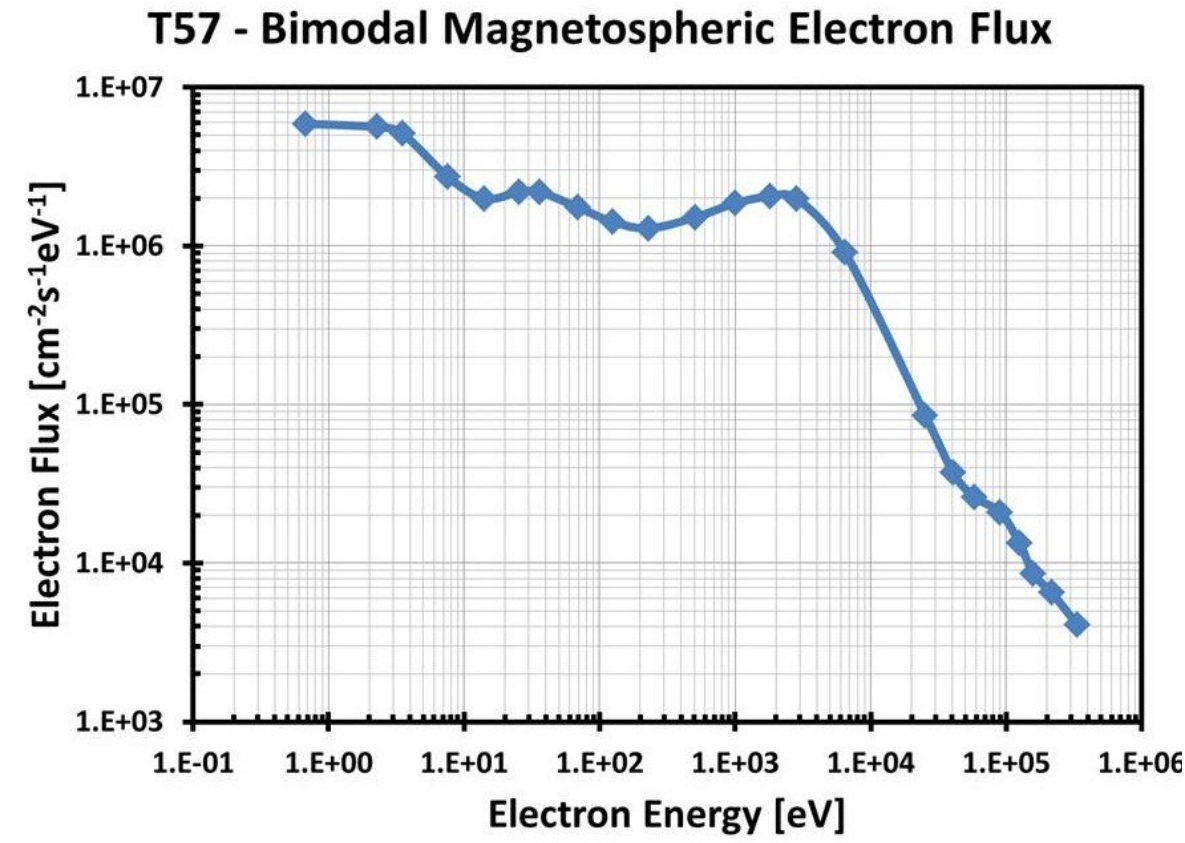

Figure 7.11 Superthermal electron fluxes in the magnetosphere measured by CAPS during the T57 encounter as reported by *Kliore et al.* [2011]. . These CAPS ELS fluxes for T57 were adopted as the boundary condition for the two-stream code. The upward electron fluxes appearing at higher energies are calculated from the model and are the result of backscattering and at lower energies are from escaping secondary electrons produced by ionization deeper in the atmosphere.

km will have a greater horizontal component near 1200 km than the parabola anchored at the surface, but less than the nested case. The field line anchored at the surface is the preferred case.

As was done in Section 7.1.1.1, the CH_3^+ density will be examined first (Figure 7.12). The CH_3^+ density profile produced using the full photochemical model (see Section 3.4) and a single parabolic magnetic field line anchored at the surface of Titan agrees with the measured INMS densities between 1350 and 1130 km to within 10%. This modeled case agrees very well with the CH_3^+ density measured at the ionospheric peak of the T57 flyby. For altitudes below 1100 km, using a single parabolic magnetic field line anchored 725 km above the surface of Titan produced CH_3^+ densities within 15% of the densities measured by INMS. This shows that the model is accurately producing enough CH_3^+, and hence the N_2^+ production is found to be produced in reasonable amounts. This follows from the earlier discussions (see Sections 3.5.2, 4.1.1, and 7.1.1.1) that make use of the fact that N_2^+ reacts with methane as the primary source of CH_3^+ production (Table 3.11). The agreement between the measured densities and modeled densities using the surface anchored parabola above 1150 and the modeled densities using the parabola anchored at 725 km below 1100 km indicates that the field line bringing magnetospheric electrons from the upper ionosphere to these lower altitudes during the T57 flyby may have a larger horizontal component than the field line bringing the electrons to the ionospheric peak observed by the Cassini spacecraft.

As the agreement between the modeled and INMS measured CH_3^+ has shown that the model is producing reasonable amounts of N_2^+, the next step, as was done in Sections 4.1.1, and 7.1.1.1, is to produce an empirical production rate of N_2^+ using the simple two-reaction model, measured INMS densities and the adjustment factor obtained by comparing the amount of CH_3^+ produced to the amount of N_2^+ produced (Figure 7.13), computed from Equation (7.4), and

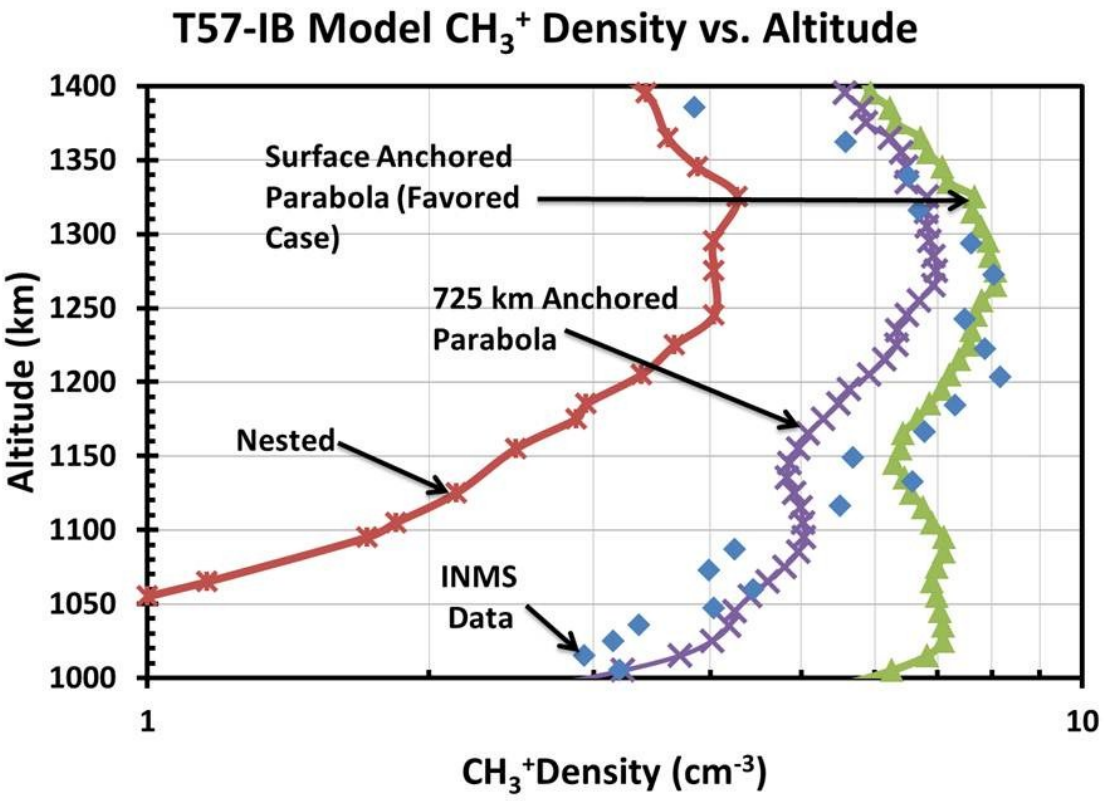

Figure 7.12 CH_3^+ density produced by the full photochemical model with magnetic field line topologies of a parabola anchored at the surface of Titan (green triangles), a parabola anchored at 725 km (purple crosses) and nested parabola (red stars) using the T57 magnetospheric electron flux measured by CAPS/ELS [*Kliore et al.*, 2011] as an input (Figure 7.11) compared to INMS data from the T57-Outbound flyby of Titan. INMS data is indicated with the blue diamonds.

compare this to the modeled production rates of N_2^+ resulting from the electron impact ionization of the upper atmosphere by magnetospheric electrons. As Figure 7.14 shows, the empirically derived production rates are within 10% of the modeled N_2^+ production rate when the single parabola anchored at the surface of Titan is adopted for the magnetic field line topology above 1140 km and for the parabolic magnetic field line anchored at 725 km at altitudes below 1140 km. Thus the modeled production rates of N_2^+ are found to be in good agreement with the empirically derived production rates and the actual magnetic field line topology is found to be closer to a surface anchored parabola at higher altitudes and a 725 km anchored parabola at the lower altitudes, consistent with what was observed in the CH_3^+ density profiles.

To ensure that reasonable amounts of CH_4^+ are being produced, the INMS measured density profile of CH_4^+ is compared to the modeled CH_4^+ density profile generated using the full photochemical model (see Section 3.4) for the three magnetic field line topologies described above (Figure 7.15). As was found in the cases of the N_2^+ production rates and the CH_3^+ density profiles, the measured INMS densities of CH_4^+ agree with the magnetic field topology of the surface anchored parabola above 1150 km and the parabola anchored at 725 km below 1140 km. In all of these instances the modeled densities of CH_4^+ are within 20% of the measured values. This trend is repeated when comparing the modeled production rates of CH_4^+, using the full chemical model (see Sections 3.5.2, 4.1.2, and 7.1.1.1) to account for the CH_5^+ reactions with H to form CH_4^+ (Table 3.14), to the empirical production rate of CH_4^+ derived from INMS data and the assumption of photochemical equilibrium (Equation (7.6)) as shown in Figure 7.16. These cases all illustrate the importance of the magnetic field line topology on the efforts to model the nightside ionosphere of Titan.

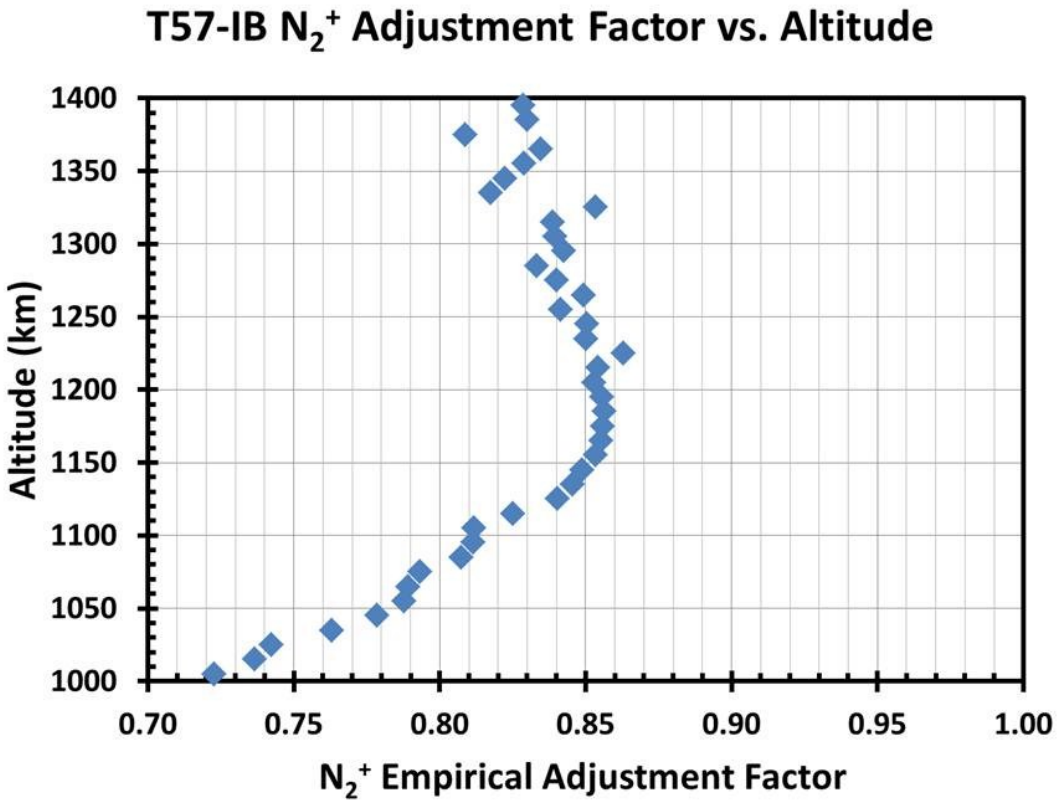

Figure 7.13 Factor used to adjust the production rate of N_2^+ derived from the simple two-reaction model using INMS data for the inbound leg of the T57 flyby of Titan. This correction factor is the ratio of N_2^+ production rate from photoionization to the N_2^+ production rate from the full photochemical model (production from photoionization and chemical pathways).

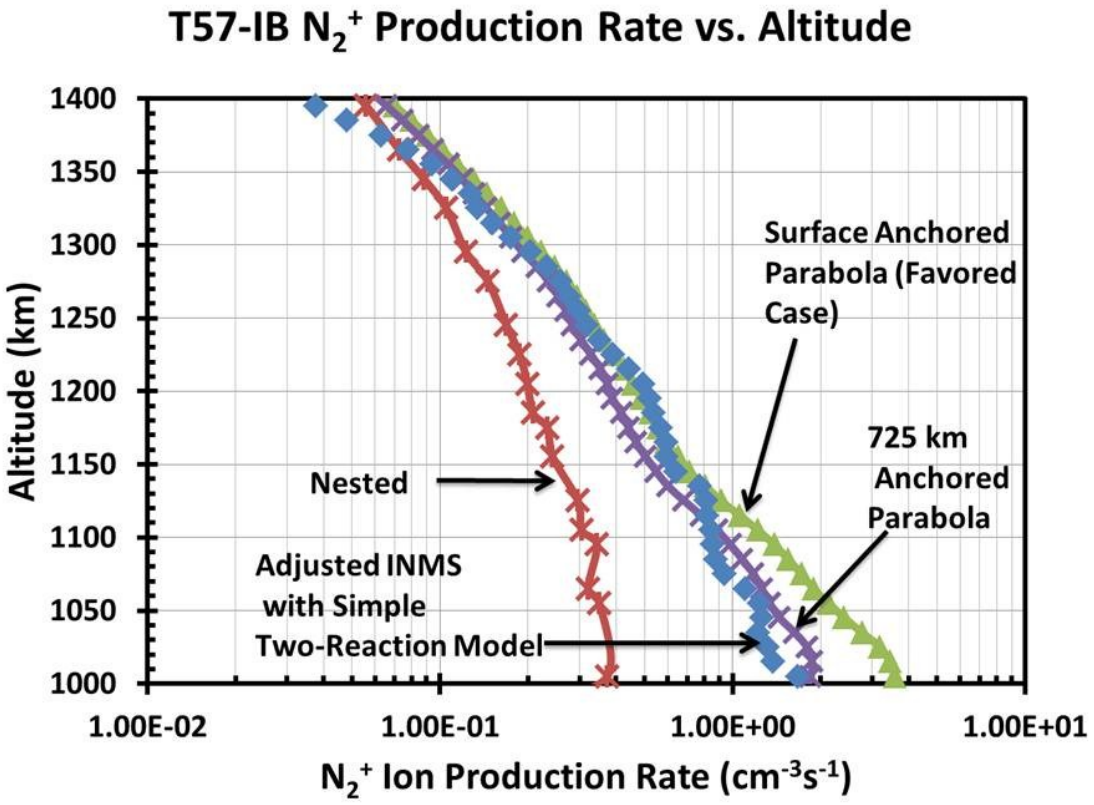

Figure 7.14 Modeled photoionization production rates of N_2^+ with magnetic field line topologies of a parabola anchored at the surface of Titan (green triangles), a parabola anchored at 725 km (purple crosses) and nested parabola (red stars) compared to the production rate of N_2^+ derived from INMS data using a simple two – reaction model adjusted by the factor shown in Figure 7.13 (blue diamonds) for the inbound leg of the T57 flyby of Titan.

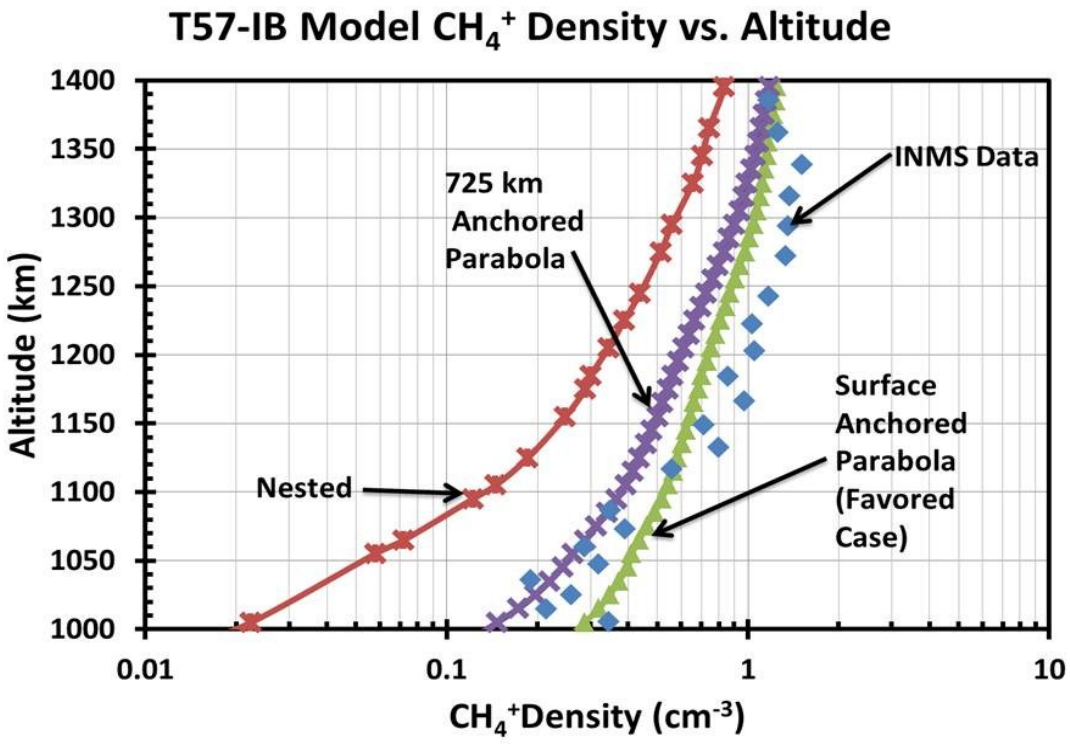

Figure 7.15 CH_4^+ density produced with the full photochemical model and magnetic field line topologies of a parabola achored at the surface of Titan (green triangles), a parabola anchored at 725 km (purple crosses) and nested parabola (red stars) compared to INMS data (blue diamonds) from the T57-Inbound flyby of Titan.

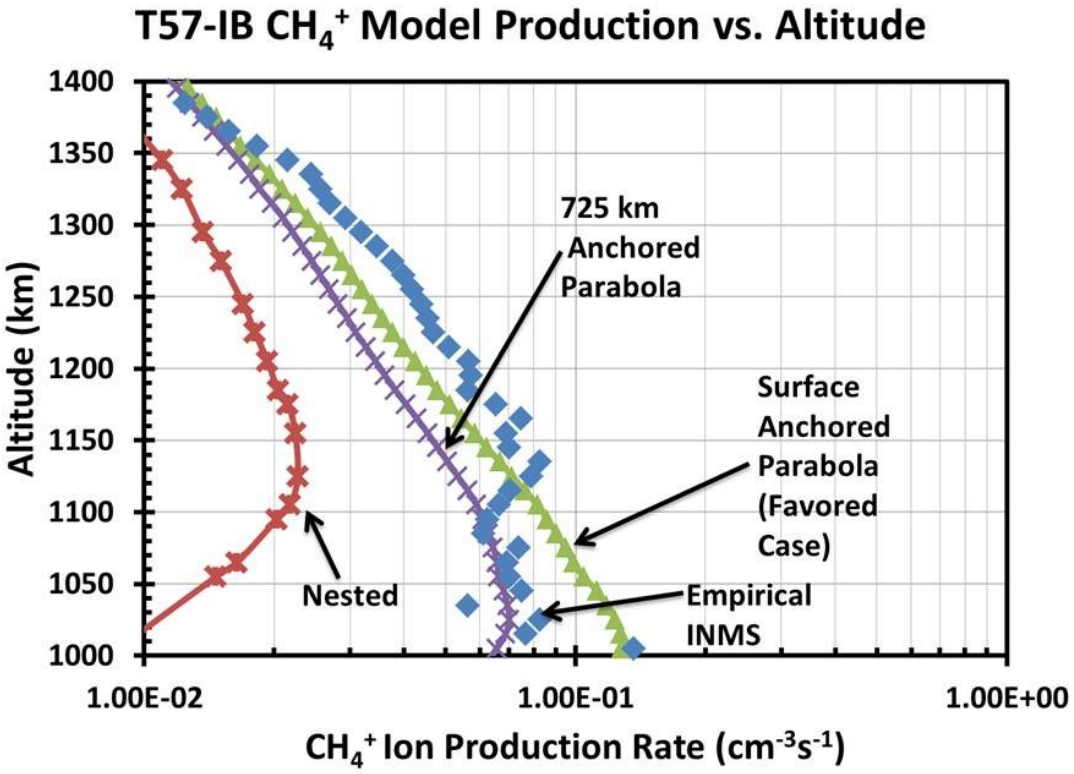

Figure 7.16 Modeled production rates of CH_4^+ with magnetic field line topologies of a parabola achored at the surface of Titan (green triangles), a parabola anchored at 725 km (purple crosses) and nested parabola (red stars) using the full photochemcial model compared to the empirical production rate of CH_4^+ derived from INMS data (blue diamonds) using the simple two-reaction chemical model for the T57-Inbound flyby of Titan.

7.1.2 Magnetospheric Electron Flux Classification of *Rymer et al.* [2009]

The material presented in the Section 7.1.1, has shown that the two-stream model (Section 3.3) in conjunction with the photochemical model (Section 3.4) is capable of producing reasonable amounts of N_2^+ and CH_4^+ by comparing modeled production rates with those determined empirically from INMS density measurements. In this section modeled production rates for the ionization products of the most abundant neutral species in Titan's ionosphere (N_2 and CH_4) will be shown using the magnetospheric electron fluxes presented by *Rymer et al.* [2009] without attenuation for their canonical magnetospheric electron flux conditions; lobe-like from the T8 flyby, plasma sheet from the T13 flyby, magnetosheath from the T32 flyby and bimodal from the T31 flyby (see Section 1.2 and Figure 7.1).

The goal of this section is to use these cases to create generic ion production profiles for the electron impact ionization of the neutral atmosphere resulting from magnetospheric electron precipitation along magnetic field lines. These production rates can then be combined with the generic solar photon produced production rates from Section 4.3 to create reasonable ion production rate profiles for various combinations of solar zenith angles and magnetospheric electron flux conditions. For all of these cases the globally averaged model of the neutral atmosphere discussed in Section 3.4.2.2 is used. Various magnetic field line topologies will be used (radial, parabola anchored at 725 km, and nested as was discussed in Section 3.1); however, only the results for the nested case will appear in this section for most flybys while the parabolic and radial field line cases will be shown in Appendix D-3 and D-4 respectively.

7.1.2.1 Products of N_2

Molecular nitrogen has two possible ionization products; N_2^+ and N^+. First, the production of N_2^+ will be examined for each of the magnetospheric electron flux categorizations

of *Rymer et al.* [2009] for nested magnetic field lines (Figure 7.17), a parabolic magnetic field line anchored at 725 km (Figure 7.18), and a radial magnetic field line (Figure 7.19).

In general higher energy electrons have smaller electron impact cross sections and will penetrated deeper into the ionosphere. This is why the lobe-like, plasma sheet and bimodal electron fluxes produce production rate profiles that peak at lower altitudes than the comparatively low energy magnetospheric electron flux of the magnetosheath. These higher energy electrons will also produce secondary electrons that can then go ionize neutral atoms resulting in a smaller peak below the main peak (see Figure 7.17). The larger the flux of precipitating electrons, the larger the ion production rate as there are more electrons to ionize the neutral atmosphere.

In addition to the impacts of energy and flux, the magnetic field line topology is important in determining where the electrons will deposit their energy [c.f. *Galand et al.*, 2010; *Gronoff et al.*, 2009b; *Robertson et al.,* 2009; *Richard et al.*, 2011]. Table 7.2 compares the peak ion production rates of N_2^+ along with the peak altitude for each of the magnetic field line topologies and each of the magnetospheric electron environments. In general the nested magnetic field line case, horizontal magnetic field lines, produces peak production rates 8-10 times lower than the parabola anchored at 725 km and 20-30 times lower than the radial magnetic field line. The peak altitude of the production rates generated with the nested magnetic field line is between approximately 150 (200) km higher than the peak altitude obtained with the parabolic magnetic field line anchored at 725 km (radial magnetic field line) for the lobe, bimodal and plasma sheet case and 200 (300) km higher for the magnetosheath case. These results are to be expected as the lower energy electrons more readily impact the neutral ions, thus

the flux will decay more rapidly than that of a higher energy electron population moving through the same amount of atmosphere.

Table 7.2 Peak production rate of N_2^+ for magnetospheric electron flux conditions of *Rymer et al.* [2009] and various magnetic field line topologies.

Magnetospheric Flux	Peak Production Rate of N_2^+ in $cm^{-3}s^{-1}$		
	Nested Magnetic Field Lines	Parabolic Magnetic Field Line Anchored at 725 km	Radial Magnetic Field Line
T8 - Lobe-like	0.02 @ 1175 km	0.2 @ 1050 km	0.5 @ 1000 km
T13 - Plasma sheet	0.08 @ 1400 km	0.6 @ 1250 km	2.0 @ 1160 km
T31 - Bimodal	0.11 @ 1200 km	0.7 @ 1040 km	3.0 @ 1000 km
T32 - Magnetosheath	0.53 @ 1550 km	0.5 @ 1350 km	1.2 @ 1275 km

It should also be noted that there are some jagged peaks that appear in Figure 7.19. This is an artifact of the model resolution as the radial field line model has a resolution of 35 km where the nested and parabolic magnetic field line geometries have 10 km resolution. The features and the peaks are still visible and can provide useful data. As the shape of the profile is similar regardless of the magnetic field line topology, only the production rates for the nested magnetic field line case will be shown. The production rate for N^+ is shown in Figure 7.20. For all of the other cases, refer to Appendix D-3 and D-4 for the parabolic magnetic field line anchored at 725 km and the radial magnetic field line cases respectively.

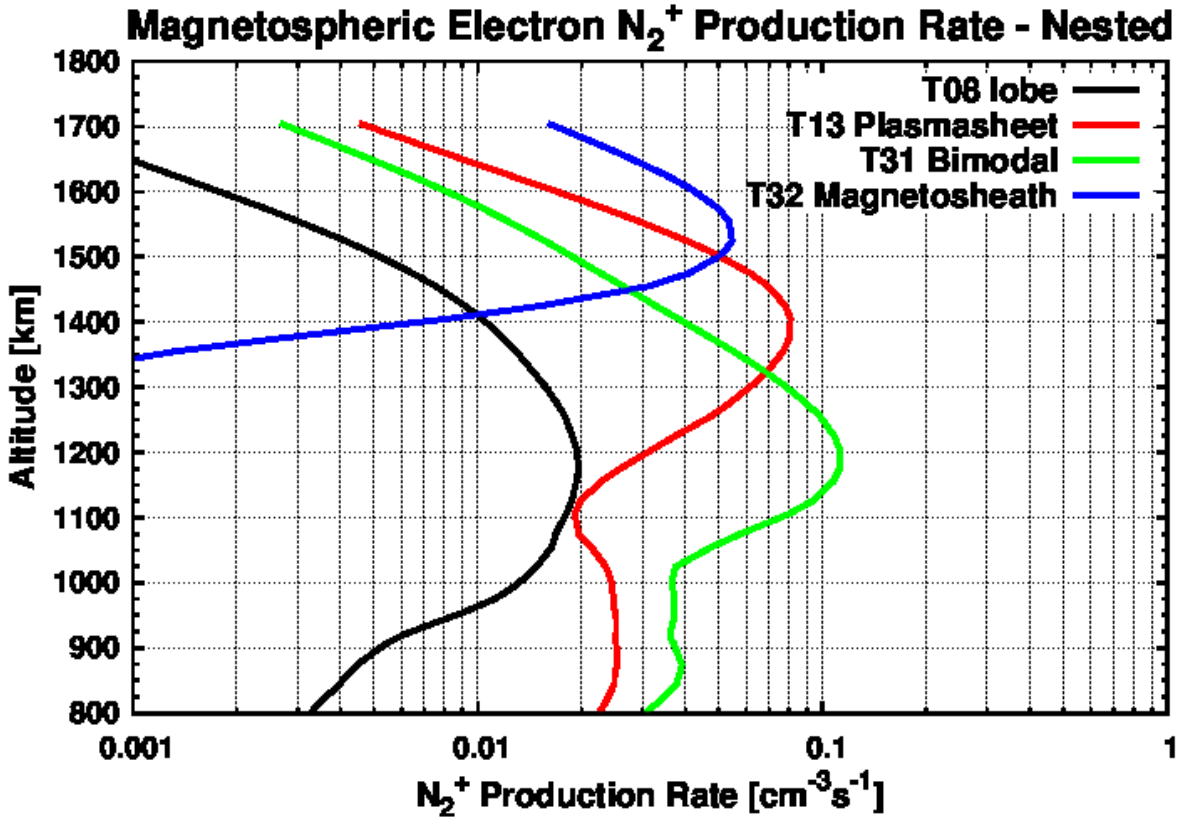

Figure 7.17 Production of N_2^+ using nested magnetic field line topology and the magnetospheric electron fluxes of the *Rymer et al.* [2009] classifications. Results are shown for model runs using the T8 lobe-like (black line), the T13 plasma sheet (red line), T31 bimodal (green line) and the T32 magnetosheath (blue line) electron fluxes measured by CAPS/ELS. The magnetospheric electron flux profiles are shown in Figure 7.3.

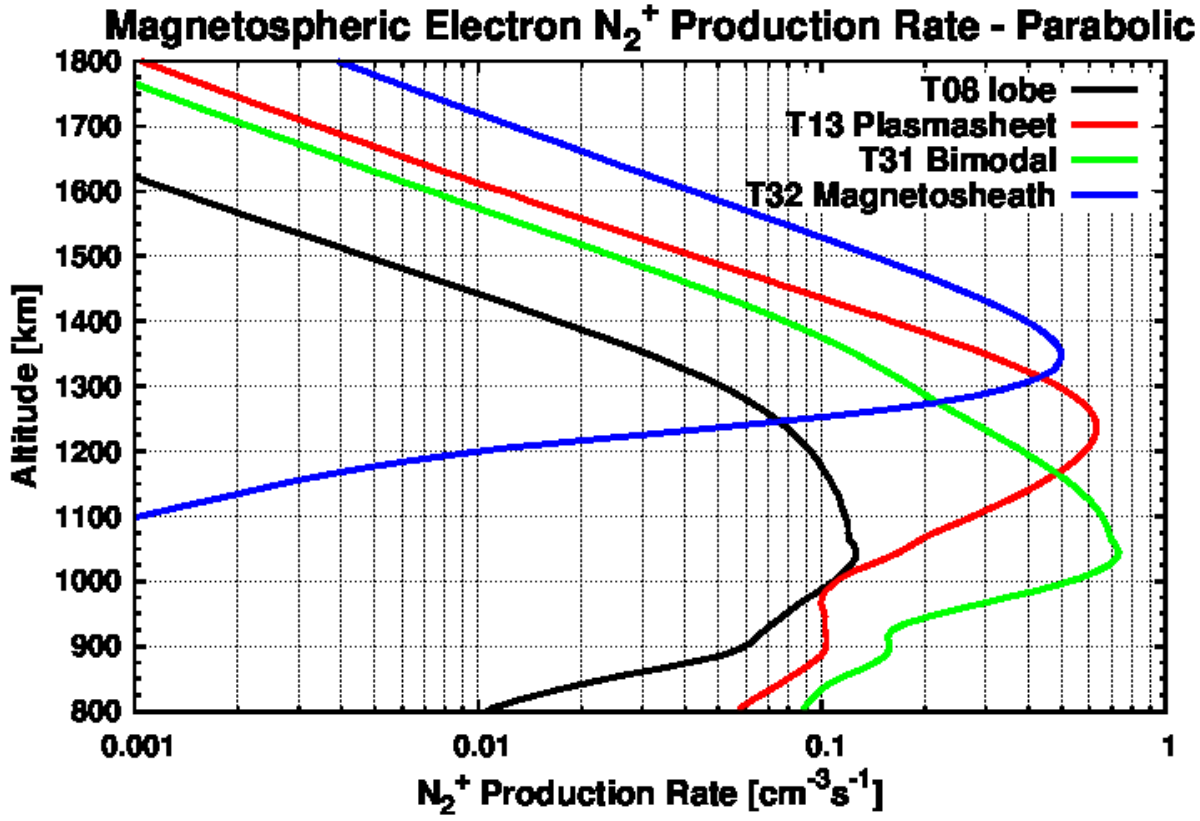

Figure 7.18 Production of N_2^+ using magnetic field line topology of a parabola anchored at 725 km and the magnetospheric electron fluxes of the *Rymer et al.* [2009] classifications. Results are shown for model runs using the T8 lobe-like (black line), the T13 plasma sheet (red line), T31 bimodal (green line) and the T32 magnetosheath (blue line) electron fluxes measured by CAPS/ELS. The magnetospheric electron flux profiles are shown in Figure 7.3.

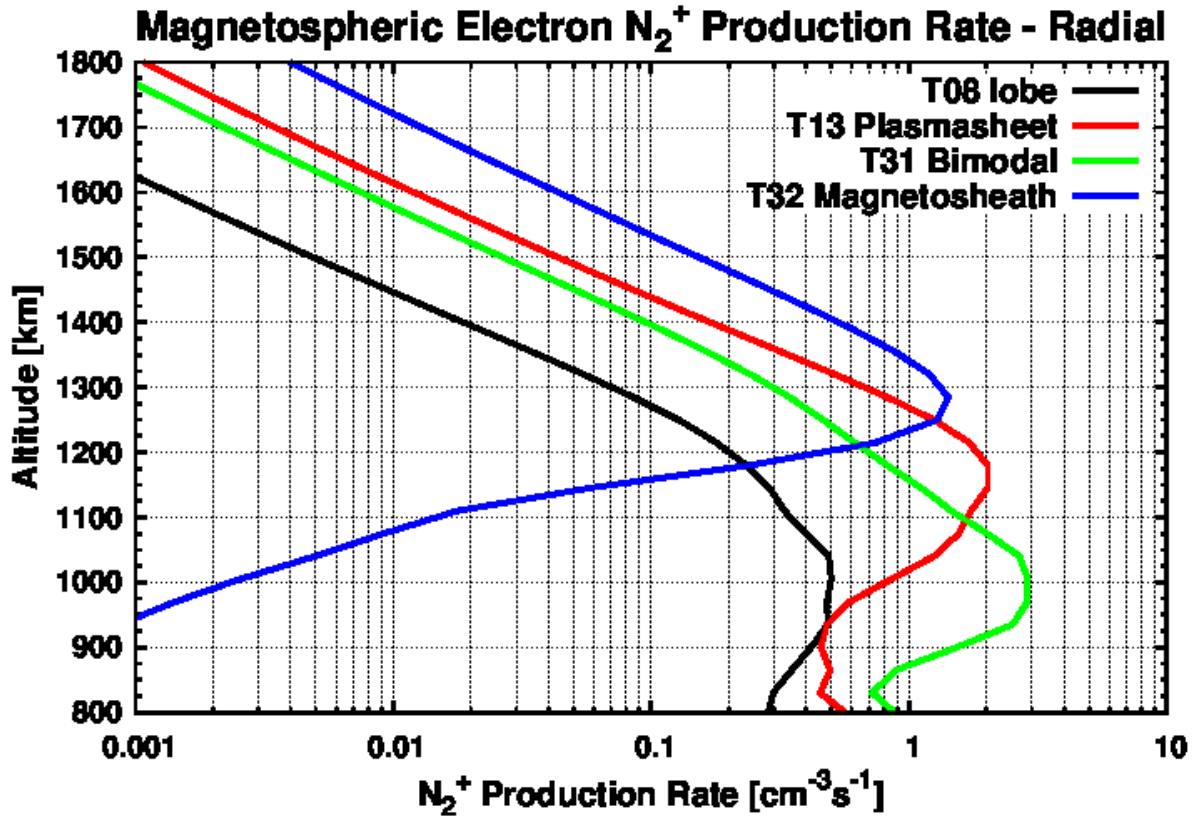

Figure 7.19 Production of N_2^+ using radial magnetic field line topology and the magnetospheric electron fluxes of the *Rymer et al.* [2009] classifications. Results are shown for model runs using the T8 lobe-like (black line), the T13 plasma sheet (red line), T31 bimodal (green line) and the T32 magnetosheath (blue line) electron fluxes measured by CAPS/ELS. The magnetospheric electron flux profiles are shown in Figure 7.3.

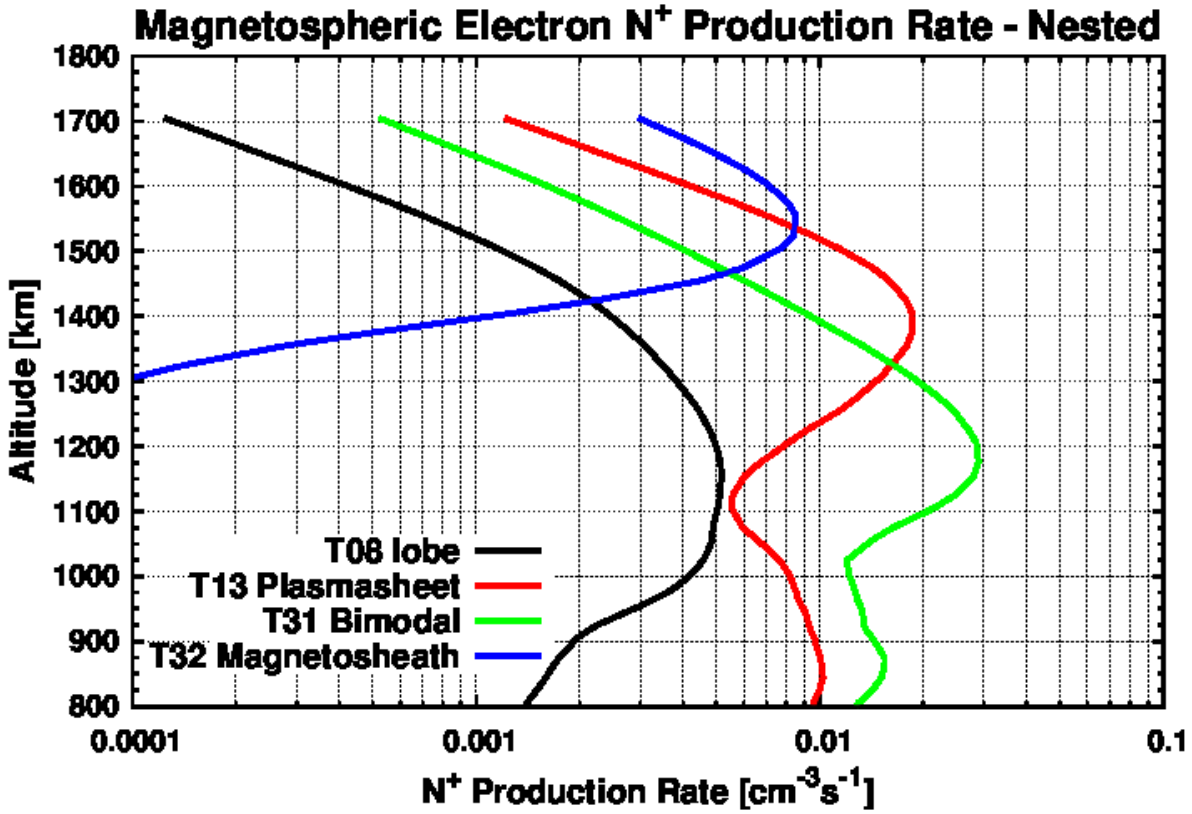

Figure 7.20 Production of N^+ using nested magnetic field line topology and the magnetospheric electron fluxes of the *Rymer et al.* [2009] classifications. Results are shown for model runs using the T8 lobe-like (black line), the T13 plasma sheet (red line), T31 bimodal (green line) and the T32 magnetosheath (blue line) electron fluxes measured by CAPS/ELS. The magnetospheric electron flux profiles are shown in Figure 7.3.

7.1.2.2 Products of CH_4

Ionization profiles have also been constructed for the ionization products of methane in the neutral atmosphere of Titan (CH_4^+, CH_3^+, CH_2^+, CH^+, C^+, H_2^+, and H^+) using the magnetospheric fluxes detailed in *Rymer et al.* [2009] (Figure 1.2) as inputs to the two-stream model (see Section 3.3). As was done in the previous section, the global average neutral atmospheric model (3.4.2.2) was used along with the three magnetic field line conditions (see Section 3.1) used in the previous section (nested, radial, and a parabola anchored at 725 km). The ion production rate profiles for CH_4^+, CH_3^+, CH_2^+, CH^+, C^+, H_2^+, and H^+ using the nested magnetic field lines (horizontal) are shown from Figure 7.21 to Figure 7.27 respectively. Ion production rate profiles generated using a parabolic magnetic field line and a radial magnetic field line are shown in Appendix D-3 and D-4.

The peak of the ionospheric production rate is shifted up or down depending on the ionization threshold of the product species. This is why the production rate of CH_4^+ peaks 25 km higher than the N_2^+ production rate, CH_4^+ has a lower ionization threshold so lower energy electrons that deposit their energy higher in the atmosphere will ionize methane. The shape of the production rate profiles for all of the ionization products are similar. Using the magnetosheath electron flux from T32 produces a production rate that peaks high in the atmosphere (between 1550 and 1650 km) with a higher production rate caused by a magnetospheric electron flux that has a higher density, but lower peak electron energy. Using the magnetospheric electron flux from the lobe-like (T8) or the plasma sheet (T13) magnetospheric electron fluxes produce ion production rates that peak between 1300 and 1450 km due to their similar peak energies; however the increased electron density in the plasma sheet causes the resulting production rates to be an order of magnitude larger than those produced when using the

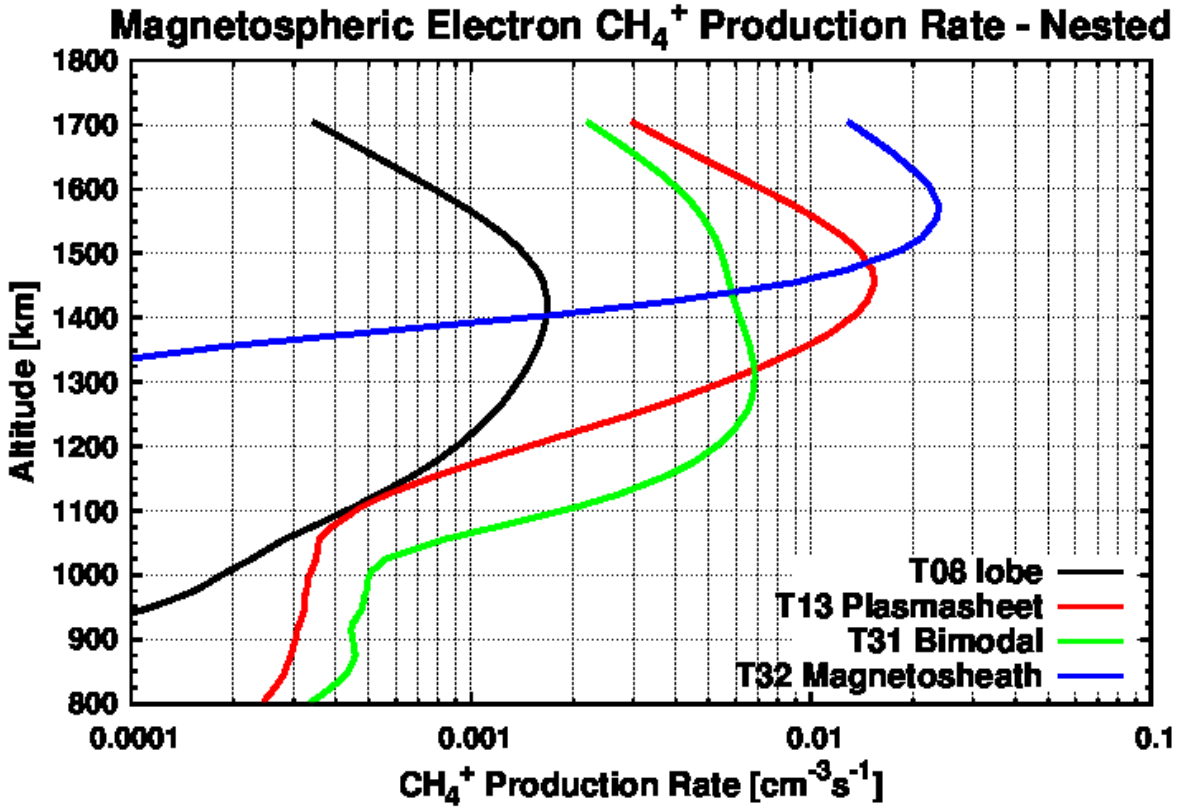

Figure 7.21 Production of CH_4^+ using nested magnetic field line topology and the magnetospheric electron fluxes of the *Rymer et al.* [2009] classifications. Results are shown for model runs using the T8 lobe-like (black line), the T13 plasma sheet (red line), T31 bimodal (green line) and the T32 magnetosheath (blue line) electron fluxes measured by CAPS/ELS. The magnetospheric electron flux profiles are shown in Figure 7.3.

lobe-like magnetospheric flux. Using the magnetospheric electron flux for the bimodal (T31) conditions of Titan generated a broader production peak than the previous cases. Here there is a small peak between 1550 and 1600 km resulting from the lower energy electrons which are the produced from ion pick-up. This transitions into the main peak between 1150 and 1300 km caused by the energy deposition from the lobe-like or plasma sheet electron population.

The production rate profiles generated in this section can be used in conjunction with the production rate profiles for the solar cases in order to create generic ion production profiles for a variety of solar zenith angles and magnetospheric electron conditions.

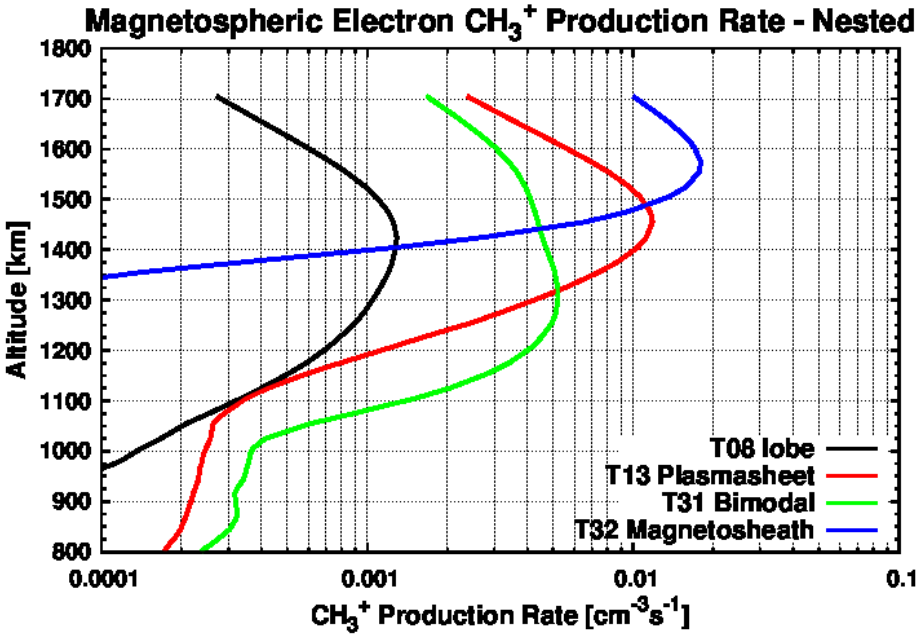

Figure 7.22 Production of CH_3^+ using nested magnetic field line topology and the magnetospheric electron fluxes of the *Rymer et al.* [2009] classifications. Results are shown for model runs using the T8 lobe-like (black line), the T13 plasma sheet (red line), T31 bimodal (green line) and the T32 magnetosheath (blue line) electron fluxes measured by CAPS/ELS. The magnetospheric electron flux profiles are shown in Figure 7.3.

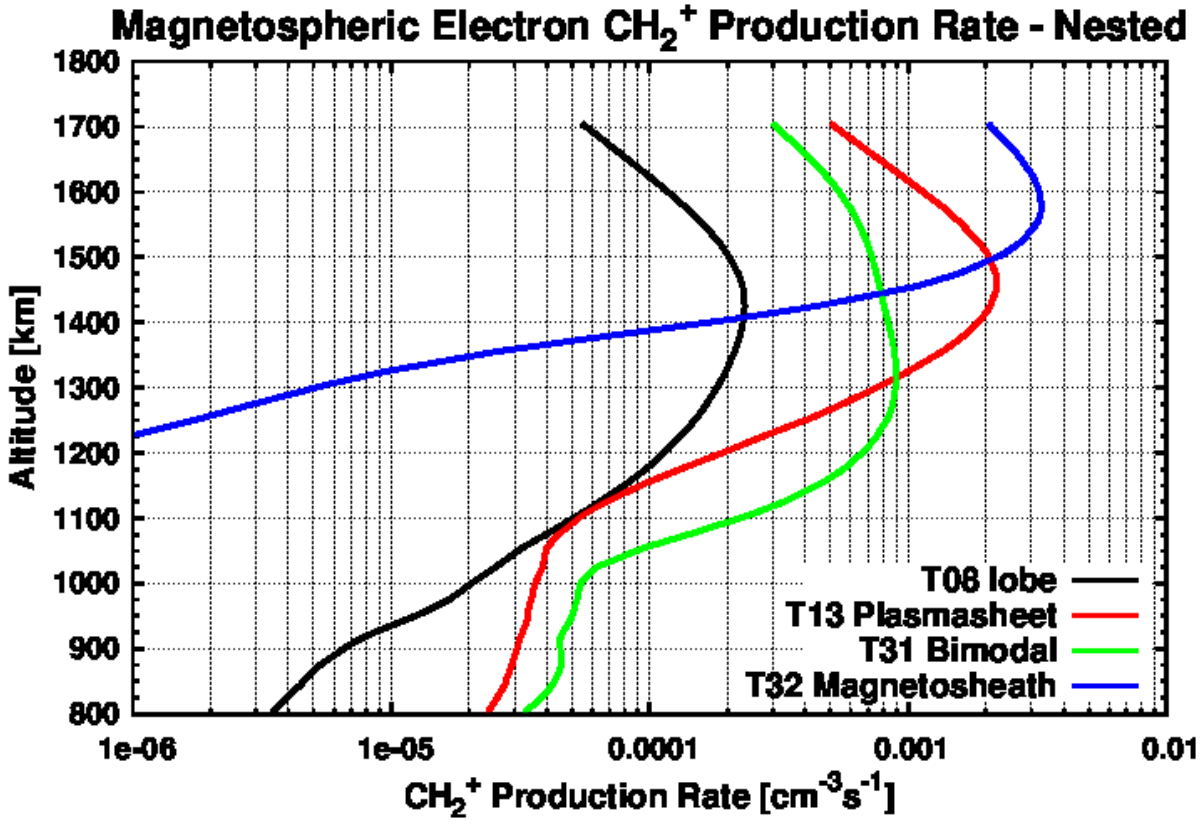

Figure 7.23 Production of CH_2^+ using nested magnetic field line topology and the magnetospheric electron fluxes of the *Rymer et al.* [2009] classifications. Results are shown for model runs using the T8 lobe-like (black line), the T13 plasma sheet (red line), T31 bimodal (green line) and the T32 magnetosheath (blue line) electron fluxes measured by CAPS/ELS. The magnetospheric electron flux profiles are shown in Figure 7.3.

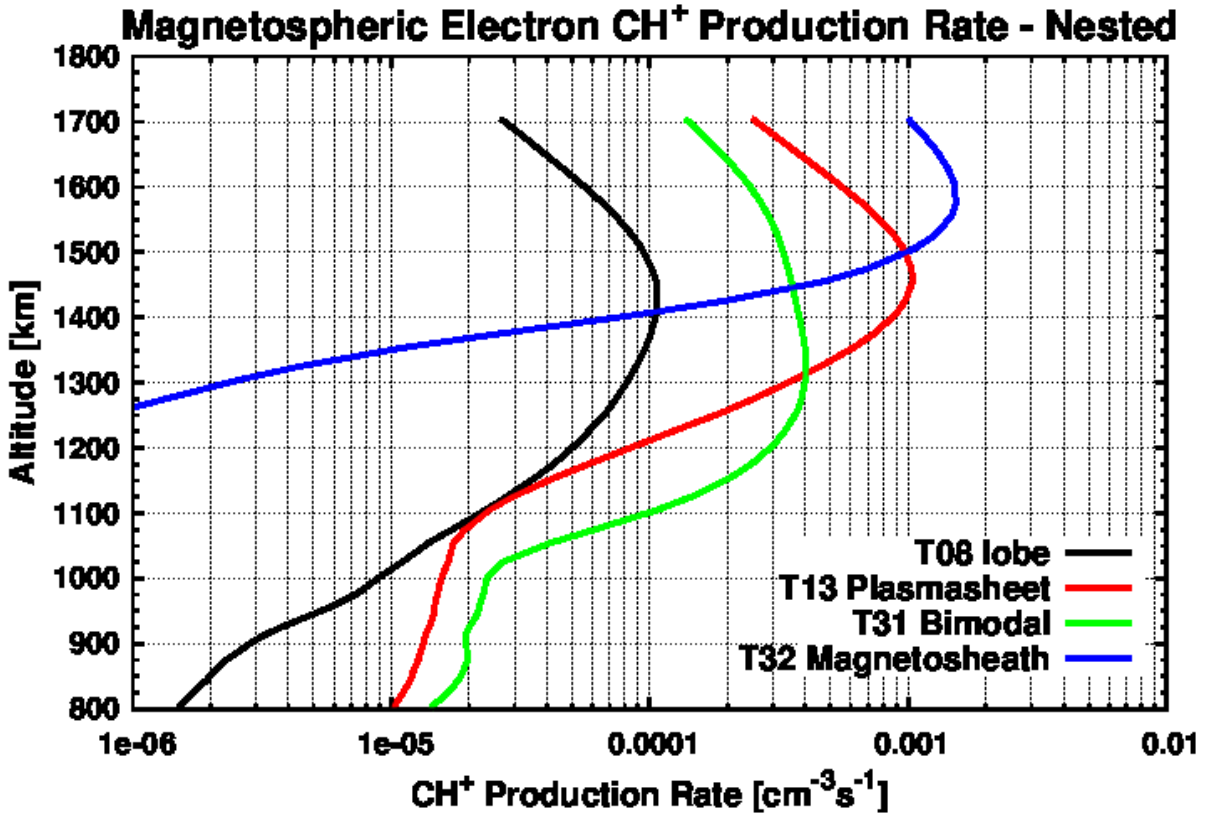

Figure 7.24 Production of CH^+ using nested magnetic field line topology and the magnetospheric electron fluxes of the *Rymer et al.* [2009] classifications. Results are shown for model runs using the T8 lobe-like (black line), the T13 plasma sheet (red line), T31 bimodal (green line) and the T32 magnetosheath (blue line) electron fluxes measured by CAPS/ELS. The magnetospheric electron flux profiles are shown in Figure 7.3.

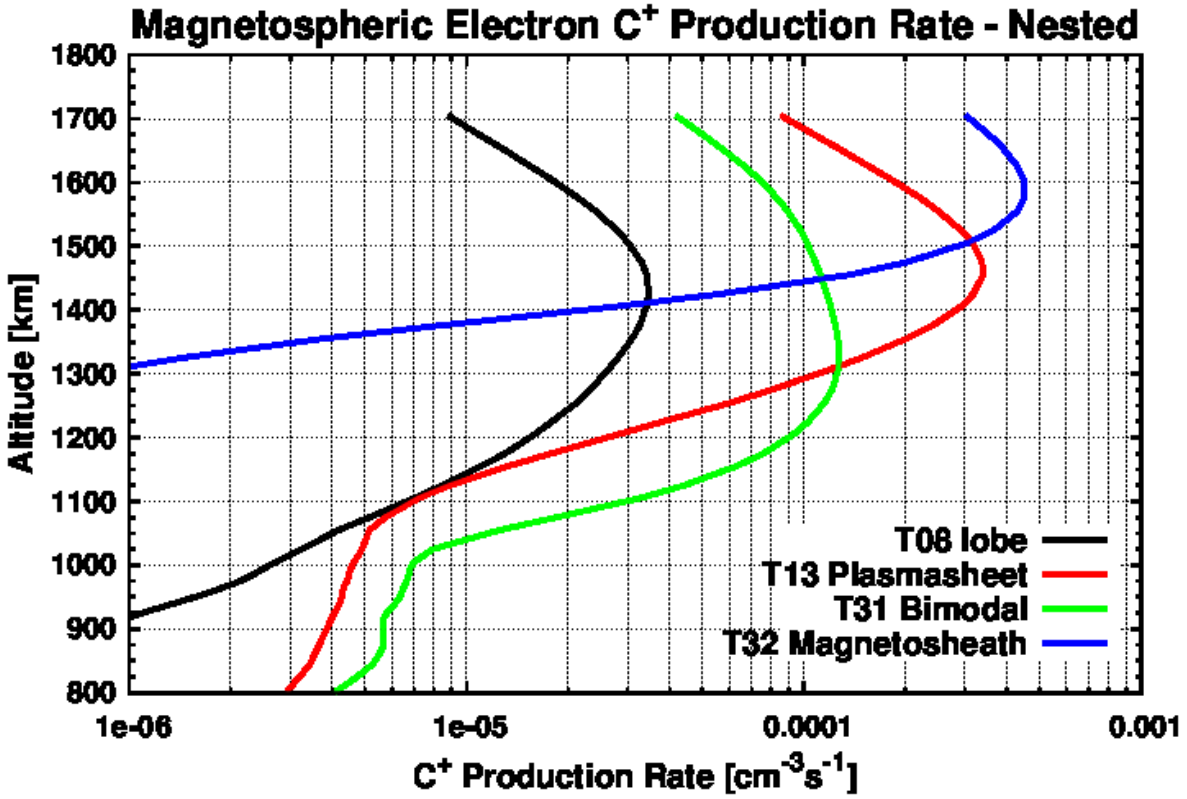

Figure 7.25 Production of C^+ using nested magnetic field line topology and the magnetospheric electron fluxes of the *Rymer et al.* [2009] classifications. Results are shown for model runs using the T8 lobe-like (black line), the T13 plasma sheet (red line), T31 bimodal (green line) and the T32 magnetosheath (blue line) electron fluxes measured by CAPS/ELS. The magnetospheric electron flux profiles are shown in Figure 7.3.

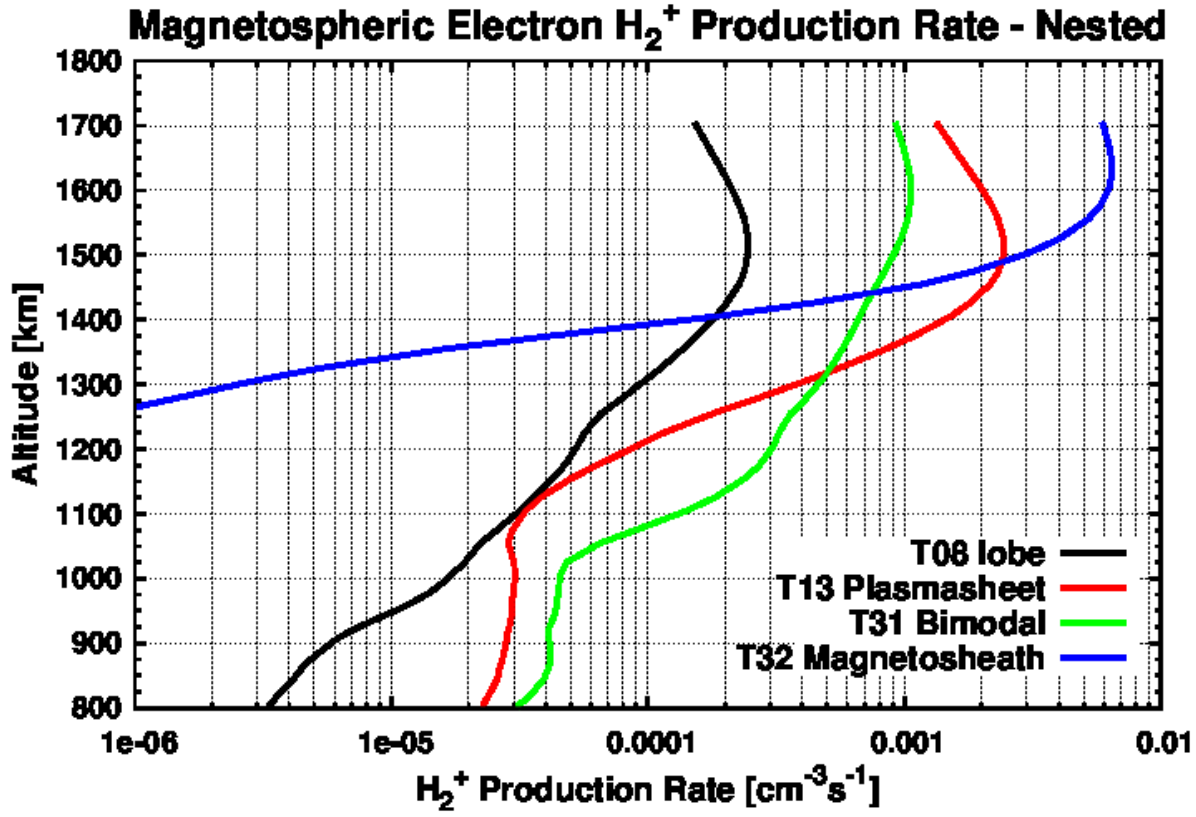

Figure 7.26 Production of H_2^+ using nested magnetic field line topology and the magnetospheric electron fluxes of the *Rymer et al.* [2009] classifications. Results are shown for model runs using the T8 lobe-like (black line), the T13 plasma sheet (red line), T31 bimodal (green line) and the T32 magnetosheath (blue line) electron fluxes measured by CAPS/ELS. The magnetospheric electron flux profiles are shown in Figure 7.3.

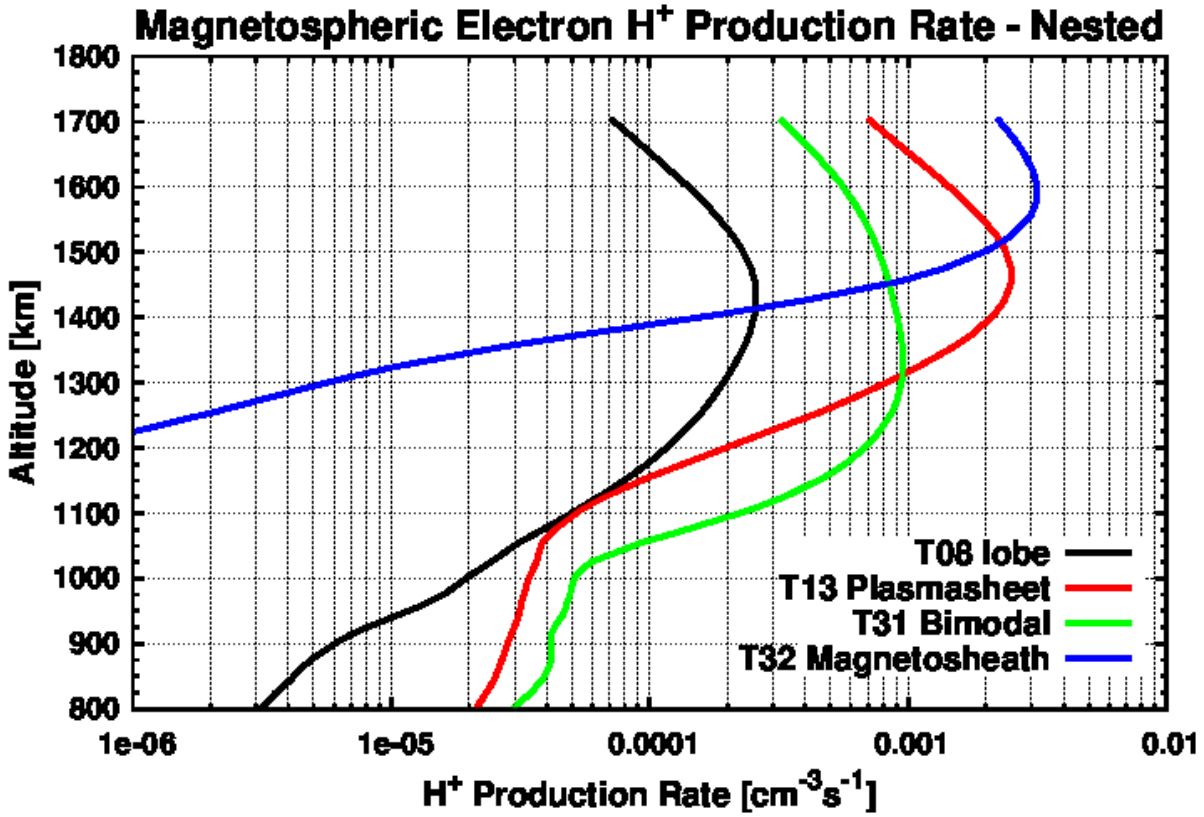

Figure 7.27 Production of H^+ using nested magnetic field line topology and the magnetospheric electron fluxes of the *Rymer et al.* [2009] classifications. Results are shown for model runs using the T8 lobe-like (black line), the T13 plasma sheet (red line), T31 bimodal (green line) and the T32 magnetosheath (blue line) electron fluxes measured by CAPS/ELS. The magnetospheric electron flux profiles are shown in Figure 7.3.

7.2 Modeling Electron and Ion Temperatures in the Nightside Ionosphere of Titan

In addition to ion production rate profiles, the two-stream electron code (3.3) also generates heating rates for the thermal electron population due to electron impact collisions between precipitating magnetospheric electrons and secondary electrons resulting from higher energy electrons in the thermal electron population creating ions in the neutral atmosphere. These heating rates are used as inputs into the temperature code which generates the electron and ion temperature profiles along a magnetic field line (see Section 3.7).

In this section, comparisons will be made between the modeled temperatures and electron temperatures measured by RPWS/LP [*Agren et al.,* 2007] and ion temperatures inferred by *Crary et al.* [2009] from measurements made by the CAPS-IBS. After the model has been verified and found to produce electron temperatures that are in agreement with the measured electron and ion temperatures, electron temperature profiles for the nightside of Titan will be generated using the globally averaged model of the neutral atmosphere with the neutral densities increased by a factor of 3.15 and the full magnetospheric electron fluxes from the cases described by *Rymer et al.* [2009] (Figure 1.2) without the use of solar inputs. Temperature profiles will be constructed for a case with nested magnetic field lines, a radial field line and parabolic magnetic field lines anchored at 725 km assuming a neutral temperature of 150 K [c.f. *Cravens et al.,* 2009b]. These temperatures can then be used in chemical models in order to establish proper electron recombination rates which are temperature dependent.

7.2.1 Electron and Ion Temperature Comparisons with T5 Data

The details of the T5 flyby of Titan have been discussed in Section 7.1.1.1. This flyby has been studied extensively as an example of Titan's nightside ionosphere [*Agren et al.,* 2007;

Cravens et al,. 2008; 2009a; *Robertson et al.,* 2009; *Richard et al.,* 2011] and will be used to evaluate the efficacy of the temperature model on the nightside of Titan in a similar manner to the work of *Richard et al.* [2011]. When modeling the temperature profile of the T5 encounter, the factor of 3.15 increase to the neutral densities was not included. If this factor was included, the modeled temperature profiles would shift upwards in altitude approximately 60 km.

Five cases are considered in our nightside model and are described below.

- C*ase N1* – Reduced Magnetospheric Electron Flux with E > 10 eV Only – This case will serve as the baseline case for the nightside model. The magnetic field line topology was a parabola anchored at the surface of Titan reflecting the 45˚ angle with respect to the radial direction observed by the magnetometer (Figure 3.2). Electron fluxes in the magnetosphere near Titan on magnetic flux tubes linked to Titan appear to be attenuated, or depleted, probably due to losses associated with interaction with Titan's ionosphere. This attenuation of the magnetospheric electron flux, which we use as our upper boundary condition, lowers ion production rates and associated thermal electron heating rates resulting from magnetospheric electron precipitation. In order to bring chemically modeled ion densities into agreement with INMS ion density measurements, *Cravens et al*. [2009a] applied an attenuation factor of 2.5 to the magnetospheric electron flux. This same reduction was applied in the current paper for this case. Only the contribution to the ionospheric energetics of the magnetospheric suprathermal population with energies above 10 eV is considered for this particular case, in order to exclude any possible spacecraft photoelectron contribution to the CAPS data; however, this also excludes the heating effects of very low energy magnetospheric electrons. Other cases will remove this restriction.

- *Case N2* – Triple Neutral Density – This case is identical to the N1 case except that the neutral densities have been tripled.
- *Case N3* – Reduced Magnetospheric Electron Flux over Full Energy Range – Suprathermal electrons with energies less than 10 eV were not used in the N1 case, but for the N3 case the full energy range (up to 5 keV) of the CAPS ELS suprathermal electron flux from *Cravens et al.* [2008] were included in the calculations.
- *Case N4* – Full Magnetospheric Electron Flux with E > 10 eV Only – Cases N1, N2, and N3 reduced the magnetospheric electron fluxes and hence the heating rates obtained with the input of CAPS-ELS magnetospheric electron fluxes for T5 by a factor of 2.5. This was needed for the modeled ion densities of *Cravens et al.* [2009a] to be brought into agreement with measured values in a model ionosphere. For case N4 the full magnetospheric electron flux rate from the external magnetospheric electron fluxes is adopted; however, only magnetospheric electrons with energies greater than 10 eV are included.
- *Case N5* – Full Magnetospheric Electron Flux over Full Energy Range – This case utilizes the full CAPS-ELS measured suprathermal electron flux over the full energy range up to 5 keV.

Using the magnetospheric electron flux measured by CAPS ELS [*Cravens et al.*, 2008] during the T5 flyby without attenuation and with electrons with E < 10 eV and a parabolic field line anchored at the surface of Titan, the two stream code (Section 3.3) generated the heating rates shown in Figure 7.28. This figure also shows that increasing the neutral densities by a factor of 3 will increase the altitude at which the heating rate peaks by 60 km.

Figure 7.29 and Figure 7.30 show the model electron temperatures for the nightside cases. Figure 7.29 shows that for the N1 case (magnetospheric electrons with energies less than 10 eV were excluded and the overall flux was reduced by a factor of 2.5) the calculated thermal electron temperatures are ~400 K lower than the temperatures reported by RPWS [*Agren et al.,* 2007] at 1200 km. Tripling the neutral densities (N2) resulted in a shift of the temperature curve up in altitude by 60-80 km, approximately one neutral scale height, but the shape of the curve is similar to the previous case. Including suprathermal electrons with energies less than 10 eV raised the thermal electron temperature at the higher altitudes (above 1300 km) by 250 K to a temperature of 900 K. Although reducing the magnetospheric electron flux (and the associated thermal electron heating rates) as was done in the N1, N2 and N3 cases provided the necessary correction to the ionospheric model densities of *Cravens et al*. [2009a] and *Agren et al.* [2007], the heat input is apparently not adequate, as the modeled electron temperatures are approximately 400 K lower than RPWS-LP values at 1200 km [*Agren et al*., 2007].

Cases N4 and N5 (Figure 7.30) show that with the full magnetospheric electron flux, and hence the full heating rate, the modeled electron temperatures agree with the RPWS measurements at 1200 km. The N4 case also shows that using the full magnetospheric electron flux (but with energies less than 10 eV excluded) produces electron temperatures that agree with RPWS measured temperatures of about 1100 K in the vicinity of 1300 km. At 1400 km the model temperatures are still somewhat lower than RPWS temperatures by 400 K. The N5 case also included magnetospheric electrons with energies less than 10 eV (no flux attenuation or reduction was included). The calculated electron temperature is now close to 1500 K at an

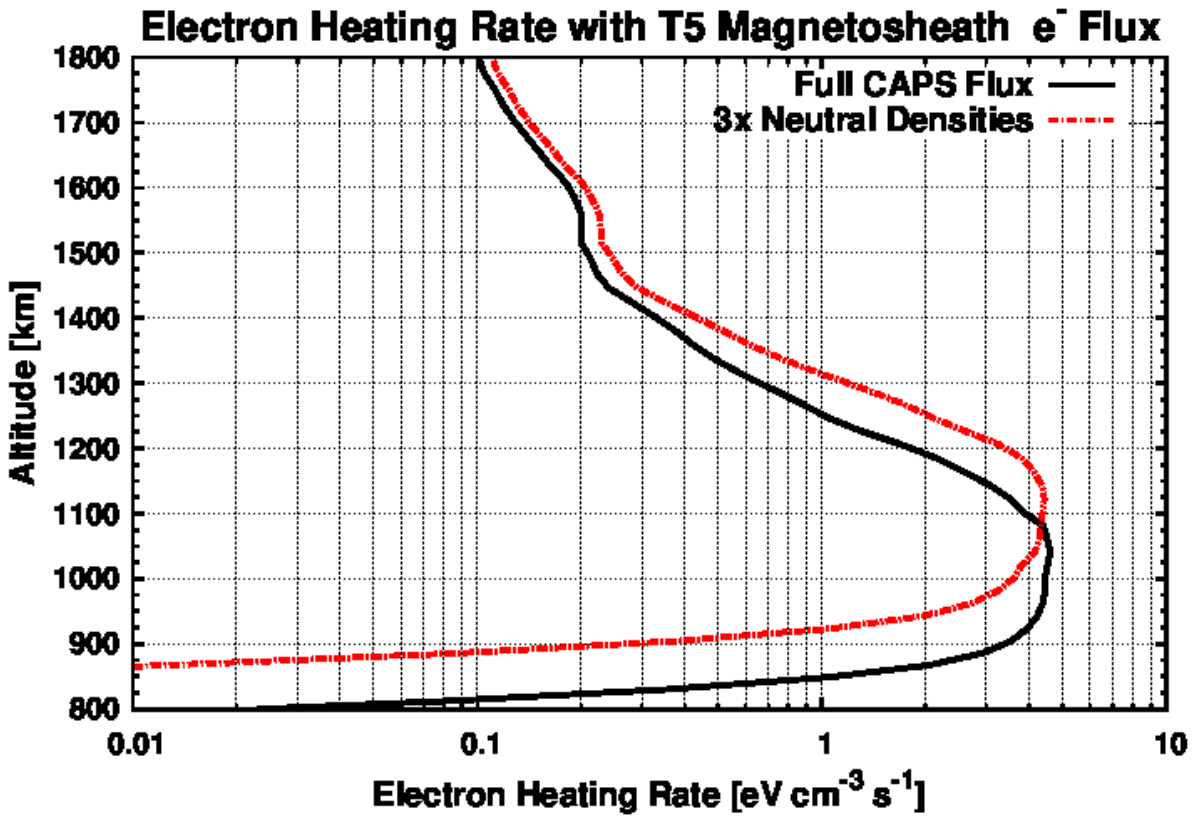

Figure 7.28 Thermal electron heating rates using the T5 magnetospheric electron fluxes measured by CAPS ELS [*Cravens et al.*, 2008] without attenuation and including electrons with energies less than 10 eV. Cases are shown for the case of a parabolic magnetic field line anchored at the surface of Titan using the T5 neutral atmosphere(black line) and a case where the T5 neutral densities have been multiplied by a factor of 3 (red line).

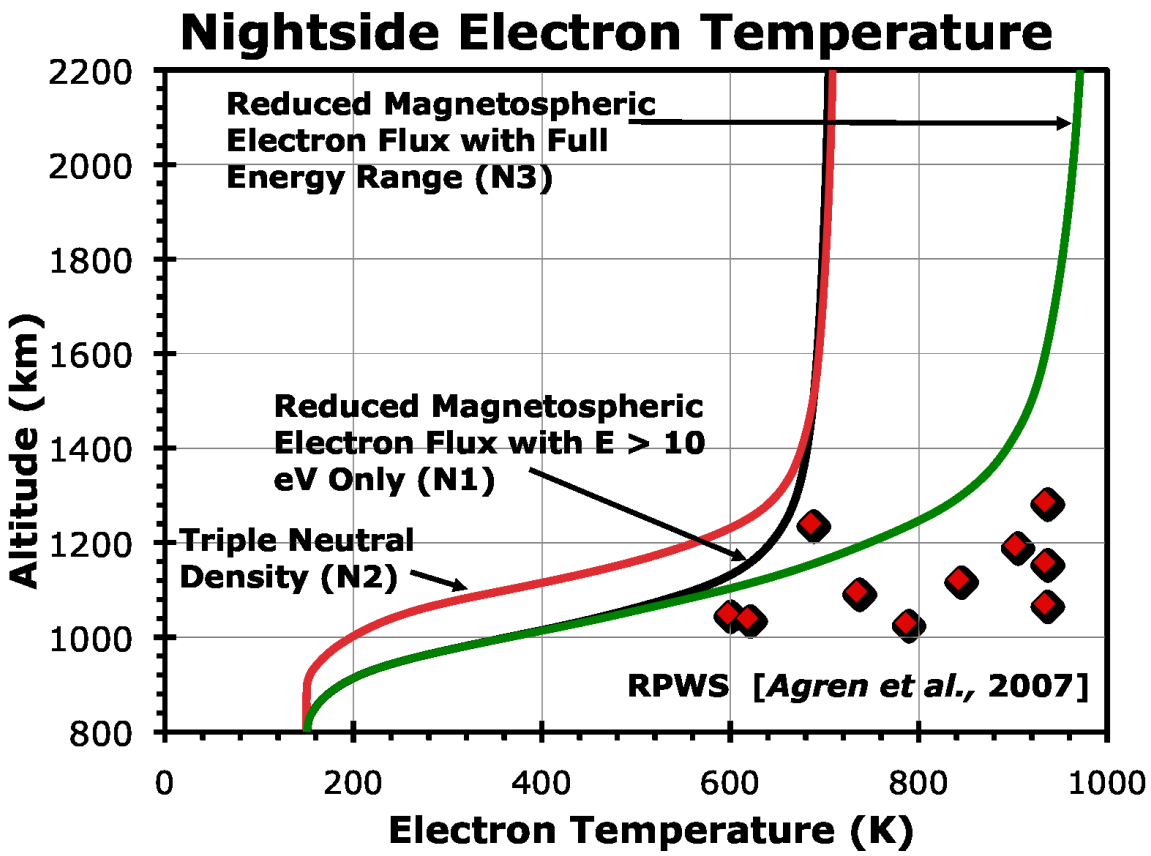

Figure 7.29 Electron temperatures vs. altitude are shown for cases N1, N2 and N3 on the nightside (see the text for the description but for these cases the magnetospheric electron fluxes measured in the magnetosphere were reduced by a factor of three before introducing them into the model, for reasons discussed in the text). The surface anchored parabolic magnetic field case was chosen to give a field direction at 1100 km in agreement with magnetometer data [cf. *Cravens et al.*, 2009]. The field has a significant radial component. The temperatures measured by the RPWS-LP during the T5 flyby [*Agren et al.*, 2007] are larger than the calculated temperatures in all cases, although the model N3 case gets close. Tripling the INMS neutral densities will just shift the temperature curve up by about 60 km (i.e., a neutral scale height).

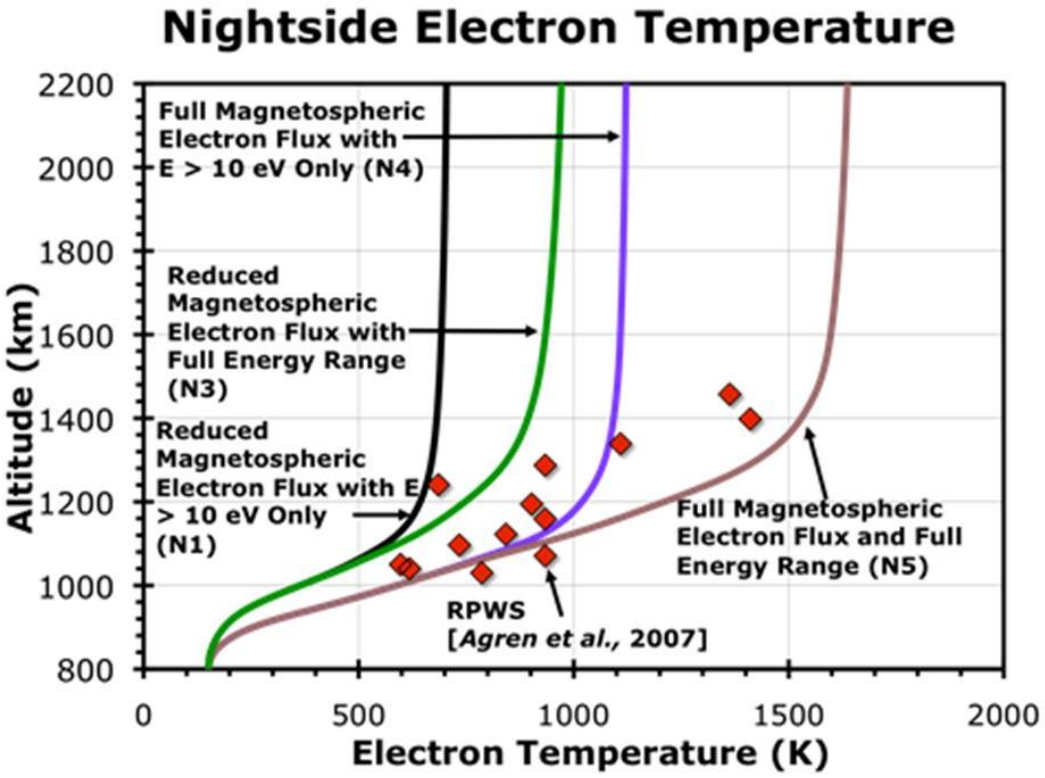

Figure 7.30 Electron temperatures vs. altitude are shown for cases N1, N3, N4 and N5 on the nightside. For cases N4 and N5, the electron fluxes input into the ionosphere in the model were not reduced from their magnetospheric values. A surface anchored parabolic magnetic field with a significant radial component was used for each case [cf. Cravens et al., 2009]. Better agreement between model and data is obtained with cases N4 and N5.

altitude of 1360 km. N5 shows the best agreement between the modeled temperatures and the RPWS [*Agren et al.*, 2007] T5 measurements, differences of only ≈ 25 K near 1100 km and ≈ 100 K a near 1400 km (i.e., within 15%). If the neutral densities were tripled the N5 curve on Figure 7.30 would be shifted upward by about 70 km and bring the modeled temperatures into even better agreement with the RPWS values. This illustrates the importance to the thermal electron energy balance of the upper ionosphere of the input of magnetospheric electrons of all energies, including lower energies below 10 eV.

The calculated ion temperatures for the above cases are presented in Figure 7.31. Note that dynamical terms were not included in the ion energy equation for these cases. As mentioned for the dayside results, the ion temperature is strongly coupled to the neutral temperature below approximately 1400 km. The model ion temperatures for the nightside case above 1400 km indicate that dynamical terms in the ion energy equation no doubt play a role in the upper ionosphere on the nightside as they do on the dayside. As the thermal electron temperature increases and the electrons become more energetic, their collisional cross-section with the thermal ions decreases [cf. *Gan et al.,* 1992, 1993], therefore lowering the ion temperature as shown.

7.2.2 Temperature Profiles for the Magnetospheric Conditions of *Rymer et al.* [2009]

After demonstrating that the energetic model (see Section 3.7) is capable of producing reasonable electron temperature profiles by comparing the modeled temperature profiles with the electron temperature measurements of the T5 flyby made by RPWS/LP and the inferred ion temperatures from *Crary et al.* [2009], generic temperature profiles for the thermal electrons and ions of mass 29 amu have been generated for the lobe-like (T8), plasma sheet (T13), magnetosheath (T32) and bimodal (T31) magnetospheric electron populations presented by

Rymer et al. [2009]. Cases are shown for nested, radial (anchored at 725 km) and parabolic (parabola anchored at 725 km) magnetic field line topologies so that the temperature profiles that are generated can be used in general modeling efforts and chosen based upon the magnetic field line observations or predictions.

7.2.2.1 Lobe-like

Using the lobe-like magnetospheric electron flux from the T8 flyby and the globally averaged neutral atmosphere (Section 3.4.2.2) as inputs into the two-stream code (Section 3.3), which computes the thermal electron heating rates, which then feed into the energetics code (Section 3.7), produces the electron temperature profiles shown in Figure 7.32. As was discussed in Section 5.2, the larger the radial component of the magnetic field the more readily energy is conducted down the magnetic field line where larger densities of atmospheric neutrals increase the cooling rate of the thermal electrons; however, this also allows magnetospheric electrons to deposit their energy deeper into the ionosphere resulting in larger heating rates lower in the ionosphere (Figure 7.33, other heating rate profiles appear in Appendix D-4). The electron temperature along the radial magnetic field line begins to deviate from the thermal electron temperature at 925 km and increases to 200 K at 1200 km.

Magnetospheric electrons travelling along the parabolic field lines pass though more of the neutral atmosphere before reaching lower altitudes and deposit their energy higher in the ionosphere. This is the reason that the electron temperature calculated for the nested and parabolic magnetic field line deviates from the thermal electron temperature at altitudes 200 and 75 km above the altitude at which the electron temperature deviates for the radial case. Above

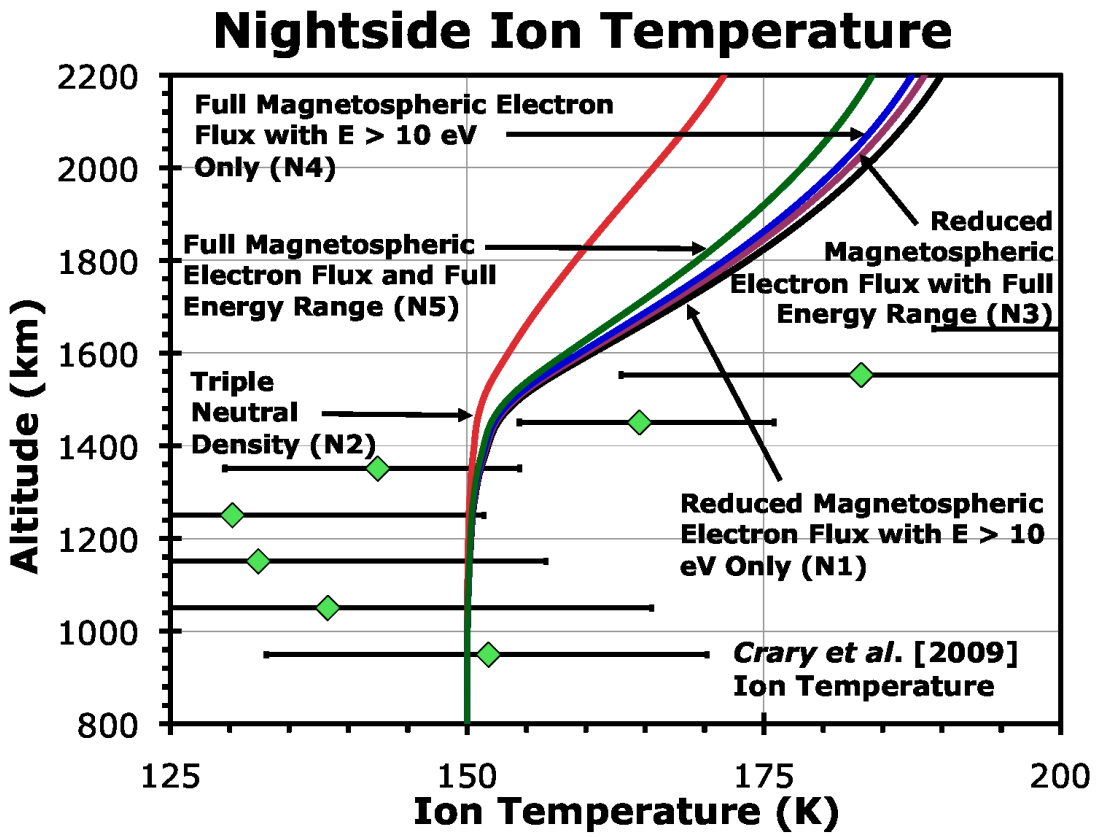

Figure 7.31 Ion temperatures as a function of altitude for the nightside (T5 flyby) of Titan. No ion dynamical terms were included. All curves are in good agreement with the measured values given by Crary et al. [2010] below about 1400 km but not at higher altitudes.

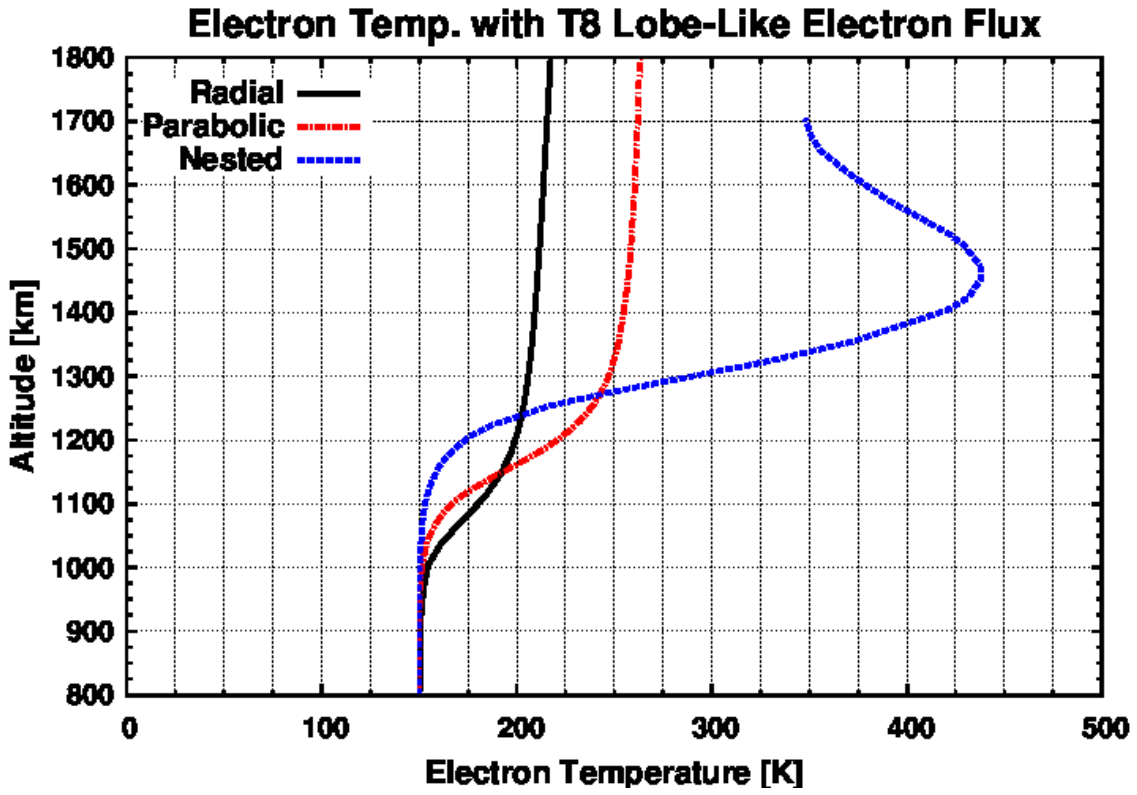

Figure 7.32 Electron temperature generated using the T8 lobe-like magnetospheric electron flux shown by *Rymer et al.* [2009] for the cases of nested magnetic field lines (blue dotted line), a parabolic magnetic field line anchored at 725 km (red dashed line), and a radial magnetic field line (black line).

1200 km the electron temperature along the parabolic magnetic field line reaches thermal equilibrium at a temperature near 250 K. The nested case exhibits more structure in its electron temperature profile as the temperatures at the subsolar points of multiple parabolic field lines have been compiled, simulating local energy deposition into the ionosphere. For this reason, the electron temperature computed for the nested magnetic field lines increases to a peak temperature of 425 K at 1450 km coinciding with the peak location of the ion production and energy deposition. Above this altitude the heating rate diminishes causing lower electron temperatures.

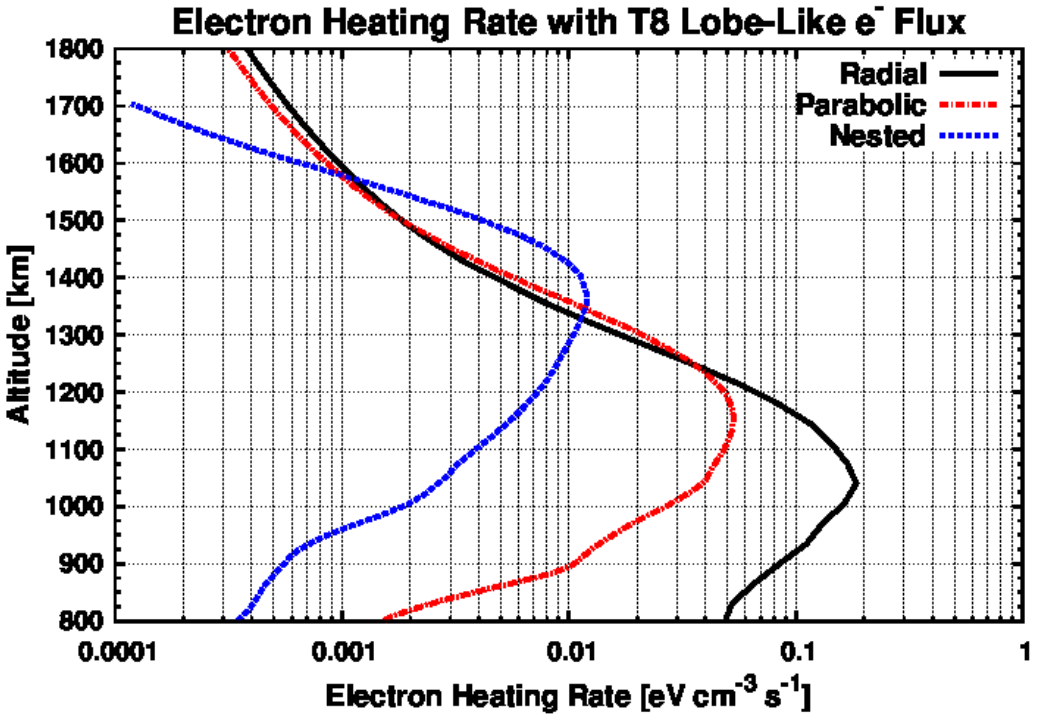

Figure 7.33 Thermal electron heating rate generated using the two-stream model using the magnetospheric flux of electrons measured by CAPS ELS [*Rymer et al.*] during the T8 lobe-like flyby of Titan. Results are shown using a radial magnetic field line anchored at 725 km (black solid line), a parabolic field line anchored at 725 km (red dashed line) and nested magnetic field line topologies (blue dotted line).

7.2.2.2 Plasma Sheet (T13)

Figure 7.34 shows the modeled electron temperatures computed with the energetics model (see Section 3.7) using the T13 plasma sheet magnetospheric electron flux. The magnetospheric electron flux for the T13 plasma sheet had a similar peak energy to the lobe-like magnetospheric flux of the T8 flyby; however, the flux of superthermal electrons for the lobe-like case is an order of magnitude lower than the electron flux observed in the plasma sheet. This results in similarity in the altitudes at which features occur in the electron temperature profiles for the two cases due to fact that the depth at which an electron deposits its energy is a function of its energy. The increased flux of superthermal electrons observed during the plasma sheet encounter of T13 causes the resulting electron temperatures to be larger than the modeled temperatures for the lobe-like distribution. Modeled electron temperatures along the radial magnetic field line begin to rise at 975 km and reach a temperature of 400 K at 1500 km. Adopting the single parabolic magnetic field line anchored at 725 km produced an electron temperature profile that deviates from the neutral temperature near 1050 km and reaches thermal equilibrium at an altitude of 1300 km at a temperature of 500 K. Electron temperatures computed using nested magnetic field lines increase the neutral temperature at an altitude above 1200 km and peak at 850 K at an altitude of 1475 km where, again matching the peak in ion production.

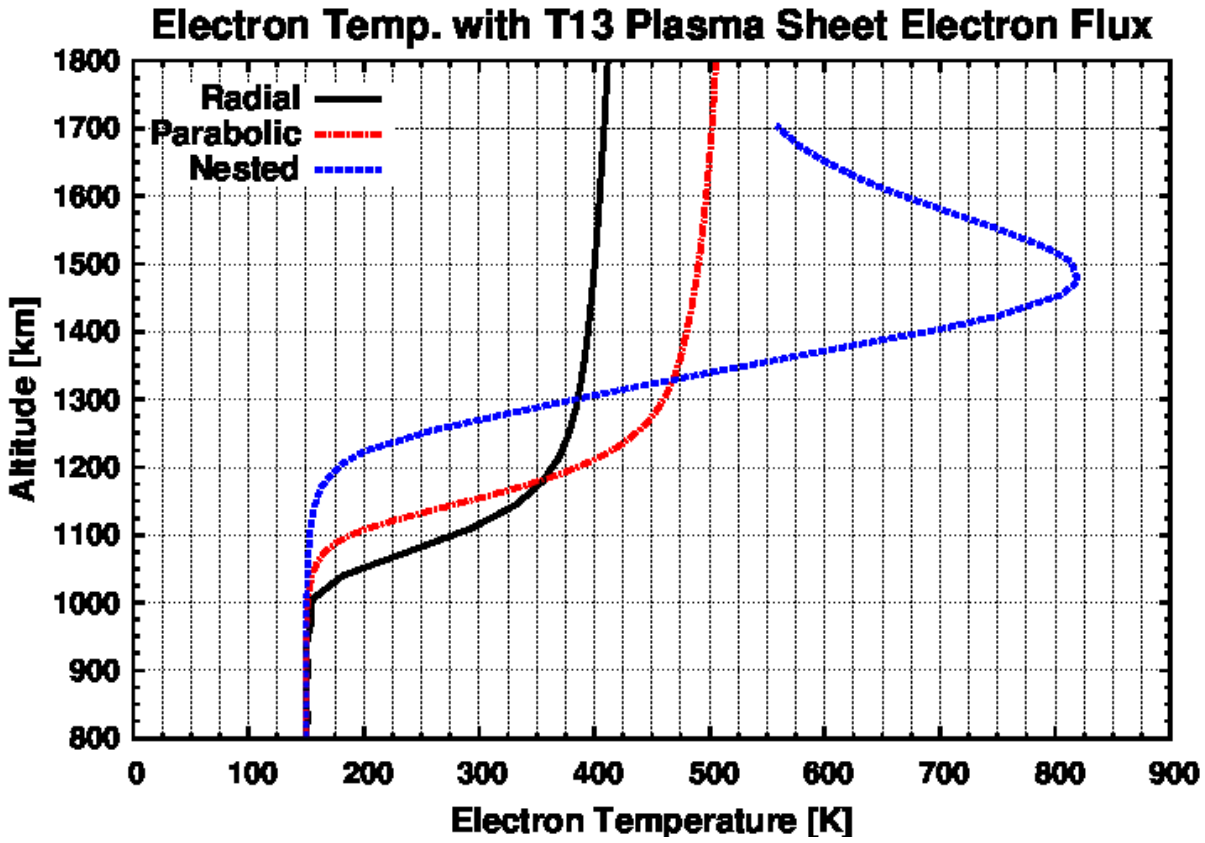

Figure 7.34 Electron temperature generated using the T13 plasma sheet magnetospheric electron flux shown by *Rymer et al.* [2009] for the cases of nested magnetic field lines (blue dotted line), a parabolic magnetic field line anchored at 725 km (red dashed line), and a radial magnetic field line (black line).

7.2.2.3 Magnetosheath (T32)

The magnetospheric electron distribution for magnetosheath conditions (T5) features a large flux of low energy electrons (Figure 1.2). In this case (Figure 7.35), electron temperatures computed along the radial magnetic field line reach a temperature of 600 K at 1600 km after an initial departure from neutral temperatures at 1000 km. Temperature profiles along the parabolic magnetic field line are strongly coupled to the neutral temperature below 1100 km and then rise to 675 K at 1700 km. The temperature profile compiled using nested magnetic field lines rises from the neutral temperature at 1250 km to small peak at 1600 km with a temperature of 1325 K. Using nested magnetic field lines limits the conduction of energy to lower altitudes, as the field lines can be thought of as parallel and horizontal, effectively constraining the energy to higher altitudes where the lower energy electrons deposit their energy. When this thermal energy is contained in the upper altitude regions, the peak electron temperature becomes comparable to the temperatures reached using the T13 plasma sheet superthermal electron flux as the large flux of superthermal electrons translates into a large amount of energy deposited into Titan's ionosphere.

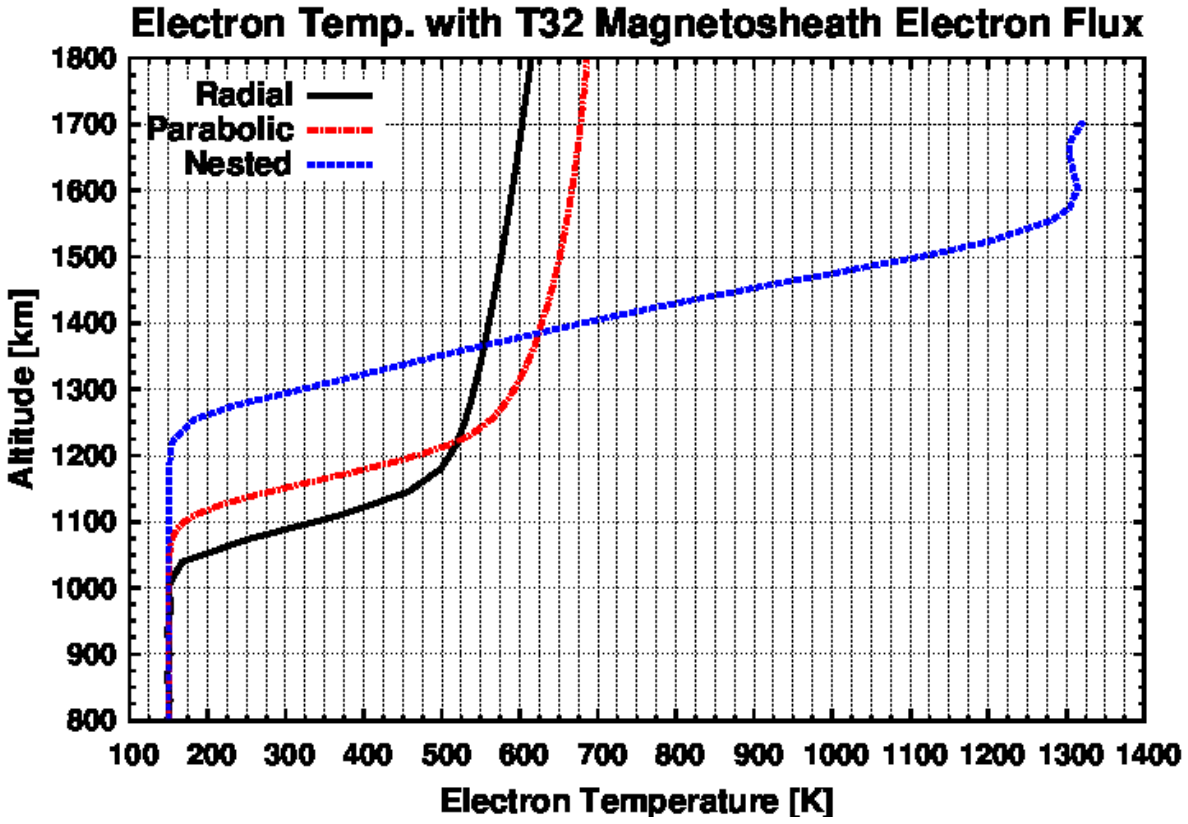

Figure 7.35 Electron temperature generated using the T32 magnetosheath magnetospheric electron flux shown by *Rymer et al.* [2009] for the cases of nested magnetic field lines (blue dotted line), a parabolic magnetic field line anchored at 725 km (red dashed line), and a radial magnetic field line (black line).

7.2.2.4 Bi-Modal (T31)

Using the bimodal magnetospheric electron flux (Figure 1.2) as input into the two-stream code (Section 3.3) to produce the thermal electron heating rates used in the energetics code (Section 3.7) produces the electron temperature profile shown in Figure 7.36. Computing the electron temperature along a radial magnetic field line results in an electron temperature coupled with the neutral temperature until 925 km where it reaches 350 K at 1600 km. For the case using the parabolic magnetic field line the electron temperature deviates from the neutral temperature at an altitude of 1000 km and reaches 400 K near 1350 km. Using the nested magnetic field line, the electron temperature begins to rise at 1100 km, increases steadily reaching a slight shelf between 725 K at 1550 km and then begins to increase steadily from there. The electron temperature uncouples from the neutral temperature near 1000 km, increasing to 750 K at 1500 km, where the temperature increase slows, and then the temperature increase resumes above 1600. This lower altitude region where the point of inflection in the temperature profile is located is caused by higher energy electrons and precipitating magnetospheric electrons, while the temperature increase at the higher altitudes is caused by lower energy electrons associated with ion pick up depositing their energy. This case best illustrates where energy is deposited as the parallel magnetic field lines limit the amount of heat transfer between altitudes.

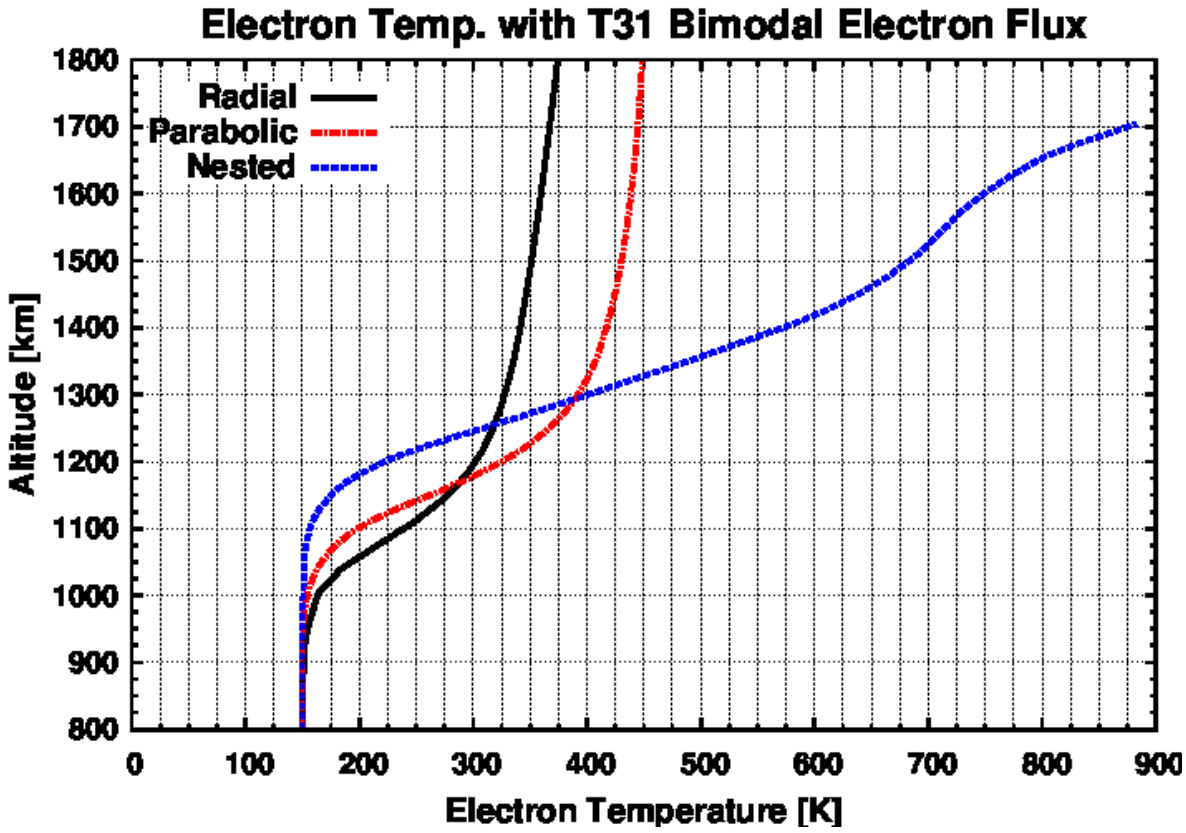

Figure 7.36 Electron temperature generated using the T31 bimodal magnetospheric electron flux shown by *Rymer et al.* [2009] for the cases of nested magnetic field lines (blue dotted line), a parabolic magnetic field line anchored at 725 km (red dashed line), and a radial magnetic field line (black line).

7.3 Conclusions

7.3.1 Ion Production Modeling

Modeled ion production rates of N_2^+ and CH_4^+ for the T5 (excluding the bite-out feature between 1160 and 1250 km) and T57 flyby have been found to agree with the production rates derived empirically from INMS measurements using the photochemical model (Section 3.4) and ion chemistry (Section 3.5) as was done in Chapter 4 to within 20%. In this derivation of an empirical production rate, photochemical equilibrium was assumed so that the production of an ion species at a given altitude is balanced by the loss rate of the ion species. As the major loss processes of CH_3^+ (Table 3.12), which serves as a proxy for N_2^+ production as most CH_3^+ is produced from N_2^+ reactions with methane (see discussion in Section 4.1.1), and CH_4^+ are well known (Table 3.10), the production rate can be set equal to the loss rate of these ion species calculated by multiplying the appropriate reaction rate coefficient by the product of the measured density of methane and the measured density of CH_3^+ or CH_4^+ (see Section 3.5.2 and Equations (7.4) and (7.6)). The empirical N_2^+ production rate obtained by dividing the CH_3^+ production rate by a correction factor obtained from the photochemical model by comparing the amount of CH_3^+ produced to N_2^+, and CH_4^+ were found to be in agreement with the modeled electron densities to within 20%. These comparisons have demonstrated that the model is capable of producing reasonable ion production rate profiles on the nightside of Titan using magnetospheric electron precipitation.

After demonstrating that the model is capable of producing reasonable production rates, ion production rate profiles have been created using the four magnetospheric flux characterizations (Figure 1.2) detailed in *Rymer et al.* [2009] for the magnetospheric conditions of Titan (lobe-like, plasma sheet, magnetosheath, and bimodal superthermal electron

distributions). Although the production rate profiles using nested magnetic field lines have been shown in this chapter, profiles generated using a parabolic magnetic field line anchored at 725 km and a radial magnetic field line are shown in Appendix D-3 and D-4. Using the ion production rates created with this model in conjunction with the production rate profiles created in Section 4.3 it is possible to create ion production profiles for a variety of solar zenith angles and magnetospheric flux conditions. This will allow researchers to create predictive models of the ionosphere for upcoming flybys based upon the spacecraft trajectory and location of Titan in the magnetosphere of Saturn.

7.3.2 Temperature Modeling

Applying the energetics model (Section 3.7) to the nightside ionosphere showed that magnetospheric electron fluxes measured by CAPS ELS in the nearby magnetosphere of Saturn during T5, as discussed by *Cravens et al.* [2008], can provide sufficient heating to bring the modeled thermal electron temperatures into agreement with the RPWS-LP data presented by *Agren et al.* [2007]. Lower energy (E < 10 eV) magnetospheric electrons are important for the thermal energy balance as well. An unresolved issue is how much magnetospheric electron fluxes are attenuated as induced magnetic field lines get caught up in Titan's ionosphere and atmosphere (see discussion by *Gan et al.* [1993] and *Cravens et al.* [2008]). The role of the magnetic field topology is also important, and although reasonable topologies were adopted for T5, the variation of thermal quantities for different flybys (and field line configurations) should be investigated.

The model ion temperatures on the nightside (T5 flyby of Titan) fall within the values presented by *Crary et al.* [2010] below 1400 km; however, they are about 25 K lower at an

altitude of ~1650 km, indicating that dynamical terms are important for ion temperatures at higher altitudes on the nightside as well as on the dayside.

7.3.3 Summary of the Conclusions of Nightside Ion Production and Temperature Modeling

In conclusion, the key findings of this study are:

1. Modeled electron ion production rates are found to be within 25% of production rates derived empirically from INMS measurements for the T5 and T57 nightside flyby of Titan.
2. Attenuation of the magnetospheric electron fluxes as proposed by *Agren et al.* [2007] and *Cravens et al.* [2009] is not needed to reproduce the primary production rates of the primary ion species or the electron temperatures.
3. Globally averaged ion production profiles have been generated for the ionization products of N_2 and CH_4 resulting from magnetospheric electron precipitation using the magnetospheric electron conditions described by *Rymer et al.* [2009].
4. On the nightside above 1400 km, magnetospheric inputs are needed to heat the electrons.
5. Dynamical terms, most notably Joule heating, play an important role at higher altitudes in the energy balance for the ions at Titan and may be needed to model the nightside ion temperatures.
6. Globally averaged temperature profiles for the thermal electron population have been generated for each of the magnetospheric flux conditions characterized by *Rymer et al.* [2009].

Chapter 8 **Conclusions**

Saturn's moon Titan has an ionosphere caused by the ionization of its neutral atmosphere from solar photons and electrons originating in Saturn's magnetosphere that precipitate down Saturnian magnetic field lines draping around Titan. Since 2004 instruments aboard the Cassini spacecraft have been making measurements of the ionospheric electron temperatures, magnetic fields, and electron and ion densities which are compared to models of the ionosphere. Modeled electron and ion densities have been found to be larger than the measured counterparts by more than a factor of three [c.f. *Robertson et al.*, 2009; *Westlake et al*., 2012] which has prompted the investigation into the possible causes of this discrepancy.

The model discussed in this paper consists of four distinct parts: (1) a photoionization code to compute photoionization and photoelectron production as a function of altitude, (2) a two-stream electron transport code which calculates the heating rate of the thermal electron population and electron impact ionization of the neutral atmosphere along a magnetic field line caused by photoelectrons, secondary electrons resulting from previous electron impact collisions with neutrals, and precipitating magnetospheric electrons, (3) an energetics code to compute the electron and ion temperatures along a magnetic field line and (4) a photochemical code that produces ion densities as a function of altitude by balancing ion production and loss rates at each altitude.

Inputs used in the model are taken from measurements made by instruments aboard Cassini. Neutral measurements made by INMS for N_2, CH_4 and H_2, multiplied by a factor of 3.15 in order to reflect a possible recalibration of the INMS instrument [*Mandt et al.*, 2012], with

the mixing ratios of *Magee et al.* [2009] and *Cui et al.* [2009] have been used to build flyby specific neutral atmospheres. Thermal electron temperature profiles and electron densities are taken from measurements made by RPWS/LP [c.f. *Agren et al.*, 2007; 2009].

Adopting an appropriate magnetic field line topology is also important for modeling the ionosphere of Titan. Electrons, both those resulting from photoionization and electron impact ionization and those of magnetospheric origin, travel along the magnetic field lines which determines how much of the neutral atmosphere an electron interacts with as it travels to lower altitudes. This influences where energy is initially deposited in the ionosphere as well as the thermal electron cooling rates which increase as the neutral density increases. Magnetic field line topology has been considered for the cases of radial, parabolic and horizontal (nested) magnetic field lines. When comparing modeled values with measurements, a magnetic field line topology was adopted in order to mimic observations made by the magnetometer on the Cassini spacecraft [*Bertucci et al.,* 2005]; however, the magnetometer only gives information along the spacecraft trajectory so it does not give information about the origin and long term-structure of the magnetic field lines.

The goal of the research presented in this dissertation is to use this model to investigate the cause of this discrepancy in the electron densities and to produce globally averaged ion production rates, electron temperature profiles and ion chemistry that can be used to accurately model processes occurring in Titan's ionosphere. The results presented in this paper may then be used to predict what Cassini will observe during future flybys of Titan based on Titan's location in Saturn's magnetosphere and the solar zenith angle.

8.1 Summary of Ion Production

It is possible that the discrepancy between the modeled and measured electron densities could be caused by an overproduction of ions resulting from photoionization or the electron impact ionization from precipitation of magnetospheric electrons. As there are no direct measurements of ion production rates in Titan's ionosphere, ion density comparisons are drawn between CH_4^+, the primary ionization product of methane, and CH_3^+, which is produced primarily from chemical reactions involving N_2^+, the primary ionization product of N_2. Density comparisons between measured and modeled N_2^+ could not be used as the mass 28 signal obtained by INMS is dominated by the most abundant ion in the ionosphere of Titan, $HCNH^+$.

Empirical production rates were then derived for CH_4^+ and CH_3^+ using INMS measured densities for neutral methane, and CH_3^+ and CH_4^+, along with ion chemistry from the photochemical model with the assumption of photochemical equilibrium. This was done by setting the production rates of the ions equal to their loss rates which are the result of chemical reactions between the ions and methane. Due to the fact that only a fraction of N_2^+ reacts with methane to produce CH_3^+, the empirical production rate of N_2^+ was then calculated by dividing the production rate of CH_3^+ by the ratio of CH_3^+ production to N_2^+ production found using the photochemical model. These empirical production rates are then compared to the ion production rates found using the full photochemical model.

Using the methodology described above the following conclusions and results were obtained:

1. Allowing 50% of solar photons with wavelengths between 800 and 1000 Å to interact with molecular nitrogen using the photoabsorption cross sections of *Gallagher et al.*

[1988] is a good approximation to the high resolution photoabsorption cross sections of *Liang et al.* [2007] and will aid the model in reproducing the lower altitude shelf in the CH_4^+ production.

2. Model ion production rates agree with empirical ion production rates determined using INMS ion neutral density profiles to within 20% for dayside comparisons and within 25% for nightside comparisons.
3. The cause of the discrepancy between modeled and measured (data taken by INMS, RSS, and RPWS-LP) electron and ion density is not due to overproduction of the primary ion species and therefore must be caused by insufficient electron recombination rates.
4. Attenuation of the magnetospheric electron fluxes as proposed by *Agren et al.* [2007] and *Cravens et al.* [2009] is not needed to reproduce the primary production rates of the primary ion species on the nightside of Titan.
5. Globally averaged ion production profiles have been generated for the ionization products of N_2 and CH_4 resulting from magnetospheric electron precipitation using the magnetospheric electron conditions described by *Rymer et al.* [2009].

8.2 Summary of Temperature Modeling

The measured electron temperature in Titan's ionosphere has been found to be larger than the neutral temperature [*Agren et al.,* 2007, 2009; *Galand et al.*2010; *Richard et al.* 2011]. Accurately modeling the electron temperatures in Titan's ionosphere has important implications for the chemical modeling of Titan's ionosphere. Ultimately, the only way that electrons leave the ionosphere of Titan is through dissociative electron recombination which is temperature dependent.

Heating of the thermal electron population (electrons with energies less than 2 eV) is caused by collisions with secondary electrons from photoionization and magnetospheric electrons precipitating down magnetic field lines. These thermal electrons are cooled via collisions with atmospheric neutrals and ions. Dynamical terms resulting from bulk plasma motion (i.e. Joule heating) have been found to be important in the energy balance for ions [*Richard et al,.* 2011]. Using the heating rates generated using the two-stream model of electron transport; the energetics code solves the energy equation (Equation (3.34)) along magnetic field lines. The key conclusions, also shown by *Richard et al.* [2011], are:

1. Below approximately 1400 km on the dayside, solar inputs sufficiently explain ionospheric electron temperatures when appropriate magnetic field lines are adopted.
2. Dynamical terms, most notably Joule heating, play an important role at higher altitudes in the energy balance for the ions at Titan.
3. Attenuation of the magnetospheric electron fluxes as proposed by *Agren et al.* [2007] and *Cravens et al.* [2009] is not needed to reproduce the electron temperature profile on the nightside of Titan.
4. Globally averaged temperature profiles for the thermal electron population have been generated for each of the magnetospheric flux conditions characterized by *Rymer et al.* [2009].

8.3 Summary of Photochemical Modeling

Photochemical models of Titan yield electron densities that are much larger than the electron densities measured in the ionosphere [c.f. *Robertson et al.,* 2009; *Westlake et al.,* 2012]. The main contributors to the enhanced electron density are the large amounts of $C_2H_5^+$, CH_5^+

and, most notably, $HCNH^+$ whose density is three times larger than the measured ion density at the ionospheric peak. These three species are chemically linked such that an increase in one affects the density of the other two and so care must be taken when manipulating the reactions between the three ions.

Comparisons between the modeled and empirical ion production rates have shown that this disparity in the electron density is not the product of overproduction of primary ion species due to photoionization and electron impact ionization. The focus of attention then becomes the loss rate of electrons in the ionosphere which can be increased by including additional reactions that convert lower mass ions into higher mass ions with larger dissociative recombination rates and the reexamination of the dissociative electron combination rates. The following results were obtained by comparing modeled ion density spectra with the INMS measured density spectrum at 1205 km during the outbound leg of the T40 flyby.

1. Using the favored ion chemical scheme (reducing the H_2O and NH_3 densities by a factor of 100, tripling the HCN, C_2H_2, and C_2H_4 densities, using the modeled electron temperature, and including reactions between C_2H_2, C_2H_4 and $HCNH^+$) requires the electron dissociative recombination coefficient of $HCNH^+$ to be increased by a factor of 10 for the modeled ion density to agree with the measured ion density, but provides agreement between most modeled ion densities and the INMS measured values to within a factor of 2.

2. Reactions between C_2H_2 andC_2H_4 and ion species proposed by *Westlake et al.* [2012] are helpful in modeling the mid- and upper mass hydrocarbon and nitrile production in the ionosphere of Titan.

3. Electron dissociative recombination accounts for nearly 70% of the loss of $HCNH^+$ and therefore, updated recombination coefficients represent a more plausible sink for $HCNH^+$ loss.

8.4 Answers to the Guiding Questions

Chapter 1 listed four guiding questions for this research endeavor as well as outlining how the questions would be answered. As this dissertation concludes, these questions will be revisited and the insights gained from this work will be presented.

1. Is the current (see Chapter 3) model employed by this study valid near the ionospheric peak?

- Empirical estimates of flow speeds within the ionosphere of Titan and diffusion magnetic diffusion coefficients calculated by *Cravens et al.* [2010] indicate the plasma flow speed and magnetic diffusion coefficient are sufficiently low so that the local approximation of the photochemical model is valid up to 1400 km.
- Ion production rate profiles generated by the model using the relevant solar inputs and INMS measured neutral atmospheres multiplied by a factor of 3.15 have been compared to empirical production rates derived from INMS measurements for the T17, T18 and T40 flybys agree within 20% at the ionospheric peak showing that the model is producing reasonable production rates for primary ions.
- Similar modeling efforts have been conducted for the nightside of Titan using the magnetospheric electron fluxes for the T5 and T57 flybys and agreement between

the modeled and empirical production rates is found to be within 20% at the ionospheric peak.

2. How can the observed electron and ion temperatures, which are much higher than the neutral temperatures, be explained?

- Solar photons provide sufficient heating on the dayside between 1000 and 1400 km to bring the modeled electron temperatures into agreement with the measured electron temperatures for the T18 flyby of Titan.
- On the nightside, magnetospheric electrons provide sufficient heating to bring the T5 modeled electron temperature into agreement with the measured values.
- Magnetospheric electron precipitation needs to be included for agreement between the measured and modeled electron temperature above 1400 km on the dayside, although the details of small scale structure of the magnetic field line topology and magnetospheric flux attenuation are not well understood.
- Magnetic field line topology is important in the energy balance; nested field lines keep energy bottled at the altitude at which it was deposited while radial field lines allow conduction of energy more readily to upper and lower altitudes.

3. What is the cause of the discrepancy between the measured and modeled electron densities [i.e. *Robertson et al.*, 2009; *Westlake et al*., 2012]?

- Ion production rate profiles generated using flyby specific solar photon fluxes or magnetospheric electron fluxes agree with empirical ion production rates derived from INMS ion and neutral density measurements and are not the source of the overabundance of electrons in Titan's ionosphere.

- Using modeled temperature profiles that are closer to the neutral temperatures at altitudes near and below 1000 km than the values obtained from the Cassini Radio and Plasma Wave Science – Langmuir Probe raises electron recombination rates of ions at lower altitudes which helps with the electron density disparity, but can only account for at most 25% of the overabundance at lower altitudes (below 1150 km).
- Implementing the changes proposed by *Westlake et al.* [2012] (tripling the mixing ratio of HCN, C_2H_2 and C_2H_4, adding reactions between $HCNH^+$ with the neutrals C_2H_2 and C_2H_4 and its reaction products) brings the modeled densities of CH_5^+, $C_2H_5^+$ and C_2-group hydrocarbons to within 15% of densities measured by INMS but increases the discrepancy in $HCNH^+$ from a factor of 3 higher than the measured value to a factor of 5 higher.
- The electron dissociative recombination coefficient of $HCNH^+$ must be increased by a factor of 5 (or more than 10 with the additions of *Westlake et al.* [2012]) in order to bring the modeled HCNH+ density into agreement with the measured value.
- Electron dissociative recombination is responsible for upwards of 70% of the loss of $HCNH^+$ which means that even though the adjustments to the ion chemistry proposed by *Westlake et al.* [2012] decrease the overall electron density, the dissociative electron recombination coefficient of $HCNH^+$ must be reevaluated as this is the most plausible sink of the ion.

4. How can this information be applied to the global picture of Titan's ionosphere and its interaction with the Saturnian magnetospheric plasma?

- Model runs yielding ion production rates for various solar zenith angles on the dayside and for the cases presented by *Rymer et al.* [2009] on the nightside were constructed using a globally averaged neutral atmosphere for cases using nested, parabolic (parabola anchored at 725 km) and radial magnetic field lines which can be combined to produce production rate profiles for varying solar and magnetospheric conditions.
- Electron temperature profiles have been created using magnetospheric electron precipitation along nested, parabolic and radial magnetic field lines for the magnetospheric electron fluxes presented by *Rymer et al.* [2009] (lobe-like, plasma sheet, magnetosheath, and bimodal) which can be combined with chemical models of Titan to approximate the nightside dissociative electron recombination rates.

8.5 Future Problems

Numerous insights into the processes occurring within the ionosphere of Titan have been gained as a result of this study. The model has proven itself to be able to compute ion production rates and electron temperatures on the day and nightside of Titan within reasonable agreement of the measured values and generic ion production and electron temperature profiles have been created for future modeling efforts of future flybys of Titan. The ion chemistry has been scrutinized and new reaction pathways have been examined which bring modeled electron densities into better agreement with the INMS measured ion densities. There are many areas of this model that can be improved upon and topics that need to be investigated in order to form a

more complete picture of Titan's ionosphere. A list of potential areas of future research appears below.

1. More realistic magnetic field line topologies from MHD models, such as those used by *Ma et al.* [2006; 2007; 2009] which are capable of modeling the draping Saturnian magnetic field lines around Titan, can be implemented which will allow models such as the one described in this paper to more accurately compute the altitude at which magnetospheric electrons deposit their energy and how readily heat is conducted to lower altitudes.

2. Chemical loss processes, the electron dissociative recombination coefficient, and the temperature dependence of $HCNH^+$ must be examined as this is the main loss process of the ion. The values currently measured in the lab, 3.5×10^{-7} and 2.8×10^{-7} cm^3s^{-1}, measured by *McLain et al.* [2004] and *Semaniak et al.* [2001] at 300 K, do not provide sufficient loss rates for the ion.

3. High mass ions [*Coates et al.*, 2007; *Crary et al.* 2009] must be considered, especially at lower altitudes, as these new production pathways will move ions from lower mass species to heavier ions that have larger dissociative electron recombination coefficients and will lower the modeled electron density.

4. Negative ions [*Coates et al.*, 2007; *Crary et al.* 2009] observed by the CAPS instrument should be considered as this will affect the electron density inferred by the INMS instrument (there would be more ions than free electrons) which would lower the discrepancy between RPWS measured electron densities and modeled electron densities.

5. Dynamical transport should be considered in the chemical model as the assumption of photochemical equilibrium is only valid below 1400 km.

6. As Cassini continues to collect data from flybys of Titan, the sun is entering a more active era which will result in a denser ionosphere, thus models of Titan's ionosphere for solar maximum conditions need to be created and evaluated.

This work has improved our understanding of the plasma interactions occurring in Titan's ionosphere. The model described in the paper has been able to reproduce key features of ion production, electron temperature and ion density measurements in the ionosphere of Titan. From this analysis, generic profiles of the ion production rates have been produced using solar and magnetospheric inputs which can be combined to model a multitude of conditions that Titan's ionosphere may be experiencing. From this work, it has been shown that an over-production of ions is not the cause of the electron density discrepancy between measured and modeled values. Temperature profiles that converge to the neutral temperature near 1000 km have been created and potential chemical reaction pathways have been investigated that will increase the dissociative electron recombination rate resulting in a decreased modeled electron density. This work has greatly contributed to our assessment and understanding of the anomalous modeled electron densities that have plagued efforts to accurately reproduce the ionosphere of Titan.

References

Acton, L., D. C. Weston, and M. E. Bruner (1999) Deriving solar X ray irradiance from Yohkoh observations, *J. Geophs. Res., 104*, 14,827-14,832.

Agren, K., and 15 colleagues (2007). On magnetospheric electron impact ionization and dynamics in Titan's ram-side and polar ionosphere—A Cassini case study, *Ann. Geophys., 25*, 2359–2369.

Agren, K., J.-E. Wahlund, P. Garnier, R. Modolo, J. Cui, M. Galand, and I. Muller-Wodarg (2009), On the ionospheric structure of Titan, *Planet. Space Sci., 57(14-15*), 1821-1827. doi: 10.1016/j.pss.2009.04.012.

Anicich, V., and M. McEwan (1997), Ion-molecule chemistry in Titan's ionosphere, *Planetary and Space Science, 45*(8), 897-921.

Anicich, V. (2003), An index of the literature for bimolecular gas phase cation-molecule reaction kinetics, *JPL Publication,* 03-19.

Arridge, C. S., N. Achilleos, M. K. Dougherty, K. K. Khurana, and C. T. Russell (2006), Modeling the size and shape of Saturn's magnetopause with variable dynamic pressure, *J. Geophys . Res . , 111*, A11 227, doi:10.1029/2005JA011574.

Arridge, C. S., N. Andre´, N. Achilleos, K. K. Khurana, C. L. Bertucci, L. K. Gilbert, G. R. Lewis, A. J. Coates, and M. K. Dougherty (2008), Thermal electron periodicities at 20RS in Saturn's magnetosphere, *Geophys. Res. Lett., 35*, L15107, doi:10.1029/2008GL034132.

Backes, H. (2004), Titan's interaction with the Saturnian magnetospheric plasma, thesis, Inst. fur Geophys. And meterol., Univ. of Cologne, Cologne, Germany.

Backes, H., F. M. Neubauer, M. K. Dougherty, H. Achilleos, N. Andre, C. S. Arridge, C. Bertucci, G. H. Jones, and K. K. Khurana (2005), Titan's magnetic field signature during the first Cassini encounter, *Science, 308*, 992–995.

Backx, C. and M. J. Van der Wiel (1975), Electron-ion coincidence measurements of CH_4, *J. Phys. B., 8*, 3020.

Banaskiewicz, M., L. M. Lara, R. Rodrigo, J. J. Lopez-Moreno, and G. J. Molina-Cuberos (2000), A coupled model of Titan's atmosphere and ionosphere, *Icarus, 147*, 386– 404.

Banks, P. M., and G. Kockarts (1973), *Aeronomy, Parts A and B*, Academic Press, Inc. New York.

Barbosa, D. D. (1987), Titan's atomic nitrogen torus: Inferred properties and consequences for the Saturnian aurora, *Icarus, 72*, 53–61,doi:10.1016/0019-1035(87)90118-7.

Bell, J., S. W. Bougher, J. H. Waite Jr., A. J. Ridley, B. Magee, K. Mandt, J. Westlake, A. D. DeJong, A. Bar-Nun, R. Jacovi, G. Toth, and V. de la Haye (2010). Simulating the one-dimensional structure of Titan's upper atmosphere, part I: Formulation of the Titan global ionosphere-thermosphere model and benchmark simulations, *J. Geophys. Res.*, *115*, E12002.

Bell, J., S. W. Bougher, J. H. Waite Jr., A. J. Ridley, B. Magee, K. Mandt., J. Westlake, A. D. DeJong, V. de la Haye, D. Gell, G. Fletcher, A. Bar-Nun, R. Jacovi, and G. Toth (2010). Simulating the one-dimensional structure of Titan's upper atmosphere, part II: Alternative scenarios for methane escape, *J. Geophys. Res.*, *115*, E12018

Bell, J., S. W. Bougher, J. H. Waite Jr., A. J. Ridley, B. Magee, K. Mandt, J. Westlake, A. D. DeJong, A. Bar-Nun, R. Jacovi, G. Toth, and V. de la Haye (2011). Simulating the one-dimensional structure of Titan's upper atmosphere, part III, *J. Geophys. Res., 116*, E11002.

Bertucci, C., et al. (2008), The magnetic memory of Titan's ionized atmosphere, *Science, 321*, 1475–1478, doi:10.1126/science.1159780.

Bertucci, C., B. Sinclair, N. Achilleos, P. Hunt, M. K. Dougherty, and C. S.Arridge (2009), The variability of Titan's magnetic environment, Planet.Space Sci., 57, 1813, doi:10.1016/j.pss.2009.02.009.

Bird, M. K., R. Dutta-Roy, S. W. Asmar, and T. A. Rebold (1997), Detection of Titan's ionosphere from Voyager 1 radio occultation observations, *Icarus, 130*, 426–436.

Brescansin, L. M., M. A. P. Lima, and V. Mckoy (1989), Cross sections for rotational excitation of CH_4 by 3-20 eV electrons, *Phys. Rev. A, 40*, no. 10, 5577.

Carbary, J. F., and S. M. Krimigis (1982), Charged particle periodicity in the Saturnian magnetosphere, *Geophys. Res. Lett., 9*, 1073 – 1076, doi:10.1029/GL009i009p01073.

Carbary, J. F., D. G. Mitchell, S. M. Krimigis, D. C. Hamilton, and N. Krupp (2007), Charged particle periodicities in Saturn's outer magnetosphere, *J. Geophys. Res., 112*, A06246, doi:10.1029/2007JA012351.

Cartwright, D. C., S. Trajmar, A. Chutjian, and W. Williams (1977), Electron impact excitation of the electronic states of N2. II Integral cross sections at incident energies from 10 to 50 eV, *Phys. Rev. A, 16* 1041.

Chen, F. F. (2006). *Introduction to plasma physics and controlled fusion volume 1: Plasma physics*. Springer Science+Business Media, LLC, New York.

Coates, A. J., F. J. Crary, D. T. Young, K. Szego, C. S. Arridge, Z. Bebesi, and E. C. Sittler Jr. (2007), Ionospheric electrons in Titan's tail: Plasma structure during the Cassini T9 encounter, *Geophys. Res. Lett,. 34*, L24505–L24519, doi:10.1029/ 2007GL030919.

Crary, F. J., B. A. Magee, K. Mandt, J. H. Waite Jr., J. Westlake, and D. T. Young (2009), Heavy ion temperatures and winds in Titan's ionosphere: Combined Cassini CAPS and INMS observations, *Planet. Space Sci., 57(14-15*), 1847-1856.

Cravens, T. E. (1997). *Physics of solar system plasmas*. Cambridge Univ. Press, Cambridge.

Cravens, T. E., C. J. Lindgren, and S. A. Ledvina (1998), A two-dimensional multifluid MHD model of Titan's plasma environment, *Planet. Space Sci., 46*, 1193.

Cravens, T. E., J. Vann, J. Clark, J. Yu, C. N. Keller, and C. Brull (2004), The ionosphere of Titan: An updated theoretical model, *Adv. Space Res, 33*, 212–215.

Cravens, T. E., and 15 colleagues (2005), Titan's ionosphere: Model comparisons with Cassini Ta data, *Geophys. Res. Lett., 32 (12)*, L12108, doi:10.1029/2005GL023249.

Cravens, T. E., J. Clark, A. Bhardwaj, R. Elsner, J. H. Waite, A. N. Maurellis, G. R. Gladstone and G. Branduardi-Raymont (2006) X –ray emission from the outer planets: Albedo for scattering and fluorescence of solar x-rays, *J. Geophys. Res., 111,* A07308, doi:10.1029/2005JA011413.

Cravens, T. E., I. P. Robertson, S. A. Ledvina, D. Mitchell, S. M. Krimigis, and J. H. Waite Jr. (2008), Energetic ion precipitation at Titan, *Geophys. Res. Lett., 35*, 03103. doi:10.1029/ 2007GL032451.

Cravens, T. E., et al., (2009a), Model–data comparisons for Titan's nightside ionosphere, *Icarus, 199*, 174.

Cravens, T. E., R. V. Yelle, J.-E. Wahlund, D. E. Shemansky, and A. F. Nagy (2009b), Composition and structure of the ionosphere and thermosphere. In: *Titan from Cassini-Huygens*. edited by R. H. Brown, J.-P. Lebreton, and J. H. Waite Jr., Springer, New York, pp. 259–296.

Cravens, T. E., et al. (2010), Dynamical and magnetic field time constants for Titan's ionosphere: Empirical estimates and comparisons with Venus, J. Geophys. Res., 115, A08319, doi:10.1029/2009JA015050.

Cui, J., et al. (2009a), Diurnal variations of Titan's ionosphere, *J. Geophys. Res., 114*, A06310, doi:10.1029/2009JA014228.

Cui, J., R. V. Yelle, V. Vuitton, J. H. Waite, Jr., W. T. Kasprzak, D. A. Gell, H. B. Niemann, I. C. F. Müller-Wodarg, N. Borggren, G. G. Fletcher, E. L. Patrick, E. Raaen, and B. Magee (2009b), Analysis of Titan's neutral upper atmosphere from Cassini Ion Neutral Mass Spectrometer measurements, *Icarus*, *200*, 581.

De La Haye, V., J. H. Waite Jr., R. E. Johnson, R. V. Yelle, T. E. Cravens, J. G. Luhmann, W. T. Kasprzak, D. A. Gell, B. Magee, F. Leblanc, M. Michael, S. Jurac, and I. P. Robertson (2007), Cassini ion and neutral mass spectrometer data in Titan's upper atmosphere and exosphere: Observation of a suprathermal corona, *J. Geophys. Res., 112*, A07309, doi:10.1029/2006JA012222.

Denne, D. R., (1970), Measurements of the ultrasoft X-ray absorption of Ar, Ne, N_2, O_2, CH_4, He and H_2, *J. Geophys. D. 3*, 1392.

Ditchburn, R. W. (1955), Absorption cross-sections in the vacuum ultra-violet, III, Methane, Proc *Roy. Soc. London, 229A*, 44.

Dougherty, M. K., et al. (2004), The Cassini magnetic field investigation, Space Sci. Rev., 114, 331–383, doi:10.1007/s11,214–004–1432–2.

Flasar, F. M., et al. (2005), Titan's atmospheric temperatures, winds, and composition, *Science, 308*, 975–978, doi:10.1126/science.1111150.

Fulchignoni, M. et al. (2005) In situ measurements of the physical characteristics of Titan's environment. *Nature 438,* 785-791.

Galand M., R. Yelle, J. Cui, J.-E. Wahlund, V. Vuitton, A. Wellbrock, and A. Coates (2010), Ionization sources in Titan's deep ionosphere, *J. Geophys. Res.*, *115*, A07312, doi: 10.1029/2009JA015100.

Galand, M., R. V. Yelle, A. J. Coates, H. Backes, and J.-E. Wahlund (2006), Electron temperature of Titan's sunlit ionosphere, *Geophys. Res. Lett., 33*, L21101, doi:10.1029/2006GL027488

Galand, M., J. Lilensten, D. Toublanc, and S. Maurice (1999), The ionosphere of Titan: Ideal diurnal and nocturnal cases, *Icarus, 140*, 92–105.

Gallagher, J. W., C. E. Brion, J. A. Samson, and P. W. Langhoff (1988), Absolute cross sections for molecular photoabsorption, partial photoionization, and ionic photofragmentation processes, *J. Phys. Chem. Ref. Data, 17*,9.

Gan, L. (1991) Electron distributions and solar wind interaction with nonmagnetic planets. Unpublished doctoral dissertation. University of Michigan.

Gan, L., C. N. Keller, and T. E. Cravens (1992), Electrons in the ionosphere of Titan, *J. Geophys. Res., 97*, 12136–12151

Gan, L., C. N. Keller, and T. E. Cravens (1993), A time-dependent model of suprathermal electrons at Titan. In: Gombosi, T. I. (Ed.) *Plasma Environments of Non-Magnetic Planets*, vol. 4, p. 171, Elsevier.

Gold, T., (1959). *J. Geophys. Res., 64*, 1219

Green, A. E. S. and S. K. Dutta (1967), Semi-empirical cross sections for electron impacts, *J. Geophsys. Res., 72,* 3933.

Green, A. E. S. and T. Sawada (1972), Ionization cross sections and secondary electron distributions, *J. Atmos. Terr. Phys., 34*, 1719.

Green, A. E. S., and R. S. Stolarski (1972), Analytic models of electron impact excitation cross sections, *Journal of Atmospheric and Terrestrial Physics. 34,* 1703-1717.

Gurnett, D. A., et al. (2004), The Cassini radio and plasma wave investigation, *Space Sci. Rev., 114*, 395.

Hartle, R. E., E. C. Sittler, Jr., K. Ogilvie, J. D. Scudder, A. J. Lazarus, and S. K. Atreya (1982), Titan's ion exosphere observed from Voyager 1, *J. Geophys. Res., 87*, 1383.

Herzberg, G. (1945), *Molecular spectra and molecular structure: II. Infrared and Ramen spectra of polyatomic molecules,* New York.

Ip, W. (1992), The nitrogen tori of Titan and Triton, *Adv. Space Res., 12*, 73 – 79, doi:10.1016/0273-1177(92)90379-C.

Itikawa, I. (2006), Cross sections for electron collisions with nitrogen molecules, *J. Phys. Chem. Ref. Data*, 35, 31-53.

Jain, A. (1986), Total (elastic + absorption) cross sections for e-CH_4 collisions in a spherical model at 0.10-500 eV, *Phys. Rev. A, 34*, no. 5, 3707.

Jain, A. and D. G. Thompson (1983), Rotational excitation of CH_4 and H_2O by slow electron impact, *J. Phys. B: Atom. Mol. Phys., 16*, 3077.

Kasprzak, W. K., et al. (1996), Cassini orbiter ion and neutral mass spectrometer, *Proc. SPIE 2803*, 129.

Keller, C. N., T. E. Cravens, and L. Gan (1992), A model of the ionosphere of Titan, *J. Geophys. Res., 97*, 12117–12135.

Keller, C. N., V. G. Anicich, and T. E. Cravens (1998), Model of Titan's ionosphere with detailed hydrocarbon chemistry, *Planet. Space Sci., 46*, 1157–1174.

Kliore, A. J., and 12 colleagues (2008), First results from the Cassini radio occultations of the Titan ionosphere, *J. Geophys. Res.,* 113, A09317, doi:10.1029/2007JA012965.

Kliore, A. .J., A. F. Nagy, T. E. Cravens, M. S. Richard, and A. M. Rymer (2011), Unusual electron density profiles observed by Cassini radio occultations in Titan's ionosphere: Effects of enhanced magnetospheric electron precipitation? *J. Geophys. Res.,* 116, A016694, doi:10.1029/2011JA016694

Krasnopolsky, V. (2009), A photochemical model of Titan's atmosphere and ionosphere. *Icarus, 201*, 226-256.

Krimigis, S. M., et al. (2004), Magnetospheric Imaging Instrument (MIMI) on the Cassini mission to Saturn/Titan, *Space Sci. Rev.*, *114*, 233

Krimigis, S. M., and 31 colleagues (2005), Dynamics of Saturn's magnetosphere from MIMI during Saturn's orbital insertion, *Science, 307*, 1270–1273.

Langhoff, P. W., S. R. Langhoff, T. N. Rescigno, J. Schirmer, L. S. Cedarbaum, W. Dorncke, and W. Won Niessen (1981), Theoretical studies of inner-valence-shell photoionization cross sections in N_2 and CO, *Chem. Phys., 58*, 71.

Lavvas, P.P., A. Coustenis, and I. M. Vardavas,(2008a), Coupling photochemistry with haze formation in Titan's atmosphere. Part I. Model description. *Planet. Space Sci. 56*, 27–66.

Lavvas, P.P., A. Coustenis, and I. M. Vardavas,(2008b), Coupling photochemistry with haze formation in Titan's atmosphere. Part II. Results and validation with Cassini/Huygens data. *Planet. Space Sci. 56*, 67–99.

Lavvas, P., M. Galand, R.V. Yelle, A.N. Heays, B.R. Lewis, G.R. Lewis, and A.J. Coates (2011), Energy deposition and primary chemical products in Titan's upper atmosphere, *Icarus*, *213*, 233-251, doi:10.1016/j.icarus.2011.03.001.

Liang, M-C., A. N. Heays, B. R. Lewis, S. T. Gibson, and Y. L. Yung (2007), Source of nitrogen isotope anomaly in HCN in the atmosphere of Titan, *Astrophysical Journal,* 664, L115-L118.

Lilensten, J., O. Witasse, C. Simon, H. Soldi-Lose, O. Dutuit, R. Thissen, and C. Alcaraz (2005a), Prediction of a N++ 2 layer in the upper atmosphere of Titan, *Geophys. Res. Lett., 32*, L03203, doi:10.1029/2004GL021432.

Lilensten, J., C. Simon, O. Witasse, O. Dutuit, R. Thissen, and C. Alcarez (2005b), A fast comparison of the diurnal secondary ion production in the ionosphere of Titan, *Icarus, 174*, 285–288.

Lindsay, B. G. and M. A. Mangan (2003), Cross sections for ion production by electron collision with molecules, in *Landolt-Börnstein, Photon- and Electron-Interaction With Molecules: Ionization and Dissociation, New. Ser.,* vol. I/17C, edited by Y. Itikawa, pp. 5-1- 5-77, Springer, New York.

Liu, X. and D. E. Shemansky (2006) Analysis of electron impact ionization properties of methane, *J. Geophys. Res.*, 111, A04303-A04319.

Lukirskii, A. P., I. A. Brytov, and T. M. Zimkina (1964), Photoionization absorption of He, Kr, Xr, CH_4 and methylal in the 23.6-250 Å region, *Opt. Sprctrosc. USSR, English transl., 17*, 234.

Ma, Y.-J., A. F. Nagy, T. E. Cravens, I. V. Sokolov, J. Clark, and K. C. Hansen (2004). 3-D global MHD model prediction for the first close flyby of Titan by Cassini, *Geophys. Res. Lett.*, *31*, L22803, doi:10.1029/2004GL021215.

Ma, Y., A. F. Nagy, T. E. Cravens, I. V. Sokolov, K. C. Hansen, J.-E. Wahlund, F. J. Crary, A. J. Coates, and M. K. Dougherty (2006), Comparisons between MHD model calculations and observations of Cassini flybys of Titan, *J. Geophys. Res., 111*, A05207, doi:10.1029/2005JA011481.

Ma, Y.-J., et al. (2007), 3D global multi-species Hall-MHD simulation of the Cassini T9 flyby, *Geophys. Res. Lett., 34,* 24, doi:10.1029/2007GL031627.

Ma, Y.-J., et al. (2009), Time-dependent global MHD simulations of Cassini T32 flyby: From magnetosphere to magnetosheath. *J. Geophys. Res. 114*, A03204, doi:10.1029/2008JA013676.

Magee, B., J. Bell, J. H. Waite Jr., K. Mandt, J. Westlake, and D. Gell (2009), INMS derived composition of Titan's upper atmosphere: Analysis methods and model comparison, *Planet. Space Sci., 57*, 1895-1916.

Mandt, K.E. et al. (2007), The 12C/13C ratio on Titan from Cassini INMS measurements and implications for the evolution of methane. *Astrophysical Journal. 749*, 160.

McEwan, M.J., and V. G. Anicich (2007), Titan's ion chemistry: A laboratory perspective. *Mass Spectrom. Rev. 26*, 281–319.

McLain, J., V. Poterya, D. Christopher, L. Babcock, and N. Adams (2004) Flowing afterglow studies of the temperature dependencies for dissociative recombination of O_2^+, CH_5^+, $C_2H_5^+$, and $C_6H_7^+$ with electrons, *the Journal of Chemistry A, 108*(32), 6704-6708.

McLain, J., and N. Adams (2009), Flowing afterglow studies of temperature dependencies for electron dissociative recombination of HCNH+, CH3CNH+, CH3CH2CNH+ and their symmetrical proton-bound dimers, *Planetary and Space Science, 57*(13), 1642-1647.

Metzger, P. H. and G. R. Cook (1964), On the continuous absorption, photoionization, and fluorescence of H_2O, NH_3, CH_4, C_2H_2, C_2H_4, and C_2H_6 in the 600-1000Å region, *J. Chem. Phys., 41*, 642.

Molina-Cuberos, G. J., H. Lammer, W. Stumptner, K. Schwingenschuh, H. O. Rucker, J. J. Lopez-Moreno, K. Rodrigo, and T. Tokano (2001), Ionosphere layer induced by meteoric ionization in Titan's atmosphere, *Planet. Space Sci., 49*, 143–153.

Muller, R., K. Jung, K.-H. Kochem, W. Sohn and H. Ehrhardt (1985), Rotational excitation of CH_4 by low-energy-electron collisions, *J. Phys. B: Atom. Mol. Phys., 18,* 3971.

Müller-Wodarg, I. C. F., R. V. Yelle, N. Borggren, and J. H. Waite Jr. (2006), Waves and horizontal structures in Titan's thermosphere, *J. Geophys. Res., 111*, A12315, doi:10.1029/2006JA011961.

Müller-Wodarg, I. C. F., R. V. Yelle, J. Cui, and J. H. Waite Jr. (2008), Horizontal structures and dynamics of Titan's thermosphere*, J. Geophys. Res., 113,* doi:10.1029/2007JE003033.

Murray, C. and S. Dermott (1999) *Solar system dynamics*. Cambridge Univ. Press, Cambridge.

Nagy, A. F., and P. M. Banks (1970), Photoelectron fluxes in the ionosphere, *J. Geophys. Res., 75*, 6260–6270.

Nagy, A.F., and T.E. Cravens (1998) Ionosphere: Energetics, in *Venus II*, edited by Univ. of Arizona Press, Tucson.

Neubauer, F. M., D. A. Gurnett, J. D. Scudder, and R. E. Hartle (1984), Titan's magnetospheric interaction. In *Saturn*, edited by T. Gehrels and M.D. Matthews, Univ. of Arizona Press, Tucson, pp. 760–787.

Osborne, D., P. Lawson, and N. Adams (2011), The effect of N-heteroatoms and CH3 substituents on dissociative electron-ion recombination of protonated single six membered ring compounds at room temperature, *Int. J. Mass. Spectrom 308*(1), 4.

Porter, H. S., C. H. Jackman, and A. E. S. Green (1976), Efficiencies for production of atomic nitrogen and oxygen by relativistic proton impact in air, *J. Chem. Phys., 65*, 154.

Press, W. H., B. P. Flannery, S. A. Teukolsky, and W. T. Vetterling (1986), *Numerical Recipes*, pp. 269-273, Cambridge University Press, New York.

Robertson, I. P., T. E. Cravens, J. H. Waite Jr., R. V. Yelle, V. Vuitton, A. J. Coates, J.-E. Wahlund, K. Agren, K. Mandt, B. Magee, and M.S. Richard (2009), Structure of Titan's ionosphere: Model comparisons with Cassini data., *Planet. Space Sci., 57*, 1834, doi:10.1016/j.pss.2009.07.011.

Richards, P.G., J . A. Fenelly and D. G.Torr (1994), EUVAC: a solar flux model for aeronomi c calculations, *J. Geophys. Res., 99*, 8981.

Roboz, A., and A. F. Nagy (1994), The energetics of Titan, *Geophys. Res., Lett., 99*, 2087–2093.

Rohr, K. (1980), Cross beam experiment for the scattering of low-energy electrons from methane, *J. Phys. B: Atom. Mol. Phys., 13*, 4897.

Rustgi, O. P. (1964), Absorption cross sections of argon and methane between 600 and 170 Å, *J. Opt. Soc. Amer., 54*, 464.

Rymer, A. M., et al. (2007), Electron sources in Saturn's magnetosphere, *J. Geophys. Res., 112*, A02201, doi:10.1029/2006JA012017.

Rymer, A. M., H. T. Smith, A. Wellbrock, A. J. Coates, and D. T. Young (2009), Discrete classification and electron energy spectra of Titan's varied magnetospheric environment, *Geophys. Res. Lett., 36,* L15109, doi:10.1029/2009GL039427.

Samson, J.A.R., T. Masuoka, P. N. Pareek, and G. C. Angel (1987), Total and dissociativephotoionization cross sections of N2from threshold to 107 eV. *J. Chem. Phys. 86*,6128–6132.

Samson, J. A. R., G. N. Haddad, T. Masuoka, P. N. Pareek, and D. A. L. Kilcoyne (1989), Ionization yields, total absoption, and dissociative photoionization cross sections of CH_4 from 110-950 Å, *J. Chem. Phys. 90*(12), 6925.

Schrijver, C. J., and G. L. Siscoe, (2009). *Heliophysics: Plasma physics of the local cosmos.* Cambridge Univ. Press, Cambridge.

Semaniak, J., et al., (2001). Dissociative recombination of $HCNH^+$: Absolute cross-sections and branching ratios*, Astrophys. J. Suppl. Ser., 135,* 275-283.

Schunk, R. W., and A. F. Nagy, (2009). *Ionospheres, Second Edition*. Cambridge Univ. Press, Cambridge.

Shemansky, D. E., A. I. F. Stewart, R. A. West, L. W. Esposito, J. T. Hallett, and X. Liu (2005), The Cassini UVIS stellar probe of the Titan atmosphere, *Science, 308*, 978–982.

Shimamura, I. (1983), Partial-sum rules for and asymmetry between rotational transitions $J\pm\Delta J \leftarrow J$, *Phys. Rev. A, 28,* no. 3, 1357.

Sittler, E. C., et al. (2008), Ion and neutral sources and sinks within Saturn's inner magnetosphere: Cassini results, *Planet. Space Sci., 56*, 3–8, doi:10.1016/j.pss.2007.06.006.

Sittler, E. C., R. E. Hartle, C. Bertucci, A. Coates, T. E. Cravens, I. Dandouras, and D. E. Shemansky (2009), Energy deposition processes in Titan's upper atmosphere and its induced magnetosphere. In *Titan from Cassini-Huygens*, edited by R. H. Brown, J.-P. Lebreton, and J.H. Waite, Springer, New York, pp. 393-454.

Smith, B.A., and 28 co-authors (1982), A new look at the Saturn system: TheVoyager 2 images, *Science, 215*, 504–537.

Smith, H. T., R. E. Johnson, and V. I. Shematovich (2004), Titan's atomic and molecular nitrogen tori, *Geophys. Res. Lett., 31*, L16804, doi:10.1029/2004GL020580.

Smith III, F. L., and C. Smith (1972), Numerical evaluations of Chapman's grazing incidence integral ch(X,x), *J. Phys. Res, 77*, 3592, doi:10,1029/JA077i019p03592.

Sohn, W., K. Jung and H. Ehrhardt (1983), Threshold structures in the cross section of low-energyelectron scattering of methane, *J. Phys. B: Atom. Mol. Phys., 16*, 891.

Solomon, S. C., P. B. Hays and V. J. Abreu (1988), The auroral 6300Å emission: Observations and modeling, *J. Geophys. Res., 93*, 9867.

Straub, H.C., D. Lin, B. G. Lindsay, K. A. Smith, and R. F. Stebbings (1997), Absolute partial cross sections for electron-impact ionization of CH4 from threshold to 1000 eV, *J. Chem. Phys.,106,* 4430-4435.

Tabata, T., T. Shirai, M. Sataka, and H. Kubo (2006) Analytic cross sections for electron impact collisions with nitrogen molecules, *atomic Data Nucl. Data Tabl.*, *92*, 375-406.

Tanaka, H., M. Kubo, N. Onodera, and A. Suzuki (1983), Vibrational excitation of CH_4 by electron impact: 3-20 eV, *J. Phys. B: Atom. Mol. Phys., 16*, 2861.

Tobiska, W. K., T. Woods, F. G. Eparvier, R. Viereck, L. Floyd, D. Bouwer, G. Rottman, and O. R. White (2000), The SOLAR2000 empirical solar irradiance model and forecast tool, *J.* Atmos. *Sol. Terr. Phys., 62* (14), 1233.

Tobiska, W.K. (2007), SOLAR 2000 v2.30 and SOLARFLARE v1.01: New capabilities for space system operations, *American Institute of Aeronautics and Astronautics, Inc.*

Toublanc, D., J. P. Parisot, J. Brillet, D. Gautier, F. Raulin, and C. P. McKay (1995a), Photochemical modeling of Titan's atmosphere, *Icarus, 113*, 2.

Toublanc, D., J. P. Parisot, J. Brillet, D. Gautier, F. Raulin, and C. P. McKay (1995b), Erratum: Photochemical modeling of Titan's atmosphere, *Icarus, 117*, 218.

Trajmar, S., D. F. Register and A. Chutjian (1983), Electron scattering by molecules II. Experimental methods and data, *Physics Reports (Review Section of Physics Letters), 97*, 219.

Ulusen., D., J. G. Luhmann, Y.-J. Ma, S. Ledvina, T. E. Cravens, K. Mandt, J. H. Waite, J.-E. Wahlund (2010), Investigation of the force balance in the Titan ionosphere: Cassini T5 flyby model/data comparisons, *Icarus, 210*, 867-880, doi: 10.1016/j.icarus.2010.07.004.

Vervack Jr., R. J., B. R. Sandel, and D. F. Strobel (2004), New perspectives on Titan's upper atmosphere from a reanalysis of the Voyager 1 UVS solar occultations, *Icarus, 170*, 91–112.

Vigren, E., M. Hamberg, V. Zhaunerchyk, M. Kaminska, R. Thomas, M. Larsson, T. Millar, C. Walsh, and W. Geppert (2009), The dissociative recombination of protonated acrylonitrile and the upper atmosphere of Titan, *The Astrophysical Journal, 695*. 317.

Vuitton, V., R. V. Yelle, and V. G. Anicich (2006), The nitrogen chemistry of Titan's upper atmosphere revealed, *Astrophys. J., 647*, L175–L178.

Vuitton, V., R. V. Yelle, and M. McEwan (2007), Ion chemistry and N-containing molecules in Titan's upper atmosphere, *Icarus, 191*, 722–742.

Vuskovic, L. and S. Trajmar (1983), Electron impact excitation of methane, *J. Chem. Phys.. 78*, 4947.

Wahlund, J.-E., and 17 colleagues (2005), Cassini measurements of cold plasma in the ionosphere of Titan, *Science, 308*, 986–989.

Wainfan, N., W. C. Walker and G. L. Weissler (1955), Photoionization efficiencies and cross sections in O_2, N_2, CO_2, Ar, H_2O, H_2, and CH_4, *Phys. Rev., 99*, 542.

Waite, J. H., et al. (2004), The Cassini ion and neutral mass spectrometer (INMS) investigation, *Space Sci. Rev., 114 (1),* 113.

Waite Jr., J. H., T. E. Cravens, W.-H. Ip, W. T. Kasprzak, J. G. Luhmann, R. L. McNutt, H. B. Niemann, R. B. Yelle, I. Meuller-Wodarg, S. A. Ledvina, and S. Scherer (2005a), Oxygen ions observed near Saturn's A ring, *Science, 307*, 1260–1262.

Waite Jr., J. H., and 21 colleagues. (2005b), Ion Neutral Mass Spectrometer (INMS) results from the first flyby of Titan, *Science, 308*, 982–986.

Waite Jr., J. H., D. T. Young, T. E. Cravens, A. J. Coates, F. J. Crary, B. Magee, and J. Westlake (2007), The process of tholin formation in Titan's upper atmosphere, *Science, 316*, 870–875.

Watanabe, K., M. Zelikoff, and E. C. Y. Inn (1953) Absorption coefficients of several atmospheric gases, *Air Force Cambridge Research Centre Tech. Rep*. 52-53.

Westlake, J. H., J. H. Waite, Jr., K. E. Mandt, N. Carrasco, J. M. Bell, B. A. Magee, and J.-E. Wahlund (2012), Titan's ionospheric composition and structure: Photochemical modeling of Cassini INMS data, *J. Geophys. Res., 117*, E01003, 21, doi:10.1029/2011JE003883.

Westlake, J. H., J. H. Waite Jr., K. E. Mandt, N. Carrasco, J. M. Bell, B. A. Magee, and J.-E. Wahlund (2012), Titan's ionospheric composition and structure: Photochemical modeling of Cassini INMS data, *J. Geophys. Res., 117*, E01003,doi:10.1029/2011JE003883.

Wight, G. R., M. J. Van der Wiel and C. E. Brion (1976), Diopole excitations, ionization and fragmentation of N_2 and CO in the 10-60 eV region, *J. Phys. B, 9*, 675.

Woodall, J.,M. Agúndez, A. J. Markwick-Kemper, and T. J. Millar (2007) The UMIST database for astrochemistry. *Astron. Astrophys. 466*, 1197–1204.

Young, D. T., and 42 colleagues (2005), Composition and dynamics of plasma in Saturn's magnetosphere, *Science 307*. 1262–1266.

Zabka, J., M. Polasek, D. Ascenzi, P. Tosi and D. Schroder (2009), Reactivity of $C_2H_5^+$ with benzene: Formation of ethylbenzenium ions and implications for Titan's ionospheric chemistry, *the Journal of Physical Chemistry A, 113*(42), 11,153-11,160.

Zipf, E. C. and R. W. McLaughkub (1978), On the dissociation of nitrogen by electron impact and by E.U.V. photo-absorption, *Planet. Space Sci., 26*, 449.

Appendix A **Incident Solar Flux for Titan Flybys T17, T18 and T40**

This section contains tabulated versions of the solar flux plots for the T17, T18 and T40 flybys of Titan. Solar fluxes are shown for the results of the EUVAC and SOLAR2000 (SIP) models.

A-1 Incident Solar Flux

Appendix Table A.1 Solar flux generated by the EUVAC and SOLAR2000 (Solar Irradiance Platform) for the T17, T18 and T40 flybys of Titan. Solar fluxes are in solar flux units (photons $cm^{-2} * 10^{-9}$).

λ_{MAX} (Å)	λ_{MIN} (Å)	T18 SOLAR2000	T18 EUVAC	T17 SOLAR2000	T17 EUVAC	T40 SOLAR2000	T40 EUVAC
1306	1304.9	7.913E-01	7.913E-01	7.913E-01	7.913E-01	7.913E-01	7.913E-01
1302.2	1302.2	7.913E-01	7.913E-01	7.913E-01	7.913E-01	7.913E-01	7.913E-01
1265	1265	2.241E-01	2.241E-01	2.241E-01	2.241E-01	2.241E-01	2.241E-01
1260.7	1260.7	2.241E-01	2.241E-01	2.241E-01	2.241E-01	2.241E-01	2.241E-01
1242.8	1242.8	2.149E-01	2.149E-01	2.149E-01	2.149E-01	2.149E-01	2.149E-01
1238.8	1238.8	2.962E-01	2.962E-01	2.962E-01	2.962E-01	2.962E-01	2.962E-01
1215.7	1215.7	4.010E+01	4.010E+01	4.010E+01	4.010E+01	3.720E+01	3.720E+01
1206.5	1206.5	1.185E+00	1.185E+00	1.185E+00	1.185E+00	7.877E-01	7.877E-01
1175	1175	4.209E-01	4.209E-01	4.209E-01	4.209E-01	3.044E-01	3.044E-01
1128.3	1128.3	2.789E-01	2.789E-01	2.789E-01	2.789E-01	2.052E-01	2.052E-01
1122.5	1122.5	2.789E-01	2.789E-01	2.789E-01	2.789E-01	2.052E-01	2.052E-01
1085	1085	1.944E-01	1.944E-01	1.944E-01	1.944E-01	1.359E-01	1.359E-01
1037.6	1037.6	3.403E+00	3.403E+00	2.568E+00	2.568E+00	2.484E+00	2.484E+00
1031.9	1031.9	6.363E+00	2.034E+00	4.800E+00	2.124E+00	4.644E+00	2.072E+00
1310	1280	1.005E+01	1.005E+01	1.005E+01	1.005E+01	1.005E+01	1.005E+01
1280	1250	4.974E+00	4.974E+00	4.974E+00	4.974E+00	4.974E+00	4.974E+00
1250	1220	7.752E+01	7.752E+01	7.752E+01	7.752E+01	7.752E+01	7.752E+01
1220	1190	3.742E+02	3.742E+02	3.742E+02	3.742E+02	3.439E+02	3.439E+02
1190	1160	5.725E+00	5.725E+00	5.725E+00	5.725E+00	4.317E+00	4.317E+00
1160	1130	2.265E+00	2.265E+00	2.265E+00	2.265E+00	1.740E+00	1.740E+00
1130	1100	4.257E+00	4.257E+00	4.257E+00	4.257E+00	3.135E+00	3.135E+00
1100	1070	4.612E+00	4.612E+00	4.612E+00	4.612E+00	3.301E+00	3.301E+00
1070	1040	2.710E+00	2.710E+00	2.710E+00	2.710E+00	1.866E+00	1.866E+00
1040	1027	1.210E+01	1.210E+01	9.129E+00	9.129E+00	8.830E+00	8.830E+00
1025.8	1025.7	8.743E+00	3.393E+00	6.596E+00	3.539E+00	6.381E+00	3.454E+00
1010.3	1010.1	1.699E-01	1.292E-02	1.282E-01	1.339E-02	1.240E-01	1.312E-02
991.6	991.5	7.644E-01	3.573E-03	5.767E-01	3.704E-03	5.578E-01	3.628E-03

λ_{MAX} (Å)	λ_{MIN} (Å)	T18 SOLAR2000	T18 EUVAC	T17 SOLAR2000	T17 EUVAC	T40 SOLAR2000	T40 EUVAC
1027	990	1.031E+00	2.390E+00	7.778E-01	2.477E+00	7.524E-01	2.426E+00
977.1	977	1.191E+01	4.297E+00	8.981E+00	4.437E+00	8.688E+00	4.356E+00
972.6	972.5	1.647E+00	3.573E-03	1.242E+00	3.704E-03	1.202E+00	3.628E-03
990	950	9.411E-01	1.429E+00	7.099E-01	1.482E+00	6.868E-01	1.451E+00
949.8	949.7	6.995E-01	4.804E-03	5.277E-01	5.003E-03	5.104E-01	4.888E-03
944.6	944.5	1.299E-01	4.804E-03	9.800E-02	5.003E-03	9.480E-02	4.888E-03
937.9	937.7	3.797E-01	9.609E-03	2.865E-01	1.001E-02	2.771E-01	9.776E-03
933.4	933.3	1.959E-01	4.804E-03	1.478E-01	5.003E-03	1.429E-01	4.888E-03
930.8	930.7	2.598E-01	4.804E-03	1.960E-01	5.003E-03	1.896E-01	4.888E-03
950	912	2.181E+00	1.826E+00	1.645E+00	1.901E+00	1.592E+00	1.857E+00
912	890	7.330E+00	1.057E+00	5.529E+00	1.101E+00	5.349E+00	1.075E+00
890	860	5.101E+00	2.051E+00	3.848E+00	2.148E+00	3.722E+00	2.092E+00
860	840	1.794E+00	1.367E+00	1.354E+00	1.432E+00	1.309E+00	1.394E+00
835	832	1.564E+00	1.008E-01	1.180E+00	1.048E-01	1.141E+00	1.025E-01
840	810	1.223E+00	1.008E+00	9.227E-01	1.048E+00	8.925E-01	1.025E+00
810	796	3.831E-01	4.702E-01	2.890E-01	4.890E-01	2.796E-01	4.781E-01
790.2	790.1	9.539E-01	6.897E-01	7.196E-01	7.083E-01	6.961E-01	6.975E-01
787.8	787.7	5.546E-01	1.304E-03	4.184E-01	1.355E-03	4.047E-01	1.325E-03
786.5	786.4	2.924E-01	1.304E-03	2.206E-01	1.355E-03	2.134E-01	1.325E-03
780.4	780.3	2.610E-01	1.304E-03	1.969E-01	1.355E-03	1.905E-01	1.325E-03
796	780	3.002E-01	2.086E-01	2.265E-01	2.168E-01	2.191E-01	2.121E-01
770.5	770.4	4.846E-01	2.403E-01	3.656E-01	2.671E-01	3.537E-01	2.515E-01
765.2	765.1	3.991E-01	1.661E-01	3.011E-01	1.714E-01	2.912E-01	1.683E-01
760.35	760.25	9.792E-03	1.304E-03	7.388E-03	1.355E-03	7.146E-03	1.325E-03
780	760	5.562E-01	2.607E-01	4.196E-01	2.711E-01	4.059E-01	2.651E-01
760	740	3.483E-01	2.607E-01	2.628E-01	2.711E-01	2.542E-01	2.651E-01
740	732	2.978E-02	2.741E-02	2.246E-02	2.849E-02	2.173E-02	2.786E-02
703.4	703.3	7.824E-01	3.535E-01	5.903E-01	3.623E-01	5.710E-01	3.572E-01
732	700	2.298E-01	1.096E-01	1.734E-01	1.139E-01	1.677E-01	1.114E-01
685.8	685.7	2.024E-01	3.198E-04	1.527E-01	3.311E-04	1.477E-01	3.245E-04
700	665	1.859E-01	1.119E-01	1.402E-01	1.159E-01	1.356E-01	1.136E-01
665	630	1.717E-01	1.119E-01	1.295E-01	1.159E-01	1.253E-01	1.136E-01
629.8	624.9	3.198E+00	1.559E+00	2.412E+00	1.601E+00	2.333E+00	1.577E+00
609.8	609.7	8.993E-01	4.792E-01	6.784E-01	5.483E-01	6.563E-01	5.082E-01
630	600	3.337E-02	3.181E-01	2.518E-02	3.506E-01	2.436E-02	3.317E-01
599.7	599.5	3.797E-01	5.811E-04	2.865E-01	5.987E-04	2.771E-01	5.885E-04
584.4	584.3	3.158E+00	1.231E+00	2.382E+00	1.284E+00	2.304E+00	1.253E+00
554.4	554.3	1.597E+00	7.061E-01	1.205E+00	7.250E-01	1.166E+00	7.140E-01
537.1	537	3.717E-01	2.857E-01	2.804E-01	3.070E-01	2.713E-01	2.946E-01
507.95	507.9	1.529E-01	1.429E-01	1.153E-01	1.535E-01	1.116E-01	1.473E-01
499.4	499.3	1.549E-01	5.562E-04	1.168E-01	6.592E-04	1.130E-01	5.994E-04

λ_{MAX} (Å)	λ_{MIN} (Å)	T18 SOLAR2000	T18 EUVAC	T17 SOLAR2000	T17 EUVAC	T40 SOLAR2000	T40 EUVAC
600	480	1.408E+00	3.487E-01	1.062E+00	3.592E-01	1.027E+00	3.531E-01
465.3	465.2	3.597E-01	2.771E-01	2.714E-01	2.946E-01	2.625E-01	2.845E-01
480	460	1.077E-01	1.112E-01	8.126E-02	1.318E-01	7.861E-02	1.199E-01
460	435	2.660E-01	1.391E-01	2.007E-01	1.648E-01	1.941E-01	1.499E-01
435	400	5.400E-01	3.662E-01	4.074E-01	3.891E-01	3.941E-01	3.758E-01
368.1	368	1.478E+00	6.246E-01	1.115E+00	6.592E-01	1.078E+00	6.391E-01
360.9	360.7	3.497E-02	2.461E-01	2.638E-02	3.385E-01	2.552E-02	2.848E-01
303.8	303.7	1.199E+01	7.445E+00	9.046E+00	7.792E+00	8.750E+00	7.591E+00
400	300	2.589E+00	8.367E-01	1.953E+00	1.011E+00	1.890E+00	9.099E-01
284.2	284.1	1.999E-01	3.879E-02	1.508E-01	2.718E-01	1.458E-01	1.365E-01
300	280	3.685E-01	4.702E-01	2.780E-01	5.891E-01	2.689E-01	5.201E-01
274.3	274.1	9.992E-02	4.702E-03	7.538E-02	5.891E-03	7.292E-02	5.201E-03
264.81	264.79	5.995E-02	4.702E-04	4.523E-02	5.891E-04	4.375E-02	5.201E-04
280	260	5.949E-01	4.702E-01	4.488E-01	5.891E-01	4.342E-01	5.201E-01
256.4	256.3	5.422E-01	4.524E-01	4.090E-01	4.627E-01	3.957E-01	4.568E-01
260	240	1.193E+00	4.702E-01	8.998E-01	5.891E-01	8.704E-01	5.201E-01
240	220	7.408E-01	1.097E+00	5.589E-01	1.292E+00	5.406E-01	1.179E+00
220	205	2.012E-01	8.229E-01	1.518E-01	9.686E-01	1.469E-01	8.840E-01
205	190	9.802E-01	8.229E-01	7.395E-01	9.686E-01	7.153E-01	8.840E-01
190	180	8.909E-01	8.500E-01	6.721E-01	9.494E-01	6.502E-01	8.917E-01
180	165	1.915E+00	1.275E+00	1.444E+00	1.424E+00	1.397E+00	1.338E+00
165	138	2.740E-01	2.295E+00	2.067E-01	2.564E+00	1.999E-01	2.408E+00
138	103	1.405E-01	4.298E-01	1.060E-01	4.555E-01	1.025E-01	4.406E-01
100.59	100.49	1.679E-02	1.228E-03	1.266E-02	1.302E-03	1.225E-02	1.259E-03
100	99.94	5.396E-03	5.859E-03	4.071E-03	6.362E-03	3.938E-03	6.070E-03
99.76	99.66	3.997E-03	9.765E-03	3.015E-03	1.060E-02	2.917E-03	1.012E-02
98.55	98.45	5.196E-03	9.765E-03	3.920E-03	1.060E-02	3.792E-03	1.012E-02
98.31	98.21	5.396E-03	9.765E-03	4.071E-03	1.060E-02	3.938E-03	1.012E-02
98.17	98.07	5.396E-03	9.765E-03	4.071E-03	1.060E-02	3.938E-03	1.012E-02
97.92	97.82	4.596E-03	9.765E-03	3.468E-03	1.060E-02	3.354E-03	1.012E-02
97.56	97.46	5.995E-03	9.765E-03	4.523E-03	1.060E-02	4.375E-03	1.012E-02
97.17	97.07	1.039E-02	9.765E-03	7.840E-03	1.060E-02	7.584E-03	1.012E-02
96.88	96.78	5.396E-03	9.765E-03	4.071E-03	1.060E-02	3.938E-03	1.012E-02
96.54	96.44	3.797E-03	9.765E-03	2.865E-03	1.060E-02	2.771E-03	1.012E-02
96.1	96	1.639E-02	9.765E-03	1.236E-02	1.060E-02	1.196E-02	1.012E-02
95.86	95.76	5.796E-03	9.765E-03	4.372E-03	1.060E-02	4.229E-03	1.012E-02
95.56	95.46	5.796E-03	9.765E-03	4.372E-03	1.060E-02	4.229E-03	1.012E-02
95.42	95.32	9.593E-03	9.765E-03	7.237E-03	1.060E-02	7.000E-03	1.012E-02
94.95	94.85	1.999E-04	9.765E-03	1.508E-04	1.060E-02	1.458E-04	1.012E-02
94.44	94.34	3.397E-03	9.765E-03	2.563E-03	1.060E-02	2.479E-03	1.012E-02
94.3	94.2	1.999E-04	9.765E-03	1.508E-04	1.060E-02	1.458E-04	1.012E-02

λ_{MAX} (Å)	λ_{MIN} (Å)	T18 SOLAR2000	T18 EUVAC	T17 SOLAR2000	T17 EUVAC	T40 SOLAR2000	T40 EUVAC
94.12	94.02	1.639E-02	9.765E-03	1.236E-02	1.060E-02	1.196E-02	1.012E-02
93.66	93.56	1.119E-02	9.765E-03	8.443E-03	1.060E-02	8.167E-03	1.012E-02
92.86	92.76	7.594E-03	9.765E-03	5.729E-03	1.060E-02	5.542E-03	1.012E-02
92.14	92.04	7.594E-03	9.765E-03	5.729E-03	1.060E-02	5.542E-03	1.012E-02
91.86	91.76	9.593E-03	9.765E-03	7.237E-03	1.060E-02	7.000E-03	1.012E-02
91.74	91.64	1.079E-02	9.765E-03	8.141E-03	1.060E-02	7.875E-03	1.012E-02
91.53	91.43	3.797E-03	9.765E-03	2.865E-03	1.060E-02	2.771E-03	1.012E-02
91.05	90.95	7.794E-03	9.765E-03	5.880E-03	1.060E-02	5.688E-03	1.012E-02
90.76	90.66	5.995E-03	9.765E-03	4.523E-03	1.060E-02	4.375E-03	1.012E-02
90.5	90.4	3.997E-03	9.765E-03	3.015E-03	1.060E-02	2.917E-03	1.012E-02
90.19	90.09	6.195E-03	9.765E-03	4.674E-03	1.060E-02	4.521E-03	1.012E-02
89.75	89.65	5.995E-03	9.765E-03	4.523E-03	1.060E-02	4.375E-03	1.012E-02
89.19	89.09	5.396E-03	9.765E-03	4.071E-03	1.060E-02	3.938E-03	1.012E-02
88.95	88.85	7.594E-03	9.765E-03	5.729E-03	1.060E-02	5.542E-03	1.012E-02
88.69	88.59	4.796E-03	9.765E-03	3.618E-03	1.060E-02	3.500E-03	1.012E-02
88.47	88.37	3.797E-03	9.765E-03	2.865E-03	1.060E-02	2.771E-03	1.012E-02
88.19	88.09	1.999E-04	9.765E-03	1.508E-04	1.060E-02	1.458E-04	1.012E-02
88.16	88.06	1.219E-02	9.765E-03	9.197E-03	1.060E-02	8.896E-03	1.012E-02
88.14	88.04	8.993E-03	9.765E-03	6.784E-03	1.060E-02	6.563E-03	1.012E-02
87.66	87.56	3.997E-03	9.765E-03	3.015E-03	1.060E-02	2.917E-03	1.012E-02
87.35	87.25	4.796E-03	9.765E-03	3.618E-03	1.060E-02	3.500E-03	1.012E-02
87.03	86.93	6.195E-03	9.765E-03	4.674E-03	1.060E-02	4.521E-03	1.012E-02
86.91	86.81	3.797E-03	9.765E-03	2.865E-03	1.060E-02	2.771E-03	1.012E-02
86.82	86.72	9.193E-03	9.765E-03	6.935E-03	1.060E-02	6.709E-03	1.012E-02
84.05	83.95	1.019E-02	9.765E-03	7.689E-03	1.060E-02	7.438E-03	1.012E-02
83.72	83.62	7.594E-03	9.765E-03	5.729E-03	1.060E-02	5.542E-03	1.012E-02
83.47	83.37	8.993E-03	9.765E-03	6.784E-03	1.060E-02	6.563E-03	1.012E-02
82.89	82.79	5.196E-03	9.765E-03	3.920E-03	1.060E-02	3.792E-03	1.012E-02
82.79	82.69	5.196E-03	9.765E-03	3.920E-03	1.060E-02	3.792E-03	1.012E-02
82.48	82.38	9.792E-03	9.765E-03	7.388E-03	1.060E-02	7.146E-03	1.012E-02
80.6	80.5	4.596E-03	9.765E-03	3.468E-03	1.060E-02	3.354E-03	1.012E-02
80.05	79.95	2.798E-03	9.765E-03	2.111E-03	1.060E-02	2.042E-03	1.012E-02
79.81	79.71	4.596E-03	9.765E-03	3.468E-03	1.060E-02	3.354E-03	1.012E-02
79.53	79.43	3.597E-03	9.765E-03	2.714E-03	1.060E-02	2.625E-03	1.012E-02
79.13	79.03	3.797E-03	9.765E-03	2.865E-03	1.060E-02	2.771E-03	1.012E-02
78.75	78.65	5.596E-03	9.765E-03	4.221E-03	1.060E-02	4.084E-03	1.012E-02
78.61	78.51	5.995E-03	9.765E-03	4.523E-03	1.060E-02	4.375E-03	1.012E-02
77.79	77.69	7.794E-03	9.765E-03	5.880E-03	1.060E-02	5.688E-03	1.012E-02
77.35	77.25	5.796E-03	9.765E-03	4.372E-03	1.060E-02	4.229E-03	1.012E-02
76.99	76.89	6.595E-03	9.765E-03	4.975E-03	1.060E-02	4.813E-03	1.012E-02
76.88	76.78	8.194E-03	9.765E-03	6.181E-03	1.060E-02	5.979E-03	1.012E-02

λ_{MAX} (Å)	λ_{MIN} (Å)	T18 SOLAR2000	T18 EUVAC	T17 SOLAR2000	T17 EUVAC	T40 SOLAR2000	T40 EUVAC
76.53	76.43	1.999E-03	9.765E-03	1.508E-03	1.060E-02	1.458E-03	1.012E-02
76.06	75.96	6.395E-03	9.765E-03	4.825E-03	1.060E-02	4.667E-03	1.012E-02
75.78	75.68	4.996E-03	9.765E-03	3.769E-03	1.060E-02	3.646E-03	1.012E-02
75.51	75.41	7.594E-03	9.765E-03	5.729E-03	1.060E-02	5.542E-03	1.012E-02
75.34	75.24	4.996E-03	9.765E-03	3.769E-03	1.060E-02	3.646E-03	1.012E-02
75.08	74.98	9.193E-03	9.765E-03	6.935E-03	1.060E-02	6.709E-03	1.012E-02
74.88	74.78	7.994E-03	9.765E-03	6.031E-03	1.060E-02	5.834E-03	1.012E-02
74.49	74.39	2.598E-03	9.765E-03	1.960E-03	1.060E-02	1.896E-03	1.012E-02
74.26	74.16	4.996E-03	9.765E-03	3.769E-03	1.060E-02	3.646E-03	1.012E-02
73.6	73.5	3.797E-03	9.765E-03	2.865E-03	1.060E-02	2.771E-03	1.012E-02
73.52	73.42	9.992E-04	9.765E-03	7.538E-04	1.060E-02	7.292E-04	1.012E-02
73	72.9	6.795E-03	9.765E-03	5.126E-03	1.060E-02	4.959E-03	1.012E-02
72.85	72.75	4.197E-03	9.765E-03	3.166E-03	1.060E-02	3.063E-03	1.012E-02
72.68	72.58	3.198E-03	9.765E-03	2.412E-03	1.060E-02	2.333E-03	1.012E-02
72.36	72.26	1.279E-02	9.765E-03	9.649E-03	1.060E-02	9.334E-03	1.012E-02
71.99	71.89	2.398E-03	9.765E-03	1.809E-03	1.060E-02	1.750E-03	1.012E-02
71.05	70.95	8.793E-03	9.765E-03	6.634E-03	1.060E-02	6.417E-03	1.012E-02
70.8	70.7	5.995E-03	9.765E-03	4.523E-03	1.060E-02	4.375E-03	1.012E-02
70.59	70.49	6.595E-03	9.765E-03	4.975E-03	1.060E-02	4.813E-03	1.012E-02
70.05	69.95	1.999E-04	9.765E-03	1.508E-04	1.060E-02	1.458E-04	1.012E-02
69.7	69.6	2.758E-02	9.765E-03	2.081E-02	1.060E-02	2.013E-02	1.012E-02
68.4	68.3	4.596E-03	9.765E-03	3.468E-03	1.060E-02	3.354E-03	1.012E-02
67.4	67.3	3.997E-03	9.765E-03	3.015E-03	1.060E-02	2.917E-03	1.012E-02
67.19	67.09	5.995E-03	9.765E-03	4.523E-03	1.060E-02	4.375E-03	1.012E-02
66.42	66.32	7.994E-04	9.765E-03	6.031E-04	1.060E-02	5.834E-04	1.012E-02
66.35	66.25	7.594E-03	9.765E-03	5.729E-03	1.060E-02	5.542E-03	1.012E-02
66.31	66.21	5.995E-04	9.765E-03	4.523E-04	1.060E-02	4.375E-04	1.012E-02
65.9	65.8	5.995E-03	9.765E-03	4.523E-03	1.060E-02	4.375E-03	1.012E-02
65.76	65.66	8.194E-03	9.765E-03	6.181E-03	1.060E-02	5.979E-03	1.012E-02
65.26	65.16	5.995E-03	9.765E-03	4.523E-03	1.060E-02	4.375E-03	1.012E-02
64.65	64.55	4.996E-03	9.765E-03	3.769E-03	1.060E-02	3.646E-03	1.012E-02
64.16	64.06	2.198E-03	9.765E-03	1.658E-03	1.060E-02	1.604E-03	1.012E-02
63.7	63.6	8.194E-03	9.765E-03	6.181E-03	1.060E-02	5.979E-03	1.012E-02
63.35	63.25	1.079E-02	9.765E-03	8.141E-03	1.060E-02	7.875E-03	1.012E-02
63.21	63.11	6.595E-03	9.765E-03	4.975E-03	1.060E-02	4.813E-03	1.012E-02
62.82	62.72	6.795E-03	9.765E-03	5.126E-03	1.060E-02	4.959E-03	1.012E-02
62.4	62.3	2.198E-03	9.765E-03	1.658E-03	1.060E-02	1.604E-03	1.012E-02
62.35	62.25	1.999E-04	9.765E-03	1.508E-04	1.060E-02	1.458E-04	1.012E-02
61.95	61.85	9.992E-03	9.765E-03	7.538E-03	1.060E-02	7.292E-03	1.012E-02
61.68	61.58	5.796E-03	9.765E-03	4.372E-03	1.060E-02	4.229E-03	1.012E-02
61.12	61.02	1.159E-02	9.765E-03	8.744E-03	1.060E-02	8.459E-03	1.012E-02

λ_{MAX} (Å)	λ_{MIN} (Å)	T18 SOLAR2000	T18 EUVAC	T17 SOLAR2000	T17 EUVAC	T40 SOLAR2000	T40 EUVAC
60.9	60.8	7.194E-03	9.765E-03	5.428E-03	1.060E-02	5.250E-03	1.012E-02
60.35	60.25	4.996E-03	9.765E-03	3.769E-03	1.060E-02	3.646E-03	1.012E-02
59.67	59.57	1.399E-03	9.765E-03	1.055E-03	1.060E-02	1.021E-03	1.012E-02
59.01	58.91	1.399E-03	9.765E-03	1.055E-03	1.060E-02	1.021E-03	1.012E-02
57.93	57.83	8.593E-03	9.765E-03	6.483E-03	1.060E-02	6.271E-03	1.012E-02
57.61	57.51	9.992E-03	9.765E-03	7.538E-03	1.060E-02	7.292E-03	1.012E-02
57.41	57.31	1.239E-02	9.765E-03	9.348E-03	1.060E-02	9.042E-03	1.012E-02
56.97	56.87	1.479E-02	9.765E-03	1.116E-02	1.060E-02	1.079E-02	1.012E-02
56.13	56.03	4.796E-03	9.765E-03	3.618E-03	1.060E-02	3.500E-03	1.012E-02
55.39	55.29	2.118E-02	9.765E-03	1.598E-02	1.060E-02	1.546E-02	1.012E-02
55.11	55.01	7.994E-03	9.765E-03	6.031E-03	1.060E-02	5.834E-03	1.012E-02
54.47	54.37	7.194E-03	9.765E-03	5.428E-03	1.060E-02	5.250E-03	1.012E-02
54.2	54.1	1.639E-02	9.765E-03	1.236E-02	1.060E-02	1.196E-02	1.012E-02
52.96	52.86	1.999E-04	9.765E-03	1.508E-04	1.060E-02	1.458E-04	1.012E-02
52.35	52.25	6.995E-03	9.765E-03	5.277E-03	1.060E-02	5.104E-03	1.012E-02
50.74	50.64	1.119E-02	9.765E-03	8.443E-03	1.060E-02	8.167E-03	1.012E-02
50.57	50.47	1.119E-02	9.765E-03	8.443E-03	1.060E-02	8.167E-03	1.012E-02
49.27	49.17	8.593E-03	8.593E-03	6.483E-03	6.483E-03	6.271E-03	6.271E-03
47.92	47.82	8.993E-03	8.993E-03	6.784E-03	6.784E-03	6.563E-03	6.563E-03
46.72	46.62	7.994E-03	7.994E-03	6.031E-03	6.031E-03	5.834E-03	5.834E-03
46.45	46.35	5.396E-03	5.396E-03	4.071E-03	4.071E-03	3.938E-03	3.938E-03
45.71	45.61	9.992E-04	9.992E-04	7.538E-04	7.538E-04	7.292E-04	7.292E-04
44.21	44.11	1.799E-03	1.799E-03	1.357E-03	1.357E-03	1.313E-03	1.313E-03
44.07	43.97	1.599E-03	1.599E-03	1.206E-03	1.206E-03	1.167E-03	1.167E-03
43.81	43.71	4.197E-03	4.197E-03	3.166E-03	3.166E-03	3.063E-03	3.063E-03
41	40.9	1.199E-03	1.199E-03	9.046E-04	9.046E-04	8.750E-04	8.750E-04
33.79	33.69	2.198E-03	2.198E-03	1.658E-03	1.658E-03	1.604E-03	1.604E-03
30.48	30.38	1.199E-03	1.199E-03	9.046E-04	9.046E-04	8.750E-04	8.750E-04
30.07	29.97	1.799E-03	1.799E-03	1.357E-03	1.357E-03	1.313E-03	1.313E-03
30	29	3.054E-03	3.054E-03	3.054E-03	3.054E-03	3.640E-03	3.640E-03
29	28	4.979E-03	4.979E-03	4.979E-03	4.979E-03	5.936E-03	5.936E-03
28	27	3.581E-03	3.581E-03	3.581E-03	3.581E-03	4.269E-03	4.269E-03
27	26	3.671E-03	3.671E-03	3.671E-03	3.671E-03	4.376E-03	4.376E-03
26	25	2.234E-03	2.234E-03	2.234E-03	2.234E-03	2.663E-03	2.663E-03
25	24	6.071E-03	6.071E-03	6.071E-03	6.071E-03	7.237E-03	7.237E-03
24	23	2.104E-03	2.104E-03	2.104E-03	2.104E-03	2.509E-03	2.509E-03
23	22	1.277E-02	1.277E-02	1.277E-02	1.277E-02	1.522E-02	1.522E-02
22	21	1.831E-02	1.831E-02	1.831E-02	1.831E-02	2.182E-02	2.182E-02
21	20	1.583E-03	1.583E-03	1.583E-03	1.583E-03	1.887E-03	1.887E-03
20	19	2.005E-04	2.005E-04	2.005E-04	2.005E-04	2.581E-04	2.581E-04
19	18	1.813E-03	1.813E-03	1.813E-03	1.813E-03	2.333E-03	2.333E-03

λ_{MAX} (Å)	λ_{MIN} (Å)	T18 SOLAR2000	T18 EUVAC	T17 SOLAR2000	T17 EUVAC	T40 SOLAR2000	T40 EUVAC
18	17	5.027E-03	5.027E-03	5.027E-03	5.027E-03	6.470E-03	6.470E-03
17	16	2.378E-03	2.378E-03	2.378E-03	2.378E-03	3.061E-03	3.061E-03
16	15	2.473E-03	2.473E-03	2.473E-03	2.473E-03	3.183E-03	3.183E-03
15	14	1.518E-04	1.518E-04	1.518E-04	1.518E-04	1.954E-04	1.954E-04
14	13	4.828E-04	4.828E-04	4.828E-04	4.828E-04	6.214E-04	6.214E-04
13	12	2.865E-04	2.865E-04	2.865E-04	2.865E-04	3.687E-04	3.687E-04
12	11	1.783E-04	1.783E-04	1.783E-04	1.783E-04	2.295E-04	2.295E-04
11	10	1.418E-04	1.418E-04	1.418E-04	1.418E-04	1.825E-04	1.825E-04
10	9.9	3.290E-05	3.290E-05	3.286E-05	3.290E-05	4.408E-05	4.410E-05
9.9	9.8	2.970E-05	2.970E-05	2.968E-05	2.970E-05	3.981E-05	3.980E-05
9.8	9.7	2.840E-05	2.840E-05	2.836E-05	2.840E-05	3.804E-05	3.800E-05
9.7	9.6	2.640E-05	2.640E-05	2.644E-05	2.640E-05	3.547E-05	3.550E-05
9.6	9.5	2.500E-05	2.500E-05	2.496E-05	2.500E-05	3.349E-05	3.350E-05
9.5	9.4	2.560E-05	2.560E-05	2.559E-05	2.560E-05	3.433E-05	3.430E-05
9.4	9.3	6.760E-05	6.760E-05	6.761E-05	6.760E-05	9.069E-05	9.070E-05
9.3	9.2	1.015E-04	1.015E-04	1.015E-04	1.015E-04	1.361E-04	1.361E-04
9.2	9.1	1.327E-04	1.327E-04	1.327E-04	1.327E-04	1.781E-04	1.781E-04
9.1	9	2.010E-05	2.010E-05	2.009E-05	2.010E-05	2.695E-05	2.690E-05
9	8.9	1.880E-05	1.880E-05	1.876E-05	1.880E-05	2.516E-05	2.520E-05
8.9	8.8	1.790E-05	1.790E-05	1.794E-05	1.790E-05	2.406E-05	2.410E-05
8.8	8.7	1.640E-05	1.640E-05	1.643E-05	1.640E-05	2.204E-05	2.200E-05
8.7	8.6	1.510E-05	1.510E-05	1.511E-05	1.510E-05	2.027E-05	2.030E-05
8.6	8.5	1.400E-05	1.400E-05	1.401E-05	1.400E-05	1.879E-05	1.880E-05
8.5	8.4	1.300E-05	1.300E-05	1.303E-05	1.300E-05	1.748E-05	1.750E-05
8.4	8.3	1.200E-05	1.200E-05	1.197E-05	1.200E-05	1.605E-05	1.610E-05
8.3	8.2	1.100E-05	1.100E-05	1.103E-05	1.100E-05	1.479E-05	1.480E-05
8.2	8.1	1.010E-05	1.010E-05	1.014E-05	1.010E-05	1.361E-05	1.360E-05
8.1	8	9.320E-06	9.320E-06	9.319E-06	9.320E-06	1.250E-05	1.250E-05
8	7.9	8.720E-06	8.720E-06	8.718E-06	8.720E-06	1.169E-05	1.170E-05
7.9	7.8	2.010E-05	2.010E-05	2.007E-05	2.010E-05	2.692E-05	2.690E-05
7.8	7.7	9.510E-06	9.510E-06	9.509E-06	9.510E-06	1.275E-05	1.280E-05
7.7	7.6	6.440E-06	6.440E-06	6.437E-06	6.440E-06	8.635E-06	8.630E-06
7.6	7.5	5.830E-06	5.830E-06	5.833E-06	5.830E-06	7.824E-06	7.820E-06
7.5	7.4	7.560E-06	7.560E-06	7.562E-06	7.560E-06	1.014E-05	1.010E-05
7.4	7.3	5.640E-06	5.640E-06	5.643E-06	5.640E-06	7.570E-06	7.570E-06
7.3	7.2	4.260E-06	4.260E-06	4.264E-06	4.260E-06	5.719E-06	5.720E-06
7.2	7.1	3.820E-06	3.820E-06	3.818E-06	3.820E-06	5.121E-06	5.120E-06
7.1	7	3.410E-06	3.410E-06	3.411E-06	3.410E-06	4.575E-06	4.570E-06
7	6.9	3.110E-06	3.110E-06	3.115E-06	3.110E-06	4.178E-06	4.180E-06
6.9	6.8	6.230E-06	6.230E-06	6.235E-06	6.230E-06	8.363E-06	8.360E-06
6.8	6.7	1.950E-05	1.950E-05	1.946E-05	1.950E-05	2.611E-05	2.610E-05

λ_{MAX} (Å)	λ_{MIN} (Å)	T18 SOLAR2000	T18 EUVAC	T17 SOLAR2000	T17 EUVAC	T40 SOLAR2000	T40 EUVAC
6.7	6.6	1.160E-05	1.160E-05	1.157E-05	1.160E-05	1.552E-05	1.550E-05
6.6	6.5	1.820E-06	1.820E-06	1.822E-06	1.820E-06	2.444E-06	2.440E-06
6.5	6.4	1.590E-06	1.590E-06	1.588E-06	1.590E-06	2.131E-06	2.130E-06
6.4	6.3	1.380E-06	1.380E-06	1.378E-06	1.380E-06	1.849E-06	1.850E-06
6.3	6.2	1.190E-06	1.190E-06	1.190E-06	1.190E-06	1.596E-06	1.600E-06
6.2	6.1	1.020E-06	1.020E-06	1.023E-06	1.020E-06	1.372E-06	1.370E-06
6.1	6	8.740E-07	8.740E-07	8.739E-07	8.740E-07	1.172E-06	1.170E-06
6	5.9	7.430E-07	7.430E-07	7.428E-07	7.430E-07	9.963E-07	9.960E-07
5.9	5.8	6.280E-07	6.280E-07	6.276E-07	6.280E-07	8.419E-07	8.420E-07
5.8	5.7	5.270E-07	5.270E-07	5.271E-07	5.270E-07	7.070E-07	7.070E-07
5.7	5.6	1.060E-06	1.060E-06	1.055E-06	1.060E-06	1.415E-06	1.420E-06
5.6	5.5	3.640E-07	3.640E-07	3.645E-07	3.640E-07	4.889E-07	4.890E-07
5.5	5.4	4.440E-07	4.440E-07	4.439E-07	4.440E-07	5.955E-07	5.950E-07
5.4	5.3	2.450E-07	2.450E-07	2.451E-07	2.450E-07	3.288E-07	3.290E-07
5.3	5.2	3.500E-07	3.500E-07	3.495E-07	3.500E-07	4.688E-07	4.690E-07
5.2	5.1	2.850E-07	2.850E-07	2.846E-07	2.850E-07	3.817E-07	3.820E-07
5.1	5	2.230E-07	2.230E-07	2.230E-07	2.230E-07	2.991E-07	2.990E-07
5	4.9	9.990E-08	9.990E-08	9.988E-08	9.990E-08	1.340E-07	1.340E-07
4.9	4.8	7.790E-08	7.790E-08	7.792E-08	7.790E-08	1.045E-07	1.050E-07
4.8	4.7	6.010E-08	6.010E-08	6.013E-08	6.010E-08	8.066E-08	8.070E-08
4.7	4.6	4.590E-08	4.590E-08	4.587E-08	4.590E-08	6.153E-08	6.150E-08
4.6	4.5	3.460E-08	3.460E-08	3.456E-08	3.460E-08	4.636E-08	4.640E-08
4.5	4.4	2.570E-08	2.570E-08	2.570E-08	2.570E-08	3.447E-08	3.450E-08
4.4	4.3	1.990E-08	1.990E-08	1.993E-08	1.990E-08	2.674E-08	2.670E-08
4.3	4.2	1.360E-08	1.360E-08	1.361E-08	1.360E-08	1.825E-08	1.830E-08
4.2	4.1	1.030E-08	1.030E-08	1.025E-08	1.030E-08	1.375E-08	1.370E-08
4.1	4	7.550E-09	7.550E-09	7.554E-09	7.550E-09	1.013E-08	1.010E-08
4	3.9	4.620E-09	4.620E-09	4.625E-09	4.620E-09	6.204E-09	6.200E-09
3.9	3.8	3.110E-09	3.110E-09	3.105E-09	3.110E-09	4.165E-09	4.170E-09
3.8	3.7	2.040E-09	2.040E-09	2.040E-09	2.040E-09	2.736E-09	2.740E-09
3.7	3.6	1.310E-09	1.310E-09	1.309E-09	1.310E-09	1.755E-09	1.760E-09
3.6	3.5	8.180E-10	8.180E-10	8.180E-10	8.180E-10	1.097E-09	1.100E-09
3.5	3.4	4.970E-10	4.970E-10	4.973E-10	4.970E-10	6.670E-10	6.670E-10
3.4	3.3	2.930E-10	2.930E-10	2.932E-10	2.930E-10	3.933E-10	3.930E-10
3.3	3.2	1.670E-10	1.670E-10	1.672E-10	1.670E-10	2.242E-10	2.240E-10
3.2	3.1	9.190E-11	9.190E-11	9.190E-11	9.190E-11	1.233E-10	1.230E-10
3.1	3	4.850E-11	4.850E-11	4.852E-11	4.850E-11	6.509E-11	6.510E-11
3	2.9	2.450E-11	2.450E-11	2.451E-11	2.450E-11	3.288E-11	3.290E-11
2.9	2.8	1.180E-11	1.180E-11	1.179E-11	1.180E-11	1.581E-11	1.580E-11
2.8	2.7	5.370E-12	5.370E-12	5.368E-12	5.370E-12	7.200E-12	7.200E-12
2.7	2.6	2.300E-12	2.300E-12	2.300E-12	2.300E-12	3.086E-12	3.090E-12

λ_{MAX} (Å)	λ_{MIN} (Å)	T18 SOLAR2000	T18 EUVAC	T17 SOLAR2000	T17 EUVAC	T40 SOLAR2000	T40 EUVAC
2.6	2.5	9.210E-13	9.210E-13	9.212E-13	9.210E-13	1.236E-12	1.240E-12
2.5	2.4	3.420E-13	3.420E-13	3.418E-13	3.420E-13	4.585E-13	4.580E-13
2.4	2.3	1.160E-13	1.160E-13	1.164E-13	1.160E-13	1.561E-13	1.560E-13
2.3	2.2	3.590E-14	3.590E-14	3.593E-14	3.590E-14	4.819E-14	4.820E-14
2.2	2.1	9.920E-15	9.920E-15	9.924E-15	9.920E-15	1.331E-14	1.330E-14
2.1	2	2.410E-15	2.410E-15	2.413E-15	2.410E-15	3.236E-15	3.240E-15

Appendix B **Cross Sections**

Cross Sections for photoabsorption, photoionization and electron impact ionization of methane and molecular nitrogen are shown here in tabular form. These are used in as inputs in the photoionization and two stream codes.

B-1 Photoabsorption Cross Sections and Branching Ratios

Appendix Table B.1 Photoabsorption and photoionization cross sections for N_2

				Branching Ratios for N_2				
λ_{Max}	λ_{Min}	σ_{abs}	σ_{ion}	X	A	B	$(2\sigma^{-1})$	N^{++}
1306	1304.9	0	0	0	0	0	0	0
1302.2	1302.2	0	0	0	0	0	0	0
1265	1265	0	0	0	0	0	0	0
1260.7	1260.7	0	0	0	0	0	0	0
1242.8	1242.8	0	0	0	0	0	0	0
1238.8	1238.8	0	0	0	0	0	0	0
1215.7	1215.7	0	0	0	0	0	0	0
1206.5	1206.5	0	0	0	0	0	0	0
1175	1175	0	0	0	0	0	0	0
1128.3	1128.3	0	0	0	0	0	0	0
1122.5	1122.5	0	0	0	0	0	0	0
1085	1085	0	0	0	0	0	0	0
1037.6	1037.6	0	0	0	0	0	0	0
1031.9	1031.9	0	0	0	0	0	0	0
1310	1280	0	0	0	0	0	0	0
1280	1250	0	0	0	0	0	0	0
1250	1220	0	0	0	0	0	0	0
1220	1190	0	0	0	0	0	0	0
1190	1160	0	0	0	0	0	0	0
1160	1130	0	0	0	0	0	0	0
1130	1100	0	0	0	0	0	0	0
1100	1070	0	0	0	0	0	0	0
1070	1040	0	0	0	0	0	0	0
1040	1027	0	0	0	0	0	0	0
1025.8	1025.7	0	0	0	0	0	0	0
1010.3	1010.1	0	0	0	0	0	0	0
991.6	991.5	0	0	0	0	0	0	0
1027	990	0	0	0	0	0	0	0

				Branching Ratios for N_2				
λ_{Max}	λ_{Min}	σ_{abs}	σ_{ion}	X	A	B	$(2\sigma^{-1})$	N^{++}
977.1	977	68.1	0	0	0	0	0	0
972.6	972.5	68.1	0	0	0	0	0	0
990	950	26.03	0	0	0	0	0	0
949.8	949.7	7.2	0	0	0	0	0	0
944.6	944.5	39.8	0	0	0	0	0	0
937.9	937.7	3.1	0	0	0	0	0	0
933.4	933.3	3.1	0	0	0	0	0	0
930.8	930.7	64.5	0	0	0	0	0	0
950	912	39.95	0	0	0	0	0	0
912	890	27.51	0	0	0	0	0	0
890	860	50.46	0	0	0	0	0	0
860	840	21.88	0	0	0	0	0	0
835	832	29.36	0	0	0	0	0	0
840	810	13.47	0	1	0	0	0	0
810	796	28.44	0	1	0	0	0	0
790.2	790.1	59.9	33.3	1	0	0	0	0
787.8	787.7	16.3	9.9	1	0	0	0	0
786.5	786.4	16.3	0	1	0	0	0	0
780.4	780.3	40.8	24.8	1	0	0	0	0
796	780	34.01	14.57	1	0	0	0	0
770.5	770.4	26.9	18.4	1	0	0	0	0
765.2	765.1	35.5	23.8	1	0	0	0	0
760.35	760.25	30.3	19.6	1	0	0	0	0
780	760	28.44	17.39	1	0	0	0	0
760	740	27.48	14.15	1	0	0	0	0
740	732	29.68	25.9	1	0	0	0	0
703.4	703.3	26.5	20.9	0.974	0.026	0	0	0
732	700	32.31	24.2	0.999	0.001	0	0	0
685.8	685.7	26.2	21.6	0.245	0.755	0	0	0
700	665	31.95	26.21	0.261	0.739	0	0	0
665	630	23.7	23.46	0.262	0.738	0	0	0
629.8	624.9	23.2	23.2	0.355	0.645	0	0	0
609.8	609.7	23.1	23.1	0.385	0.613	0.002	0	0
630	600	23.2	23.2	0.377	0.623	0.001	0	0
599.7	599.5	23.1	23.1	0.397	0.584	0.018	0	0
584.4	584.3	22.82	22.82	0.384	0.51	0.107	0	0
554.4	554.3	24.3	24.3	0.386	0.517	0.097	0	0
537.1	537	25.2	25.2	0.384	0.524	0.092	0	0
507.95	507.9	24	24	0.379	0.536	0.085	0	0
499.4	499.3	22	22	0.382	0.532	0.086	0	0

				Branching Ratios for N_2				
λ_{Max}	λ_{Min}	σ_{abs}	σ_{ion}	X	A	B	$(2\sigma^{-1})$	N^{++}
600	480	23.93	23.93	0.384	0.523	0.093	0	0
465.3	465.2	21.8	21.8	0.398	0.511	0.091	0	0
480	460	21.73	21.73	0.394	0.515	0.09	0	0
460	435	21.92	21.92	0.431	0.479	0.089	0	0
435	400	20.906	20.906	0.448	0.465	0.087	0	0
368.1	368	17.212	17.212	0.404	0.5	0.096	0	0
360.9	360.7	16.608	16.608	0.389	0.511	0.099	0	0
303.8	303.7	12.4	12.4	0.304	0.503	0.123	0.07	0
400	300	14.1	14.1	0.365	0.528	0.106	0	0
284.2	284.1	10.69	10.69	0.29	0.482	0.119	0.109	0
300	280	11.14	11.14	0.291	0.491	0.121	0.097	0
274.3	274.1	10.3	10.3	0.282	0.459	0.116	0.143	0
264.81	264.79	10.14	10.14	0.282	0.437	0.116	0.165	0
280	260	10.19	10.19	0.281	0.45	0.116	0.153	0
256.4	256.3	9.65	9.65	0.287	0.418	0.119	0.176	0
260	240	9.59	9.59	0.29	0.404	0.12	0.185	0
240	220	8.37	8.37	0.309	0.368	0.129	0.194	0
220	205	7.44	7.44	0.333	0.343	0.14	0.185	0
205	190	6.31	6.31	0.354	0.318	0.149	0.179	0
190	180	5.6	5.6	0.371	0.295	0.157	0.177	0
180	165	5.05	5.05	0.389	0.272	0.165	0.174	0
165	138	3.94	3.94	0.421	0.231	0.181	0.167	0
138	103	1.915	1.915	0.474	0.168	0.205	0.152	0
100.59	100.49	1.24	1.24	0.509	0.13	0.223	0.138	0
100	99.94	1.224	1.224	0.51	0.129	0.224	0.137	0
99.76	99.66	1.215	1.215	0.51	0.129	0.224	0.137	0
98.55	98.45	1.18	1.18	0.512	0.126	0.225	0.136	0
98.31	98.21	1.173	1.173	0.513	0.126	0.226	0.136	0
98.17	98.07	1.169	1.169	0.513	0.126	0.226	0.136	0
97.92	97.82	1.162	1.162	0.513	0.125	0.226	0.135	0
97.56	97.46	1.152	1.152	0.514	0.125	0.226	0.135	0
97.17	97.07	1.141	1.141	0.515	0.124	0.227	0.135	0
96.88	96.78	1.133	1.133	0.515	0.123	0.227	0.135	0
96.54	96.44	1.123	1.123	0.516	0.123	0.227	0.134	0
96.1	96	1.111	1.111	0.517	0.122	0.228	0.134	0
95.86	95.76	1.104	1.104	0.517	0.121	0.228	0.134	0
95.56	95.46	1.096	1.096	0.517	0.121	0.228	0.133	0
95.42	95.32	1.092	1.092	0.518	0.121	0.228	0.133	0
94.95	94.85	1.079	1.079	0.519	0.12	0.229	0.133	0
94.44	94.34	1.065	1.065	0.519	0.119	0.229	0.133	0

				Branching Ratios for N_2				
λ_{Max}	λ_{Min}	σ_{abs}	σ_{ion}	X	A	B	$(2\sigma^{-1})$	N^{++}
94.3	94.2	1.062	1.062	0.52	0.119	0.229	0.132	0
94.12	94.02	1.057	1.057	0.52	0.118	0.23	0.132	0
93.66	93.56	1.044	1.044	0.521	0.117	0.23	0.132	0
92.86	92.76	1.023	1.023	0.522	0.116	0.231	0.131	0
92.14	92.04	1.004	1.004	0.523	0.115	0.232	0.131	0
91.86	91.76	0.997	0.997	0.524	0.114	0.232	0.13	0
91.74	91.64	0.994	0.994	0.524	0.114	0.232	0.13	0
91.53	91.43	0.988	0.988	0.524	0.114	0.232	0.13	0
91.05	90.95	0.976	0.976	0.525	0.113	0.233	0.13	0
90.76	90.66	0.968	0.968	0.526	0.112	0.233	0.129	0
90.5	90.4	0.962	0.962	0.526	0.112	0.233	0.129	0
90.19	90.09	0.954	0.954	0.527	0.111	0.233	0.129	0
89.75	89.65	0.943	0.943	0.528	0.11	0.234	0.129	0
89.19	89.09	0.929	0.929	0.529	0.109	0.234	0.128	0
88.95	88.85	0.923	0.923	0.529	0.109	0.235	0.128	0
88.69	88.59	0.916	0.916	0.529	0.108	0.235	0.128	0
88.47	88.37	0.911	0.911	0.53	0.108	0.235	0.127	0
88.19	88.09	0.904	0.904	0.53	0.108	0.235	0.127	0
88.16	88.06	0.903	0.903	0.53	0.107	0.236	0.127	0
88.14	88.04	0.903	0.903	0.53	0.107	0.236	0.127	0
87.66	87.56	0.891	0.891	0.531	0.107	0.236	0.127	0
87.35	87.25	0.883	0.883	0.532	0.106	0.236	0.126	0
87.03	86.93	0.876	0.876	0.532	0.105	0.237	0.126	0
86.91	86.81	0.873	0.873	0.532	0.105	0.237	0.126	0
86.82	86.72	0.87	0.87	0.533	0.105	0.237	0.126	0
84.05	83.95	0.805	0.805	0.537	0.1	0.24	0.123	0
83.72	83.62	0.798	0.798	0.538	0.1	0.24	0.123	0
83.47	83.37	0.792	0.792	0.538	0.099	0.24	0.123	0
82.89	82.79	0.779	0.779	0.539	0.098	0.241	0.122	0
82.79	82.69	0.777	0.777	0.54	0.098	0.241	0.122	0
82.48	82.38	0.77	0.77	0.54	0.097	0.241	0.122	0
80.6	80.5	0.728	0.728	0.543	0.094	0.243	0.12	0
80.05	79.95	0.716	0.716	0.544	0.093	0.244	0.12	0
79.81	79.71	0.711	0.711	0.545	0.093	0.244	0.119	0
79.53	79.43	0.705	0.705	0.545	0.092	0.244	0.119	0
79.13	79.03	0.697	0.697	0.546	0.091	0.245	0.119	0
78.75	78.65	0.689	0.689	0.547	0.091	0.245	0.118	0
78.61	78.51	0.686	0.686	0.547	0.09	0.245	0.118	0
77.79	77.69	0.669	0.669	0.548	0.089	0.246	0.117	0
77.35	77.25	0.66	0.66	0.549	0.088	0.247	0.117	0

				Branching Ratios for N_2				
λ_{Max}	λ_{Min}	σ_{abs}	σ_{ion}	X	A	B	$(2\sigma^{-1})$	N^{++}
76.99	76.89	0.652	0.652	0.55	0.088	0.247	0.117	0
76.88	76.78	0.65	0.65	0.55	0.088	0.247	0.116	0
76.53	76.43	0.643	0.643	0.55	0.087	0.247	0.116	0
76.06	75.96	0.633	0.633	0.551	0.086	0.248	0.116	0
75.78	75.68	0.628	0.628	0.552	0.086	0.248	0.115	0
75.51	75.41	0.622	0.622	0.552	0.085	0.248	0.115	0
75.34	75.24	0.619	0.619	0.553	0.085	0.249	0.115	0
75.08	74.98	0.614	0.614	0.553	0.084	0.249	0.115	0
74.88	74.78	0.61	0.61	0.553	0.084	0.249	0.114	0
74.49	74.39	0.602	0.602	0.554	0.083	0.25	0.114	0
74.26	74.16	0.598	0.598	0.554	0.083	0.25	0.114	0
73.6	73.5	0.585	0.585	0.556	0.082	0.25	0.113	0
73.52	73.42	0.584	0.584	0.556	0.082	0.251	0.113	0
73	72.9	0.574	0.574	0.557	0.081	0.251	0.113	0
72.85	72.75	0.571	0.571	0.557	0.081	0.251	0.112	0
72.68	72.58	0.568	0.568	0.557	0.08	0.251	0.112	0
72.36	72.26	0.562	0.562	0.558	0.08	0.252	0.112	0
71.99	71.89	0.555	0.555	0.558	0.079	0.252	0.111	0
71.05	70.95	0.538	0.538	0.56	0.078	0.253	0.11	0
70.8	70.7	0.533	0.533	0.56	0.077	0.253	0.11	0
70.59	70.49	0.529	0.529	0.561	0.077	0.254	0.11	0
70.05	69.95	0.52	0.52	0.562	0.076	0.254	0.109	0
69.7	69.6	0.513	0.513	0.562	0.075	0.255	0.109	0
68.4	68.3	0.491	0.491	0.565	0.073	0.256	0.108	0
67.4	67.3	0.474	0.474	0.566	0.071	0.257	0.107	0
67.19	67.09	0.47	0.47	0.567	0.071	0.257	0.106	0
66.42	66.32	0.457	0.457	0.568	0.07	0.258	0.105	0
66.35	66.25	0.456	0.456	0.568	0.07	0.258	0.105	0
66.31	66.21	0.455	0.455	0.568	0.07	0.258	0.105	0
65.9	65.8	0.449	0.449	0.569	0.069	0.259	0.105	0
65.76	65.66	0.446	0.446	0.569	0.069	0.259	0.105	0
65.26	65.16	0.438	0.438	0.57	0.068	0.259	0.104	0
64.65	64.55	0.429	0.429	0.571	0.067	0.26	0.103	0
64.16	64.06	0.421	0.421	0.572	0.066	0.261	0.103	0
63.7	63.6	0.414	0.414	0.573	0.065	0.261	0.102	0
63.35	63.25	0.408	0.408	0.573	0.065	0.261	0.102	0
63.21	63.11	0.406	0.406	0.573	0.065	0.262	0.102	0
62.82	62.72	0.4	0.4	0.574	0.064	0.262	0.101	0
62.4	62.3	0.394	0.394	0.575	0.063	0.263	0.101	0
62.35	62.25	0.393	0.393	0.575	0.063	0.263	0.101	0

				Branching Ratios for N_2				
λ_{Max}	λ_{Min}	σ_{abs}	σ_{ion}	X	A	B	$(2\sigma^{-1})$	N^{++}
61.95	61.85	0.387	0.387	0.576	0.062	0.263	0.1	0
61.68	61.58	0.383	0.383	0.576	0.062	0.263	0.1	0
61.12	61.02	0.374	0.374	0.577	0.061	0.264	0.099	0
60.9	60.8	0.371	0.371	0.577	0.061	0.264	0.099	0
60.35	60.25	0.363	0.363	0.578	0.06	0.265	0.098	0
59.67	59.57	0.353	0.353	0.579	0.059	0.266	0.098	0
59.01	58.91	0.344	0.344	0.58	0.058	0.266	0.097	0
57.93	57.83	0.329	0.329	0.582	0.056	0.267	0.095	0
57.61	57.51	0.325	0.325	0.583	0.056	0.268	0.095	0
57.41	57.31	0.322	0.322	0.583	0.055	0.268	0.095	0
56.97	56.87	0.316	0.316	0.584	0.055	0.269	0.094	0
56.13	56.03	0.305	0.305	0.585	0.053	0.269	0.093	0
55.39	55.29	0.295	0.295	0.586	0.052	0.27	0.092	0
55.11	55.01	0.292	0.292	0.587	0.052	0.271	0.092	0
54.47	54.37	0.284	0.284	0.588	0.051	0.271	0.091	0
54.2	54.1	0.28	0.28	0.588	0.05	0.272	0.091	0
52.96	52.86	0.265	0.265	0.591	0.048	0.273	0.089	0
52.35	52.25	0.258	0.258	0.592	0.047	0.274	0.088	0
50.74	50.64	0.239	0.239	0.594	0.045	0.276	0.086	0
50.57	50.47	0.237	0.237	0.595	0.045	0.276	0.086	0
49.27	49.17	0.223	0.223	0.597	0.043	0.277	0.084	0
47.92	47.82	0.209	0.209	0.599	0.041	0.279	0.082	0
46.72	46.62	0.196	0.196	0.601	0.039	0.28	0.081	0
46.45	46.35	0.193	0.193	0.601	0.038	0.281	0.08	0
45.71	45.61	0.186	0.186	0.603	0.037	0.281	0.079	0
44.21	44.11	0.172	0.172	0.605	0.035	0.283	0.077	0
44.07	43.97	0.17	0.17	0.605	0.035	0.283	0.077	0
43.81	43.71	0.168	0.168	0.606	0.035	0.284	0.077	0
41	40.9	0.143	0.143	0.61	0.03	0.287	0.073	0
33.79	33.69	0.09	0.09	0.622	0.021	0.296	0.061	0
30.48	30.38	0.075	0.075	0.627	0.016	0.3	0.056	0
30.07	29.97	1.56	1.56	0.03	0.001	0.014	0.003	0.952
30	29	1.489	1.489	0.03	0.001	0.014	0.003	0.952
29	28	1.359	1.359	0.03	0.001	0.014	0.003	0.952
28	27	1.236	1.236	0.03	0.001	0.015	0.002	0.952
27	26	1.121	1.121	0.03	0.001	0.015	0.002	0.952
26	25	1.016	1.016	0.03	0.001	0.015	0.002	0.952
25	24	0.91	0.91	0.03	0.001	0.015	0.002	0.952
24	23	0.815	0.815	0.031	0	0.015	0.002	0.952
23	22	0.726	0.726	0.031	0	0.015	0.002	0.952

				Branching Ratios for N_2				
λ_{Max}	λ_{Min}	σ_{abs}	σ_{ion}	X	A	B	$(2\sigma^{-1})$	N^{++}
22	21	0.644	0.644	0.031	0	0.015	0.002	0.952
21	20	0.567	0.567	0.031	0	0.015	0.002	0.952
20	19	0.497	0.497	0.031	0	0.015	0.002	0.952
19	18	0.432	0.432	0.031	0	0.015	0.002	0.952
18	17	0.373	0.373	0.031	0	0.016	0.001	0.952
17	16	0.319	0.319	0.031	0	0.016	0.001	0.952
16	15	0.27	0.27	0.031	0	0.016	0.001	0.952
15	14	0.226	0.226	0.031	0	0.016	0.001	0.952
14	13	0.187	0.187	0.031	0	0.016	0.001	0.952
13	12	0.153	0.153	0.031	0	0.016	0.001	0.952
12	11	0.122	0.122	0.031	0	0.016	0.001	0.952
11	10	0.096	0.096	0.031	0	0.016	0.001	0.952
10	9.9	0.083	0.083	0.031	0	0.016	0.001	0.952
9.9	9.8	0.081	0.081	0.031	0	0.016	0.001	0.952
9.8	9.7	0.079	0.079	0.031	0	0.016	0.001	0.952
9.7	9.6	0.077	0.077	0.031	0	0.016	0.001	0.952
9.6	9.5	0.075	0.075	0.031	0	0.016	0.001	0.952
9.5	9.4	0.072	0.072	0.031	0	0.016	0.001	0.952
9.4	9.3	0.07	0.07	0.031	0	0.016	0.001	0.952
9.3	9.2	0.068	0.068	0.031	0	0.016	0.001	0.952
9.2	9.1	0.067	0.067	0.031	0	0.016	0.001	0.952
9.1	9	0.065	0.065	0.031	0	0.016	0.001	0.952
9	8.9	0.063	0.063	0.031	0	0.016	0.001	0.952
8.9	8.8	0.061	0.061	0.031	0	0.016	0.001	0.952
8.8	8.7	0.059	0.059	0.031	0	0.016	0.001	0.952
8.7	8.6	0.057	0.057	0.031	0	0.016	0.001	0.952
8.6	8.5	0.056	0.056	0.031	0	0.016	0.001	0.952
8.5	8.4	0.054	0.054	0.031	0	0.016	0.001	0.952
8.4	8.3	0.052	0.052	0.031	0	0.016	0.001	0.952
8.3	8.2	0.05	0.05	0.031	0	0.016	0.001	0.952
8.2	8.1	0.049	0.049	0.031	0	0.016	0.001	0.952
8.1	8	0.047	0.047	0.031	0	0.016	0.001	0.952
8	7.9	0.046	0.046	0.031	0	0.016	0.001	0.952
7.9	7.8	0.044	0.044	0.031	0	0.016	0.001	0.952
7.8	7.7	0.043	0.043	0.031	0	0.016	0.001	0.952
7.7	7.6	0.041	0.041	0.031	0	0.016	0.001	0.952
7.6	7.5	0.04	0.04	0.031	0	0.016	0.001	0.952
7.5	7.4	0.039	0.039	0.031	0	0.016	0.001	0.952
7.4	7.3	0.037	0.037	0.031	0	0.016	0.001	0.952
7.3	7.2	0.036	0.036	0.031	0	0.016	0.001	0.952

				Branching Ratios for N_2				
λ_{Max}	λ_{Min}	σ_{abs}	σ_{ion}	X	A	B	$(2\sigma^{-1})$	N^{++}
7.2	7.1	0.035	0.035	0.031	0	0.016	0.001	0.952
7.1	7	0.033	0.033	0.031	0	0.016	0.001	0.952
7	6.9	0.032	0.032	0.031	0	0.016	0.001	0.952
6.9	6.8	0.031	0.031	0.031	0	0.016	0.001	0.952
6.8	6.7	0.03	0.03	0.031	0	0.016	0.001	0.952
6.7	6.6	0.028	0.028	0.031	0	0.016	0.001	0.952
6.6	6.5	0.027	0.027	0.031	0	0.016	0.001	0.952
6.5	6.4	0.026	0.026	0.031	0	0.016	0.001	0.952
6.4	6.3	0.025	0.025	0.031	0	0.016	0.001	0.952
6.3	6.2	0.024	0.024	0.031	0	0.016	0.001	0.952
6.2	6.1	0.023	0.023	0.031	0	0.016	0.001	0.952
6.1	6	0.022	0.022	0.031	0	0.016	0.001	0.952
6	5.9	0.021	0.021	0.031	0	0.016	0.001	0.952
5.9	5.8	0.02	0.02	0.031	0	0.016	0.001	0.952
5.8	5.7	0.019	0.019	0.031	0	0.016	0.001	0.952
5.7	5.6	0.018	0.018	0.031	0	0.016	0.001	0.952
5.6	5.5	0.018	0.018	0.031	0	0.016	0.001	0.952
5.5	5.4	0.017	0.017	0.031	0	0.016	0.001	0.952
5.4	5.3	0.016	0.016	0.031	0	0.016	0.001	0.952
5.3	5.2	0.015	0.015	0.031	0	0.016	0.001	0.952
5.2	5.1	0.014	0.014	0.031	0	0.016	0.001	0.952
5.1	5	0.014	0.014	0.031	0	0.016	0.001	0.952
5	4.9	0.013	0.013	0.031	0	0.016	0.001	0.952

Appendix Table B.2 Photoabsorption and photoionization cross sections for CH_4

				Branching Ratios for CH_4						
λ_{Max}	λ_{Min}	σ_{abs}	σ_{ion}	CH_4^+	CH_3^+	CH_2^+	$CH^+(X)$	$CH^+(A)$	$H^+(X)$	$H^+(A)$
1306	1304.9	14.889	0	0	0	0	0	0	0	0
1302.2	1302.2	15.413	0	0	0	0	0	0	0	0
1265	1265	18.977	0	0	0	0	0	0	0	0
1260.7	1260.7	18.994	0	0	0	0	0	0	0	0
1242.8	1242.8	18.31	0	0	0	0	0	0	0	0
1238.8	1238.8	18.157	0	0	0	0	0	0	0	0
1215.7	1215.7	18.079	0	0	0	0	0	0	0	0
1206.5	1206.5	18.179	0	0	0	0	0	0	0	0
1175	1175	18.523	0	0	0	0	0	0	0	0
1128.3	1128.3	19.032	0	0	0	0	0	0	0	0
1122.5	1122.5	19.095	0	0	0	0	0	0	0	0

				Branching Ratios for CH_4						
λ_{Max}	λ_{Min}	σ_{abs}	σ_{ion}	$CH_4^{\pm}$	$CH_3^{\pm}$	$CH_2^{\pm}$	$CH^+(X)$	$CH^+(A)$	$H^+(X)$	$H^+(A)$
1085	1085	24.311	0	0	0	0	0	0	0	0
1037.6	1037.6	32.281	0	0	0	0	0	0	0	0
1031.9	1031.9	33.176	0	0	0	0	0	0	0	0
1310	1280	16.573	0	0	0	0	0	0	0	0
1280	1250	18.977	0	0	0	0	0	0	0	0
1250	1220	18.011	0	0	0	0	0	0	0	0
1220	1190	18.195	0	0	0	0	0	0	0	0
1190	1160	18.523	0	0	0	0	0	0	0	0
1160	1130	18.85	0	0	0	0	0	0	0	0
1130	1100	19.177	0	0	0	0	0	0	0	0
1100	1070	24.311	0	0	0	0	0	0	0	0
1070	1040	29.517	0	0	0	0	0	0	0	0
1040	1027	32.932	0	0	0	0	0	0	0	0
1025.8	1025.7	34.039	0	0	0	0	0	0	0	0
1010.3	1010.1	36.22	0	0	0	0	0	0	0	0
991.6	991.5	38.835	0	0	0	0	0	0	0	0
1027	990	36.45	0	0	0	0	0	0	0	0
977.1	977	40.869	0.651	1	0	0	0	0	0	0
972.6	972.5	41.5	1.21	1	0	0	0	0	0	0
990	950	41.857	1.527	1	0	0	0	0	0	0
949.8	949.7	44.669	5.536	1	0	0	0	0	0	0
944.6	944.5	45.372	6.619	1	0	0	0	0	0	0
937.9	937.7	46.285	8.024	1	0	0	0	0	0	0
933.4	933.3	46.887	8.95	1	0	0	0	0	0	0
930.8	930.7	47.239	9.492	1	0	0	0	0	0	0
950	912	47.205	9.439	1	0	0	0	0	0	0
912	890	49.77	15.486	1	0	0	0	0	0	0
890	860	50.29	20.04	0.986	0.014	0	0	0	0	0
860	840	48.756	23.827	0.945	0.055	0	0	0	0	0
835	832	47.705	34.616	0.687	0.313	0	0	0	0	0
840	810	47.153	36.601	0.657	0.343	0	0	0	0	0
810	796	45.724	40.611	0.59	0.41	0.001	0	0	0	0
790.2	790.1	44.89	42.176	0.56	0.438	0.002	0	0	0	0
787.8	787.7	44.734	42.425	0.554	0.443	0.003	0	0	0	0
786.5	786.4	44.65	42.562	0.551	0.445	0.004	0	0	0	0
780.4	780.3	44.254	43.112	0.538	0.455	0.006	0	0	0	0
796	780	44.75	42.398	0.555	0.442	0.003	0	0	0	0
770.5	770.4	43.611	43.276	0.527	0.462	0.011	0	0	0	0
765.2	765.1	43.306	43.306	0.521	0.466	0.014	0	0	0	0
760.35	760.25	43.08	43.08	0.516	0.469	0.015	0	0	0	0

				Branching Ratios for CH_4						
λ_{Max}	λ_{Min}	σ_{abs}	σ_{ion}	$CH_4^{\pm}$	$CH_3^{\pm}$	$CH_2^{\pm}$	$CH^+(X)$	$CH^+(A)$	$H^+(X)$	$H^+(A)$
780	760	43.582	43.582	0.527	0.462	0.011	0	0	0	0
760	740	42.608	42.608	0.506	0.478	0.017	0	0	0	0
740	732	41.964	41.964	0.501	0.482	0.018	0	0	0	0
703.4	703.3	39.767	39.767	0.492	0.49	0.018	0	0	0	0
732	700	40.831	40.831	0.495	0.487	0.018	0	0	0	0
685.8	685.7	38.286	38.286	0.489	0.493	0.019	0	0	0	0
700	665	38.012	38.012	0.488	0.493	0.019	0	0	0	0
665	630	35.067	35.067	0.479	0.501	0.02	0	0	0	0
629.8	624.9	33.371	33.371	0.476	0.504	0.02	0	0	0	0
609.8	609.7	31.89	31.89	0.473	0.506	0.021	0	0	0	0
630	600	32.332	32.332	0.474	0.505	0.021	0	0	0	0
599.7	599.5	31.036	31.036	0.472	0.507	0.021	0	0	0	0
584.4	584.3	29.678	29.678	0.47	0.508	0.022	0	0	0	0
554.4	554.3	26.901	26.901	0.468	0.507	0.024	0.001	0	0	0
537.1	537	25.3	25.3	0.462	0.501	0.031	0.003	0	0.003	0
507.95	507.9	22.583	22.583	0.457	0.487	0.04	0.006	0	0.009	0
499.4	499.3	21.78	21.78	0.457	0.484	0.043	0.007	0	0.01	0
600	480	25.57	25.57	0.463	0.503	0.029	0.002	0	0.003	0
465.3	465.2	18.577	18.577	0.449	0.47	0.058	0.007	0.004	0.012	0
480	460	19.023	19.023	0.45	0.473	0.055	0.007	0.003	0.012	0
460	435	16.91	16.91	0.447	0.456	0.066	0.007	0.009	0.012	0.003
435	400	14.19	14.19	0.438	0.436	0.078	0.006	0.019	0.011	0.013
368.1	368	9.964	9.964	0.415	0.415	0.082	0.004	0.032	0.008	0.043
360.9	360.7	9.503	9.503	0.407	0.416	0.084	0.004	0.034	0.007	0.048
303.8	303.7	5.874	5.874	0.373	0.36	0.115	0.002	0.046	0.006	0.098
400	300	8.816	8.816	0.398	0.412	0.088	0.004	0.036	0.007	0.055
284.2	284.1	5.135	5.135	0.349	0.355	0.125	0.002	0.049	0.005	0.116
300	280	5.269	5.269	0.357	0.356	0.122	0.002	0.048	0.005	0.11
274.3	274.1	4.907	4.907	0.333	0.352	0.131	0.002	0.05	0.005	0.127
264.81	264.79	4.691	4.691	0.316	0.349	0.137	0.002	0.052	0.004	0.14
280	260	4.811	4.811	0.326	0.351	0.133	0.002	0.051	0.005	0.133
256.4	256.3	4.499	4.499	0.309	0.343	0.143	0.002	0.053	0.004	0.146
260	240	4.354	4.354	0.305	0.337	0.147	0.002	0.054	0.004	0.151
240	220	3.66	3.66	0.296	0.32	0.157	0.001	0.058	0.004	0.164
220	205	3.04	3.04	0.279	0.319	0.168	0.001	0.062	0.003	0.169
205	190	2.509	2.509	0.28	0.31	0.171	0	0.065	0.003	0.172
190	180	2.106	2.106	0.289	0.296	0.17	0	0.068	0.002	0.175
180	165	1.719	1.719	0.295	0.292	0.166	0	0.071	0.002	0.175
165	138	1.204	1.204	0.291	0.312	0.157	0	0.074	0	0.166
138	103	0.643	0.643	0.275	0.333	0.154	0	0.083	0	0.155

				Branching Ratios for CH_4						
λ_{Max}	λ_{Min}	σ_{abs}	σ_{ion}	$CH_4^{\pm}$	$CH_3^{\pm}$	$CH_2^{\pm}$	$CH^+(X)$	$CH^+(A)$	$H^+(X)$	$H^+(A)$
100.59	100.49	0.391	0.391	0.252	0.36	0.154	0	0.092	0	0.143
100	99.94	0.385	0.385	0.251	0.361	0.154	0	0.095	0	0.142
99.76	99.66	0.383	0.383	0.251	0.362	0.154	0	0.093	0	0.142
98.55	98.45	0.37	0.37	0.249	0.364	0.154	0	0.094	0	0.141
98.31	98.21	0.367	0.367	0.248	0.364	0.154	0	0.094	0	0.141
98.17	98.07	0.366	0.366	0.248	0.364	0.154	0	0.094	0	0.141
97.92	97.82	0.363	0.363	0.248	0.365	0.154	0	0.094	0	0.141
97.56	97.46	0.36	0.36	0.247	0.365	0.154	0	0.094	0	0.14
97.17	97.07	0.356	0.356	0.246	0.366	0.154	0	0.095	0	0.14
96.88	96.78	0.353	0.353	0.246	0.367	0.154	0	0.095	0	0.14
96.54	96.44	0.35	0.35	0.246	0.367	0.154	0	0.095	0	0.139
96.1	96	0.345	0.345	0.245	0.368	0.154	0	0.095	0	0.139
95.86	95.76	0.343	0.343	0.244	0.369	0.154	0	0.095	0	0.139
95.56	95.46	0.34	0.34	0.244	0.369	0.154	0	0.096	0	0.139
95.42	95.32	0.339	0.339	0.244	0.37	0.154	0	0.096	0	0.138
94.95	94.85	0.334	0.334	0.243	0.37	0.154	0	0.096	0	0.138
94.44	94.34	0.329	0.329	0.242	0.371	0.154	0	0.096	0	0.138
94.3	94.2	0.328	0.328	0.242	0.372	0.154	0	0.097	0	0.137
94.12	94.02	0.326	0.326	0.241	0.372	0.154	0	0.097	0	0.137
93.66	93.56	0.322	0.322	0.24	0.373	0.154	0	0.097	0	0.137
92.86	92.76	0.314	0.314	0.239	0.375	0.154	0	0.098	0	0.136
92.14	92.04	0.308	0.308	0.238	0.376	0.154	0	0.098	0	0.135
91.86	91.76	0.305	0.305	0.237	0.377	0.154	0	0.098	0	0.135
91.74	91.64	0.304	0.304	0.237	0.377	0.154	0	0.098	0	0.135
91.53	91.43	0.302	0.302	0.237	0.377	0.154	0	0.099	0	0.135
91.05	90.95	0.298	0.298	0.236	0.378	0.154	0	0.099	0	0.134
90.76	90.66	0.295	0.295	0.235	0.379	0.154	0	0.099	0	0.134
90.5	90.4	0.293	0.293	0.235	0.38	0.154	0	0.099	0	0.134
90.19	90.09	0.29	0.29	0.234	0.38	0.154	0	0.1	0	0.134
89.75	89.65	0.286	0.286	0.233	0.381	0.154	0	0.1	0	0.133
89.19	89.09	0.281	0.281	0.232	0.383	0.154	0	0.1	0	0.133
88.95	88.85	0.279	0.279	0.232	0.383	0.154	0	0.101	0	0.132
88.69	88.59	0.277	0.277	0.231	0.384	0.154	0	0.101	0	0.132
88.47	88.37	0.275	0.275	0.231	0.384	0.154	0	0.101	0	0.132
88.19	88.09	0.273	0.273	0.23	0.385	0.154	0	0.101	0	0.131
88.16	88.06	0.272	0.272	0.23	0.385	0.154	0	0.101	0	0.131
88.14	88.04	0.272	0.272	0.23	0.385	0.154	0	0.101	0	0.131
87.66	87.56	0.268	0.268	0.229	0.386	0.154	0	0.102	0	0.131
87.35	87.25	0.266	0.266	0.228	0.387	0.154	0	0.102	0	0.131
87.03	86.93	0.263	0.263	0.228	0.388	0.154	0	0.102	0	0.13

				Branching Ratios for CH_4						
λ_{Max}	λ_{Min}	σ_{abs}	σ_{ion}	$CH_4^{\pm}$	$CH_3^{\pm}$	$CH_2^{\pm}$	$CH^+(X)$	$CH^+(A)$	$H^+(X)$	$H^+(A)$
86.91	86.81	0.262	0.262	0.227	0.388	0.154	0	0.102	0	0.13
86.82	86.72	0.261	0.261	0.227	0.388	0.154	0	0.102	0	0.13
84.05	83.95	0.239	0.239	0.221	0.395	0.154	0	0.105	0	0.127
83.72	83.62	0.236	0.236	0.221	0.396	0.154	0	0.105	0	0.126
83.47	83.37	0.234	0.234	0.22	0.396	0.154	0	0.105	0	0.126
82.89	82.79	0.23	0.23	0.219	0.398	0.154	0	0.106	0	0.126
82.79	82.69	0.229	0.229	0.218	0.398	0.154	0	0.106	0	0.125
82.48	82.38	0.227	0.227	0.218	0.399	0.154	0	0.106	0	0.125
80.6	80.5	0.213	0.213	0.213	0.404	0.154	0	0.108	0	0.123
80.05	79.95	0.209	0.209	0.212	0.406	0.154	0	0.109	0	0.122
79.81	79.71	0.207	0.207	0.211	0.406	0.154	0	0.109	0	0.122
79.53	79.43	0.205	0.205	0.211	0.407	0.154	0	0.109	0	0.121
79.13	79.03	0.202	0.202	0.21	0.408	0.154	0	0.11	0	0.121
78.75	78.65	0.2	0.2	0.209	0.409	0.154	0	0.11	0	0.12
78.61	78.51	0.199	0.199	0.208	0.41	0.154	0	0.11	0	0.12
77.79	77.69	0.193	0.193	0.206	0.412	0.153	0	0.111	0	0.119
77.35	77.25	0.19	0.19	0.205	0.413	0.153	0	0.111	0	0.118
76.99	76.89	0.188	0.188	0.204	0.414	0.153	0	0.112	0	0.118
76.88	76.78	0.187	0.187	0.204	0.415	0.153	0	0.112	0	0.118
76.53	76.43	0.185	0.185	0.203	0.416	0.153	0	0.112	0	0.117
76.06	75.96	0.182	0.182	0.202	0.417	0.153	0	0.113	0	0.117
75.78	75.68	0.18	0.18	0.201	0.418	0.153	0	0.113	0	0.116
75.51	75.41	0.178	0.178	0.2	0.419	0.153	0	0.113	0	0.116
75.34	75.24	0.177	0.177	0.2	0.419	0.153	0	0.114	0	0.116
75.08	74.98	0.175	0.175	0.199	0.42	0.153	0	0.114	0	0.115
74.88	74.78	0.174	0.174	0.199	0.421	0.153	0	0.114	0	0.115
74.49	74.39	0.171	0.171	0.198	0.422	0.153	0	0.115	0	0.114
74.26	74.16	0.17	0.17	0.197	0.423	0.153	0	0.115	0	0.114
73.6	73.5	0.166	0.166	0.195	0.425	0.153	0	0.116	0	0.113
73.52	73.42	0.165	0.165	0.195	0.425	0.153	0	0.116	0	0.113
73	72.9	0.162	0.162	0.194	0.427	0.153	0	0.116	0	0.112
72.85	72.75	0.161	0.161	0.193	0.427	0.153	0	0.116	0	0.112
72.68	72.58	0.16	0.16	0.193	0.428	0.153	0	0.117	0	0.112
72.36	72.26	0.158	0.158	0.192	0.429	0.153	0	0.117	0	0.111
71.99	71.89	0.156	0.156	0.191	0.43	0.153	0	0.117	0	0.111
71.05	70.95	0.151	0.151	0.188	0.433	0.153	0	0.119	0	0.109
70.8	70.7	0.149	0.149	0.187	0.434	0.153	0	0.119	0	0.109
70.59	70.49	0.148	0.148	0.187	0.435	0.153	0	0.119	0	0.108
70.05	69.95	0.145	0.145	0.185	0.437	0.153	0	0.12	0	0.108
69.7	69.6	0.143	0.143	0.184	0.438	0.153	0	0.12	0	0.107

				Branching Ratios for CH_4						
λ_{Max}	λ_{Min}	σ_{abs}	σ_{ion}	$CH_4^{\pm}$	$CH_3^{\pm}$	$CH_2^{\pm}$	$CH^+(X)$	$CH^+(A)$	$H^+(X)$	$H^+(A)$
68.4	68.3	0.136	0.136	0.18	0.443	0.153	0	0.122	0	0.105
67.4	67.3	0.13	0.13	0.177	0.446	0.153	0	0.123	0	0.103
67.19	67.09	0.126	0.126	0.176	0.447	0.152	0	0.123	0	0.103
66.42	66.32	0.125	0.125	0.174	0.45	0.152	0	0.124	0	0.101
66.35	66.25	0.125	0.125	0.174	0.45	0.152	0	0.124	0	0.101
66.31	66.21	0.125	0.125	0.174	0.45	0.152	0	0.124	0	0.101
65.9	65.8	0.122	0.122	0.172	0.452	0.152	0	0.125	0	0.101
65.76	65.66	0.122	0.122	0.172	0.453	0.152	0	0.125	0	0.1
65.26	65.16	0.119	0.119	0.17	0.454	0.152	0	0.126	0	0.099
64.65	64.55	0.116	0.116	0.168	0.457	0.152	0	0.127	0	0.098
64.16	64.06	0.114	0.114	0.167	0.459	0.152	0	0.127	0	0.097
63.7	63.6	0.112	0.112	0.165	0.461	0.152	0	0.128	0	0.097
63.35	63.25	0.11	0.11	0.164	0.462	0.152	0	0.129	0	0.096
63.21	63.11	0.109	0.109	0.163	0.463	0.152	0	0.129	0	0.096
62.82	62.72	0.107	0.107	0.162	0.464	0.152	0	0.129	0	0.095
62.4	62.3	0.105	0.105	0.161	0.466	0.152	0	0.13	0	0.094
62.35	62.25	0.105	0.105	0.16	0.466	0.152	0	0.13	0	0.094
61.95	61.85	0.103	0.103	0.159	0.468	0.152	0	0.13	0	0.093
61.68	61.58	0.102	0.102	0.158	0.469	0.152	0	0.131	0	0.093
61.12	61.02	0.1	0.1	0.156	0.471	0.152	0	0.132	0	0.092
60.9	60.8	0.099	0.099	0.155	0.472	0.152	0	0.132	0	0.091
60.35	60.25	0.096	0.096	0.154	0.474	0.151	0	0.133	0	0.09
59.67	59.57	0.093	0.093	0.151	0.477	0.151	0	0.134	0	0.089
59.01	58.91	0.09	0.09	0.149	0.48	0.151	0	0.135	0	0.087
57.93	57.83	0.086	0.086	0.145	0.485	0.151	0	0.136	0	0.085
57.61	57.51	0.085	0.085	0.144	0.486	0.151	0	0.137	0	0.085
57.41	57.31	0.084	0.084	0.143	0.487	0.151	0	0.137	0	0.084
56.97	56.87	0.082	0.082	0.141	0.489	0.151	0	0.138	0	0.083
56.13	56.03	0.079	0.079	0.138	0.493	0.151	0	0.139	0	0.081
55.39	55.29	0.076	0.076	0.135	0.497	0.15	0	0.14	0	0.08
55.11	55.01	0.075	0.075	0.134	0.498	0.15	0	0.141	0	0.079
54.47	54.37	0.072	0.072	0.131	0.501	0.15	0	0.142	0	0.078
54.2	54.1	0.071	0.071	0.13	0.502	0.15	0	0.142	0	0.077
52.96	52.86	0.067	0.067	0.125	0.508	0.15	0	0.144	0	0.074
52.35	52.25	0.065	0.065	0.123	0.511	0.15	0	0.146	0	0.073
50.74	50.64	0.06	0.06	0.116	0.519	0.149	0	0.148	0	0.069
50.57	50.47	0.059	0.059	0.116	0.52	0.149	0	0.149	0	0.069
49.27	49.17	0.055	0.055	0.11	0.527	0.149	0	0.151	0	0.066
47.92	47.82	0.051	0.051	0.104	0.534	0.148	0	0.153	0	0.062
46.72	46.62	0.047	0.047	0.099	0.541	0.148	0	0.156	0	0.059

				Branching Ratios for CH_4						
λ_{Max}	λ_{Min}	σ_{abs}	σ_{ion}	$CH_4^{\pm}$	$CH_3^{\pm}$	$CH_2^{\pm}$	$CH^+(X)$	$CH^+(A)$	$H^+(X)$	$H^+(A)$
46.45	46.35	0.047	0.047	0.098	0.542	0.148	0	0.156	0	0.059
45.71	45.61	0.045	0.045	0.094	0.546	0.148	0	0.157	0	0.057
44.21	44.11	0.044	0.044	0.087	0.555	0.147	0	0.16	0	0.053
44.07	43.97	0.04	0.04	0.087	0.556	0.147	0	0.161	0	0.052
43.81	43.71	0.04	0.04	0.086	0.557	0.147	0	0.161	0	0.052
41	40.9	0.958	0.958	0	0.027	0.006	0	0.008	0	0
33.79	33.69	0.574	0.574	0	0.027	0.006	0	0.008	0	0
30.48	30.38	0.469	0.469	0	0.028	0.006	0	0.008	0	0
30.07	29.97	0.451	0.451	0	0.028	0.006	0	0.008	0	0
30	29	0.429	0.429	0	0.028	0.006	0	0.008	0	0
29	28	0.386	0.386	0	0.028	0.005	0	0.009	0	0
28	27	0.35	0.35	0	0.028	0.005	0	0.009	0	0
27	26	0.314	0.314	0	0.028	0.005	0	0.009	0	0
26	25	0.281	0.281	0	0.028	0.005	0	0.009	0	0
25	24	0.25	0.25	0	0.028	0.005	0	0.009	0	0
24	23	0.222	0.222	0	0.029	0.004	0	0.009	0	0
23	22	0.195	0.195	0	0.029	0.004	0	0.009	0	0
22	21	0.171	0.171	0	0.029	0.004	0	0.009	0	0
21	20	0.149	0.149	0	0.029	0.004	0	0.009	0	0
20	19	0.129	0.129	0	0.029	0.004	0	0.009	0	0
19	18	0.111	0.111	0	0.029	0.003	0	0.009	0	0
18	17	0.094	0.094	0	0.029	0.003	0	0.009	0	0
17	16	0.079	0.079	0	0.029	0.003	0	0.01	0	0
16	15	0.066	0.066	0	0.029	0.003	0	0.01	0	0
15	14	0.054	0.054	0	0.03	0.003	0	0.01	0	0
14	13	0.044	0.044	0	0.03	0.003	0	0.01	0	0
13	12	0.035	0.035	0	0.03	0.003	0	0.01	0	0
12	11	0.028	0.028	0	0.03	0.003	0	0.01	0	0
11	10	0.021	0.021	0	0.03	0.003	0	0.01	0	0
10	9.9	0.018	0.018	0	0.03	0.003	0	0.01	0	0
9.9	9.8	0.017	0.017	0	0.03	0.003	0	0.01	0	0
9.8	9.7	0.017	0.017	0	0.03	0.003	0	0.01	0	0
9.7	9.6	0.016	0.016	0	0.03	0.003	0	0.01	0	0
9.6	9.5	0.016	0.016	0	0.03	0.003	0	0.01	0	0
9.5	9.4	0.015	0.015	0	0.03	0.003	0	0.01	0	0
9.4	9.3	0.015	0.015	0	0.03	0.003	0	0.01	0	0
9.3	9.2	0.014	0.014	0	0.03	0.002	0	0.01	0	0
9.2	9.1	0.014	0.014	0	0.03	0.002	0	0.01	0	0
9.1	9	0.014	0.014	0	0.03	0.002	0	0.01	0	0
9	8.9	0.013	0.013	0	0.03	0.002	0	0.01	0	0

				Branching Ratios for CH_4						
λ_{Max}	λ_{Min}	σ_{abs}	σ_{ion}	$CH_4^{\pm}$	$CH_3^{\pm}$	$CH_2^{\pm}$	$CH^+(X)$	$CH^+(A)$	$H^+(X)$	$H^+(A)$
8.9	8.8	0.013	0.013	0	0.03	0.002	0	0.01	0	0
8.8	8.7	0.012	0.012	0	0.03	0.002	0	0.01	0	0
8.7	8.6	0.012	0.012	0	0.03	0.002	0	0.01	0	0
8.6	8.5	0.011	0.011	0	0.03	0.002	0	0.01	0	0
8.5	8.4	0.011	0.011	0	0.03	0.002	0	0.01	0	0
8.4	8.3	0.011	0.011	0	0.03	0.002	0	0.01	0	0
8.3	8.2	0.01	0.01	0	0.03	0.002	0	0.01	0	0
8.2	8.1	0.01	0.01	0	0.03	0.002	0	0.01	0	0
8.1	8	0.009	0.009	0	0.03	0.002	0	0.01	0	0
8	7.9	0.009	0.009	0	0.03	0.002	0	0.01	0	0
7.9	7.8	0.009	0.009	0	0.03	0.002	0	0.01	0	0
7.8	7.7	0.008	0.008	0	0.03	0.002	0	0.01	0	0
7.7	7.6	0.008	0.008	0	0.03	0.002	0	0.01	0	0
7.6	7.5	0.008	0.008	0	0.03	0.002	0	0.01	0	0
7.5	7.4	0.007	0.007	0	0.03	0.002	0	0.01	0	0
7.4	7.3	0.007	0.007	0	0.03	0.002	0	0.01	0	0
7.3	7.2	0.007	0.007	0	0.03	0.002	0	0.01	0	0
7.2	7.1	0.007	0.007	0	0.03	0.002	0	0.01	0	0
7.1	7	0.006	0.006	0	0.03	0.002	0	0.01	0	0
7	6.9	0.006	0.006	0	0.03	0.002	0	0.01	0	0
6.9	6.8	0.006	0.006	0	0.03	0.002	0	0.01	0	0
6.8	6.7	0.006	0.006	0	0.03	0.002	0	0.01	0	0
6.7	6.6	0.005	0.005	0	0.03	0.002	0	0.01	0	0
6.6	6.5	0.005	0.005	0	0.03	0.002	0	0.01	0	0
6.5	6.4	0.005	0.005	0	0.03	0.002	0	0.01	0	0
6.4	6.3	0.005	0.005	0	0.03	0.002	0	0.01	0	0
6.3	6.2	0.004	0.004	0	0.03	0.002	0	0.01	0	0
6.2	6.1	0.004	0.004	0	0.03	0.002	0	0.01	0	0
6.1	6	0.004	0.004	0	0.03	0.002	0	0.01	0	0
6	5.9	0.004	0.004	0	0.03	0.002	0	0.01	0	0
5.9	5.8	0.003	0.003	0	0.03	0.002	0	0.01	0	0
5.8	5.7	0.003	0.003	0	0.03	0.002	0	0.01	0	0
5.7	5.6	0.003	0.003	0	0.03	0.002	0	0.01	0	0
5.6	5.5	0.003	0.003	0	0.03	0.002	0	0.01	0	0
5.5	5.4	0.003	0.003	0	0.03	0.002	0	0.01	0	0
5.4	5.3	0.003	0.003	0	0.03	0.002	0	0.01	0	0
5.3	5.2	0.002	0.002	0	0.03	0.002	0	0.01	0	0
5.2	5.1	0.002	0.002	0	0.03	0.002	0	0.01	0	0
5.1	5	0.002	0.002	0	0.03	0.002	0	0.01	0	0
5	4.9	0.002	0.002	0	0.03	0.001	0	0.01	0	0

Appendix Table B.3 Electron impact ionization cross sections for N_2 from *Itikawa* [2006]. Labels indicate the final product.

E(eV)	$\rightarrow N_2^+$ ($10^{-16}cm^{-2}$)	$\rightarrow N^+$ ($10^{-16}cm^{-2}$)	$\rightarrow N^{++}$ ($10^{-16}cm^{-2}$)
15.7387	0.020261		
16.8761	0.07134		
17.1731	0.096977		
18.0957	0.163431		
19.0679	0.229087		
20.0923	0.301995		
21.1718	0.386071		
22.7018	0.50894		
24.7708	0.670914		
29.4915	0.912011	0.032112	
34.5047	1.16591	0.091201	
39.6721	1.38341	0.163431	
44.0493	1.53697	0.243594	
48.9096	1.63431	0.311411	
54.3061	1.68526	0.386071	
59.2553	1.7378	0.436516	
65.7933	1.79198	0.490531	
69.3281	1.79198	0.50894	
74.3382	1.8197	0.54117	
76.9775	1.84785	0.566674	
79.7104	1.84785	0.593381	0.001166
83.9929	1.84785	0.593381	0.001965
85.4709	1.84785	0.593381	0.002314
88.5054	1.84785	0.608135	0.003211
91.6476	1.84785	0.623256	0.003599
93.2603	1.85733	0.630957	0.00381
100	1.89574	0.650629	0.004786
109.114	1.81412	0.670914	0.007432
119.058	1.83654	0.650629	0.00912
157.387	1.7378	0.633383	0.013183
177.828	1.68526	0.593381	0.014905
197.449	1.63431	0.558042	0.015213
247.708	1.4905	0.493552	0.014259
294.915	1.40174	0.436516	0.013082
345.047	1.2784	0.386071	0.011659
396.721	1.20226	0.352101	0.010633

E(eV)	$\rightarrow N_2^+$ ($10^{-16}cm^{-2}$)	$\rightarrow N^+$ ($10^{-16}cm^{-2}$)	$\rightarrow N^{++}$ ($10^{-16}cm^{-2}$)
440.493	1.13066	0.331131	0.00912
497.702	1.06333	0.287519	0.008191
552.617	1	0.261684	0.00772
592.553	0.940445	0.251189	0.007282
635.375	0.898118	0.236229	0.006709
693.281	0.84463	0.215443	0.006146
730.527	0.823295	0.20893	0.005873
797.104	0.782228	0.199526	0.00558
854.709	0.758578	0.187643	0.005248
900.628	0.735642	0.181041	0.005012
965.714	0.691831	0.171133	0.004713
982.707	0.681292	0.168526	0.004642

Appendix Table B.4 GOS parameters for the electron impact ionization of N_2. See Section 3.3.2.1

Final State	I (eV)	K	K_b	J	J_b	T_s	T_a	T_b	Γ_s	Γ_b
$X^2\Sigma^+_g$	15.58	2.42	0	1.74	0	4.71	1000	31.16	13.8	15.58
$A^2\Pi_u$	16.73	1.06	0	1.74	0	4.71	1000	33.46	13.8	16.73
$B^2\Sigma^+_u$	18.75	0.551	0	1.74	0	4.71	1000	37.5	13.8	18.75
$D^2\Pi_g$	22	0.371	0	1.74	0	4.71	1000	44	13.8	22
$C^2\Sigma^+_u$	23.6	0.371	0	1.74	0	4.71	1000	47.2	13.8	23.6
40-eV state	40	0.53	0	1.74	0	4.71	1000	80	13.8	40

Appendix Table B.5 Parameters for the excitation of N_2

v	Ω	f_0C_0	β	P_{auto}	Notes
4.530	3.000	2.770	1.420	0.000	A+B+W
4.780	3.000	0.114	3.540	0.000	B’
4.320	3.000	0.179	12.700	0.000	C
4.050	1.000	9.990E-02	5.200	0.000	a+a’+w
1.470	0.750	0.876	0.860	0.000	$^1\Pi_u$
1.270	0.750	0.601	0.450	0.000	$^1\Sigma_u$
3.000	0.750	1.890	1.000	0.000	Rydbergs
1.580	8.000	1.350	1.000	0.000	vibrations

Appendix Table B.6 Revised *Straub et al.* [1997] cross sections for the electron impact ionization of methane from *Lindsay and Mangan* [2003]. Labels indicated the final ionization product.

E(eV)	→ CH_4^+ (cm^{-2})	→ CH_3^+ (cm^{-2})	→ CH_2^+ (cm^{-2})	→ CH^+ (cm^{-2})	→ C^+ (cm^{-2})	→ $H2^+$ (cm^{-2})	→ H^+ (cm^{-2})	Total (cm^{-2})
12.6	1.00E-36							1.00E-36
14	4.35E-25	1.00E-36						4.35E-25
15	1.82E-17	3.50E-18						2.17E-17
15.1	1.90E-17	3.79E-18	1.00E-36					2.28E-17
17.5	4.79E-17	2.20E-17	5.00E-19					7.04E-17
19.6	7.60E-17	4.22E-17	1.32E-18					1.20E-16
20	8.25E-17	4.74E-17	1.57E-18	1.00E-36	6.75E-36			1.31E-16
22.5	1.03E-16	6.85E-17	2.64E-18	1.98E-27	4.63E-31			1.74E-16
22.58	1.04E-16	6.90E-17	2.70E-18	3.77E-27	6.47E-31		1.00E-36	1.75E-16
23.49	1.10E-16	7.51E-17	3.48E-18	4.96E-24	2.71E-29	1.00E-36	8.37E-30	1.88E-16
25	1.20E-16	8.57E-17	5.19E-18	4.10E-19	9.80E-27	2.17E-32	6.90E-19	2.12E-16
30	1.36E-16	1.05E-16	1.31E-17	2.92E-18	3.00E-19	1.06E-19	2.87E-18	2.60E-16
35	1.41E-16	1.11E-16	2.03E-17	7.46E-18	1.41E-18	6.02E-19	7.00E-18	2.89E-16
40	1.45E-16	1.14E-16	2.48E-17	1.12E-17	2.74E-18	1.50E-18	1.30E-17	3.12E-16
45	1.50E-16	1.19E-16	2.79E-17	1.36E-17	3.44E-18	2.23E-18	1.96E-17	3.36E-16
50	1.53E-16	1.22E-16	2.88E-17	1.44E-17	4.27E-18	2.68E-18	2.49E-17	3.50E-16
60	1.55E-16	1.26E-16	3.02E-17	1.63E-17	4.92E-18	3.21E-18	3.29E-17	3.69E-16
70	1.56E-16	1.27E-16	3.07E-17	1.73E-17	5.55E-18	3.52E-18	3.80E-17	3.78E-16
80	1.55E-16	1.26E-16	3.11E-17	1.72E-17	5.97E-18	3.64E-18	4.10E-17	3.80E-16
90	1.54E-16	1.26E-16	3.04E-17	1.74E-17	5.94E-18	3.71E-18	4.28E-17	3.80E-16
100	1.52E-16	1.24E-16	3.04E-17	1.67E-17	5.92E-18	3.69E-18	4.30E-17	3.76E-16
110	1.49E-16	1.22E-16	3.00E-17	1.63E-17	5.98E-18	3.59E-18	4.29E-17	3.70E-16
125	1.44E-16	1.19E-16	2.87E-17	1.54E-17	5.78E-18	3.45E-18	4.12E-17	3.58E-16
150	1.38E-16	1.13E-16	2.66E-17	1.40E-17	5.32E-18	3.22E-18	3.81E-17	3.38E-16
175	1.31E-16	1.08E-16	2.46E-17	1.27E-17	4.81E-18	2.84E-18	3.53E-17	3.19E-16
200	1.25E-16	1.03E-16	2.33E-17	1.16E-17	4.44E-18	2.53E-18	3.28E-17	3.03E-16
250	1.13E-16	9.34E-17	1.99E-17	9.81E-18	3.56E-18	2.14E-18	2.68E-17	2.69E-16
300	1.04E-16	8.55E-17	1.77E-17	8.44E-18	3.10E-18	1.89E-18	2.30E-17	2.44E-16
400	8.91E-17	7.19E-17	1.39E-17	6.43E-18	2.13E-18	1.38E-18	1.77E-17	2.03E-16
500	7.78E-17	6.38E-17	1.19E-17	5.24E-18	1.70E-18	1.11E-18	1.43E-17	1.76E-16
600	6.86E-17	5.60E-17	1.03E-17	4.35E-18	1.43E-18	9.91E-19	1.20E-17	1.54E-16
700	6.22E-17	5.07E-17	8.92E-18	3.78E-18	1.25E-18	8.34E-19	1.01E-17	1.38E-16
800	5.52E-17	4.54E-17	7.98E-18	3.27E-18	9.72E-19	7.21E-19	8.71E-18	1.22E-16
900	5.16E-17	4.20E-17	7.26E-18	3.02E-18	9.26E-19	5.88E-19	7.74E-18	1.13E-16
1000	4.76E-17	3.85E-17	6.54E-18	2.72E-18	8.27E-19	5.42E-19	6.88E-18	1.04E-16

Appendix Table B.7 GOS parameters for the electron impact ionization of methane. See Section 3.3.2.1

Final State	I (eV)	K	K_b	J	J_b	T_s	T_a	T_b	Γ_s	Γ_b
CH_4^+	12.6	1.31	0	3.5	30.17	3.7	0	0	44.5	81
CH_3^+	14.0	5.2	0	9.5	10.59	-37.2	0	0	27.2	2.4
CH_2^+	15.1	0.25	0	1	-20.0	-24.1	0	0	39.2	-36.2
CH^+	20.0	0.26	0	175	6.879	-59.3	0	0	61.2	-61.4
C^+	19.6	0.038	0	175	60.85	31.5	0	0	20.4	-64
H_2^+	23.49	0.024	0	2	46	24.2	0	0	14.6	-58.7
H^+	22.58	0.35	0	3.5	2.646	22.2	0	0	14.1	-65.3

Appendix Table B.8 Parameters for the excitation of CH_4

v	Ω	f_0C_0	β	P_{auto}	Notes
0.641	1.129	5.870E-03	1.000	0.000	7.5-9.0 eV
1.549	0.838	0.179	1.000	0.000	9.0-10.5 eV
0.880	0.807	0.280	1.000	0.000	10.5-12.0 eV
0.835	0.620	0.432	1.000	0.000	12.0-13.5 eV
0.908	0.681	0.533	1.000	0.000	13.5-15.0 eV

Appendix C Reaction List

The full chemical reaction list used in the model appears in this section. Dissociative electron recombination coefficients (see Equation (3.20)) are presented first followed by the list of ion – neutral reactions.

C-1 Electron Dissociative Recombination Rates

Appendix Table C.1 Electron dissociative recombination coefficients and temperature dependencies

Ion	α [cm^3s^{-1}]	β
N_2^+	1.70E-07	0.3
N^+	4.00E-12	0.58
CH_5^+	1.10E-06	1.5 T_e>300K
		0.7 T_e<300K
CH_4^+	3.50E-07	0.5
CH_3^+	2.97E-07	0.5
CH_2^+	6.40E-07	0.6
CH^+	1.50E-07	0.42
C^+	4.67E-12	0.6
H_3^+	6.70E-08	0.52
$H2^+$	1.60E-08	0.43
H^+	3.50E-12	0.75
HN^+	4.30E-08	0.5
HN_2^+	1.70E-07	0.92
CN^+	1.80E-07	0.5
CHN^+	2.00E-07	0.5
CH_2N^+	3.50E-07	1.38
$C_2H_6^+$	3.00E-07	0.5
$C_2H_5^+$	1.20E-06	1.2 T_e>300K
		0.8T_e<300K
$C_2H_4^+$	5.60E-07	0.76
$C_2H_3^+$	5.00E-07	0.84
$C_2H_2^+$	2.70E-07	0.5
C_2H^+	2.69E-07	0.76
$lC_3H_3^+$	7.00E-07	0.5
$C_3H_5^+$	1.50E-06	1.4 T_e>300K
		0.7 T_e<300K
$cC_3H_3^+$	7.00E-07	0.5
H_3O^+	4.32E-07	0.5

Ion	α [$cm^3 s^{-1}$]	β
H_2O^+	4.30E-07	0.5
C_3H^+	3.00E-07	0.5
$C_3H_2^+$	4.80E-07	0.5
$C_3H_4^+$	3.01E-06	0.67
$C_3H_6^+$	3.00E-07	0.5
$C_3H_7^+$	3.00E-07	0.5
$C_4H_5^+$	3.00E-07	0.5
$C_4H_7^+$	3.00E-07	0.5
$C_5H_3^+$	9.00E-07	0.5
$C_5H_5^+$	1.50E-06	1.4 T_e>300K 0.7 T_e< 300K
$C_6H_7^+$	2.80E-06	1.3
$C_7H_7^+$	2.80E-06	1.3
$C_{11}H_9^+$	1.10E-06	0.5
C_3HN^+	1.38E-06	0.6
$C_3H_2N^+$	1.50E-06	0.58
$C_5H_5N^+$	1.10E-06	0.5
$C_4H_2^+$	3.00E-07	0.5
$C_4H_3^+$	1.50E-06	0.7
$C_5H_7^+$	1.10E-06	1.4 T_e>300K 0.7 T_e< 300K
$C_5H_9^+$	1.10E-06	0.5
CNC^+	3.00E-07	0.5
$C_6H_5^+$	2.80E-06	1.3
NO^+	4.30E-07	0.37
NH_4^+	1.34E-06	0.5
$CH_2NH_2^+$	3.00E-07	0.5
$CH_3NH_2^+$	3.00E-07	0.7
CH_3CN^+	3.00E-07	0.5
CH_3CNH^+	3.40E-07	1.03
$HC_2N_2^+$	6.00E-07	0.5
$C_2H_3CN^+$	1.00E-07	0.5
$C_2H_3CNH^+$	1.78E-06	0.8
$C_2H_5CNH^+$	4.60E-07	0.81
$CH_3NH_3^+$	3.00E-07	0.7
$C_6H_3^+$	2.00E-06	0.3
$C_7H_5^+$	7.00E-07	0.3
$C_7H_9^+$	3.80E-07	0.7
$C_8H_3^+$	2.00E-06	0.3
$C_4H_3NH^+$	1.00E-06	0.3
$C_4H_5NH^+$	4.00E-07	0.7
HC_5NH^+	3.50E-07	0.7

Ion	α [$cm^3 s^{-1}$]	β
$C_7H_7NH^+$	3.50E-07	0.7
$C_6H_3NH^+$	2.00E-06	0.3
$C_5H_6N^+$	8.50E-07	0.7
$C_5H_4N^+$	3.00E-07	0.7
$CH_3C_5H_5N^+$	2.83E-07	0.7
$C_9H_7^+$	1.00E-06	0.7
$C_{10}H_9^+$	1.00E-06	0.7
$C_{12}H_9^+$	1.00E-06	0.7
$C_{12}H_{10}^+$	1.00E-06	0.7
$C_7H_6^+$	1.00E-06	0.7
$C_7H_8^+$	1.00E-06	0.7
$C_8H_6^+$	1.00E-06	0.7
$C_8H_7^+$	1.00E-06	0.7
$C_8H_8^+$	1.00E-06	0.7
$C_9H_8^+$	1.00E-06	0.7
$C_9H_9^+$	1.00E-06	0.7
$C_{10}H_8^+$	1.00E-06	0.7
$C_{10}H_{10}^+$	1.00E-06	0.7
$C_{11}H_8^+$	1.00E-06	0.7
$C_{11}H_{10}^+$	1.00E-06	0.7
$C_{11}H_{11}^+$	1.00E-06	0.7
C_7N^+	2.00E-06	0.3
HC_7N^+	2.00E-06	0.3
$H_2C_7N^+$	2.00E-06	0.3
$H_3C_7N^+$	2.00E-06	0.3
C_7H^+	2.00E-06	0.3
$C_7H_2^+$	2.00E-06	0.3
$C_7H_3^+$	2.00E-06	0.3
$C_7H_4^+$	2.00E-06	0.3
$CH_3C_4H^+$	2.00E-06	0.3
$C_5H_3N^+$	2.00E-06	0.3
$C_7H_5N^+$	1.00E-06	0.7
$C_9H_7N^+$	1.00E-06	0.7
$C_{11}H_9N^+$	1.00E-06	0.7
$C_{13}H_{11}N^+$	1.00E-06	0.7
C_9N^+	2.00E-06	0.3
HC_9N^+	2.00E-06	0.3
$H_2C_9N^+$	2.00E-06	0.3
C_9^+	2.00E-06	0.3
C_9H^+	2.00E-06	0.3
$C_9H_2^+$	2.00E-06	0.3

Ion	α [$cm^3 s^{-1}$]	β
$C_9H_3^+$	2.00E-06	0.3
HC_3O^+	3.00E-07	0.5
OCN^+	3.00E-07	0.5
$C_3H_3N_2^+$	6.00E-07	0.5
H_3CO^+	6.00E-07	0.5
C_4N^+	3.00E-07	0.5
CH_2CN^+	3.00E-07	0.5
C_2HN^+	3.00E-07	0.5
$C_2N_2^+$	3.00E-07	0.5
C_3^+	3.00E-07	0.5
HC_5N^+	3.00E-07	0.5
$HNCO^+$	3.00E-07	0.5
HC_4N^+	3.00E-07	0.5
NH_3^+	3.10E-07	0.5
NH_2^+	3.05E-07	0.9
CO^+	2.00E-07	0.48
HCO^+	2.40E-07	0.69
$C_5H_2^+$	3.00E-07	0.5
$C_2H_7^+$	3.00E-07	0.5
C_4H^+	3.00E-07	0.5
$C_4H_4^+$	3.30E-07	0.5
$C_8H_5^+$	3.00E-07	0.5
$C_8H_9^+$	2.00E-06	0.3
$C_8H_{11}^+$	2.00E-06	0.3
$C_9H_{11}^+$	2.00E-06	0.3
$C_{12}H_{11}^+$	2.00E-06	0.3

C-2 Ion-Neutral Reaction List

Appendix Table C.2 Ion-Neutral Chemical Reaction List

Ion	+	Neutral	→	Product	Rate [$cm^3 s^{-1}$]
N2+	+	CH4	→	CH3+	1.04E-09
N2+	+	CH4	→	CH2+	1.03E-10
N2+	+	CH4	→	HN2+	1.71E-10
N2+	+	H2	→	HN2+	2.00E-09
N2+	+	N	→	N+	1.00E-11
N2+	+	NH	→	HN+	6.50E-10
N2+	+	C2H2	→	HN2+	2.40E-10

Ion	+	Neutral	→	Product	Rate [cm^3s^{-1}]
N2+	+	C2H2	→	CHN+	1.20E-11
N2+	+	C2H2	→	C2H2+	1.48E-10
N2+	+	C2H4	→	HN2+	1.30E-10
N2+	+	C2H4	→	CHN+	1.30E-10
N2+	+	C2H4	→	CH2N+	1.30E-10
N2+	+	C2H4	→	C2H3+	6.50E-10
N2+	+	C2H4	→	C2H2+	2.60E-10
N2+	+	HCN	→	CHN+	3.90E-10
N2+	+	C2H6	→	CH2N+	1.30E-10
N2+	+	C2H6	→	C2H6+	1.30E-10
N2+	+	C2H6	→	C2H5+	2.16E-10
N2+	+	C2H6	→	C2H4+	4.32E-10
N2+	+	C2H6	→	C2H3+	5.04E-10
N2+	+	C2H6	→	C2H2+	2.88E-10
N2+	+	HC3N	→	HN2+	1.05E-09
N2+	+	HC3N	→	C3HN+	3.50E-09
N2+	+	H2O	→	HN2+	5.04E-10
N2+	+	H2O	→	H2O+	1.90E-09
N2+	+	CO	→	CO+	7.30E-11
N2+	+	C2N2	→	C2N2+	9.30E-10
N2+	+	NH3	→	NH4+	1.95E-09
N2+	+	NH3	→	NH3+	1.90E-09
N2+	+	O	→	NO+	1.30E-10
N2+	+	CH3CN	→	CH3CN+	3.15E-10
N2+	+	CH3CN	→	CH2CN+	1.37E-09
N2+	+	CH3CN	→	C2HN+	4.20E-10
N2+	+	C2H5CN	→	CH3+	6.80E-10
N2+	+	C2H5CN	→	C2H2+	5.10E-10
N2+	+	C2H5CN	→	C2H3CNH+	2.21E-09
N2+	+	CH3NH2	→	CH2NH2+	8.80E-10
N2+	+	CH3NH2	→	CH3NH2+	7.20E-11
N+	+	CH4	→	CH4+	5.75E-11
N+	+	CH4	→	CH3+	5.75E-10
N+	+	CH4	→	CHN+	4.14E-10
N+	+	CH4	→	CH2N+	4.14E-10
N+	+	H2	→	HN+	1.00E-09
N+	+	NH	→	N2+	3.70E-10
N+	+	NH	→	HN+	3.70E-10
N+	+	C2H2	→	C2H2+	1.05E-09
N+	+	C2H2	→	CNC+	2.25E-10
N+	+	C2H2	→	C2HN+	2.25E-10

Ion	+	Neutral	→	Product	Rate [cm^3s^{-1}]
N+	+	C2H4	→	CHN+	1.50E-10
N+	+	C2H4	→	CH2N+	2.25E-10
N+	+	C2H4	→	C2H4+	5.25E-10
N+	+	C2H4	→	C2H3+	3.75E-10
N+	+	C2H4	→	C2H2+	1.50E-10
N+	+	C2H4	→	C2HN+	7.50E-11
N+	+	HCN	→	CH+	1.30E-09
N+	+	HCN	→	CHN+	2.41E-09
N+	+	C2H6	→	CH2N+	1.30E-10
N+	+	C2H6	→	C2H5+	1.30E-10
N+	+	C2H6	→	C2H4+	7.15E-10
N+	+	C2H6	→	C2H3+	3.25E-10
N+	+	HC3N	→	C3H+	1.60E-09
N+	+	HC3N	→	C3HN+	2.65E-09
N+	+	H2O	→	H2O+	2.70E-09
N+	+	CO	→	C+	5.60E-13
N+	+	CO	→	NO+	6.16E-12
N+	+	CO	→	CO+	4.93E-11
N+	+	C2N2	→	C2H2+	3.40E-10
N+	+	C2N2	→	CNC+	1.36E-09
N+	+	C2N2	→	C2N2+	1.40E-09
N+	+	NH3	→	NH4+	2.40E-09
N+	+	NH3	→	NH2+	2.16E-10
N+	+	CH3CN	→	CH3CN+	5.00E-10
N+	+	C2H5CN	→	N2+	2.31E-09
N+	+	C2H5CN	→	lC3H3+	4.20E-10
N+	+	C2H5CN	→	cC3H3+	4.20E-10
N+	+	C2H5CN	→	C2H3CNH+	1.05E-09
N+	+	CH3NH2	→	CH2NH2+	9.80E-10
CH5+	+	NH	→	NH2+	7.10E-10
CH5+	+	C2H2	→	C2H3+	1.48E-09
CH5+	+	C2H4	→	C2H5+	1.00E-09
CH5+	+	HCN	→	CH2N+	2.70E-09
CH5+	+	C2H6	→	C2H5+	2.03E-10
CH5+	+	C2H6	→	C2H7+	1.15E-09
CH5+	+	H	→	CH4+	1.50E-10
CH5+	+	HC3N	→	C3H2N+	4.50E-09
CH5+	+	H2O	→	H3O+	3.70E-07
CH5+	+	CO	→	HCO+	9.90E-10
CH5+	+	NH3	→	NH4+	2.50E-09
CH5+	+	O	→	H3CO+	4.40E-12

Ion	+	Neutral	→	Product	Rate [cm^3s^{-1}]
CH5+	+	CH2NH	→	CH2NH2+	2.09E-09
CH5+	+	CH3CN	→	CH3CNH+	4.90E-09
CH5+	+	CH3NH2	→	CH2NH2+	1.00E-09
CH5+	+	C6H6	→	C6H7+	2.00E-09
CH4+	+	CH4	→	CH5+	1.14E-09
CH4+	+	H2	→	CH5+	3.50E-11
CH4+	+	C2H2	→	C2H3+	1.12E-09
CH4+	+	C2H2	→	C2H2+	1.44E-09
CH4+	+	C2H2	→	lC3H3+	1.63E-10
CH4+	+	C2H2	→	cC3H3+	1.51E-10
CH4+	+	C2H4	→	C2H5+	4.23E-10
CH4+	+	C2H4	→	C2H4+	1.38E-09
CH4+	+	C2H4	→	cC3H3+	6.00E-11
CH4+	+	HCN	→	CH2N+	3.23E-09
CH4+	+	HCN	→	CH3CNH+	6.60E-11
CH4+	+	C2H6	→	C2H4+	1.91E-09
CH4+	+	HC3N	→	C3H2N+	2.50E-09
CH4+	+	H2O	→	H3O+	2.50E-09
CH4+	+	CO	→	HCO+	1.04E-09
CH4+	+	NH3	→	NH4+	1.15E-09
CH4+	+	NH3	→	NH3+	1.65E-09
CH4+	+	CH3CN	→	CH3CNH+	3.90E-09
CH4+	+	C2H3CN	→	C3HN+	5.00E-11
CH4+	+	C2H3CN	→	C3H2N+	3.50E-11
CH4+	+	C2H3CN	→	C2H3CN+	3.50E-10
CH4+	+	CH3NH2	→	CH2NH2+	8.80E-10
CH4+	+	CH3NH2	→	CH3NH2+	1.32E-09
CH3+	+	CH4	→	C2H5+	1.10E-09
CH3+	+	H2	→	CH5+	5.00E-13
CH3+	+	N	→	CHN+	3.35E-11
CH3+	+	N	→	CH2N+	3.35E-11
CH3+	+	NH	→	CH2N+	7.40E-10
CH3+	+	C2H2	→	lC3H3+	5.75E-10
CH3+	+	C2H2	→	cC3H3+	5.75E-10
CH3+	+	C2H4	→	C2H5+	2.60E-10
CH3+	+	C2H4	→	C2H4+	1.70E-09
CH3+	+	C2H4	→	C2H3+	4.88E-10
CH3+	+	C2H4	→	lC3H3+	4.24E-11
CH3+	+	C2H4	→	C3H5+	6.00E-11
CH3+	+	C2H4	→	cC3H3+	4.60E-11
CH3+	+	HCN	→	CH3CNH+	2.00E-10

Ion		Neutral	→	Product	Rate [cm^3s^{-1}]
CH3+	+	C2H6	→	C2H5+	1.48E-09
CH3+	+	C2H6	→	C3H5+	1.57E-10
CH3+	+	C2H6	→	cC3H3+	1.57E-10
CH3+	+	C2H6	→	C3H7+	1.04E-10
CH3+	+	HC3N	→	cC3H3+	2.11E-09
CH3+	+	HC3N	→	C4H3NH+	2.19E-09
CH3+	+	C3H4	→	C2H5+	1.24E-09
CH3+	+	C3H4	→	C2H3+	2.85E-10
CH3+	+	C3H4	→	lC3H3+	1.43E-10
CH3+	+	C3H4	→	cC3H3+	1.43E-10
CH3+	+	C3H4	→	C4H5+	1.90E-10
CH3+	+	C4H2	→	lC3H3+	1.17E-09
CH3+	+	C4H2	→	cC3H3+	1.27E-09
CH3+	+	C4H2	→	C5H3+	1.30E-10
CH3+	+	C2N2	→	C3H3N2+	8.00E-12
CH3+	+	C2N2	→	CH2CN+	7.20E-11
CH3+	+	C3H2	→	C4H3+	2.70E-09
CH3+	+	NH3	→	NH4+	3.04E-10
CH3+	+	NH3	→	CH2NH2+	1.30E-09
CH3+	+	O	→	HCO+	4.00E-10
CH3+	+	CH3CN	→	CH2N+	1.04E-09
CH3+	+	CH3CN	→	C2H5+	6.66E-10
CH3+	+	CH3CN	→	CH3CNH+	1.10E-09
CH3+	+	CH3CN	→	C2H5CNH+	9.00E-11
CH3+	+	CH3CN	→	CH3NH3+	9.00E-11
CH3+	+	C2H3CN	→	CH3CNH+	4.30E-09
CH3+	+	C2H3CN	→	C2H3CNH+	2.60E-10
CH3+	+	CH3NH2	→	CH2NH2+	1.44E-09
CH3+	+	CH3NH2	→	CH3NH2+	1.76E-09
CH3+	+	C6H2	→	C7H3+	1.20E-09
CH3+	+	C8H2	→	C9H3+	1.20E-09
CH3+	+	C5H5N	→	C5H5N+	6.59E-10
CH3+	+	C5H5N	→	C5H6N+	2.83E-10
CH3+	+	C5H5N	→	C5H4N+	6.28E-10
CH3+	+	C5H5N	→	CH3C5H5N+	1.57E-09
CH2+	+	CH4	→	C2H5+	3.90E-10
CH2+	+	CH4	→	C2H4+	9.10E-10
CH2+	+	H2	→	CH3+	1.10E-09
CH2+	+	N	→	CN+	1.10E-10
CH2+	+	N	→	CHN+	1.10E-10
CH2+	+	NH	→	CH2N+	7.50E-10

Ion	+	Neutral	→	Product	Rate [cm^3s^{-1}]
CH2+	+	C2H2	→	cC3H3+	2.50E-09
CH2+	+	HCN	→	CH2CN+	1.80E-09
CH2+	+	HC3N	→	C3H2N+	4.10E-09
CH2+	+	H2O	→	H3CO+	2.05E-09
CH2+	+	NH3	→	NH4+	1.26E-09
CH2+	+	O	→	HCO+	7.50E-10
CH2+	+	C2H3CN	→	C2H3CN+	2.30E-09
CH2+	+	CH3NH2	→	CH2NH2+	1.15E-09
CH2+	+	CH3NH2	→	CH3NH2+	7.70E-10
CH+	+	CH4	→	C2H4+	6.50E-11
CH+	+	CH4	→	C2H3+	1.09E-09
CH+	+	CH4	→	C2H2+	1.43E-10
CH+	+	H2	→	CH2+	1.20E-09
CH+	+	N	→	CN+	1.90E-10
CH+	+	NH	→	CN+	7.60E-10
CH+	+	C2H2	→	C3H2+	2.40E-09
CH+	+	HCN	→	CH2N+	2.10E-09
CH+	+	HCN	→	CNC+	4.20E-10
CH+	+	HCN	→	C2HN+	2.80E-10
CH+	+	H	→	C+	7.50E-10
CH+	+	H2O	→	H3O+	1.45E-09
CH+	+	H2O	→	HCO+	1.45E-09
CH+	+	CO	→	HCO+	7.00E-12
CH+	+	NH3	→	NH4+	4.05E-10
CH+	+	NH3	→	NH3+	4.59E-10
CH+	+	O	→	CO+	3.50E-10
C+	+	CH4	→	C2H3+	9.36E-10
C+	+	CH4	→	C2H2+	3.64E-10
C+	+	H2	→	CH+	1.20E-16
C+	+	NH	→	CN+	7.80E-10
C+	+	C2H2	→	C3H+	2.63E-09
C+	+	C2H4	→	C2H4+	2.25E-10
C+	+	C2H4	→	C2H3+	1.20E-10
C+	+	C2H4	→	lC3H3+	6.30E-10
C+	+	C2H4	→	cC3H3+	1.02E-09
C+	+	C2H4	→	C3H+	7.50E-11
C+	+	C2H4	→	C3H2+	4.35E-10
C+	+	HCN	→	CNC+	2.95E-09
C+	+	C2H6	→	C2H5+	2.31E-10
C+	+	C2H6	→	C2H4+	1.16E-10
C+	+	C2H6	→	C2H3+	4.95E-10

Ion	+	Neutral	→	Product	Rate [cm^3s^{-1}]
C+	+	C2H6	→	C2H2+	8.25E-11
C+	+	C2H6	→	cC3H3+	7.10E-10
C+	+	C2H6	→	C3H2+	1.65E-11
C+	+	HC3N	→	C3H+	3.85E-09
C+	+	HC3N	→	CNC+	1.10E-10
C+	+	HC3N	→	C4N+	1.27E-09
C+	+	HC3N	→	C3+	2.75E-10
C+	+	HC3N	→	C4H+	1.40E-09
C+	+	C3H4	→	C2H3+	1.90E-10
C+	+	C3H4	→	C2H2+	1.90E-10
C+	+	C3H4	→	lC3H3+	3.80E-10
C+	+	C3H4	→	C3H5+	5.70E-10
C+	+	C3H4	→	C4H2+	5.70E-10
C+	+	H2O	→	H2O+	2.40E-10
C+	+	H2O	→	HCO+	2.16E-09
C+	+	C3H8	→	C2H3+	6.30E-10
C+	+	C3H8	→	cC3H3+	3.60E-10
C+	+	C3H8	→	C3H7+	5.40E-10
C+	+	C3H8	→	C4H5+	9.00E-11
C+	+	C4H2	→	C3H+	1.45E-10
C+	+	C4H2	→	C4H2+	1.31E-09
C+	+	C3H6	→	C2H3+	6.00E-10
C+	+	C3H6	→	C2H2+	3.00E-10
C+	+	C3H6	→	lC3H3+	1.50E-10
C+	+	C3H6	→	C3H5+	4.00E-10
C+	+	C3H6	→	cC3H3+	1.50E-10
C+	+	C3H6	→	C3H6+	2.00E-10
C+	+	C3H6	→	C4H3+	2.00E-10
C+	+	C2N2	→	CNC+	1.90E-09
C+	+	C3H2	→	C4H+	1.00E-09
C+	+	NH3	→	NH3+	5.06E-10
C+	+	O	→	CO+	2.50E-18
C+	+	C6H2	→	C7H+	1.20E-09
C+	+	C7H4	→	C7H3+	7.50E-10
C+	+	C8H2	→	C9+	1.20E-09
C+	+	C8H2	→	C9H+	1.20E-09
C+	+	C4H3N	→	C4H3+	5.00E-09
C+	+	C6H3N	→	C6H3+	5.00E-09
H3+	+	N2	→	HN2+	1.86E-09
H3+	+	CH4	→	CH5+	2.40E-09
H3+	+	NH	→	NH2+	1.30E-09

Ion	+	Neutral	→	Product	Rate [cm^3s^{-1}]
H3+	+	C2H2	→	C2H3+	3.20E-09
H3+	+	C2H4	→	C2H5+	8.70E-10
H3+	+	C2H4	→	C2H3+	2.03E-09
H3+	+	HCN	→	CH2N+	7.50E-09
H3+	+	C2H6	→	C2H5+	2.90E-09
H3+	+	HC3N	→	C3H2N+	9.80E-09
H3+	+	C3H4	→	C2H3+	9.00E-10
H3+	+	C3H4	→	C3H5+	2.10E-09
H3+	+	H2O	→	H3O+	5.30E-09
H3+	+	C4H2	→	C4H3+	2.60E-09
H3+	+	CO	→	HCO+	1.74E-09
H3+	+	C3H6	→	C2H3+	9.30E-10
H3+	+	C3H6	→	C3H5+	2.17E-09
H3+	+	C2N2	→	HC2N2+	2.80E-09
H3+	+	NH3	→	NH4+	4.39E-09
H3+	+	CH3CN	→	CH3CNH+	8.90E-09
H3+	+	C2H3CN	→	C4H3NH+	9.00E-09
H3+	+	C2H5CN	→	C2H5CNH+	8.90E-09
H3+	+	C6H2	→	C6H3+	2.00E-09
H3+	+	C7H4	→	C7H5+	2.50E-09
H3+	+	C8H2	→	C8H3+	2.00E-09
H2+	+	N2	→	HN2+	2.00E-09
H2+	+	CH4	→	CH5+	1.14E-10
H2+	+	CH4	→	CH4+	1.41E-09
H2+	+	CH4	→	CH3+	2.28E-09
H2+	+	H2	→	H3+	2.00E-09
H2+	+	N	→	HN+	1.90E-09
H2+	+	NH	→	HN+	7.60E-10
H2+	+	C2H2	→	C2H3+	4.77E-10
H2+	+	C2H2	→	C2H2+	4.82E-09
H2+	+	C2H4	→	C2H4+	2.21E-09
H2+	+	C2H4	→	C2H3+	1.81E-09
H2+	+	C2H4	→	C2H2+	8.82E-10
H2+	+	C2H6	→	C2H6+	2.94E-10
H2+	+	C2H6	→	C2H5+	1.37E-09
H2+	+	C2H6	→	C2H4+	2.35E-09
H2+	+	C2H6	→	C2H3+	6.86E-10
H2+	+	C2H6	→	C2H2+	1.96E-10
H2+	+	H	→	H+	6.40E-10
H2+	+	H2O	→	H3O+	3.43E-09
H2+	+	H2O	→	H2O+	3.87E-09

Ion	+	Neutral	→	Product	Rate [cm^3s^{-1}]
H2+	+	CO	→	CO+	6.44E-10
H2+	+	CO	→	HCO+	2.90E-09
H2+	+	NH3	→	NH3+	5.70E-09
H+	+	CH4	→	CH4+	7.47E-10
H+	+	CH4	→	CH3+	3.40E-09
H+	+	H2	→	H3+	1.30E-16
H+	+	NH	→	HN+	2.10E-09
H+	+	C2H2	→	C2H2+	5.40E-10
H+	+	C2H4	→	C2H4+	9.80E-10
H+	+	C2H4	→	C2H3+	2.94E-09
H+	+	C2H4	→	C2H2+	9.80E-10
H+	+	HCN	→	CHN+	1.10E-08
H+	+	C2H6	→	CH3+	2.45E-10
H+	+	C2H6	→	C2H5+	2.45E-10
H+	+	C2H6	→	C2H4+	1.47E-09
H+	+	C2H6	→	C2H3+	2.94E-09
H+	+	HC3N	→	C3HN+	4.00E-09
H+	+	H2O	→	H2O+	6.90E-09
H+	+	C4H2	→	C4H2+	2.00E-09
H+	+	C4H2	→	C4H+	2.00E-09
H+	+	NH3	→	NH3+	3.70E-09
H+	+	CH2NH	→	NH2+	1.00E-09
H+	+	CH3CN	→	CH3+	3.00E-09
H+	+	CH3CN	→	CH3CN+	8.40E-09
H+	+	CH3CN	→	CH2CN+	6.00E-10
H+	+	C7H4	→	C7H3+	2.00E-09
H+	+	C7H4	→	C7H4+	2.00E-09
H+	+	HC5N	→	HC5N+	4.00E-09
HN+	+	N2	→	HN2+	6.50E-10
HN+	+	CH4	→	CH5+	9.60E-11
HN+	+	CH4	→	CH2N+	6.72E-10
HN+	+	CH4	→	NH2+	1.92E-10
HN+	+	H2	→	H3+	1.85E-10
HN+	+	H2	→	NH2+	1.05E-09
HN+	+	NH	→	NH2+	1.00E-09
HN+	+	C2H4	→	CH2N+	3.00E-10
HN+	+	C2H4	→	C2H4+	3.75E-10
HN+	+	C2H4	→	C2H3+	3.75E-10
HN+	+	C2H4	→	C2H2+	1.50E-10
HN+	+	C2H4	→	CH3CN+	1.50E-10
HN+	+	H2O	→	H3O+	1.05E-09

Ion	+	Neutral	→	Product	Rate [cm^3s^{-1}]
HN+	+	H2O	→	H2O+	1.05E-09
HN+	+	H2O	→	NH3+	1.75E-10
HN+	+	H2O	→	NH2+	8.75E-10
HN+	+	CO	→	OCN+	5.39E-10
HN+	+	CO	→	HCO+	4.41E-10
HN+	+	NH3	→	NH4+	6.00E-10
HN+	+	NH3	→	NH3+	1.80E-09
HN2+	+	N2	→	H3+	5.10E-18
HN2+	+	CH4	→	CH5+	8.90E-10
HN2+	+	H2	→	H3+	5.10E-18
HN2+	+	NH	→	NH2+	6.40E-10
HN2+	+	C2H2	→	C2H3+	1.40E-09
HN2+	+	HCN	→	CH2N+	3.20E-09
HN2+	+	C2H6	→	CH5+	1.13E-09
HN2+	+	C2H6	→	C2H5+	1.13E-09
HN2+	+	C2H6	→	C2H7+	1.69E-10
HN2+	+	HC3N	→	C3H2N+	4.20E-09
HN2+	+	C3H4	→	lC3H3+	7.50E-10
HN2+	+	C3H4	→	cC3H3+	7.50E-10
HN2+	+	H2O	→	H3O+	2.60E-09
HN2+	+	C4H2	→	C4H3+	1.10E-09
HN2+	+	CO	→	HCO+	8.80E-10
HN2+	+	C2N2	→	HC2N2+	1.20E-09
HN2+	+	NH3	→	NH4+	2.30E-09
HN2+	+	CH3CN	→	CH3CNH+	4.10E-09
HN2+	+	C2H3CN	→	C2H3CNH+	1.50E-09
CN+	+	CH4	→	CH4+	1.50E-10
CN+	+	CH4	→	CH3+	5.00E-10
CN+	+	CH4	→	CHN+	1.50E-10
CN+	+	CH4	→	CH2N+	1.00E-10
CN+	+	CH4	→	CH2CN+	1.00E-10
CN+	+	H2	→	CHN+	1.60E-09
CN+	+	N	→	N2+	6.10E-10
CN+	+	C2H2	→	C2H2+	8.00E-10
CN+	+	C2H2	→	C3HN+	2.00E-10
CN+	+	C2H4	→	CHN+	3.25E-10
CN+	+	C2H4	→	C2H4+	9.10E-10
CN+	+	C2H4	→	C3H2N+	6.50E-11
CN+	+	HCN	→	CHN+	2.24E-09
CN+	+	HCN	→	C2N2+	4.59E-10
CN+	+	C2H6	→	C2H5+	3.80E-10

Ion	+	Neutral	→	Product	Rate [cm^3s^{-1}]
CN+	+	C2H6	→	C2H4+	1.24E-09
CN+	+	C2H6	→	C2H3+	2.85E-10
CN+	+	H	→	H+	6.40E-10
CN+	+	HC3N	→	C3HN+	3.68E-09
CN+	+	H2O	→	CHN+	1.60E-09
CN+	+	H2O	→	CH2N+	4.80E-10
CN+	+	H2O	→	H2O+	3.20E-10
CN+	+	H2O	→	HNCO+	6.40E-10
CN+	+	H2O	→	HCO+	1.60E-10
CN+	+	C4H2	→	C4H2+	7.28E-10
CN+	+	C4H2	→	HC5N+	2.43E-10
CN+	+	CO	→	CO+	4.40E-10
CN+	+	C2N2	→	CNC+	5.25E-11
CN+	+	C2N2	→	C2N2+	1.63E-09
CN+	+	CH3CN	→	CH3+	6.80E-10
CN+	+	CH3CN	→	C2H3+	3.40E-10
CN+	+	CH3CN	→	CH3CN+	1.70E-09
CN+	+	CH3CN	→	CH2CN+	6.80E-10
CHN+	+	CH4	→	CH2N+	1.14E-09
CHN+	+	CH4	→	C2H3+	1.27E-10
CHN+	+	H2	→	CH2N+	8.80E-10
CHN+	+	N	→	CH+	2.20E-10
CHN+	+	NH	→	NH2+	6.50E-10
CHN+	+	C2H2	→	C2H4+	1.15E-09
CHN+	+	C2H2	→	C2H3+	2.03E-10
CHN+	+	C2H2	→	C2H2+	6.00E-10
CHN+	+	C2H2	→	C3H2N+	9.00E-10
CHN+	+	HCN	→	CH2N+	1.45E-09
CHN+	+	H	→	H+	3.70E-11
CHN+	+	HC3N	→	C3HN+	2.39E-09
CHN+	+	HC3N	→	C3H2N+	2.21E-09
CHN+	+	H2O	→	CH2N+	1.80E-10
CHN+	+	H2O	→	H3O+	1.80E-09
CHN+	+	H2O	→	H2O+	1.80E-09
CHN+	+	CO	→	HCO+	1.38E-10
CHN+	+	NH3	→	NH3+	1.68E-09
CHN+	+	CH3CN	→	CH3CNH+	1.90E-09
HCNH+	+	C2H2	→	C3H2N+	5.00E-11
HCNH+	+	C2H2	→	C3H2N+	2.50E-10
HCNH+	+	C2H4	→	C2H5CNH+	2.00E-11
HCNH+	+	C2H4	→	C2H3CNH+	5.00E-11

Ion	+	Neutral	→	Product	Rate [cm^3s^{-1}]
HCNH+	+	C2H4	→	C2H3CNH+	2.50E-10
CH2N+	+	HC3N	→	C3H2N+	3.40E-09
CH2N+	+	H2O	→	H3O+	8.80E-13
CH2N+	+	C4H2	→	C4H3+	1.80E-09
CH2N+	+	NH3	→	NH4+	2.40E-09
CH2N+	+	CH2NH	→	CH2NH2+	2.70E-09
CH2N+	+	CH3CN	→	CH3CNH+	3.80E-09
CH2N+	+	C2H3CN	→	C2H3CNH+	4.50E-09
CH2N+	+	C2H5CN	→	C2H5CNH+	4.20E-09
CH2N+	+	C6H6	→	C6H7+	1.10E-09
CH2N+	+	C6H6	→	CH3NH3+	2.00E-09
CH2N+	+	C6H2	→	C6H3+	3.00E-09
CH2N+	+	C7H4	→	C7H5+	3.00E-09
CH2N+	+	C7H8	→	C7H9+	3.00E-09
CH2N+	+	C8H2	→	C8H3+	3.00E-09
CH2N+	+	C4H3N	→	C4H3NH+	3.00E-09
CH2N+	+	HC5N	→	HC5NH+	3.00E-09
CH2N+	+	C5H5N	→	C5H5N+	3.00E-09
CH2N+	+	C6H3N	→	C6H3NH+	3.00E-09
CH2N+	+	C6H7N	→	C7H7NH+	3.00E-09
C2H6+	+	C2H2	→	C2H5+	2.47E-10
C2H6+	+	C2H2	→	C3H5+	9.10E-10
C2H6+	+	C2H2	→	C4H7+	1.43E-10
C2H6+	+	C2H4	→	C2H4+	1.15E-09
C2H6+	+	HCN	→	CH2N+	1.14E-09
C2H6+	+	HCN	→	C2H5CNH+	6.00E-11
C2H6+	+	H	→	C2H5+	1.00E-10
C2H6+	+	H2O	→	H3O+	2.95E-09
C2H6+	+	NH3	→	NH4+	1.61E-09
C2H6+	+	NH3	→	NH3+	6.24E-10
C2H5+	+	CH4	→	C3H7+	9.00E-14
C2H5+	+	C2H2	→	lC3H3+	6.84E-11
C2H5+	+	C2H2	→	cC3H3+	6.84E-11
C2H5+	+	C2H2	→	C4H5+	1.22E-10
C2H5+	+	C2H4	→	C3H5+	3.55E-10
C2H5+	+	HCN	→	CH2N+	5.00E-09
C2H5+	+	C2H6	→	C3H7+	5.46E-12
C2H5+	+	H	→	C2H4+	1.00E-11
C2H5+	+	HC3N	→	C3H2N+	3.55E-10
C2H5+	+	C3H4	→	C3H5+	1.26E-09
C2H5+	+	C3H4	→	C4H5+	1.40E-10

Ion		Neutral	→	Product	Rate [cm^3s^{-1}]
C2H5+	+	H2O	→	H3O+	1.89E-09
C2H5+	+	H2O	→	HC2N2+	1.20E-09
C2H5+	+	C3H8	→	C3H7+	6.30E-10
C2H5+	+	C4H2	→	C4H3+	3.00E-09
C2H5+	+	C2N2	→	HC2N2+	8.00E-11
C2H5+	+	NH3	→	NH4+	2.10E-09
C2H5+	+	CH2NH	→	CH2NH2+	2.57E-09
C2H5+	+	CH3CN	→	CH3CNH+	3.80E-09
C2H5+	+	C2H3CN	→	C2H3CNH+	3.00E-09
C2H5+	+	C2H5CN	→	C2H5CNH+	4.09E-09
C2H5+	+	C6H6	→	C6H7+	2.60E-09
C2H5+	+	C6H6	→	CH3NH3+	1.52E-09
C2H5+	+	C6H2	→	C6H3+	3.00E-09
C2H5+	+	C7H4	→	C7H5+	3.00E-09
C2H5+	+	C7H8	→	C7H9+	3.00E-09
C2H5+	+	C8H2	→	C8H3+	3.00E-09
C2H5+	+	C4H3N	→	C4H3NH+	3.00E-09
C2H5+	+	HC5N	→	HC5NH+	3.00E-09
C2H5+	+	C5H5N	→	C5H5N+	3.00E-09
C2H5+	+	C6H3N	→	C6H3NH+	3.00E-09
C2H5+	+	C6H7N	→	C7H7NH+	3.00E-09
C2H4+	+	N	→	CH3CN+	3.00E-10
C2H4+	+	C2H2	→	cC3H3+	6.47E-10
C2H4+	+	C2H2	→	C4H5+	1.93E-10
C2H4+	+	C2H4	→	C3H5+	7.03E-10
C2H4+	+	C2H4	→	C3H4+	4.74E-11
C2H4+	+	C2H4	→	C4H7+	4.74E-11
C2H4+	+	C2H6	→	C3H6+	3.61E-13
C2H4+	+	C2H6	→	C3H7+	4.79E-12
C2H4+	+	H	→	C2H3+	3.00E-10
C2H4+	+	HC3N	→	C3H2N+	1.28E-09
C2H4+	+	HC3N	→	C5H4N+	2.25E-10
C2H4+	+	C3H4	→	C3H4+	2.20E-10
C2H4+	+	C3H4	→	C4H5+	3.30E-10
C2H4+	+	C3H4	→	C5H7+	5.50E-10
C2H4+	+	C3H8	→	C3H6+	6.60E-10
C2H4+	+	C3H8	→	C3H7+	5.40E-10
C2H4+	+	C3H6	→	C3H6+	1.17E-10
C2H4+	+	C3H6	→	C4H7+	1.30E-11
C2H4+	+	C3H2	→	C4H3+	1.50E-09
C2H4+	+	NH3	→	NH4+	1.80E-09

Ion		Neutral	→	Product	Rate [cm^3s^{-1}]
C2H4+	+	NH3	→	NH3+	1.80E-09
C2H4+	+	O	→	HCO+	8.40E-11
C2H4+	+	CH3CN	→	CH3CNH+	2.70E-09
C2H4+	+	C2H5CN	→	C2H5CNH+	4.50E-09
C2H4+	+	C6H2	→	C7H3+	5.00E-10
C2H3+	+	CH4	→	C3H5+	1.90E-10
C2H3+	+	N	→	CH2N+	2.40E-11
C2H3+	+	N	→	CH2CN+	2.20E-12
C2H3+	+	N	→	C2HN+	1.98E-11
C2H3+	+	C2H2	→	C2H3+	5.04E-10
C2H3+	+	C2H2	→	C4H3+	2.16E-10
C2H3+	+	C2H4	→	C2H5+	8.20E-10
C2H3+	+	HCN	→	CH2N+	2.30E-09
C2H3+	+	C2H6	→	C2H5+	2.91E-10
C2H3+	+	C2H6	→	C3H5+	2.48E-10
C2H3+	+	C2H6	→	C4H7+	8.06E-11
C2H3+	+	H	→	C2H2+	6.80E-11
C2H3+	+	HC3N	→	C3H2N+	3.80E-09
C2H3+	+	C3H4	→	C3H5+	1.50E-09
C2H3+	+	H2O	→	H3O+	1.10E-09
C2H3+	+	C4H2	→	C4H3+	3.00E-10
C2H3+	+	C4H2	→	C6H3+	3.00E-10
C2H3+	+	C3H6	→	C4H7+	8.70E-10
C2H3+	+	C2N2	→	C3H+	5.50E-10
C2H3+	+	C2N2	→	HC2N2+	1.10E-09
C2H3+	+	C3H2	→	CH3C4H+	8.00E-10
C2H3+	+	NH3	→	NH4+	2.50E-09
C2H3+	+	C2H3CN	→	C2H3CNH+	3.50E-09
C2H3+	+	C6H6	→	C6H7+	1.60E-09
C2H3+	+	C6H2	→	C6H3+	3.00E-10
C2H3+	+	C6H2	→	C8H3+	3.00E-10
C2H2+	+	CH4	→	C3H5+	7.03E-10
C2H2+	+	CH4	→	C3H4+	1.87E-10
C2H2+	+	H2	→	C2H3+	1.00E-11
C2H2+	+	N	→	CH+	2.50E-11
C2H2+	+	N	→	CNC+	7.50E-11
C2H2+	+	N	→	C2HN+	1.50E-10
C2H2+	+	NH	→	CH2CN+	6.50E-10
C2H2+	+	C2H2	→	C4H2+	4.48E-10
C2H2+	+	C2H2	→	C4H3+	9.52E-10
C2H2+	+	C2H4	→	C2H5+	1.24E-10

Ion		Neutral	→	Product	Rate [cm^3s^{-1}]
C2H2+	+	C2H4	→	C2H4+	2.48E-10
C2H2+	+	C2H4	→	C3H5+	7.45E-10
C2H2+	+	C2H4	→	cC3H3+	8.28E-11
C2H2+	+	C2H4	→	C3H4+	1.38E-11
C2H2+	+	C2H4	→	C4H5+	6.90E-11
C2H2+	+	C2H4	→	C4H7+	1.24E-10
C2H2+	+	HCN	→	CH2N+	2.38E-10
C2H2+	+	HCN	→	C3H2N+	1.22E-10
C2H2+	+	C2H6	→	C2H5+	1.24E-10
C2H2+	+	C2H6	→	C2H4+	2.48E-10
C2H2+	+	C2H6	→	C3H5+	7.45E-10
C2H2+	+	C2H6	→	cC3H3+	8.28E-11
C2H2+	+	C2H6	→	C3H4+	1.38E-11
C2H2+	+	C2H6	→	C4H5+	6.90E-11
C2H2+	+	C2H6	→	C4H7+	1.24E-10
C2H2+	+	HC3N	→	C4H2+	3.70E-10
C2H2+	+	HC3N	→	C5H3N+	2.00E-12
C2H2+	+	C3H4	→	C3H5+	7.50E-11
C2H2+	+	C3H4	→	C3H4+	7.50E-10
C2H2+	+	C3H4	→	C5H5+	6.75E-10
C2H2+	+	H2O	→	H3O+	2.20E-10
C2H2+	+	C3H8	→	C3H6+	1.95E-10
C2H2+	+	C3H8	→	C3H7+	6.50E-10
C2H2+	+	C3H8	→	C4H7+	6.50E-11
C2H2+	+	C4H2	→	C4H2+	1.53E-09
C2H2+	+	C4H2	→	C6H3+	1.40E-10
C2H2+	+	C3H6	→	C3H6+	1.30E-09
C2H2+	+	C3H2	→	C5H2+	7.00E-10
C2H2+	+	NH3	→	NH4+	9.61E-10
C2H2+	+	NH3	→	NH3+	2.14E-09
C2H2+	+	O	→	HCO+	8.50E-11
C2H2+	+	CH3CN	→	C3H5+	1.06E-09
C2H2+	+	CH3CN	→	C3H4+	1.06E-09
C2H2+	+	CH3CN	→	CH2NH2+	2.90E-09
C2H2+	+	CH3CN	→	CH3CNH+	8.36E-10
C2H2+	+	C2H3CN	→	C2H3CNH+	6.50E-10
C2H2+	+	C2H5CN	→	C3H5+	3.99E-09
C2H2+	+	C2H5CN	→	C2H5CNH+	2.10E-10
C2H2+	+	CH3NH2	→	CH2NH2+	7.00E-10
C2H2+	+	CH3NH2	→	CH3NH2+	8.00E-10
C2H2+	+	CH3NH2	→	CH3NH3+	1.30E-09

Ion	+	Neutral	→	Product	Rate [cm^3s^{-1}]
C2H2+	+	C6H2	→	C8H3+	5.00E-10
C2H2+	+	HC5N	→	H3C7N+	2.00E-12
C2H+	+	CH4	→	C2H2+	3.74E-10
C2H+	+	CH4	→	lC3H3+	3.74E-10
C2H+	+	CH4	→	C3H5+	2.20E-10
C2H+	+	CH4	→	cC3H3+	3.74E-10
C2H+	+	CH4	→	C3H4+	1.32E-10
C2H+	+	H2	→	C2H2+	1.24E-09
C2H+	+	N	→	CH+	9.50E-11
C2H+	+	C2H2	→	C4H2+	1.85E-09
C2H+	+	HCN	→	CH2N+	9.45E-10
C2H+	+	HCN	→	C2H2+	5.40E-10
C2H+	+	HCN	→	C3HN+	1.22E-09
C2H+	+	HC3N	→	C3H2N+	1.41E-09
C2H+	+	HC3N	→	C4H2+	4.56E-10
C2H+	+	HC3N	→	HC5N+	1.18E-09
C2H+	+	HC3N	→	C4H+	7.60E-10
C2H+	+	NH3	→	NH4+	5.50E-10
C2H+	+	NH3	→	CH2CN+	5.50E-10
C2H+	+	O	→	HCO+	3.30E-10
lC3H3+	+	N	→	C3HN+	5.80E-11
lC3H3+	+	N	→	C3H2N+	1.30E-10
lC3H3+	+	C2H2	→	cC3H3+	2.00E-10
lC3H3+	+	C2H2	→	C5H3+	1.00E-09
lC3H3+	+	C2H4	→	C5H5+	1.10E-09
lC3H3+	+	HCN	→	C4H3NH+	4.80E-10
lC3H3+	+	H2O	→	H3O+	3.20E-12
lC3H3+	+	C3H8	→	C3H7+	8.04E-10
lC3H3+	+	C3H8	→	C4H7+	3.96E-10
lC3H3+	+	C4H2	→	cC3H3+	3.36E-10
lC3H3+	+	C4H2	→	C5H3+	1.06E-09
lC3H3+	+	C4H2	→	C7H5+	1.00E-13
lC3H3+	+	C3H2	→	C6H3+	1.00E-09
lC3H3+	+	NH3	→	NH4+	1.10E-09
lC3H3+	+	O	→	HCO+	2.00E-10
lC3H3+	+	CH3CN	→	CH3CN+	1.60E-10
lC3H3+	+	C2H5CN	→	CH3C5H5N+	3.00E-10
lC3H3+	+	C6H6	→	C7H7+	7.00E-10
lC3H3+	+	C6H2	→	C9H3+	1.00E-09
C3H5+	+	N	→	C2H4+	1.10E-10
C3H5+	+	N	→	C2H3CN+	1.50E-11

Ion		Neutral	→	Product	Rate [cm^3s^{-1}]
C3H5+	+	C2H2	→	C5H5+	3.80E-10
C3H5+	+	C2H4	→	C5H7+	8.90E-11
C3H5+	+	C2H4	→	C5H9+	5.10E-11
C3H5+	+	HCN	→	C4H5NH+	1.50E-10
C3H5+	+	H	→	C2H3+	9.50E-12
C3H5+	+	H	→	C2H2+	5.00E-13
C3H5+	+	HC3N	→	C3H2N+	3.80E-10
C3H5+	+	C3H4	→	C6H7+	3.50E-10
C3H5+	+	C3H8	→	C3H7+	3.90E-10
C3H5+	+	C3H8	→	C4H7+	2.82E-11
C3H5+	+	C4H2	→	C5H5+	1.50E-10
C3H5+	+	CO	→	C5H5+	3.80E-10
C3H5+	+	C3H6	→	C4H7+	1.00E-09
C3H5+	+	CH2NH	→	CH2NH2+	1.75E-09
C3H5+	+	C2H3CN	→	C2H3CNH+	1.00E-09
C3H5+	+	C2H5CN	→	C2H5CNH+	2.67E-09
C3H5+	+	C6H6	→	C6H7+	1.15E-10
C3H5+	+	C6H6	→	C7H7+	1.04E-09
C3H5+	+	C6H6	→	CH2NH2+	4.75E-10
C3H5+	+	C6H6	→	CH3NH3+	7.60E-10
cC3H3+	+	C4H2	→	C7H5+	1.00E-13
cC3H3+	+	C3H2	→	C6H3+	1.00E-09
cC3H3+	+	NH3	→	NH4+	1.10E-09
cC3H3+	+	C2H5CN	→	CH3C5H5N+	3.00E-10
cC3H3+	+	C6H2	→	C9H3+	1.00E-09
H3O+	+	C2H4	→	C2H5+	2.00E-12
H3O+	+	HCN	→	CH2N+	3.80E-09
H3O+	+	HC3N	→	C3H2N+	3.90E-09
H3O+	+	C3H4	→	C3H5+	1.80E-09
H3O+	+	C4H2	→	C4H3+	1.10E-09
H3O+	+	NH3	→	NH4+	2.20E-09
H3O+	+	CH2NH	→	CH2NH2+	3.00E-09
H3O+	+	CH3CN	→	CH3CNH+	4.50E-09
H3O+	+	C2H5CN	→	C3H5+	4.60E-09
H3O+	+	C6H6	→	CH3NH3+	2.10E-09
H2O+	+	CH4	→	H3O+	1.12E-09
H2O+	+	H2	→	H3O+	7.60E-10
H2O+	+	N	→	NO+	2.80E-11
H2O+	+	C2H2	→	C2H2+	1.90E-09
H2O+	+	C2H4	→	C2H5+	1.50E-09
H2O+	+	C2H4	→	C2H4+	1.50E-09

Ion		Neutral	→	Product	Rate [cm^3s^{-1}]
H2O+	+	HCN	→	CH2N+	1.05E-09
H2O+	+	HCN	→	H3O+	1.05E-09
H2O+	+	C2H6	→	C2H6+	6.40E-11
H2O+	+	C2H6	→	C2H5+	1.60E-11
H2O+	+	C2H6	→	C2H4+	1.92E-10
H2O+	+	C2H6	→	H3O+	1.33E-09
H2O+	+	H	→	H3O+	7.60E-10
H2O+	+	H2O	→	H3O+	1.85E-09
H2O+	+	CO	→	HCO+	4.25E-09
H2O+	+	C2N2	→	HC2N2+	1.00E-09
H2O+	+	NH3	→	NH4+	9.45E-10
H2O+	+	NH3	→	NH3+	2.21E-09
C3H+	+	CH4	→	C2H3+	7.83E-10
C3H+	+	CH4	→	cC3H3+	1.10E-10
C3H+	+	CH4	→	C4H3+	8.70E-11
C3H+	+	H2	→	lC3H3+	1.69E-12
C3H+	+	H2	→	cC3H3+	1.69E-12
C3H+	+	H2	→	C3H2+	5.20E-12
C3H+	+	H2	→	C6H3+	1.35E-11
C3H+	+	N	→	C3HN+	2.70E-11
C3H+	+	C2H2	→	C5H2+	8.40E-10
C3H+	+	C2H4	→	lC3H3+	9.03E-10
C3H+	+	C2H4	→	cC3H3+	9.00E-10
C3H+	+	C2H4	→	C5H3+	4.75E-11
C3H+	+	HCN	→	CH2N+	4.40E-10
C3H+	+	C3H4	→	C4H3+	1.40E-09
C3H+	+	H2O	→	C2H3+	4.50E-10
C3H+	+	H2O	→	HC3O+	2.25E-11
C3H+	+	H2O	→	HCO+	4.50E-10
C3H+	+	C4H2	→	C4H2+	6.00E-11
C3H+	+	C4H2	→	C5H2+	1.02E-09
C3H+	+	NH3	→	NH4+	8.00E-10
C3H+	+	NH3	→	C2H3CN+	1.65E-09
C3H+	+	NH3	→	NH3+	3.20E-10
C3H+	+	CH3CN	→	C2H3+	6.00E-10
C3H+	+	CH3CN	→	C3H2N+	9.90E-10
C3H+	+	CH3CN	→	CH3CNH+	4.50E-10
C3H+	+	CH3CN	→	C5H4N+	9.00E-10
C3H+	+	CH3NH2	→	CH2NH2+	1.90E-09
C3H2+	+	CH4	→	cC3H3+	4.68E-10
C3H2+	+	CH4	→	C4H5+	8.25E-11

Ion		Neutral	→	Product	Rate [cm^3s^{-1}]
C3H2+	+	N	→	CH2N+	6.60E-12
C3H2+	+	N	→	C2H2+	3.74E-11
C3H2+	+	C2H2	→	C5H3+	2.00E-09
C3H2+	+	C2H4	→	lC3H3+	2.75E-10
C3H2+	+	C2H4	→	C3H4+	6.60E-10
C3H2+	+	C2H4	→	C5H3+	2.75E-10
C3H2+	+	C2H4	→	C5H5+	4.40E-10
C3H2+	+	H	→	C3H+	6.00E-11
C3H2+	+	C3H4	→	C5H3+	2.34E-10
C3H2+	+	C3H4	→	C4H2+	1.17E-10
C3H2+	+	C3H4	→	C4H3+	1.56E-10
C3H2+	+	C3H4	→	C6H5+	2.60E-10
C3H2+	+	C3H4	→	C4H4+	5.33E-10
C3H2+	+	H2O	→	C2H4+	4.80E-11
C3H2+	+	C3H8	→	lC3H3+	1.80E-10
C3H2+	+	C3H8	→	cC3H3+	1.80E-10
C3H2+	+	C3H8	→	C3H7+	5.40E-10
C3H2+	+	C3H8	→	C5H7+	1.20E-10
C3H2+	+	C4H2	→	C7H2+	3.00E-10
C3H2+	+	C4H2	→	C7H3+	3.00E-10
C3H2+	+	C3H2	→	C6H3+	1.00E-09
C3H2+	+	NH3	→	C2H3CNH+	1.20E-09
C3H2+	+	O	→	HCO+	2.00E-10
C3H2+	+	C6H2	→	C9H2+	3.00E-10
C3H2+	+	C6H2	→	C9H3+	3.00E-10
C3H4+	+	C2H2	→	C5H5+	4.20E-10
C3H4+	+	C2H4	→	C4H5+	9.13E-11
C3H4+	+	C2H4	→	C5H7+	7.39E-10
C3H4+	+	H	→	cC3H3+	3.00E-11
C3H4+	+	HC3N	→	C3H2N+	1.80E-10
C3H4+	+	C3H4	→	C3H5+	1.98E-10
C3H4+	+	C3H4	→	C5H5+	2.20E-11
C3H4+	+	C3H4	→	C6H7+	7.48E-10
C3H4+	+	C3H4	→	C6H5+	8.80E-11
C3H4+	+	C3H4	→	C4H4+	2.20E-11
C3H4+	+	C4H2	→	C7H5+	1.67E-09
C3H4+	+	C4H2	→	CH3C4H+	1.26E-10
C3H4+	+	O	→	HCO+	2.00E-10
C3H4+	+	C2H5CN	→	C2H5CNH+	3.71E-09
C3H4+	+	C2H5CN	→	CH3C5H5N+	1.95E-10
C3H6+	+	C2H2	→	C4H5+	8.04E-11

Ion		Neutral	→	Product	Rate [cm^3s^{-1}]
C3H6+	+	C2H2	→	C5H7+	5.90E-10
C3H6+	+	C2H4	→	C4H7+	1.80E-27
C3H6+	+	HCN	→	CH3CN+	1.60E-10
C3H6+	+	HCN	→	C4H5NH+	2.40E-10
C3H6+	+	C3H6	→	C3H7+	2.10E-10
C3H6+	+	C3H6	→	C4H7+	2.80E-10
C3H6+	+	C3H6	→	C5H9+	4.20E-10
C3H6+	+	NH3	→	NH4+	3.00E-10
C3H7+	+	H	→	C3H6+	3.70E-11
C4H5+	+	N	→	C4H3NH+	1.00E-10
C4H5+	+	C2H2	→	C6H5+	1.60E-10
C4H5+	+	C2H4	→	C6H7+	7.30E-11
C4H5+	+	C3H4	→	C7H7+	1.50E-10
C4H5+	+	C3H4	→	C6H5+	5.00E-11
C4H5+	+	C4H2	→	C6H5+	1.00E-09
C4H7+	+	C3H4	→	C7H9+	1.50E-10
C4H7+	+	CH3CN	→	CH3CNH+	5.20E-11
C5H3+	+	O	→	HCO+	2.00E-10
C5H5+	+	N	→	C5H3N+	1.00E-10
C5H5+	+	C2H2	→	C7H7+	1.70E-10
C5H5+	+	C2H2	→	C7H5+	1.00E-09
C5H5+	+	C3H4	→	C6H7+	5.60E-10
C5H5+	+	C3H4	→	C8H6P	9.00E-11
C5H5+	+	C3H4	→	C8H8P	7.50E-10
C5H5+	+	C4H2	→	C7H7+	2.20E-10
C5H5+	+	C4H2	→	C7H5+	2.20E-10
C5H5+	+	NH3	→	NH4+	6.50E-10
C5H5+	+	CH2NH	→	CH2NH2+	3.20E-10
C5H5+	+	CH3CN	→	C7H7+	7.33E-11
C5H5+	+	CH3CN	→	C7H5+	7.33E-11
C5H5+	+	CH3CN	→	C9H7+	7.33E-11
C5H5+	+	C6H6	→	CH2NH2+	2.50E-11
C5H5+	+	C6H6	→	CH3NH3+	2.00E-10
C6H7+	+	C3H4	→	C7H7+	9.70E-11
C7H7+	+	CH4	→	C8H5+	3.00E-11
C7H7+	+	C2H2	→	C11H9+	1.00E-09
C7H7+	+	C2H2	→	C9H8P	5.00E-10
C7H7+	+	C2H2	→	C9H9P	1.00E-10
C7H7+	+	C2H2	→	C11H8P	1.00E-09
C7H7+	+	C2H4	→	C9H8P	5.00E-10
C7H7+	+	C2H4	→	C9H9P	5.00E-10

Ion		Neutral	→	Product	Rate [cm^3s^{-1}]
C7H7+	+	C2H4	→	C8H5+	2.00E-10
C7H7+	+	C2H6	→	C8H8P	2.00E-10
C7H7+	+	C3H4	→	C10H9+	5.00E-10
C7H7+	+	C3H4	→	C8H8P	5.60E-10
C7H7+	+	C3H4	→	C10H10P	5.00E-10
C7H7+	+	C4H2	→	C11H9+	1.00E-09
C7H7+	+	C4H2	→	C11H9N+	1.00E-09
C7H7+	+	CH2NH	→	CH2NH2+	3.40E-11
C7H7+	+	C6H6	→	CH3NH2+	1.80E-12
C7H7+	+	C6H6	→	CH3NH3+	1.62E-11
C3HN+	+	CH4	→	C3H5+	2.28E-10
C3HN+	+	CH4	→	C3H4+	8.30E-11
C3HN+	+	CH4	→	C3H2N+	2.91E-10
C3HN+	+	CH4	→	CH3CN+	2.28E-10
C3HN+	+	H2	→	C2H2+	1.65E-12
C3HN+	+	H2	→	C3H2N+	2.80E-12
C3HN+	+	N	→	C3H+	9.60E-11
C3HN+	+	N	→	CNC+	1.44E-10
C3HN+	+	C2H2	→	C2H4+	1.28E-10
C3HN+	+	C2H2	→	C2H2+	1.28E-10
C3HN+	+	C2H2	→	C4H2+	5.12E-10
C3HN+	+	C2H4	→	C2H4+	5.36E-10
C3HN+	+	C2H4	→	C3H2N+	1.34E-10
C3HN+	+	HCN	→	CH2N+	3.90E-10
C3HN+	+	HC3N	→	HC5N+	1.17E-09
C3HN+	+	H2O	→	C3H2N+	6.70E-10
C3HN+	+	C4H2	→	C4H2+	8.90E-10
C3HN+	+	NH3	→	NH4+	1.70E-09
C3HN+	+	NH3	→	NH3+	1.70E-09
C3HN+	+	C8H2	→	NH3+	1.70E-09
C3H2N+	+	C2H4	→	C5H5N+	1.30E-09
C3H2N+	+	C2H4	→	C4H5NH+	1.00E-11
C3H2N+	+	NH3	→	NH4+	2.00E-09
C3H2N+	+	CH2NH	→	CH2NH2+	2.40E-09
C3H2N+	+	CH3CN	→	CH3CNH+	1.28E-09
C3H2N+	+	CH3CN	→	C5H4N+	3.20E-10
C3H2N+	+	C2H5CN	→	C2H5CNH+	1.90E-09
C3H2N+	+	C6H6	→	CH3NH3+	1.60E-09
C4H2+	+	CH4	→	C5H5+	5.00E-10
C4H2+	+	CH4	→	CH3C4H+	2.00E-10
C4H2+	+	N	→	CH2N+	9.00E-12

Ion	+	Neutral	→	Product	Rate [cm^3s^{-1}]
C4H2+	+	N	→	C3H+	1.62E-10
C4H2+	+	N	→	HC4N+	9.00E-12
C4H2+	+	C2H2	→	C6H3+	1.40E-11
C4H2+	+	C2H4	→	C3H2N+	7.35E-10
C4H2+	+	C2H4	→	C6H5+	7.60E-10
C4H2+	+	C2H4	→	C7H3+	2.20E-09
C4H2+	+	C2H4	→	C4H4+	7.05E-10
C4H2+	+	H	→	C4H3+	7.00E-11
C4H2+	+	HC3N	→	H3C7N+	1.70E-09
C4H2+	+	C3H4	→	C7H5+	1.17E-09
C4H2+	+	C3H4	→	CH3C4H+	1.30E-10
C4H2+	+	C4H2	→	C8H3+	1.00E-09
C4H2+	+	C3H2	→	C7H3+	2.20E-09
C4H2+	+	O	→	C3H2+	1.08E-10
C4H2+	+	O	→	HC3O+	1.35E-11
C4H3+	+	CH4	→	C5H5+	5.00E-10
C4H3+	+	C2H2	→	C6H5+	2.20E-10
C4H3+	+	C2H4	→	C6H5+	1.20E-10
C4H3+	+	H	→	C4H4+	6.00E-14
C4H3+	+	C3H4	→	C5H5+	1.40E-09
C4H3+	+	C3H4	→	C6H5+	4.00E-11
C4H3+	+	C3H4	→	C7H5+	1.00E-09
C4H3+	+	C4H2	→	C6H3+	7.40E-10
C4H3+	+	C4H2	→	C8H5+	1.00E-13
C4H3+	+	C3H2	→	C7H4+	1.50E-09
C4H3+	+	CH2NH	→	CH2NH2+	1.92E-09
C4H3+	+	C6H6	→	C6H7+	1.30E-09
C4H3+	+	C6H6	→	CH2NH2+	5.00E-10
C4H3+	+	C6H6	→	CH3NH2+	2.00E-10
C4H3+	+	C6H6	→	CH3NH3+	1.30E-09
C4H3+	+	C6H2	→	C8H3+	7.40E-10
CNC+	+	CH4	→	CH2N+	2.10E-10
CNC+	+	CH4	→	C2H3+	4.20E-10
CNC+	+	CH4	→	C3H2N+	7.00E-11
CNC+	+	H2	→	CH2N+	8.10E-10
CNC+	+	H2	→	CH2CN+	9.00E-11
CNC+	+	N	→	CH2N+	1.28E-10
CNC+	+	N	→	C3H+	1.47E-09
CNC+	+	C2H2	→	C3H+	8.00E-10
CNC+	+	C2H2	→	C4H2+	4.00E-10
CNC+	+	C2H4	→	C2H4+	1.30E-10

Ion		Neutral	→	Product	Rate [cm^3s^{-1}]
CNC+	+	C2H4	→	lC3H3+	1.95E-10
CNC+	+	C2H4	→	cC3H3+	1.95E-10
CNC+	+	C2H4	→	CH2CN+	6.50E-10
CNC+	+	C2H6	→	C2H5+	3.00E-10
CNC+	+	C2H6	→	C2H3+	1.20E-10
CNC+	+	C2H6	→	lC3H3+	1.80E-10
CNC+	+	C2H6	→	C3H5+	1.20E-10
CNC+	+	C2H6	→	cC3H3+	1.80E-10
CNC+	+	C2H6	→	C3H2N+	3.00E-10
CNC+	+	C2H6	→	CH2CN+	3.00E-10
CNC+	+	HC3N	→	C3H+	3.30E-09
CNC+	+	H2O	→	CH2N+	1.30E-10
CNC+	+	H2O	→	C2HN+	1.75E-11
CNC+	+	H2O	→	HCO+	1.50E-09
CNC+	+	C4H2	→	C4H2+	2.60E-10
CNC+	+	C4H2	→	CNC+	2.60E-10
CNC+	+	NH3	→	CH2N+	1.90E-09
CNC+	+	CH3CN	→	C2H3+	4.10E-09
C6H5+	+	CH4	→	C7H7+	7.50E-11
C6H5+	+	H2	→	C6H7+	6.00E-11
C6H5+	+	N	→	CH3C4H+	3.70E-11
C6H5+	+	C2H2	→	C8H6P	7.80E-11
C6H5+	+	C2H2	→	C8H7P	5.20E-11
C6H5+	+	C2H4	→	C6H7+	1.02E-10
C6H5+	+	C2H4	→	C8H7P	6.80E-11
C6H5+	+	C2H4	→	C8H8P	6.00E-11
C6H5+	+	C2H6	→	C6H7+	1.26E-10
C6H5+	+	C2H6	→	C7H7+	3.90E-12
C6H5+	+	C3H4	→	C7H7+	4.14E-11
C6H5+	+	C3H4	→	C9H7+	1.79E-10
C6H5+	+	C3H4	→	C9H8P	1.15E-11
C6H5+	+	C3H6	→	C7H7+	3.40E-10
C6H5+	+	C6H6	→	C9H7+	2.82E-11
C6H5+	+	C6H6	→	C10H9+	2.33E-11
C6H5+	+	C6H6	→	C12H9+	2.30E-10
C6H5+	+	C6H6	→	C12H10+	5.17E-11
C6H5+	+	C6H6	→	C10H8P	1.41E-11
C6H5+	+	C6H6	→	C8H5+	8.46E-11
CH2NH2+	+	CH3NH2	→	CH3NH3+	1.40E-09
CH3CN+	+	H2	→	CH3CNH+	5.70E-10
CH3CN+	+	CO	→	HCO+	2.00E-09

Ion	+	Neutral	→	Product	Rate [cm^3s^{-1}]
CH3CNH+	+	CH2NH	→	CH2NH2+	2.50E-09
CH3CNH+	+	C2H5CN	→	C2H5CNH+	4.09E-09
CH3CNH+	+	C6H6	→	CH3NH3+	1.80E-09
HC2N2+	+	C2H4	→	C2H5+	5.60E-10
HC2N2+	+	HCN	→	CH2N+	2.00E-09
HC2N2+	+	H2O	→	H3O+	5.10E-10
HC2N2+	+	NH3	→	NH4+	2.00E-09
C2H3CN+	+	CH4	→	CH3CN+	1.82E-11
C2H3CN+	+	CH4	→	C2H3CNH+	6.50E-12
C2H3CN+	+	CH4	→	C4H5NH+	1.30E-12
C2H3CN+	+	H2	→	C2H3CNH+	1.20E-11
C2H3CN+	+	C2H2	→	lC3H3+	3.72E-11
C2H3CN+	+	C2H2	→	cC3H3+	3.72E-11
C2H3CN+	+	C2H2	→	C6H5+	5.10E-10
C2H3CN+	+	C2H2	→	C5H4N+	1.49E-10
C2H3CN+	+	C2H2	→	C4H4+	5.12E-10
C2H3CN+	+	NH3	→	NH4+	1.90E-10
C2H3CN+	+	C2H3CN	→	C2H3CNH+	2.50E-09
C2H3CNH+	+	NH3	→	NH4+	1.70E-09
C2H3CNH+	+	CH2NH	→	CH2NH2+	2.40E-09
C2H3CNH+	+	C6H6	→	CH3NH3+	1.70E-09
C6H3+	+	O	→	HCO+	2.00E-10
C7H5+	+	N	→	H3C7N+	1.00E-10
C8H3+	+	O	→	HCO+	2.00E-10
C9H7+	+	C2H2	→	C9H8P	1.25E-10
C9H7+	+	C2H2	→	C9H9P	1.25E-10
C9H7+	+	C2H2	→	C10H8P	5.00E-10
C9H7+	+	C2H4	→	C9H8P	1.25E-10
C9H7+	+	C2H4	→	C9H9P	1.25E-10
C9H7+	+	C2H4	→	C10H8P	5.00E-10
C9H7+	+	C3H4	→	C8H5+	2.80E-09
C10H9+	+	C2H2	→	C11H9+	5.00E-11
C10H9+	+	C2H2	→	C10H10P	5.00E-10
C10H9+	+	C2H2	→	C11H10P	5.00E-11
C10H9+	+	C2H4	→	C11H9+	5.00E-11
C10H9+	+	C2H4	→	C10H10P	5.00E-10
C10H9+	+	C2H4	→	C11H10P	5.00E-11
C10H9+	+	C2H6	→	C11H9+	5.00E-11
C10H9+	+	C2H6	→	C11H10P	5.00E-11
C10H9+	+	C2H6	→	C11H11P	5.00E-11
C7H6P	+	C2H4	→	C8H8P	1.00E-09

Ion		Neutral		Product	Rate [cm^3s^{-1}]
C7H6P	+	C2H6	→	C7H7+	2.00E-10
C7H6P	+	C2H6	→	C7H8P	2.00E-10
C7H6P	+	C3H4	→	C10H9+	5.00E-10
C7H6P	+	C3H4	→	C8H8P	1.00E-09
C7H6P	+	C3H4	→	C10H8P	5.00E-10
C8H6P	+	C2H4	→	C8H7P	5.00E-10
C8H6P	+	C2H4	→	C8H8P	5.00E-10
C8H7P	+	C2H2	→	C6H5+	1.70E-10
C8H7P	+	C2H4	→	C6H5+	4.80E-11
C8H7P	+	C2H4	→	C8H8P	5.00E-10
C8H7P	+	C2H4	→	C9H9P	4.00E-10
C8H7P	+	HCN	→	C11H9+	5.00E-11
C8H7P	+	HCN	→	C11H8P	5.00E-11
C8H7P	+	HCN	→	C11H10P	5.00E-11
C8H7P	+	C2H6	→	C9H9P	4.00E-10
C8H7P	+	C3H4	→	C9H8P	5.00E-10
C8H7P	+	C3H4	→	C9H9P	5.00E-10
C8H8P	+	C2H2	→	C10H9+	5.00E-10
C8H8P	+	C2H2	→	C10H10P	5.00E-10
C8H8P	+	C2H4	→	C10H9+	5.00E-10
C8H8P	+	C2H4	→	C10H10P	5.00E-10
C8H8P	+	C2H6	→	C9H9P	4.00E-10
C8H8P	+	C3H4	→	C11H9+	5.00E-11
C8H8P	+	C3H4	→	C11H10P	5.00E-11
C8H8P	+	C3H4	→	C11H11P	5.00E-11
C9H8P	+	C2H2	→	C10H9+	5.00E-10
C9H8P	+	C2H2	→	C9H9P	5.00E-10
C9H8P	+	C2H4	→	C10H9+	5.00E-10
C9H8P	+	C2H4	→	C9H9P	5.00E-10
C9H9P	+	C2H2	→	C10H9+	5.00E-10
C9H9P	+	C2H2	→	C10H10P	5.00E-10
C9H9P	+	C2H4	→	C10H9+	5.00E-10
C9H9P	+	C2H4	→	C10H10P	5.00E-10
C9H9P	+	C2H6	→	C10H9+	5.00E-10
C9H9P	+	C2H6	→	C10H10P	5.00E-10
C10H8P	+	C2H2	→	C11H9+	5.00E-11
C10H8P	+	C2H2	→	C11H8P	5.00E-11
C10H8P	+	C2H4	→	C11H9+	5.00E-11
C10H8P	+	C2H4	→	C11H8P	5.00E-11
C10H8P	+	C2H6	→	C11H9+	5.00E-11
C10H8P	+	C2H6	→	C11H10P	5.00E-11

Ion		Neutral		Product	Rate [cm^3s^{-1}]
C10H8P	+	C2H6	→	C11H11P	5.00E-11
C10H10P	+	C2H2	→	C11H10P	5.00E-11
C10H10P	+	C2H2	→	C11H11P	5.00E-11
C10H10P	+	C2H4	→	C11H10P	5.00E-11
C10H10P	+	C2H4	→	C11H11P	5.00E-11
C10H10P	+	C2H6	→	C11H9+	5.00E-11
C10H10P	+	C2H6	→	C11H10P	5.00E-11
C10H10P	+	C2H6	→	C11H11P	5.00E-11
C7N+	+	H2	→	HC7N+	1.50E-09
HC7N+	+	H2	→	H2C7N+	5.00E-12
C7H+	+	H2	→	C7H2+	1.00E-17
C7H+	+	N	→	C7N+	2.00E-10
C7H+	+	O	→	HCO+	2.00E-10
C7H2+	+	N	→	HC7N+	2.00E-10
C7H2+	+	C2H2	→	C9H2+	3.00E-10
C7H2+	+	O	→	HCO+	2.00E-10
C7H3+	+	N	→	H2C7N+	2.00E-10
C7H3+	+	O	→	HCO+	2.00E-10
C7H4+	+	N	→	H3C7N+	1.00E-10
CH3C4H+	+	N	→	C5H3N+	1.00E-10
C5H3N+	+	C2H4	→	C7H5N+	1.00E-10
C7H5N+	+	C2H4	→	C9H7N+	1.00E-10
C9H7N+	+	C2H4	→	C11H9N+	1.00E-10
C11H9N+	+	C2H4	→	C13H11N+	1.00E-10
C9N+	+	H2	→	HC9N+	1.50E-09
HC9N+	+	H2	→	H2C9N+	5.00E-12
C9H+	+	N	→	C9N+	2.00E-10
C9H+	+	O	→	HCO+	2.00E-10
C9H2+	+	N	→	HC9N+	2.00E-10
C9H2+	+	O	→	HCO+	2.00E-10
C9H3+	+	O	→	HCO+	2.00E-10
H3CO+	+	H2	→	H3O+	2.30E-10
H3CO+	+	HCN	→	CH2N+	1.30E-09
H3CO+	+	H2O	→	H3O+	2.30E-10
H3CO+	+	C4H2	→	C4H3+	9.30E-10
H3CO+	+	NH3	→	NH4+	2.30E-09
C4N+	+	CH4	→	C2H3+	1.43E-10
C4N+	+	CH4	→	C3H2N+	2.00E-10
C4N+	+	CH4	→	C4H3+	1.71E-10
C4N+	+	CH4	→	HC5NH+	2.85E-11
C4N+	+	H2	→	C3H+	2.20E-11

Ion		Neutral	→	Product	Rate [cm^3s^{-1}]
C4N+	+	H2O	→	HCO+	7.50E-10
C2N2+	+	H2	→	HC2N2+	8.80E-10
C2N2+	+	C2H2	→	C2H2+	1.00E-10
C2N2+	+	C2H2	→	C4H2+	3.00E-11
C2N2+	+	C2H4	→	C2H4+	1.30E-09
C2N2+	+	HCN	→	CHN+	5.40E-10
C2N2+	+	HCN	→	HC2N2+	2.03E-09
C2N2+	+	H	→	CHN+	4.96E-10
C2N2+	+	H	→	C2H+	1.24E-10
C2N2+	+	HC3N	→	C3HN+	1.60E-09
C2N2+	+	H2O	→	H2O+	2.34E-10
C2N2+	+	H2O	→	HC2N2+	2.37E-09
C2N2+	+	C4H2	→	C4H3+	1.08E-09
C3+	+	CH4	→	C3H+	2.38E-10
C3+	+	CH4	→	C4H2+	3.61E-10
C3+	+	CH4	→	C4H3+	3.52E-10
C3+	+	H2	→	C3H+	2.40E-10
C3+	+	C2H4	→	C2H4+	3.96E-10
C3+	+	C2H4	→	C3H2+	1.35E-10
C3+	+	C2H4	→	C5H3+	1.35E-10
C3+	+	C2H4	→	C5H2+	2.34E-10
C3+	+	HCN	→	C3H+	2.60E-10
C3+	+	HCN	→	C4N+	1.04E-09
C3+	+	HCN	→	C4H+	1.04E-09
HC5N+	+	H2	→	HC5NH+	1.00E-09
HC5N+	+	C2H4	→	HC5NH+	9.00E-10
HC5N+	+	C2H4	→	C7H5N+	2.40E-10
HC4N+	+	H2	→	HC5NH+	1.00E-09
NH3+	+	CH4	→	NH4+	4.80E-10
NH3+	+	H2	→	NH4+	4.40E-13
NH3+	+	NH	→	NH4+	7.10E-10
NH3+	+	C2H4	→	NH4+	1.40E-09
NH3+	+	H2O	→	NH4+	2.50E-10
NH3+	+	NH3	→	NH4+	2.10E-09
NH2+	+	CH4	→	NH3+	9.20E-10
NH2+	+	H2	→	NH3+	1.95E-10
NH2+	+	N	→	HN2+	9.10E-11
NH2+	+	C2H4	→	C2H4+	4.50E-10
NH2+	+	C2H4	→	C2H3+	3.00E-10
NH2+	+	C2H4	→	CH2NH2+	4.50E-10
NH2+	+	HCN	→	CH2N+	1.20E-09

Ion	+	Neutral	→	Product	Rate [cm^3s^{-1}]
NH2+	+	H2O	→	H3O+	2.73E-09
NH2+	+	H2O	→	NH4+	1.16E-10
NH2+	+	H2O	→	NH3+	8.70E-11
NH2+	+	NH3	→	NH4+	1.61E-09
NH2+	+	NH3	→	NH3+	6.90E-10
CO+	+	CH4	→	CH4+	8.98E-10
CO+	+	CH4	→	HCO+	3.75E-10
CO+	+	H2	→	HCO+	1.40E-09
CO+	+	N	→	NO+	8.20E-11
CO+	+	NH	→	HN+	3.20E-10
CO+	+	NH	→	HCO+	3.20E-10
CO+	+	C2H2	→	C2H2+	4.10E-10
CO+	+	HCN	→	CHN+	3.06E-09
CO+	+	HCN	→	HCO+	3.40E-10
CO+	+	C2H6	→	CH3+	2.78E-11
CO+	+	C2H6	→	C2H5+	5.00E-10
CO+	+	C2H6	→	C2H4+	8.62E-10
CO+	+	H	→	H+	4.00E-10
CO+	+	HC3N	→	C3HN+	3.10E-09
CO+	+	H2O	→	H2O+	1.56E-09
CO+	+	H2O	→	HCO+	8.40E-10
CO+	+	C3H8	→	C2H5+	6.60E-10
CO+	+	C3H8	→	C2H4+	1.80E-10
CO+	+	C3H8	→	C3H6+	3.00E-11
CO+	+	C3H8	→	C3H7+	1.30E-10
CO+	+	NH3	→	NH3+	2.02E-09
CO+	+	NH3	→	HCO+	4.08E-11
CO+	+	CH3CN	→	CH3CN+	2.25E-09
CO+	+	CH3CN	→	CH2CN+	7.50E-10
HCO+	+	N2	→	HN2+	6.60E-10
HCO+	+	CH4	→	CH3+	1.10E-09
HCO+	+	H2	→	HCO+	3.80E-10
HCO+	+	NH	→	NH2+	6.40E-10
HCO+	+	C2H2	→	C2H3+	1.36E-09
HCO+	+	C2H4	→	C2H5+	1.40E-09
HCO+	+	HCN	→	CH2N+	3.50E-09
HCO+	+	C2H6	→	C2H7+	1.20E-10
HCO+	+	HC3N	→	C3H2N+	3.80E-09
HCO+	+	C3H4	→	C3H5+	1.40E-09
HCO+	+	H2O	→	H3O+	2.60E-09
HCO+	+	C4H2	→	C4H3+	1.40E-09

Ion	+	Neutral	→	Product	Rate [cm^3s^{-1}]
HCO+	+	CO	→	HCO+	4.00E-10
HCO+	+	C2N2	→	HC2N2+	1.30E-09
HCO+	+	C3H2	→	cC3H3+	1.40E-09
HCO+	+	C3H2	→	C3H4+	1.40E-09
HCO+	+	NH3	→	NH4+	2.20E-09
HCO+	+	CH2NH	→	CH2NH2+	1.00E-09
HCO+	+	CH3CN	→	CH3CNH+	4.10E-09
HCO+	+	C2H3CN	→	C4H3NH+	4.00E-09
HCO+	+	C6H6	→	C6H7+	1.60E-09
HCO+	+	C6H2	→	C6H3+	1.40E-09
HCO+	+	C7H4	→	HN2+	2.00E-09
HCO+	+	C7H4	→	C7H5+	2.00E-09
HCO+	+	C8H2	→	C8H3+	1.40E-09
HCO+	+	HC5N	→	HC5NH+	8.00E-09
HCO+	+	C6H3N	→	C6H3NH+	4.00E-09
C5H2+	+	CH4	→	C6H5+	8.00E-10
C5H2+	+	N	→	HC5N+	2.00E-10
C5H2+	+	C2H4	→	C7H5+	5.00E-10
C5H2+	+	C2H4	→	C7H4+	5.00E-10
C5H2+	+	C4H2	→	C7H3+	6.00E-10
C5H2+	+	C3H2	→	C8H3+	1.20E-09
C5H2+	+	O	→	HCO+	2.00E-10
C2H7+	+	HCN	→	CH2N+	1.98E-09
C2H7+	+	HCN	→	CH3CNH+	2.20E-10
C2H7+	+	NH3	→	NH4+	2.00E-09
C4H+	+	CH4	→	C5H3+	1.10E-09
C4H+	+	H2	→	C3H+	2.20E-11
C4H+	+	H2	→	C4H2+	1.65E-10
C4H+	+	C2H4	→	C4H3+	7.50E-10
C4H+	+	HCN	→	C4H2+	9.45E-11
C4H+	+	HCN	→	HC5N+	1.23E-09
C4H+	+	C3H4	→	C7H4+	1.20E-09
C4H+	+	H2O	→	C3H2N+	7.50E-10
C4H+	+	H2O	→	HCO+	7.50E-10
C4H+	+	C4H2	→	C9H2+	1.50E-09
C4H+	+	C3H2	→	C7H2+	2.00E-09
C4H+	+	O	→	HCO+	2.00E-10
C4H4+	+	C2H2	→	C6H5+	8.80E-11
C8H5+	+	C3H4	→	C5H7+	7.00E-10

Solar Driven Primary Ion Production

In this section figures that were omitted from the text pertaining to the ion production rate comparisons for the dayside of Titan using only solar inputs. The nested magnetic field line topology has been adopted for all of the models.

C-3 Ion Production Comparisons for the Inbound Leg of the T40 Flyby

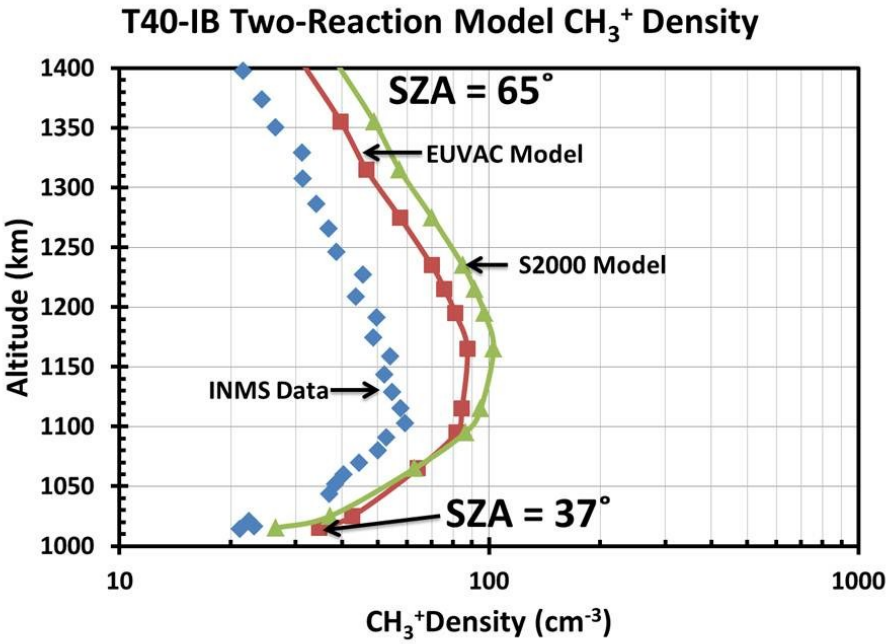

Appendix Figure C.1 Density of CH_3^+ derived from model production rates using a simple two reaction chemical model compared to INMS data from the T40-Inbound flyby of Titan. INMS data is indicated with the blue diamonds, results for the Solar 2000 and EUVAC models of the solar flux are shown with green triangles and red squares respectively. The orange crosses indicate the CH_3^+ density derived from model production rates and the more complex ion chemistry given in Equation (4.5). The solar zenith angle at closest approach and at the uppermost altitude is indicated at the bottom and top of the figure. The solar zenith angle is adjusted to reflect the conditions observed by the Cassini spacecraft.

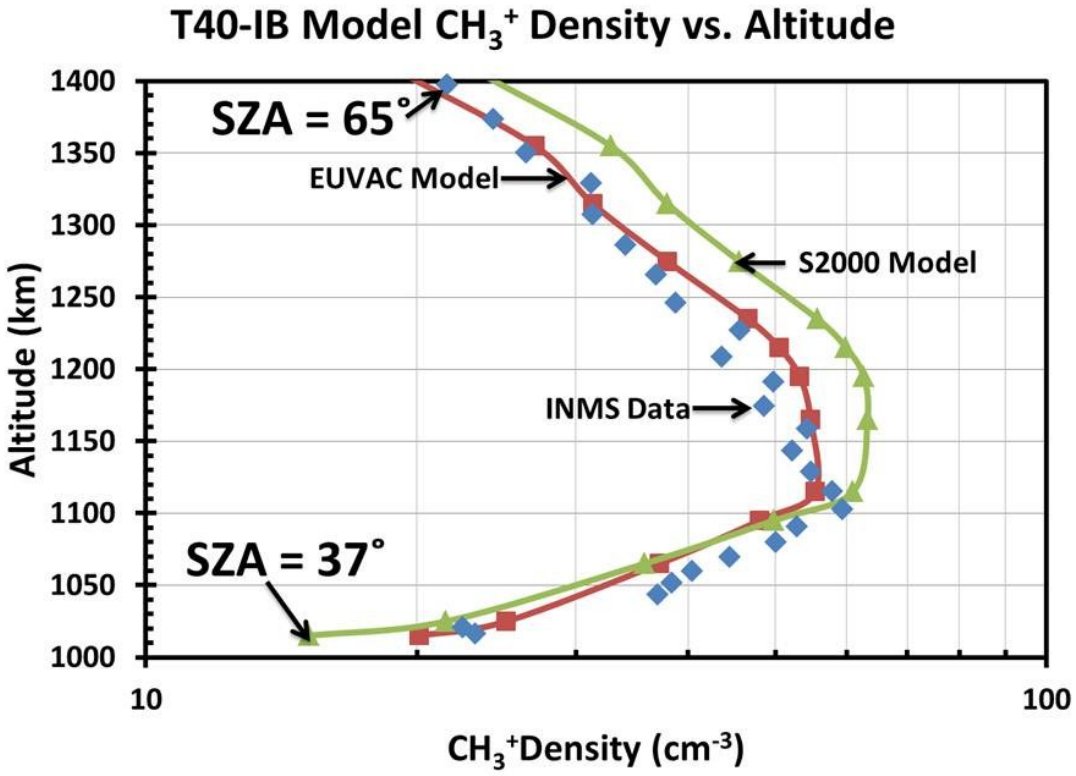

Appendix Figure C.2 CH_3^+ density produced by the full photochemical model compared to INMS data from the T40-Inbound flyby of Titan. INMS data is indicated with the blue diamonds, results for the Solar 2000 and EUVAC models of the solar flux are shown with green triangles and red squares respectively. The solar zenith angle at closest approach and at the uppermost altitude is indicated at the bottom and top of the figure. The solar zenith angle is adjusted to reflect the conditions observed by the Cassini spacecraft

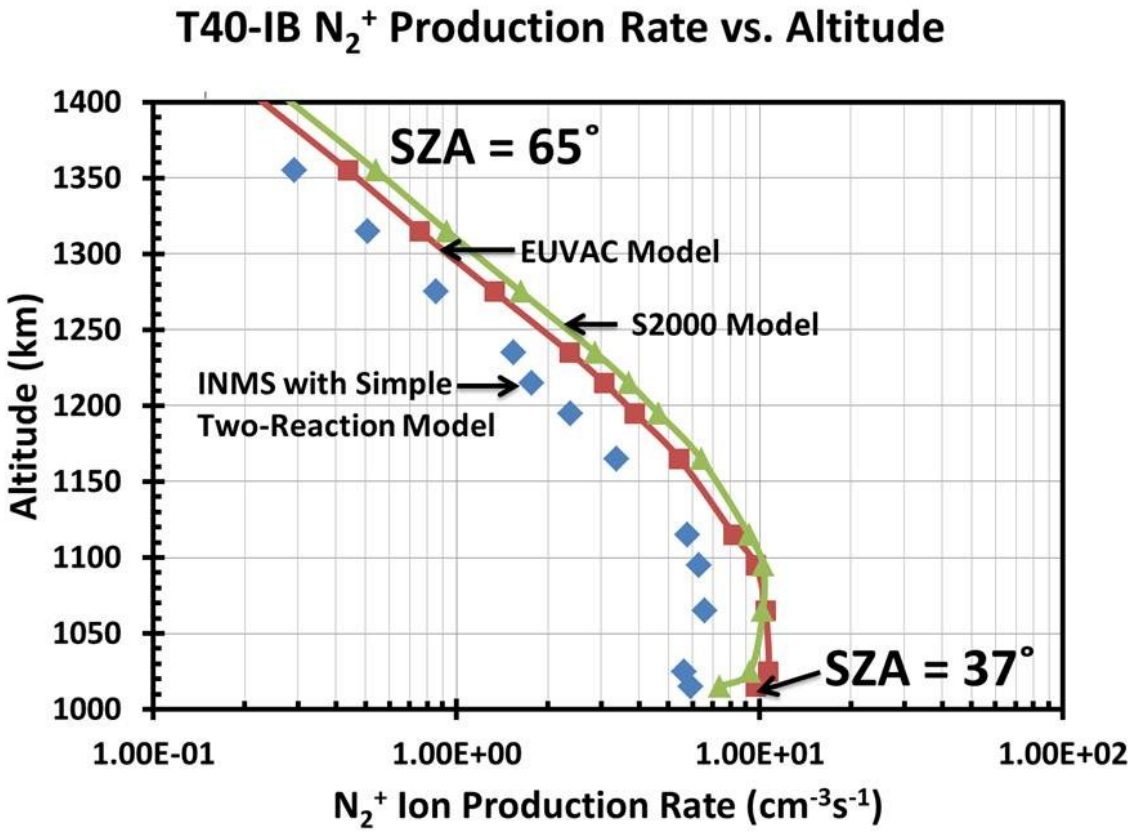

Appendix Figure C.3 Modeled photoionization production rates of N_2^+ compared to the empirical production rate of N_2^+ derived from INMS data from the T40-Inbound flyby of Titan using the simple two reaction chemical model. INMS data is indicated with the blue diamonds, results for the Solar 2000 and EUVAC models of the solar flux are shown with green triangles and red squares respectively. All N_2^+ production is assumed to produce CH_3^+. The solar zenith angle at closest approach and at the uppermost altitude is indicated at the bottom and top of the figure. The solar zenith angle is adjusted to reflect the conditions observed by the Cassini spacecraft

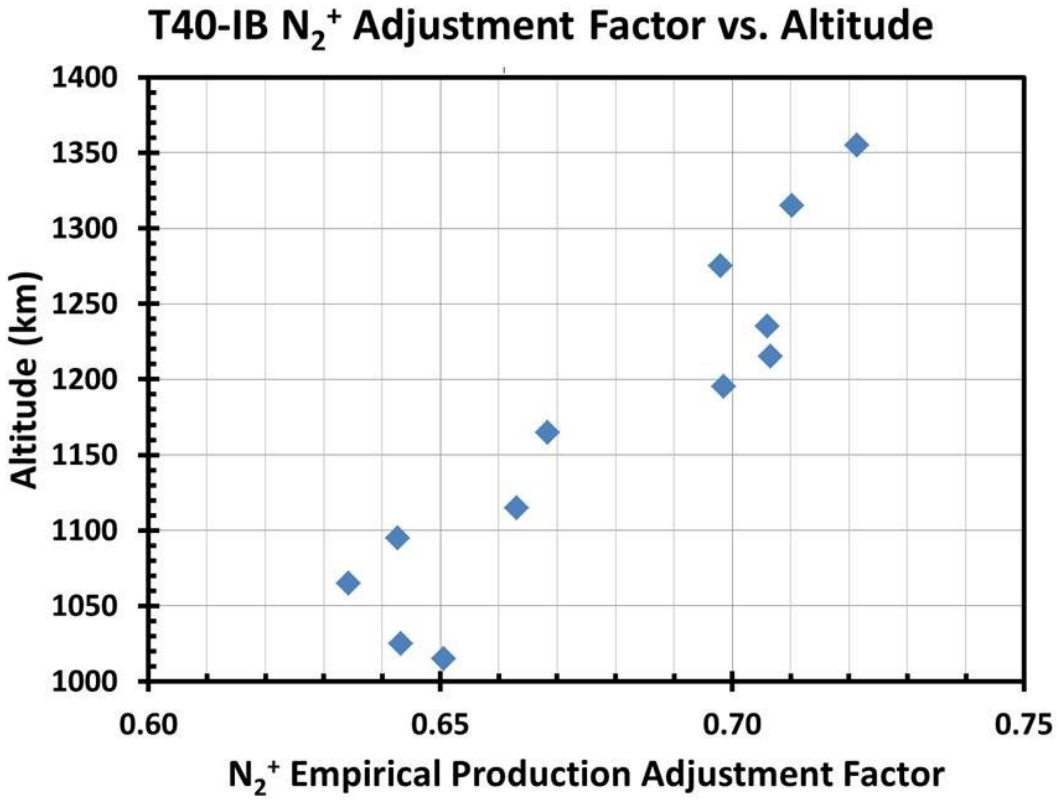

Appendix Figure C.4 Factor used to adjust the empirical INMS N_2^+ production rate for the T40-Inbound flyby of Titan. This correction factor is the ratio of N_2^+ production rate from photoionization to the N_2^+ production rate from the full photochemical model (production from photoionization and chemical pathways).

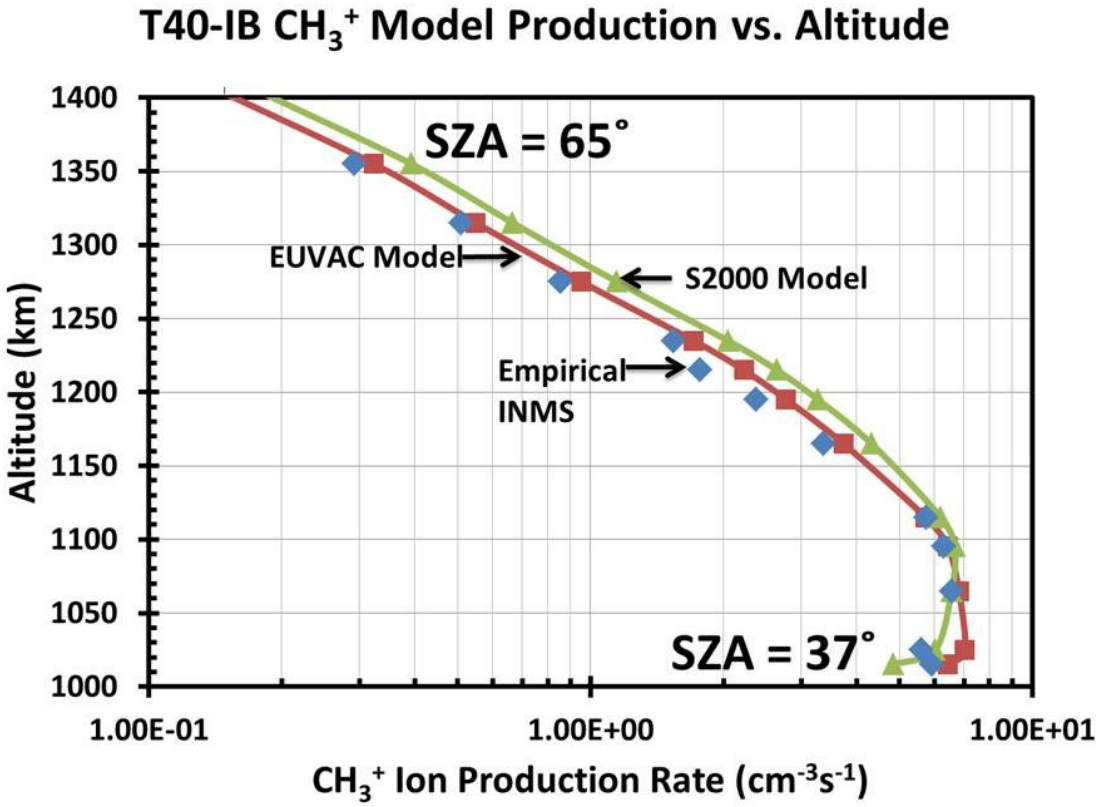

Appendix Figure C.5 A comparison of the modeled production rates of CH_3^+ to the empirical production rate of CH_3^+ derived from INMS data from the T40-Inbound flyby of Titan. INMS data is indicated with the blue diamonds, results for the Solar 2000 and EUVAC models of the solar flux are shown with green triangles and red squares respectively. The solar zenith angle at closest approach and at the uppermost altitude is indicated at the bottom and top of the figure. The solar zenith angle is adjusted to reflect the conditions observed by the Cassini spacecraft.

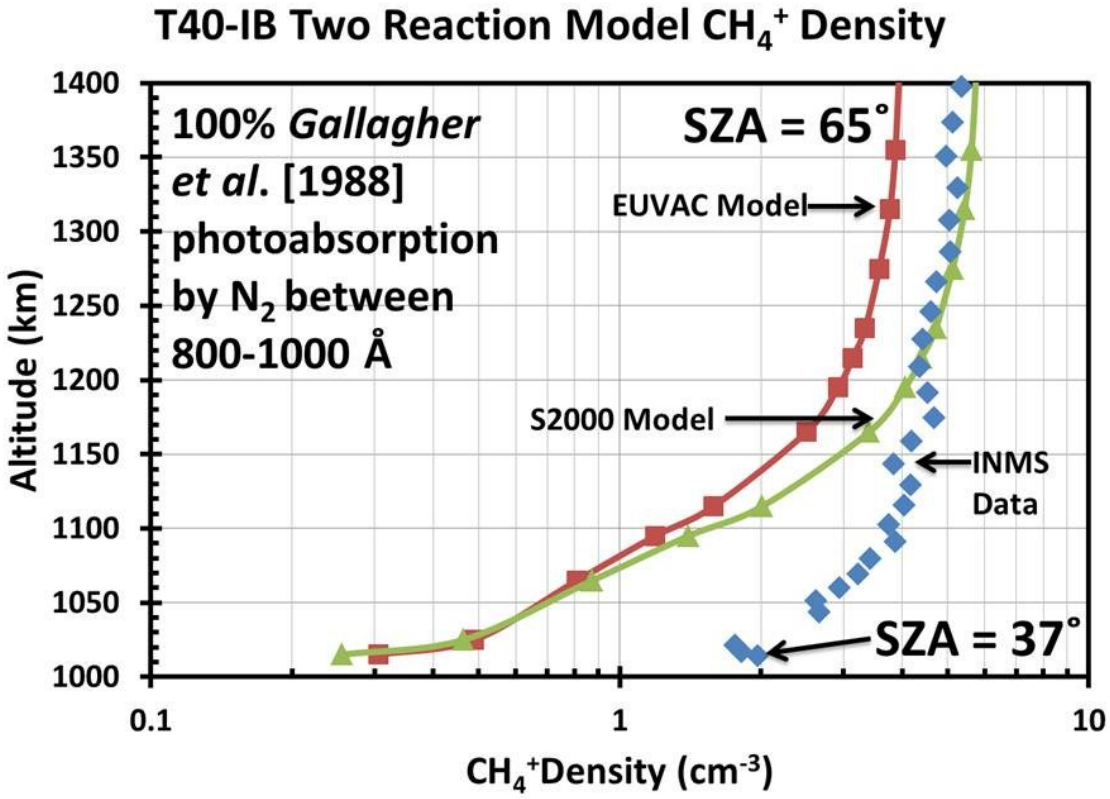

Appendix Figure C.6 Density of CH_4^+ calculated using the simple two reaction chemical model (Equation (4.10)) and the photoionization model compared to INMS data from the T40-Inbound flyby of Titan. N_2 photoabsorption cross sections for photons with wavelengths between 800 and 1000 Å of *Gallagher et al.* [1988] were used. INMS data is indicated with the blue diamonds, results for the Solar 2000 and EUVAC models of the solar flux are shown with green triangles and red squares respectively. The solar zenith angle at closest approach and at the uppermost altitude is indicated at the bottom and top of the figure. The solar zenith angle is adjusted to reflect the conditions observed by the Cassini spacecraft.

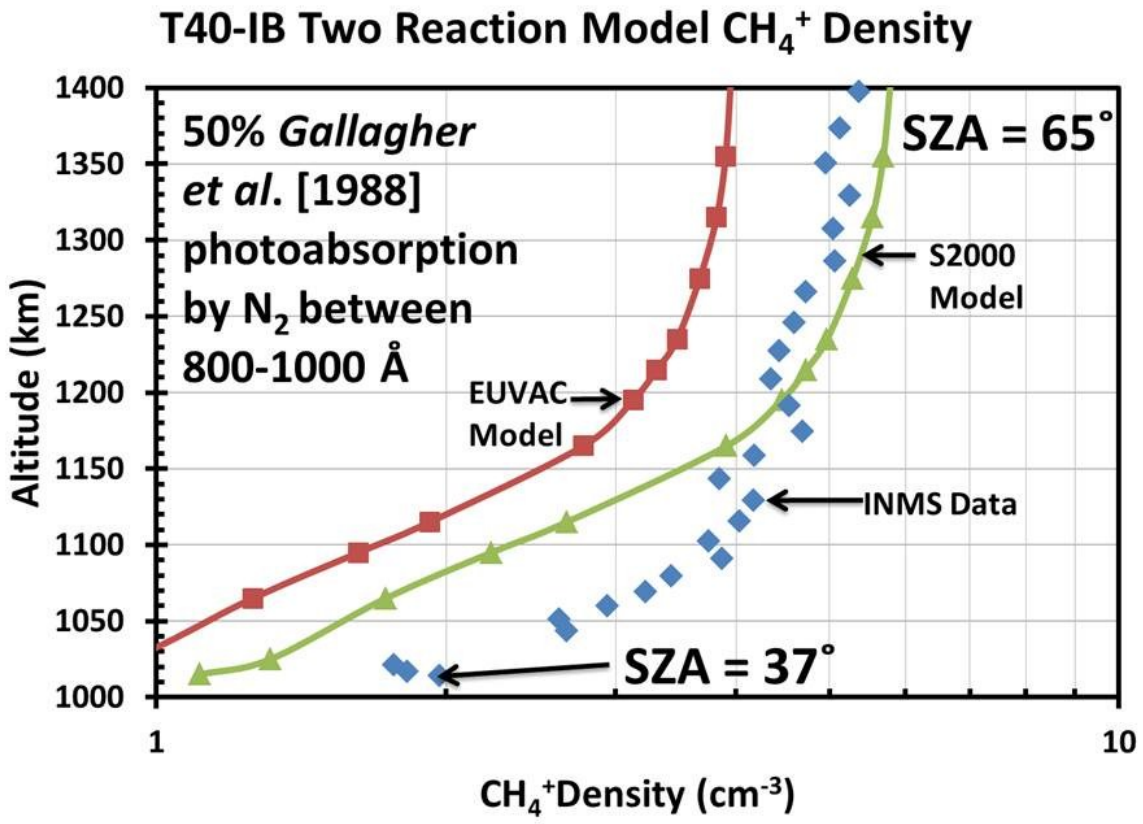

Appendix Figure C.7 Density of CH_4^+ calculated using the simple two reaction chemical model (Equation (4.10)) and the photoionization model compared to INMS data from the T40-Inbound flyby of Titan. 50% of solar photons with wavelengths between 800 and 1000 Å interact with N_2 using photoabsorption cross sections of *Gallagher et al.* [1988]. INMS data is indicated with the blue diamonds, results for the Solar 2000 and EUVAC models of the solar flux are shown with green triangles and red squares respectively. The solar zenith angle at closest approach and at the uppermost altitude is indicated at the bottom and top of the figure. The solar zenith angle is adjusted to reflect the conditions observed by the Cassini spacecraft.

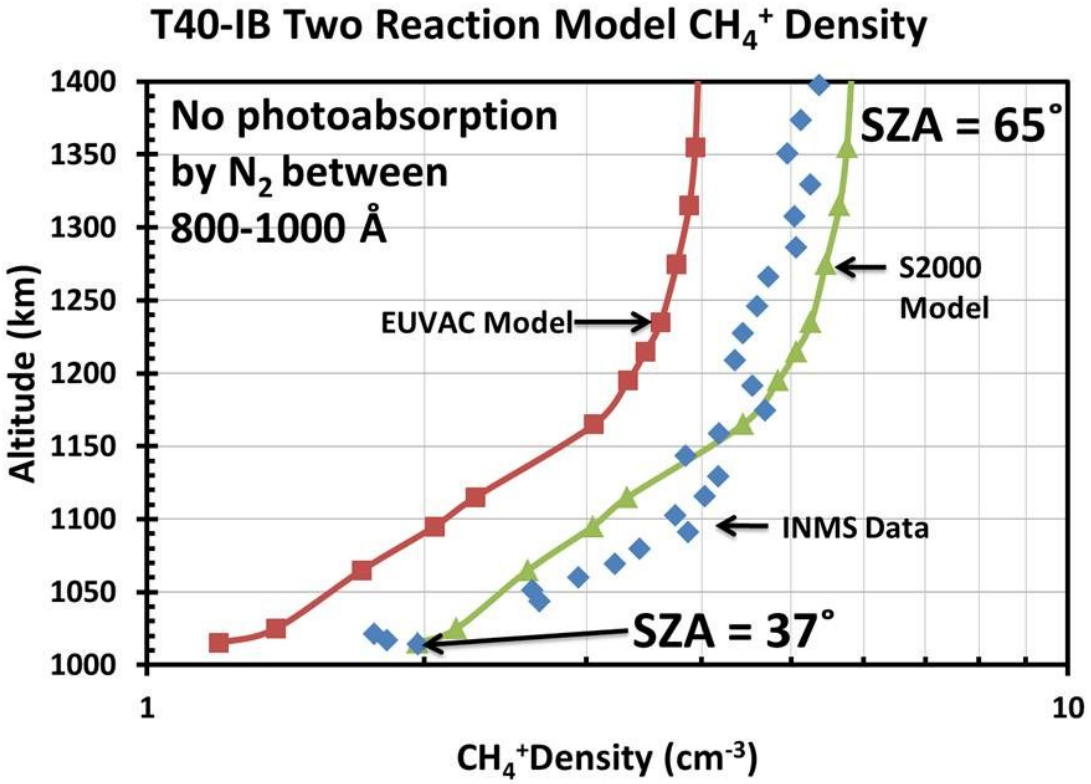

Appendix Figure C.8 Density of CH_4^+ calculated using the simple two reaction chemical model (Equation (4.10)) and the photoionization model compared to INMS data from the T40-Inbound flyby of Titan. Solar photons with wavelengths between 800 and 1000 Å did not interact with N_2. INMS data is indicated with the blue diamonds, results for the Solar 2000 and EUVAC models of the solar flux are shown with green triangles and red squares respectively. The solar zenith angle at closest approach and at the uppermost altitude is indicated at the bottom and top of the figure. The solar zenith angle is adjusted to reflect the conditions observed by the Cassini spacecraft.

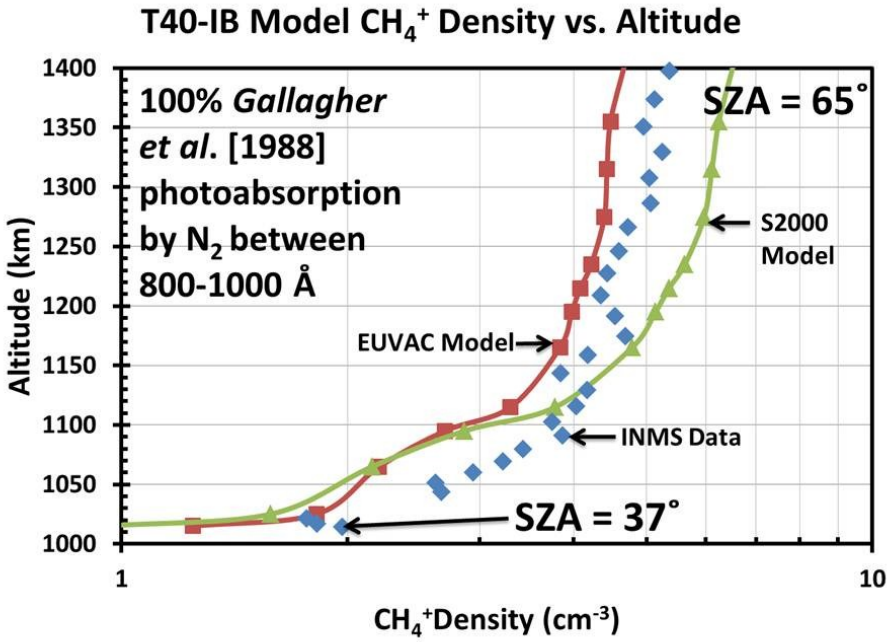

Appendix Figure C.9 CH_4^+ density produced with the full photochemical model compared to INMS data from the T40-Inbound flyby of Titan. N_2 photoabsorption cross sections for photons with wavelengths between 800 and 1000 Å of Gallagher et al. [1988] were used. INMS data is indicated with the blue diamonds, results for the Solar 2000 and EUVAC models of the solar flux are shown with green triangles and red squares respectively. The solar zenith angle at closest approach and at the uppermost altitude is indicated at the bottom and top of the figure. The solar zenith angle is adjusted to reflect the conditions observed by the Cassini spacecraft.

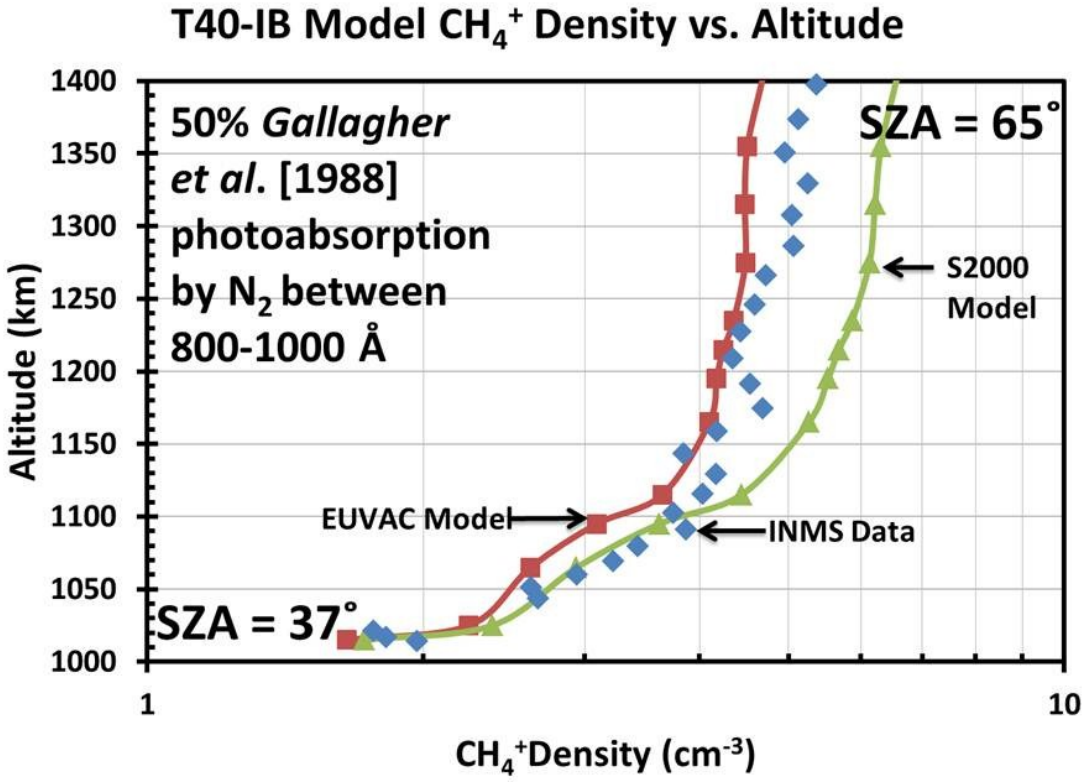

Appendix Figure C.10 CH_4^+ density produced by the full photochemical model compared to INMS data from the T40-Inbound flyby of Titan. 50% of solar photons with wavelengths between 800 and 1000 Å interact with N_2 photoabsorption using cross sections of *Gallagher et al.* [1988]. INMS data is indicated with the blue diamonds, results for the Solar 2000 and EUVAC models of the solar flux are shown with green triangles and red squares respectively. The solar zenith angle at closest approach and at the uppermost altitude is indicated at the bottom and top of the figure. The solar zenith angle is adjusted to reflect the conditions observed by the Cassini spacecraft.

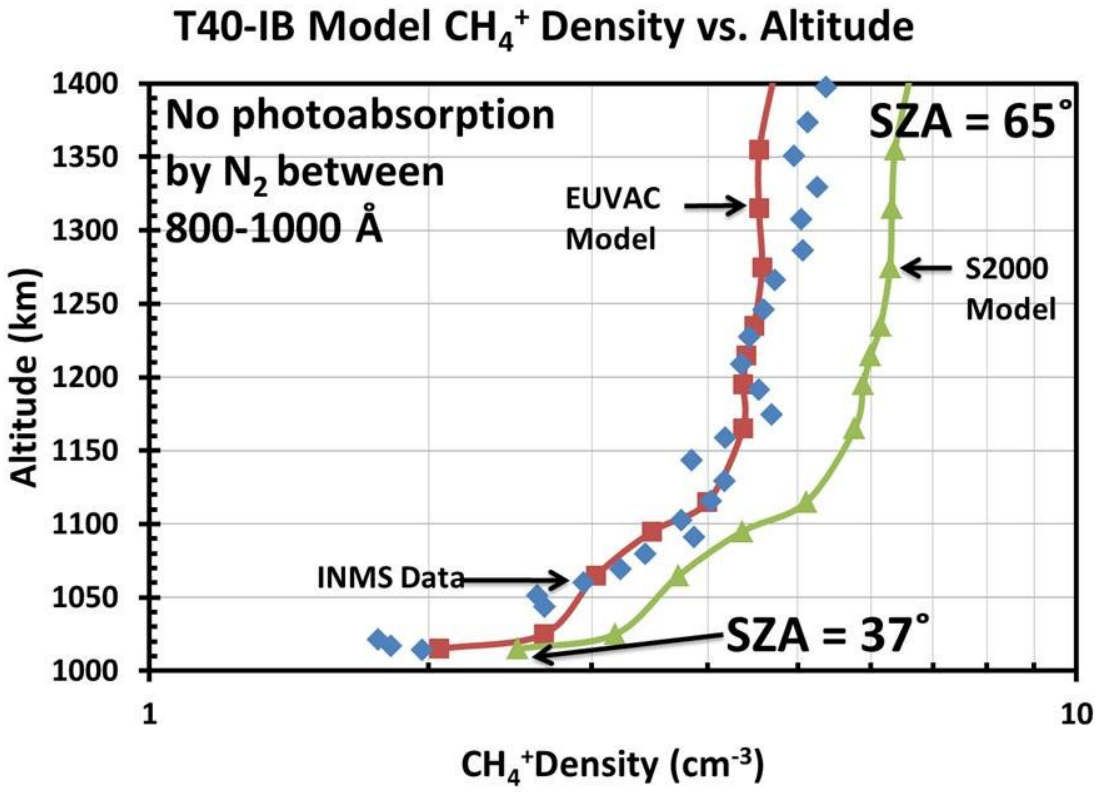

Appendix Figure C.11 CH_4^+ density produced by the full photochemical model compared to INMS data from the T40-Inbound flyby of Titan. Solar photons with wavelengths between 800 and 1000 Å did not interact with N_2. INMS data is indicated with the blue diamonds, results for the Solar 2000 and EUVAC models of the solar flux are shown with green triangles and red squares respectively. The solar zenith angle at closest approach and at the uppermost altitude is indicated at the bottom and top of the figure. The solar zenith angle is adjusted to reflect the conditions observed by the Cassini spacecraft.

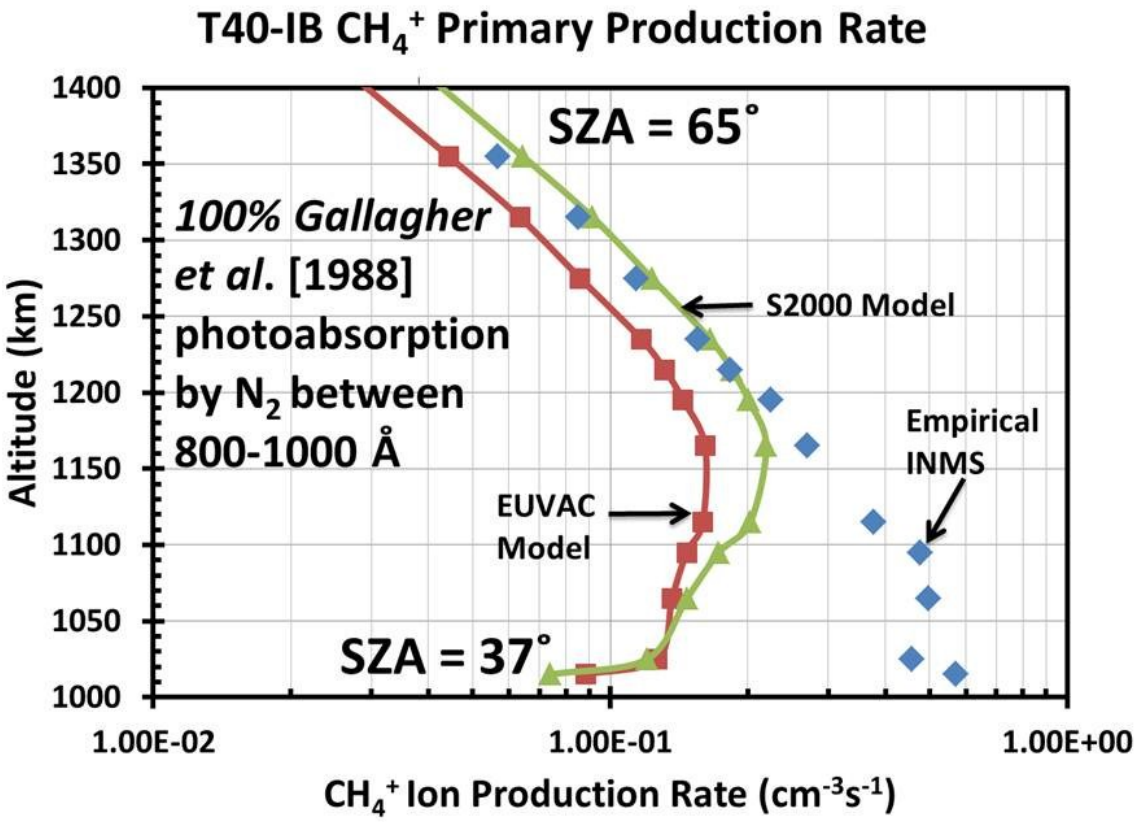

Appendix Figure C.12 Modeled photoionization production rates of CH_4^+ from photoionization and electron impact ionization by photoelectrons compared to the empirical production rate of CH_4^+ derived from INMS data from the T40-Inbound flyby of Titan. 100% of solar photons with wavelengths between 800 and 1000 Å interact with N_2 using photoabsorption cross sections of *Gallagher et al.* [1988]. INMS data is indicated with the blue diamonds, results for the Solar 2000 and EUVAC models of the solar flux are shown with green triangles and red squares respectively. The solar zenith angle at closest approach and at the uppermost altitude is indicated at the bottom and top of the figure. The solar zenith angle is adjusted to reflect the conditions observed by the Cassini spacecraft.

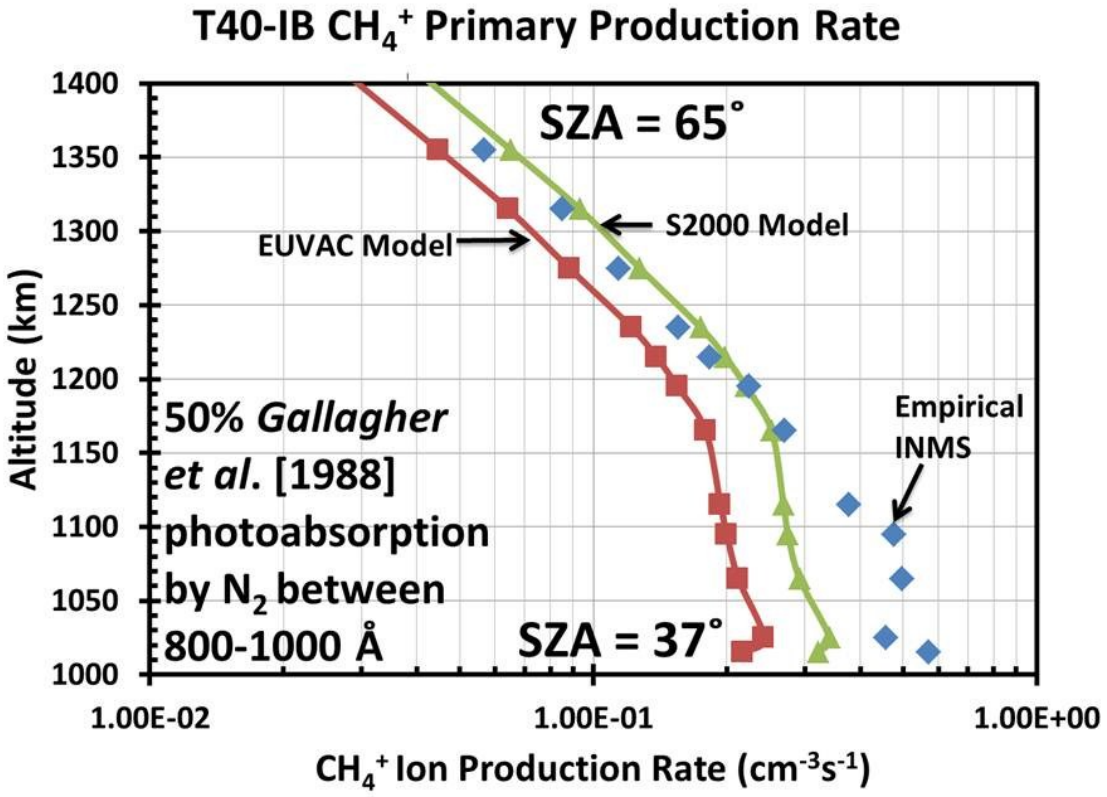

Appendix Figure C.13 Modeled photoionization production rates of CH_4^+ from photoionization and electron impact ionization by photoelectrons compared to the empirical production rate of CH_4^+ derived from INMS data from the T40-Inbound flyby of Titan. 50% of solar photons with wavelengths between 800 and 1000 Å interact with N_2 using photoabsorption cross sections of *Gallagher et al.* [1988]. INMS data is indicated with the blue diamonds, results for the Solar 2000 and EUVAC models of the solar flux are shown with green triangles and red squares respectively. The solar zenith angle at closest approach and at the uppermost altitude is indicated at the bottom and top of the figure. The solar zenith angle is adjusted to reflect the conditions observed by the Cassini spacecraft.

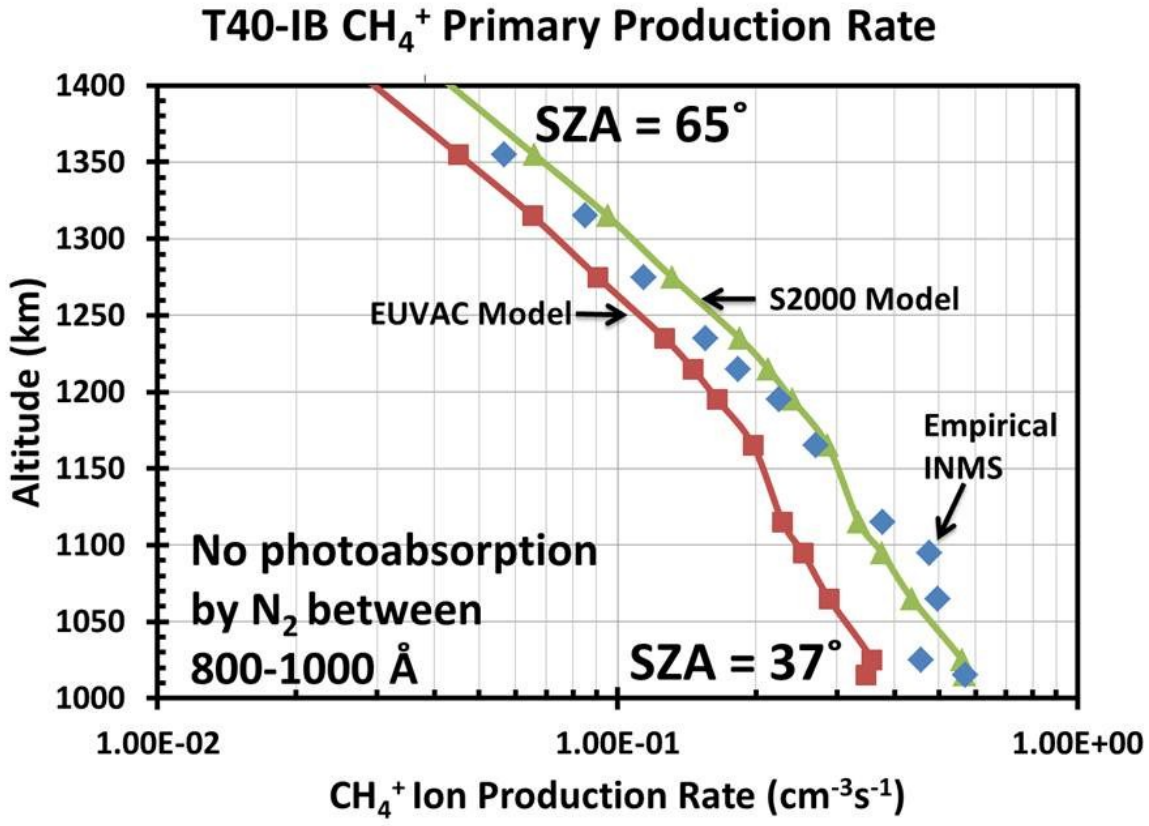

Appendix Figure C.14 Modeled photoionization production rates of CH_4^+ from photoionization and electron impact ionization by photoelectrons compared to the empirical production rate of CH_4^+ derived from INMS data from the T40-Inbound flyby of Titan. Solar photons with wavelengths between 800 and 1000 Å did not interact with N_2. INMS data is indicated with the blue diamonds, results for the Solar 2000 and EUVAC models of the solar flux are shown with green triangles and red squares respectively. The solar zenith angle at closest approach and at the uppermost altitude is indicated at the bottom and top of the figure. The solar zenith angle is adjusted to reflect the conditions observed by the Cassini spacecraft.

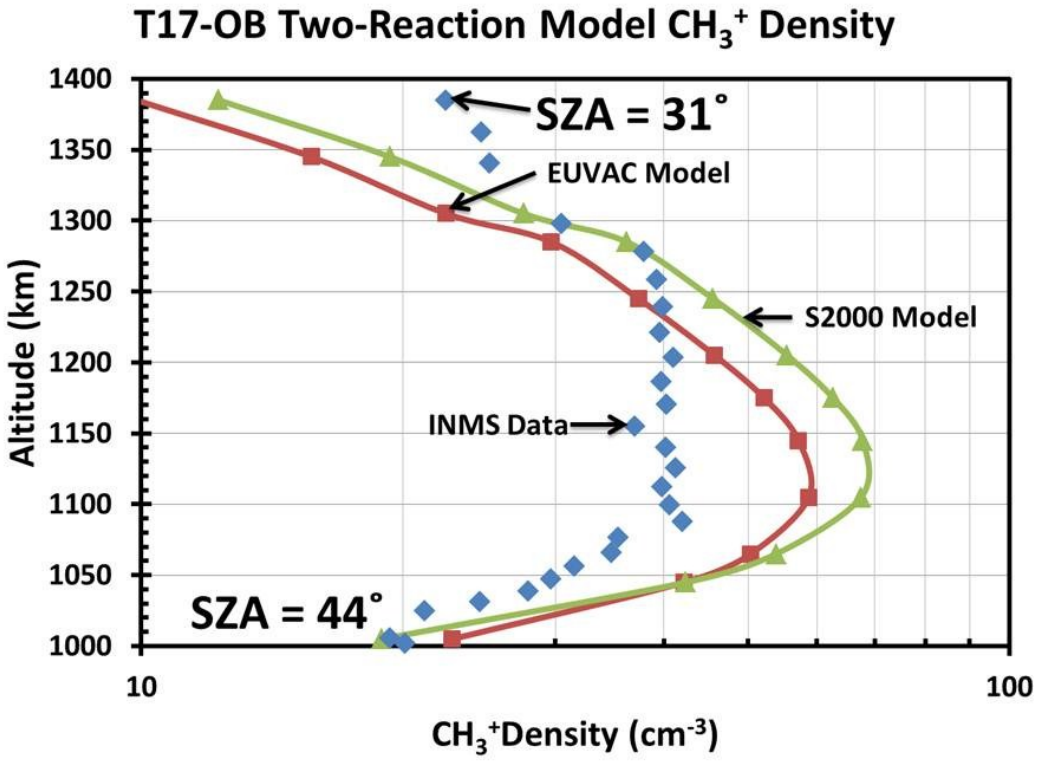

Appendix Figure C.15 Density of CH_3^+ derived from model production rates using a simple two reaction chemical model compared to INMS data from the T17-Outbound flyby of Titan. INMS data is indicated with the blue diamonds, results for the Solar 2000 and EUVAC models of the solar flux are shown with green triangles and red squares respectively. The orange crosses indicate the CH_3^+ density derived from model production rates and the more complex ion chemistry given in Equation (4.5). The solar zenith angle at closest approach and at the uppermost altitude is indicated at the bottom and top of the figure. The solar zenith angle is adjusted to reflect the conditions observed by the Cassini spacecraft.

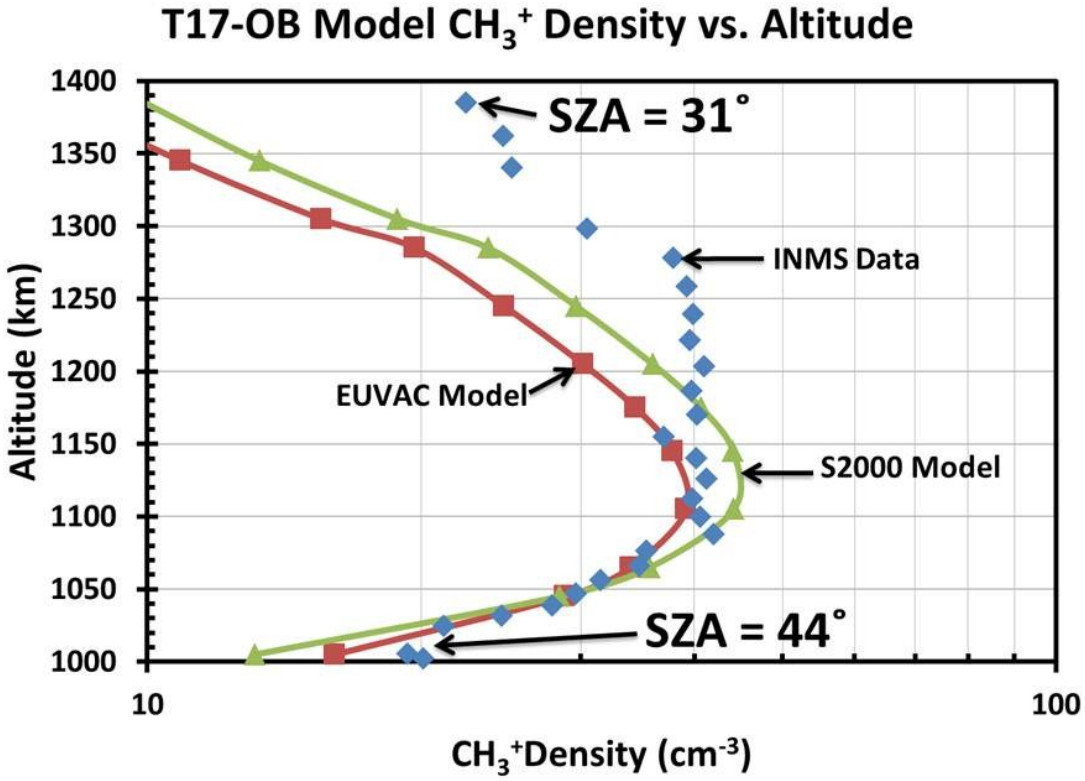

Appendix Figure C.16 CH_3^+ density produced by the full photochemical model compared to INMS data from the T17-Outbound flyby of Titan. INMS data is indicated with the blue diamonds, results for the Solar 2000 and EUVAC models of the solar flux are shown with green triangles and red squares respectively. The solar zenith angle at closest approach and at the uppermost altitude is indicated at the bottom and top of the figure. The solar zenith angle is adjusted to reflect the conditions observed by the Cassini spacecraft.

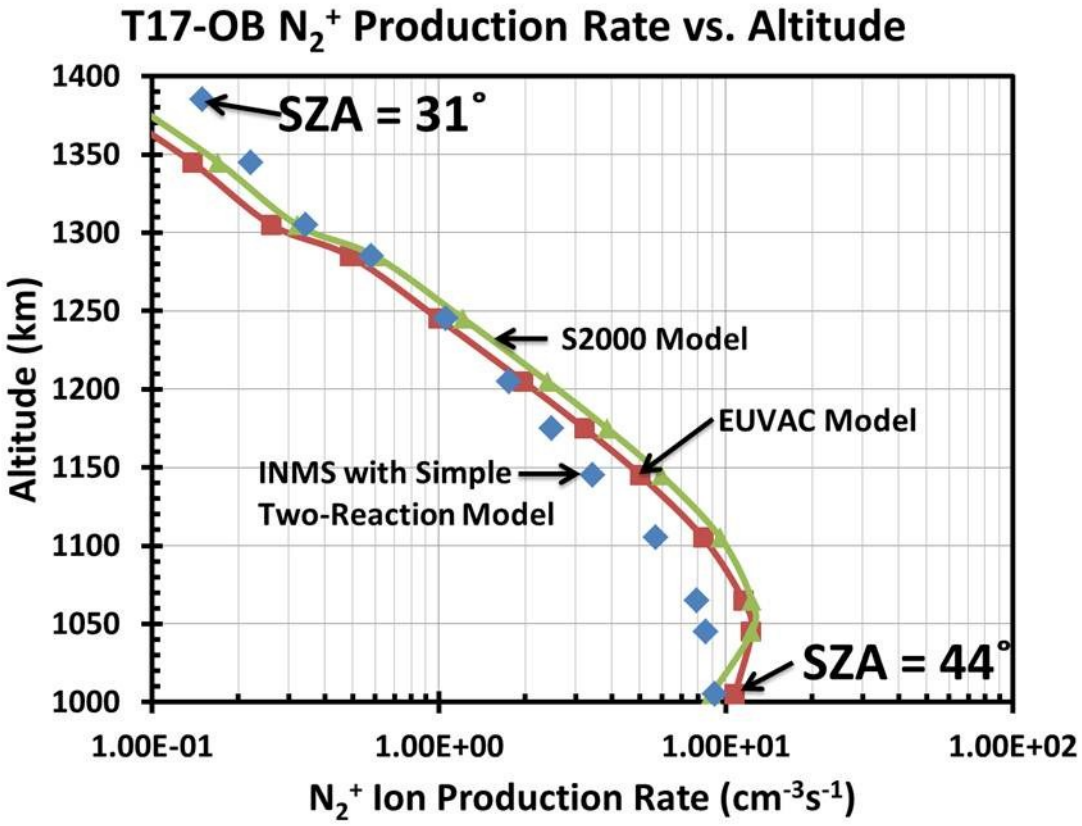

Appendix Figure C.17 Modeled photoionization production rates of N_2^+ compared to the empirical production rate of N_2^+ derived from INMS data from the T17-Outbound flyby of Titan using the simple two reaction chemical model. INMS data is indicated with the blue diamonds, results for the Solar 2000 and EUVAC models of the solar flux are shown with green triangles and red squares respectively. All N_2^+ production is assumed to produce CH_3^+. The solar zenith angle at closest approach and at the uppermost altitude is indicated at the bottom and top of the figure. The solar zenith angle is adjusted to reflect the conditions observed by the Cassini spacecraft.

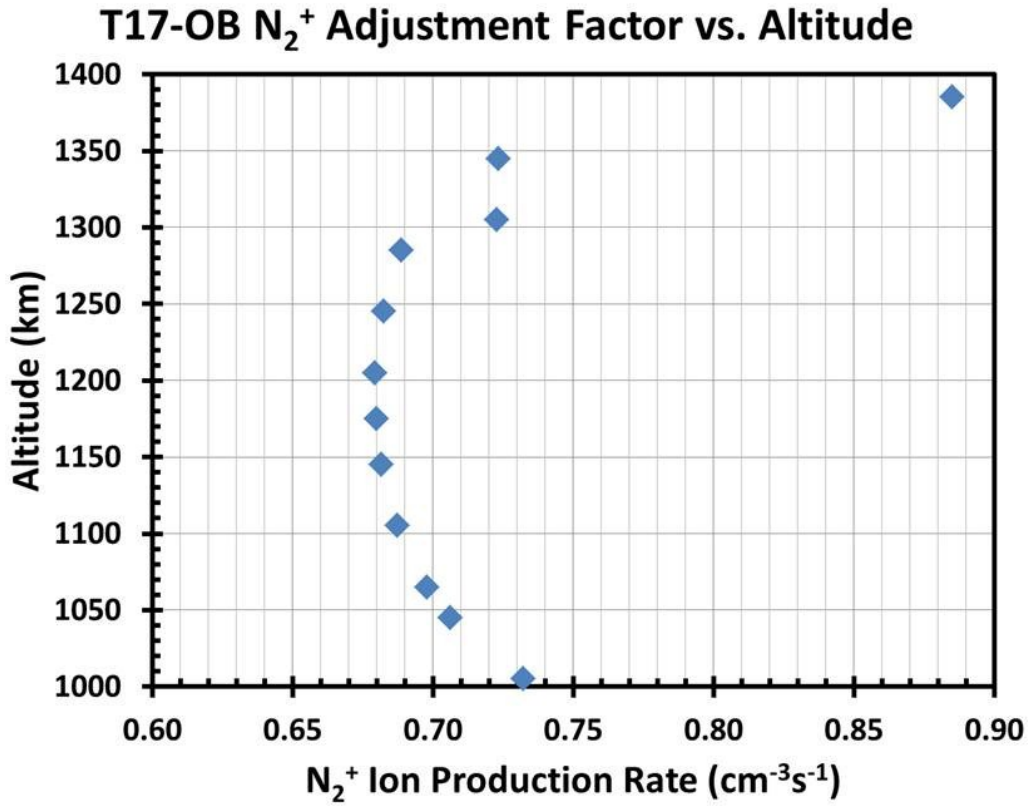

Appendix Figure C.18 Factor used to adjust the empirical INMS N_2^+ production rate for the T17-Outbound flyby of Titan. This correction factor is the ratio of N_2^+ production rate from photoionization to the N_2^+ production rate from the full photochemical model (production from photoionization and chemical pathways).

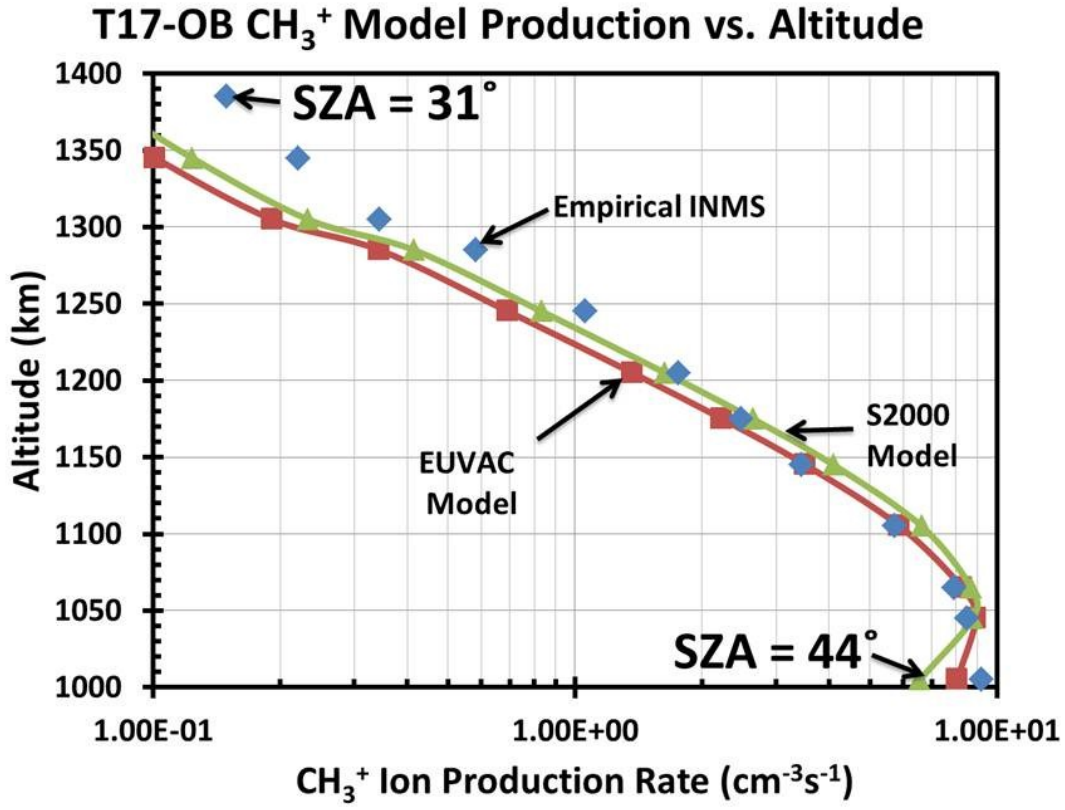

Appendix Figure C.19 A comparison of the modeled production rates of CH_3^+ to the empirical production rate of CH_3^+ derived from INMS data from the T17-Outbound flyby of Titan. INMS data is indicated with the blue diamonds, results for the Solar 2000 and EUVAC models of the solar flux are shown with green triangles and red squares respectively. The solar zenith angle at closest approach and at the uppermost altitude is indicated at the bottom and top of the figure. The solar zenith angle is adjusted to reflect the conditions observed by the Cassini spacecraft.

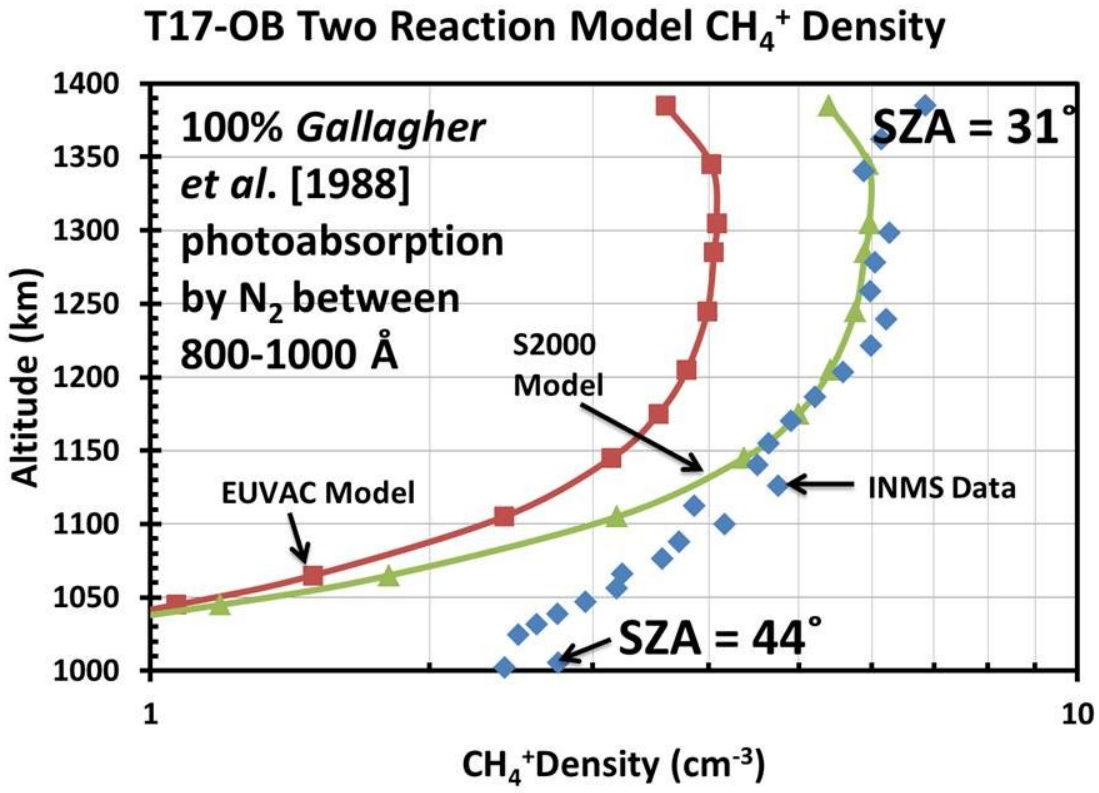

Appendix Figure C.20 Density of CH_4^+ calculated using the simple two reaction chemical model (Equation (4.10)) and the photoionization model compared to INMS data from the T17-Outbound flyby of Titan. N_2 photoabsorption cross sections for photons with wavelengths between 800 and 1000 Å of *Gallagher et al.* [1988] were used. INMS data is indicated with the blue diamonds, results for the Solar 2000 and EUVAC models of the solar flux are shown with green triangles and red squares respectively. The solar zenith angle at closest approach and at the uppermost altitude is indicated at the bottom and top of the figure. The solar zenith angle is adjusted to reflect the conditions observed by the Cassini spacecraft.

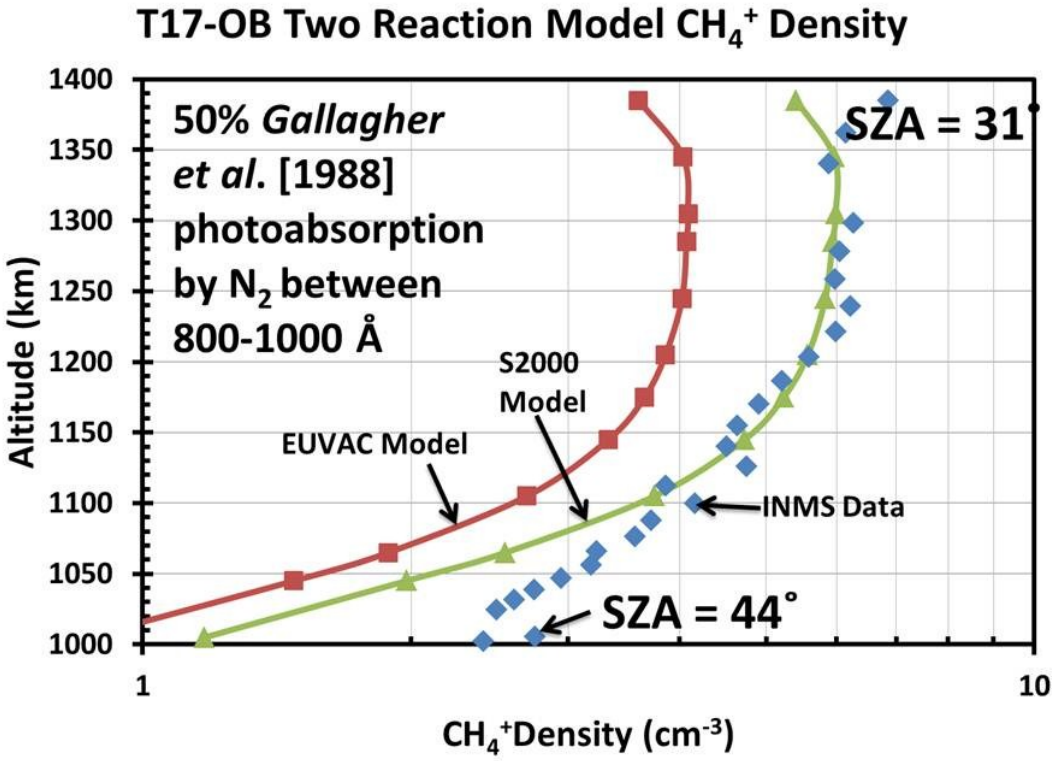

Appendix Figure C.21 Density of CH_4^+ calculated using the simple two reaction chemical model (Equation (4.10)) and the photoionization model compared to INMS data from the T17-Outbound flyby of Titan. 50% of solar photons with wavelengths between 800 and 1000 Å interact with N_2 using photoabsorption cross sections of *Gallagher et al.* [1988]. INMS data is indicated with the blue diamonds, results for the Solar 2000 and EUVAC models of the solar flux are shown with green triangles and red squares respectively. The solar zenith angle at closest approach and at the uppermost altitude is indicated at the bottom and top of the figure. The solar zenith angle is adjusted to reflect the conditions observed by the Cassini spacecraft.

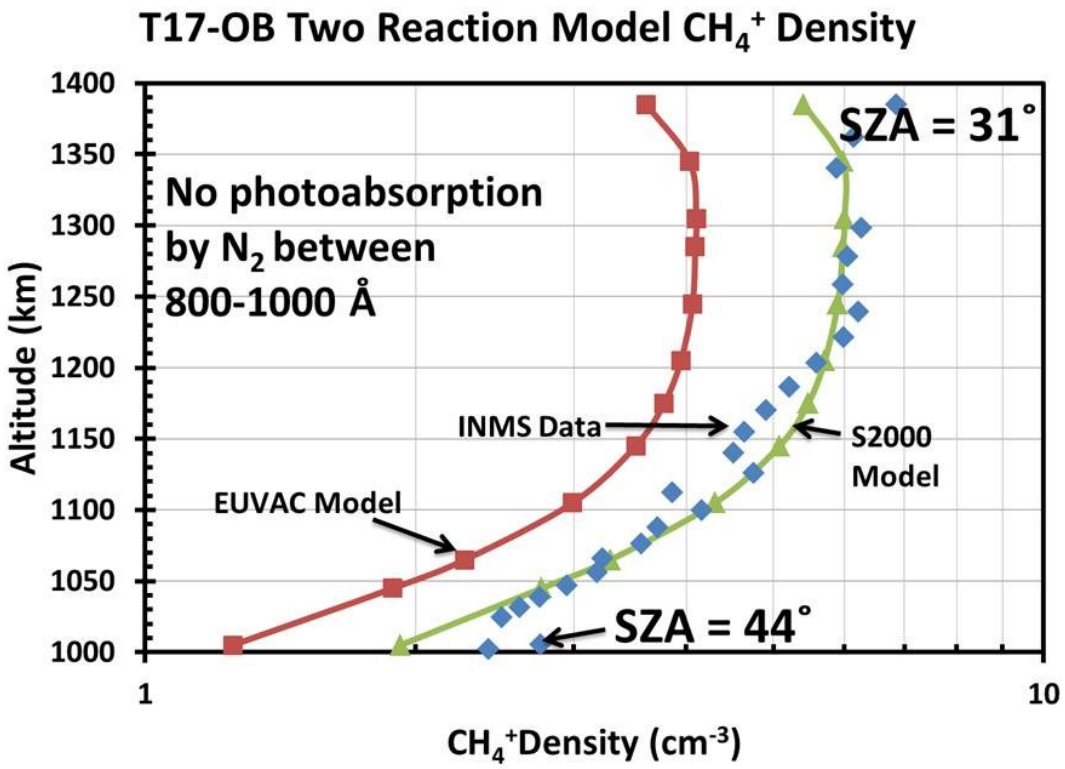

Appendix Figure C.22 Density of CH_4^+ calculated using the simple two reaction chemical model (Equation (4.10)) and the photoionization model compared to INMS data from the T17-Outbound flyby of Titan. Solar photons with wavelengths between 800 and 1000 Å did not interact with N_2. INMS data is indicated with the blue diamonds, results for the Solar 2000 and EUVAC models of the solar flux are shown with green triangles and red squares respectively. The solar zenith angle at closest approach and at the uppermost altitude is indicated at the bottom and top of the figure. The solar zenith angle is adjusted to reflect the conditions observed by the Cassini spacecraft.

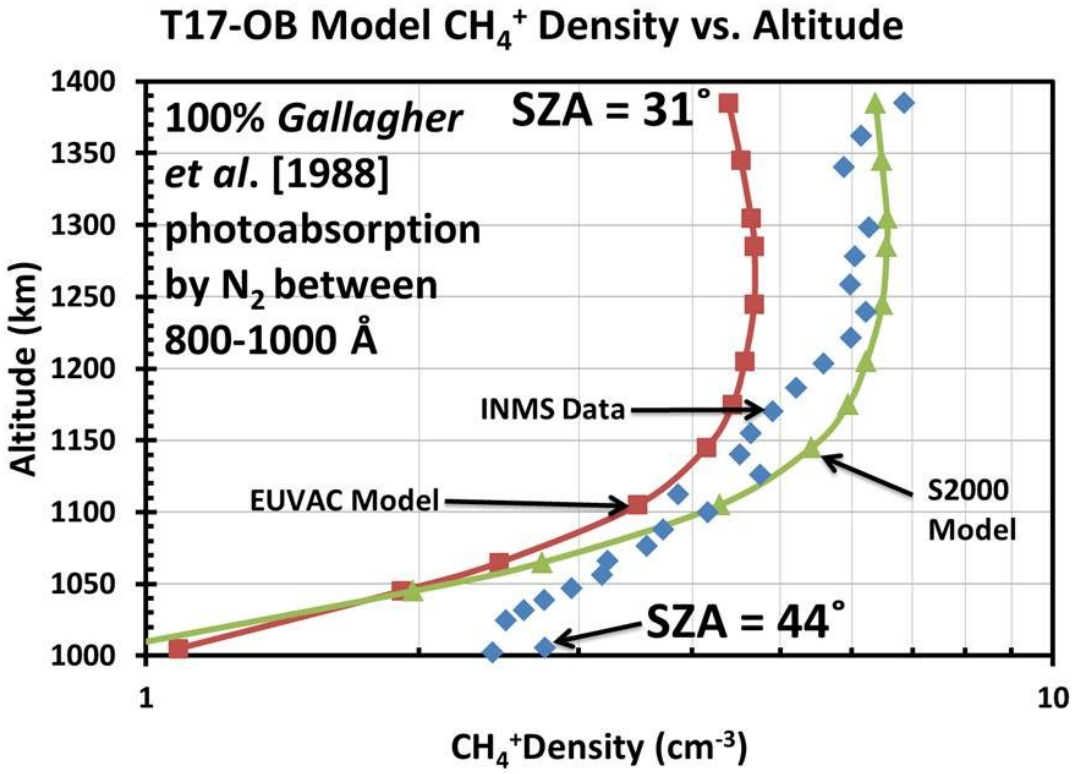

Appendix Figure C.23 CH_4^+ density produced with the full photochemical model compared to INMS data from the T17-Outbound flyby of Titan. N_2 photoabsorption cross sections for photons with wavelengths between 800 and 1000 Å of Gallagher et al. [1988] were used. INMS data is indicated with the blue diamonds, results for the Solar 2000 and EUVAC models of the solar flux are shown with green triangles and red squares respectively. The solar zenith angle at closest approach and at the uppermost altitude is indicated at the bottom and top of the figure. The solar zenith angle is adjusted to reflect the conditions observed by the Cassini spacecraft.

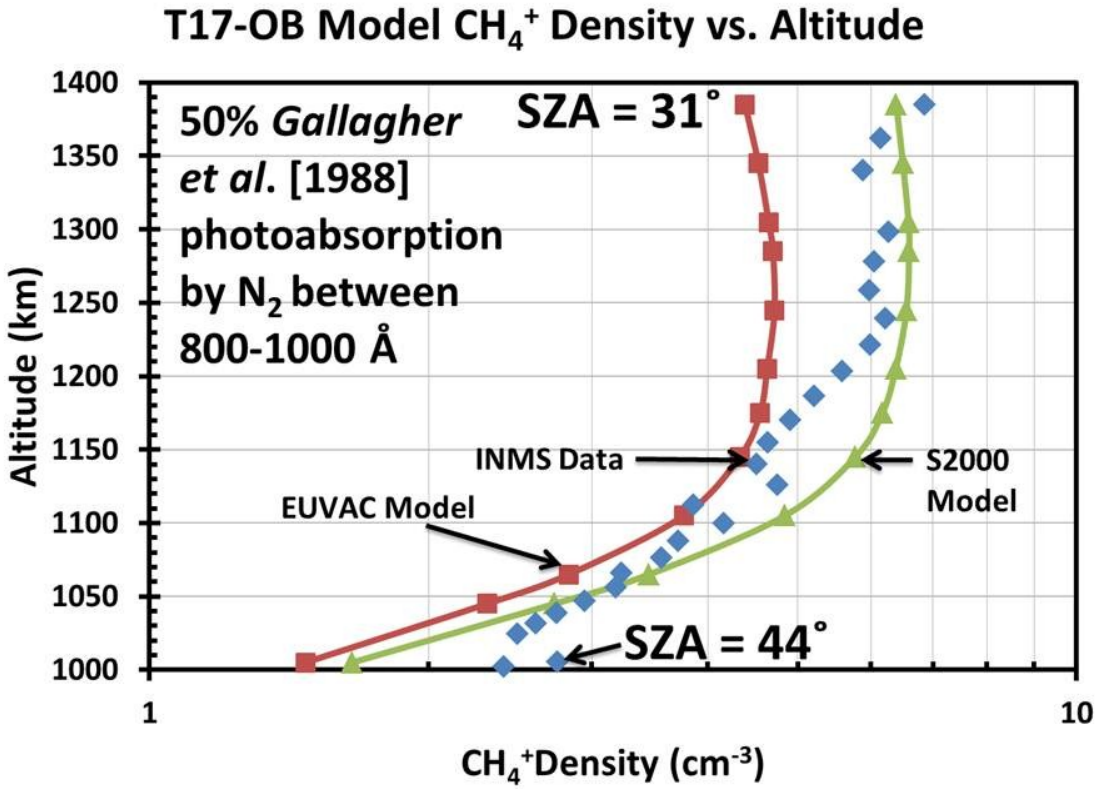

Appendix Figure C.24 CH_4^+ density produced by the full photochemical model compared to INMS data from the T17-Outbound flyby of Titan. 50% of solar photons with wavelengths between 800 and 1000 Å interact with N_2 photoabsorption using cross sections of *Gallagher et al.* [1988]. INMS data is indicated with the blue diamonds, results for the Solar 2000 and EUVAC models of the solar flux are shown with green triangles and red squares respectively. The solar zenith angle at closest approach and at the uppermost altitude is indicated at the bottom and top of the figure. The solar zenith angle is adjusted to reflect the conditions observed by the Cassini spacecraft.

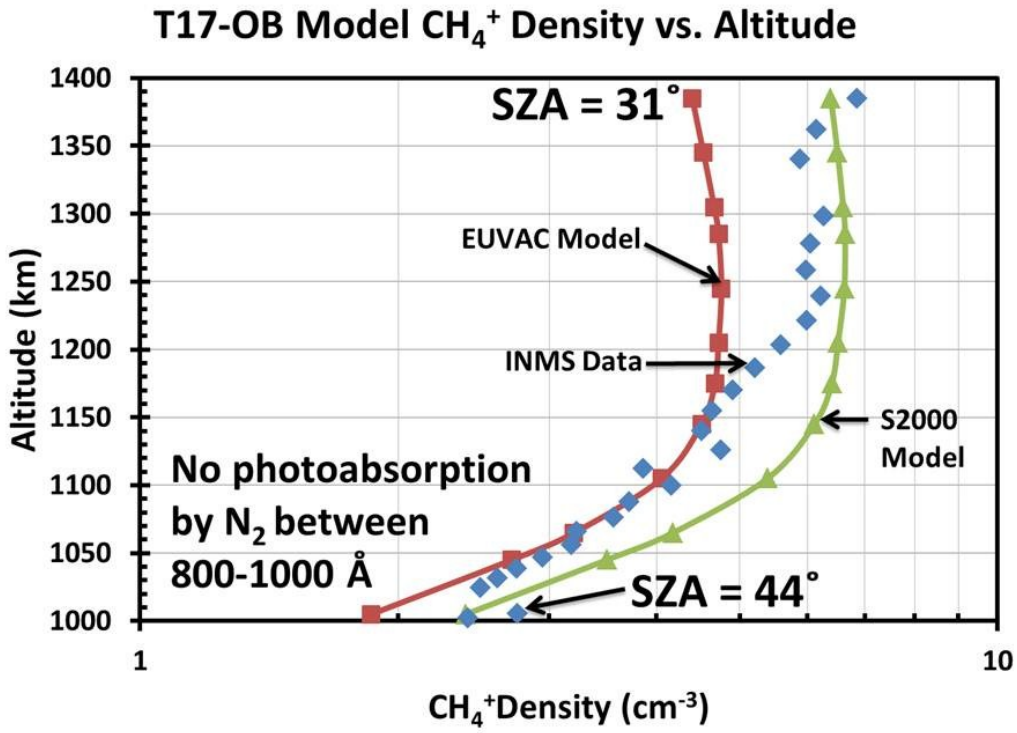

Appendix Figure C.25 CH_4^+ density produced by the full photochemical model compared to INMS data from the T17-Outbound flyby of Titan. Solar photons with wavelengths between 800 and 1000 Å did not interact with N_2. INMS data is indicated with the blue diamonds, results for the Solar 2000 and EUVAC models of the solar flux are shown with green triangles and red squares respectively. The solar zenith angle at closest approach and at the uppermost altitude is indicated at the bottom and top of the figure. The solar zenith angle is adjusted to reflect the conditions observed by the Cassini spacecraft.

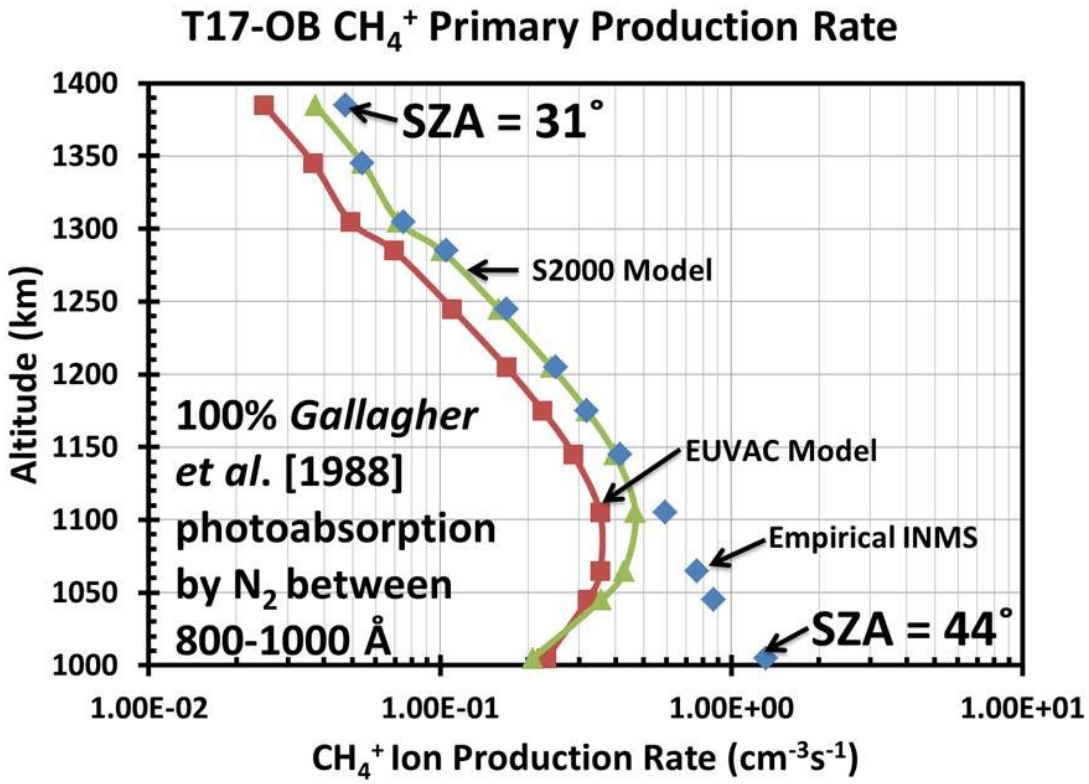

Appendix Figure C.26 Modeled photoionization production rates of CH_4^+ from photoionization and electron impact ionization by photoelectrons compared to the empirical production rate of CH_4^+ derived from INMS data from the T17-Outbound flyby of Titan. 100% of solar photons with wavelengths between 800 and 1000 Å interact with N_2 using photoabsorption cross sections of *Gallagher et al.* [1988]. INMS data is indicated with the blue diamonds, results for the Solar 2000 and EUVAC models of the solar flux are shown with green triangles and red squares respectively. The solar zenith angle at closest approach and at the uppermost altitude is indicated at the bottom and top of the figure. The solar zenith angle is adjusted to reflect the conditions observed by the Cassini spacecraft.

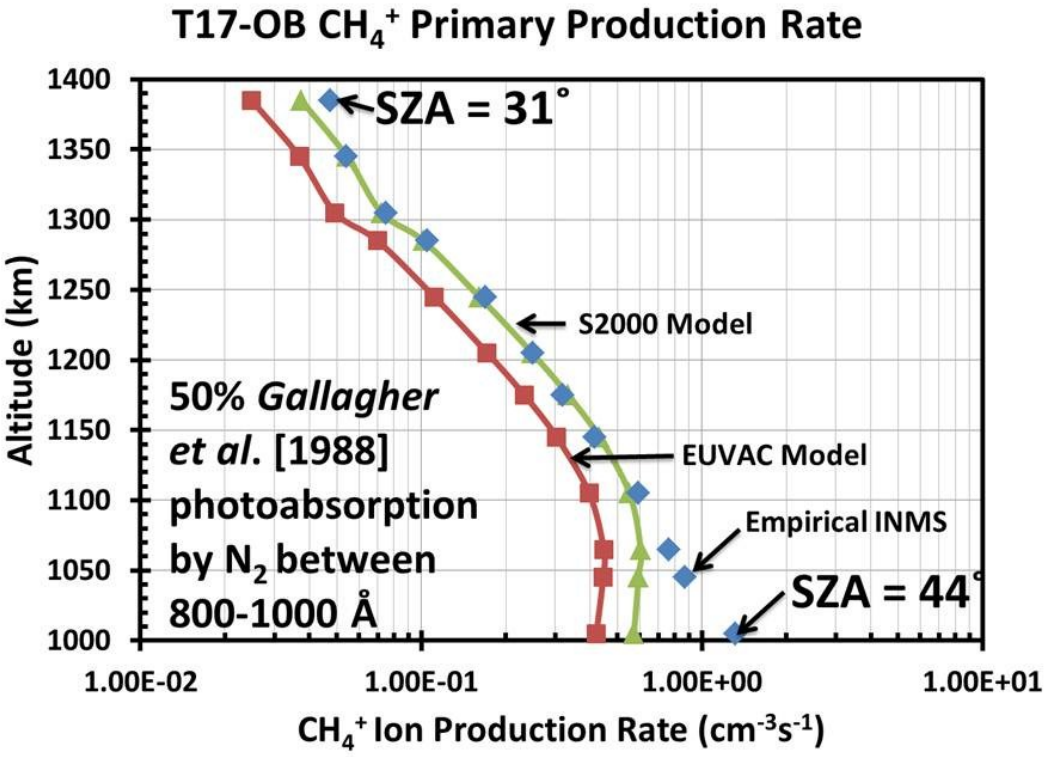

Appendix Figure C.27 Modeled photoionization production rates of CH_4^+ from photoionization and electron impact ionization by photoelectrons compared to the empirical production rate of CH_4^+ derived from INMS data from the T17-Outbound flyby of Titan. 50% of solar photons with wavelengths between 800 and 1000 Å interact with N_2 using photoabsorption cross sections of *Gallagher et al.* [1988]. INMS data is indicated with the blue diamonds, results for the Solar 2000 and EUVAC models of the solar flux are shown with green triangles and red squares respectively. The solar zenith angle at closest approach and at the uppermost altitude is indicated at the bottom and top of the figure. The solar zenith angle is adjusted to reflect the conditions observed by the Cassini spacecraft.

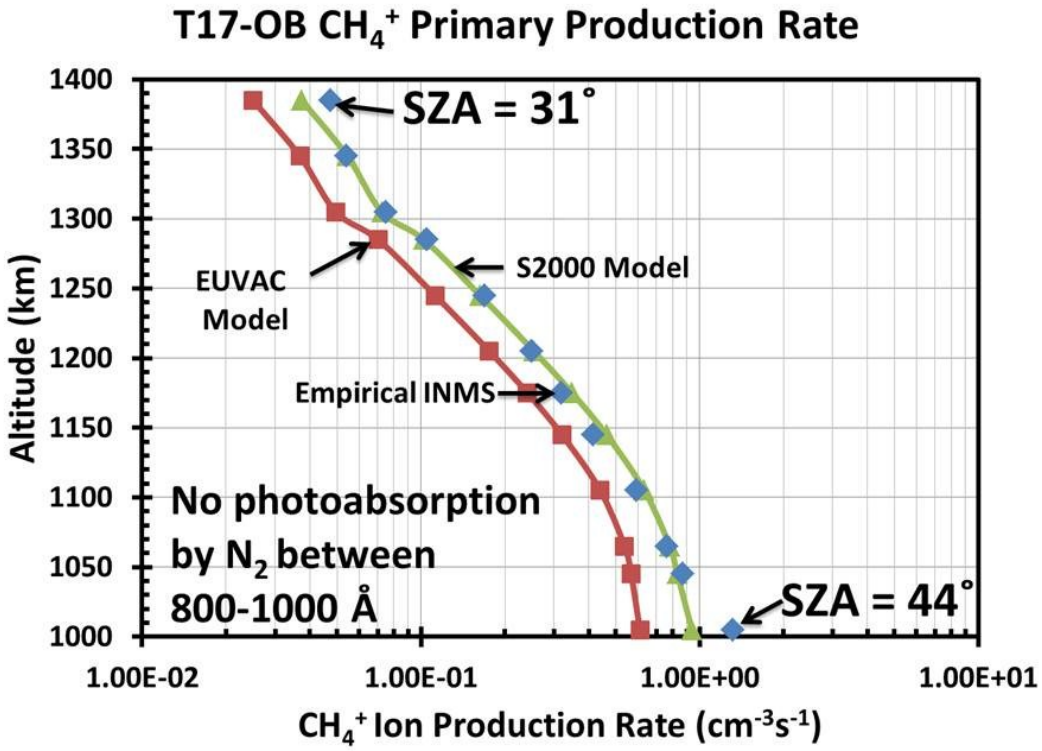

Appendix Figure C.28 Modeled photoionization production rates of CH_4^+ from photoionization and electron impact ionization by photoelectrons compared to the empirical production rate of CH_4^+ derived from INMS data from the T17-Outbound flyby of Titan. Solar photons with wavelengths between 800 and 1000 Å did not interact with N_2. INMS data is indicated with the blue diamonds, results for the Solar 2000 and EUVAC models of the solar flux are shown with green triangles and red squares respectively. The solar zenith angle at closest approach and at the uppermost altitude is indicated at the bottom and top of the figure. The solar zenith angle is adjusted to reflect the conditions observed by the Cassini spacecraft.

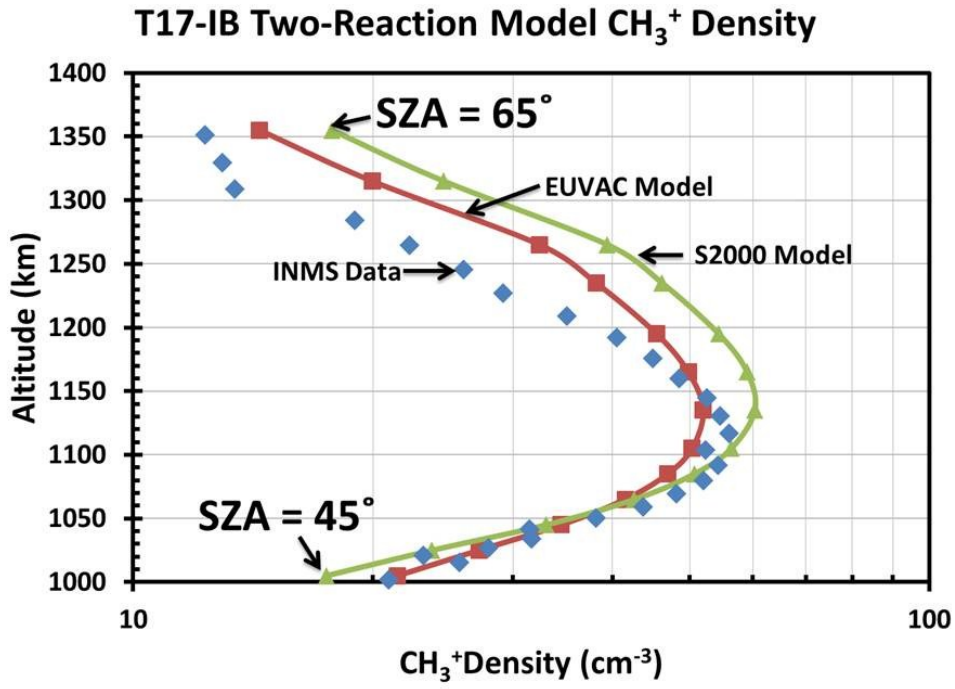

Appendix Figure C.29 Density of CH_3^+ derived from model production rates using a simple two reaction chemical model compared to INMS data from the T17-Inbound flyby of Titan. INMS data is indicated with the blue diamonds, results for the Solar 2000 and EUVAC models of the solar flux are shown with green triangles and red squares respectively. The orange crosses indicate the CH_3^+ density derived from model production rates and the more complex ion chemistry given in Equation (4.5). The solar zenith angle at closest approach and at the uppermost altitude is indicated at the bottom and top of the figure. The solar zenith angle is adjusted to reflect the conditions observed by the Cassini spacecraft.

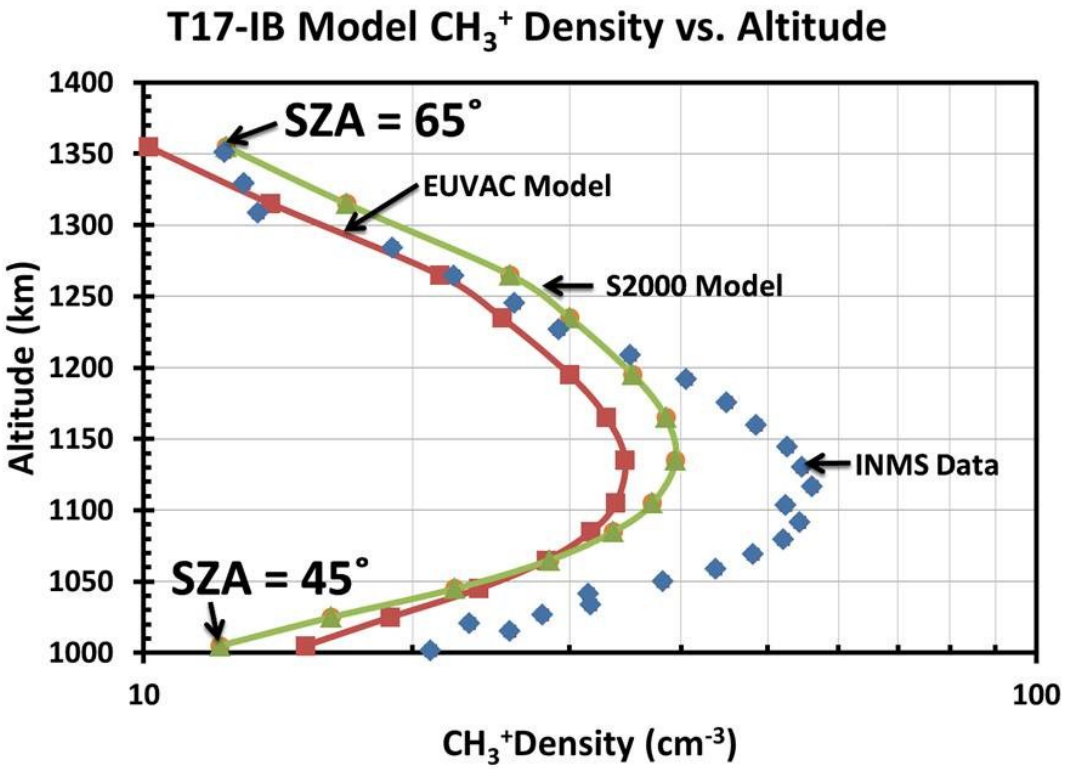

Appendix Figure C.30 CH_3^+ density produced by the full photochemical model compared to INMS data from the T17-Inbound flyby of Titan. INMS data is indicated with the blue diamonds, results for the Solar 2000 and EUVAC models of the solar flux are shown with green triangles and red squares respectively. The solar zenith angle at closest approach and at the uppermost altitude is indicated at the bottom and top of the figure. The solar zenith angle is adjusted to reflect the conditions observed by the Cassini spacecraft.

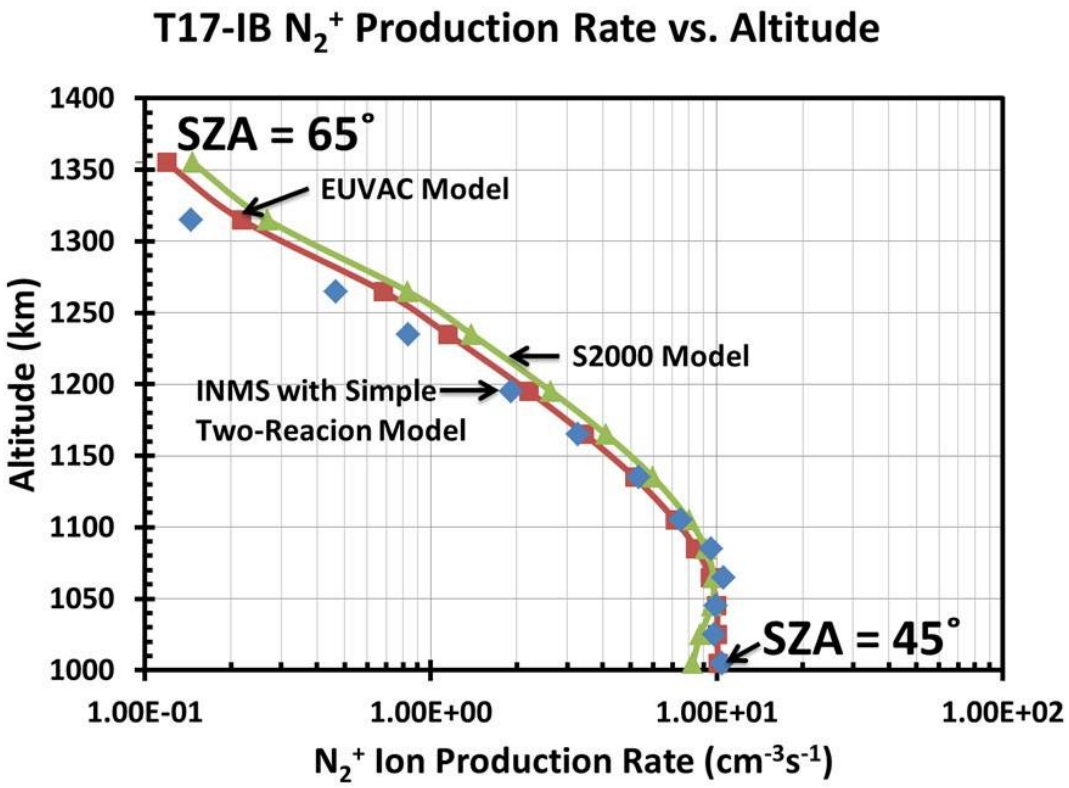

Appendix Figure C.31 Modeled photoionization production rates of N_2^+ compared to the empirical production rate of N_2^+ derived from INMS data from the T17-Inbound flyby of Titan using the simple two reaction chemical model. INMS data is indicated with the blue diamonds, results for the Solar 2000 and EUVAC models of the solar flux are shown with green triangles and red squares respectively. All N_2^+ production is assumed to produce CH_3^+. The solar zenith angle at closest approach and at the uppermost altitude is indicated at the bottom and top of the figure. The solar zenith angle is adjusted to reflect the conditions observed by the Cassini spacecraft.

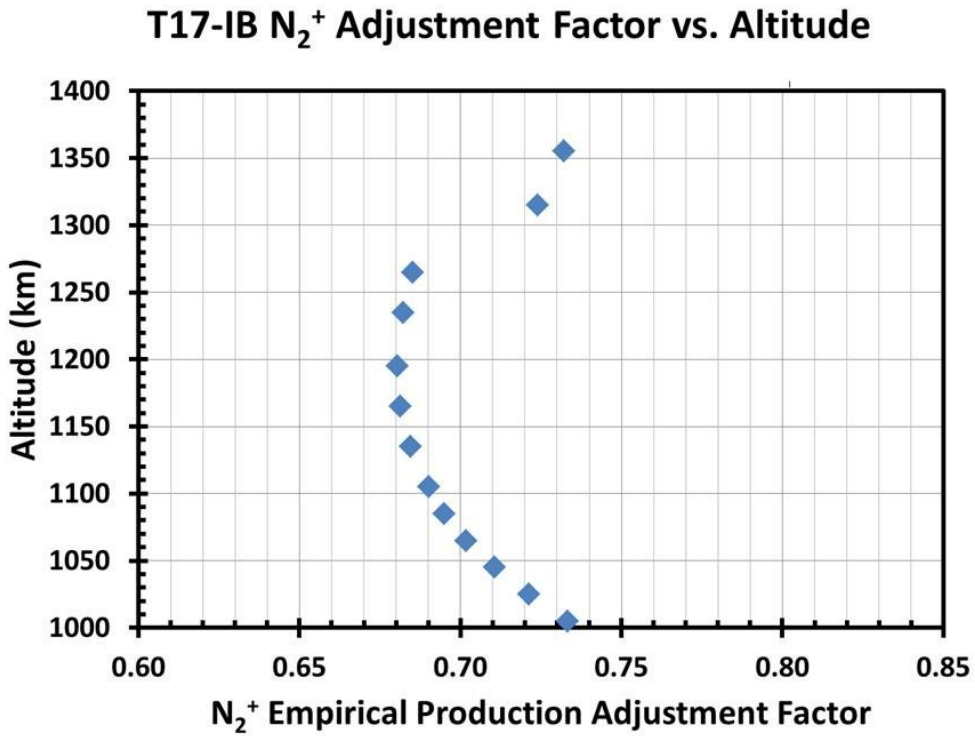

Appendix Figure C.32 Factor used to adjust the empirical INMS N_2^+ production rate for the T17-Inbound flyby of Titan. This correction factor is the ratio of N_2^+ production rate from photoionization to the N_2^+ production rate from the full photochemical model (production from photoionization and chemical pathways).

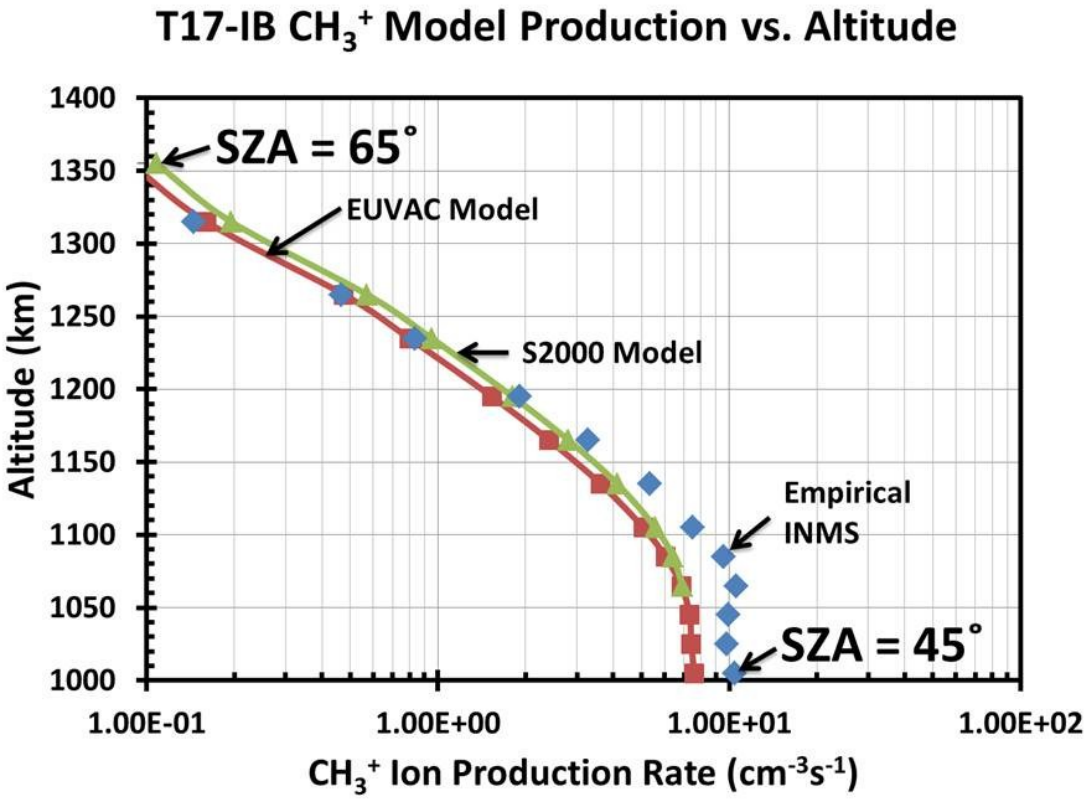

Appendix Figure C.33 A comparison of the modeled production rates of CH_3^+ to the empirical production rate of CH_3^+ derived from INMS data from the T17-Inbound flyby of Titan. INMS data is indicated with the blue diamonds, results for the Solar 2000 and EUVAC models of the solar flux are shown with green triangles and red squares respectively. The solar zenith angle at closest approach and at the uppermost altitude is indicated at the bottom and top of the figure. The solar zenith angle is adjusted to reflect the conditions observed by the Cassini spacecraft.

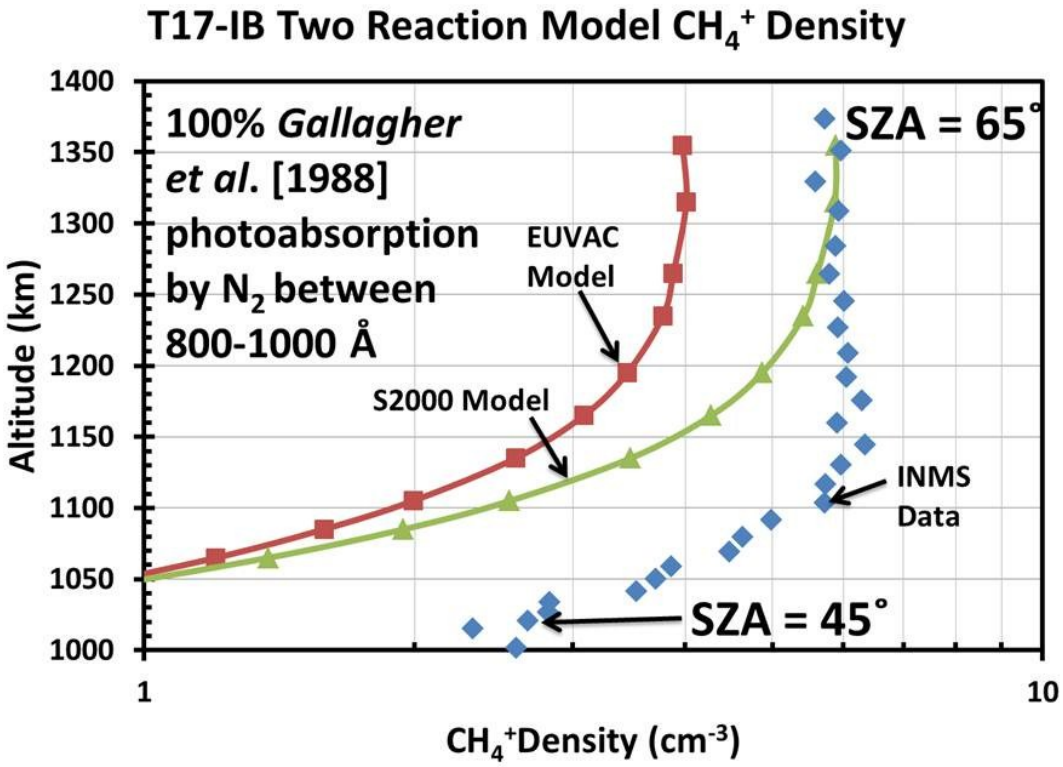

Appendix Figure C.34 Density of CH_4^+ calculated using the simple two reaction chemical model (Equation (4.10)) and the photoionization model compared to INMS data from the T17-Inbound flyby of Titan. N_2 photoabsorption cross sections for photons with wavelengths between 800 and 1000 Å of *Gallagher et al.* [1988] were used. INMS data is indicated with the blue diamonds, results for the Solar 2000 and EUVAC models of the solar flux are shown with green triangles and red squares respectively. The solar zenith angle at closest approach and at the uppermost altitude is indicated at the bottom and top of the figure. The solar zenith angle is adjusted to reflect the conditions observed by the Cassini spacecraft.

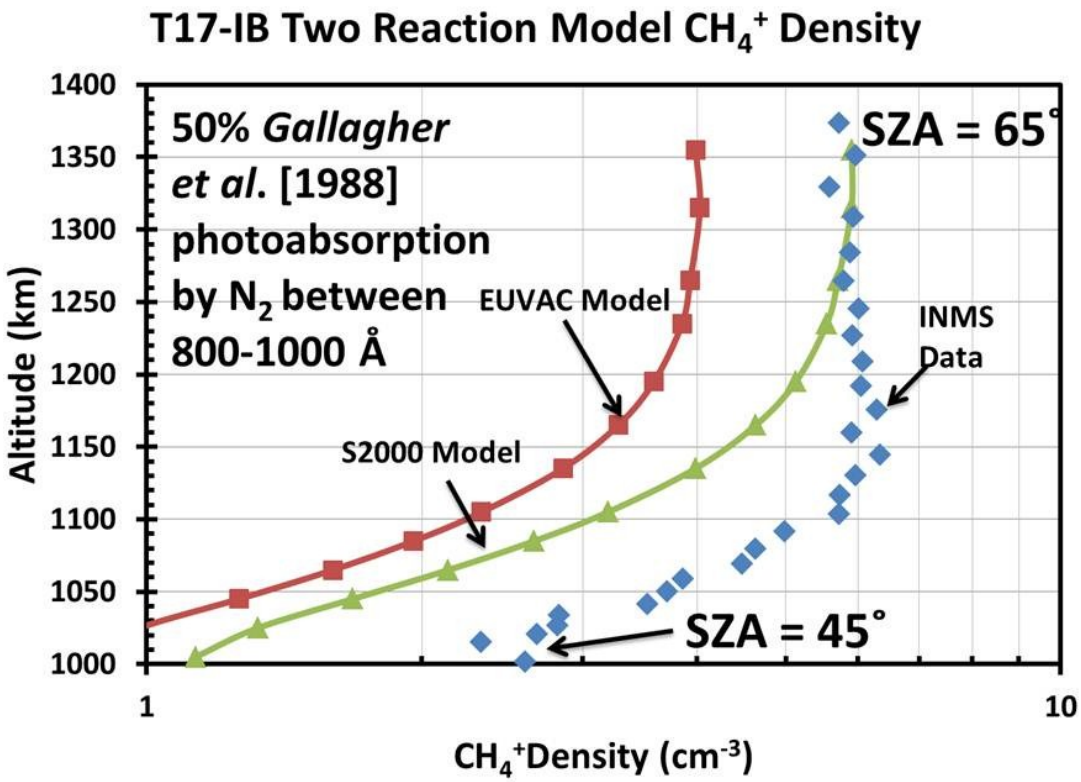

Appendix Figure C.35 Density of CH_4^+ calculated using the simple two reaction chemical model (Equation (4.10)) and the photoionization model compared to INMS data from the T17-Inbound flyby of Titan. 50% of solar photons with wavelengths between 800 and 1000 Å interact with N_2 using photoabsorption cross sections of *Gallagher et al.* [1988]. INMS data is indicated with the blue diamonds, results for the Solar 2000 and EUVAC models of the solar flux are shown with green triangles and red squares respectively. The solar zenith angle at closest approach and at the uppermost altitude is indicated at the bottom and top of the figure. The solar zenith angle is adjusted to reflect the conditions observed by the Cassini spacecraft.

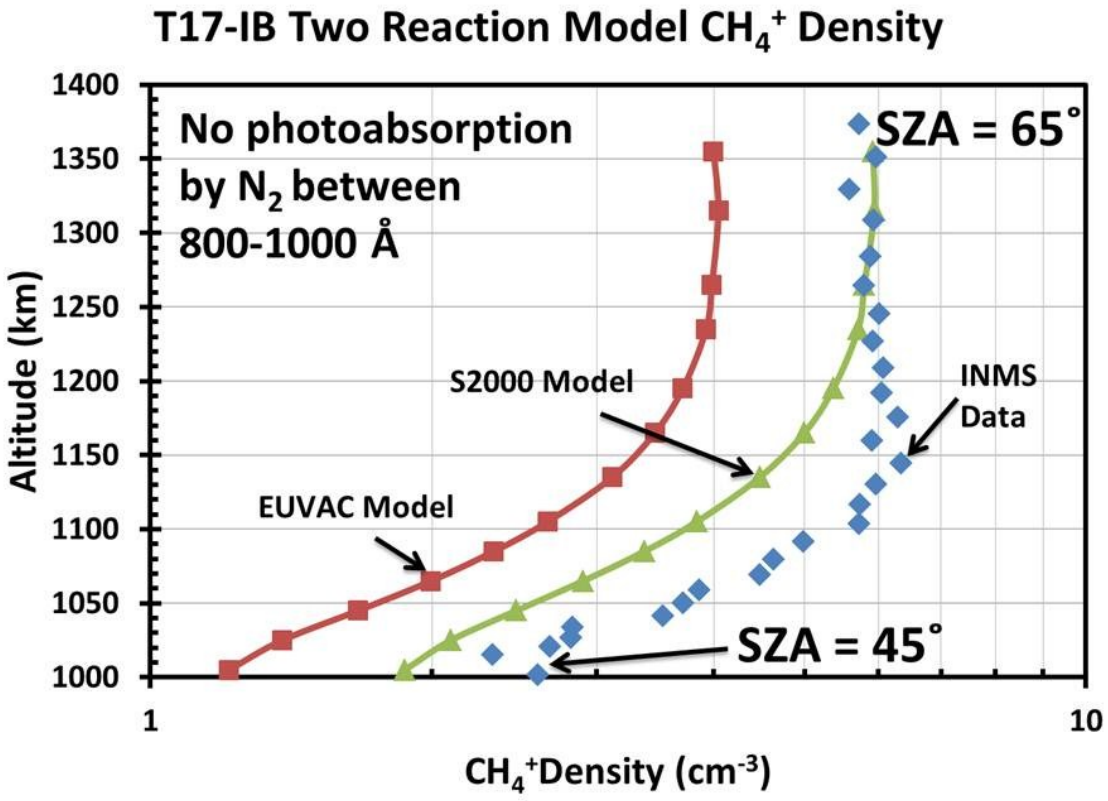

Appendix Figure C.36 Density of CH_4^+ calculated using the simple two reaction chemical model (Equation (4.10)) and the photoionization model compared to INMS data from the T17-Inbound flyby of Titan. Solar photons with wavelengths between 800 and 1000 Å did not interact with N2. INMS data is indicated with the blue diamonds, results for the Solar 2000 and EUVAC models of the solar flux are shown with green triangles and red squares respectively. The solar zenith angle at closest approach and at the uppermost altitude is indicated at the bottom and top of the figure. The solar zenith angle is adjusted to reflect the conditions observed by the Cassini spacecraft.

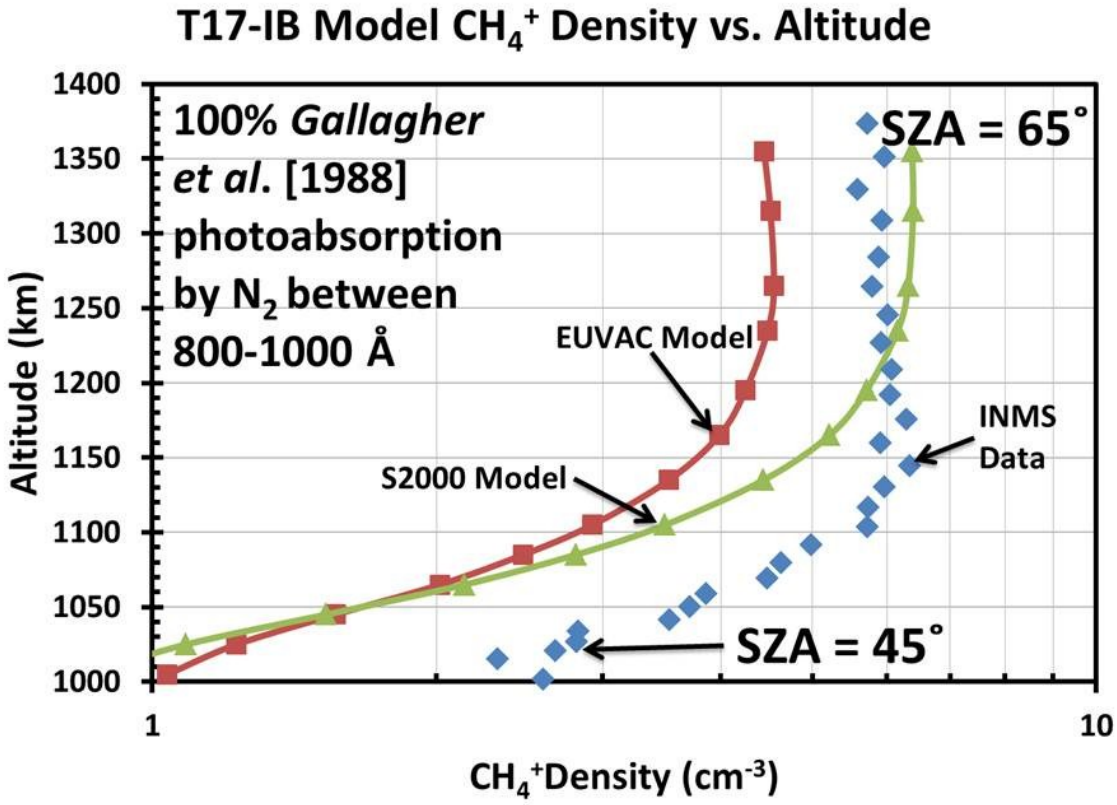

Appendix Figure C.37 CH_4^+ density produced with the full photochemical model compared to INMS data from the T17-Inbound flyby of Titan. N_2 photoabsorption cross sections for photons with wavelengths between 800 and 1000 Å of Gallagher et al. [1988] were used. INMS data is indicated with the blue diamonds, results for the Solar 2000 and EUVAC models of the solar flux are shown with green triangles and red squares respectively. The solar zenith angle at closest approach and at the uppermost altitude is indicated at the bottom and top of the figure. The solar zenith angle is adjusted to reflect the conditions observed by the Cassini spacecraft.

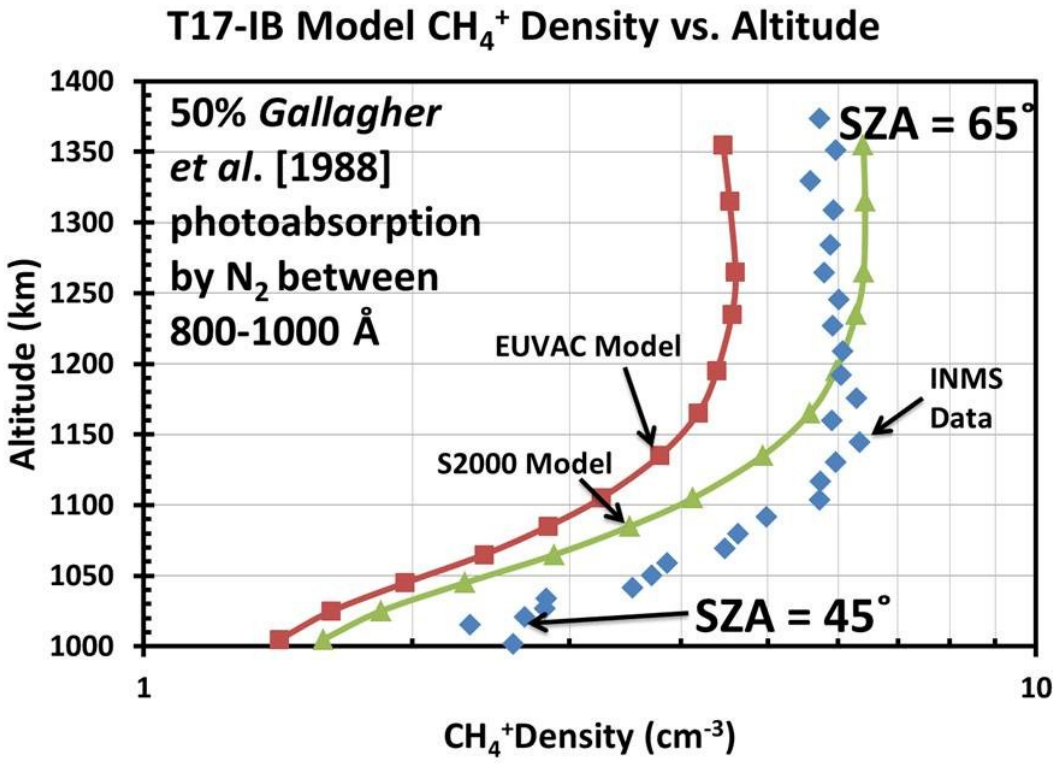

Appendix Figure C.38 CH_4^+ density produced by the full photochemical model compared to INMS data from the T17-Inbound flyby of Titan. 50% of solar photons with wavelengths between 800 and 1000 Å interact with N_2 photoabsorption using cross sections of *Gallagher et al.* [1988]. INMS data is indicated with the blue diamonds, results for the Solar 2000 and EUVAC models of the solar flux are shown with green triangles and red squares respectively. The solar zenith angle at closest approach and at the uppermost altitude is indicated at the bottom and top of the figure. The solar zenith angle is adjusted to reflect the conditions observed by the Cassini spacecraft.

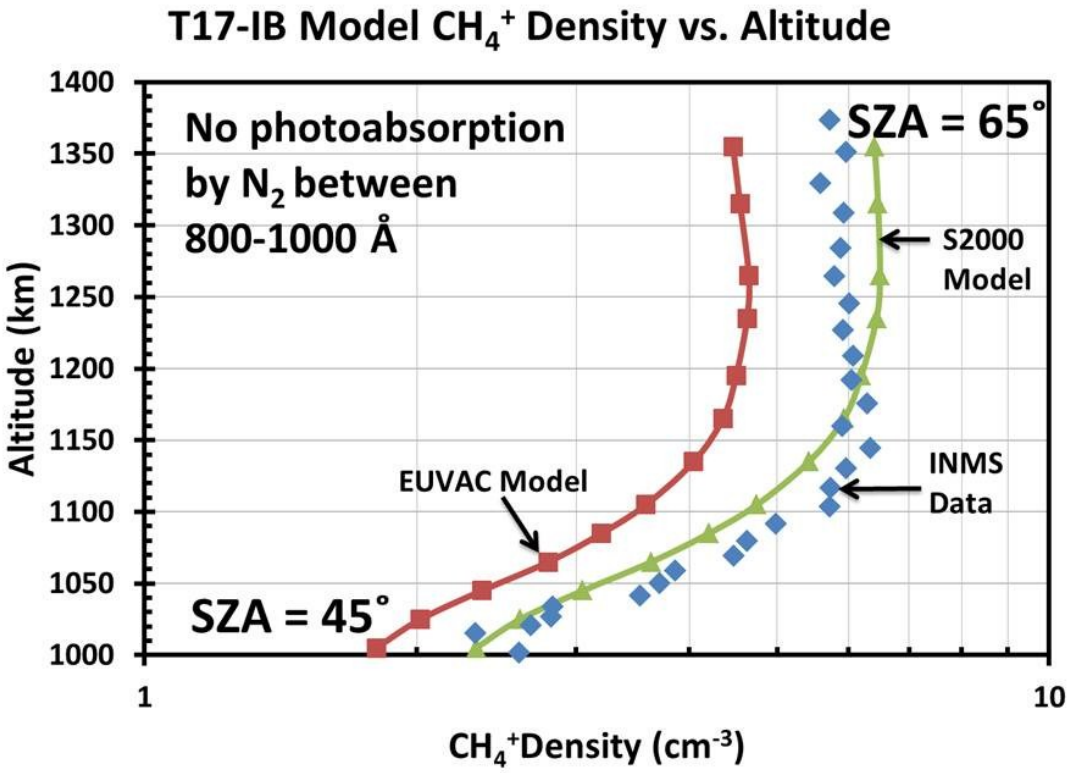

Appendix Figure C.39 CH_4^+ density produced by the full photochemical model compared to INMS data from the T17-Inbound flyby of Titan. Solar photons with wavelengths between 800 and 1000 Å did not interact with N_2. INMS data is indicated with the blue diamonds, results for the Solar 2000 and EUVAC models of the solar flux are shown with green triangles and red squares respectively. The solar zenith angle at closest approach and at the uppermost altitude is indicated at the bottom and top of the figure. The solar zenith angle is adjusted to reflect the conditions observed by the Cassini spacecraft.

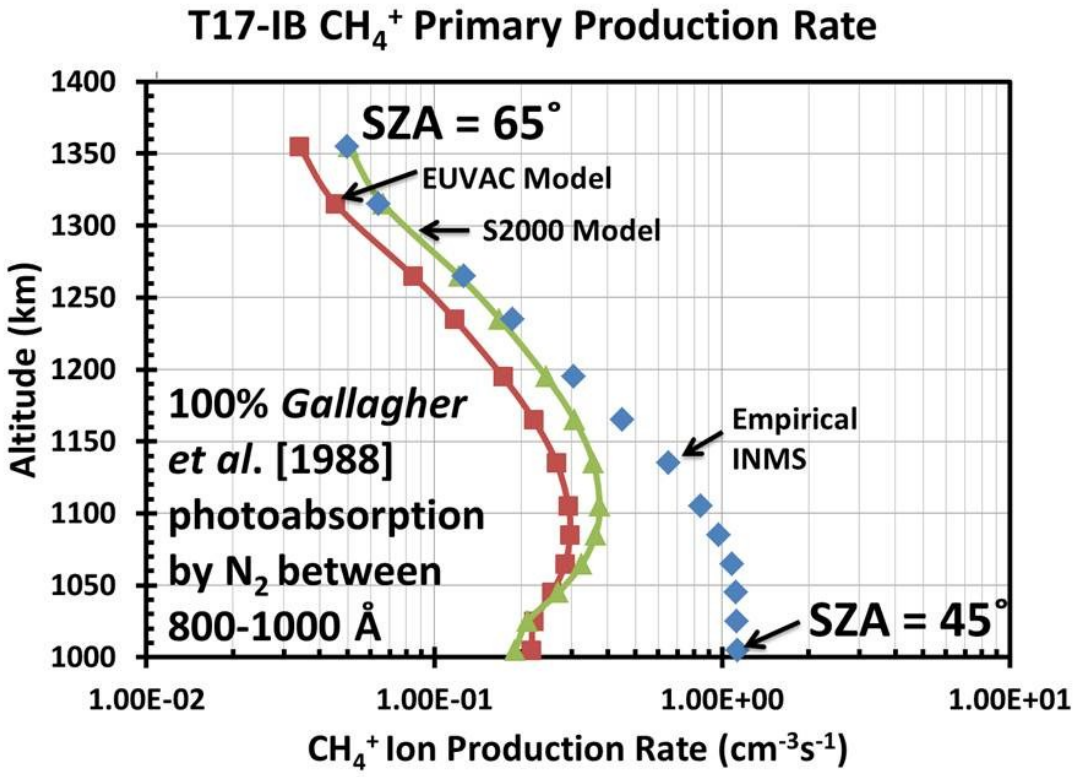

Appendix Figure C.40 Modeled photoionization production rates of CH_4^+ from photoionization and electron impact ionization by photoelectrons compared to the empirical production rate of CH_4^+ derived from INMS data from the T17-Inbound flyby of Titan. 100% of solar photons with wavelengths between 800 and 1000 Å interact with N_2 using photoabsorption cross sections of *Gallagher et al.* [1988]. INMS data is indicated with the blue diamonds, results for the Solar 2000 and EUVAC models of the solar flux are shown with green triangles and red squares respectively. The solar zenith angle at closest approach and at the uppermost altitude is indicated at the bottom and top of the figure. The solar zenith angle is adjusted to reflect the conditions observed by the Cassini spacecraft.

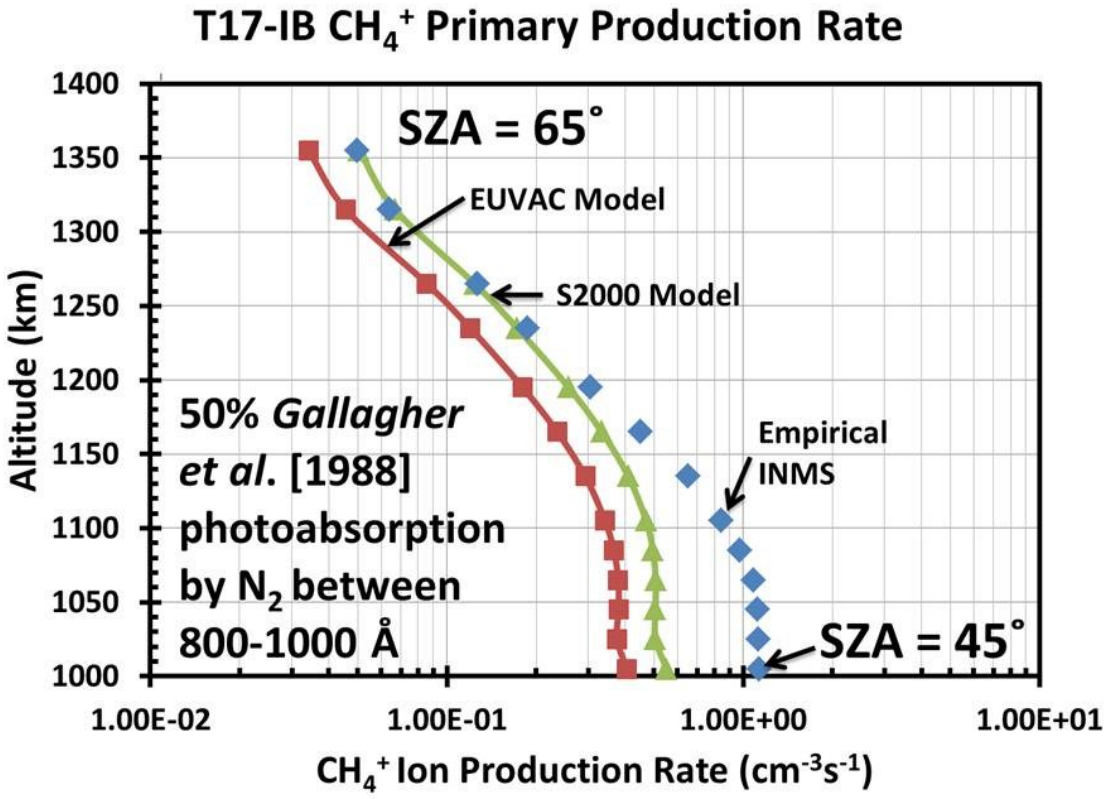

Appendix Figure C.41 Modeled photoionization production rates of CH_4^+ from photoionization and electron impact ionization by photoelectrons compared to the empirical production rate of CH_4^+ derived from INMS data from the T17-Inbound flyby of Titan. 50% of solar photons with wavelengths between 800 and 1000 Å interact with N_2 using photoabsorption cross sections of *Gallagher et al.* [1988]. INMS data is indicated with the blue diamonds, results for the Solar 2000 and EUVAC models of the solar flux are shown with green triangles and red squares respectively. The solar zenith angle at closest approach and at the uppermost altitude is indicated at the bottom and top of the figure. The solar zenith angle is adjusted to reflect the conditions observed by the Cassini spacecraft.

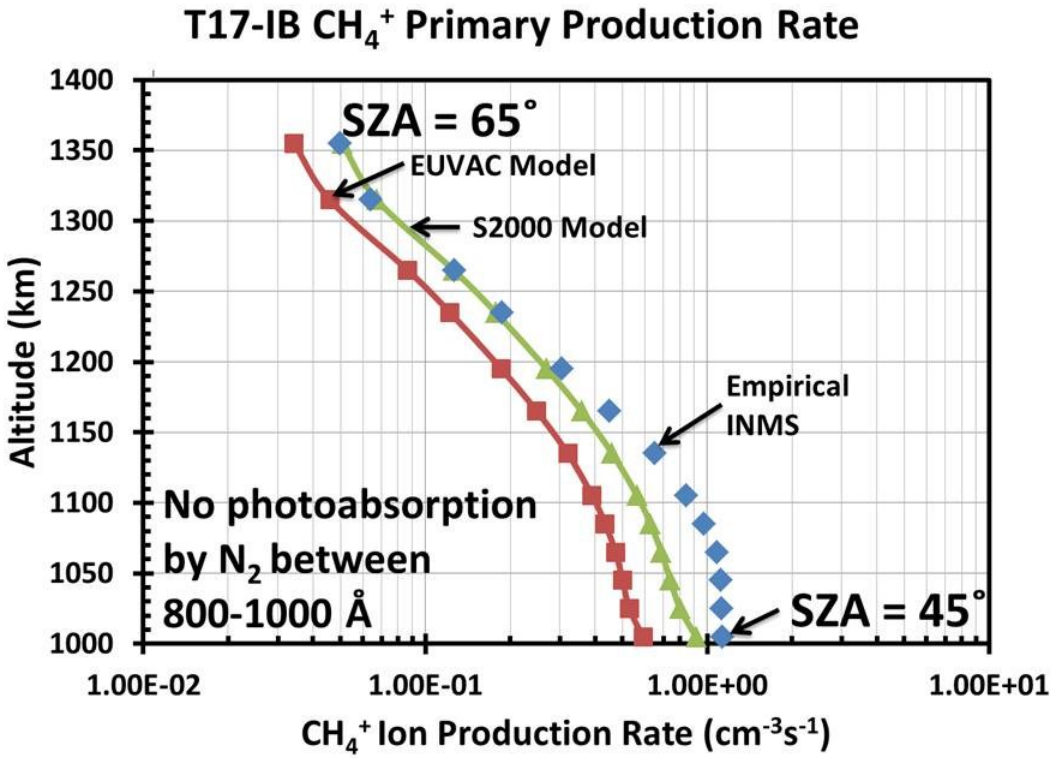

Appendix Figure C.42 Modeled photoionization production rates of CH_4^+ from photoionization and electron impact ionization by photoelectrons compared to the empirical production rate of CH_4^+ derived from INMS data from the T17-Inbound flyby of Titan. Solar photons with wavelengths between 800 and 1000 Å did not interact with N_2. INMS data is indicated with the blue diamonds, results for the Solar 2000 and EUVAC models of the solar flux are shown with green triangles and red squares respectively. The solar zenith angle at closest approach and at the uppermost altitude is indicated at the bottom and top of the figure. The solar zenith angle is adjusted to reflect the conditions observed by the Cassini spacecraft.

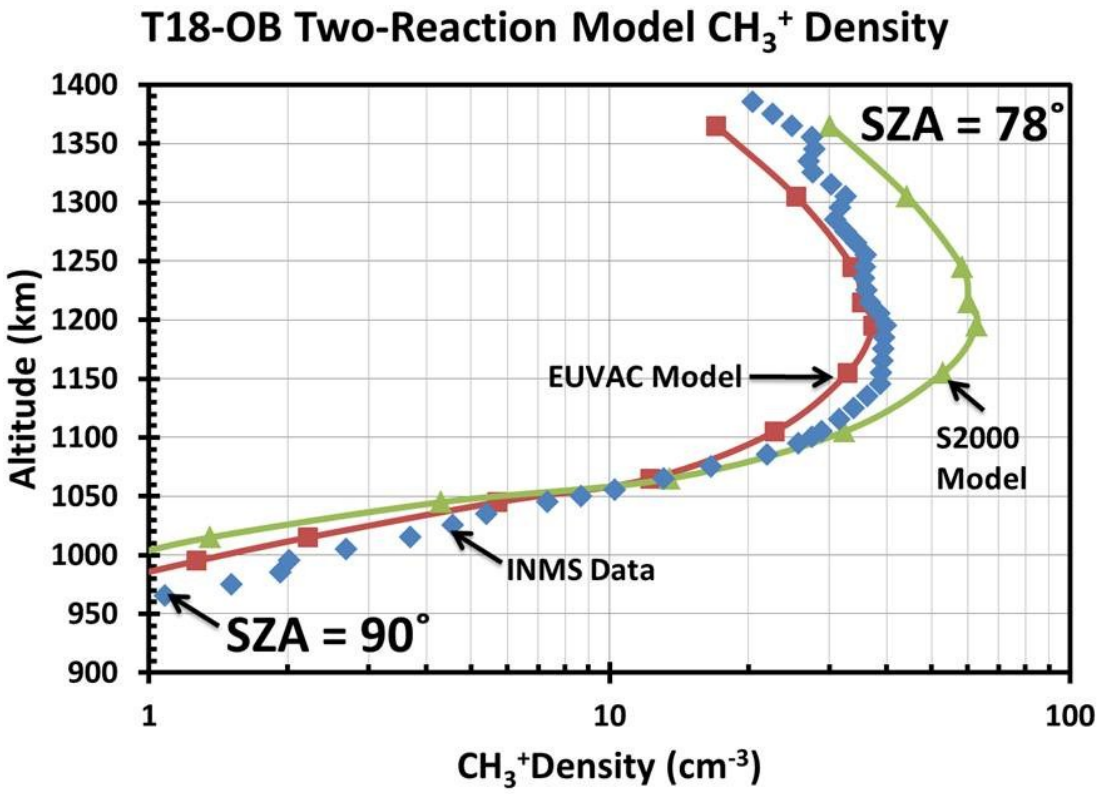

Appendix Figure C.43 Density of CH_3^+ derived from model production rates using a simple two reaction chemical model compared to INMS data from the T18-Outbound flyby of Titan. INMS data is indicated with the blue diamonds, results for the Solar 2000 and EUVAC models of the solar flux are shown with green triangles and red squares respectively. The orange crosses indicate the CH_3^+ density derived from model production rates and the more complex ion chemistry given in Equation (4.5). The solar zenith angle at closest approach and at the uppermost altitude is indicated at the bottom and top of the figure. The solar zenith angle is adjusted to reflect the conditions observed by the Cassini spacecraft.

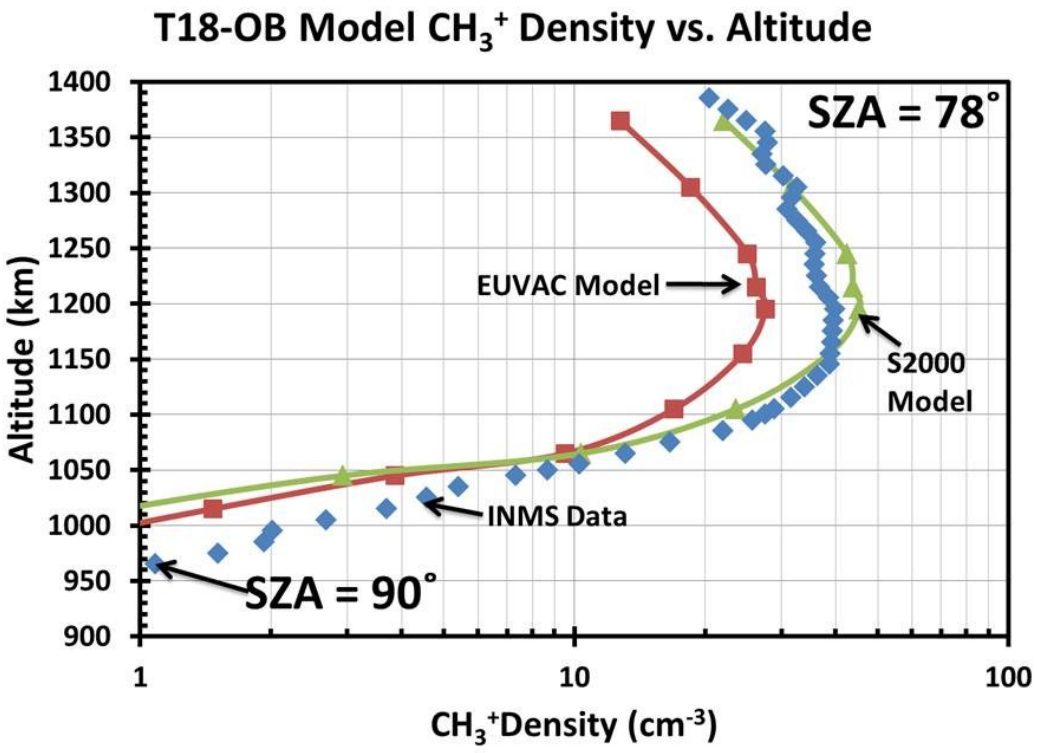

Appendix Figure C.44 CH_3^+ density produced by the full photochemical model compared to INMS data from the T18-Outbound flyby of Titan. INMS data is indicated with the blue diamonds, results for the Solar 2000 and EUVAC models of the solar flux are shown with green triangles and red squares respectively. The solar zenith angle at closest approach and at the uppermost altitude is indicated at the bottom and top of the figure. The solar zenith angle is adjusted to reflect the conditions observed by the Cassini spacecraft.

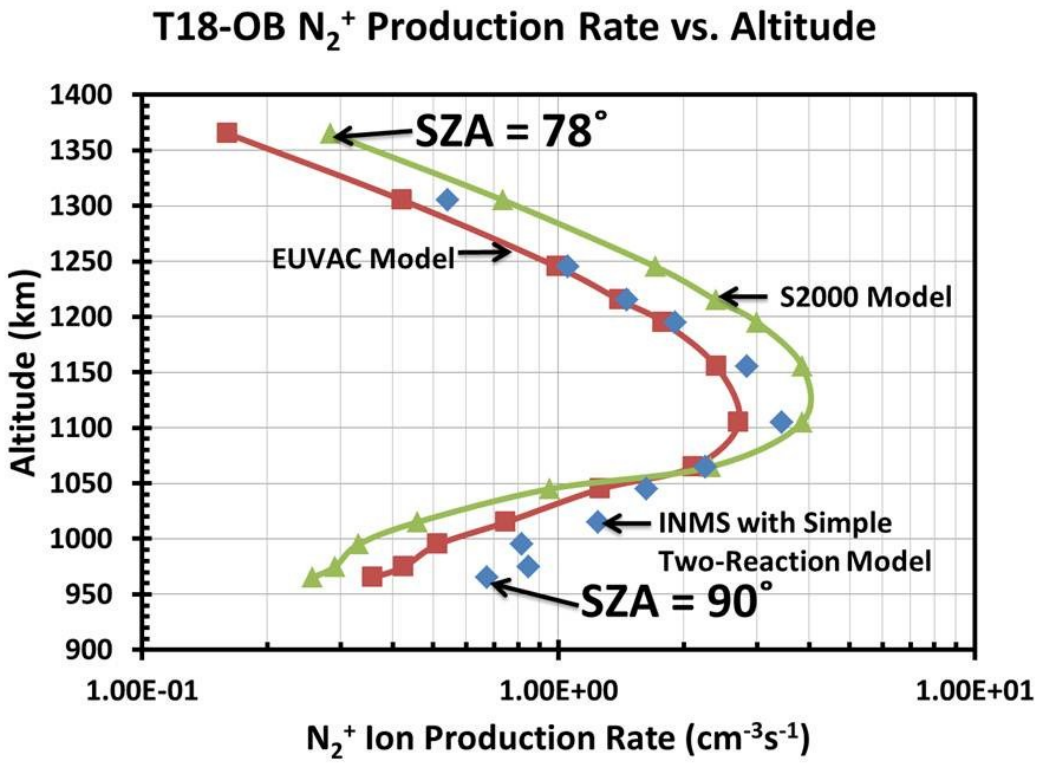

Appendix Figure C.45 Modeled photoionization production rates of N_2^+ compared to the empirical production rate of N_2^+ derived from INMS data from the T18-Outbound flyby of Titan using the simple two reaction chemical model. INMS data is indicated with the blue diamonds, results for the Solar 2000 and EUVAC models of the solar flux are shown with green triangles and red squares respectively. All N_2^+ production is assumed to produce CH_3^+. The solar zenith angle at closest approach and at the uppermost altitude is indicated at the bottom and top of the figure. The solar zenith angle is adjusted to reflect the conditions observed by the Cassini spacecraft.

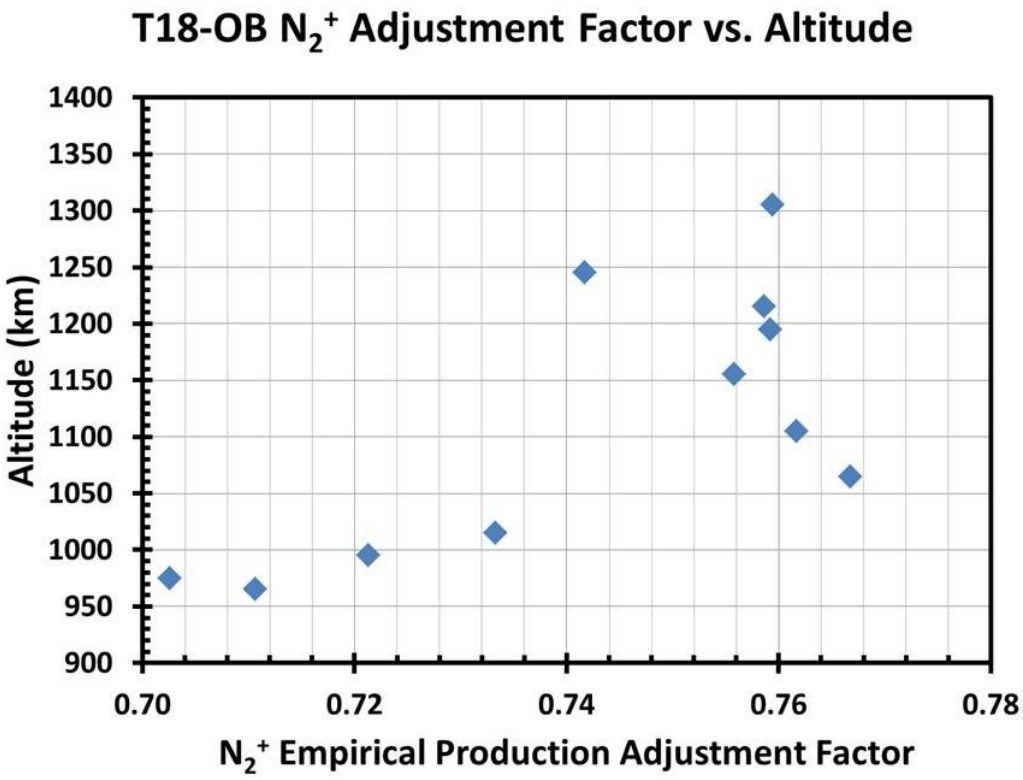

Appendix Figure C.46 Factor used to adjust the empirical INMS N_2^+ production rate for the T18-Outbound flyby of Titan. This correction factor is the ratio of N_2^+ production rate from photoionization to the N_2^+ production rate from the full photochemical model (production from photoionization and chemical pathways).

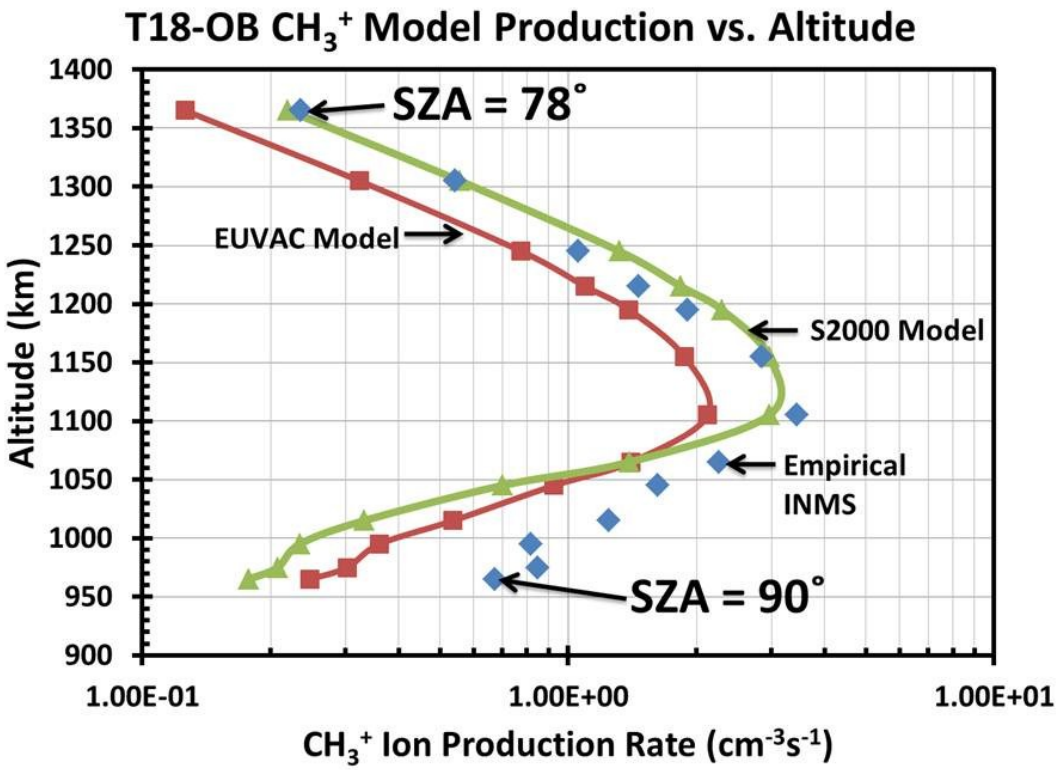

Appendix Figure C.47 A comparison of the modeled production rates of CH_3^+ to the empirical production rate of CH_3^+ derived from INMS data from the T18-Outbound flyby of Titan. INMS data is indicated with the blue diamonds, results for the Solar 2000 and EUVAC models of the solar flux are shown with green triangles and red squares respectively. The solar zenith angle at closest approach and at the uppermost altitude is indicated at the bottom and top of the figure. The solar zenith angle is adjusted to reflect the conditions observed by the Cassini spacecraft.

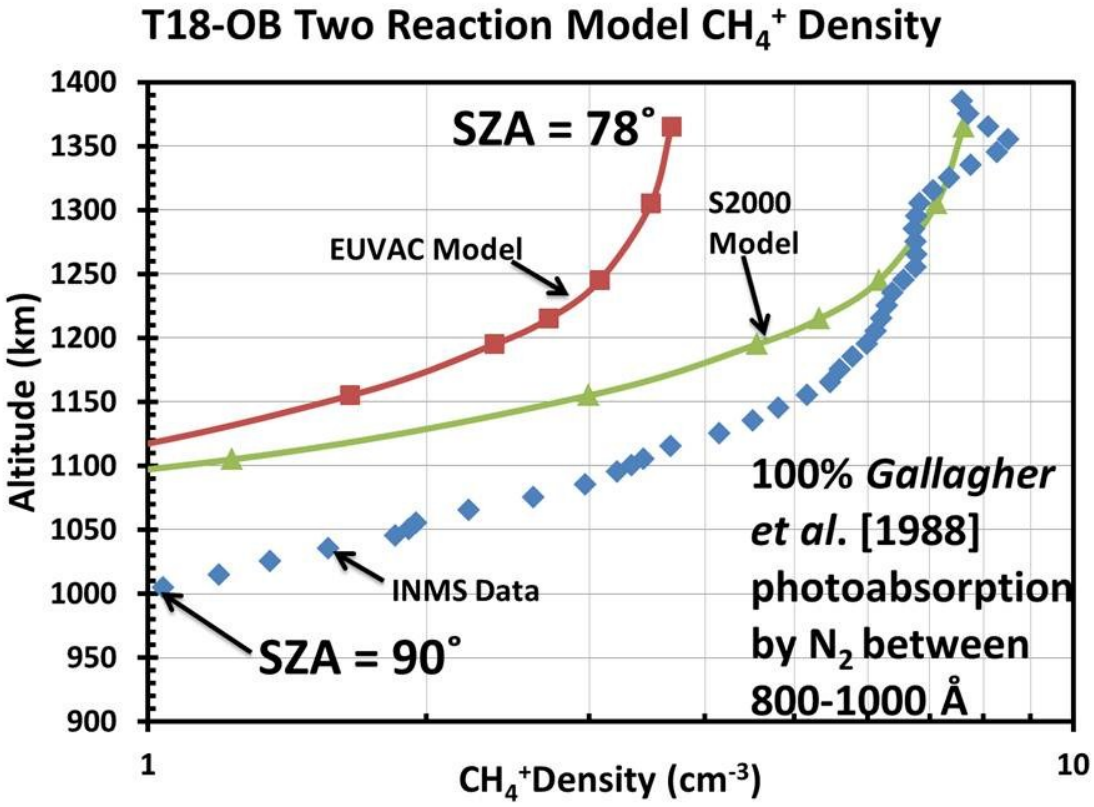

Appendix Figure C.48 Density of CH_4^+ calculated using the simple two reaction chemical model (Equation (4.10)) and the photoionization model compared to INMS data from the T18-Outbound flyby of Titan. N_2 photoabsorption cross sections for photons with wavelengths between 800 and 1000 Å of *Gallagher et al.* [1988] were used. INMS data is indicated with the blue diamonds, results for the Solar 2000 and EUVAC models of the solar flux are shown with green triangles and red squares respectively. The solar zenith angle at closest approach and at the uppermost altitude is indicated at the bottom and top of the figure. The solar zenith angle is adjusted to reflect the conditions observed by the Cassini spacecraft.

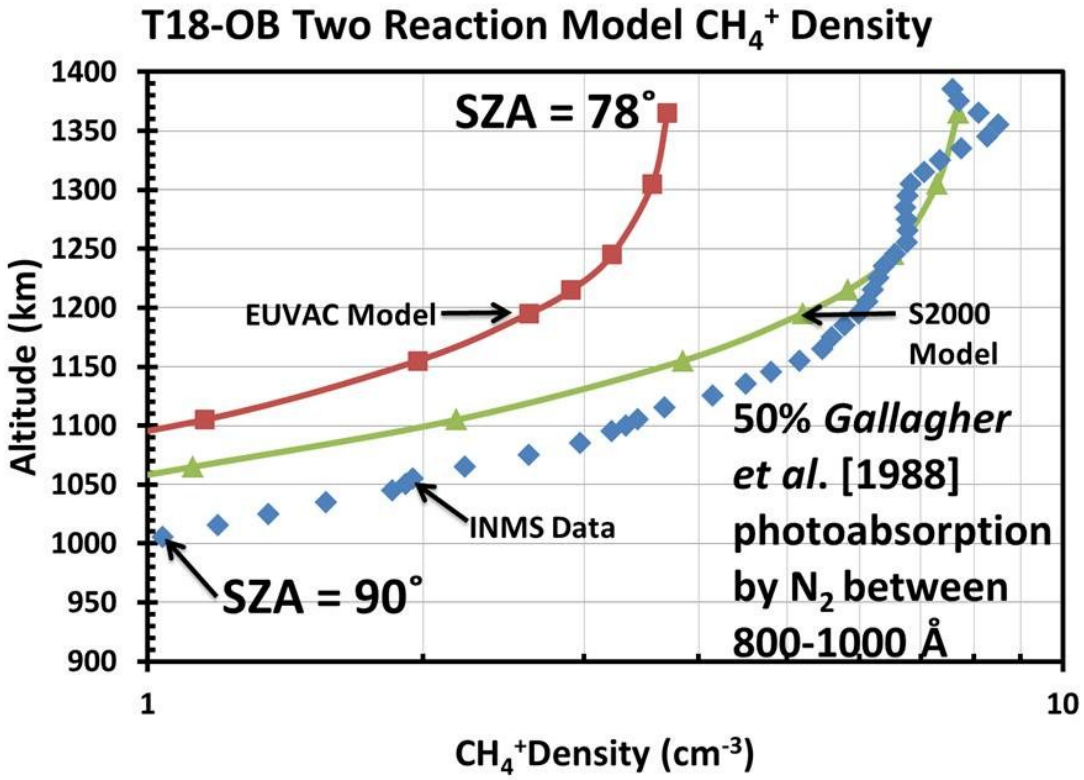

Appendix Figure C.49 Density of CH_4^+ calculated using the simple two reaction chemical model (Equation (4.10)) and the photoionization model compared to INMS data from the T18-Outbound flyby of Titan. 50% of solar photons with wavelengths between 800 and 1000 Å interact with N_2 using photoabsorption cross sections of *Gallagher et al.* [1988]. INMS data is indicated with the blue diamonds, results for the Solar 2000 and EUVAC models of the solar flux are shown with green triangles and red squares respectively. The solar zenith angle at closest approach and at the uppermost altitude is indicated at the bottom and top of the figure. The solar zenith angle is adjusted to reflect the conditions observed by the Cassini spacecraft.

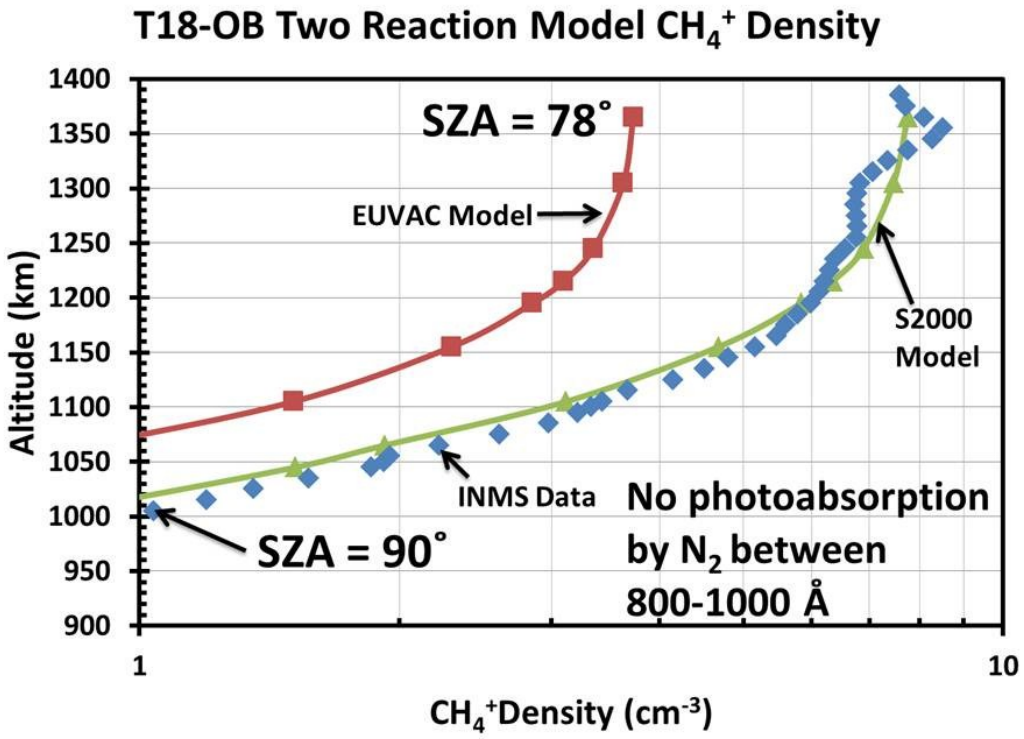

Appendix Figure C.50 Density of CH_4^+ calculated using the simple two reaction chemical model (Equation (4.10)) and the photoionization model compared to INMS data from the T18-Outbound flyby of Titan. Solar photons with wavelengths between 800 and 1000 Å did not interact with N2. INMS data is indicated with the blue diamonds, results for the Solar 2000 and EUVAC models of the solar flux are shown with green triangles and red squares respectively. The solar zenith angle at closest approach and at the uppermost altitude is indicated at the bottom and top of the figure. The solar zenith angle is adjusted to reflect the conditions observed by the Cassini spacecraft.

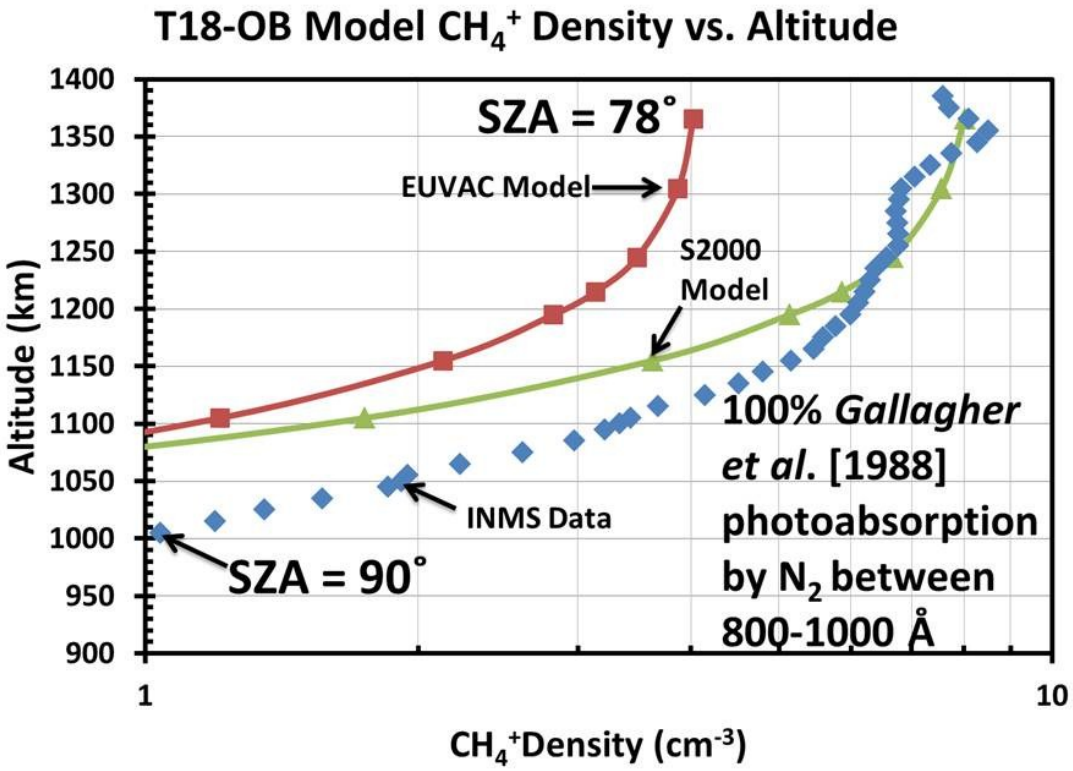

Appendix Figure C.51 CH_4^+ density produced with the full photochemical model compared to INMS data from the T18-Outbound flyby of Titan. N_2 photoabsorption cross sections for photons with wavelengths between 800 and 1000 Å of Gallagher et al. [1988] were used. INMS data is indicated with the blue diamonds, results for the Solar 2000 and EUVAC models of the solar flux are shown with green triangles and red squares respectively. The solar zenith angle at closest approach and at the uppermost altitude is indicated at the bottom and top of the figure. The solar zenith angle is adjusted to reflect the conditions observed by the Cassini spacecraft.

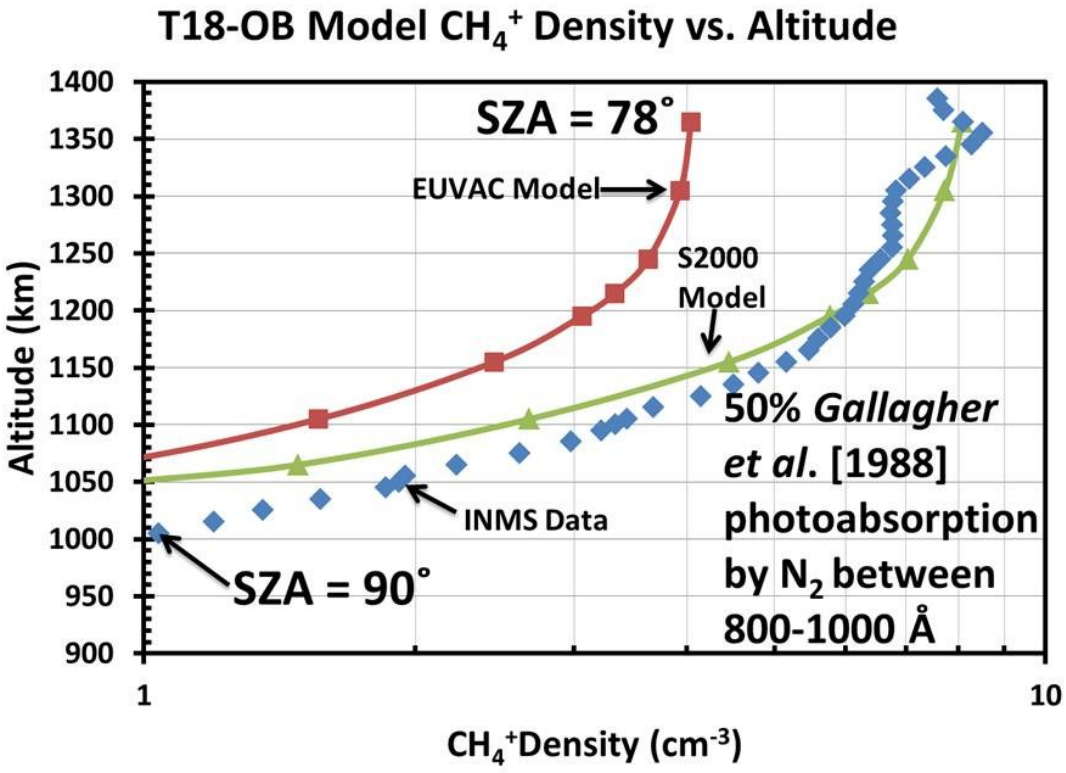

Appendix Figure C.52 CH_4^+ density produced by the full photochemical model compared to INMS data from the T18-Outbound flyby of Titan. 50% of solar photons with wavelengths between 800 and 1000 Å interact with N_2 photoabsorption using cross sections of *Gallagher et al.* [1988]. INMS data is indicated with the blue diamonds, results for the Solar 2000 and EUVAC models of the solar flux are shown with green triangles and red squares respectively. The solar zenith angle at closest approach and at the uppermost altitude is indicated at the bottom and top of the figure. The solar zenith angle is adjusted to reflect the conditions observed by the Cassini spacecraft.

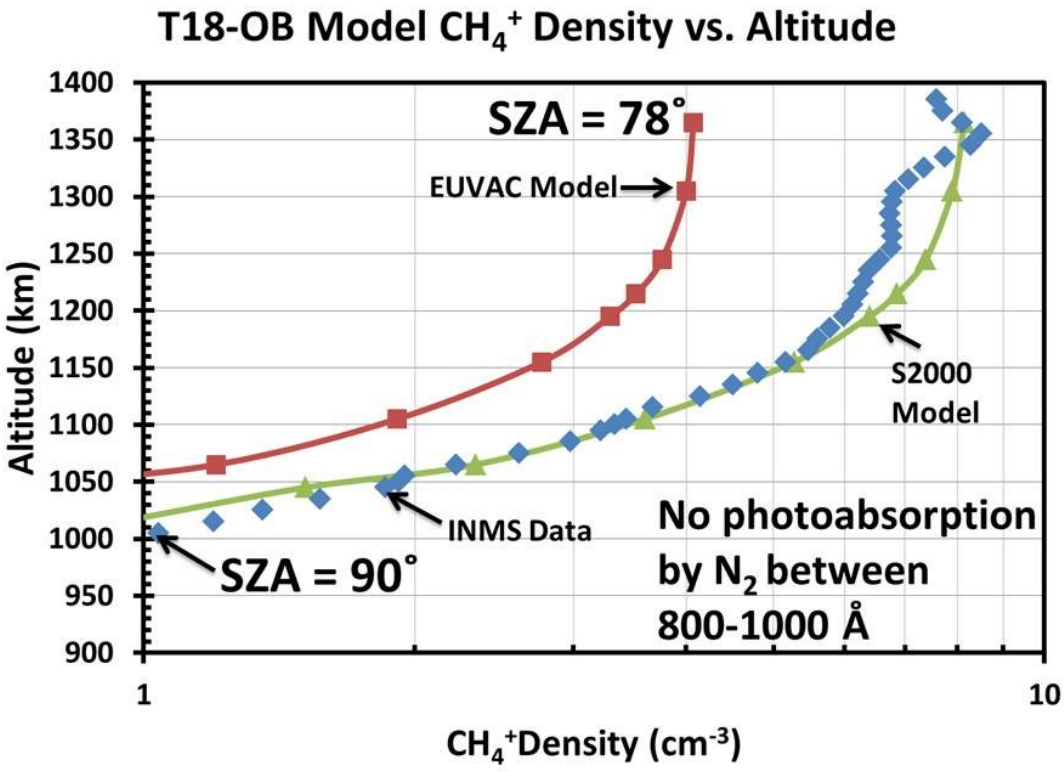

Appendix Figure C.53 CH_4^+ density produced by the full photochemical model compared to INMS data from the T18-Outbound flyby of Titan. Solar photons with wavelengths between 800 and 1000 Å did not interact with N_2. INMS data is indicated with the blue diamonds, results for the Solar 2000 and EUVAC models of the solar flux are shown with green triangles and red squares respectively. The solar zenith angle at closest approach and at the uppermost altitude is indicated at the bottom and top of the figure. The solar zenith angle is adjusted to reflect the conditions observed by the Cassini spacecraft.

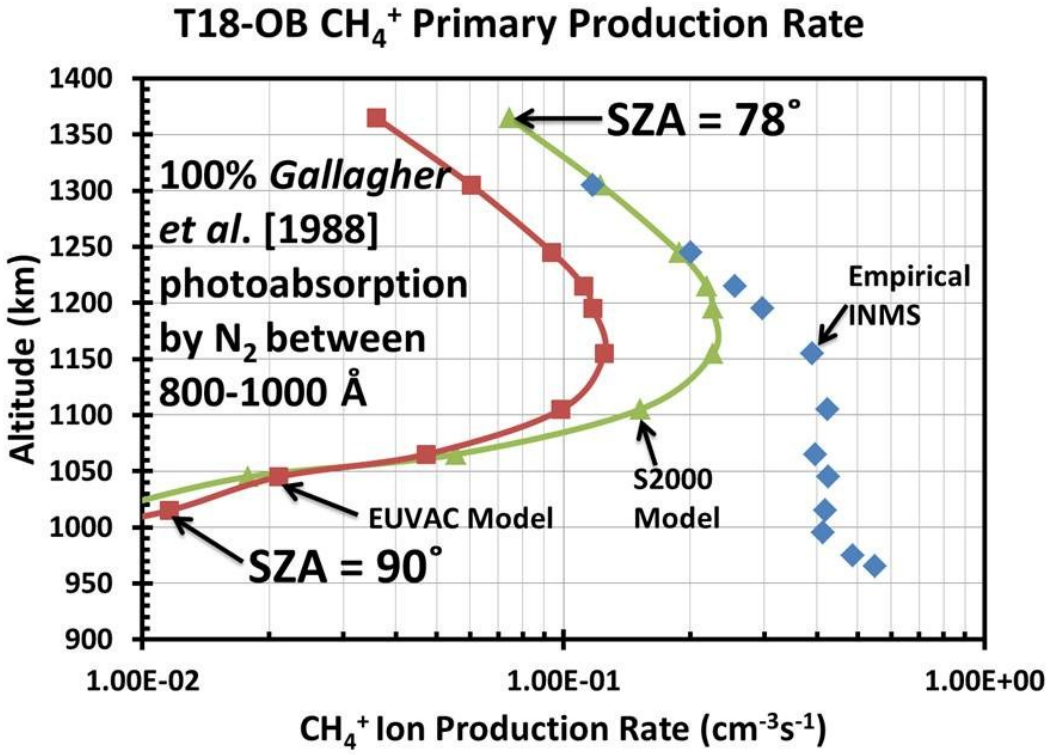

Appendix Figure C.54 Modeled photoionization production rates of CH_4^+ from photoionization and electron impact ionization by photoelectrons compared to the empirical production rate of CH_4^+ derived from INMS data from the T18-Outbound flyby of Titan. 100% of solar photons with wavelengths between 800 and 1000 Å interact with N_2 using photoabsorption cross sections of *Gallagher et al.* [1988]. INMS data is indicated with the blue diamonds, results for the Solar 2000 and EUVAC models of the solar flux are shown with green triangles and red squares respectively. The solar zenith angle at closest approach and at the uppermost altitude is indicated at the bottom and top of the figure. The solar zenith angle is adjusted to reflect the conditions observed by the Cassini spacecraft.

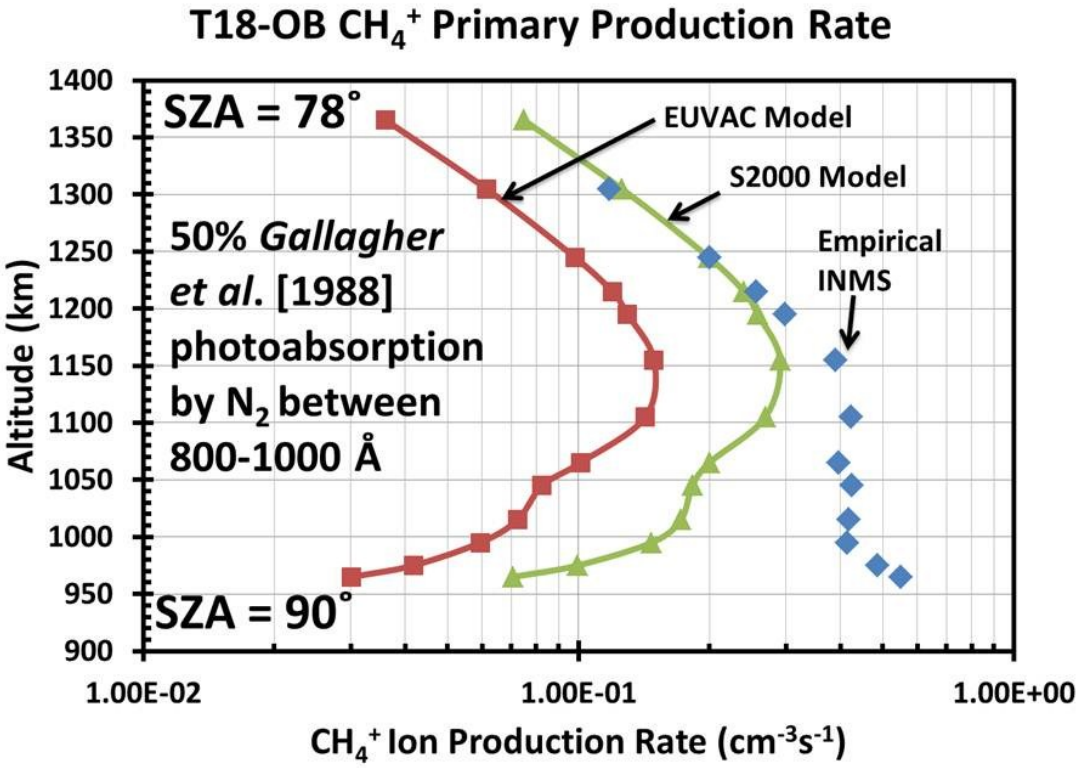

Appendix Figure C.55 Modeled photoionization production rates of CH_4^+ from photoionization and electron impact ionization by photoelectrons compared to the empirical production rate of CH_4^+ derived from INMS data from the T18-Outbound flyby of Titan. 50% of solar photons with wavelengths between 800 and 1000 Å interact with N_2 using photoabsorption cross sections of *Gallagher et al.* [1988]. INMS data is indicated with the blue diamonds, results for the Solar 2000 and EUVAC models of the solar flux are shown with green triangles and red squares respectively. The solar zenith angle at closest approach and at the uppermost altitude is indicated at the bottom and top of the figure. The solar zenith angle is adjusted to reflect the conditions observed by the Cassini spacecraft.

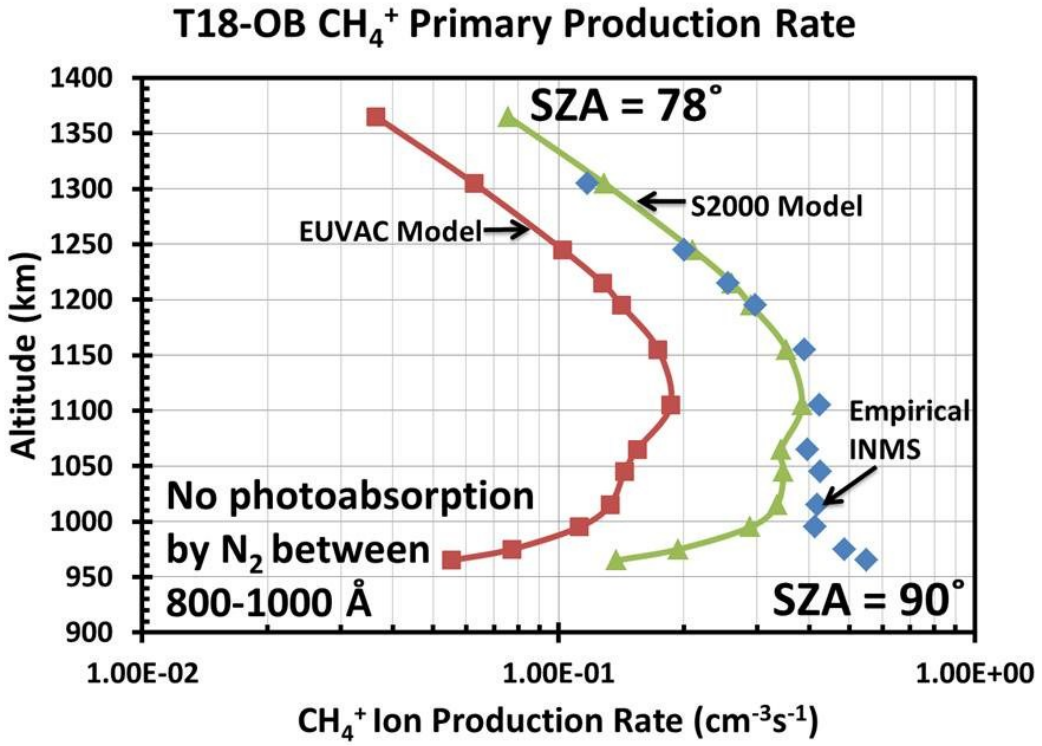

Appendix Figure C.56 Modeled photoionization production rates of CH_4^+ from photoionization and electron impact ionization by photoelectrons compared to the empirical production rate of CH_4^+ derived from INMS data from the T18-Outbound flyby of Titan. Solar photons with wavelengths between 800 and 1000 Å did not interact with N_2. INMS data is indicated with the blue diamonds, results for the Solar 2000 and EUVAC models of the solar flux are shown with green triangles and red squares respectively. The solar zenith angle at closest approach and at the uppermost altitude is indicated at the bottom and top of the figure. The solar zenith angle is adjusted to reflect the conditions observed by the Cassini spacecraft.

C-7 Globally Averaged Ion Production Rates for Various Solar Zenith Angles Using a Radial Magnetic Field Line and the T40 SOLAR2000 Model of the Solar Flux

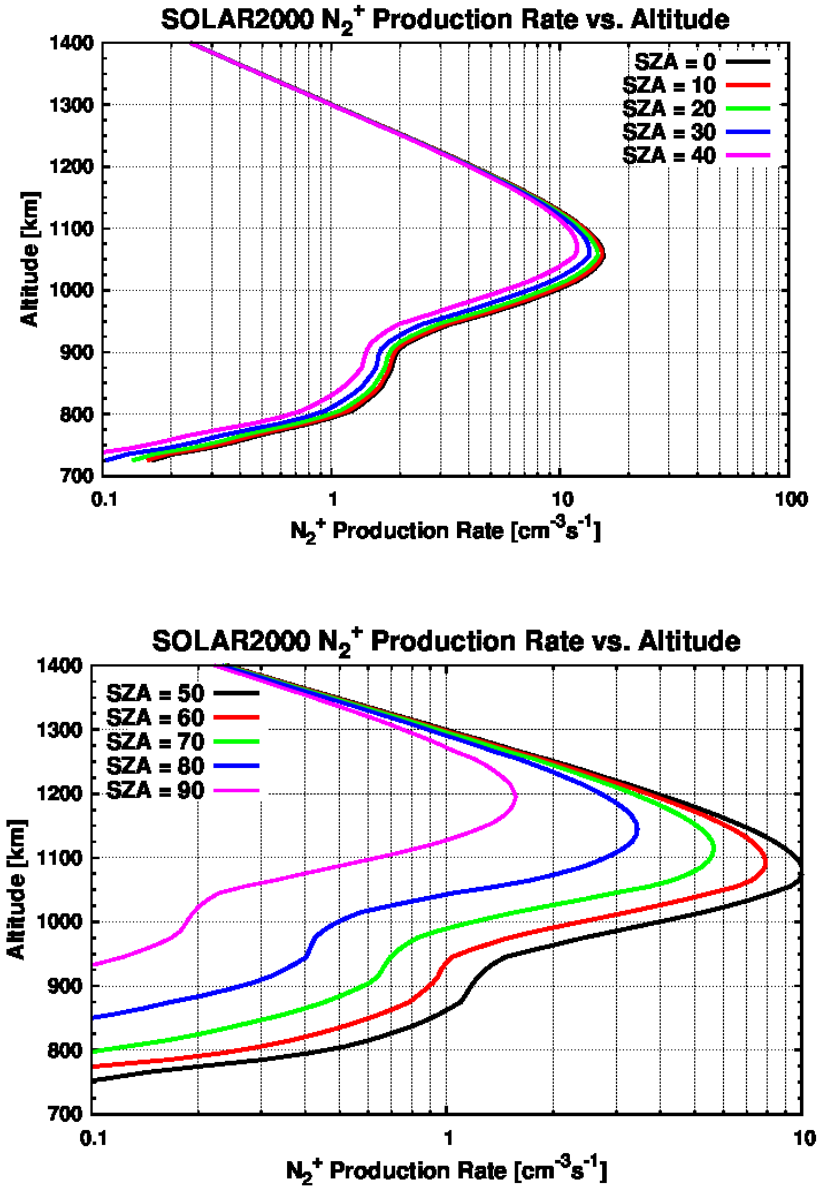

Appendix Figure C.57 Production rate of N_2^+ resulting from the photoionization and photoelectron impact ionization of the global average model of the ionosphere of Titan using the SOLAR2000 model of the solar photon flux for T40 conditions and a radial magnetic field line for solar zenith angles between 0° and 40° (above) and between 50° and 90° (below).

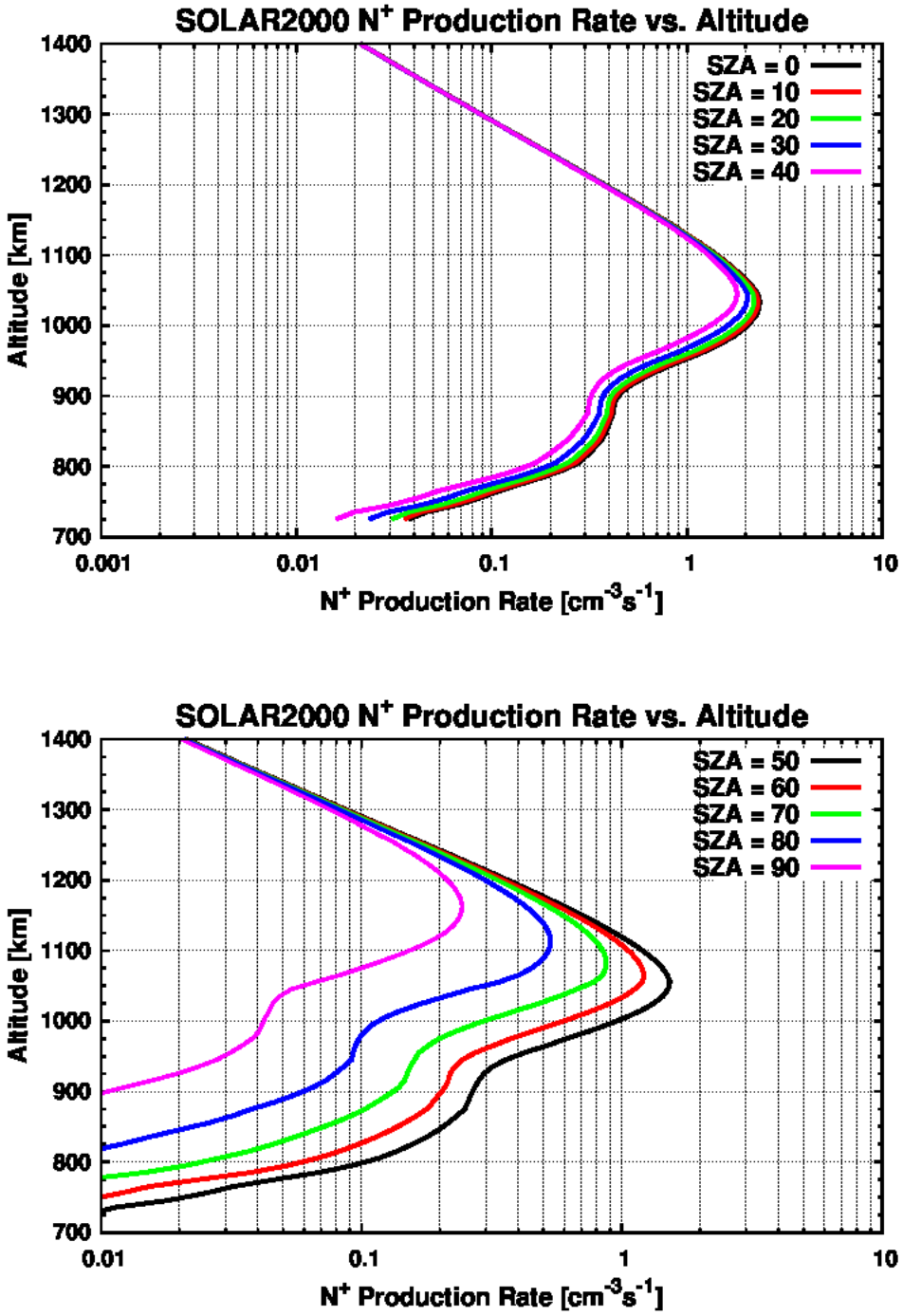

Appendix Figure C.58 Production rate of N^+ resulting from the photoionization and photoelectron impact ionization of the global average model of the ionosphere of Titan using the SOLAR2000 model of the solar photon flux for T40 conditions and a radial magnetic field line for solar zenith angles between 0° and 40° (above) and between 50° and 90° (below).

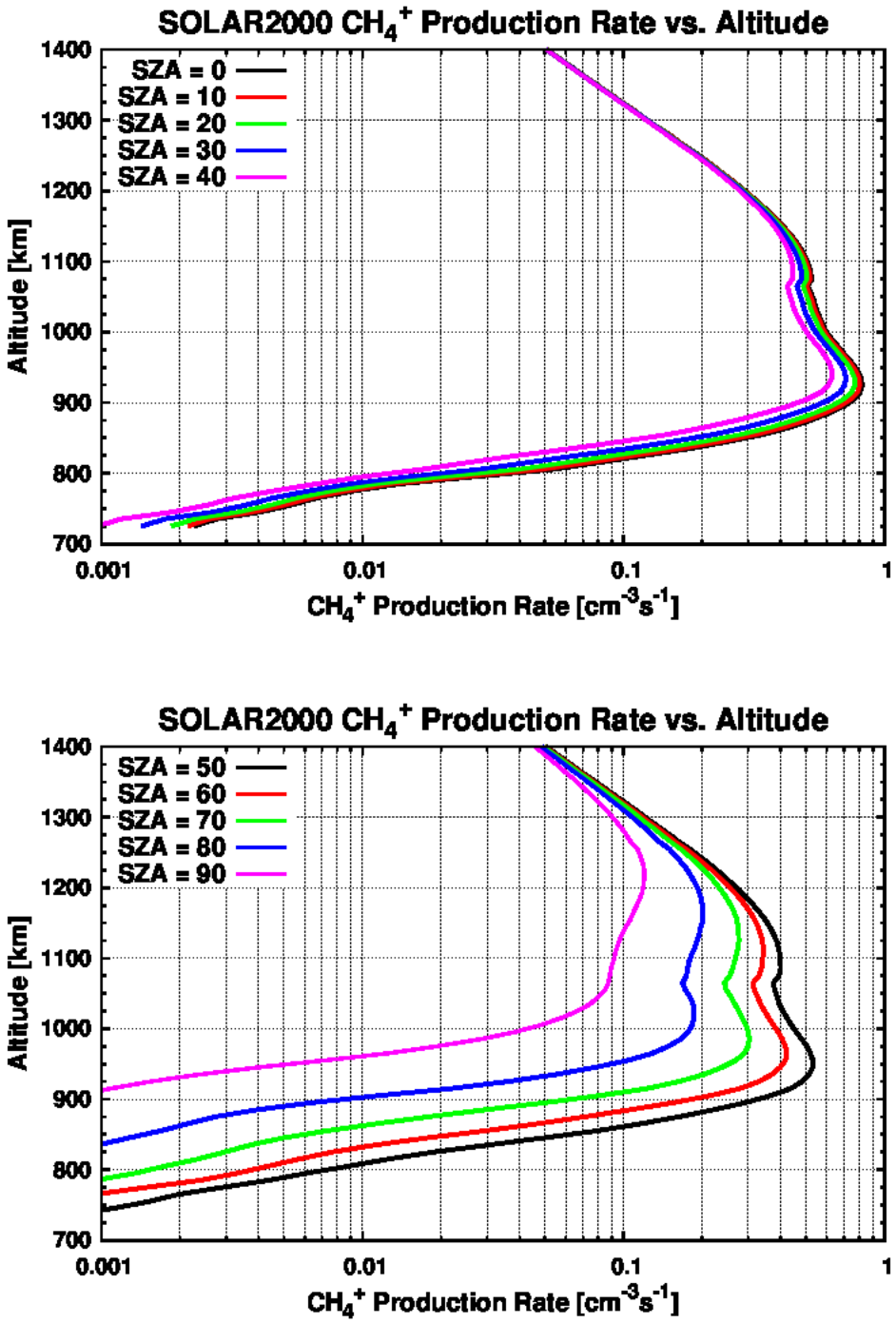

Appendix Figure C.59 Production rate of CH_4^+ resulting from the photoionization and photoelectron impact ionization of the global average model of the ionosphere of Titan using the SOLAR2000 model of the solar photon flux for T40 conditions and a radial magnetic field line for solar zenith angles between 0° and 40° (above) and between 50° and 90° (below).

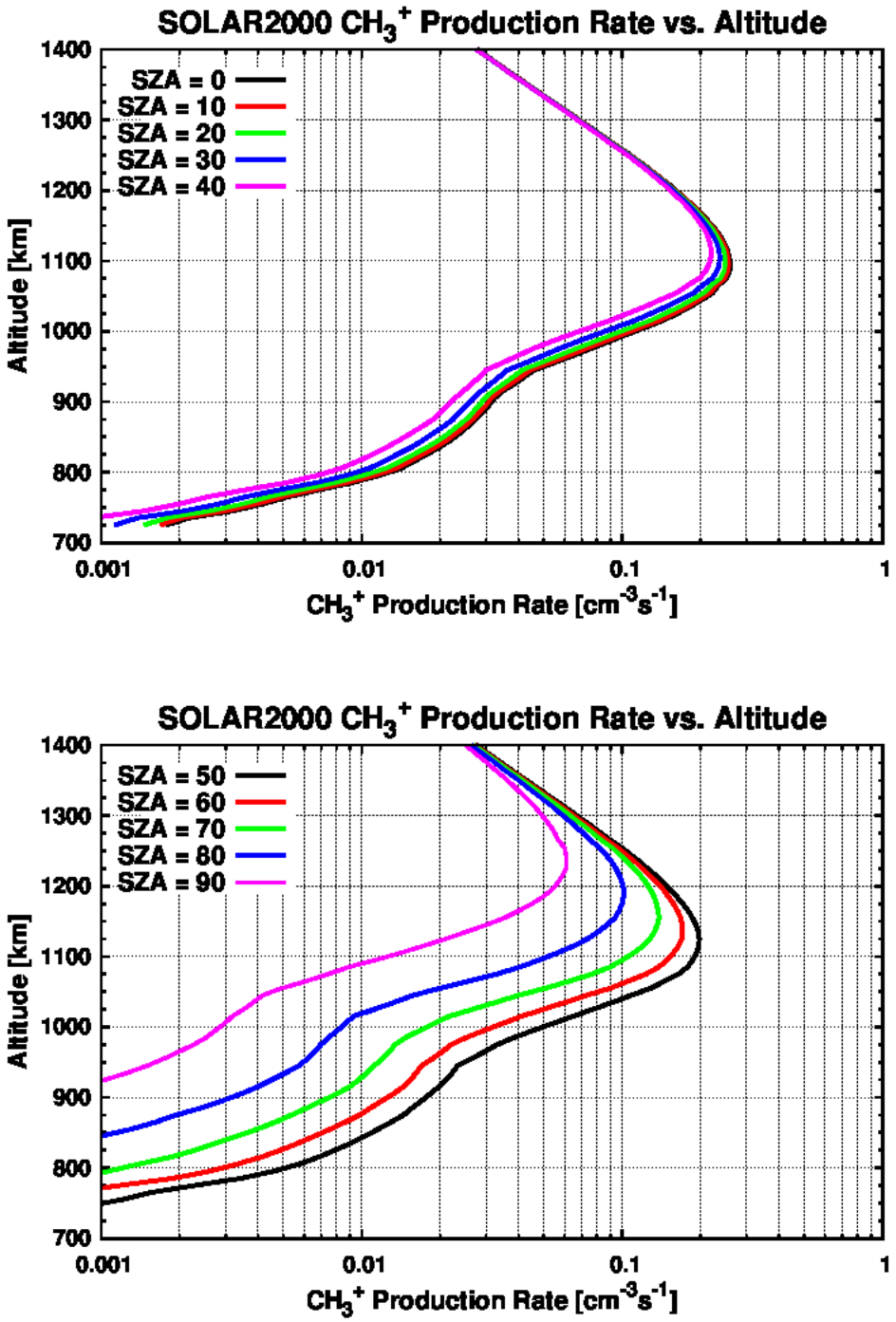

Appendix Figure C.60 Production rate of CH_3^+ resulting from the photoionization and photoelectron impact ionization of the global average model of the ionosphere of Titan using the SOLAR2000 model of the solar photon flux for T40 conditions and a radial magnetic field line for solar zenith angles between 0° and 40° (above) and between 50° and 90° (below).

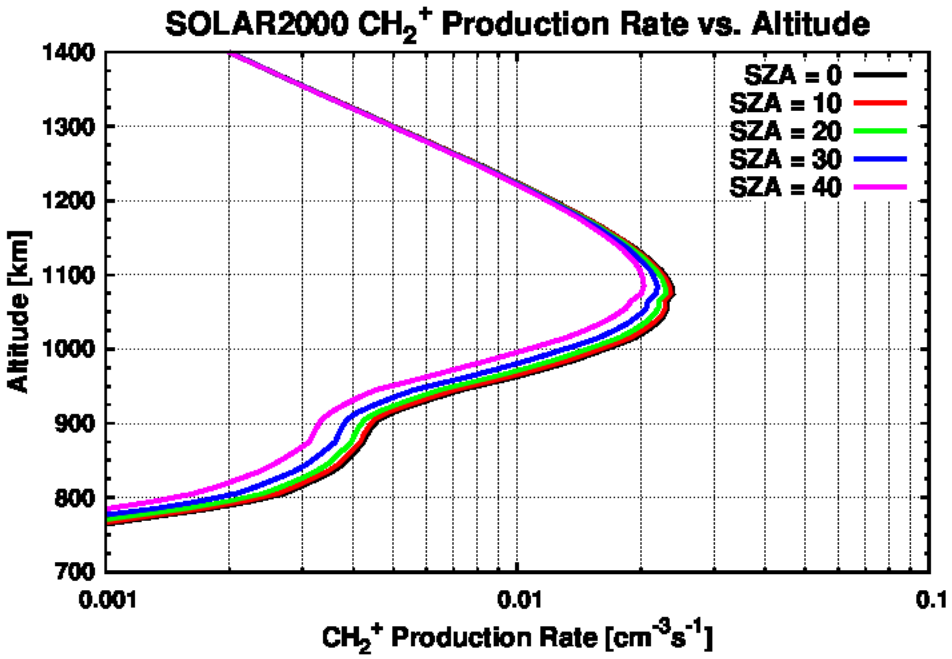

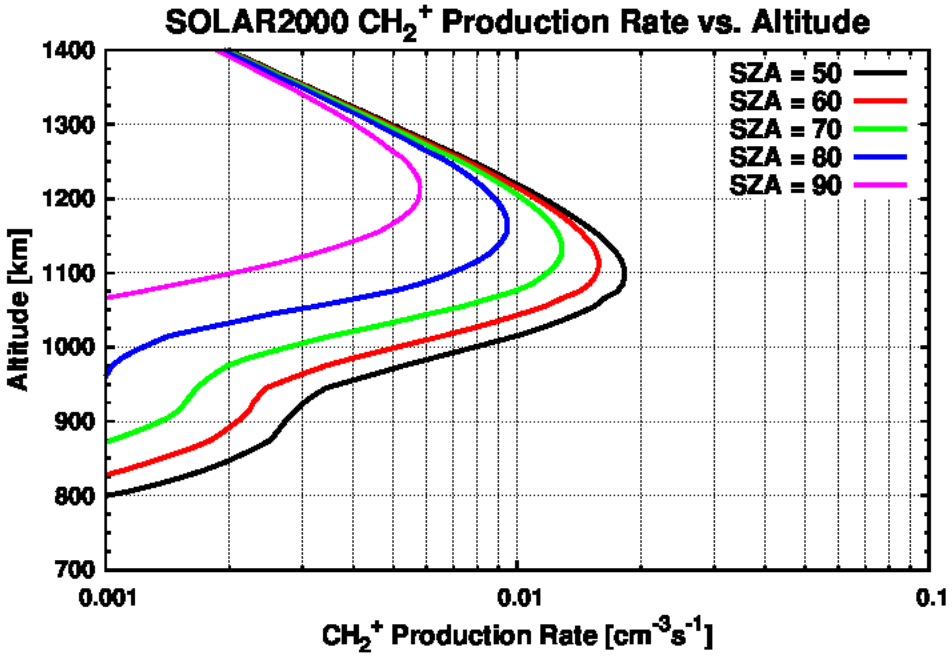

Appendix Figure C.61 Production rate of CH_2^+ resulting from the photoionization and photoelectron impact ionization of the global average model of the ionosphere of Titan using the SOLAR2000 model of the solar photon flux for T40 conditions and a radial magnetic field line for solar zenith angles between 0˚ and 40˚ (above) and between 50˚ and 90˚ (below).

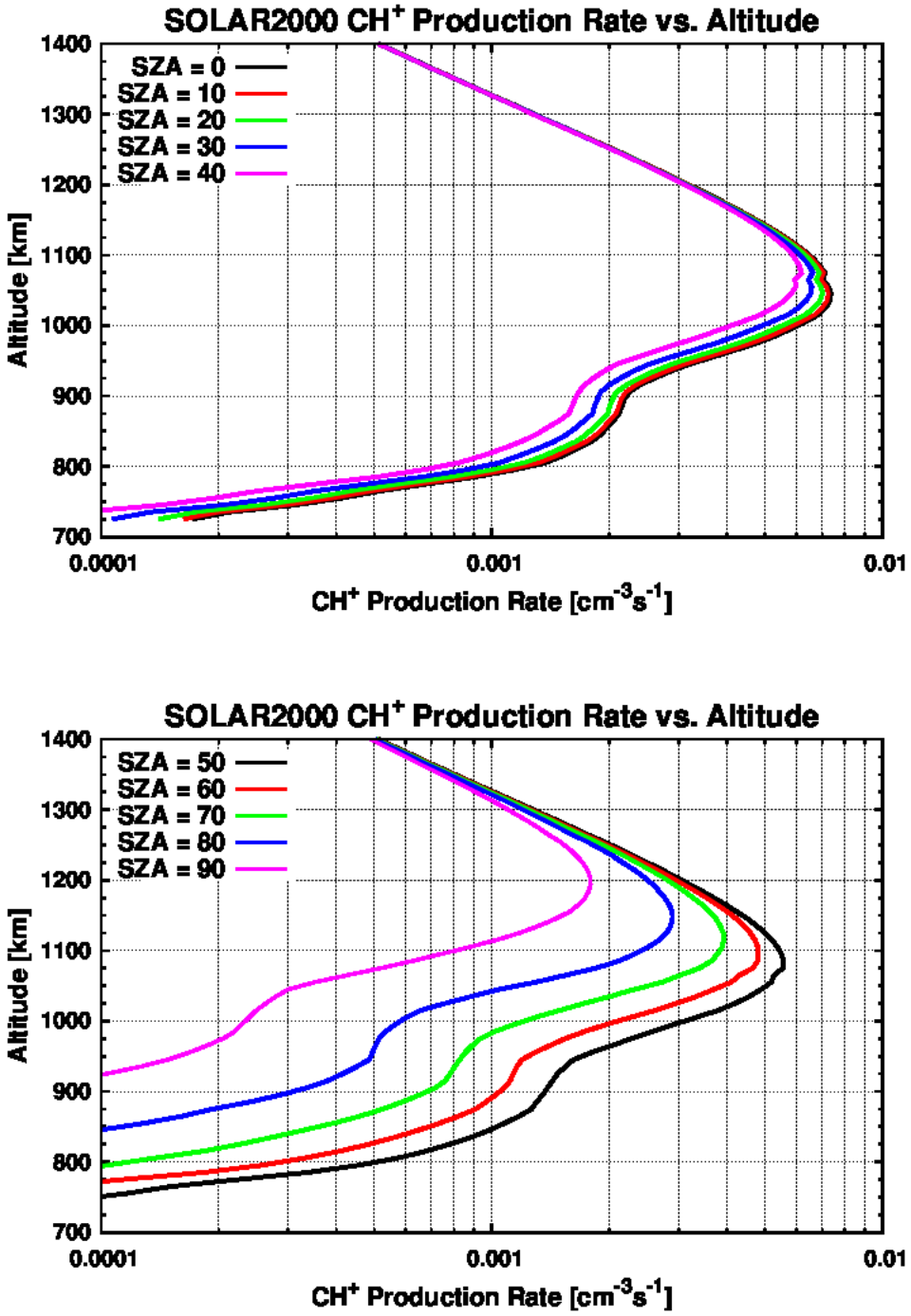

Appendix Figure C.62 Production rate of CH^+ resulting from the photoionization and photoelectron impact ionization of the global average model of the ionosphere of Titan using the SOLAR2000 model of the solar photon flux for T40 conditions and a radial magnetic field line for solar zenith angles between 0° and 40° (above) and between 50° and 90° (below).

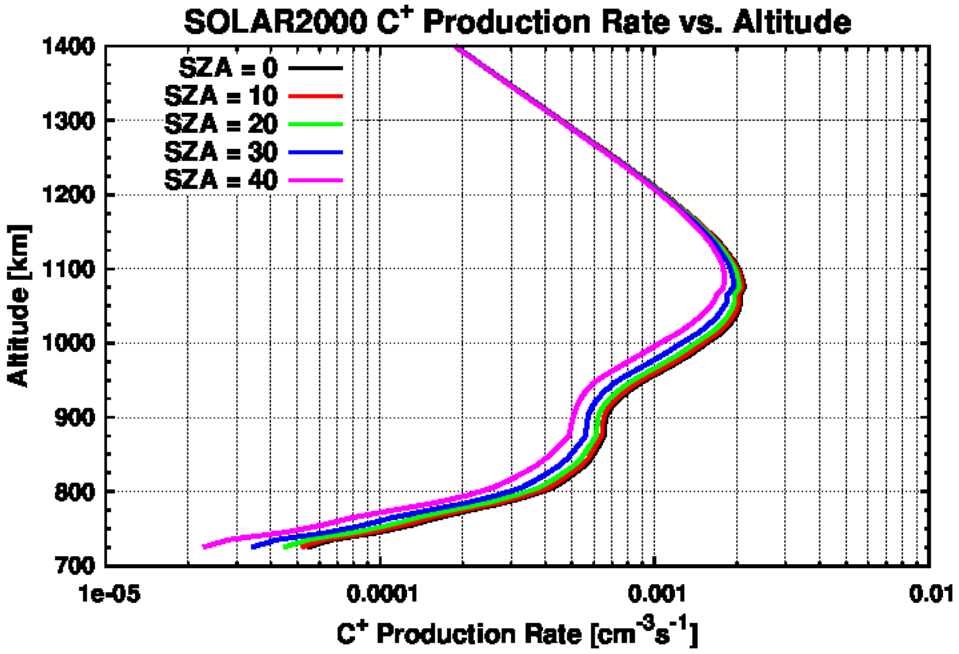

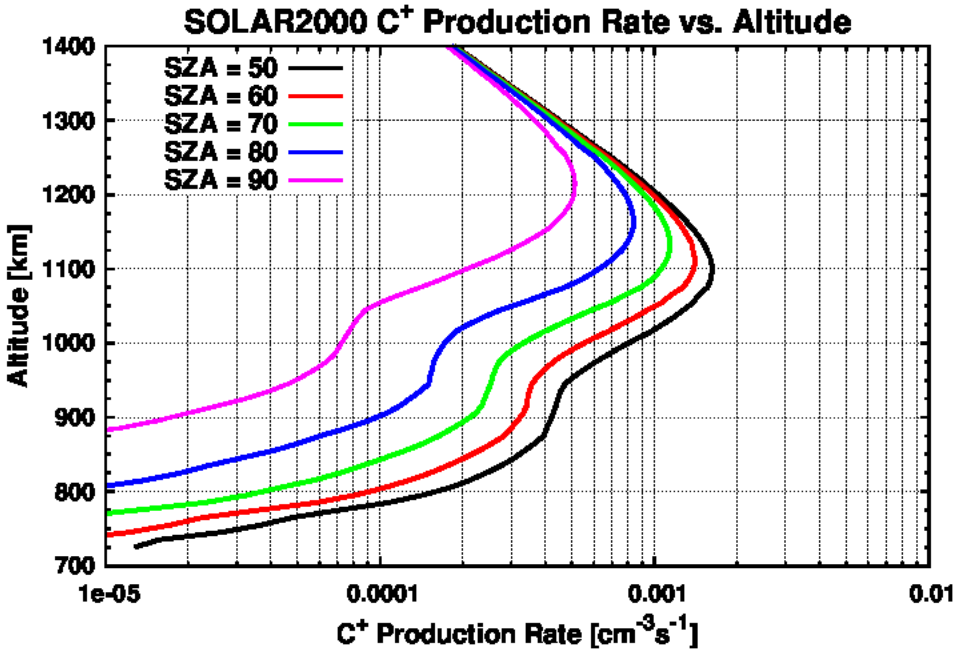

Appendix Figure C.63 Production rate of C^+ resulting from the photoionization and photoelectron impact ionization of the global average model of the ionosphere of Titan using the SOLAR2000 model of the solar photon flux for T40 conditions and a radial magnetic field line for solar zenith angles between 0° and 40° (above) and between 50° and 90° (below).

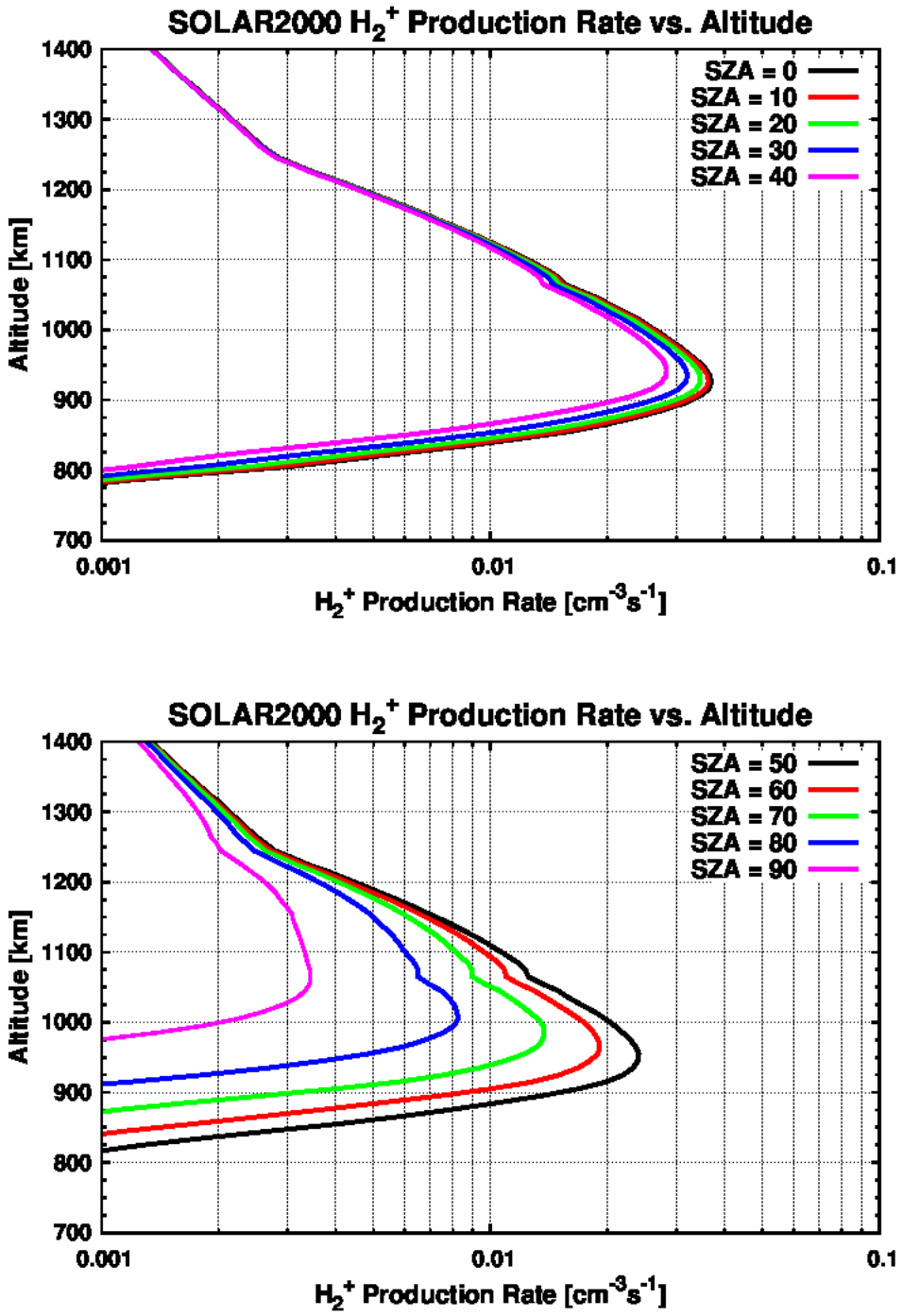

Appendix Figure C.64 Production rate of H_2^+ resulting from the photoionization and photoelectron impact ionization of the global average model of the ionosphere of Titan using the SOLAR2000 model of the solar photon flux for T40 conditions and a radial magnetic field line for solar zenith angles between 0° and 40° (above) and between 50° and 90° (below).

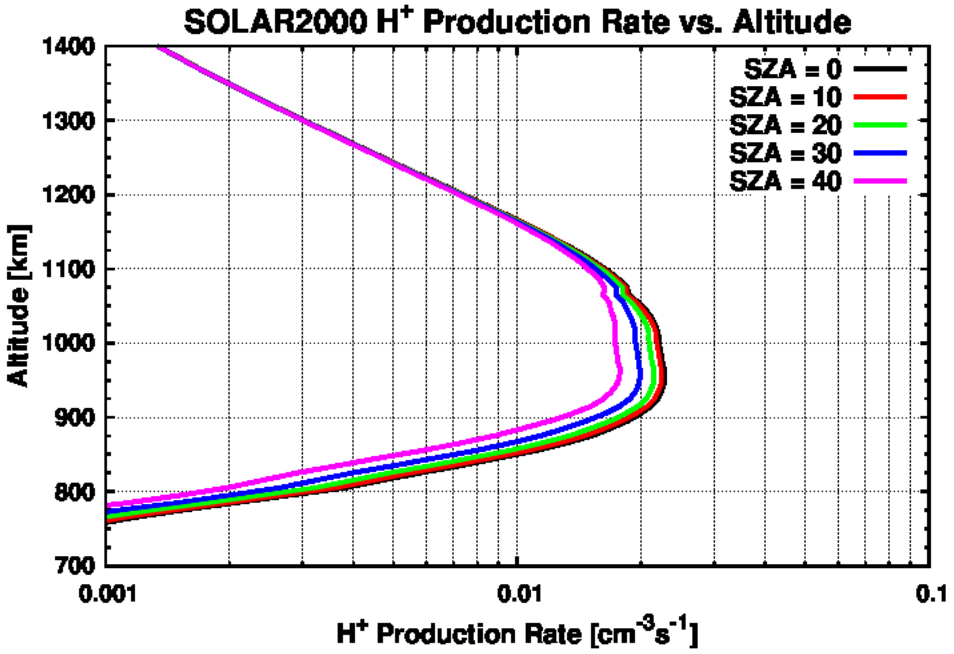

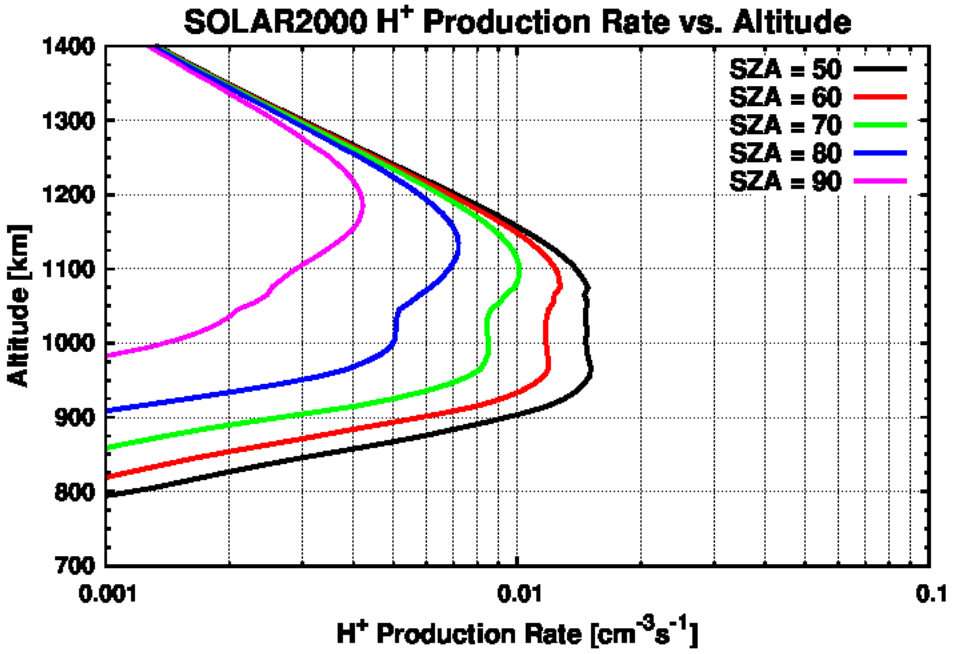

Appendix Figure C.65 Production rate of H^+ resulting from the photoionization and photoelectron impact ionization of the global average model of the ionosphere of Titan using the SOLAR2000 model of the solar photon flux for T40 conditions and a radial magnetic field line for solar zenith angles between 0° and 40° (above) and between 50° and 90° (below).

Appendix D Magnetospheric Electron Ion Production

Ion production rate comparisons, not shown in the text, for the T5 and T57 nightside flybys of Titan will be shown in this appendix. The rates shown here are generated using the full magnetospheric electron fluxes observed by the CAPS ELS instrument. Following this, production rate profiles for the primary ionization products of N_2 and CH_4 will be shown using radial and parabolic, both anchored at 725 km, magnetic field line topologies.

D-1 Ion Production Comparisons for the T5 Flyby

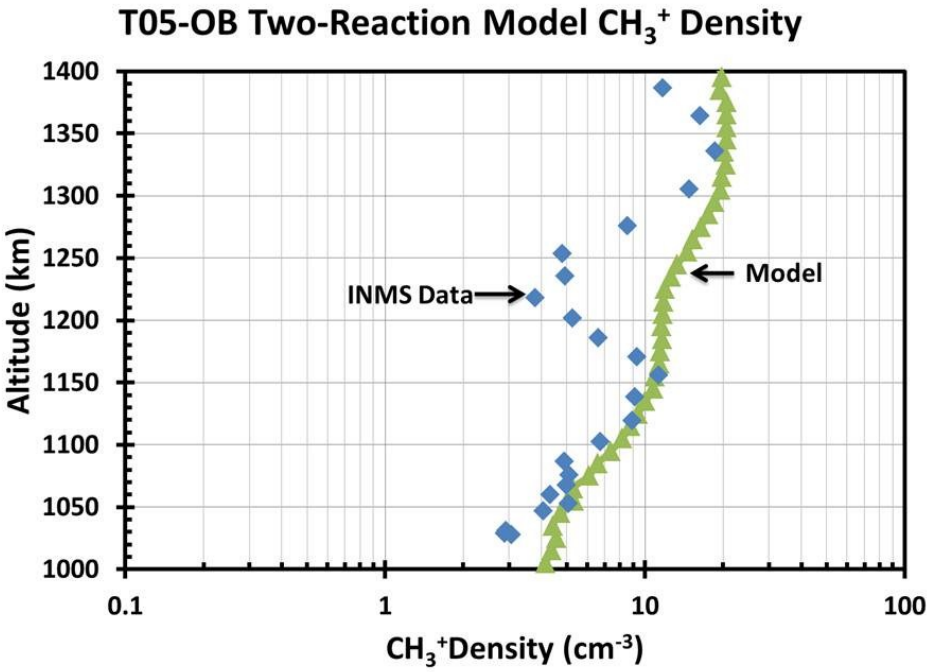

Appendix Figure D.1 Density of CH_3^+ derived from model production rates from a simple two reaction chemical model using the full T5 magnetospheric electron flux measured by CAPS/ELS [*Cravens et al.*, 2008] as an input (Figure 7.3) compared to INMS data from the T5-Outbound flyby of Titan. INMS data are indicated with the blue diamonds. This model uses the magnetic field topology of a single parabola anchored at the surface of Titan to simulate a curved field line with a large radial component.

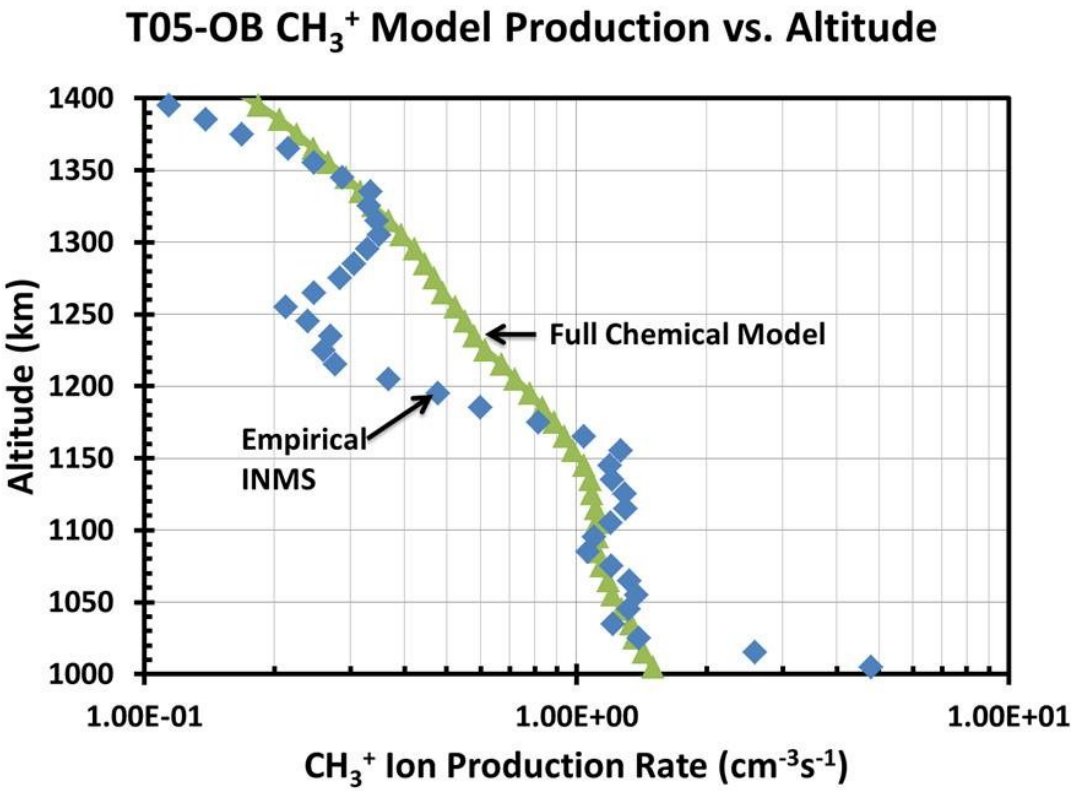

Appendix Figure D.2 CH_3^+ density produced by the full photochemical model using the full T5 magnetospheric electron flux measured by CAPS/ELS [*Cravens et al.*, 2008] as an input (Figure 7.3) compared to INMS data from the T5-Outbound flyby of Titan. INMS data are indicated with the blue diamonds. This model uses the magnetic field topology of a single parabola anchored at the surface of Titan to simulate a curved field line with a large radial component.

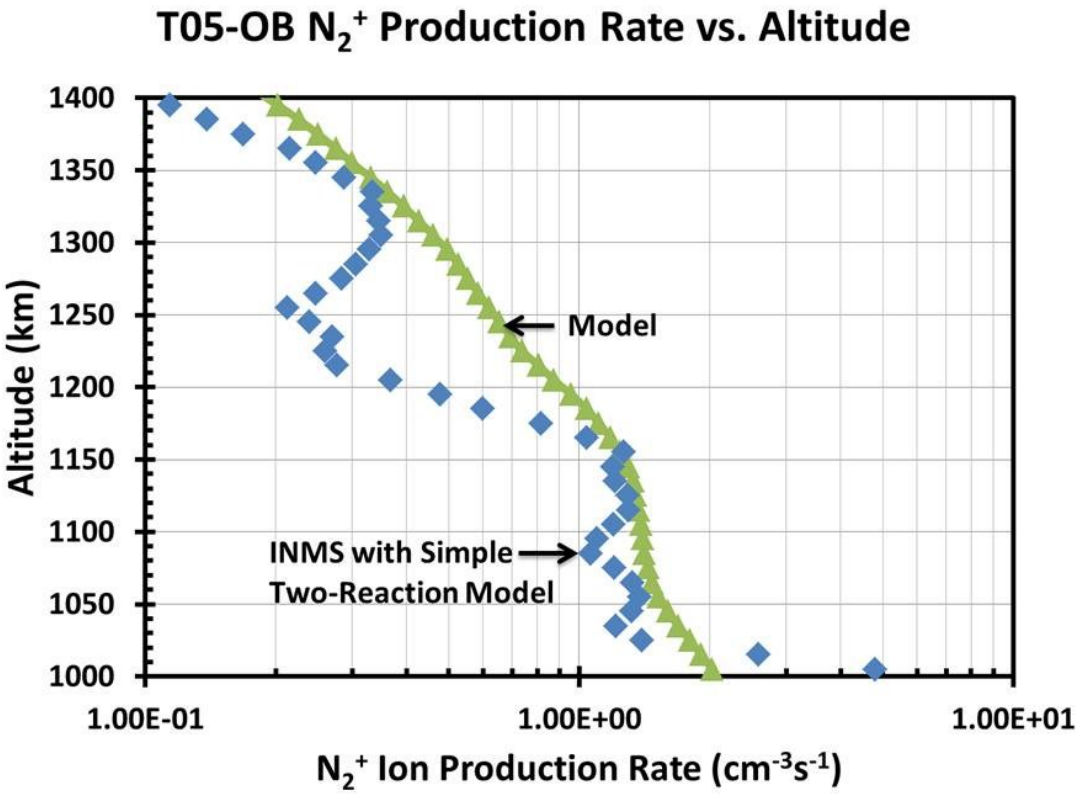

Appendix Figure D.3 Modeled electron impact ionization production rates of N_2^+ using the full T5 magnetospheric electron flux measured by CAPS/ELS [*Cravens et al.*, 2008] as an input (Figure 7.3) compared to the empirical production rate of N_2^+ derived from INMS data (blue diamonds) from the T5-Outbound flyby of Titan. This model uses the magnetic field topology of a single parabola anchored at the surface of Titan to simulate a curved field line with a large radial component.

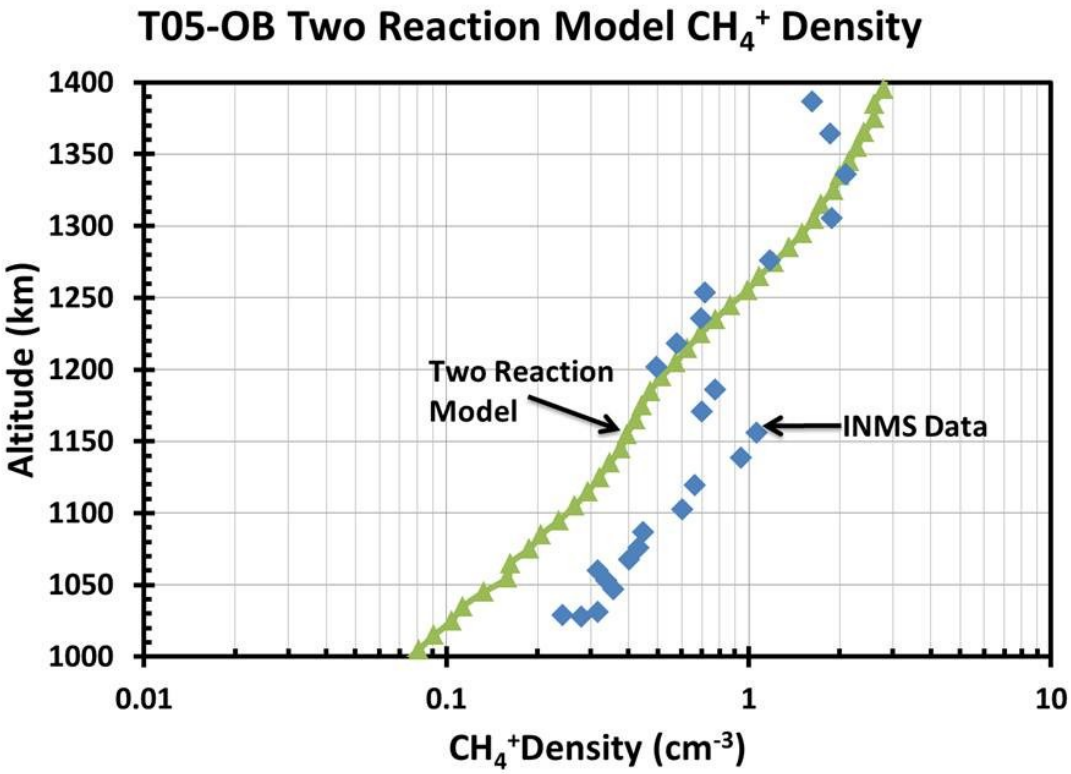

Appendix Figure D.4 Density of CH_4^+ calculated using the simple two reaction chemical model (Equation (4.10)) and the electron impact ionization model using the full T5 magnetospheric electron flux measured by CAPS/ELS [*Cravens et al.*, 2008] as an input (Figure 7.3) compared to INMS data from the T5-Outbound flyby of Titan. INMS data are indicated with the blue diamonds. This model uses the magnetic field topology of a single parabola anchored at the surface of Titan to simulate a curved field line with a large radial component.

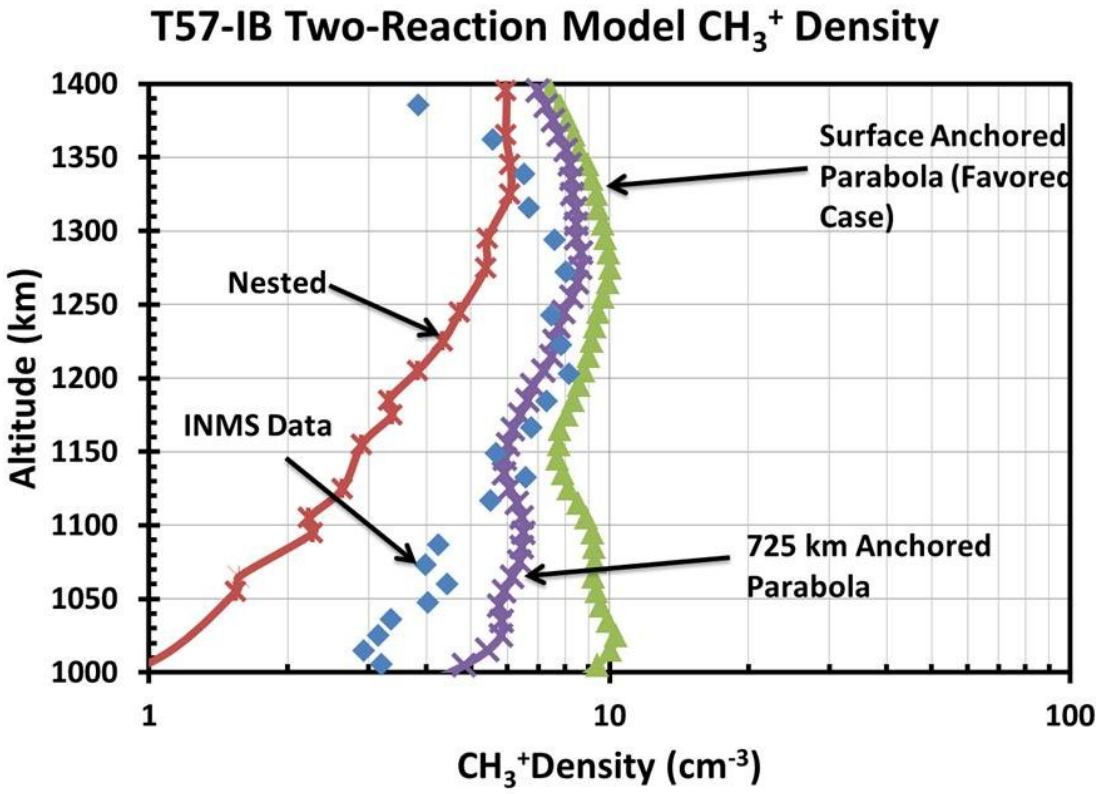

Appendix Figure D.5 Density of CH_3^+ derived from model production rates using a simple two reaction chemical model with magnetic field line topologies of a parabola achored at the surface of Titan (green triangles), a parabola anchored at 725 km (purple crosses) and nested parabola (red stars) using the T57 magnetospheric electron flux measured by CAPS/ELS [*Kliore et al.*, 2011] as an input (Figure 7.11) compared to INMS data from the T57-Outbound flyby of Titan. INMS data are indicated with the blue diamonds.

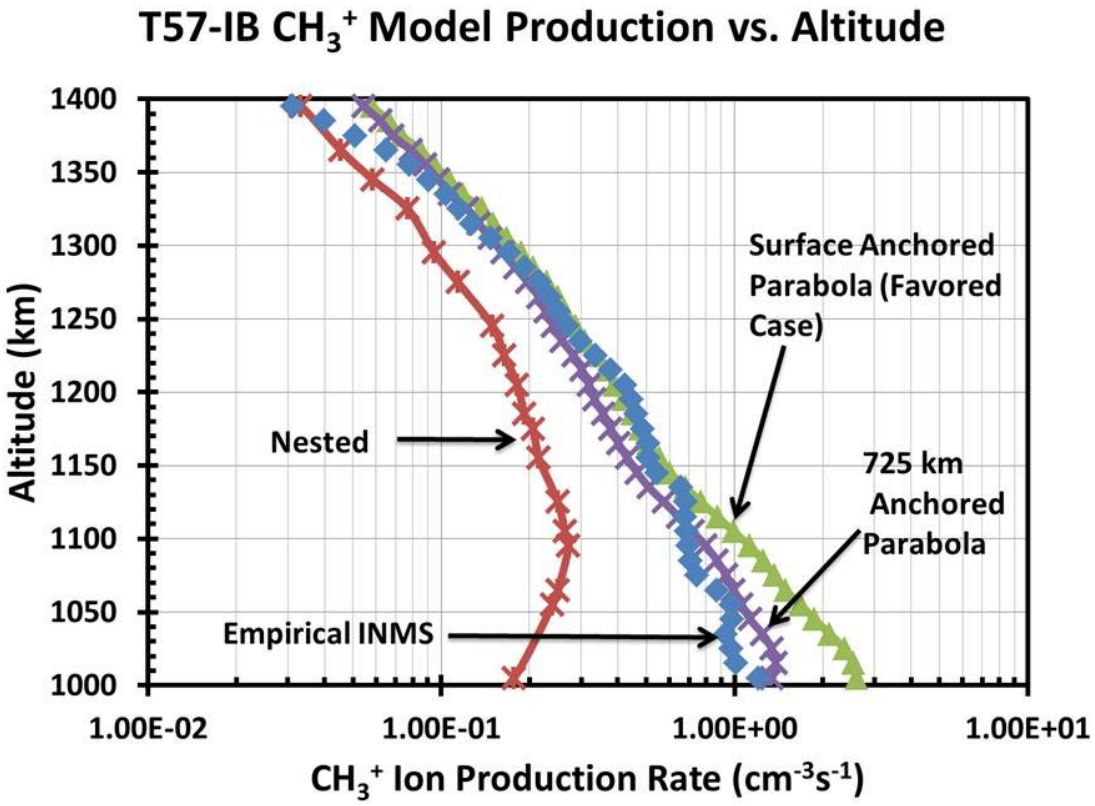

Appendix Figure D.6 CH_3^+ density produced by the full photochemical model with magnetic field line topologies of a parabola achored at the surface of Titan (green triangles), a parabola anchored at 725 km (purple crosses) and nested parabola (red stars) using the T57 magnetospheric electron flux measured by CAPS/ELS [*Kliore et al.*, 2011] as an input (Figure 7.11) compared to INMS data from the T57-Outbound flyby of Titan. INMS data are indicated with the blue diamonds.

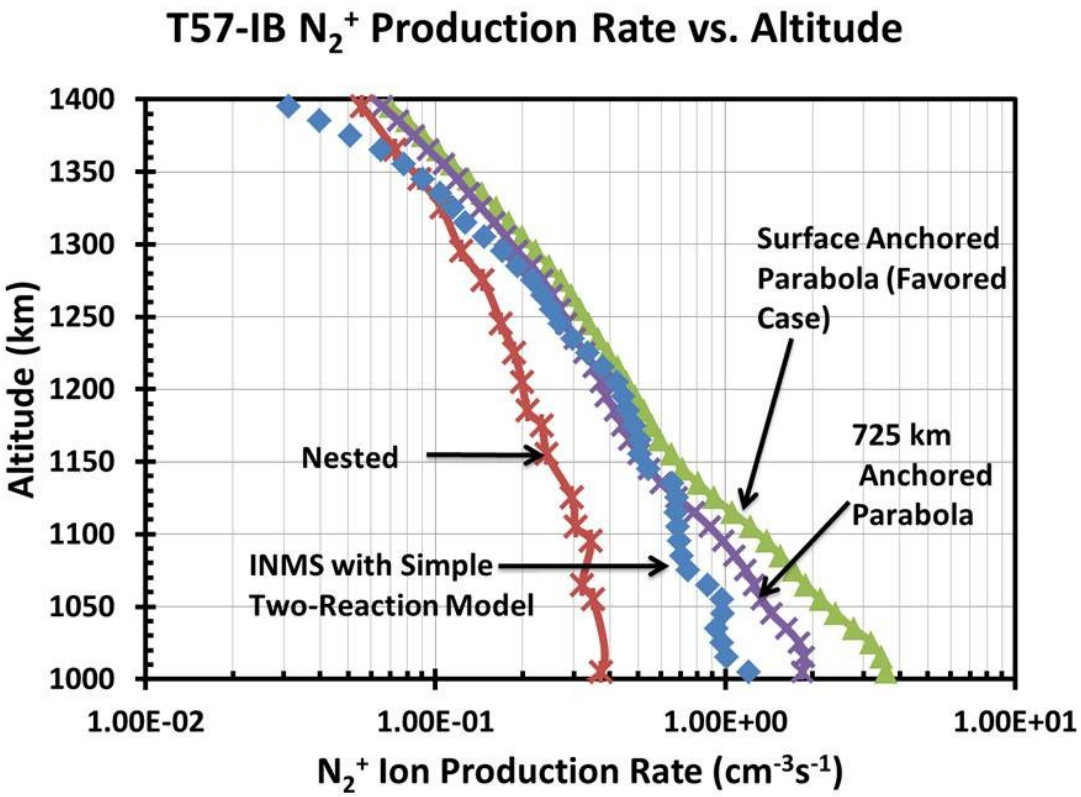

Appendix Figure D.7 Modeled electron impact ionization production rates of N_2^+ compared to the empirical production rate of N_2^+ derived from INMS data with magnetic field line topologies of a parabola achored at the surface of Titan (green triangles), a parabola anchored at 725 km (purple crosses) and nested parabola (red stars) using the T57 magnetospheric electron flux measured by CAPS/ELS [*Kliore et al.*, 2011] as an input (Figure 7.11) compared to INMS data from the T57-Outbound flyby of Titan.

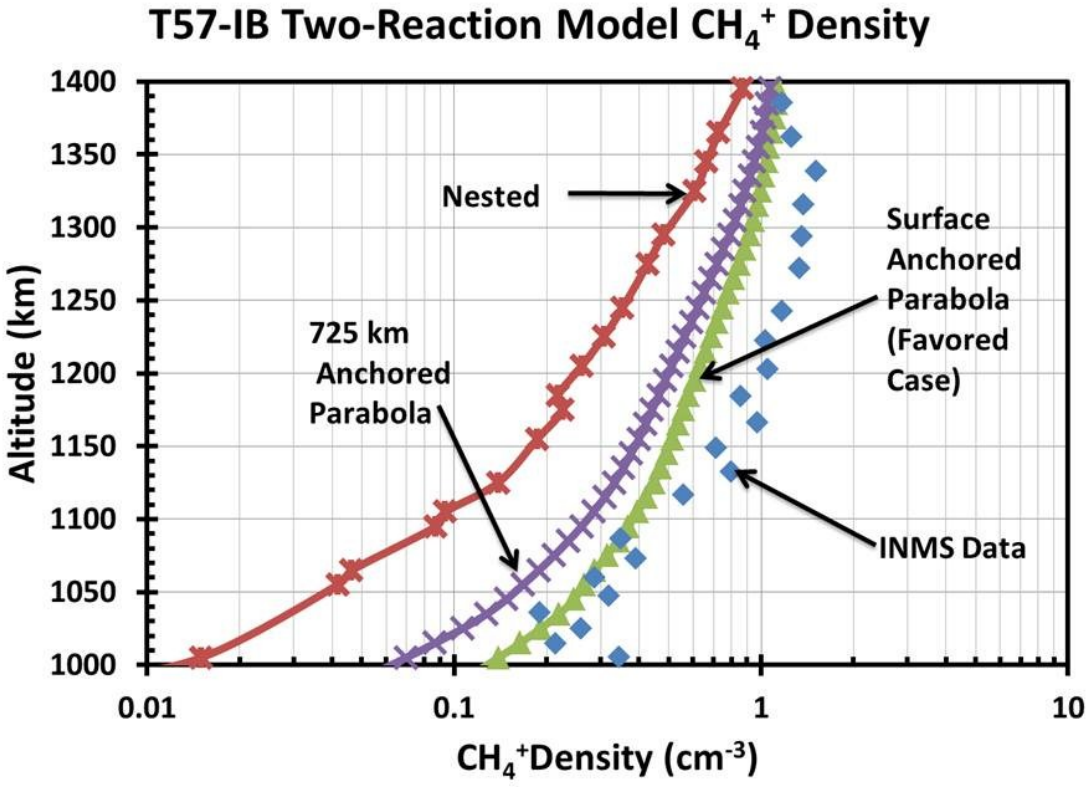

Appendix Figure D.8 Density of CH_4^+ calculated using the simple two reaction chemical model (Equation (4.10)) and the electron impact ionization model with magnetic field line topologies of a parabola achored at the surface of Titan (green triangles), a parabola anchored at 725 km (purple crosses) and nested parabola (red stars) using the T57 magnetospheric electron flux measured by CAPS/ELS [*Kliore et al.*, 2011] as an input (Figure 7.11) compared to INMS data from the T57-Outbound flyby of Titan. INMS data are indicated with the blue diamonds.

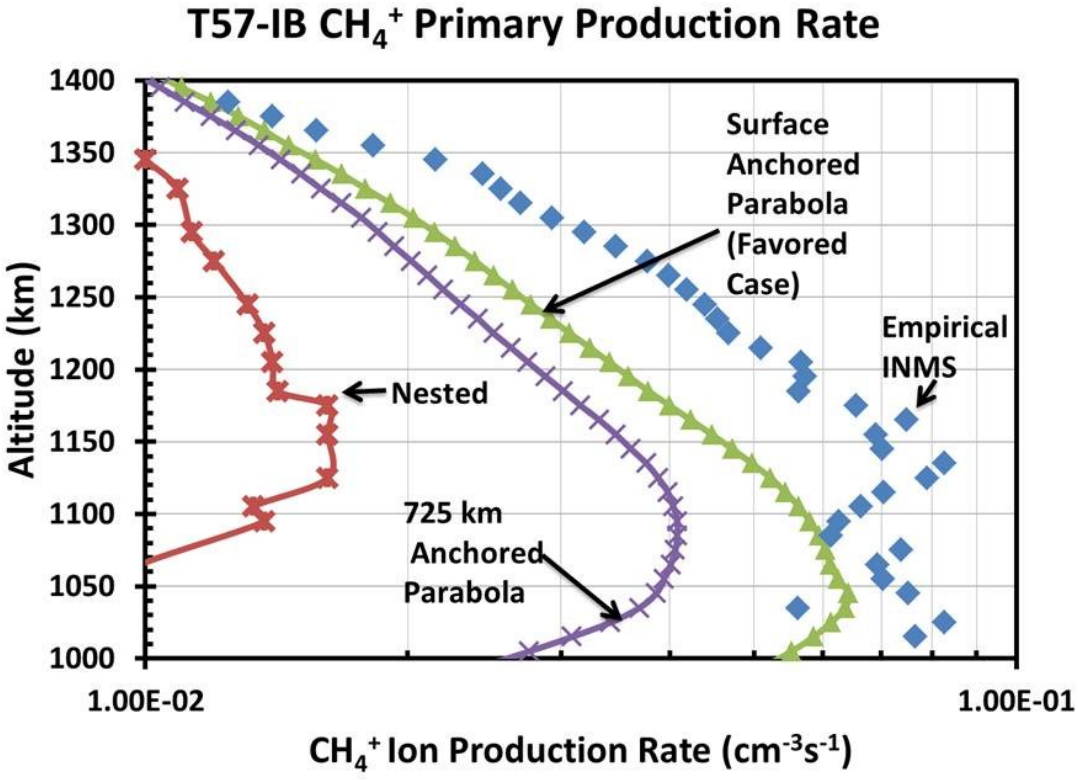

Appendix Figure D.9 Modeled electron impact ionization production rates of CH_4^+ using magnetic field line topologies of a parabola achored at the surface of Titan (green triangles), a parabola anchored at 725 km (purple crosses) and nested parabola (red stars) using the T57 magnetospheric electron flux measured by CAPS/ELS [*Kliore et al.*, 2011] as an input (Figure 7.11) compared to empirical production rates of CH_4^+ derived from INMS data from the T57-Outbound flyby of Titan (blue diamonds).

D-3 Generic Ion Production Rates Using a Parabolic Field Line Anchored at 725 km and Magnetospheric Electron Fluxes from *Rymer et al.* [2009]

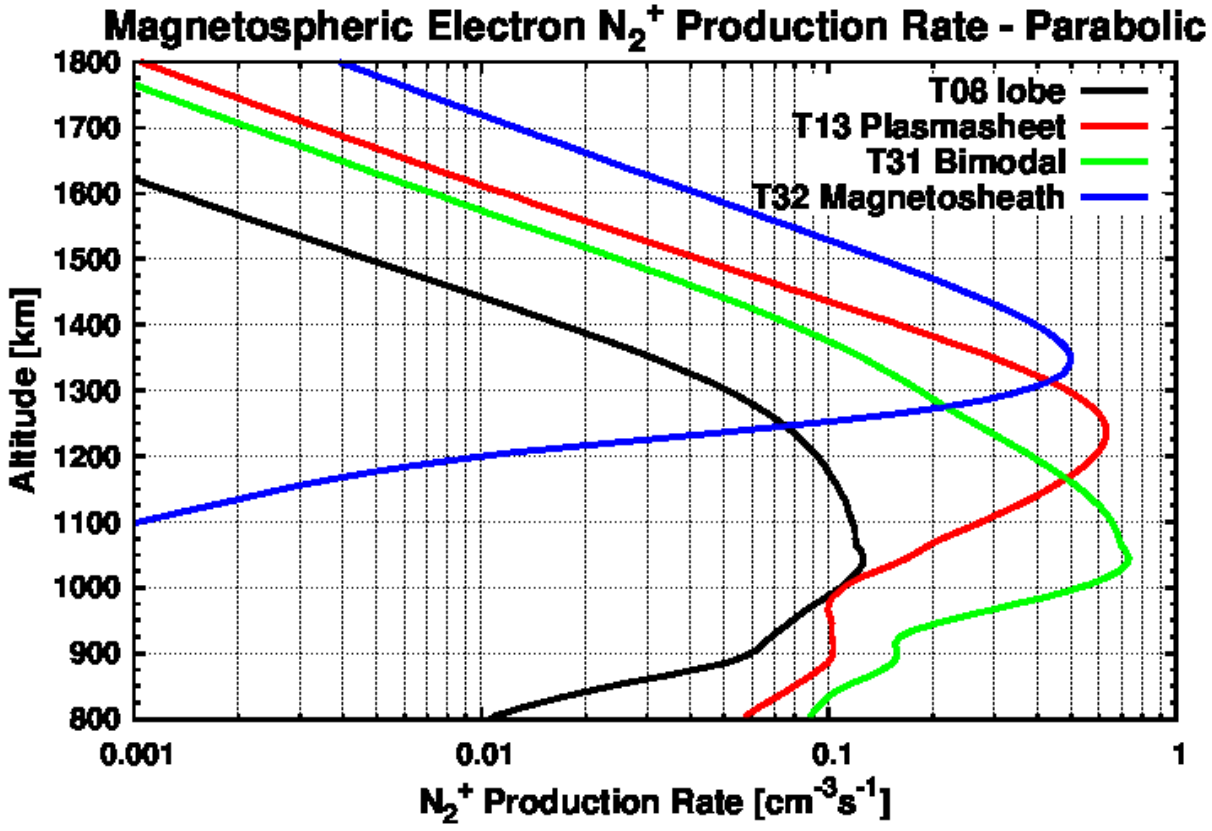

Appendix Figure D.10 Production of N_2^+ using a parabolic magnetic field line anchored at 725km and the magnetospheric electron fluxes of the *Rymer et al.* [2009] classifications. Results are shown for model runs using the T8 lobe-like (black line), the T13 plasma sheet (red line), T31 bimodal (green line) and the T32 magnetosheath (blue line) electron fluxes measured by CAPS/ELS. The magnetospheric electron flux profiles are shown in Figure 7.2.

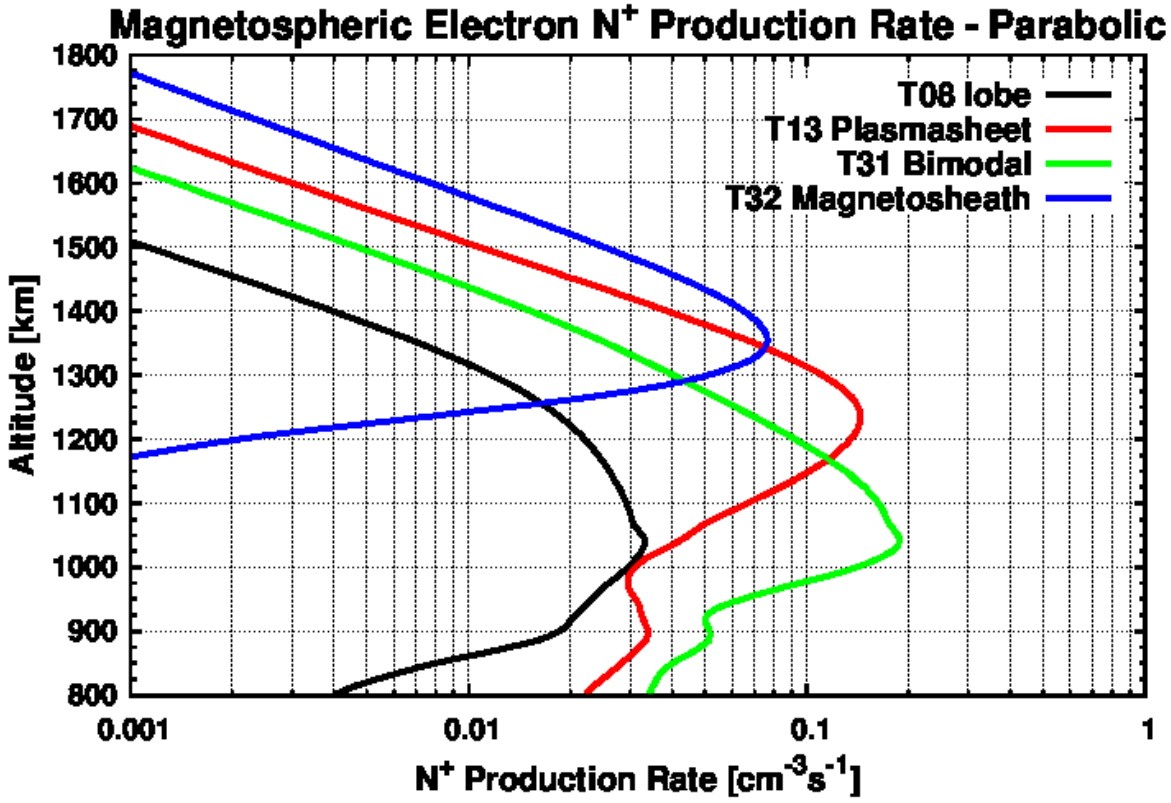

Appendix Figure D.11 Production of N^+ using a parabolic magnetic field line anchored at 725km and the magnetospheric electron fluxes of the *Rymer et al.* [2009] classifications. Results are shown for model runs using the T8 lobe-like (black line), the T13 plasma sheet (red line), T31 bimodal (green line) and the T32 magnetosheath (blue line) electron fluxes measured by CAPS/ELS. The magnetospheric electron flux profiles are shown in Figure 7.2.

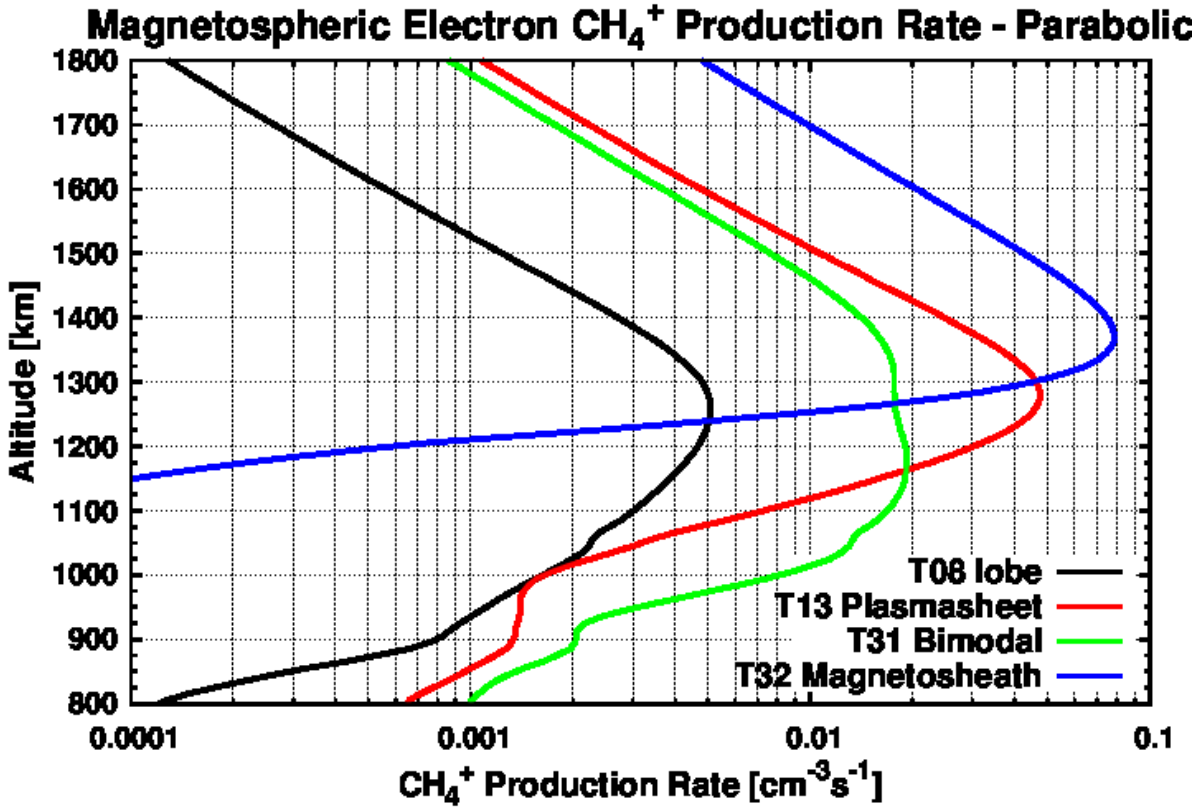

Appendix Figure D.12 Production of CH_4^+ using a parabolic magnetic field line anchored at 725km and the magnetospheric electron fluxes of the *Rymer et al.* [2009] classifications. Results are shown for model runs using the T8 lobe-like (black line), the T13 plasma sheet (red line), T31 bimodal (green line) and the T32 magnetosheath (blue line) electron fluxes measured by CAPS/ELS. The magnetospheric electron flux profiles are shown in Figure 7.2.

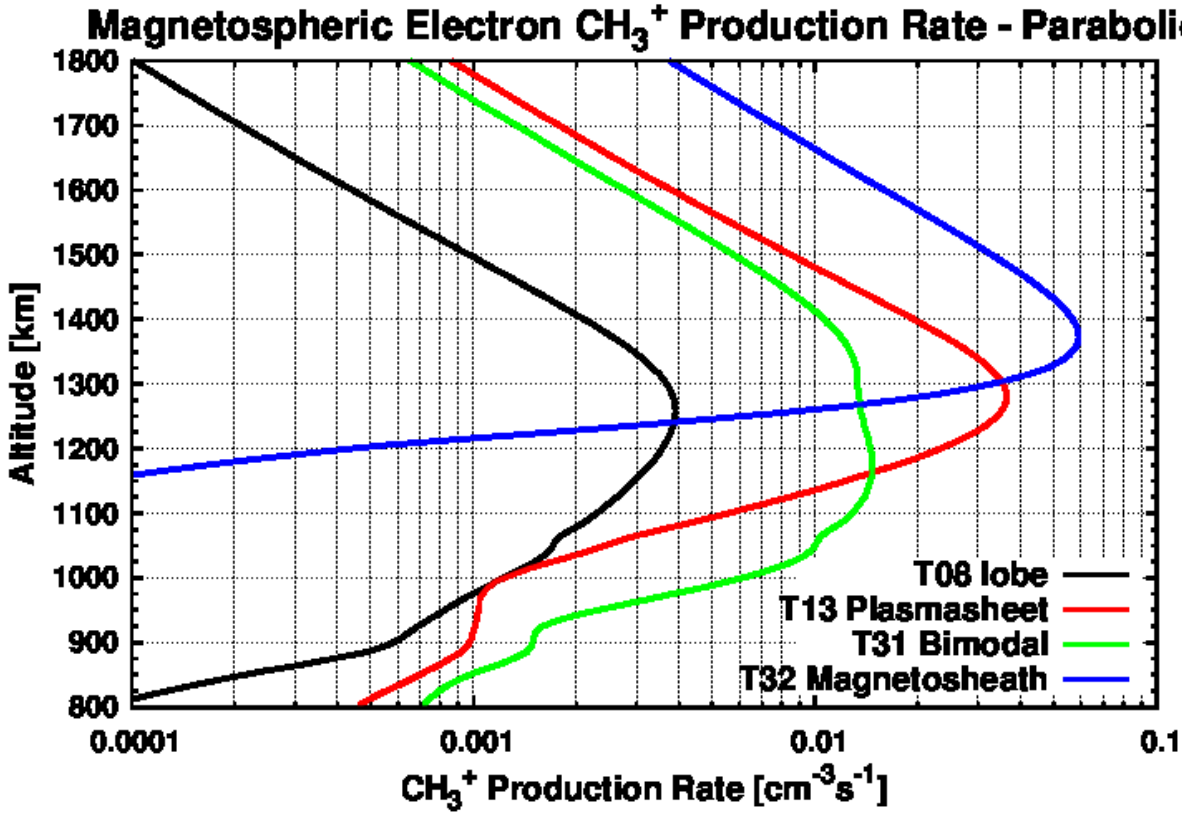

Appendix Figure D.13 Production of CH_3^+ using a parabolic magnetic field line anchored at 725km and the magnetospheric electron fluxes of the *Rymer et al.* [2009] classifications. Results are shown for model runs using the T8 lobe-like (black line), the T13 plasma sheet (red line), T31 bimodal (green line) and the T32 magnetosheath (blue line) electron fluxes measured by CAPS/ELS. The magnetospheric electron flux profiles are shown in Figure 7.2.

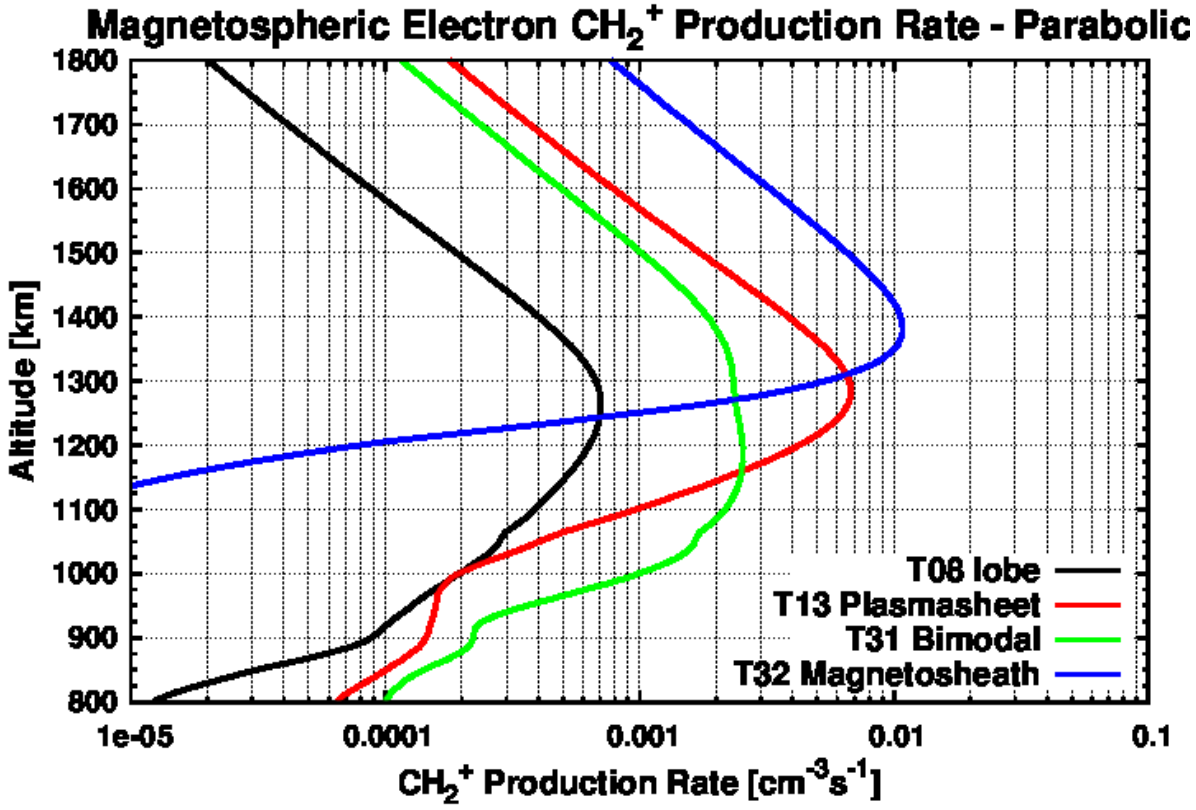

Appendix Figure D.14 Production of CH_2^+ using a parabolic magnetic field line anchored at 725km and the magnetospheric electron fluxes of the *Rymer et al.* [2009] classifications. Results are shown for model runs using the T8 lobe-like (black line), the T13 plasma sheet (red line), T31 bimodal (green line) and the T32 magnetosheath (blue line) electron fluxes measured by CAPS/ELS. The magnetospheric electron flux profiles are shown in Figure 7.2.

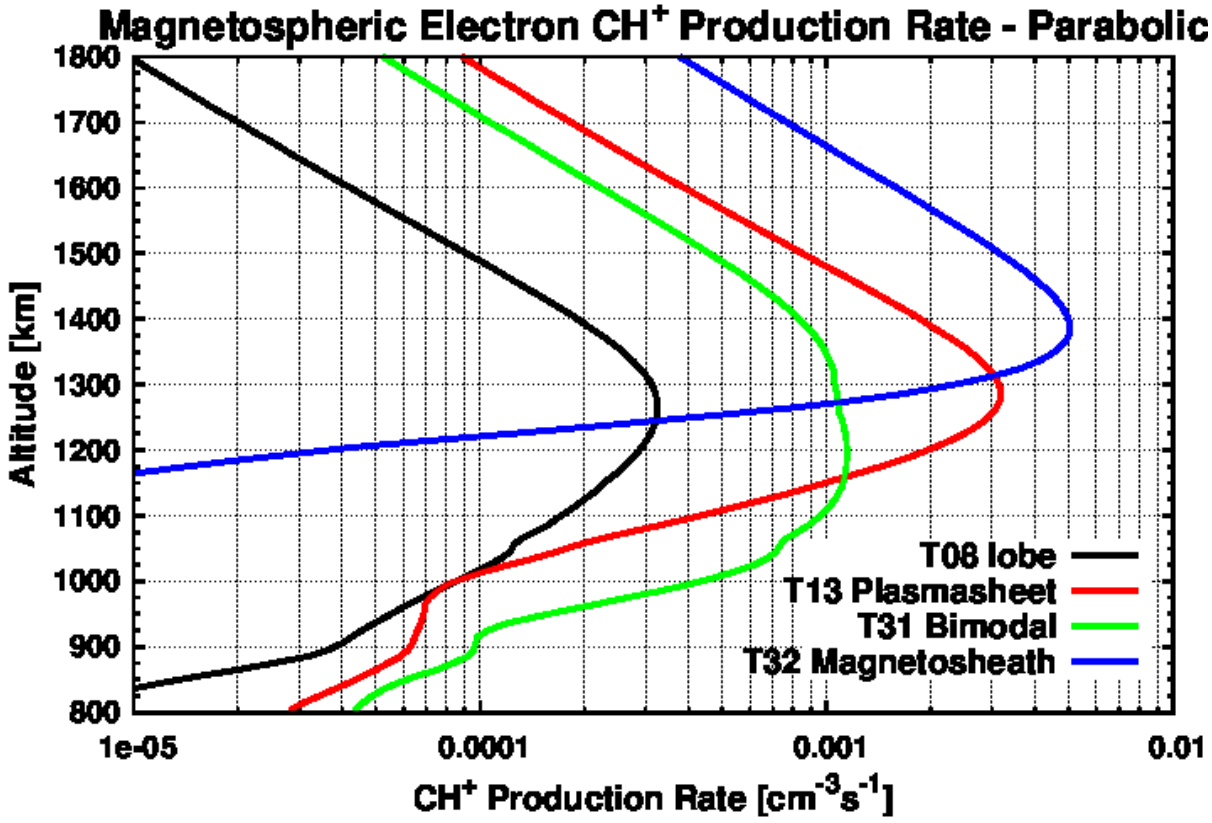

Appendix Figure D.15 Production of CH^+ using a parabolic magnetic field line anchored at 725km and the magnetospheric electron fluxes of the *Rymer et al.* [2009] classifications. Results are shown for model runs using the T8 lobe-like (black line), the T13 plasma sheet (red line), T31 bimodal (green line) and the T32 magnetosheath (blue line) electron fluxes measured by CAPS/ELS. The magnetospheric electron flux profiles are shown in Figure 7.2.

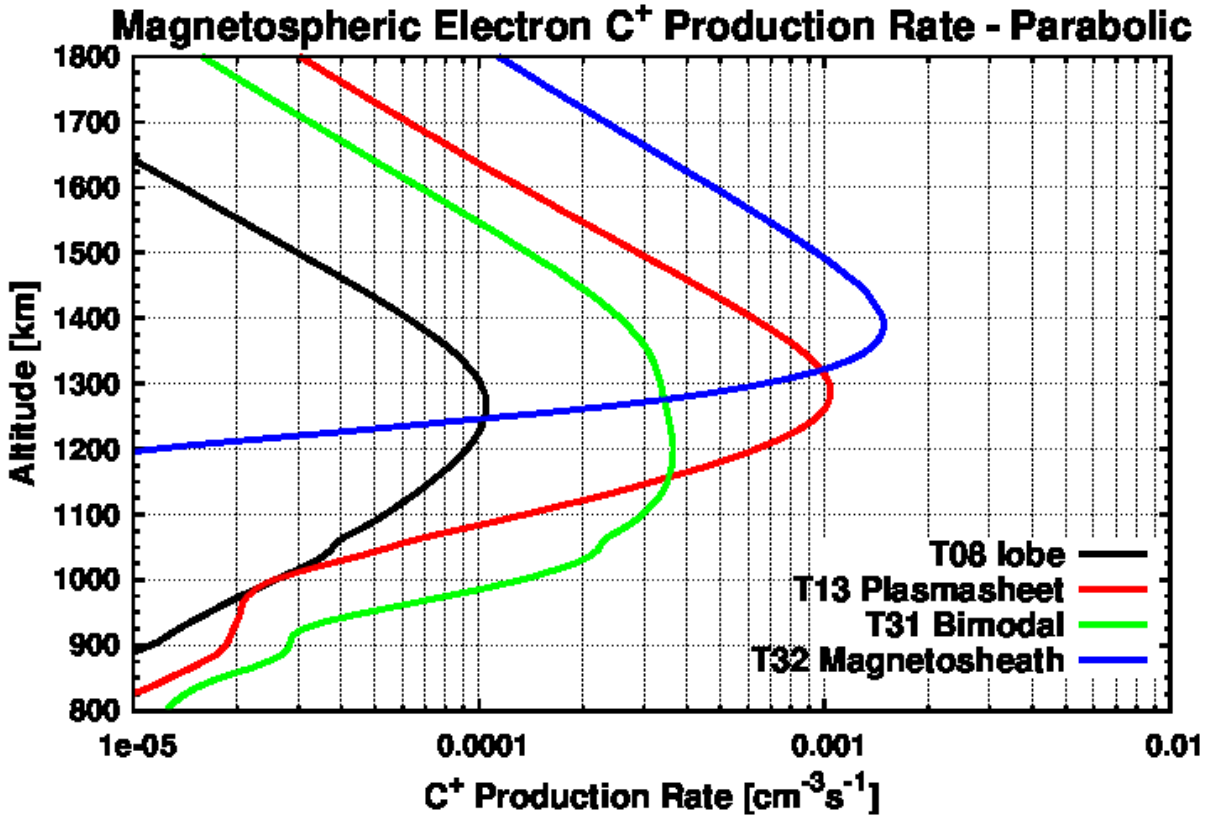

Appendix Figure D.16 Production of C^+ using a parabolic magnetic field line anchored at 725km and the magnetospheric electron fluxes of the *Rymer et al.* [2009] classifications. Results are shown for model runs using the T8 lobe-like (black line), the T13 plasma sheet (red line), T31 bimodal (green line) and the T32 magnetosheath (blue line) electron fluxes measured by CAPS/ELS. The magnetospheric electron flux profiles are shown in Figure 7.2.

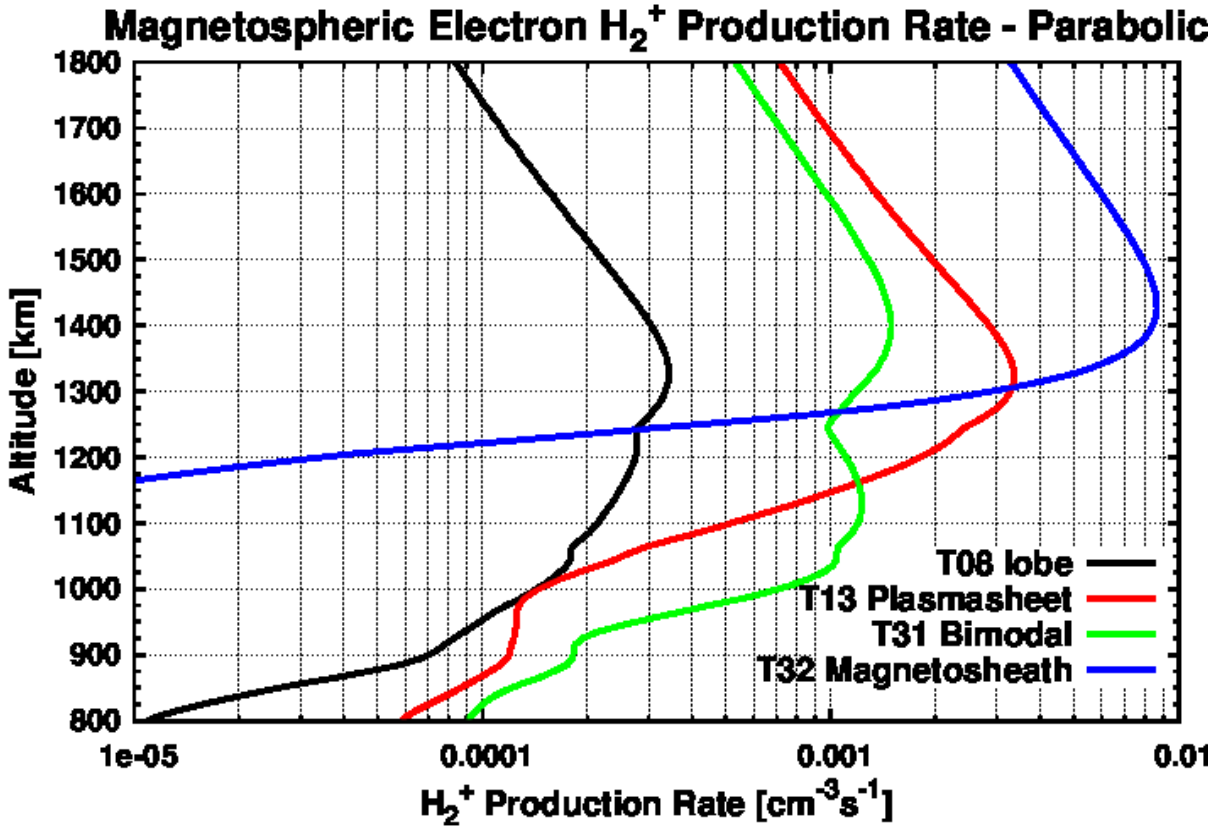

Appendix Figure D.17 Production of H_2^+ using a parabolic magnetic field line anchored at 725km and the magnetospheric electron fluxes of the *Rymer et al.* [2009] classifications. Results are shown for model runs using the T8 lobe-like (black line), the T13 plasma sheet (red line), T31 bimodal (green line) and the T32 magnetosheath (blue line) electron fluxes measured by CAPS/ELS. The magnetospheric electron flux profiles are shown in Figure 7.2.

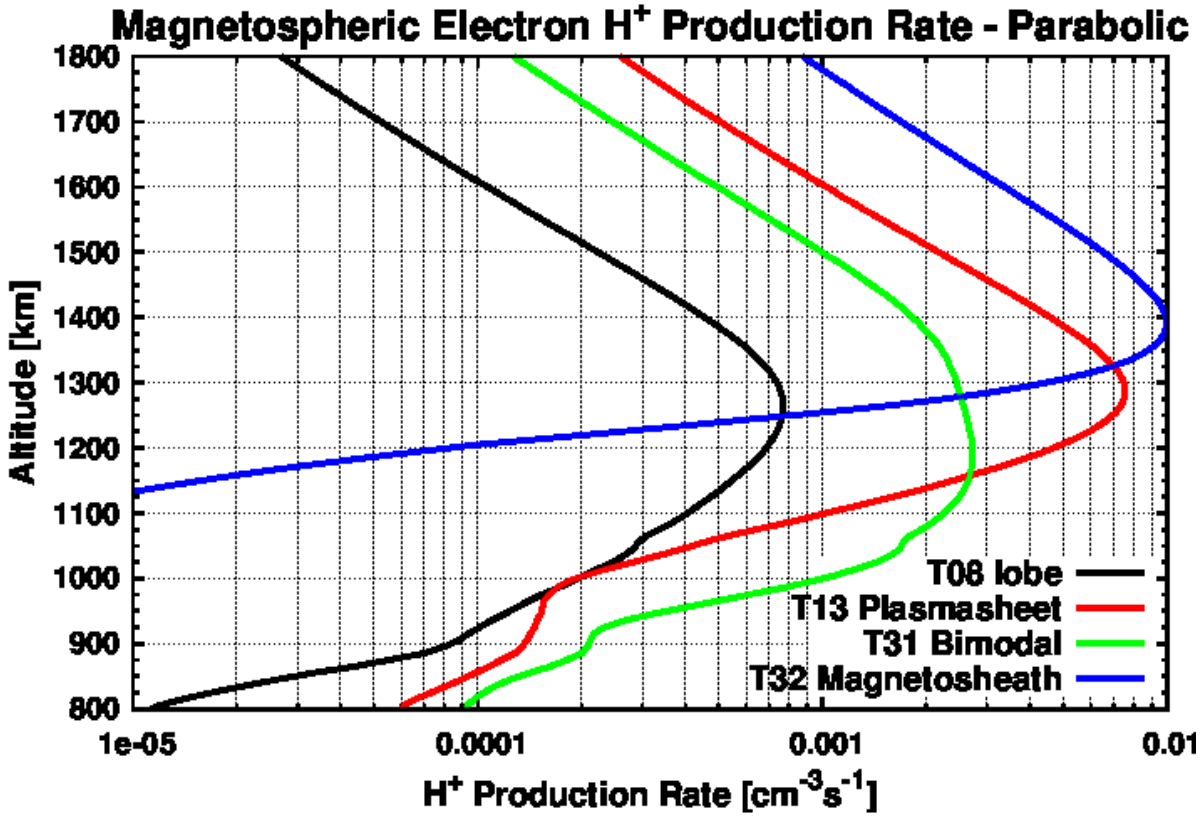

Appendix Figure D.18 Production of H^+ using a parabolic magnetic field line anchored at 725km and the magnetospheric electron fluxes of the *Rymer et al.* [2009] classifications. Results are shown for model runs using the T8 lobe-like (black line), the T13 plasma sheet (red line), T31 bimodal (green line) and the T32 magnetosheath (blue line) electron fluxes measured by CAPS/ELS. The magnetospheric electron flux profiles are shown in Figure 7.2.

D-4 Generic Ion Production Rates Using a Radial Field Line Anchored at 725 km and Magnetospheric Electron Fluxes from *Rymer et al.* [2009]

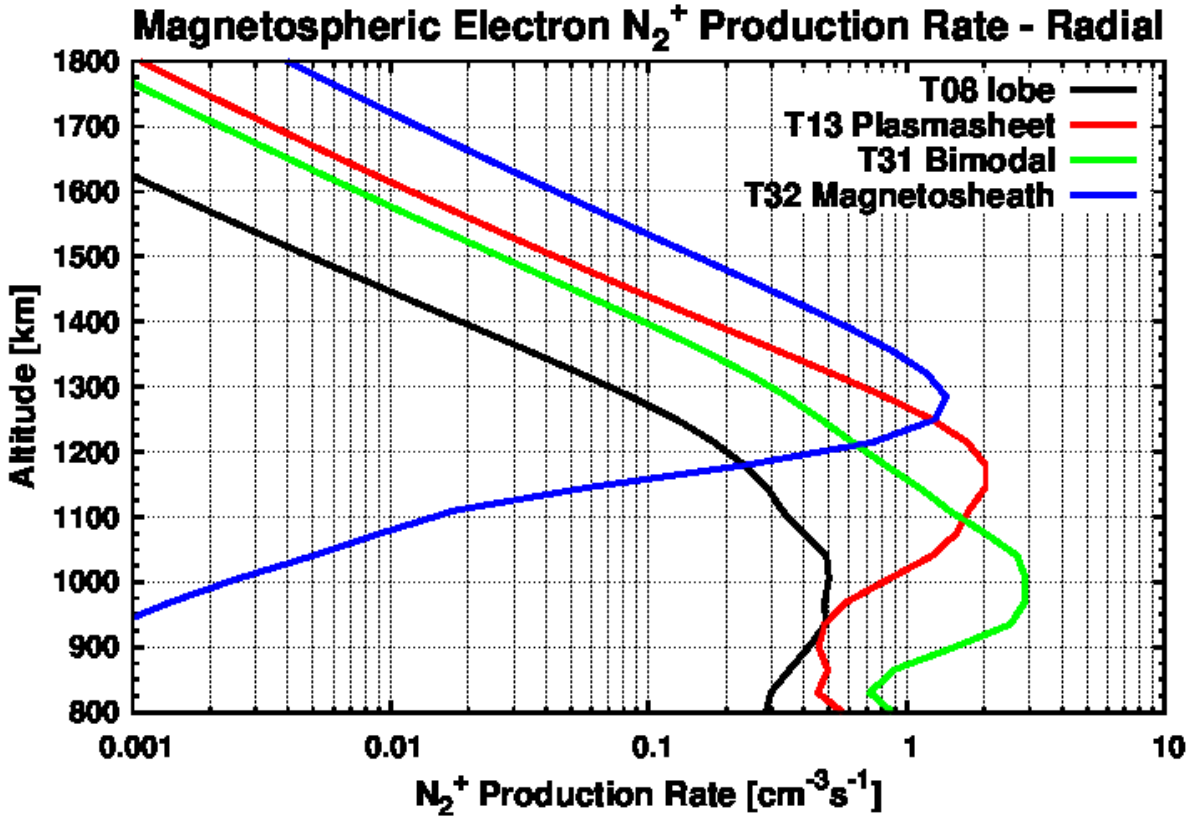

Appendix Figure D.19 Production of N_2^+ using a radial magnetic field line anchored at 725km and the magnetospheric electron fluxes of the *Rymer et al.* [2009] classifications. Results are shown for model runs using the T8 lobe-like (black line), the T13 plasma sheet (red line), T31 bimodal (green line) and the T32 magnetosheath (blue line) electron fluxes measured by CAPS/ELS. The magnetospheric electron flux profiles are shown in Figure 7.2.

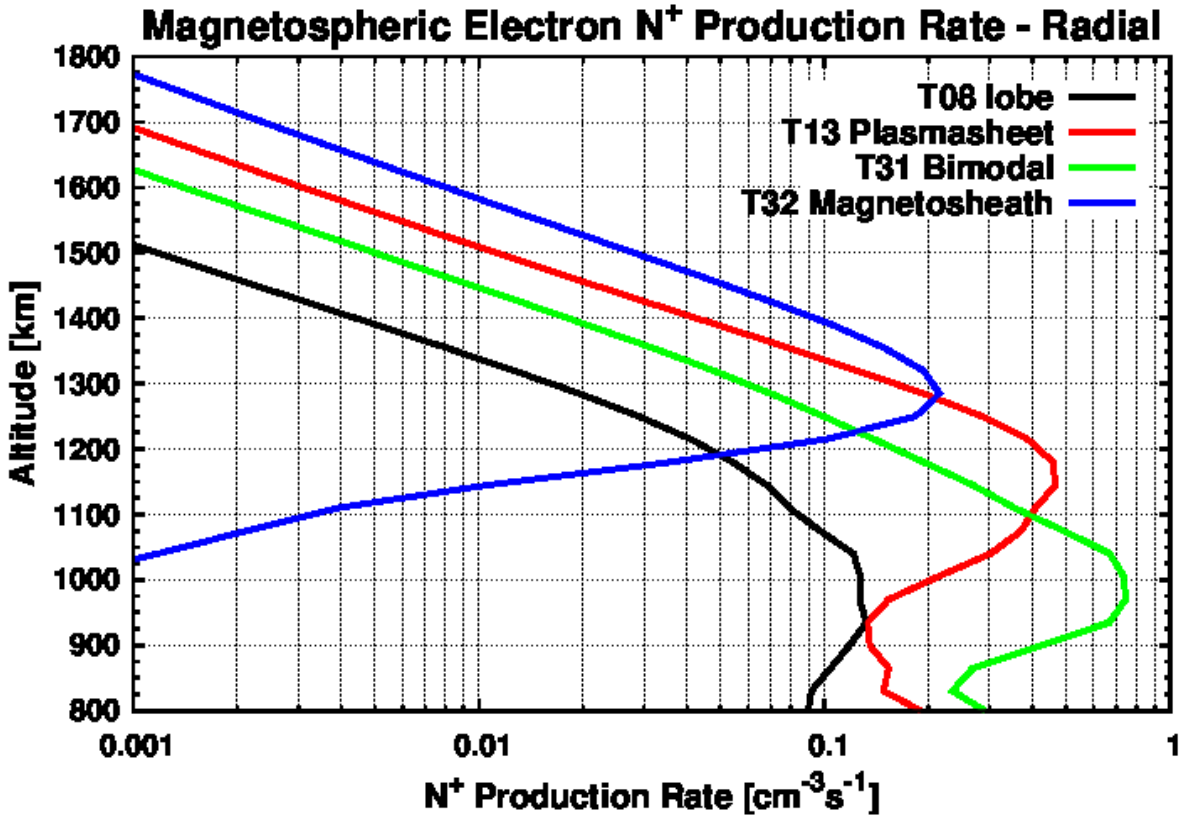

Appendix Figure D.20 Production of N^+ using a radial magnetic field line anchored at 725km and the magnetospheric electron fluxes of the *Rymer et al.* [2009] classifications. Results are shown for model runs using the T8 lobe-like (black line), the T13 plasma sheet (red line), T31 bimodal (green line) and the T32 magnetosheath (blue line) electron fluxes measured by CAPS/ELS. The magnetospheric electron flux profiles are shown in Figure 7.2.

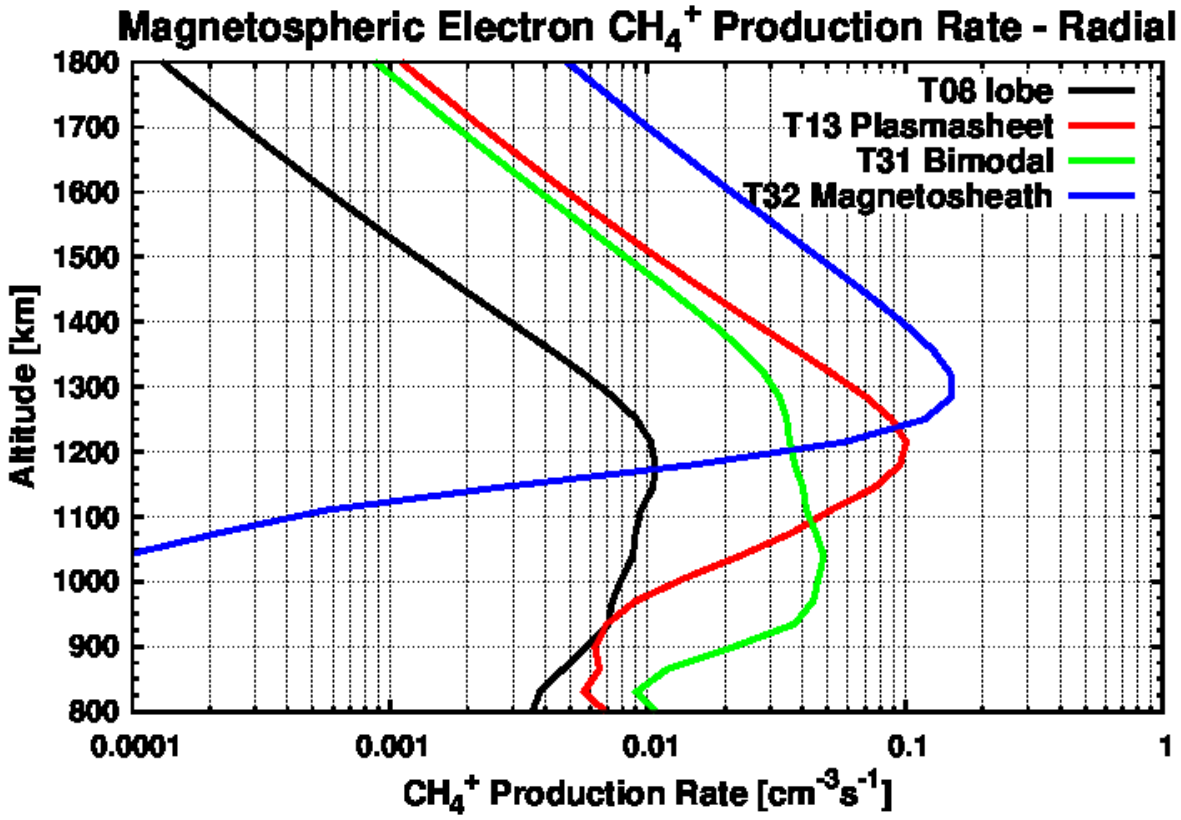

Appendix Figure D.21 Production of CH_4^+ using a radial magnetic field line anchored at 725km and the magnetospheric electron fluxes of the *Rymer et al.* [2009] classifications. Results are shown for model runs using the T8 lobe-like (black line), the T13 plasma sheet (red line), T31 bimodal (green line) and the T32 magnetosheath (blue line) electron fluxes measured by CAPS/ELS. The magnetospheric electron flux profiles are shown in Figure 7.2.

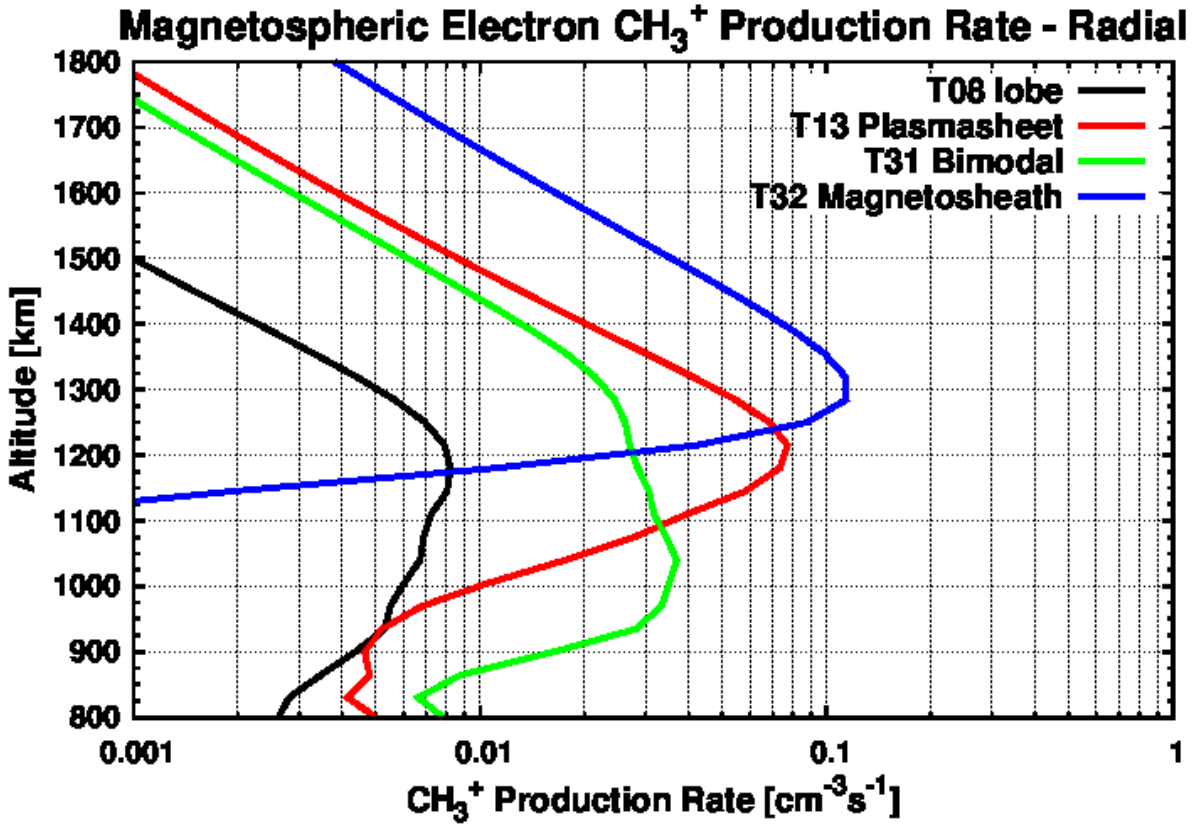

Appendix Figure D.22 Production of CH_3^+ using a radial magnetic field line anchored at 725km and the magnetospheric electron fluxes of the *Rymer et al.* [2009] classifications. Results are shown for model runs using the T8 lobe-like (black line), the T13 plasma sheet (red line), T31 bimodal (green line) and the T32 magnetosheath (blue line) electron fluxes measured by CAPS/ELS. The magnetospheric electron flux profiles are shown in Figure 7.2.

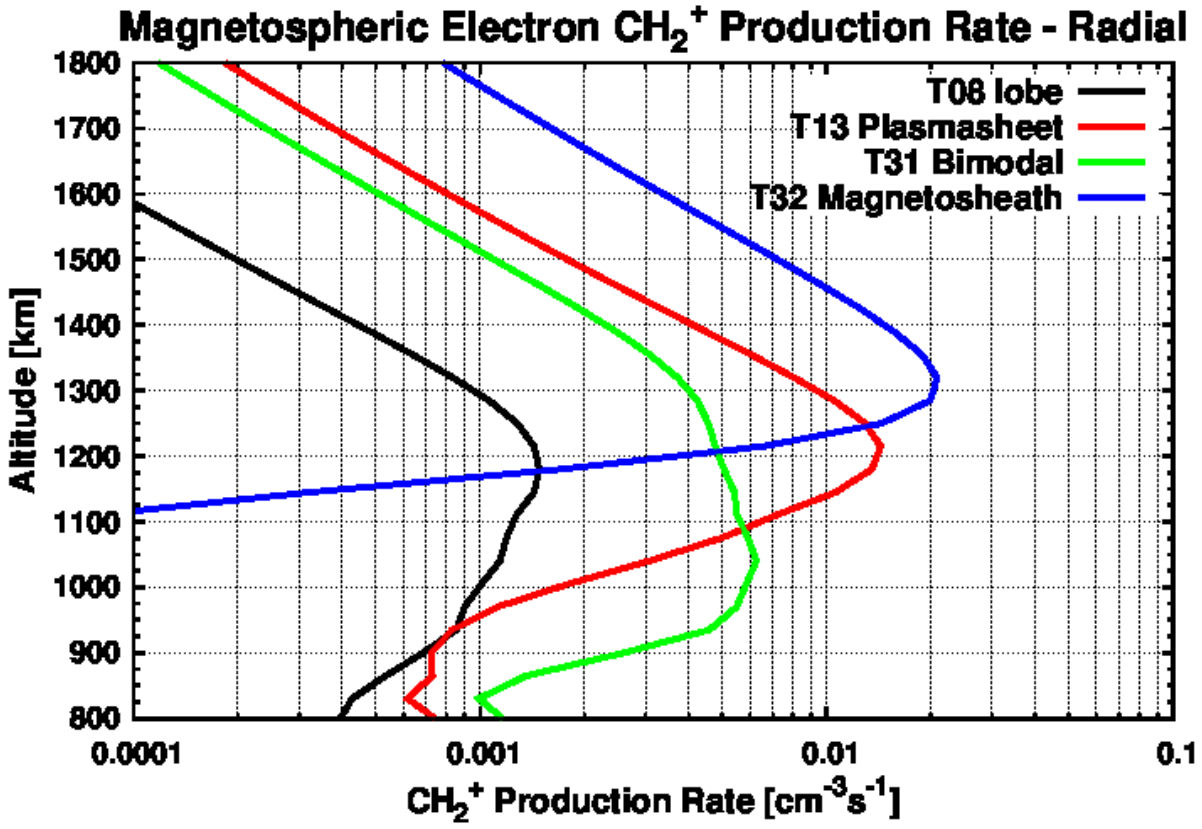

Appendix Figure D.23 Production of CH_2^+ using a radial magnetic field line anchored at 725km and the magnetospheric electron fluxes of the *Rymer et al.* [2009] classifications. Results are shown for model runs using the T8 lobe-like (black line), the T13 plasma sheet (red line), T31 bimodal (green line) and the T32 magnetosheath (blue line) electron fluxes measured by CAPS/ELS. The magnetospheric electron flux profiles are shown in Figure 7.2.

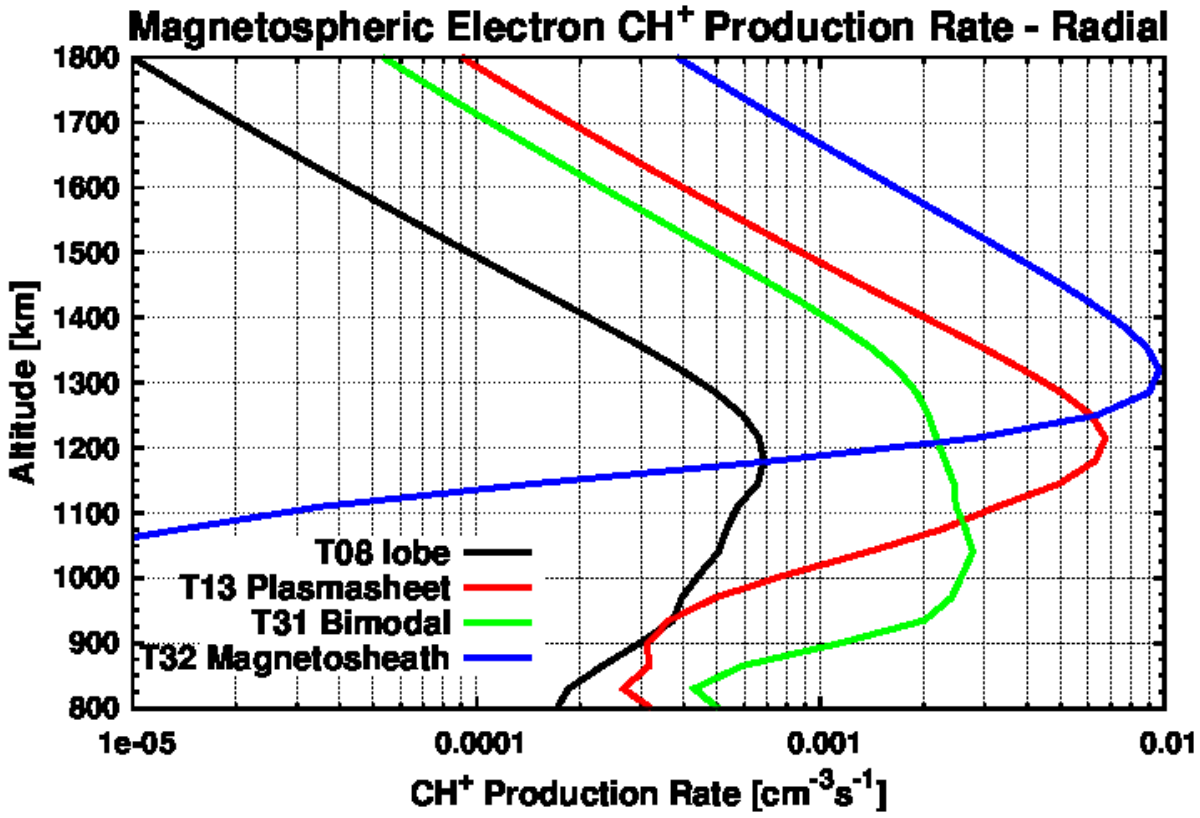

Appendix Figure D.24 Production of CH^+ using a radial magnetic field line anchored at 725km and the magnetospheric electron fluxes of the *Rymer et al.* [2009] classifications. Results are shown for model runs using the T8 lobe-like (black line), the T13 plasma sheet (red line), T31 bimodal (green line) and the T32 magnetosheath (blue line) electron fluxes measured by CAPS/ELS. The magnetospheric electron flux profiles are shown in Figure 7.2.

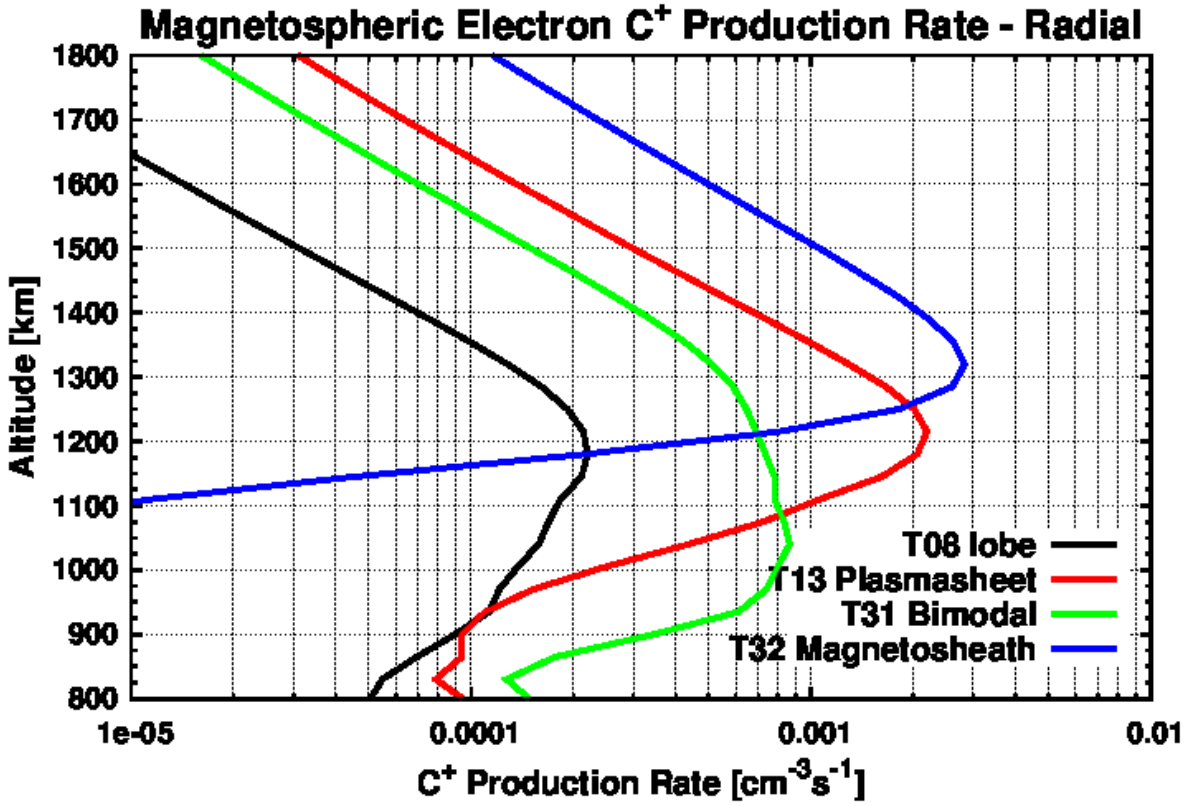

Appendix Figure D.25 Production of C^+ using a radial magnetic field line anchored at 725km and the magnetospheric electron fluxes of the *Rymer et al.* [2009] classifications. Results are shown for model runs using the T8 lobe-like (black line), the T13 plasma sheet (red line), T31 bimodal (green line) and the T32 magnetosheath (blue line) electron fluxes measured by CAPS/ELS. The magnetospheric electron flux profiles are shown in Figure 7.2.

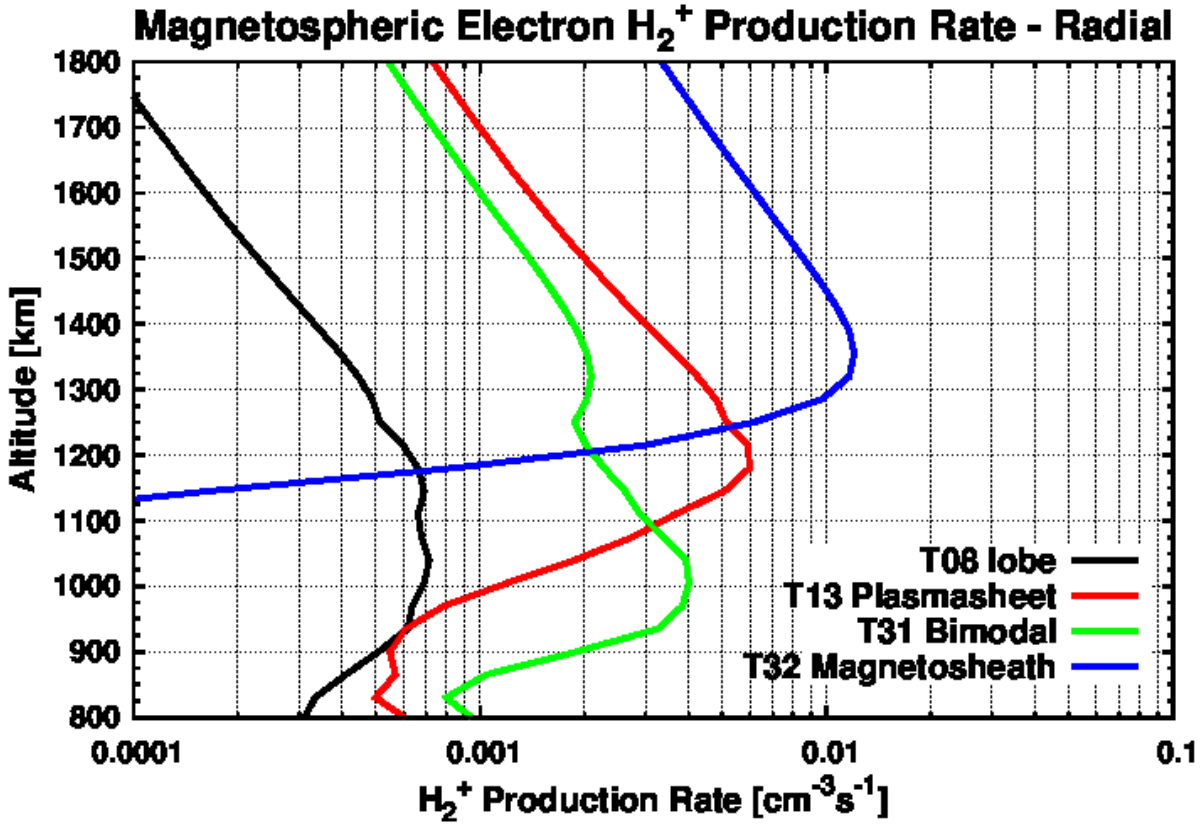

Appendix Figure D.26 Production of H_2^+ using a radial magnetic field line anchored at 725km and the magnetospheric electron fluxes of the *Rymer et al.* [2009] classifications. Results are shown for model runs using the T8 lobe-like (black line), the T13 plasma sheet (red line), T31 bimodal (green line) and the T32 magnetosheath (blue line) electron fluxes measured by CAPS/ELS. The magnetospheric electron flux profiles are shown in Figure 7.2.

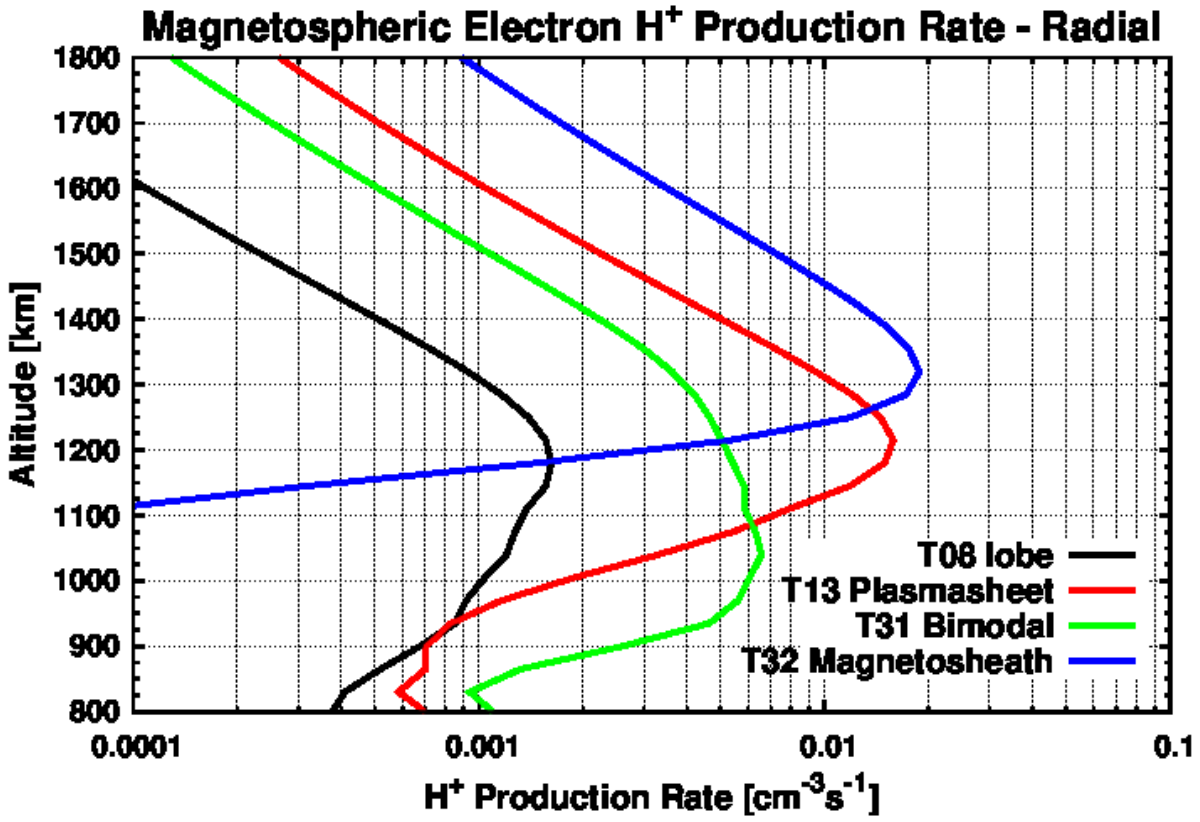

Appendix Figure D.27 Production of H^+ using a radial magnetic field line anchored at 725km and the magnetospheric electron fluxes of the *Rymer et al.* [2009] classifications. Results are shown for model runs using the T8 lobe-like (black line), the T13 plasma sheet (red line), T31 bimodal (green line) and the T32 magnetosheath (blue line) electron fluxes measured by CAPS/ELS. The magnetospheric electron flux profiles are shown in Figure 7.2.

Appendix E Thermal Electron Heating Rates on the Nightside of Titan

In this section, plots of the thermal electron heating rates using the full magnetospheric electron flux measured by CAPS ELS in the magnetosphere of Saturn are shown for the magnetospheric classifications outlined by *Rymer et al.* [2009] (except lobe-like which appears in the text). Cases are shown using a radial magnetic field line anchored at 725 km, a parabolic magnetic field line anchored at 725 km and nested magnetic field lines.

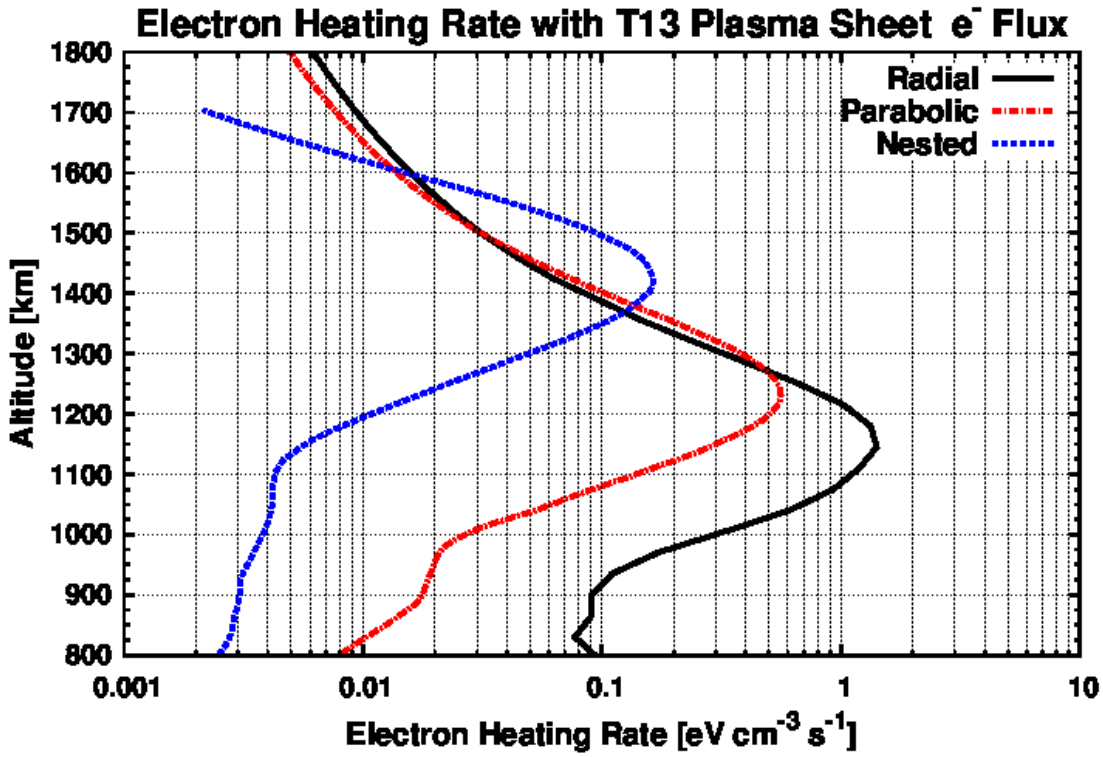

Appendix Figure E.1 Thermal electron heating rate generated using the two-stream model using the magnetospheric flux of electrons measured by CAPS ELS [*Rymer et al.*] during the T13 plasma sheet flyby of Titan. Results are shown using a radial magnetic field line anchored at 725 km (black solid line), a parabolic field line anchored at 725 km (red dashed line) and nested magnetic field line topologies (blue dotted line).

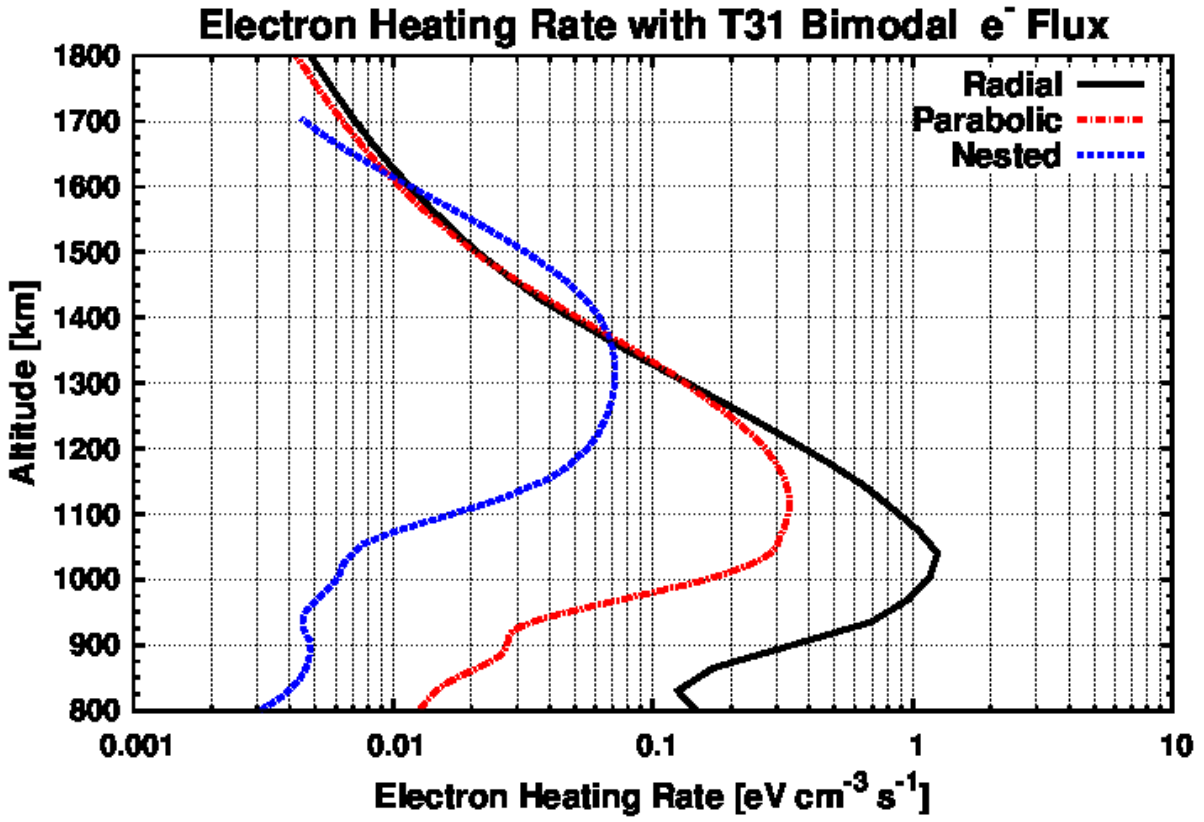

Appendix Figure E.2 Thermal electron heating rate generated using the two-stream model using the magnetospheric flux of electrons measured by CAPS ELS [*Rymer et al.*] during the T31 bimodal flyby of Titan. Results are shown using a radial magnetic field line anchored at 725 km (black solid line), a parabolic field line anchored at 725 km (red dashed line) and nested magnetic field line topologies (blue dotted line).

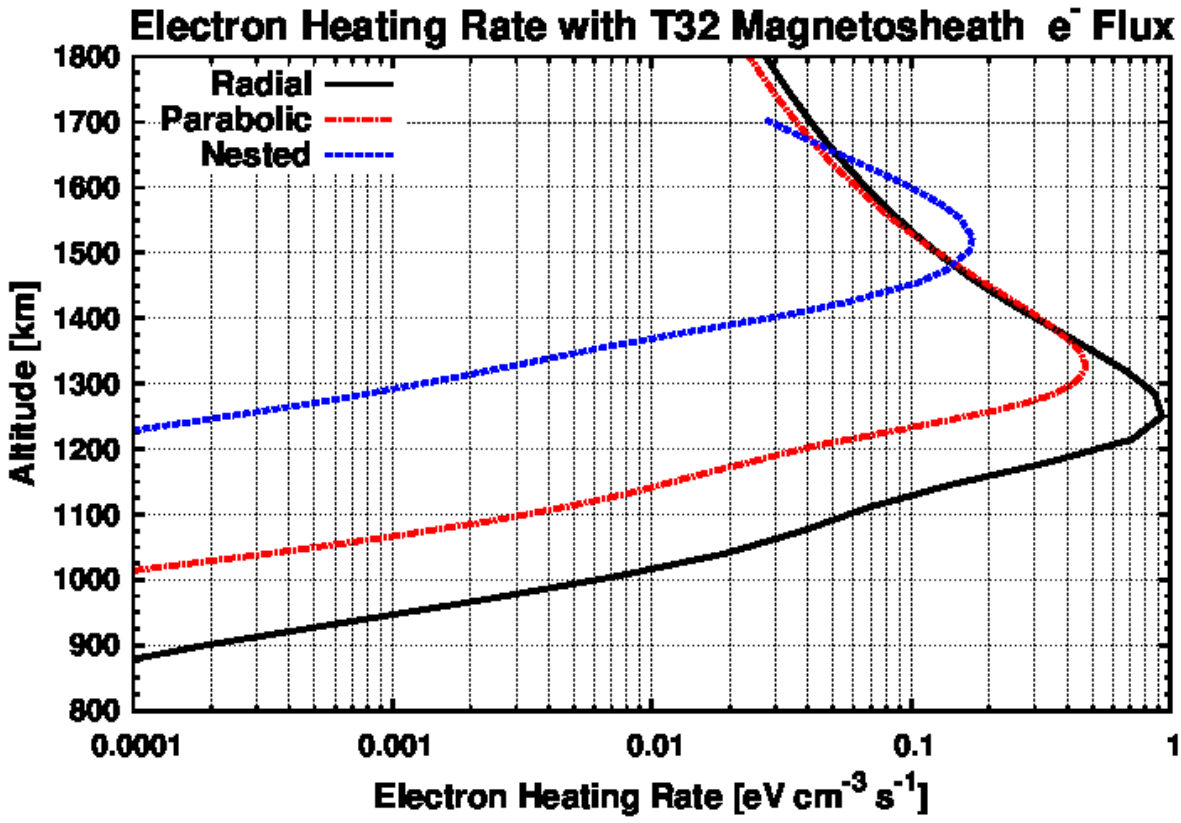

Appendix Figure E.3 Thermal electron heating rate generated using the two-stream model using the magnetospheric flux of electrons measured by CAPS ELS [*Rymer et al.*] during the T32 magnetosheath flyby of Titan. Results are shown using a radial magnetic field line anchored at 725 km (black solid line), a parabolic field line anchored at 725 km (red dashed line) and nested magnetic field line topologies (blue dotted line).